

 Open access • Report • DOI:10.2172/6174404

Laboratory setup and results of experiments on two-dimensional multiphase flow in porous media — [Source link](#)

J.F. McBride, D.N. Graham, H.O. Schiegg, Zurich (Switzerland)

Published on: 01 Oct 1990

Topics: Multiphase flow and Porous medium

Related papers:

- [Measurement and simulation of one-dimensional transient three phase flow for monotonic liquid drainage](#)
- [A model for hysteretic constitutive relations governing multiphase flow: 1. Saturation-pressure relations](#)
- [A closed-form equation for predicting the hydraulic conductivity of unsaturated soils](#)
- [Experimental validation of the theory of extending two-phase saturation-pressure relations to three-fluid phase systems for monotonic drainage paths](#)
- [Measurement and prediction of saturation-pressure relationships in three-phase porous media systems](#)

Share this paper:    

View more about this paper here: <https://typeset.io/papers/laboratory-setup-and-results-of-experiments-on-two-3bwhw1e3vv>

PNL--7453

DE91 006611

Laboratory Setup and Results of Experiments on Two-Dimensional Multiphase Flow in Porous Media

H. O. Schiegg
Editors of English Translation
J. F. McBride
D. N. Graham

October 1990

Prepared for the U.S. Department of Energy
under Contract DE-AC06-76RLO 1830

Pacific Northwest Laboratory
Operated for the U.S. Department of Energy
by Battelle Memorial Institute



PNL-7453

MASTER

DISCLAIMER

This report was prepared as an account of work sponsored by an agency of the United States Government. Neither the United States Government nor any agency thereof, nor Battelle Memorial Institute, nor any of their employees, makes any warranty, expressed or implied, or assumes any legal liability or responsibility for the accuracy, completeness, or usefulness of any information, apparatus, product, or process disclosed, or represents that its use would not infringe privately owned rights. Reference herein to any specific commercial product, process, or service by trade name, trademark, manufacturer, or otherwise, does not necessarily constitute or imply its endorsement, recommendation, or favoring by the United States Government or any agency thereof, or Battelle Memorial Institute. The views and opinions of authors expressed herein do not necessarily state or reflect those of the United States Government or any agency thereof.

PACIFIC NORTHWEST LABORATORY
operated by
BATTELLE MEMORIAL INSTITUTE
for the
UNITED STATES DEPARTMENT OF ENERGY
under Contract DE-AC06-76RLO 1830

Printed in the United States of America

Available to DOE and DOE contractors from the
Office of Scientific and Technical Information, P.O. Box 62, Oak Ridge, TN 37831;
prices available from (615) 576-8401. FTS 626-8401.

Available to the public from the National Technical Information Service,
U.S. Department of Commerce, 5285 Port Royal Rd., Springfield, VA 22161.

NTIS Price Codes, Microfiche A01

Printed Copy

Price Code	Page Range	Price Code	Page Range
A02	1- 10	A15	326-350
A03	11- 50	A16	351-375
A04	51- 75	A17	376-400
A05	76-100	A18	401-425
A06	101-125	A19	426-450
A07	126-150	A20	451-475
A08	151-175	A21	476-500
A09	176-200	A22	501-525
A10	201-225	A23	526-550
A11	226-250	A24	551-575
A12	251-275	A25	576-600
A13	276-300	A99	601-Up
A14	301-325		

LABORATORY SETUP AND RESULTS OF
EXPERIMENTS ON TWO-DIMENSIONAL
MULTIPHASE FLOW IN POROUS MEDIA

H. O. Schiegg^(a)

Editors of English Translation
J. F. McBride
D. N. Graham^(a)

October 1990

Prepared for
the U.S. Department of Energy
under Contract DE-AC06-76RLC 1830

Pacific Northwest Laboratory
Richland, Washington 99352

(a) Simultec Ltd.
Zürich, Switzerland.

SUMMARY

In the event of an accidental release into the earth's subsurface of an immiscible organic liquid, such as a petroleum hydrocarbon or chlorinated organic solvent, the spatial and temporal distribution of the organic liquid is of great interest when considering efforts to prevent groundwater contamination or restore contaminated groundwater. An accurate prediction of immiscible organic liquid migration requires the incorporation of relevant physical principles in models of multiphase flow in porous media; these physical principles must be determined from physical experiments. This report presents a series of such experiments performed during the 1970s at the Swiss Federal Institute of Technology (ETH) in Zürich, Switzerland. The experiments were designed to study the transient, two-dimensional displacement of three immiscible fluids in a porous medium. This experimental study appears to be the most detailed published to date. The data obtained from these experiments are suitable for the validation and test calibration of multiphase flow codes.

The flume in which the experiments were performed was constructed with an inside length of 280 cm, an inside height of 60 cm, and an inside width of 15 cm. The front and back walls of the flume each consisted of single glass plates that prevented preferential wetting of the walls by the oil, as would have occurred, for example, with acrylic plates. The flume was designed to allow the water table height and slope to be adjusted during the course of the experiments. A uniform sand with a mean grain diameter of 0.33 mm was carefully applied in 0.15-mm layers with a funnel mounted on an automated cart. The 15-cm width was theoretically calculated to minimize the error in cross-sectional porosity caused by the larger pores next to the walls. In addition, to remove the larger pores next to the walls, a finer sand was simultaneously applied along the glass walls. The variation in porosity with height was less than 0.003. Hydrophilic and hydrophobic pressure probes were installed and connected to pressure transducers. The response time of the pressure probe system was less than 0.10 sec, and the resolution was less than 0.2-mm H_2O piezometric head. A dual-energy gamma attenuation system was used to measure fluid saturations across the width of the flume. A 1.0-Ci cesium source

(0.662 MeV) and a 2,000-Ci thulium source (0.084 MeV) were used with a 10-sec counting time to obtain a standard deviation of the fluid saturation lower than 2%.

An immiscible organic liquid less dense than water (oil) was used in the two-dimensional experiments and in one-dimensional experiments. From the one-dimensional experiments, the static two- and three-phase capillary pressure head-saturation relationships were obtained. The two-dimensional experiments were performed with various initial and boundary conditions to simulate different oil release scenarios. The results are presented as nearly instantaneous fluid saturation and liquid potential distributions after selected time intervals.

ACKNOWLEDGMENTS

This report was funded by the U.S. Department of Energy's Office of Health and Environmental Research through its national Subsurface Science Program and its Environmental Science Research Center (ESRC) at Pacific Northwest Laboratory. We thank F. J. Wobber of the Subsurface Science Program and R. E. Wildung of the ESRC for their support of this report. We also thank Professor D. Vischer for permission to publish this English translation of reports issued through the Laboratory of Hydraulics, Hydrology, and Glaciology at the Swiss Federal Institute of Technology in Zürich, Switzerland. Finally, we want to recognize the efforts of L. Snyder in translating the German-language reports, J. M. Gephart in editing this report, and the Sigma V text processing team.

CONTENTS

SUMMARY.	iii
ACKNOWLEDGMENTS.	v
1.0 INTRODUCTION.	1.1
2.0 FUNDAMENTALS	2.1
2.1 HYDRODYNAMIC DISPLACEMENT	2.1
2.2 HYDRODYNAMIC DISPERSION	2.3
2.3 EQUATION SYSTEM FOR THE DESCRIPTION OF GROUNDWATER CONTAMINATION BY OIL DERIVATIVES	2.5
2.4 SATURATION DIAGRAM	2.9
2.5 NUMERICAL INTEGRATION	2.12
2.6 PARAMETERS TO BE MEASURED	2.13
3.0 POROUS MEDIUM	3.1
3.1 CHARACTERISTICS OF THE POROUS MEDIUM	3.1
3.2 THICKNESS OF THE POROUS MEDIUM	3.4
3.3 POROUS MEDIUM CONTAINERS	3.5
3.3.1 Plexicolumn for the One-Dimensional Static Experiments	3.5
3.3.2 Flume for the Two-Dimensional Dynamic Experiments	3.7
3.4 APPARATUS FOR PACKING A HOMOGENOUS ISOTROPIC POROUS MEDIUM	3.22
4.0 PRESSURE GAGE APPARATUS	4.1
4.1 REQUIREMENTS	4.1
4.2 CONSTRUCTION OF THE PRESSURE GAGE SYSTEM	4.2
4.2.1 Probes	4.2
4.2.2 Pressure Transducer	4.13

4.2.3	Switching Apparatus	4.21
4.2.4	Tubing System	4.24
4.2.5	Response Time of the Pressure Gage System	4.38
4.2.6	Minimum Measuring Time	4.43
5.0	SATURATION MEASUREMENT APPARATUS	5.1
5.1	MEASUREMENT APPARATUS	5.1
5.2	SOURCE SHIELDS	5.2
5.3	COLLIMATION	5.9
5.4	DETECTOR	5.11
5.5	IMPULSE HEIGHT ANALYZER	5.17
5.6	SOURCE-DETECTOR SCANNING SYSTEM	5.17
6.0	DEVELOPMENT OF A METHOD FOR DETERMINING SATURATIONS DURING EXPERIMENTS ON THE DISPLACEMENT OF WATER, OIL, AND AIR IN POROUS MEDIA	6.1
6.1	THE DEFINITION OF SATURATION	6.1
6.2	REQUIREMENTS OF THE SATURATION MEASUREMENT METHOD	6.1
6.3	PROPOSAL OF SOLUTIONS TO MEET STATED REQUIREMENTS	6.2
6.3.1	Alternative Methods	6.2
6.3.2	Attenuation of Gamma Radiation	6.2
6.3.3	Use of Radioactive Tracers	6.10
6.3.4	Conclusion	6.14
6.4	CONSEQUENCES FROM THE REQUIREMENT OF THE VALIDITY OF THE INEQUALITY STATED IN EQUATION (6.16)	6.14
6.4.1	Mass Attenuation Coefficient	6.14
6.4.2	The Relationship Between the Mass Attenuation Coefficients of Water and Oil as a Function of Energy	6.24
6.4.3	Possibilities Relating to the Selection of Radiation Sources	6.26

6.4.4	Conclusions	6.44
6.5	CONSIDERATION OF THE STANDARD ERROR OF THE SATURATION MEASUREMENT	6.45
6.5.1	Determination of the Separate Differential Quotients	6.46
6.5.2	Estimate of the Values and Standard Errors of the Separate Variables	6.49
6.6	RAISING THE MASS ATTENUATION COEFFICIENT OF THE PETROLEUM DERIVATIVE WITH AN ELEMENT WITH A HIGHER ATOMIC NUMBER	6.63
6.7	SELECTION OF Tm-170 AS A SECOND RADIATION SOURCE AND MERCURY AS AN ELEMENT WITH HIGHER ATOMIC NUMBER FOR DOPING THE PETROLEUM DERIVATIVE	6.76
6.8	PRODUCTION OF Cs-137 AND Tm-170	6.79
6.9	Tm-170 SPECTRA	6.84
6.10	MEASURES FOR THE ELIMINATION OF THE DECELERATION SPECTRUM	6.87
6.10.1	Elimination of the Characteristic Radiation	6.89
6.10.2	Mathematical Function to Describe the Deceleration Radiation Spectrum	6.89
6.10.3	Consequences of Unreliable Impulse Count Rate Determinations on Steep Portions of the Deceleration Spectrum	6.98
6.10.4	Final Observations on the Radiation Attenuation Method Used to Measure Fluid Saturations	6.99
6.11	SEMIGRAPHIC DETERMINATION OF THE FLUID SATURATIONS	6.100
7.0	CAPILLARY PRESSURE HEAD CURVES MEASURED IN A ONE-DIMENSIONAL COLUMN.	7.1
7.1	CAPILLARY PRESSURE HEAD CURVES	7.1
7.2	SERIES A AND B SATURATION DIAGRAMS	7.4
7.3	COMMENTS ON EXPERIMENTAL SERIES A	7.39
7.4	COMMENTS ON EXPERIMENTAL SERIES B	7.59
7.5	COMPARISON OF THE CAPILLARY PRESSURE HEAD CURVES	7.62
7.6	ACCURACY OF THE SATURATION MEASUREMENT	7.66

7.7	MAXIMUM RESIDUAL SATURATIONS	7.66
8.0	TWO-DIMENSIONAL PROPAGATION EXPERIMENTS	8.1
8.1	PARAMETERS TO BE MEASURED	8.1
8.2	CAPILLARY PRESSURE HEAD CURVES AND POROUS MEDIUM	8.2
8.3	MEASUREMENT METHODS	8.5
8.4	OIL APPLICATION AND BOUNDARY CONDITIONS	8.8
8.5	LEGEND FOR THE SATURATION AND POTENTIAL TIMELINE FOR EXPERIMENTS A THROUGH E	8.10
8.5.1	Selected Characteristics for Experiments A Through E	8.11
8.6	EXPERIMENT A	8.12
8.7	EXPERIMENTS B, C, AND D	8.32
8.7.1	Experiment B	8.33
8.7.2	Experiment C	8.43
8.7.3	Experiment D	8.46
8.8	SATURATION AND POTENTIAL TIMELINE FOR EXPERIMENTS A THROUGH E	In Envelope
9.0	SUMMARY OF REMAINING TWO-DIMENSIONAL PROPAGATION EXPERIMENTS . .	9.1
9.1	COMPARISON OF THE DIFFERENT EXPERIMENTS	9.1
9.2	INITIAL AND BOUNDARY CONDITIONS	9.3
9.3	LEGEND FOR THE SATURATION AND POTENTIAL TIMELINE FOR EXPERIMENTS 1 THROUGH 3	9.8
9.3.1	Selected Characteristics for Experiments 1 through 3	9.10
9.4	PHOTOGRAPHS OF EXPERIMENT	9.10
9.5	SATURATION AND POTENTIAL TIMELINE FOR EXPERIMENTS 1 THROUGH 3	In Envelope
10.0	REFERENCES AND BIBLIOGRAPHY	10.1
	APPENDIX A - EXPLANATION OF SYMBOLS AND INDICES	A.1

APPENDIX B - THE HALLUX PHENOMENON AND ITS EXPLANATION	B.1
APPENDIX C - FIELD INFILTRATION AS A METHOD FOR THE DISPOSAL OF OIL-IN-WATER EMULSIONS FROM THE RESTORATION OF OIL-POLLUTED AQUIFERS	C.1
APPENDIX D - EXPERIMENTAL CONTRIBUTION TO THE DYNAMIC CAPILLARY FRINGE	D.1
APPENDIX E - LIQUID-AIR DISPLACEMENTS IN A HOMOGENEOUS, ISOTROPIC, UNLIMITED POROUS MEDIA	E.1

FIGURES

2.1	Static Saturation Distribution in the Water-Air Capillary Fringe of the Quartz Sand Used in the Majority of Experiments	2.3
2.2	Saturation Diagram	2.8
2.3	Experimentally Measured $k^r = k^r(S)$ from Wyckoff and Botset	2.9
2.4	Experiment Setup Developed to Study Oil Propagation in an Aquifer	2.15
2.5	Engineering Sketch of Experiment Setup	2.16
3.1	Quartz Sand (a) Grain-Size Distribution Curve and (b) Shape of Grains	3.2
3.2	Effect of Wall on the Porosity of Packed Spheres	3.5
3.3	Schematic Diagram of the Plexicolumn and the Measurement Range	3.6
3.4	Photograph of the Plexicolumn	3.7
3.5	Photograph of the Experimental Flume	3.9
3.6	Flume Supports (a) at the Hinged Connection and (b) at the Threaded Jack Connection	3.10
3.7	Concrete Base and Dike Above Floor	3.11
3.8	Brace Plates of the Flume	3.12
3.9	Glass Plate Supports	3.13
3.10	Arrangement of the Ports for the Pressure Probes	3.14
3.11	Comparison of the Oil Front Position Between Glass Plates to That of Oil Fronts Between Acrylic Plates Subjected to Different Surface Treatments	3.19
3.12	Propagation Forms (a) Along Glass Wall, (b) Along Acrylic Wall Previously Treated with Fomblin	3.19
3.13	Stratified Filling in Flume	3.23
3.14	Sand Container and Slit	3.23
3.15	Sand Cart and Sand Container	3.24
3.16	Motor Drive of the Sand Cart	3.25

3.17	Device to Switch the Direction of the Sand Cart	3.26
3.18	Sand Container Lifting Device	3.27
3.19	Sand Filling Mechanism (a) Full View (b) Tube Coming from Upper Floor	3.28
3.20	Fine-Sand Applicator	3.29
3.21	Sidewall Sheet Metal Lifting Device	3.31
4.1	Sketch of the Pressure Gage System	4.3
4.2	Plate, Rod, and Probe of Sintered Quartz Glass	4.6
4.3	Photograph and Sketch of Probe and Probe Holder	4.6
4.4	Conductance (a) and Flow Rate (b) of the Probes as a Function of the Pressure Difference	4.7
4.5	Experiment Setup to Illustrate Principle of Selective Pressure Measurement	4.9
4.6	Gluing of Probe and Steel Tubes	4.11
4.7	Porous Medium (a) Before Insertion, (b) During Insertion and (c) After Removal of Probe	4.12
4.8	Diagram of the Developed Pressure Transducer	4.16
4.9	Schematic Diagram of a CEC-4-327 for Low-Pressure Range	4.20
4.10	Prototype 1	4.23
4.11	Prototype 2	4.24
4.12	Prototype 3	4.25
4.13	Prototype 4	4.26
4.14	Prototype 5	4.27
4.15	Prototype 6	4.28
4.16	Prototype 7	4.29
4.17	Prototype 8	4.30
4.18	Three-Dimensional Drawing of Prototype 8	4.31
4.19	Sketch and Photograph of a Stopcock Manifold Composed of Prototype 8 Stopcocks	4.32

4.20	Sketch of the Apparatus for the Determination of the Fluid Loss Resulting from Diffusion Through the Tubing Walls	4.33
4.21	Net Subsidence, a , as a Function of Time Resulting from Diffusion Through the Walls of Different Lengths of Plastic Tubing	4.34
4.22	Time Function of Diffusion Through the Wall of 1-m-Long Tubes of Plastic, Rubber, and Vibon	4.34
4.23	Apparatus for the Determination of the Volume Change of Vibon Hose Resulting from a Pressure Change	4.35
4.24	Oil Drop Displacement as a Function of the Pressure Change in Vibon Hose	4.35
4.25	Experiment Setup for the Determination of the Volume Change in Vibon Hose as a Function of the Temperature Change	4.36
4.26	Meniscus Displacement Resulting from Volume Change in an 80-cm Vibon Hose Caused by Rapid Temperature Changes, ΔT	4.37
4.27	End Value of the Meniscus Displacement Resulting from the Volume Change in an 80-cm Vibon Tube as a Function of Rapid Temperature Changes	4.38
4.28	Schematic Illustration of Pressure Gage System	4.39
4.29	Diagram of the Experimental Progression of Pressure Detected by the Pressure Transducer After Switching to a Lower Pressure	4.40
5.1	Schematic Diagram of the Source-Detector Pair	5.1
5.2	Photograph of Measurement Apparatus	5.2
5.3	Components of the Thulium Source Shield	5.7
5.4	Schematic Diagram of the Thulium Source Shield	5.8
5.5	Schematic Diagram of the Cesium Source Shield	5.10
5.6	Influence of Different Collimator Configurations on the A/B Ratio	5.12
5.7	Impulse Count Rate Versus Energy Showing the Integral A and B	5.13
5.8	A/B Ratio Versus Collimation Length for Different Configurations	5.14

5.9	The Selected Collimator Setup for the Cs-137 and Tm-170 Source-Detector Pairs	5.14
5.10	Schematic Diagram of the Detector Components	5.15
5.11	Plot of Impulse Count Rate Versus High Voltage Used to Select a Favorable High Voltage for the Scintillation Counters	5.18
5.12	Vernier Scale Used to Determine the Position of Each Source-Detector Pair	5.19
5.13	Bridge Connecting a Source Table and a Detector Table	5.20
5.14	Stress Diagram on One of the Beams Carrying the Source-Detector Carts	5.23
5.15	Graphic Integration to Calculate the Area Moment	5.25
5.16	Schematic Diagram of Rail-Beam Assembly	5.31
6.1	Realistic Representation of the Sand Porous Medium Filled with Water, Oil, and Air	6.5
6.2	Schematic Representation of Incremental Path Lengths of the Various Components Traversed by the Radiation Beam	6.5
6.3	Schematic Representation of the Summation of Path Lengths of the Various Components Traversed by the Radiation Beam	6.7
6.4	Generation of Infinitesimal Impulse Count Rate Reaching the Detector by the Tracer Method	6.12
6.5	Schematic Representation of the Types of Attenuation	6.15
6.6	Values for the Separate Mass Attenuation Coefficients and Their Summation as a Function of Energy for (a) Water and (b) Lead	6.17
6.7	Isolines Representing the Atomic Numbers at Which the Proportion of τ and σ and of σ and κ are Equal	6.19
6.8	Mass Attenuation Coefficients as a Function of Energy for Lead, Water, Air, Quartz Sand, and a Representative Petroleum Derivative, as Well as Additional Elements or Compounds	6.23
6.9	Plot of the Ratio of the Mass Attenuation Coefficient of Water to That of Oil as a Function of Energy	6.25
6.10	Schematic Explaining Geometric Attenuation and Self Adsorption	6.30

6.11	Expected Values of the Maximum Material Attenuation to be Observed During the Two-Dimensional Experiments	6.34
6.12	X-Ray Spectrum of a Molybdenum Anode at 35-kV Tube Voltage	6.44
6.13	Binomial Distribution of the Exiting Impulse Count Rate, J Assuming a Constant Entering Impulse Count Rate, J_k	6.53
6.14	Marginal Distribution of the Exiting Impulse Count Rates for an Entering Impulse Count Rate That Satisfies a Poisson Distribution	6.54
6.15	Fluid Densities as a Function of Temperature	6.56
6.16	Determination of the Irradiation or Flume Width B	6.58
6.17	$m_{S_0}(E_{II}, S_0)$	6.66
6.18	Standard Error of 4% Oil Saturation, S_{KWB} , as a Function of the Energy of the Second Radiation Source, E_{II} , with Lead Weight Fractions, g_{pb} , of 1%, 5%, or 10% in the Oil	6.74
6.19	Schematic Diagram of the Equipment Used to Experimentally Verify Theoretical Standard Error Estimates Shown in Figure 6 18	6.75
6.20	Schematic Diagram of the Tm-170 Source Vial	6.83
6.21	Unattenuated Tm-170 Energy Spectrum Determined by Using a Silicon Semiconductor Detector	6.84
6.22	Unattenuated Tm-170 Energy Spectrum Emitted by the 2000-Ci Source Manufactured at Mol, as Determined by NaI(Tl) Scintillation Counting	6.85
6.23	Tm-170 Spectra Obtained for Various Levels of Attenuation with the 1-Ci Test Source	6.86
6.24	Unshielded 2000-Ci Tm-170 Spectra	6.88
6.25	Use of Conic Section as Mathematical Function to Describe Deceleration Spectrum	6.90
6.26	Use of Exponential Function as Mathematical Function to Describe Deceleration Spectrum Associated with Maximum and Minimum Attenuation	6.92
6.27	Plot of Deceleration Spectrum Showing the Tangent, m, Intersecting at the Third Point, D	6.93
6.28	Use of Descartes Function as Mathematical Function to Describe Deceleration Spectrum	6.94

6.29	Flattening of the Deceleration Spectrum Obtained by Using a Zinc Plate and a Combination of Thallium, Lead, and Bismuth Plates	6.99
6.30	Flattening of the Deceleration Spectrum Shown to be Independent of Attenuation Levels	6.100
6.31	Auxiliary Diagram for Plotting the Nomograph Used to Determine Fluid Saturations	6.101
6.32	Nomograph for the Semigraphic Determination of Fluid Saturations	6.102
7.1	Theoretical Capillary Pressure Head Curves for Oil as Well as for the Contaminated Water Based on the Experimentally Determined Virgin Water Curves and the Scaling Parameter, Ω	7.2
7.2	Measured and Calculated Saturation Diagram, WOIM	7.41
7.3	Measured and Calculated Saturation Diagram, WODR	7.42
7.4	Distribution of the Residual Oil in the Water-Air Capillary Fringe	7.45
7.5	Measured and Calculated Saturation Diagram, OLIM	7.46
7.6	Measured and Calculated Saturation Diagram, OLDR	7.47
7.7	Measured and Calculated Saturation Diagram, $WLDR_{bef1}$	7.48
7.8	Measured and Calculated Saturation Diagram, $WLIM_{bef1}$	7.49
7.9	Measured Saturation Diagram for $WLIM_{jfr1}$	7.59
7.10	Measured Saturation Diagram for $WLDR_{jfr1}$	7.60
7.11	Photograph of WO Imbibition in Three Quartz Glass Capillaries	7.64
7.12	$S_w^C = f(\phi^R)$	7.65
8.1	Grain-Size Distribution Curve	8.3
8.2	Capillary Pressure Head Curves	8.4
8.3	Saturation Diagram for Experiments A Through E	8.10
8.4	Potential Histogram and Timeline for Experiments A Through E	8.11
8.5	Estimated Static Saturation Diagram 1 Day After the Beginning of Experiment A	8.16

8.6	Nomograph Displaying the Development of the Form and Position of the Flattest Oil-Air Meniscus up to the Second Saturation Diagram of Experiment A	8.18
8.7	Conversion from the Drainage to the Imbibition Capillary Pressure Head Curve	8.18
8.8	Conceptual Representation of a Three-Dimensional Oil Propagation Process	8.21
8.9	Nomograph Displaying the Complete Development of the Form and Position of the Flattest Oil Menisci Between 23 Hours and 12 Days Since the Start of Experiment A	8.28
8.10	Oil Propagation Forms for Experiments B, C, and D	8.34
8.11	Saturation Diagram Including the Hallux Phenomenon	8.37
8.12	Diagram of Water Displacement by Oil Infiltration	8.37
8.13	Nomograph Displaying the Development of the Form and Position of the Flattest Oil Menisci in the Oil Application Profile During Experiment B	8.40
8.14	Saturation Diagrams for the Oil Application Profile (a), 8, (b) 17, and (c) 19 Days into Experiment C	8.44
8.15	Photographs Taken During the First 7 Days of Experiment C	8.45
8.16	Saturation Diagram 1 Day After Lowering the Water Table in Experiment C	8.46
8.17	Photographs of Oil Propagation During Experiment D	8.47
8.18	Nomograph Showing the Development of the Form and Position of the Flattest Oil Menisci During the First 53 Days of Experiment D	8.50
8.19	Final Extent of Oil Propagation in Experiment E	8.51
8.20	Minimum Oil-Pool Thickness Estimated with the ACOLIM Curve and the ACWODR Curve	8.56
8.21	Oil-Pool Thickness in Experiment D	8.58
8.22	Minimum Oil-Pool Thickness Estimated with the ACWODR Curve and the ACWLDR _(befl) Curve	8.59
9.1	Saturation Diagram For Experiments 1 Through 8	9.8
9.2	Potential Histogram and Timeline for Experiments 1 Through 8	9.9
9.3	Photographs of Experiment 9	9.11

TABLES

1.1	Schiegg (1979 VAW No. 40) Contents	1.4
1.2	Schiegg (1980 VAW No. 43) Contents	1.5
3.1	Spreadsheet Calculations for the Arrangement of Supports . . .	3.15
4.1	Experimentally Determined Nonwetting Fluid Bubbling Pressures in the Probes Saturated with Wetting Fluids	4.10
4.2	Specific Diffusion Volumes for Plastic Tubing	4.30
5.1	Percentage Count Loss Resulting from Dead Time as a Function of Quantum Rate	5.15
5.2	Calculation of Maximum and Minimum $\int MM'dx$	5.29
6.1	Calculation of the Mass Attenuation Coefficients of Water, Quartz Sand, and Oil	6.20
6.2	Ratio of the Mass Attenuation Coefficient of Water to That of Oil as a Function of Energy	6.24
6.3	Isotope Evaluation for Second Radiation Source	6.28
6.4	Calculation of the Expected Standard Error of the Mass Attenuation Coefficients	6.61
6.5	Calculation of the Expected Standard Error of the Mass Attenuation Coefficients for SiO_2 or Quartz Sand or Glass	6.62
6.6	Standard Error at 4%, 20%, and 70% Oil Saturation, According to Equation (6.60), as a Function of the Energy of the Second Radiation Source, E_{II} , with Cs-137 as the First Radiation Source	6.64
6.7	Standard Error of a 4% Hydrocarbon-Lead Compound Saturation with 1%, 5%, or 10% Lead Concentration as a Function of the Energy of the Second Radiation Source, Given Cs-137 as the First Radiation Source	6.69
6.8	Experimental Determination of a 4% Oil Saturation with 4% Lead Content According to Equation (6.15)	6.76
8.1	Initial and Boundary Conditions, Experiments A-E	8.14
9.1	Initial and Boundary Conditions, Experiments 1-8	9.4

1.0 INTRODUCTION

The production of many of the goods and services that we are accustomed to depends on a wide variety of organic chemicals that are immiscible with water. When these chemicals are accidentally released to the environment, they often provide a long-term source of contamination. In the event of such a release, it is essential to understand the spatial and temporal distribution of the immiscible organic liquid. Such knowledge aids in assessing the potential hazard to groundwater and in selecting measures to prevent groundwater contamination or restore contaminated groundwater. Public and private support exists for developing methods to predict the extent of groundwater contamination resulting from releases of immiscible organic liquids and to aid in selecting cost efficient methods to restore polluted groundwater aquifers. To successfully develop these methods, it is assumed that the physical and chemical processes involved in the contamination of groundwater by immiscible organic liquids can be described quantitatively by applying fundamental physical and chemical principles. An important foundation for the treatment of multiphase flow is provided in the petroleum engineering literature. In petroleum production, multiphase flow occurs in response to gradients in a positive pressure field. Yet, the propagation of immiscible organic liquids in the subsurface after a spill is generally dominated by gradients in capillary pressure and elevation in the vadose zone. Thus, the soil physics literature on unsaturated water flow in porous media provides another important foundation.

The infiltration and migration of immiscible organic liquids in the subsurface are not easily described unless many simplifying assumptions are made. Recent attempts to more rigorously describe and predict the fate of immiscible organic liquids have produced increasingly more complex numerical models (e.g., Abriola 1984; Abriola and Pinder 1985a, 1985b; Allen 1985; Baehr and Corapcioglu 1984; Faust 1985; Faust and Rumbaugh 1986; Faust et al. 1989; Kuppusamy et al. 1987; Kaluarachchi and Parker 1989; Osborne and Sykes 1986; Parker et al. 1987). However, one major impediment to developing better predictive models is the lack of experimental data with which to verify numerical models and their assumptions (Streile and Simmons 1986; Abriola 1988). In an

effort to resolve this dilemma, several papers have recently appeared in the English-language literature detailing quantitative experiments of three-phase flow in porous media (e.g., Eckberg and Sunada 1984; Lenhard et al. 1988; Høst-Madsen 1988; Cary et al. 1989).

European countries have been traditionally active in multiphase flow research (e.g., Dracos 1966; Lippok 1966; Mull 1969; Schwille 1971a, 1971b, 1971c; Zilliox and Muntzer 1976; van Dam 1967). Much of the work, however, has not been published in English. During the 1970s, a series of two-dimensional, transient, three-phase flow experiments were performed at the Swiss Federal Institute of Technology (ETH), in Zürich. The results were published in two German-language reports (Schiegg 1979, 1980).

At the time this research was initiated, predominantly qualitative descriptions of petroleum hydrocarbon migration in the subsurface were found in the majority of the existing literature. A generally valid, quantitative, and simple description of petroleum hydrocarbon migration at atmospheric pressure and at which capillary pressure effects were not negligible was unknown for the following main reasons:

- Numerical methods must be used to solve the system of equations that describe the process.
- There is an abundance of possible initial and boundary conditions.
- The parameters are often poorly defined. Furthermore, the functional relationships among the parameters themselves and with other variables continues to be poorly understood.

van Dam (1967) has been one of the few researchers to produce quantitative determinations based on theoretical considerations.

Based on the mechanistic understanding gained in the research at ETH, a numerical model was developed in conjunction with the two-dimensional experiments described in this report. The numerical model was, however, highly unstable and prone to crashes unless coddled by the programmer; therefore, it was decided not to make the model publicly available. Nevertheless, a semi-analytical two-dimensional model was developed to estimate the propagation of petroleum hydrocarbons in the vadose zone and on the surface of the water table. The model and its simplifying assumptions are summarized in Schiegg

(1977b) and applied to field cases (BUNR 1986; Schiegg 1985). Numerical multiphase flow models are still considered expensive to use (Abriola 1988) and difficult to use (McKee and Bumb 1988) by individuals without the necessary mathematical or computer training. Thus, analytical or semianalytical models are still popular for practical applications (McKee and Bumb 1988). The data from these two-dimensional three-phase flow experiments can be used for the validation and initial calibration of other multiphase flow models.

Table 1.1 presents the contents of Schiegg (1979) and Table 1.2 presents the contents of Schiegg (1980). The darkened chapters have been omitted from this report. Those chapters deal with fundamental microscopic and macroscopic principles concerning immiscible fluids in porous media and some of the mechanistic concepts developed for practical applications such as 1) the saturation diagram used to describe the saturation distribution of the three fluids (water, hydrocarbon, and air) based on the locations of the water-air, water-oil, and oil-air levels, 2) the virgin and contaminated water-air menisci, 3) the hydrocarbon propagation plane, 4) the transition oil potential, 5) the minimum oil lens thickness, and 6) the hallow phenomenon. These chapters were omitted because the information is available in other English-language publications, such as Schiegg (1984), Schiegg (1988), and Schiegg and Schuille (1989). A detailed summary of the experiment setup can also be found in Schiegg and McBride (1987). At the time of publication, copies of Schiegg (1979) and (1980) were still available from ETH.

In the following eight chapters, the sense of the original German text has been maintained wherever possible. The text has not been modified to reflect more recent knowledge nor embellished with outside information. However, obvious printing errors have been corrected. To avoid introducing inaccuracies, all of the equations, figures, and tables have been reproduced directly from the original text. Text appearing in the figures and tables has been translated but no attempt was made to translate equation variables or their indices. Furthermore, numbers in the equations and tables use the European decimal system. Variables appearing directly in the body of the text are printed in a slightly different text font compared to the equations, but are still easily recognizable. Appendix A provides a more detailed explanation of the nomenclature and abbreviations. Within the text, numerous

TABLE I.1. Schiegg (1979 VAW No. 40) Contents

SYNOPSIS	9	4.3 PROPOSAL OF SOLUTIONS TO MEET STATED REQUIREMENTS	119
1.0 STATEMENT OF PROBLEM, LITERATURE REVIEW, AND STRUCTURE OF THE REPORT	13	4.4 CONSEQUENCES FROM THE REQUIREMENT OF THE VALIDITY OF THE INEQUALITY STATED IN EQUATION (15)	127
2.0 THEORETICAL FOUNDATION FOR THE MATHEMATICAL SIMULATIONS	14	4.5 CONSIDERATION OF THE STANDARD ERROR OF THE SATURATION MEASUREMENT	153
2.1 EQUATION DESCRIBING FLOW WITHIN A POROUS MEDIUM FROM A MICROSCOPIC PERSPECTIVE	15	4.6 RAISING THE MASS ATTENUATION COEFFICIENT OF THE PETROLEUM DERIVATIVE WITH AN ELEMENT WITH A HIGHER ATOMIC NUMBER	172
2.2 EQUATION DESCRIBING FLOW WITHIN A POROUS MEDIUM FROM A MACROSCOPIC PERSPECTIVE	16	4.7 SELECTION OF Tm-170 AS SECOND RADIATION SOURCE AND SELECTION OF MERCURY AS ELEMENT WITH HIGHER ATOMIC NUMBER FOR DOPING THE PETROLEUM DERIVATIVE	185
2.3 CONTINUITY EQUATION	17	4.8 PRODUCTION OF THE TWO RADIATION SOURCES: Cs-137 AND Tm-170	187
2.4 MATHEMATICAL DESCRIPTION OF DISPLACEMENT PROCESS	18	4.9 Tm-170 SPECTRA	191
2.5 INITIAL AND BOUNDARY CONDITIONS	19	4.10 MEASURES FOR THE ELIMINATION OF THE DECELERATION SPECTRUM	194
2.6 OPTIONS FOR SOLVING SET OF EQUATIONS	21	4.11 SEMI-GRAPHICAL METHOD TO DETERMINE THE FLUID SATURATIONS	202
3.0 CONCEPTS FOR THE SIMULATION OF THE THREE-FLUID FLOW BASED ON CAPILLARITY	23	5.0 RESULTS OF TWO-DIMENSIONAL THREE-PHASE FLOW EXPERIMENTS (A, B, C, AND D)	205
3.1 CAPILLARITY FROM A MICROSCOPIC PERSPECTIVE	24	5.1 PARAMETERS TO BE MEASURED	205
3.2 CAPILLARITY FROM A MACROSCOPIC PERSPECTIVE	51	5.2 CAPILLARY PRESSURE-HEAD CURVES AND POROUS MEDIUM	206
3.3 RESIDUAL OIL SATURATION	70	5.3 MEASUREMENT METHODS	208
3.4 CONCEPT OF VIRGIN AND CONTAMINATED AIR-WATER FLUID SYSTEM	78	5.4 OIL APPLICATION AND BOUNDARY CONDITIONS	210
3.5 FLUID SATURATION DIAGRAM	83	5.5 EXPERIMENT A	212
3.6 DEFINITION OF PLANE FOR HORIZONTAL OIL PROPAGATION	88	5.6 EXPERIMENTS B, C, AND D	226
3.7 TRANSITION OIL POTENTIAL	89	DEFINITION OF SYMBOLS	246
3.8 OIL-LENS THICKNESS	96	LIST OF FIGURES	253
3.9 HYSTERESIS OF THREE-PHASE FLUID FLOW IN A POROUS MEDIUM	98	LIST OF TABLES	258
4.0 SELECTION OF HIGH AND LOW-ENERGY RADIATION SOURCE AND TESTING OF GAMMA-RAY ATTENUATION METHOD TO MEASURE FLUID SATURATIONS	118	REFERENCES	259
4.1 THE DEFINITION OF SATURATION	118	APPENDIX (TABLES α , δ , and δ')	
4.2 REQUIREMENTS OF THE SATURATION MEASUREMENT METHOD	118	LIQUID POTENTIAL AND FLUID SATURATION TIMELINE FOR EXPERIMENTS A, B, AND D	

TABLE 1.2. Schiegg (1980 VAW No. 43) Contents

SYNOPSIS	4.2 SOURCE SHIELDS	81
1.0 FUNDAMENTALS	4.3 COLLIMATION	87
1.1 HYDRODYNAMIC DISPLACEMENT	4.4 DETECTOR	90
1.2 HYDRODYNAMIC DISPERSION	4.5 IMPULSE HEIGHT ANALYZER	92
1.3 EQUATION SYSTEM FOR THE DESCRIPTION OF GROUNDWATER CONTAMINATION BY OIL DERIVATIVES	4.6 SOURCE-DETECTOR SCANNING SYSTEM	93
1.4 SATURATION DIAGRAM	5.0 CAPILLARY RISE-SATURATION DIAGRAMS MEASURED IN A ONE-DIMENSIONAL COLUMN	103
1.5 NUMERICAL INTEGRATION	5.1 CAPILLARY PRESSURE-HEAD CURVES	103
1.6 PARAMETERS TO BE MEASURED	5.2 SERIES A AND B SATURATION DIAGRAMS	105
2.0 POROUS MEDIUM	5.3 COMMENTS ON EXPERIMENTAL SERIES F	106
2.1 CHARACTERISTICS OF THE POROUS MEDIUM	5.4 COMMENTS ON EXPERIMENTAL SERIES B	147
2.2 THICKNESS OF THE POROUS MEDIUM	5.5 COMPARISON OF THE CAPILLARY PRESSURE-HEAD CURVES	155
2.3 POROUS MEDIUM CONTAINERS	5.6 ACCURACY OF THE SATURATION MEASUREMENT	160
2.3.1 Plexicolumn for the One-Dimensional Static Experiments	5.7 MAXIMUM RESIDUAL SATURATIONS	161
2.3.2 Flume for the Two-Dimensional Dynamic Experiments	6.0 RESULTS OF TWO-DIMENSIONAL EXPERIMENTS	162
2.4 APPARATUS FOR PACKING A HOMOGENEOUS ISOTROPIC POROUS MEDIUM	6.1 COMPARISON OF EXPERIMENTS 1 THROUGH 9	162
3.0 PRESSURE GAGE APPARATUS	6.2 INITIAL AND BOUNDARY CONDITIONS	164
3.1 REQUIREMENTS	6.3 SELECTED CHARACTERISTICS	168
3.2 CONSTRUCTION OF THE PRESSURE GAGE SYSTEM	6.4 LEGEND FOR THE SATURATION AND POTENTIAL TIMELINE FOR EXPERIMENTS 1 THROUGH 8	168
3.2.1 Probes	6.5 SATURATION AND POTENTIAL TIMELINE FOLD-OUTS	170
3.2.2 Pressure Transducer	7.0 RESIDUAL OIL SATURATION OF DIFFERENT SANDS, AND MINIMUM OIL LENS THICKNESS ON SLOPED GROUNDWATER TABLES	171
3.2.3 Switching Apparatus	7.1 PENEBULAR OIL SATURATION AT RESIDUAL WATER SATURATION	173
3.2.4 Tubing System	7.2 MINIMUM OIL LENS THICKNESS	178
3.2.5 Response Time of the Pressure Gage System	EXPLANATION OF SYMBOLS	181
3.2.6 Minimum Measuring Time	LIST OF FIGURES AND TABLES	185
4.0 DUAL GAMMA-RAY RADIATION SATURATION MEASUREMENT	REFERENCES	189
4.1 MEASUREMENT APPARATUS		

references are made to figures, tables, and sections appearing in other chapters. If the referenced object is not included in this document, then the original table, figure, or section number in Schiegg (1979) or (1980) has been used.

The experiments presented herein should be considered as stepping stones to additional future experiments. Additional experiments are necessary to verify 1) the quantitative descriptions of organic liquid migration in aquifers (the descriptions are still extensively generalized with regard to nonstationary conditions, heterogeneities, and anisotropies), and 2) the numerical simulations. Future researchers who perform multiphase flow experiments in large containers filled with porous media must bear in mind that the quality of their data will reflect their ability to minimize experimental errors contributed by the instrument systems and the container materials. By providing a detailed description of the measurement techniques and the experiment setups used in the ETH study, it is hoped that future researchers can build experiment setups that are best suited to their experimental objectives.

This report is organized into 10 chapters and five appendices. This chapter gives the reader an appreciation of the scope of the work performed at ETH during the 1970s and the extent to which that work is reported in this PNL report. Chapter 2.0 presents the system of equations used to describe groundwater contamination by petroleum hydrocarbons. This system of equations defines the parameters that must be measured to quantify multiphase flow in porous media.

In Chapters 3.0, 4.0, 5.0, and 6.0, details of the laboratory setups are presented. Chapter 3.0 discusses the characteristics of the porous medium that was used in all the experiments. An important experimental specification was the thickness of the porous medium, which was chosen to minimize the influence of the wall effect. The design of the flume and the apparatus used to homogeneously pack the medium is also presented. Chapter 4.0 describes the system used to measure the liquid pressures in the water and oil. Chapter 5.0 discusses the dual-energy gamma-radiation saturation measurement system. A major experimental obstacle was the selection of the lower-energy gamma radiation source used in conjunction with the Cs-137 source. Thus, Chapter 6.0

presents details of the theoretical development and confirming tests that led to the use of Tm-170 as the second source.

Chapters 7.0, 8.0, and 9.0 present the results of the one- and two-dimensional experiments. A fundamental constitutive relationship in multiphase flow is the capillary pressure-saturation relationship. Chapter 7.0 presents 41 capillary pressure head curves defining the eight different relationships needed: the drainage and imbibition curves for the water-oil, oil-air, and virgin and contaminated water-air curves. Chapter 8.0 presents a detailed discussion of four two-dimensional experiments. Chapter 9.0 provides a brief description of nine more two-dimensional experiments. The liquid potential and fluid saturations, measured over time in the two-dimensional experiments, are presented in graphical form in fold-outs included in the envelope provided with this report. Chapter 10.0 lists references cited and provides a bibliography of works cited from those portions of Schregg (1979, 1980) not covered in this report. Appendix A is the definition of symbols and list of abbreviations. For completeness, four English publications by H. O. Schiegg are included in Appendices B, C, D, and E.

2.0 FUNDAMENTALS

To determine which parameters should be measured during an experimental simulation, we must first consider the fundamental mathematical description of groundwater contamination by petroleum derivatives and the method of mathematical solution.

The physical and chemical process of groundwater contamination by a petroleum derivative is the sum of several smaller connected problems that can be considered individually. Petroleum derivatives will be designated as "oils" in the remainder of this document.

2.1 HYDRODYNAMIC DISPLACEMENT

Propagation of the nonwater-soluble portion of an oil is called a hydrodynamic displacement process.

A hydrodynamic displacement process implies that the oil is in a funicular saturation state. The first stage of the oil propagation occurs predominantly in the vertical direction between the application site and the water-air capillary fringe (see Figure 8.8). The second stage consists mainly of propagation in the water-air capillary fringe parallel to the water table. After interrupting the application of oil, the funicular oil saturation disintegrates to residual oil saturation.

According to Versluys (1931), a saturation state is designated funicular if the separate fluid parts are connected to one another. A potential difference between these parts leads to flow, and accordingly, the relative permeability is greater than zero. A saturation state is designated residual if the separate fluid parts are not connected with one another, a potential difference between these parts does not lead to flow, and the relative permeability is equal to zero. The residual saturation state of a wetting fluid is designated pendular, and the residual saturation state of a nonwetting fluid is termed insular. According to Schiegg (1979, p. 71), the maximum pendular saturation (RS_{\max}^{pend}) can be set, as a first approximation, equal to half of the maximum insular saturation (RS_{\max}^{ins}).

$$RS_{\max}^{\text{pend}} \approx 0.5 RS_{\max}^{\text{ins}} \quad (2.1)$$

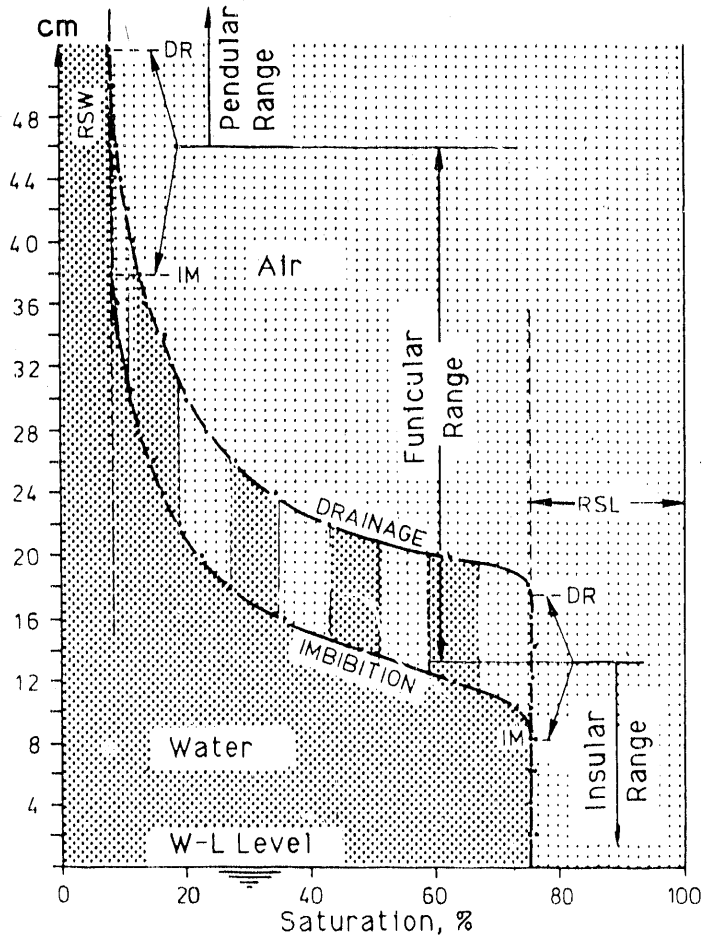
A fluid whose contact angle versus the solid is acute is a wetting fluid. Accordingly, the contact angle of a nonwetting fluid must be obtuse. The contact or wetting angle is the angle at the interface between two fluids and a solid. Imbibition, IM, is understood as the displacement of the nonwetting fluid by the wetting fluid. Drainage, DR, is the reverse process.

Figure 2.1 shows, for both imbibition and drainage, the measured saturation distribution in the water-air capillary fringe of the quartz-sand material used in the experiments discussed in Chapters 7.0, 8.0, and 9.0. RSW is the residual saturation of water, and RSL is the residual saturation of air. The range where the wetting fluid is residual is labeled the pendular range. The range where the nonwetting fluid is residual is called the insular range. In between, where both fluids are funicular, lies the funicular range.

The propagation of oil in the water-air capillary fringe parallel to the water table occurs along the so-called propagation surface. The vertical position of the propagation surface above the water table is, as a first approximation, given by the equivalent capillary water column elevation associated with the transition from funicular to insular nonwetting fluid saturation. Its actual position is defined by Schiegg (1979, p. 96).

By definition, residual oil cannot move by hydrodynamic displacement within the porous medium. Thus, residual oil constitutes hydrodynamically nondisplaceable contamination of the aquifer. However, changes in the residual oil saturations are possible by transport of the oil as fine drops in water.

Fine drops of oil suspended in water are known as an oil-in-water emulsion. A practical example of the transport of an emulsion is given in Appendix C. In practice, the reduction of the residual oil saturation is mostly the result of diffusion and bacterial degradation.



W = Water
 L = Air
 RS = Residual Saturation
 DR = Drainage
 IM = Imbibition

FIGURE 2.1. Static Saturation Distribution in the Water-Air Capillary Fringe of the Quartz Sand Used in the Majority of Experiments

2.2 HYDRODYNAMIC DISPERSION

The propagation of the water-soluble portions of an oil is known as hydrodynamic dispersion. Dispersion means that one material (the dispersed phase) is finely distributed in another (the dispersion medium). Examples of dispersions are suspensions (solid particles in a liquid), emulsions (liquid droplets in another liquid), smoke (solid particles in a gas), and mist and aerosols (liquid droplets in a gas). With a suspension or emulsion, the particle diameters lie between 1 and 50 μm . If the particle diameters of the

dispersed phase are between 1 and 100 nm, then a sol is formed. With still smaller particle diameters (i.e., those of molecular size) the dispersed phase goes into solution.

Hydrodynamic dispersion is the macroscopic propagation of a dispersed phase in a fluid flowing through a porous medium. It is the result of various particle effects, which will be described separately. Convective flow is the flow of the carrier fluid.

Mechanical dispersion or convective diffusion describes the macroscopic propagation of the dispersed phase in the carrier fluid, which results from the different particle flow paths and velocities on a microscopic scale. The concepts of microscopic and macroscopic scales are defined by Schiegg (1979, pp. 15-16). Mechanical dispersion assumes the existence of a convective fluid.

Physicochemical dispersion or molecular diffusion describes the propagation of a dispersed phase in a fluid resulting from a chemical concentration gradient. This process is described by Fick's second law of diffusion.

Finally, the mass balance of a hydrodynamic dispersion process must include both the transfer of the dispersed phase across the interfaces of the dispersion medium by adsorption, desorption, ion exchange, etc., and the natural production and decomposition of the dispersed phase.

The mass balance for the hydrodynamic dispersion of a dispersed phase β in a dispersion medium α can be formulated mathematically as Equation (2.2) (Bear 1978) based on the macroscopic continuum law, or as it was given in a microscopic, differential representation by Truesdell and Toupin (1960, p. 468).

$$\frac{\partial \theta_\alpha \langle c_\alpha \rangle^\alpha}{\partial t} = -\nabla \cdot \{ \langle c_\alpha \rangle^\alpha \cdot \underline{q}_\alpha \} - \theta_\alpha \left(D_{ij} \frac{\partial \langle c_\alpha \rangle^\alpha}{\partial x_j} \right) - \langle D_d \nabla c_\alpha \rangle - \frac{1}{U_0} \int f(c_\alpha, \dots) + \theta_\alpha \langle \rho_\alpha \Gamma(c_\alpha) \rangle^\alpha \quad (2.2)$$

- convective flow of α
- mechanical dispersion (convective diffusion of β)
- physiochemical dispersion (molecular diffusion of β)
- adsorption, desorption, etc. of β
- production, decomposition of β

where θ_α is the volumetric fraction of the fluid α in the representative elementary volume, whose size is equal to U_0 , c_α is the concentration of the dispersed phase β in the dispersion medium α , ρ_α is the density of the fluid α , D_{ij} represents the tensor of the mechanical dispersion, and D_d is the coefficient of the molecular diffusion. The symbol $\langle \rangle$ indicates that value is a macroscopic average of the microscopic values, and when subscripted as $\langle \rangle^\alpha$, it refers to a macroscopic average for fluid α , such that $\langle \rangle^\alpha = (1/\theta_\alpha) \langle \rangle$. Thus, for example, the macroscopic flux, q , = $\langle v \rangle = \theta_\alpha \langle v \rangle^\alpha$, where v represents the microscopic velocity of α .

2.2 EQUATION SYSTEM FOR THE DESCRIPTION OF GROUNDWATER CONTAMINATION BY OIL DERIVATIVES

Groundwater contamination by oil derivatives is the result of hydrodynamic displacement of the three immiscible fluidic fluids: water, air, and oil (not including the water-soluble or volatile fractions) and the hydrodynamic dispersion of the water-soluble oil fraction as a dispersed phase in the water. Both processes are correlated because the initial concentration (i.e., the initial and boundary conditions for the dispersion) is dependent on the mathematical solution of the displacement process.

If the convective flow of groundwater contaminated by petroleum derivatives, α_1 , is the result of a displacement process with an immiscible fluid, then for the mathematical formulation of the displacement process for each of the participating fluids, a relation analogous to Equation (2.2) must be established. From this, $\langle c_{\alpha i} \rangle^\alpha$ represents the dependent variables in the

first part of Equation (2.2). Consequently, the remaining parts must be known for the solution of the equation system. Likewise, the initial and boundary conditions must be assumed for each specific case.

Because the dependence of hydrodynamic dispersion on hydrodynamic displacement is known, it seemed reasonable for the quantitative determination of groundwater contamination by petroleum derivatives to limit this inquiry to the understanding of the displacement process; thus, the existence of water-soluble oil constituents was disregarded. Therefore, water is assumed to be a pure fluid with no dispersion, similar to air, and neither water-soluble nor volatile oil fractions exist. Thus, no β_j dispersed phases exist, and $\langle c_{\alpha_j} \rangle^{\alpha_i}$ in Equation (2.2) becomes equal to 1. In this way, the right side of Equation (2.2) is reduced to the sum of the convective flows. This results in relations that can be obtained for unsaturated flow and also directly from the basic equation of continuity (Bear 1978, p. 14)

$$\frac{\partial \theta_i}{\partial t} + \nabla \cdot \underline{q}_i \quad (2.3)$$

where i stands for water, oil, or air.

Equation (2.3) formulates a continuity condition (as in Equation [2.2]), specifically that of a volume balance. In unsaturated water theory, θ is moisture content. θ can be replaced by the product of porosity, n , and the saturation, S , which describes the percentage of pore space occupied by a fluid. Further, if the flux, q , in Equation (2.3) is replaced by Darcy's generalized relation, which equals the negative product of the relative permeability, k^r , the intrinsic permeability, K , and the gradient of the total potential, ϕ , divided by the dynamic viscosity, μ , then the result is a relation similar to the equation of Richards (1931)

$$n \frac{\partial S_i}{\partial t} + \nabla \cdot \left(k^r_i \frac{K}{\mu_i} \nabla \phi_i \right) \quad (2.4)$$

Because "n" was placed before the partial differential, a constant porosity is assumed. To determine the immiscible fluid displacement in incompressible porous media, Equation (2.4), with the given boundary and initial conditions, must be set up for each of the participating fluids.

Compared to water and oil, the density and viscosity of air are smaller by an order of magnitude. Thus, the variability of the potential in the air is negligibly small in contrast to that in the water or oil. The air potential at funicular air saturation remains practically constant and equal to its initial value, zero. Thus, the differential equation for air is ignored, and the equation system that describes a displacement process between water, oil, and air is reduced to

$$\begin{aligned} n \frac{\partial \Phi_O}{\partial t}(\Phi_W, \Phi_O, \Phi_L) &= V \cdot \left(\frac{k}{\mu_O} f_O^r(S_W, S_O) \cdot \nabla \Phi_O \right) \\ n \frac{\partial \Phi_W}{\partial t}(\Phi_W, \Phi_O, \Phi_L) &= V \cdot \left(\frac{k}{\mu_W} f_W^r(S_W, S_O) \cdot \nabla \Phi_W \right) \end{aligned} \quad (2.5)$$

The two potentials, Φ_W and Φ_O , are the independent variables or the two unknowns. In addition to the initial and boundary conditions, the following relations are assumed as known:

$$\begin{aligned} \Phi_O &= \Phi_O(\Phi_W, \Phi_O, \Phi_L) & f_O^r &= f_O^r(S_W, S_O) \\ S_O &= 1 - (S_W, S_L) & f_W^r &= f_W^r(S_W, S_O) \\ \Phi_W &= \Phi_W(\Phi_W, \Phi_O, \Phi_L) & & \end{aligned} \quad (2.6)$$

$$n = n(x, y, z); \quad \underline{k} = \underline{k}(x, y, z); \quad \mu_O = \mu_1; \quad \mu_W = \mu_2$$

The functions $S_L = S_L(\Phi_i)$, where S_L is air saturation, and $S_W = S_W(\Phi_i)$ define the saturation diagram (Figure 2.2). The summation function, $S_O = S_O(S_W, S_L)$, is a result of the mutual dependence of the contaminated capillary rise curve between water and air and the water-oil and oil-air capillary rise curves

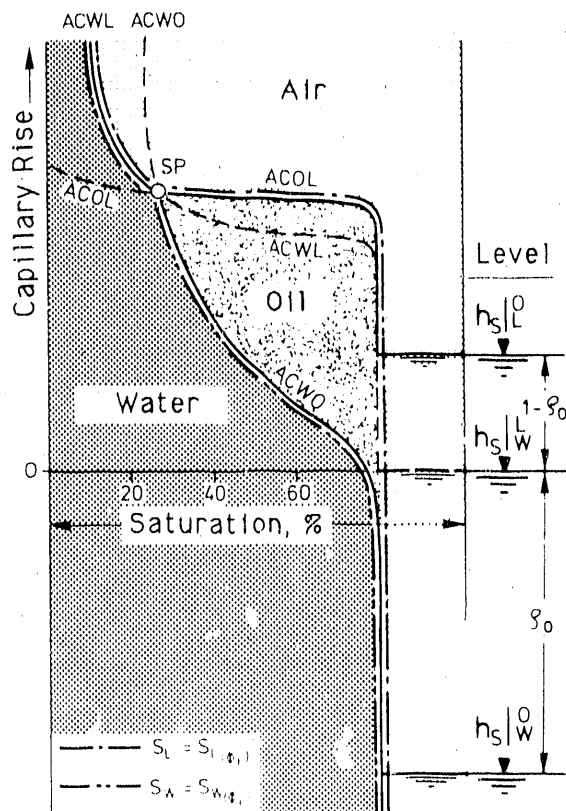


FIGURE 2.2. Saturation Diagram

based on the contamination concept from Schiegg (1979, p. 78), in which the concepts of the saturation, as well as the capillary rise curves were explained.

The relative permeabilities ($k_i^r = k_i^r(S)$) are experimentally determined functions of the saturations. Figure 2.3 shows relative permeability data measured by Wyckoff and Botset (1936). In an anisotropic porous medium, the intrinsic permeability, K , is a tensor. In an isotropic porous medium, K is a scalar. In a heterogenous porous medium, the porosity, n ; the intrinsic permeability, K ; the saturation diagram; and relative permeability-saturation relationship are functions of position. For the case of homogeneity and isotropy, these parameters become constants over space. For homogenous fluids, viscosity is constant. Because Equation (2.4) assumes incompressibility of

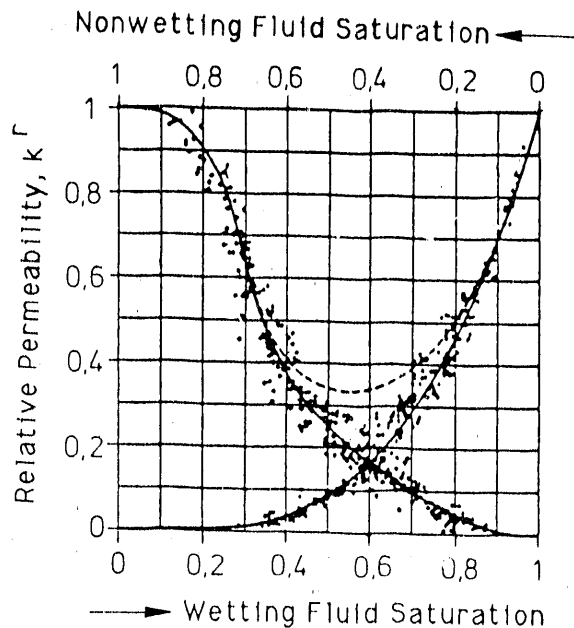


FIGURE 2.3. Experimentally Measured $k^r = k^r(S)$ from Wyckoff and Botset (1936)

the porous medium, the functions for the porosity and the intrinsic permeability can be considered time-independent relations.

2.4 SATURATION DIAGRAM

A saturation diagram, as shown in Figure 2.2, shows the local distribution of water, oil, and air in a homogenous and isotropic porous medium. A saturation diagram is constructed by superpositioning the three capillary rise curves. A capillary rise curve, AC, describes the relationship between capillary rise and saturation. This technique is limited by the validity range, which is a function of the intersection point, SP (Schiegg 1979, p. 78). Thus, superpositioning is not interpreted in the usual sense as an addition, but means a superimposed tracing of the separate curves in a common plane versus a common basis for the potentials.

Capillary rise is a function of the capillary pressure head. The capillary pressure head is dependent on the capillary pressure. This is the pressure difference between the wetting and nonwetting fluid across their

interface. The wetting fluid in a porous medium exists under a capillary suction and for this reason, the pressure in the wetting fluid is smaller than in the nonwetting one. This pressure difference is designated as the capillary pressure, p_c .

$$p_c \Big|_b^{nb} = p_{nb} - p_b \quad (2.7)$$

where the indices nb and b signify the nonwetting and wetting fluids respectively. If p_c is divided by the density difference times the gravitational constant, g , then the capillary pressure head, h_c , is obtained

$$h_c \Big|_b^{nb} = p_c \Big|_b^{nb} / (\rho_b - \rho_{nb})g \quad (2.8)$$

where h_c represents the pressure difference across a meniscus in the form of a piezometric height. h_c is also designated the capillary potential. A capillary pressure head curve, HC, describes the relation between capillary pressure head and saturation. Capillary potential and saturation assume a macroscopic perspective.

In statics, the capillary pressure head equals the increase in the elevation of the menisci resulting from capillary pressure. In dynamics, that is when the potential distribution over the domain is transient, a different capillary rise results (Schiegg 1979, p. 46). However, according to existing knowledge, the capillary pressure head is independent of dynamics (see Appendix D). The actual capillary rise is designated as the capillary rise, a_c . In statics, the capillary rise, a_c , and the capillary pressure head, h_c , are identical.

As with the capillary pressure head curve, HC, the capillary rise curve, AC, is derived from macroscopic observations. The AC curve describes the relation between capillary rise and saturation. The capillary rise refers to the distance normal from the free-fluid level to a point with a specific saturation. Thus, the AC curve describes the saturation distribution within the

capillary fringe normal to the free-fluid level. Only in statics can the saturation distribution also be described by an HC curve. In dynamics, the saturation distribution (and thus the AC curve) characterizes the momentary position function of the two potentials. In statics, both potential functions are reduced to two constant potential values over space.

The concept of the capillary rise or the capillary rise curve is a simple description of the saturation distribution in dynamics. A dynamic saturation diagram characterizes the momentary position function of the three potentials. With regard to hysteresis, a saturation diagram helps describe the development of the potentials. A static saturation diagram shows the saturation distribution for three constant potentials over the domain.

The three AC curves to be superimposed for a saturation diagram are those between water and air, ACWL; between oil and air, ACOL; and between water and oil, ACWO. Because of hysteresis, each of the three AC curves depends on the position of the pertinent free-fluid level, and thus the temporal progress of the actual potential pair. The potentials are those in the water, the oil, and the air. For simplification, hysteresis loops are not shown in Figure 2.2.

To determine the position of the three AC curves to be superimposed for the saturation diagram (ACWL, ACOL, and ACWO), the elevations of the three free-fluid levels must be calculated based on the three momentary potentials in the water, oil, and air. The equation for the free-fluid level ($h_S|_b^{nb}$) in a large diameter tube as a function of the potentials is

$$h_S|_b^{nb} = (\phi_{nb} - \phi_b) / \{(\rho_{nb} - \rho_b)g\} \quad (2.9)$$

The ACWL curve is then placed on the free water-air level, the ACOL curve is placed on the free oil-air level, and the ACWO curve is placed on the free water-oil level.

With an increase in the relative oil potential (i.e., of the oil potential relative to the water-air level), the oil-air level increases and the

water-oil level decreases versus the water-air level. The ACOL curve is displaced toward the top and the ACWO curve toward the bottom, and therefore they move in the opposite directions from the ACWL curve. In this way, the intersection point, SP, moves along the ACWL curve toward the top left. With decreasing relative oil potential, the scenario is reversed. The intersection point, SP, moves from the top left toward the bottom right, and the ACOL curve and ACWO curve approach one another until they converge on the ACWL curve.

2.5 NUMERICAL INTEGRATION

The system of equations produced from Equations (2.5) and (2.6) and from the initial and boundary conditions is nonlinear. The nonlinearity results not only from the nonlinearity of the differential equations based on the saturation, potential, and the relative permeability, but also from the boundary conditions along the interfaces with the other fluids. Such interfaces are designated as fronts. Front-boundary conditions are nonlinear because their locations, by definition, are temporal. Therefore, front-boundary conditions are also designated as transient boundary conditions. Their mathematical formulation is given in Schiegg (1979, p. 19). Because of this nonlinearity and because the relationships between the potential versus the relative permeability and saturation must be determined experimentally, an analytical solution is impossible. Only a numerical solution is possible.

In the present case, the numerical integration can be discretized in time and thus made quasi-stationary. Quasi-stationary means that the time-dependent variables are held constant within a time step.

The nonlinearity of the quasi-stationary equation system requires linearization for its solution. The differential equations can be linearized such that the nonlinearity of the relative permeability, caused by its dependency on the potentials, is disregarded.

Although the boundary function for a front in a quasi-stationary treatment is independent of time, it is still a function of the potential difference at each time step. Thus, the positions of the front boundaries, which are not known in advance, are dependent on the unknown potentials. However,

for an integration, all boundaries of an integration area must be given. Because of the solution dependency of the front boundaries, the potentials must be calculated iteratively. The saturation diagram must be constructed from the potentials, and based on this, the new position of the boundary determined. With this new boundary position, the potentials must be calculated again, a new saturation diagram constructed, and so forth.

The equation system to be solved iteratively in this way is composed of linearized, discrete equations for water and oil at each node of the spatial discretization. The solution of the symmetrical matrix must be selected from the various available algorithms.

The iterative recalculation of the saturations, front positions, and potentials continues until the set convergence requirement is met for the potentials at each node. The final potential distribution represents the solution for the current time step.

The relative permeabilities are determined from the calculated saturations using the experimentally determined relation: $k^r = k^r(S)$. This must happen at each node, but for simplification can be limited to the last solution in a time step.

With homogeneity and isotropy in the porous medium, porosity and intrinsic permeability are constant scalars. Nonhomogeneity and anisotropy do not produce a systematic aggravation of the numerical solution method, but stipulate that the experimentally determined relations $k^r = k^r(S)$ and $S = S(\phi)$ must be known for the different structures of the porous medium. For practical problems, this is a very unrealistic requirement.

2.6 PARAMETERS TO BE MEASURED

From the previous discussion, it can be seen that to verify predicted oil propagation in aquifers by experiment, the potentials of the three fluids (above all, that of water and oil) as a function of place and time must be measured. In principle, fluid saturations as a function of space and time can be calculated from the measured potentials.

Such calculations, in the range of saturations of interest, make use of various simplifying assumptions and models. Thus it is advisable, for the verification as well as for the control of the experimentally determined potentials, to also measure the saturations of water and oil as a function of space and time.

These requirements necessitate the development of methods and equipment for the determination of fluid pressures and fluid saturations over space and time. Figures 2.4 and 2.5 are a photograph and engineering sketch, respectively, of the experiment setup developed to study oil propagation in a two-dimensional physical model of an aquifer and capillary fringe. This setup includes instruments to measure fluid pressures and saturations over space and time.

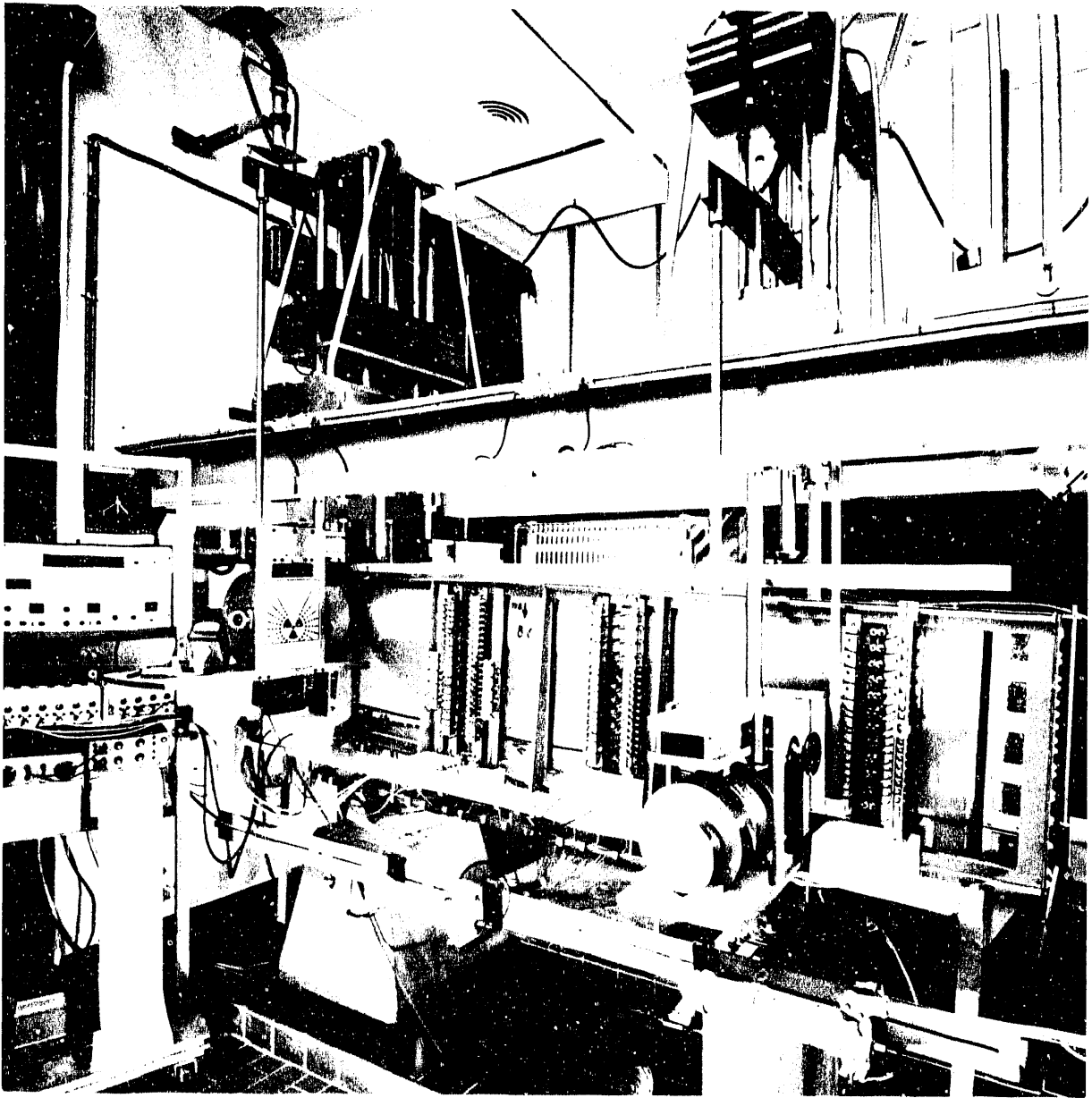


FIGURE 2.4. Experiment Setup Developed to Study Oil Propagation in an Aquifer. Fluid pressures and saturations were measured over space and time.

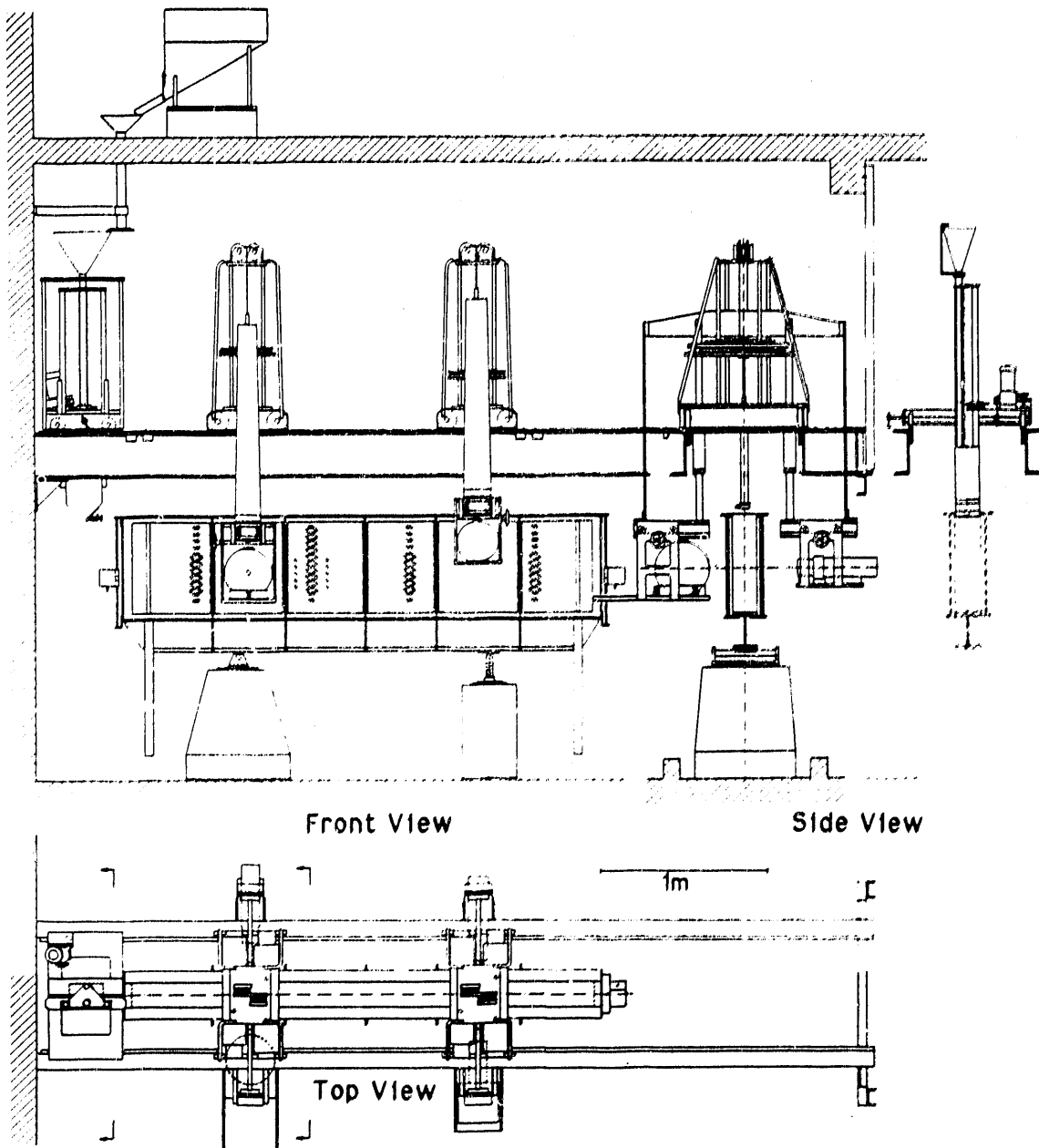


FIGURE 2.5. Engineering Sketch of Experiment Setup

3.0 POROUS MEDIUM

3.1 CHARACTERISTICS OF THE POROUS MEDIUM

A porous medium is a conglomerate of individual, nonbonded, solid particles. A porous medium is also a solid with hollow spaces called pores. Pores can exist isolated from one another or can be connected. In fluid dynamics, a porous medium is assumed to have connected pore spaces.

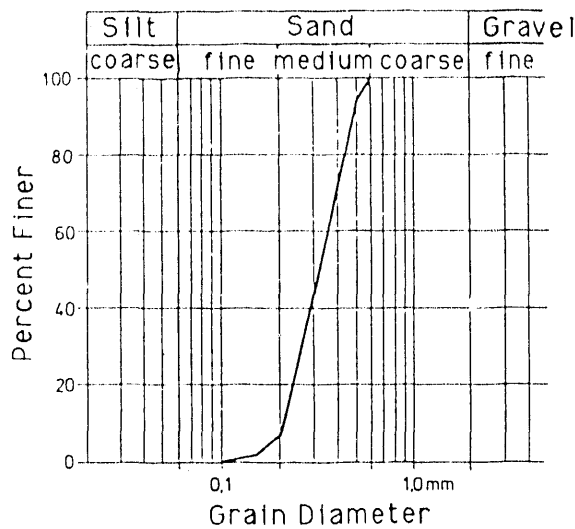
The characteristics of a porous medium are determined by the shape, surface features, and particle-size distribution of the grains. The porous medium is also characterized by the arrangement and position of the particles, which are a function of the applied packing energy (von Englehardt 1960; Childs 1967; Manegold 1955, 1960). The characteristics are further determined by the chemical properties of the grains. For example, limestone, quartz, and clay are inorganic minerals, whereas humus, peat, and coal are of an organic nature. With flow through a porous medium, it is primarily not the solid structure of the porous medium that is of interest, but rather the characteristics of the pore spaces. A pore space is determined by the shape and arrangement of the individual pores and their interconnections.

Compared to other parameters, such as tortuosity, the most important parameter for describing the pore spaces is the porosity. Porosity is the pore volume divided by the total bulk volume and is therefore dimensionless. If the pore volume is defined as the sum of all the hollow spaces, then total porosity is obtained. If the pore volume is defined as the volume of connected hollow spaces that allow fluid to flow through the porous medium, then the effective porosity is obtained. In the following discussion, the effective porosity is designated the porosity, n .

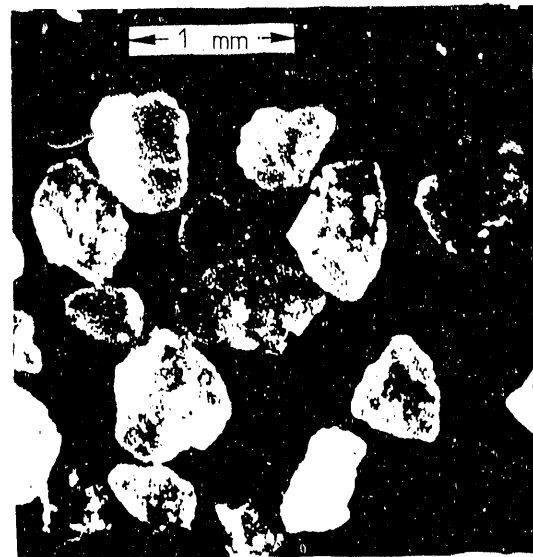
A pure quartz sand with uniform grains was chosen as the porous medium. Quartz was preferred over other minerals, such as limestone, because quartz, SiO_2 , has the same chemical elements as glass. Thus, experiments with microscopic fluid parameters (the contact angle and the radius of curvature, which determine capillarity in quartz sand) could be carried out in glass capillary tubes. This has several advantages. Glass is transparent, and glass capillary tubes in various forms and styles are readily available. Capillary

influences are more difficult to discern (less clear) in a porous medium than in the hollow space of a capillary because of hysteresis caused by the diameter variation between pores. The grain-size distribution of the quartz sand is shown in Figure 3.1a. The shape of the separate grains can be seen in Figure 3.1b. The particle density was determined as 2.65 g/cm^3 .

Heterogeneity and anisotropy result in spatial geometric differences between pore spaces. A different geometry implies a different capillary effect. The capillary effects are described by the capillary pressure, whose dependence on the pore space geometry is given by Laplace's equation of capillarity (Schiegg 1979, p. 24). Different capillary effects mean different radii of curvature for the same potential field. The variation in the radius of curvature corresponds to the variance of the capillary rise. In statics, the variance according to Equation (2.8) results from the division of the capillary-pressure variance by $\Delta\rho g$. This equation can be interpreted physically as weight minus buoyancy. For a liquid and air, the density difference or the very slight buoyancy of the liquid in air is equal to the density of



(a)



(b)

FIGURE 3.1. Quartz Sand (a) Grain-Size Distribution Curve and (b) Shape of Grains

the liquid, because the air density is practically negligible. Between water and oil, the density difference is five to ten times smaller than between either of these liquids and air. The buoyancy can no longer be ignored. Thus, the buoyancy difference resulting from the heterogeneity or anisotropy at the interface between the water or oil and the air is also five to ten times greater. From these observations, one can see that for the experimental simulation of displacement processes between water and oil, much higher requirements must be placed on homogeneity and isotropy than for liquid-air displacements, in which equal saturation deviations were tolerated.

Quartz is hydrophilic; thus, the porous medium is more wettable by water not only compared to oil but also to air. Compared to air, quartz is more wettable by oil.

The most interesting characteristic parameters of the porous medium are

$$\begin{aligned} \rho &= 2,65 \pm 0,01 \text{ g/cm}^3 & n &= 0,428 \pm 0,002 \\ k_{(S_L=0,02)} &= (4,4 \pm 0,1) \cdot 10^{-2} \text{ cm/sec} & & (3.1) \text{ (a)} \\ k_{(S_L=0,21)} &= (1,9 \pm 0,1) \cdot 10^{-2} \text{ cm/sec} \end{aligned}$$

The particle density was determined gravimetrically by displacement of water. The porosity was calculated by gamma-ray attenuation using Cs-137 (see Chapter 6.0). The hydraulic permeability, k , was determined from Darcy-type experiments (Scheidegger 1960, p. 69). At a minimum residual air saturation of 2%, a value of $4.4 \cdot 10^{-2}$ cm/sec was obtained. At a maximum residual air saturation of 21%, a value of $1.9 \cdot 10^{-2}$ cm/sec was obtained. This reduction of the relative permeability by about one-half as a result of 20% air saturation is similar to the values obtained experimentally by Wyckoff and Botset (1936) (see Figure 2.3).

(a) Equations were taken directly from the German text and, in some cases, use a different notation. For example, 0,01 = 1/100, whereas in this text, 1/100 would be shown as 0.01. Multiplication is indicated by a dot in the equations and in the text.

3.2 THICKNESS OF THE POROUS MEDIUM

The thickness of the porous medium is its expansion from a one- or two-dimensional geometry. Thickness is also equal to the irradiation width in the radiation attenuation method used to determine the fluid saturations. The attenuation of radiation increases exponentially with the thickness of the irradiated material (see Chapter 6.0). Thus, optimizing the irradiation width was important. From the requirement of a constant average error, and thus a constant attenuated radiation flux, the required activity of the isotope also increased exponentially with the thickness of the irradiated sand. The maximum isotope activity that could be produced in a nuclear reactor was a decisive factor in evaluating the isotopes under consideration (see Chapter 6.0).

Based on the above considerations, we endeavored to find the minimum necessary width of the porous medium. This was determined by the condition that the porosity introduced by the wall effect be negligible. Figure 3.2 shows that the porosity of a porous medium along a smooth wall is greater than within porous medium. This is valid for every type of packing. The smaller the distance from the wall, the larger the local porosity. According to Figure 3.2, this influence extends over four to five grain diameters. From the conversion of area $A + C$ into the equal-area rectangle $B + C$, it is seen that the wall effect causes a 25% increase in the porosity, over a distance of between four and five grain diameters. The minimum width, B , of the porous medium was defined by the requirement that the error in saturation due to the walls (calculated as one-quarter of the pore volume over nine grain diameters) did not exceed one-fourth of the tolerable standard deviation of $\pm 2\%$ fluid saturation (see Chapter 6.0), or $\pm 0.5\%$ of the pore volume over the total width

$$(n \cdot 0,25) \cdot (9 \cdot \phi) = (n \cdot 0,005) \cdot B \quad (3.2)$$

With a standard grain diameter, ϕ , of 0.33 mm (Figure 3.1a), the minimum necessary width of the porous medium is

$$B = 15 \text{ cm} \quad (3.3)$$

Preliminary experiments showed that the calculated influence of the wall effect (assumed from Figure 3.2 to be 1.5 mm long [$4.25 \cdot 0.33$ mm]) represented the lower limit of the wall effect measured experimentally. This meant that to achieve the above requirements, the thickness of the porous medium should not be less than 15 cm.

3.3 POROUS MEDIUM CONTAINERS

3.3.1 Plexicolumn for the One-Dimensional Static Experiments

The plexicolumn shown in Figures 3.3 and 3.4 was constructed for the one-dimensional static experiments (see Chapter 7.0) used to verify the theoretically determined capillary pressure head curves for oil, based on the fluid-media scaling method (Ω -values) of Schiegg (1979, p. 52). The migration of the saturation distribution as a function of the changes in potential was also observed during the experiments.

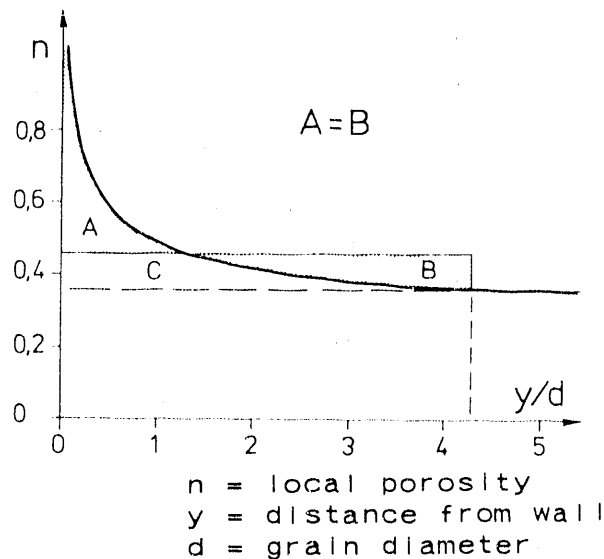


FIGURE 3.2. Effect of Wall on the Porosity of Packed Spheres

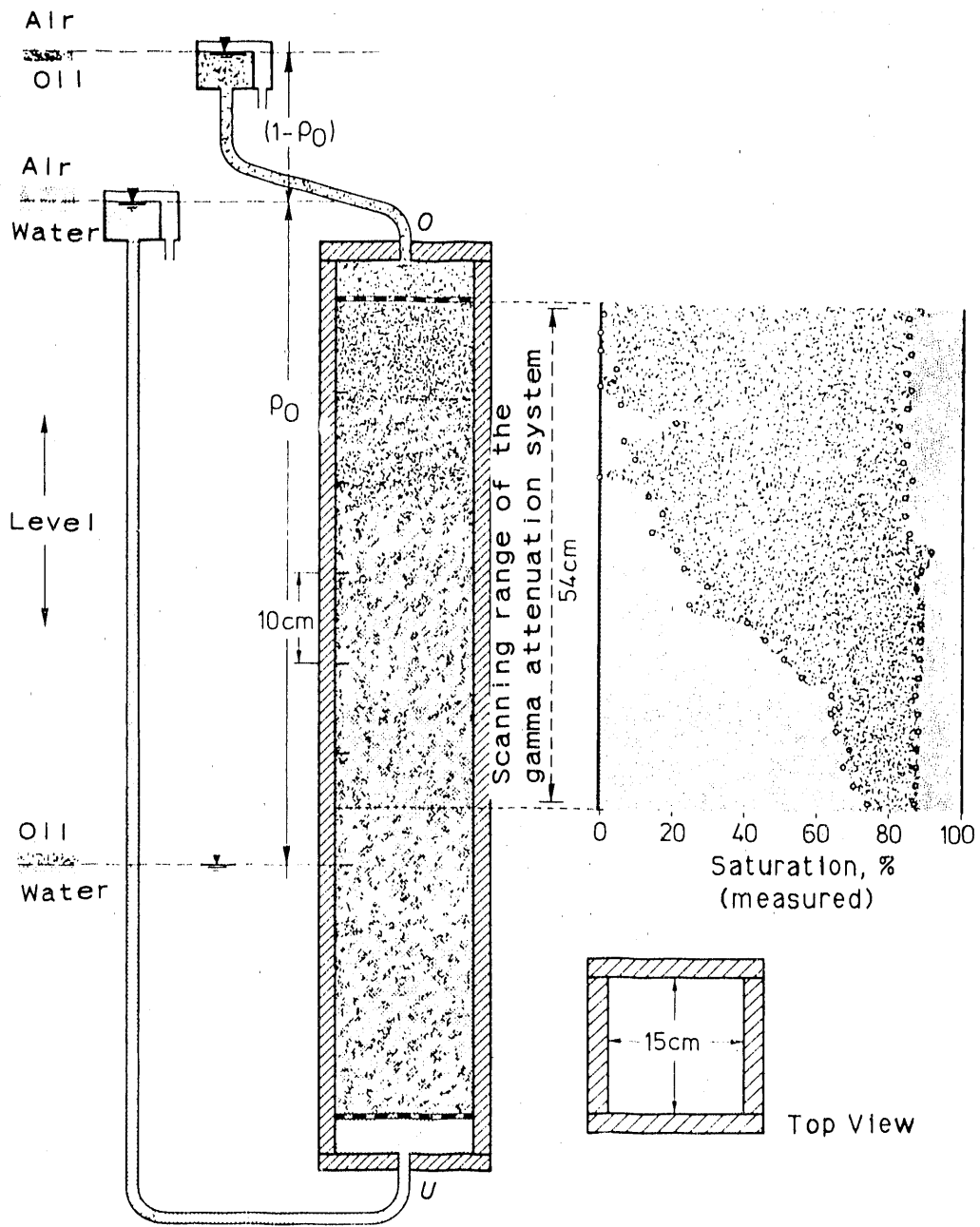


FIGURE 3.3. Schematic Diagram of the Plexicolumn and the Measurement Range



FIGURE 3.4. Photograph of the Plexicolumn (note the vent tube on the end plate)

Based on Equation (3.3), the inside width of the plexicolumn was chosen as 15 cm. At the two ends, the porous medium was held in place by two perforated screens. Overflow containers were connected to the ends such that any of the three fluids (water, oil, or air) could be introduced at both ends at a given potential.

3.3.2 Flume for the Two-Dimensional Dynamic Experiments

The laboratory space available for the experiments was 5.2 m • 5.6 m. The room was suitable because it had a northern exposure and masonry walls on all sides, which helped maintain a constant temperature. During the winter, the daily temperature variation was greater than in the summer; 1.7°C at most. The requirement for the smallest possible temperature variation arose from the required stability of the electronics and from striving for very slight fluid displacement in the pressure gage system resulting from temperature changes.

The thickness or width of the porous medium was determined from Equation (3.3) as 15 cm. The length of the porous medium was limited to about 2.6 m by the spatial configuration of the sand-filling apparatus and the gamma-ray attenuation system (explained in Section 3.4).

From the following deliberations, the height of the porous medium was established as 60 cm. The propagation of oil, which infiltrated above the

water-air capillary fringe, initially occurs primarily in the vertical direction. The propagation surface is found in the capillary fringe between water and air (see Figure 2.1). Specifically, the propagation surface occurs at the boundary between the funicular and insular nonwetting fluid saturation range. The moment the oil front reaches the propagation surface, the oil propagates in a direction predominantly parallel to the propagation surface. Thus, to obtain good oil propagation simulations, it is important that the capillary fringe extend to the highest possible height.

With small pore diameters, the funicular nonwetting fluid range lies farther away from the fluid level than with large pore diameters. For a gently sloping grain-size distribution curve, the funicular range is greater than for a steep grain-size distribution curve. However, with a gently sloping grain-size distribution curve, the packing of a homogenous and isotropic porous medium is more difficult. A compromise relating to these conflicting properties led to the selection of the material with the grain-size distribution shown in Figure 3.1a.

Preliminary experiments showed that free packing of such quartz sand yielded capillary fringe heights of a few decimeters (see Figure 2.1). Therefore, a minimum porous medium height of about 50 cm was chosen. The maximum height was restricted to about 70 cm. Because of the gamma-ray attenuation system (described in Chapter 5.0), we wanted the top of the porous medium to reach the favorable working height of about 150 cm above the floor.

The porous medium (unconsolidated sand) was packed in the experimental flume shown in Figure 3.5. The supporting element of the flume was a 256-cm-long I-beam (DIN 20). The I-beam also served as the base plate for the flume, and thus came into contact with water, but also eventually with Super-Ad-It^(a), a mercury-based fungicide dissolved in an organic solvent. Super-Ad-It diluted with an extra-light petroleum fraction, designated as SAI, was used as a representative of a petroleum derivative (see Chapter 6.0). The I-beam surface was sanded and given a chlorinated rubber coating to make it

(a) Available from the Borchers Brothers Company, Goslar, Federal Republic of Germany, under license by Hüls America, Piscataway, New Jersey.

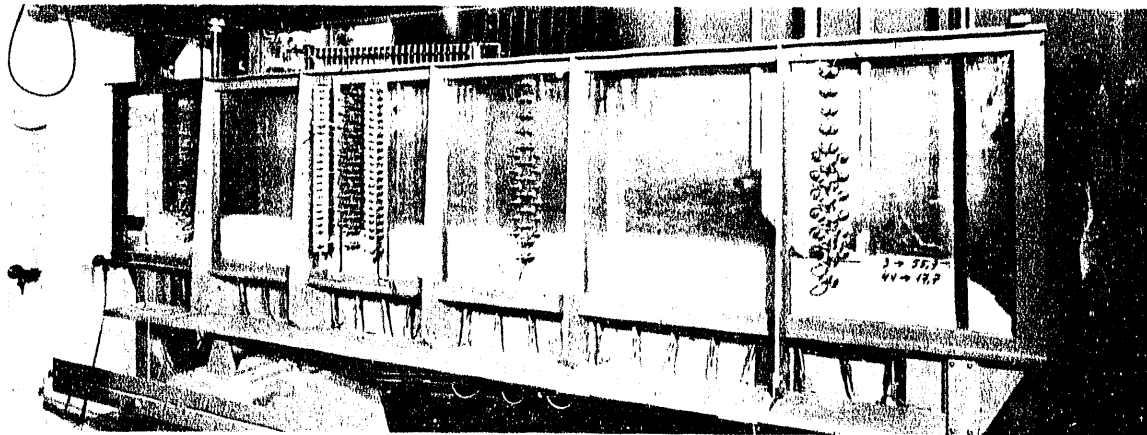


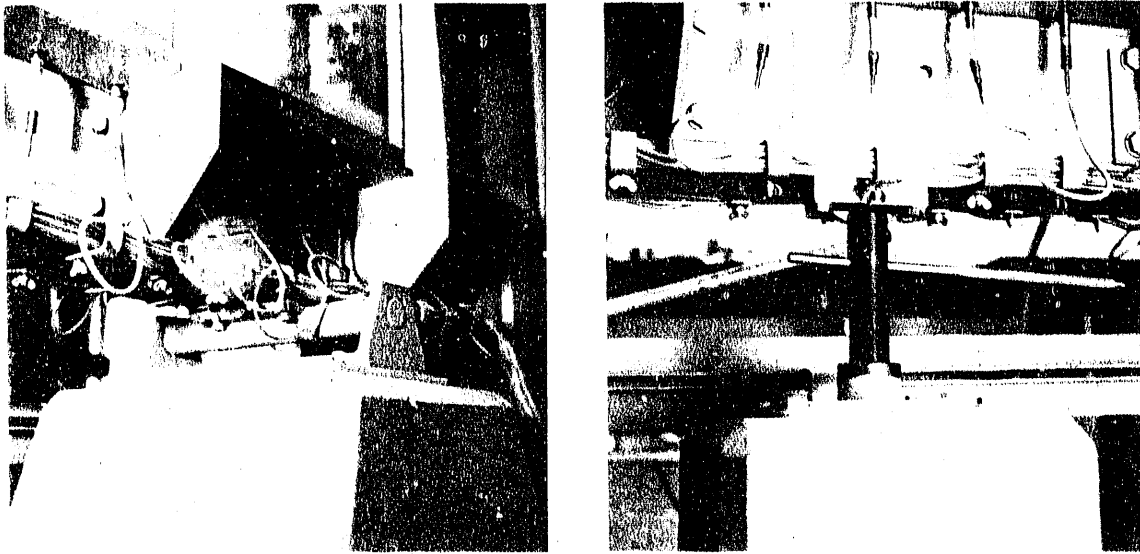
FIGURE 3.5. Photograph of the Experimental Flume

resistant to both fluids. The side walls of the flume consisted of two glass plates with the dimensions 280 cm • 60 cm • 2 cm. Each of the glass walls was supported by vertical beams to transfer the horizontal loads.

At the two ends of the flume, a screen was placed in front of the porous medium. At both ends, 5-cm-long sections of medium-coarse and coarse gravel were deposited between the quartz sand and the screen. These served to minimize end effects. The occurrence of end effects is described in Commentary A4 in Section 7.3.

A 4-cm-long water reservoir was attached to each end between the screen and the end of the flume. In each of the two water reservoirs, the water level could be regulated with an overflow vessel that could be moved vertically.

The flume was open at the top, and the porous medium was in contact with the free atmosphere above its surface. The I-beam, and thus the whole flume, was supported at two points (Figure 3.6). One support consisted of a hinge with a horizontal axis; the other was a vertical threaded bolt. The bolt was adjustable against a threaded nut fixed to the surface of the concrete base. The threaded bolt could be screwed down into a cavity in the concrete base. With this mechanism, the slope of the flume could be adjusted between 0 and 10%.



(a)

(b)

FIGURE 3.6. Flume Supports (a) at the Hinged Connection and (b) at the Threaded Jack Connection

The concrete bases were not poured directly onto the brick floor, but were built on 1.2-mm-thick rubber plates. This elastic layer served to dampen any building vibrations. This precaution was taken so that the porous medium, which was relatively loosely packed with a porosity of 40%, would not be compressed by building vibrations during the experiments. The constant position of the upper sand surface was considered proof that the constant porosity did not change during the experiments.

The flume and concrete bases were surrounded by a 12-cm-high dike so that any eventual spill of water, oil, or cleaning fluids during the cleaning phase would be contained (Figure 3.7).

The use of the proposed graphical method (see Chapter 6.0) to determine saturation required a nomograph of standard measurements. So that the nomograph was generally valid and did not have to be determined for each measuring point, the porosity had to be constant in time, and the measurements in the dry porous media had to be constant in space. This required a homogeneous

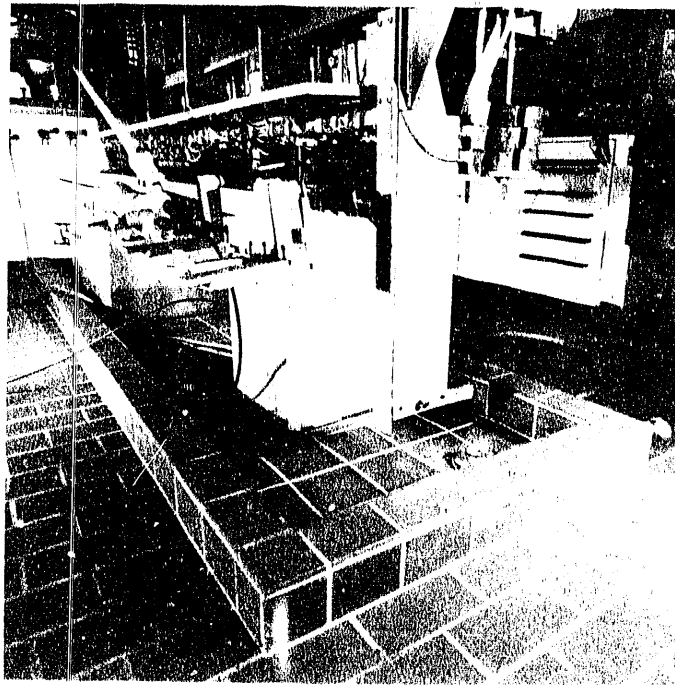


FIGURE 3.7. Concrete Base and Dike Above Floor

uniform glass thickness. In agreement with the earlier requirement that the systematic error not be greater than one-fourth of the tolerable average error of $\pm 2\%$ of the pore volume, the tolerable variance of the width of the flume, ΔB , for a 40% porosity is

$$\Delta B = B \cdot 0.02 \cdot K_1 = 150 \text{ mm} \cdot 0.02 \cdot 0.4 = 1.2 \text{ mm} \quad (3.4)$$

Therefore, the result of Equation (3.4) required that, assuming constant wall strength, the wall deflection amount to not more than 0.15 mm. To fulfill this requirement, the glass plates had to be reinforced with several vertical steel bars. This, however, did limit the view of the propagation process.

To increase the strength of the steel bars, a steel brace plate was welded along each of the vertical bars perpendicular to the glass. Because earth and water pressure increase with depth, the steel brace plate was wider near the bottom. The apparatus used to fill the flume did not allow the use

near the bottom. The apparatus used to fill the flume did not allow the use of tie rods across the top of the flume. Therefore, the steel brace plates were cut around the base plate and welded to two angle irons, which were then screwed to the I-beams (Figure 3.8).

The number and position of the vertical supports (Figure 3.9) had to be chosen so that the expected maximum deflection of the glass walls did not exceed the tolerable value of 0.15 mm [according to Equation (3.4)]. Furthermore, the supports had to be arranged so that each area that had been weakened by the holes drilled for the pressure probes lay in an area where the sum of the moments was equal to 0. This was to minimize the risk of glass failure. A search was made for the location of minimum moments on the perforated glass plates (Figure 3.10) after glass specialists expressed general doubts concerning the load capacity of such perforated glass plates. A moment distribution with a satisfactory number and position of supports had to be found by trial and error.



FIGURE 3.8. Brace Plates of the Flume



FIGURE 3.9. Glass Plate Supports

The calculation of the actual moments was made by using the simplifying assumption of a continuous beam with a constant stiffness on movable supports and under uniform load. Table 3.1 shows the calculation of the moments to obtain the most favorable arrangement of the supports. The calculation was done according to the iterative method of Cross (Hofacker 1962, Vol. XI, p. 15).

The careful selection of the two glass plates based on their uniform thickness was confirmed by gamma-ray attenuation measurements. The maximum variance of the gamma impulse count rate was smaller than an equivalent water thickness of 0.3 mm. This variance was measured on the empty flume and is smaller than the tolerable error $\pm 0.5\%$ saturation from this source of error. The cross-sectional width of the empty flume varied less than 0.2 mm.

A theoretical estimate of the maximum deflection of the glass plates was not possible before the flume was filled because a modulus of elasticity does not exist for glass. Measurements showed that the maximum deflection of the glass plates, due to the dry sandfill, came to 0.21 mm. During the highest water level in the experiments, the deflection of the glass plates was a maximum of 0.3 mm halfway up the evaluating area. The maximum variance of the flume width came to 0.6 mm. This is twice as large as the maximum tolerable value of 0.3 mm according to Equation (3.4). Thus, in an extreme case, the

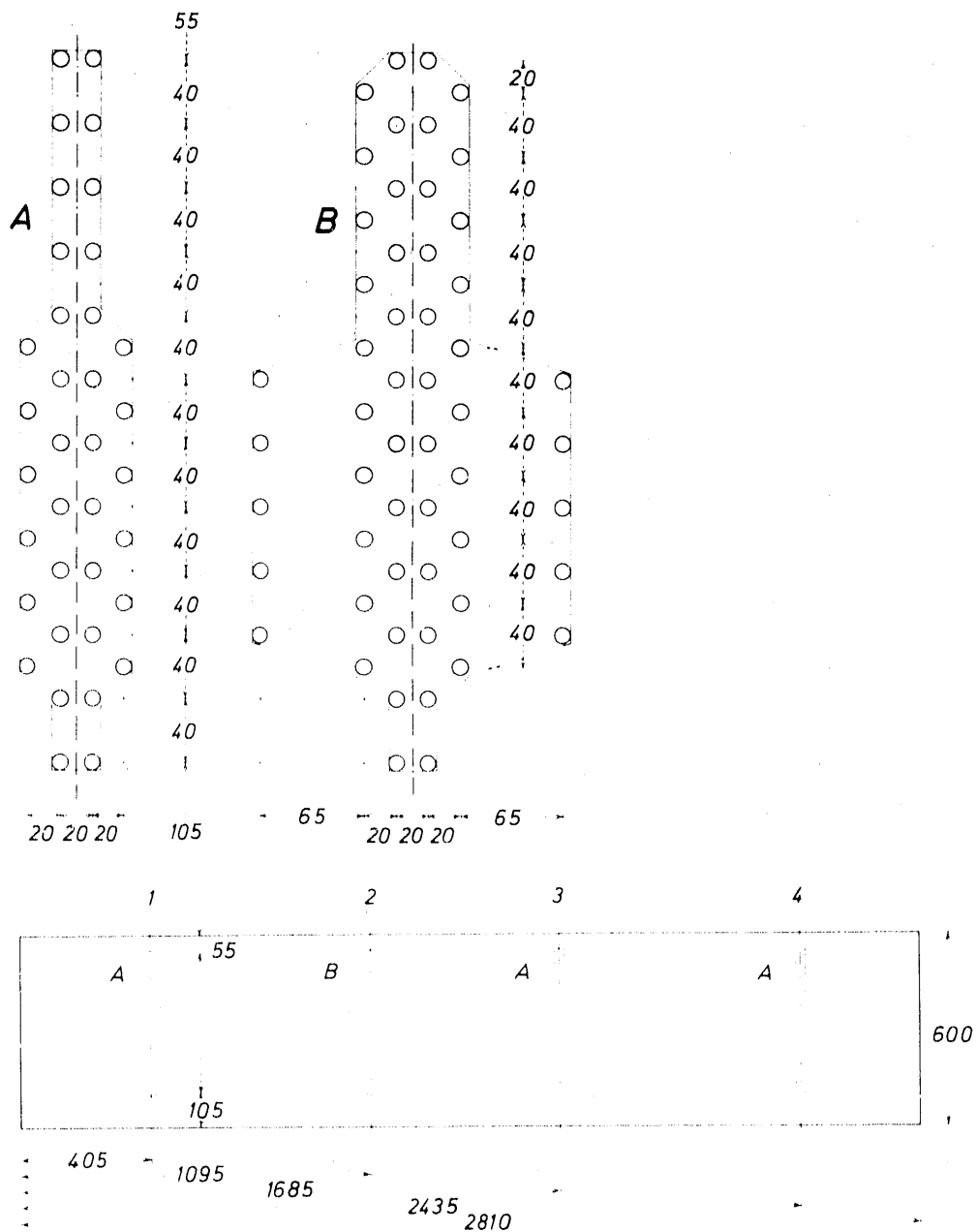


FIGURE 3.10. Arrangement of the Ports for the Pressure Probes (in millimeters)

error caused by the variable thickness of the porous medium in the irradiation direction was half of the maximum tolerable standard error of the saturations, not a fourth.

Each glass wall consisted of a single plate. It could not be constructed of several smaller plates because no hydrophilic and SAI-resistant material could be found to caulk the joints, and the open joints constituted extremely large pore passages. The oil could have perhaps migrated down the open joints and reached the base plate coated with chlorinated rubber, which is oleophilic. Because of the tendency of the oleophilic base plate to imbibe oil, the oil could have found its way to one of the outlets, in which case mechanical, not hydrodynamic, oil drainage and spreading would have occurred (Schiegg 1979, p. 33).

The joints between the front sides of the glass plates and the steel supports were filled with a permanent SAI-resistant plastic spacer in case the temperature did not remain constant and stresses built up because of the different elasticity coefficients of glass and steel. These stresses could have led to the formation of cracks in the glass plates.

To support the glass plates as evenly as possible with the steel bars, the open interval between the glass and steel was backfilled with portland cement, which was strengthened with very fine sand. With a less firm support, the variance of the clearance would have probably been somewhat larger than the upper limit of 0.6 mm.

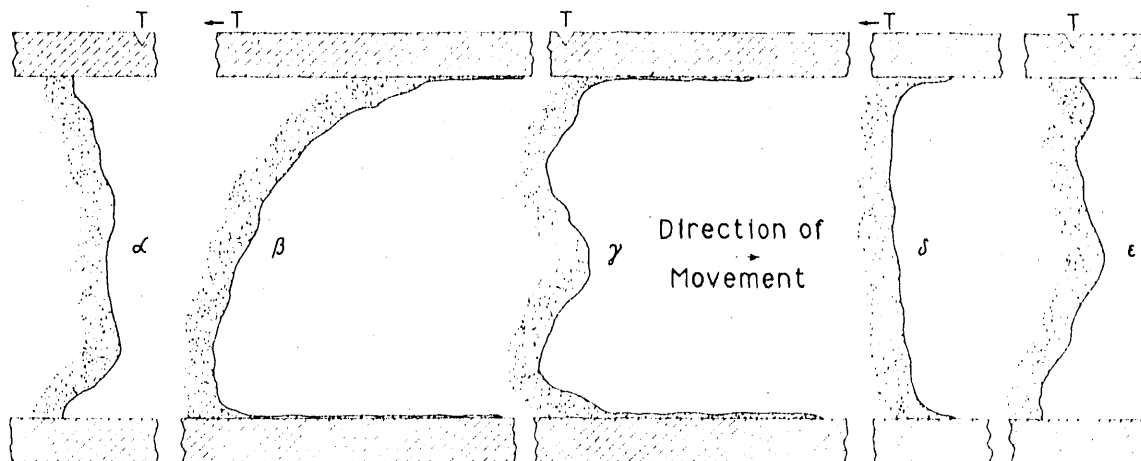
The two most important properties, in addition to a small deflection and unbreakability, of the two longitudinal walls of the flume were 1) transparency, to see the migration of the oil in the experiments, and 2) hydrophilicity or oleophobicity. This second property was required because the oil that came in contact with the wall should not spread out along it. A preferential propagation of the oil along the walls would have been undesirable for three reasons. First, the saturation conditions would have been incorrect. Second, spreading along the walls could have led to the contact of the funicular oil in the porous medium with a discharge point, and consequently to the unwanted drainage of the oil. Third, visual observations would have described a completely false propagation form. Accordingly, quartz glass (SiO_2 , chemically the same as the quartz sand used as the porous medium) was chosen as the material for the longitudinal walls of the flume.

The distribution of the ports for the pressure probes in the one glass wall was designed in advance. The ports were positioned regularly and appropriately for the different propagation experiments under consideration. The position of the ports for the pressure probes is seen in Figure 3.10. The glass wall was weakened by the strong concentration of the ports for pressure probes.

Specialists were brought in to drill the ports, but they agreed to do the job only if they would not be held accountable if the glass plate failed under a load. Thus, we attempted to find a plastic material as good as glass that would fulfill the criteria of transparency, slight deflection, and unbreakability. The workability of plastic is better than that of glass. The big problem in using plastic was that as a hydrocarbon compound, plastic has a natural oleophilic character. So the question was asked whether it would be possible to satisfy the requirement of oleophobicity by treating the plastic surface.

First, we sought to find hydrophilic coating agents that could be applied on the plastic plates in thin transparent layers. For all the different coatings considered, the adhesion of the coating to the plastic was determined by mechanical abrasion. A low adhesion indicated hydrophilic effectiveness. For the different coatings, identical propagation experiments were compared to that in the glass walls. Figure 3.11 shows the oil front advance in these experiments in relation to the point "T" 1 day after the addition of oil. The oil fronts shown in Figure 3.11 were observed by removing horizontal layers of material down to the propagation surface.

Based on the results in Figure 3.11, we concluded that treating acrylic plates with Fomblin could yield characteristics comparable with those of glass. However, during a two-dimensional experiment, a clearly established difference in propagation was obtained along the back glass plate in contrast to the front acrylic plate, which had been previously treated with Fomblin (Figure 3.12).



- α Glass
- β Acrylic plate, untreated
- γ Acrylic plate with bonded cellophane layer
- δ Acrylic plate treated with household cleaner, washed and dried
- ε Acrylic plate coated with Fomblin

FIGURE 3.11. Comparison of the Oil Front Position Between Glass Plates to That of Oil Fronts Between Acrylic Plates Subjected to Different Surface Treatments

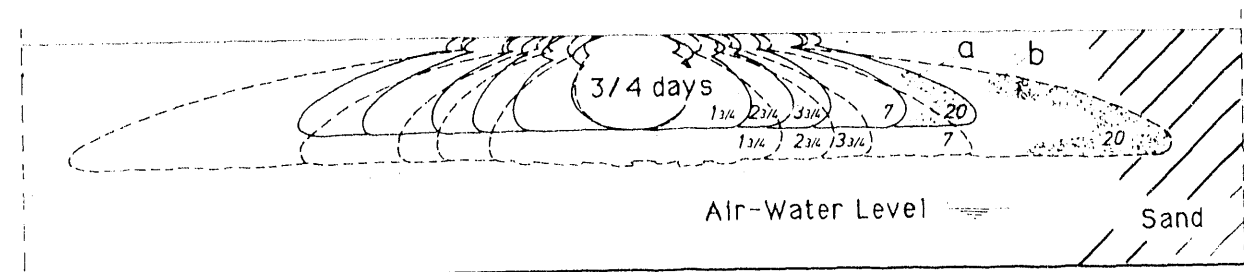
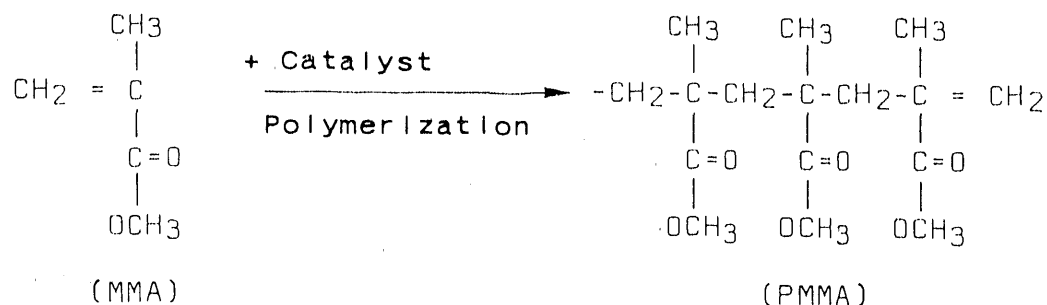


FIGURE 3.12. Propagation Forms (a) Along Glass Wall, (b) Along Acrylic Wall Previously Treated with Fomblin

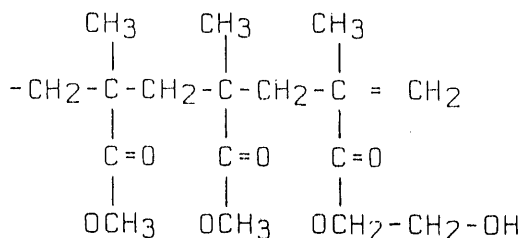
As seen in Figure 3.12, the surface treatment with Fomblin did not yield a propagation of oil similar to that for glass walls. Thus, we dropped the idea of applying a hydrophilic coating. Next, we investigated whether it would be possible to reach the same hydrophobicity by chemical conversion of the plastic surface.

Hydrophilicity implies that the surface must be chemically polar. Molecules of saturated hydrocarbons are nonpolar on the whole. The idea was developed of creating a hydroxyl group, -OH, on the nonpolar plastic surface because the polar OH-bond reacts very easily. The reaction depends on the fact that hydroxyl groups, which are similar to water, can receive as well as give off H⁺ ions and produce acids as well as bases. It had to be proven whether the hydroxyl group bound to the plastic surface would perform better by polymerizing the plate or by grafting the polymerized plate.

Polymerization means the connection and linkage of separate molecules. Polymethyl methacrylate plates are obtained by the polymerization of methacrylate (MMA) by means of a catalyst such as benzoyl peroxide or azobisisobutyronitrile.



Glycols are compounds that possess two adjacent carbon atoms for each OH group. By adding glycolmethacrylate at a suitable time before the final polymerization of the surface, hydrophilization should be obtained because the above polymethyl methacrylate (PMMA) converts into:



In addition to the use of glycolmethacrylate, identical experiments were also carried out with HEMA-96% (2-hydroxyethyl methacrylate-96%) 200-ppm

hydroquinone from Rohm and Haas, Co., Philadelphia, Pennsylvania. The optimum amount of catalyst and polymerization temperature, as well as the best time to add the hydroxyl donor had to be found experimentally. All of the experiments were unsuccessful.

On the basis of work performed in the Department of Chemistry at ETH, the graftability of four unsaturated organic groups containing silicone (OF-Silicone U of the 201, 212, 222, and 701 types; Bayer, Leverkusen, Federal Republic of Germany) was investigated on PMMA as well as on hard polyvinyl chloride (PVC) plates. Silicone 222 and 701 were successfully grafted onto the surface of PMMA plates. An additional graft of Silicone 701 on PVC succeeded. With Silicone 212, no or only a very weak graft was possible. However, even with only a slight graft of any of the silicones, transparency was lost.

The surfaces of the grafted plates were investigated with an infrared radiation (IR) spectroscope to determine the thickness of the graft. The plates became transparent again only after nearly the entire grafted silicone layer had been polished off with a clay and water paste. The grafting was shown to be practically ineffective with regard to hydrophilization. The grafted surfaces were approximately as oleophilic as each of the nontreated plastics.

The problem of the hydrophilization of plastic is by no means trivial. This is shown by the fact that even up to now the optical and cosmetics industries have not found a generally satisfactory solution. Their interest in the hydrophilization of transparent plastic stems from the manufacture of contact lenses for correcting vision.

Because of our inability to find an alternative to glass, we were forced to manufacture the hole arrangement, shown in Figure 3.10, in glass plates despite the doubt of the glass specialists. The careful planning regarding the selection of the material and the procedure for the manufacture, installation, and reinforcement of the quartz glass plates had its reward. The flume walls held up to all loads and fulfilled their purpose with complete satisfaction.

3.4 APPARATUS FOR PACKING A HOMOGENOUS ISOTROPIC POROUS MEDIUM

For the experimental simulation of water-oil displacement, the maximum possible homogeneity and isotropy of the porous medium was necessary. To develop a method to pack the most homogenous and isotropic porous medium possible, different methods for filling the flume with sand were investigated. Among other methods tried were filling the flume while it was full of water (a type of sedimentation) and sifting the sand by hand, which was very time consuming. In spite of the relatively steep grain-size distribution curve (Figure 3.1a) and thus a smaller possibility of particle segregation, small differences in the release height above the sand fill led to visually observable variations in the arrangement and the thickness of the porous medium (Figure 3.13).

By far the best results were produced when the sand was applied, with little free fall, as a thin layer over the width of the flume (15 cm) on the already existing fill, which caused negligible compression of the underlying layer. This was accomplished by allowing the sand to trickle through a slit from a container filled with sand, while the container moved back and forth over the length of the flume (Figure 3.14). The slit opening had to be adjusted to match the grain diameter and the filling velocity.

The slit length was chosen as large as possible and was about the same as the flume width. The slit on the sand container was placed exactly above the fill being built up. Then, the sand container was raised synchronously as the sand fill increased in height. In this way, the earlier conditions of no free fall at the moment of introduction and negligible compression were fulfilled.

The sand container could move vertically and was mounted on a cart (Figure 3.15). The cart could be moved horizontally on rails parallel to the flume. In preliminary tests, the sand container, which was fixed to the cart moving back and forth over the flume, was gradually raised. The effects of each jump and the variability of the conveyor velocity were visually discernible in the fill (Figure 3.13). From this, we concluded that the sand container must be moved with a very constant velocity and raised with as small steps as possible to minimize stratification. This meant that the sand container movement apparatus had to be completely automated.

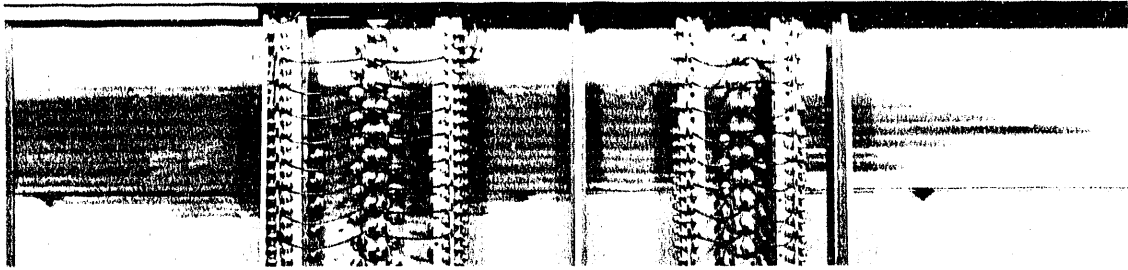


FIGURE 3.13. Stratified Filling in Flume

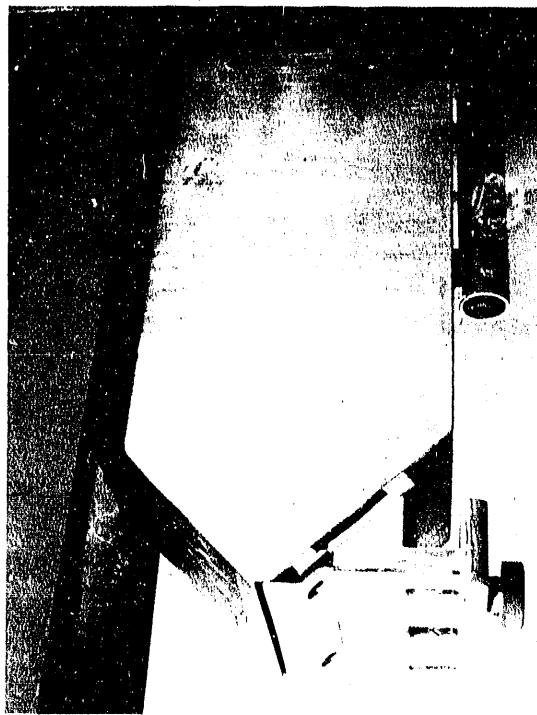


FIGURE 3.14. Sand Container and Slit

To avoid vibrations and the resulting compression of the porous medium, the rails could not be mounted on the flume. We were forced to use the overhead rails used by the gamma attenuation source-detector cart (see Chapter 5.0). To guarantee the constant velocity of the sand container during its passage along the flume, a space was provided on both ends of the flume for

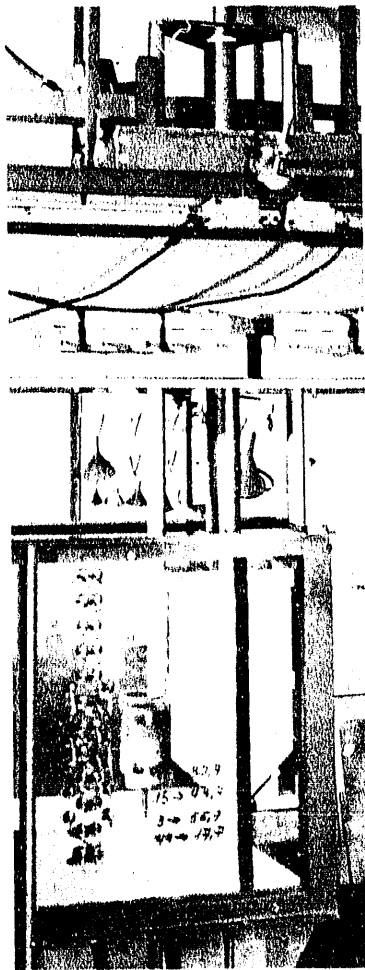


FIGURE 3.15. Sand Cart and Sand Container

the acceleration of the cart after it reversed direction. Moreover, we had to be able to push the source-detector cart to the side during sand filling. Thus, the overhead rails were 4.8 m in length compared to the flume length of 2.85 m.

Long steel bars were used to reinforce the sand cart on the rails of the source-detector cart and to lower the sand container to the bottom of the flume. Based on the requirement that the width of the container slit should be almost the same as the width of the flume, the sand container could only be slightly narrower than the width of the porous medium. Because no vibrations

of the flume were allowed, lateral movement of the sand container against the flume walls had to be prevented. The small clearance of the sand container from the flume walls, the weight of the container (several kilograms), and the acceleration of 1 m/sec^2 required that a very stable and precise supporting frame be built for the sand container. Without the necessary rigidity and precision of the vertical lift for the sand container, the container (as shown by experiment) vibrated more easily and touched the nearby flume walls, whereby the vibrations became still stronger, and consequently, the in-place porous medium was compressed.

The horizontal drive of the sand cart was powered by a 0.08-hp electric motor (Figure 3.16). The strength of the motor was selected to accelerate the sand cart (consisting of sand container, bars, and sand filling apparatus) to the required driving velocity. The acceleration of the sand cart occurred on a stretch of the overhead rails beyond the length of the flume so that when the sand cart entered the flume, it had already reached its constant working velocity. The reversal in the direction of the cart occurred automatically by using contact switches mounted on the rails. They were activated by a guide shoe attached to the cart (Figure 3.17).

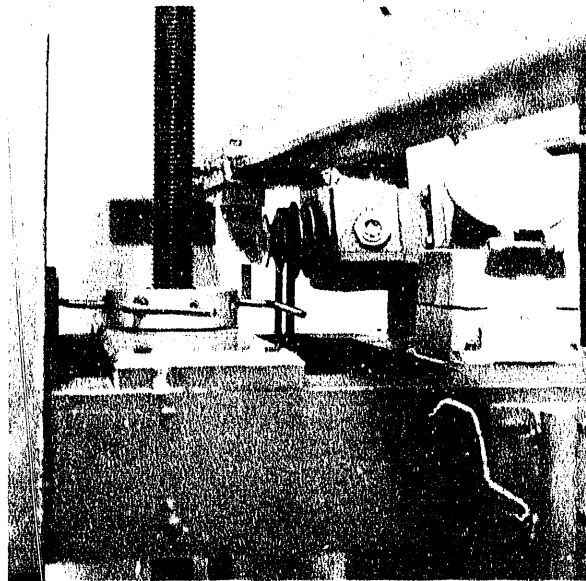


FIGURE 3.16. Motor Drive of the Sand Cart

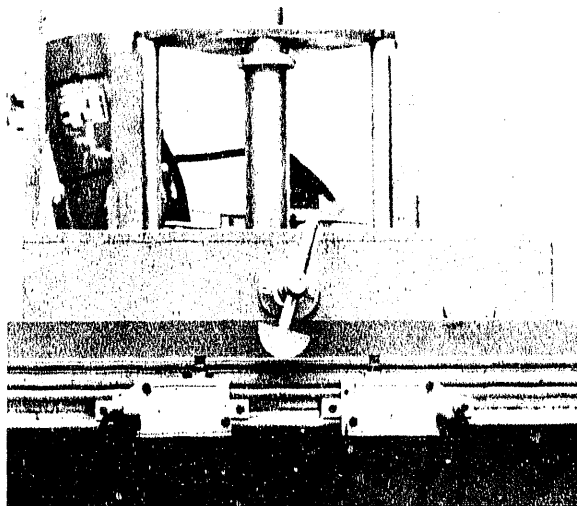


FIGURE 3.17. Device to Switch the Direction of the Sand Cart

The lifting of the sand container had to occur synchronously with the ascent of the porous medium. To do this, a threaded rod was mounted adjacent to the support rods of the sand container (Figure 3.18). A threaded collar nut sitting on a Teflon[®](a) pad turned on the threaded rod. The collar nut was supported by a plate mounted on the sand cart.

Buffer cams at each end of the overhead rails rotated the collar nut an adjusted amount on each pass, thereby lifting the sand container. The rotation of the collar nut also produced a braking action on the sand cart, which was a welcomed bonus, shortly before it reversed direction.

The running speed of the cart, regulated in three stages, was 1 m/sec. The incremental height increase per passage equaled 0.15 mm, thus less than half the average grain diameter. The packing of a porous medium to a height of 60 cm required 4000 passages. With a flume length of 3 m, this equaled 12 km, which required 12000 sec at a velocity of 1 m/sec. Thus, approximately 4 h had to be allotted to fill the flume and allow the cart to reverse directions.

(a) Teflon is a trademark of E. I. duPont de Nemours Co., Inc., Wilmington, Delaware.

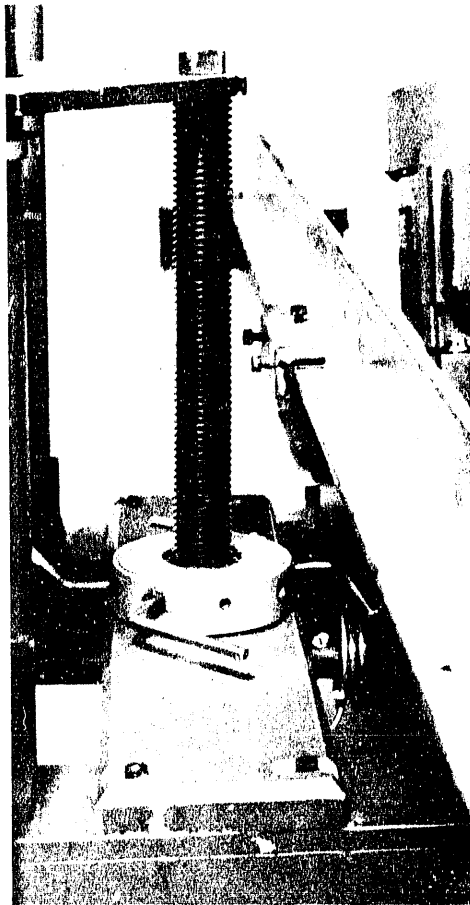
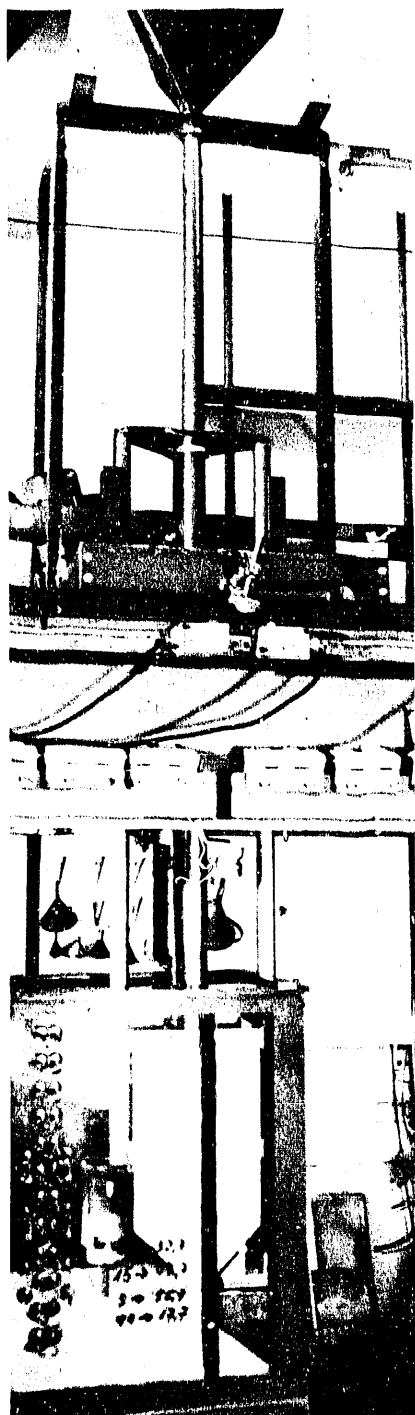


FIGURE 3.18. Sand Container Lifting Device

The sand container was filled with sand through a tube connected to a sand bin on the upstairs floor (Figure 3.19). A funnel was attached to the sand cart and supported by a frame. At one of the ends of the overhead rails, a cam attached to a louver in the tube could be triggered, thereby releasing sand from the bin and feeding the funnel. The volume of sand could be regulated by adjusting the frame.

In a quartz-sand porous medium, a petroleum derivative is the nonwetting fluid compared to water. Accordingly, a petroleum derivative will stay in the larger pores of an area with high water saturation. This fact and the fact that there are larger pores along a smooth wall (Figure 3.2) are the reasons why a petroleum derivative collects preferentially along a hydrophilic wall. To reduce this phenomenon, which would have altered flow near the wall, a



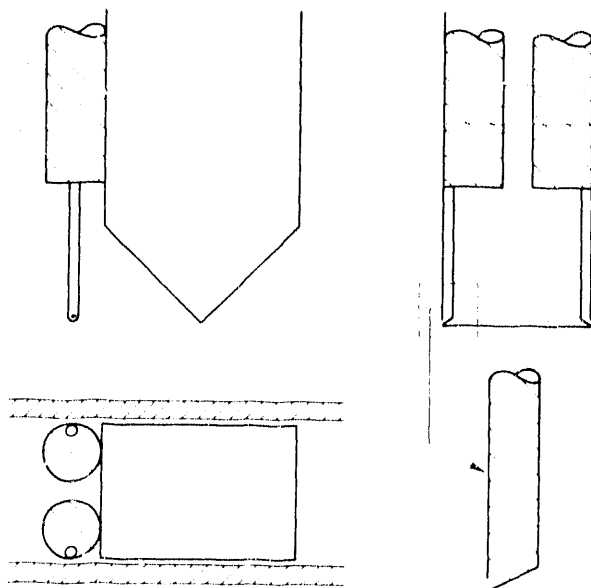
(a)



(b)

FIGURE 3.19. Sand Filling Mechanism (a) Full View and (b) Tube Coming from Upper Floor

relatively fine sand was applied along the flume walls during filling. This was done over a very local area, limited to four to five grain diameters (Figure 3.2). The particle diameter of the fine sand was calculated based on the packing model for spheres (Manegold 1955; von Englehardt 1960) and was 5% to 10% of the diameter of the quartz sand. The fine sand was applied from two adjacent jars attached to the main container. The jars were filled with the fine sand at the start of the filling procedure. Nozzles directed the fine sand against the walls. The flow of the sand could be regulated by opening slits (see Figures 3.20a and b).



(a) Engineering Sketch

(b) Photograph

FIGURE 3.20. Fine-Sand Applicator

To maximize the available flume length, vertical sliding end walls were designed. Bromatized steel sheets were automatically raised from below as the sand filled the flume. Each metal sheet was bolted to a metal bar, and the metal bar was welded to a collar nut on a vertical spindle (Figure 3.21). The seat for the rotatable spindle was bolted to the floor. The metal end walls were raised as the spindles rotated an adjustable amount with each passage of the sand cart. The rotation of the spindle was initiated by a cam, attached to the cart, which struck cogs on the spindle.

To eliminate the danger of several sand grains wedging between the steel plate and glass wall, the distance from the front of the steel plate to the glass walls was chosen larger than one grain diameter. Grain wedging could have resulted in a point load and thus a definite cracking danger for the glass. To prevent sand from trickling between the steel plate and glass wall, thin rubber strips were pasted on the glass walls to fill the gap between the steel plate and glass wall. The rubber strips were covered with a thin copper foil so that if the sand container touched them, they would not be damaged. The copper foil was pasted onto the glass wall and both sides of the rubber strips with an SAI-resistant glue.



FIGURE 3.21. Sidewall Sheet Metal Lifting Device

4.0 PRESSURE GAGE APPARATUS

Both the viscosity and density of air are smaller than the viscosity and density of water or of the petroleum derivative (SAI). Accordingly, the potential gradient or pressure gradient in air must be smaller than those in water or the SAI. In any case, they are so small that the air potential and thus also the air pressure can be, in practice, assumed constant over space and time. Therefore, it was unnecessary to measure the air pressure. Thus, the problem was limited to the development of a pressure gage system for the selective measurement of the pressure in the water and the petroleum derivative.

4.1 REQUIREMENTS

The requirements of the pressure gage system were

1. a pressure measurement accuracy of ± 0.5 -mm H₂O resulting from the required saturation measurement accuracy of $\pm 2\%$ (see Chapter 6.0) - On the flattest part of the quartz-sand capillary pressure head curve, a change of 1 cm H₂O produced a 40% change in saturation. Thus

$$(2\%/40\%) (10 \text{ mm H}_2\text{O}) = 0.5 \text{ mm H}_2\text{O}$$

2. a tolerated volume displacement of less than 1 mm³ - The fluid in the pressure measurement system was free to flow in and out. Volume changes in the pressure measurement system were caused by pressure changes in the porous media and external pressure and temperature changes, as well as volume displacements during the automated switching to sense pressure at multiple probes. A change in the internal fluid volume was equivalent to a change in saturation in the porous media. Thus, the degree of error in the pressure measurement can be inferred from the capillary pressure head curve. A volume displacement of less than 1 mm³ was tolerated because this was smaller than the volume of several pores.
3. a response time that did not exceed 1 sec
4. the flexibility of a selective pressure measurement over time and space - Selective pressure measurement refers to the pressure measurement of one of the immiscible fluids (water or oil) with the measurement independent of the pressure in the other fluid.

4.2 CONSTRUCTION OF THE PRESSURE GAGE SYSTEM

The pressure gage system consisted of probes as pressure sensors, connecting tubes and stopcocks, and a device for recording the pressure (Figure 4.1). Because of the experimental pressure range, a transformation of the measured pressure into an electrical signal was needed. Thus, the pressure recording apparatus consisted of a linear response pressure transducer. The experimental determination of the spatial and temporal progress of the pressure in both fluids was limited to pressure measurements at individual locations. Thus, one pressure gage system had to be constructed for each of the fluids.

4.2.1 Probes

A probe is similar to a diaphragm. The main function of a probe is to selectively transmit the pressure of the specific fluid for which it was designed. Selective pressure transmission can be attained by the suitable choice of surface chemistry for the probe material. The porous probe material must be more wetted by the fluid whose pressure is to be measured. The porosity or the maximum allowable pore size, and thus the grain diameter of the probe material, must be selected so that the initial bubbling pressure of the nonwetting fluid is larger than the maximum possible pressure that might be encountered. Furthermore, a probe should prevent sand particles from entering the pressure gage system. Finally, the probe should be chemically resistant to the various fluids with which it might come in contact.

The above requirements for the probe material stipulated a porous hydrophilic material for pressure measurement of the water and a porous oleophilic material for pressure measurement of the petroleum derivative. Known hydrophilic porous materials are mineralogical filters from diatomaceous soil, as well as sintered quartz glass spheres. Porous plastics are of organic nature and are thus oleophilic. The wetting characteristics of sintered bronze or steel filters are less clear and less stable than those of the other materials.

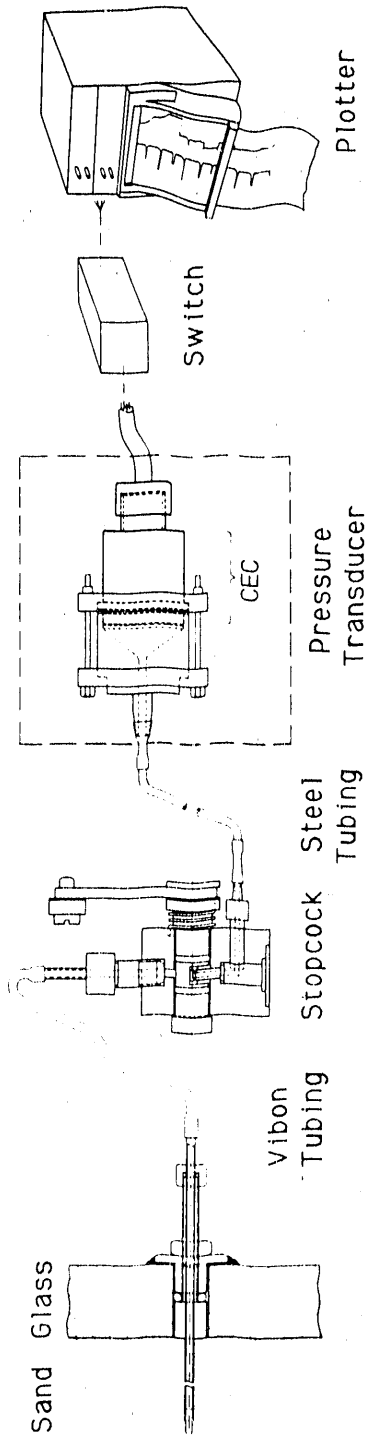


FIGURE 4.1. Sketch of the Pressure Gage System

From the desired nonwetting fluid bubbling pressure, a maximum allowable pore size was chosen. In addition, we were interested in good permeability for the probe material, based on the requirement of a small response time. From these contrasting requirements arose the need for a probe material with a pore-size distribution curve that was steep and equal to the value of the maximum acceptable pore size. Sintered glass with pores of a very uniform size is obtainable commercially. Sintered quartz glass was finally used as the material for both the hydrophilic and oleophilic probes because of the exacting and favorable characteristics of sintered quartz glass compared to that of porous plastic and because the glass could be made oleophilic by a surface treatment with silicone. The advantage of the sintered quartz glass was that it allowed a uniform probe fabrication technique, independent of whether the probes would be hydrophilic or oleophilic.

The shape of the probes was selected to yield the largest surface area possible. A large surface area was desired so that at small saturations, and consequently a relatively small contact surface with the wetting fluid, a representative pressure could be obtained. A larger surface area also yielded a smaller response time. The initial required pressure accuracy of ± 0.5 mm H₂O, the generally nonlinear pressure distribution in the unsaturated zone, and the requirement that the probes minimally compress the unconsolidated sand grains when inserted dictated that the probes be small in the measurement plane of the two-dimensional experiment. In addition, two-dimensional experiments imply that the parameters are constant in the third dimension; thus, any size could be chosen for the third dimension. These arguments led us to select the longest possible cylindrical shape with the smallest possible diameter and the deepest possible hollow core to allow easy and fast fluid exchange.

Because of the fragility of thin layers of sintered glass, the inside diameter of the probe had to be as small as that allowed by the manufacturing process. The front of each probe was finished to a point. This was done to lower the amount of sand compression while inserting the probe, but also to lower the frequency of breaking while pushing the probe into the unconsolidated sand.

For the first attempt to manufacture the probes, the largest and flattest filter plates of sintered quartz glass obtainable commercially were chosen. These filter plates had a diameter of 40 mm, a thickness of 3 mm, and a pore diameter of between 20 to 40 μm (Pyrex:^(a) 4-812-42). The selected average porosity of 0.3 was a compromise between the goal of the smallest possible pore diameter for a high bubbling pressure and the goal of a short response time produced by high permeability. The plate permeability specified by the manufacturer was not representative of the probes because the permeability of the probes was lowered during the manufacturing process.

The first manufacturing process consisted of sawing the filter plate into square bars. These square bars were then shaped into cylinders by using a centerless grinder consisting of two large, closely spaced grinding rollers turning against each other. The cylinders were given a point and a hollow core using a lathe. Figure 4.2 shows the stages of manufacture. In relation to the starting material, the permeability of the machined probes was reduced by a factor of 50 because of the accumulation of grinding dust in the pores.

Because of the great reduction in permeability and the relatively high damage rate during manufacture, a second manufacturing technique was devised. In this technique, the cylindrical bars of sintered glass were obtained directly from holes made in the starting material using a diamond drill. Finally, the hollow core was drilled out and the point turned. The permeability of a probe manufactured by this method was only five times smaller than that of the starting material. A decrease in pore plugging could not be obtained by treating the completed probes in an ultrasound bath. Only boring at the steepest possible angle of attack relative to the cutting surface brought improvement.

Figure 4.3 shows a sketch with the dimensions and a photographic enlargement of a probe manufactured using the second technique.

(a) Pyrex is a trademark of Corning Glass Works, Corning, New York.

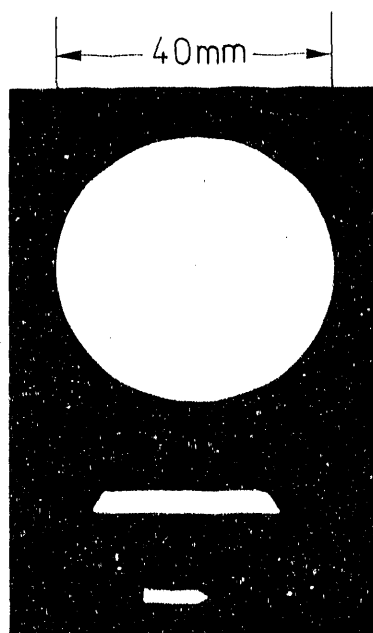


FIGURE 4.2. Plate, Rod, and Probe of Sintered Quartz Glass (from top to bottom)

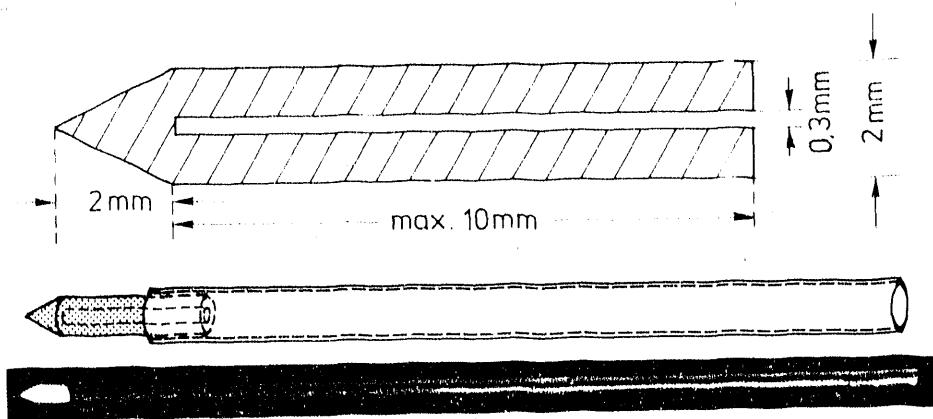


FIGURE 4.3. Photograph and Sketch of Probe and Probe Holder

The conductance, L ($L^2 T^{-1}$), of the probes was calculated as the flow rate, Q ($L^3 T^{-1}$), divided by the pressure difference across the probe, Δh (L). Figure 4.4a shows a plot of the conductance versus the pressure difference for

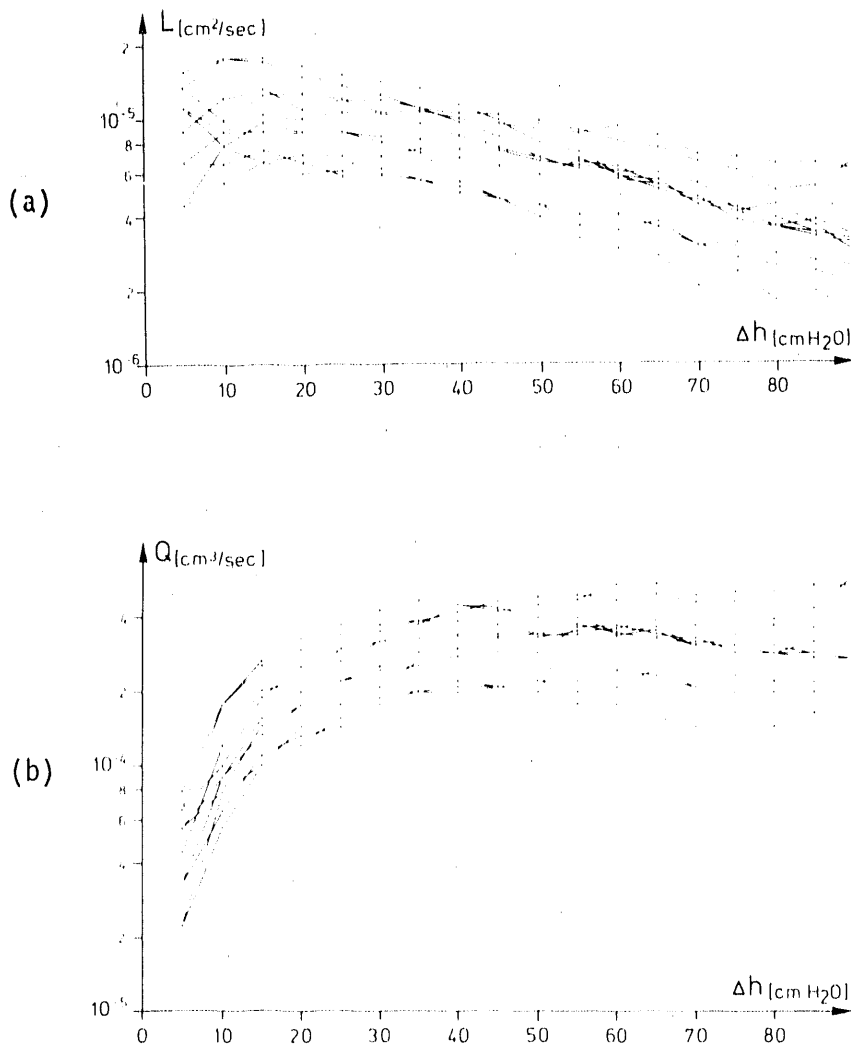


FIGURE 4.4. Conductance (a) and Flow Rate (b) of the Probes as a Function of the Pressure Difference

randomly chosen probes. From Figure 4.4a, one can see that the average conductance of the probes came to $\approx 8 \cdot 10^{-6} \text{ cm}^2/\text{sec}$, assuming laminar flow. The decrease of the conductance at larger pressure differences is probably a result of the transition to turbulent flow and thus a more quadratic velocity-pressure relation. Figure 4.4b shows a leveling of the flow rate, Q , to a constant value for pressure differences greater than 25 to 30 cm. Only when Δh was less than 20 cm was Δh proportional to Q .

Some probes were treated with a silicone solution to render them oleophilic. The probes were cured in a 35-fold dilution of the Bayer silicone emulsion H for 3 h at 240°C. It was demonstrated experimentally that such a silicone film was resistant against the very aggressive SAI, which was used as a representative petroleum derivative. The use of SAI was stipulated by the saturation measurement method used.

The experimental determination of the nonwetting fluid bubbling pressure was performed according to the setup shown in Figure 4.5. The experiment shows the principle of selective pressure measurement. With an untreated quartz-glass filter plate saturated with water, the water was the wetting fluid and fuel oil was the nonwetting fluid. When the filter plate was previously treated with the silicone solution, the water was the nonwetting fluid, the fuel oil was the wetting fluid, and the plate was consequently saturated with oil. The experiment confirmed that the wetting fluid pressure remained constant while the nonwetting fluid pressure was varied, so long as the pressure difference did not exceed the bubbling pressure of the filter plate.

The experimental determination of the bubbling pressures in the probes yielded the average values shown in Table 4.1. The nonwetting fluid bubbling pressure of the probes, H_E , is exactly the opposite of the capillary suction of the wetting fluid in the probe's largest pores.

To prevent drainage of the probes by the oven-dried porous medium, the maximum suction of the porous medium (the capillary suction of the smallest pores in the porous medium, on the fluid in the probes) must be smaller than the minimum suction of the probes (the capillary suction of the largest pores of the probe). According to Figure 2.1, the maximum suction of the sand used in the experiments was about 50 cm H_2O for water relative to air. Thus, for a petroleum derivative, the maximum suction relative to air was about half of that, or about 25 cm of oil-column height. With $\rho_o = 0.85$, this equals about 21 cm H_2O (Schiegg 1979, p. 45). These values clearly lie below the experimentally determined average bubbling pressures listed in Table 4.1; that

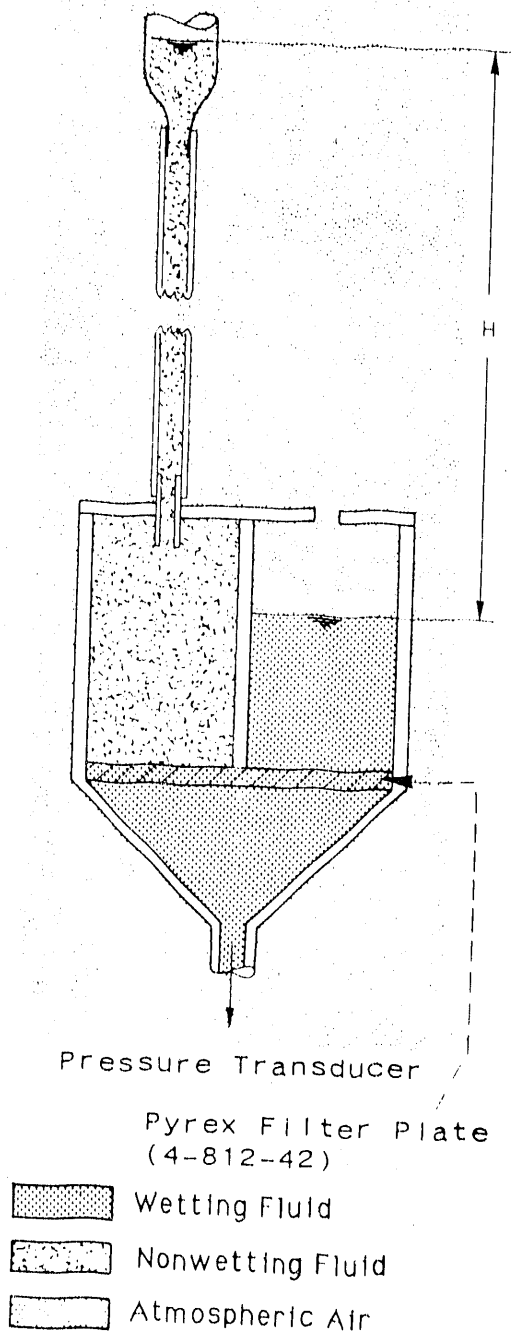


FIGURE 4.5. Experiment Setup to Illustrate Principle of Selective Pressure Measurement

TABLE 4.1. Experimentally Determined Nonwetting Fluid Bubbling Pressures in the Probes Saturated with Wetting Fluids

<u>Wetting Fluid</u>	<u>Bubbling Pressure</u>	<u>H_c in cm H₂O</u>
Water	Air	108
	Fuel oil	36
Fuel oil	Air	56
	Water	62

is, 108 cm H₂O for air-entry into a water-saturated probe and 56 cm H₂O for air entry into an oil-saturated probe. Therefore, the danger of the oven-dried porous medium draining the probes, thus allowing air to enter the probes, did not exist.

To thrust the probes into the unconsolidated dry sand, the probes were attached to the thinnest-walled, most rigid stainless-steel tubes available. These tubes were medical syringes with an inside diameter of 2.05 mm and an outside diameter of 2.5 mm. To ensure that the two-dimensional experiments were constant in the third dimension (along the axes of the probes), the steel tubes were cut to various lengths. The probes were then pushed into the porous medium to various horizontal depths.

Because of capillary suction in the porous probe material, there was a danger that while gluing the probes into the steel tubes, the glue would plug up the hollow core. To prevent this, tests were made to find the best method to glue the probes into the steel tubes along the length l shown in Figure 4.6. A thin layer of fast-bonding glue was used. However, upon shearing the probes, the tests showed that the cross section was extensively plugged with the glue. Thus, even the extremely short bonding time of only a few seconds was too long to prevent the very runny glue from infiltrating the probes. Household araldite was found to be nonresistant to SAI. However, a chemically resistant and very viscous special araldite from Ciba-Geigy Corporation (Greensboro, North Carolina) gave satisfactory results. This special araldite consisted of two components, AV 138 and H. 998. Although a longer bonding time was required at room temperature, the relatively high viscosity produced only a slight entry of araldite into the probe.

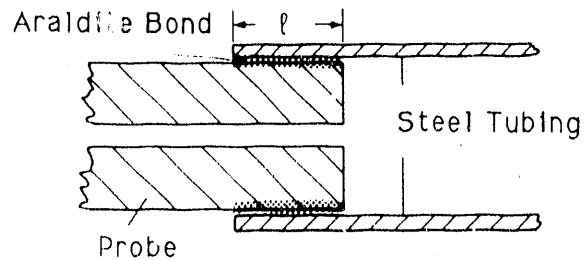


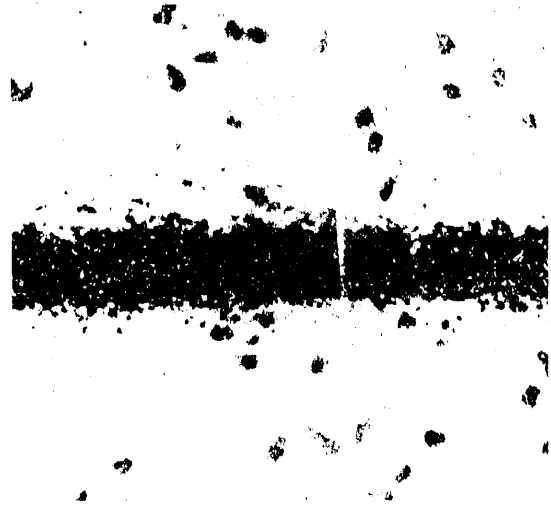
FIGURE 4.6. Gluing of Probe and Steel Tubes

The probes were inserted horizontally into the packed, oven-dried sand using a guide rod. The probes were installed through holes drilled in the glass walls of the flume. The probes could be inserted only after the flume was completely filled with sand because the filling process would have been disturbed. Although the installed probes limited the visual observation of the experiments, and the borings in the glass wall caused structural weakness, the idea of inserting probes vertically through the upper, open surface of the porous medium was abandoned for two reasons. First, the probes would have been limited to very short lengths. This would have severely increased the relative error as a result of volume displacement and increased the response time. Second, the undesired phenomenon of preferential flow of the petroleum derivative along the vertical steel tubes would be unavoidable even after going to great expense to minimize the problem.

To get an idea of the size of the disturbed area resulting from the horizontal insertion of the probes, the experiment illustrated in Figure 4.7 was performed. To see a disturbed area, a probe was inserted into a porous medium composed of clear grains and a band of black grains placed along a horizontal wall. The probe was then removed. In Figure 4.7b, one can observe from the blurred zone around the tube that the influence area of an inserted probe is probably 20 to 30 times that of the tube diameter of 2.5 mm. A comparison of the location and orientation of the grains before and after the thrusting of the probes (Figures 4.7a and 4.7c) shows that the disturbed area on both sides of the tube was two to three times smaller than the outside diameter of the influenced area, a maximum of about 0.5 cm.



(a)



(b)



(c)

FIGURE 4.7. Porous Medium (a) Before Insertion, (b) During Insertion, and (c) After Removal of Probe

Under certain experimental conditions (for example, when the local porous medium remained oven-dry for several days), the inserted probes had to be kept ready for a later pressure measurement. To prevent drying of the liquid-saturated probes, steaming the porous medium was considered, but not tried. Preliminary experiments were done to determine the performance of the pressure probes in a drying environment. The evaporation caused by a stream of warm air located 20 cm away from a water-saturated probe produced a continuous increase in the capillary suction. This was a result of the increasing curvature of the water meniscus as water was withdrawn. If the suction increased beyond the bubbling pressure of air, then the sudden entry of air caused a clear break in the progression of the measurement. If probes, initially completely water saturated, were set up in a draft-free place at room temperature, then several hours passed before the entry of air. With probes completely water saturated and inserted in oven-dried sand, the entry of air did not occur for several days. The drying of oil-saturated probes progressed even more slowly. Because of the slow drying of the probes in the oven-dried sand, fluid could be added periodically to keep the capillary suction in the probe tip below the bubbling pressure of air. Thus, every 2 to 3 days about 1 mm^3 of the fluid with which the probe was saturated was injected into the probe system. In this way, the probes could be kept ready, over an extended time, for an eventual pressure measurement.

4.2.2 Pressure Transducer

A pressure transducer converts the hydromechanical pressure of a fluid into an electrical signal. A pressure measurement can be made by detecting either a surface-specific stress or a deflection of a diaphragm, which seals off the fluid-filled system.

Detecting the deflection of a diaphragm is a distance measurement. A distance measurement can be converted into an electrical signal by using electrical induction, electrical capacitance, or a wire strain gage. A change in induction can be measured when a metal rod attached to the center of the diaphragm moves through a stationary coil within which an electric current is passing. The electric capacitance changes when the distance between the

diaphragm and a stationary plane changes. The resistance of a wire strain gage attached to the diaphragm changes in response to a deformation of the diaphragm.

The transformation of the surface-specific stress into an electrical signal can be accomplished with a semiconductor or with a diaphragm over a piezoelectric crystal. All of the above methods are found in commercially obtainable pressure transducers.

Systems based on the piezoelectric pressure gage had to be excluded from further evaluation on account of stability problems. Furthermore, because a large force on the crystal is needed to sense even the small pressures, a large diaphragm would be necessary, and this would not fulfill the requirement of a volume displacement of less than 1 mm^3 .

On the same grounds (that is, the large volume displacement and thus a poor response time and a large error in the unsaturated zone), the commercially available inductive pressure measurement systems were also excluded.

With semiconductor pressure gage instruments, the volume displacement was very small, and no undetermined stability problems were present. Yet, they were barely able to satisfy the required pressure measurement accuracy of $\pm 0.5 \text{ mm H}_2\text{O}$.

The pressure transducers based on the capacitance-measuring principle were able to satisfy the requirements as well as the wire strain gage pressure transducers that were eventually used. Moreover, the price for both types of pressure transducers was about the same. The original electrical signal from a wire strain gage could be fed directly to a chart recorder. On the other hand, the capacitance pressure transducers required an expensive oscillator and a central switching apparatus for a multiple pressure gage system, which cost several times the cost of the transducer. For cost reasons, the capacitive pressure gage system was rejected.

A single potential pressure measurement method remained using wire strain gages. We already had some experience with this type of pressure

transducer in earlier laboratory experiments. This pressure transducer satisfied the specified requirements, but the disadvantage of a wire strain gage is sensitivity to careless handling. Slight pressure on the diaphragm (contact or slight heating of the closed system by sun irradiation) was enough to damage the wire strain gage. The price was not low enough for the strain gage to be a regular stock item. Repair and delivery time took several months. The fragility of the strain gage construction was probably required for measuring vibrations, which we did not need.

On the basis of the unsatisfactory characteristics of the evaluated pressure transducers, we decided to try (in cooperation with the electronics workshop at ETH) to develop a pressure transducer that met our requirements. This was done in the hope that, after development costs, the number of pieces to be assembled would be inexpensive enough that one pressure transducer could be installed at each pressure probe site, saving us the very expensive development of special manifolds.

The specifications of the pressure transducer to be developed were overstressability, a volume displacement smaller than 1 mm^3 , and a maximum pressure gage error of $0.5 \text{ mm H}_2\text{O}$ in the measuring range of 0- to $2\text{-m H}_2\text{O}$. Because the volume displacement should be small, the diaphragm chosen must be small and rigid. The relatively small central displacement of the diaphragm required a precise method for measuring a change in position.

Our conceptual solution is shown in Figure 4.8. Our precise measuring method relied on the displacement of two lubricated glass plates sliding one on top of the other. Each glass plate had fine parallel bands, whose width equaled their distance apart. The width also equaled the maximum displacement of the diaphragm center. The attenuation of a collimated light ray through the glass plates was measured with a photo diode on the other side of the plates. The attenuation was a measurement of how much the bands overlapped, and thus of the displacement of the diaphragm center from a pre-stress position.

The main problem was the manufacture of the finest and most precise grid possible. Through photographic reduction, glass plates could be produced with

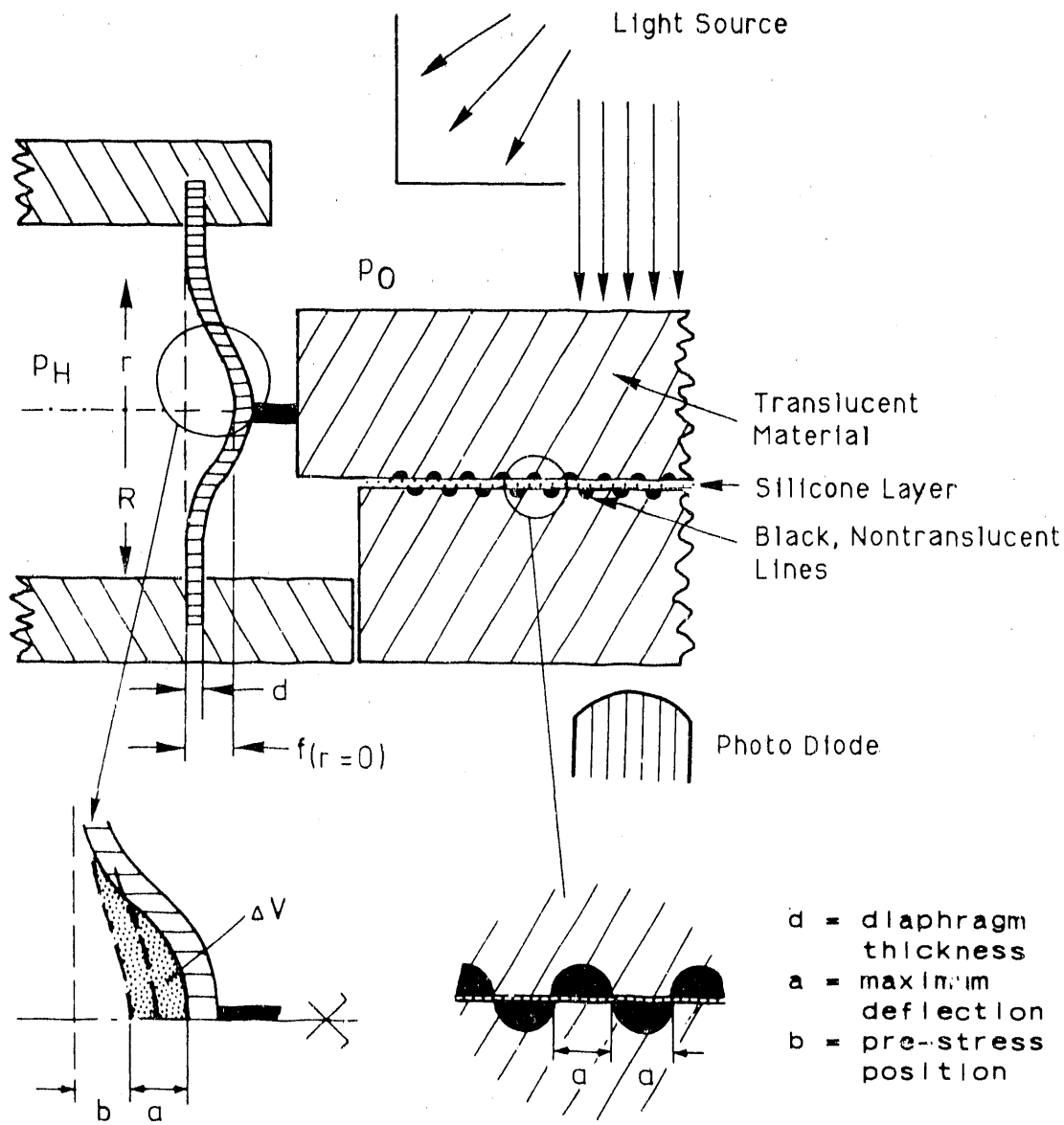


FIGURE 4.8. Diagram of the Developed Pressure Transducer

10 to 20 bands/mm. A special firm that performs precision work could produce a plate with 60 bands/mm. Another firm offered almost double the density, but for 10 times the price, which was already two-thirds the price of a wire strain gage. The maximum possible density of 100 bands/mm defined the maximum deflection, a (see Figure 4.8), in the diaphragm middle as $5 \cdot 10^{-3}$ mm for

200 cm H₂O. Because the deflection, b, resulting from the pre-stress was essentially smaller than a, then $f(r = 0) = 5 \cdot 10^{-3}$ mm could be used in the first approximation.

To size the diaphragm, we assumed that its smallest possible manufacturable radius equaled about 2 mm, thus $R_{\min} = 2 \cdot 10^{-1}$ cm. The diaphragm thickness, d, is defined explicitly in Equation (4.2) for the maximum deflection in the center of the diaphragm (at $r = 0$). The deflection of an attached diaphragm as a function of the distance, r, from the diaphragm center, and as a function of the pressure difference, geometry, and material constants amounts (DISA 1970, p. 54) to

$$f(r) = \frac{3}{16} (\rho_H - \rho_0) \cdot \frac{1 - \mu^2}{E \cdot d^3} \cdot R^4 \left(1 - \left(\frac{r}{R}\right)^2\right)^2 \quad (4.1)$$

where $(\rho_H - \rho_0)$ is the pressure difference, Δp , μ is the Poisson number, E is the modulus of elasticity, d is the diaphragm thickness, and R is the diaphragm radius. The deflection at the center of the diaphragm (at $r = 0$) is defined from Equation (4.1) as

$$f(r=0) = \frac{3}{16} (\Delta p) \cdot \frac{1 - \mu^2}{E \cdot d^3} \cdot R^4 \quad (4.2)$$

With $\mu = 0.3$ and $E = 2.1 \cdot 10^6$ kg/cm², with the deflection (tolerated for 200 cm H₂O or for $\Delta p = 0.2$ kg/cm²) in the diaphragm middle = $5 \cdot 10^{-4}$ cm, and with $R = R_{\min} = 2 \cdot 10^{-1}$ cm, the diaphragm thickness of a steel diaphragm is calculated from Equation (4.2) as

$$d = \sqrt[3]{\frac{3}{16} \cdot 0,2 \cdot \frac{(1-0,09)}{2,1 \cdot 10^6 \cdot 5 \cdot 10^{-4}} \cdot (24 \cdot 10^{-4})} = 0,0037 \text{ cm} \quad (4.3)(a)$$

(a) Equations were taken directly from the German text and, in some cases, use a different notation. For example, 0,01 = 1/100; whereas in this text, 1/100 would be shown as 0.01.

A steel diaphragm 0.0037 cm thick could be manufactured.

The infinitesimal portion of the volume displacement as a function of the local deflection of the diaphragm is

$$d(\Delta V) = 2 \cdot \pi \cdot r \cdot dr \cdot f(r) \quad (4.4)$$

The integration of Equation (4.4) over the entire diaphragm leads to the determination of the volume displacement function, ΔV :

$$\begin{aligned} \Delta V &= 2 \cdot \pi \cdot \int_0^R f(r) \cdot r \cdot dr && \text{substituting Equations (4.1) and (4.2)} \\ &= 2 \cdot \pi \cdot f(r=0) \int_0^R \left(1 - \left(\frac{r}{R}\right)^2\right)^2 \cdot r \cdot dr \\ &= 2 \cdot \pi \cdot f(r=0) \int_0^R \left(1 - 2\left(\frac{r}{R}\right)^2 + \left(\frac{r}{R}\right)^4\right) \cdot r \cdot dr \\ &= 2 \cdot \pi \cdot f(r=0) \left\{ \int_0^R r \cdot dr - \frac{2}{R^2} \int_0^R r^3 \cdot dr + \frac{1}{R^4} \int_0^R r^5 \cdot dr \right\} \\ &= 2 \cdot \pi \cdot f(r=0) \left\{ \frac{R^2}{2} - \frac{2}{R^2} \left(\frac{R^4}{4}\right) + \frac{1}{R^4} \left(\frac{R^6}{6}\right) \right\} \\ &= 2 \cdot \pi \cdot f(r=0) \left\{ \left(\frac{1}{2} - \frac{1}{2} + \frac{1}{6}\right) \cdot R^2 \right\} \\ &= \frac{1}{3} \cdot \pi \cdot f(r=0) \cdot R^2 = \frac{\pi}{16} \cdot (\Delta p) \cdot \frac{1 - \mu^2}{E \cdot d^3} \cdot R^6 \end{aligned} \quad (4.5)$$

From Equation (4.5), the maximum volume displacement associated with a pressure difference of 200 cm H₂O equals

$$\Delta V_{max} = \frac{\pi}{3} \cdot 5 \cdot 10^{-4} \cdot (2 \cdot 10^{-1})^2 = 2,1 \cdot 10^{-5} \text{ cm}^3 = 0,021 \text{ mm}^3 \quad (4.6)$$

Although a maximum volume displacement of only 2/100 mm³ was more satisfactory compared to the wire strain gage and the capacitive pressure gage

methods, and although damaging the pressure transformer by overloading was excluded, the further development of the light attenuation pressure transducer had to be discontinued because the intensity of the light source could not be held stable enough. No improvement could be attained by using a reference light source or by any other economical methods.

Thus, allowance was made for the fragility of the wire strain gage. Four CEC-4-437-type pressure transducers for a low-pressure range were ordered. The most important specifications of these strain gages were

- pressure range - 0 to 10 psi = 0 to 0.7 kg/cm^2 = 0 to 7 m H₂O.
- overloadability - Twofold nominal pressure over 3 min caused a zero error <0.5% of the maximum initial current.
- maximum feed current - 12-V direct current voltage or alternating current.
- maximum initial current - 40 mV.
- linearity and hysteresis - Error by nonlinearity and hysteresis lay within $\pm 1\%$ of the maximum initial current (based on adjusted straight line).
- thermal sensitivity - Within 0.018% of the full deflection per 1°C in the compensated temperature range of -54° to +121°C.
- special characteristics - The initial current allowed the signal to be led directly to a recorder without strengthening. The volume displacement for 7 m H₂O came to $5 \cdot 10^{-4} \text{ cm}^3$. By using Equation (4.5), a volume displacement of 0.143 mm³ was calculated for 2 m H₂O, which is approximately seven times larger than that calculated in Equation (4.6). The fluid whose pressure is measured comes in contact with stainless steel, which was found to be resistant to the SAI and caused no mercury precipitation.

The CEC-4-327 pressure transducers (Figure 4.9) are differential transducers because they measure a difference between the fluid pressure and the pressure on the back side of the diaphragm. Because the back side of the diaphragm is in contact with the free atmosphere during the experiments, the actual pressure of the fluid was determined relative to the instantaneous atmospheric pressure, P_0 . This assumes that the air pressure within the porous medium was the same as the atmospheric pressure at the pressure probe.

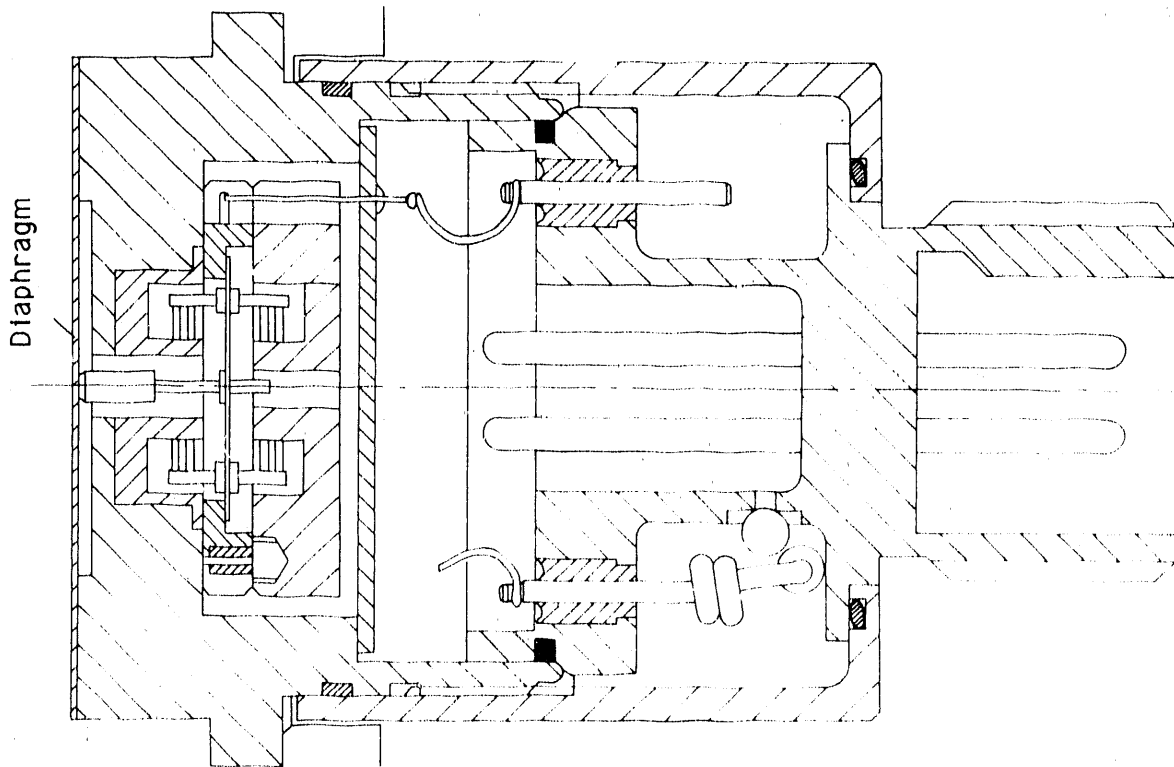


FIGURE 4.9. Schematic Diagram of a CEC-4-327 for Low-Pressure Range

The differential pressure transducer was found to be more convenient because barometric pressure fluctuations could not influence the pressure measurements compared to an absolute pressure gage, whose diaphragm seals a vacuum on the back side. Despite closed doors and windows during very windy weather, the air pressure within the porous media was not equal to the instantaneous atmospheric pressure. The delayed pressure adjustment within the porous medium made an exact pressure measurement impossible to achieve.

Test experiments showed that the pressure transducers performed more poorly than the specifications given by the manufacturer. To compensate for somewhat longer delivery terms, the manufacturer declared its willingness to screen for four pressure transducers with the smallest possible error caused by nonlinearity and hysteresis. Because we needed only about one-seventh of the available working range, we could search for the most favorable location

with respect to linearity and hysteresis. The permanent pre-stress of the diaphragm, so as not to fall into the area of its zero point, was assumed to be 2 to 3 dm in an effort to not unnecessarily lengthen the tubing system. Because of the precautions mentioned, the error caused by nonlinearity and hysteresis was found to be negligible. The attained pressure gage accuracy at more than 1 m H₂O lay below 0.20 mm H₂O. The pressure transducers were isolated by small Sagex (Bio Medical Products, Inc., Boulder, Colorado) containers to carefully protect them from local temperature variations.

4.2.3 Switching Apparatus

The price of each pressure transducer came to about 1500 Swiss francs (U.S. \$1000). For the money available, so few transducers could be purchased that simultaneous pressure measurements would be limited to a relatively small number of pressure probe sites. A switching apparatus had to be installed so that a pressure transducer could be used alternately for several pressure probe sites. The number of connections per pressure transducer was about 24. Such an apparatus requires a switching manifold with many connection ports on a main conduit leading to the pressure transducer.

Because one of the most standard requirements for the pressure transducer was a small volume displacement (about 0.10 mm³/2 m H₂O pressure difference), the same requirement must also be set for the switching manifold. Considering the desired minimum volume displacement, the switching manifold, as well as the whole pressure gage system, had to be capable of being completely filled with either one of the two liquids as easily as possible and with the certainty that no air would enter. A switching port was considered sealed if the liquid loss within 24 h at a pressure of 150 cm H₂O came to less than 0.1 mm³.

Scanivalve switching manifolds (Scanivalve Co., San Diego, California) were very compact, small, handy, and available with a motor to make the switching process automatic. However, precipitation and deposition of mercury from the SAI was caused by the materials in the switching manifold, which led

to clogging and looseness. Repairs to the manifold were very difficult to make. Considering the very high price of the switching manifold, it did not seem sensible to buy it.

Precision glass stopcocks would have met the requirement of a small volume displacement. However, they were rejected for two reasons. First, no lubricant could be found that would not loosen when in contact with the SAI nor cause a permanent locking of the stopcocks. Second, precision glass stopcocks could not be manufactured in small sizes, and thus a glass stopcock manifold of two dozen three-way stopcocks would have been very large and thus have obstructed the visual observation of the oil propagation. In an effort to obtain the shortest possible connection span, the stopcock manifolds were placed beside the pressure probes, on the transparent glass side wall.

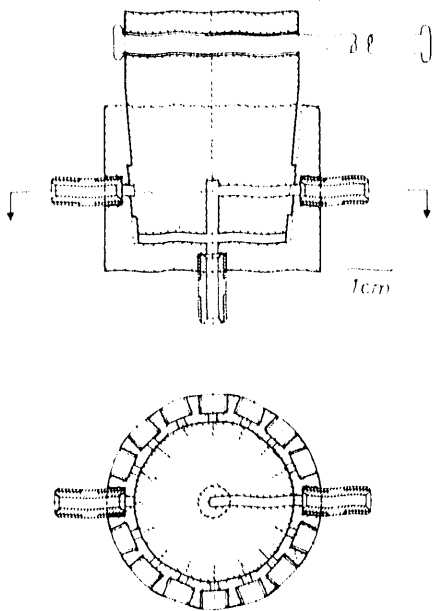
Because affordable switching manifolds were not satisfactory, we had to construct our own. The goal was a multiple-connection stopcock that, in addition to fulfilling the above requirements, had to be relatively inexpensive to manufacture, easy to clean, and simple to disassemble, so that clogged or damaged parts could be replaced individually without great difficulty. The specifications were as follows:

- about 20 connecting ports
- a volume displacement per switching process of clearly less than 0.10 mm^3
- a fluid loss from leaks of not only water but also of SAI of less than $0.10 \text{ mm}^3/24 \text{ h}$ for the case of $150 \text{ cm H}_2\text{O}$ pressure difference
- no kink, angle, or corner within the inner volume so that complete filling of the pressure gage system could be accomplished by either of the two liquids
- transparency of the stopcock manifold for simpler control of air purging
- no aluminum parts, thus preventing the danger of precipitating mercury from the SAI
- compact building method, small dimension, and simple disassembly.

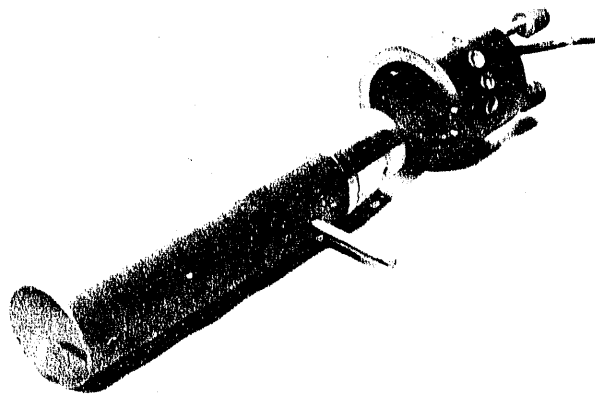
Based on these specifications, plexiglass was used as the building material. By heat tempering (warming to about 70°C) the plexiglass before use, satisfactory results were obtained.

Figures 4.10 to 4.19 are illustrations of the various prototypes. The captions contain the ideas, and the results describe the development of the stopcock manifold to the final model. To obtain the required "n" connections, a stopcock manifold of "n" separate stopcocks had to be assembled.

Considering the underrated difficulties of developing the stopcocks, it probably would have been more satisfactory to fill the oil measurement pressure gage system with a petroleum derivative without mercury, but of the same density as the SAI. In this manner, precipitation of mercury could have been avoided, and the commercially obtainable Scanivalve stopcocks could have been used.

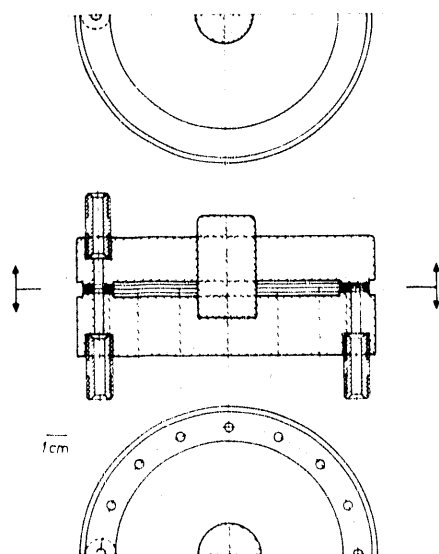


(a) Schematic

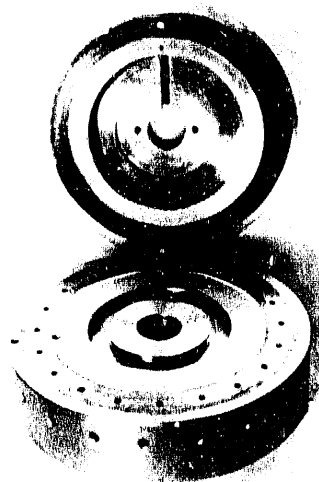


(b) Photograph

FIGURE 4.10. Prototype 1. Idea: Heavy cone inserted in a cap along which the ports are drilled. Results: Required fluid seal not reached.



(a) Schematic



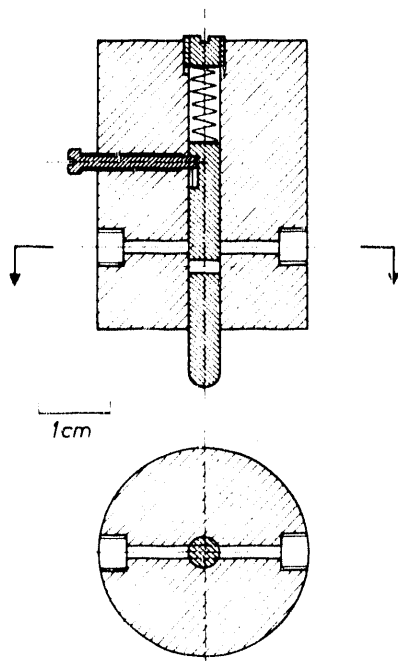
(b) Photograph

FIGURE 4.11. Prototype 2. Idea: Contact surface developed from smooth planes. Result: Despite using a hydrophilic coating, and also constructing the contact surface from glass, the required fluid seal for oil could not be reached. Such precautions seemed promising because the fluid seal for water was satisfactory.

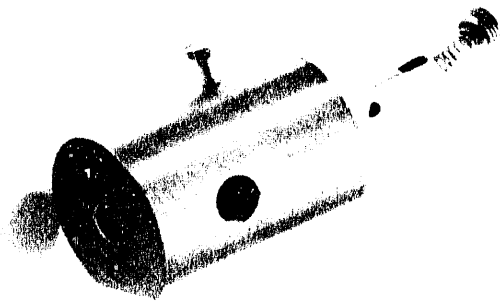
4.2.4 Tubing System

The requirement for the smallest possible fluid exchange was the result of an interest in the smallest possible error of the saturation measurement and the smallest possible response time of the pressure gage system. Fluid exchange refers to the sum of the volume changes resulting from temperature and pressure changes in the tubing system, diffusion, diaphragm deflection within the pressure transducer, and volume exchange in the stopcocks.

To keep the influence of any diffusion and long-term temperature and pressure fluctuations as small as possible, we strove for the shortest possible connection between the probes and the pressure transducers. The suitability of glass tubing stemmed from its stability with respect to temperature and pressure changes, and its transparency, which would have



(a) Schematic

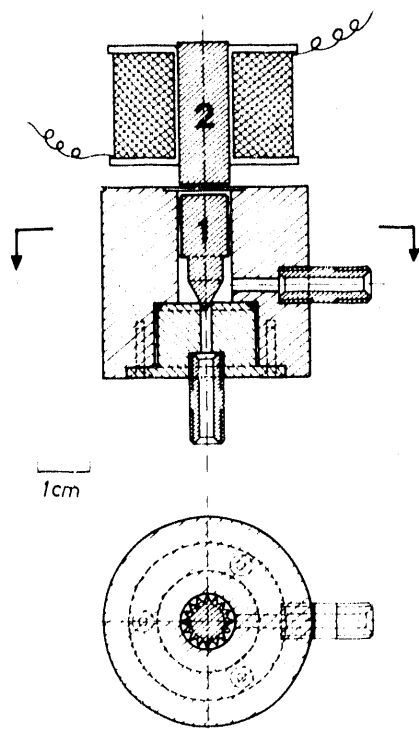


(b) Photograph

FIGURE 4.12. Prototype 3. Idea: Stopcocks of bolts, which were movable along the axes. Result: No improvement of fluid seal.

simplified the control of the complete purging of air from the system. Because of the fragility of a glass tubing system, it seemed more advisable to use instead the thin-walled, easily bendable, and constant-volume steel tubing with an inside diameter of 2 mm that was already being used for the probe holder. The steel tubing was resistant against corrosion by water and SAI, and it caused no precipitation of mercury from the SAI.

However, it was more practical to use flexible connections, rather than steel tubing, between the probe holder and the stopcock. Naturally, larger volume changes, caused by temperature and pressure changes, were to be expected with hose connection. The fluid loss caused by diffusion through the walls also had to be calculated. The fluid displacements caused by temperature changes and diffusion in the tubing between the probe holder and the stopcock probably had no influence on the response time of the pressure gage



(a) Schematic

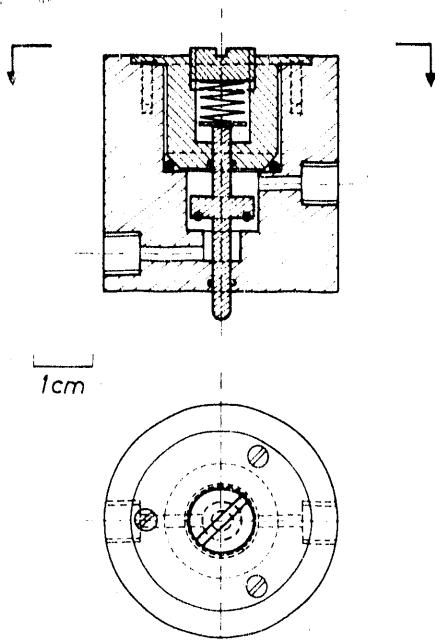


(b) Photograph

FIGURE 4.13. Prototype 4. Idea: A cone fitting into a circular opening. Opening occurs by lifting cone (1 on figure) in the sealed central space by using a magnet (2). Result: The requirements of fluid seal could not be satisfied.

system because the fluid within the tubing was connected to the fluid in the probe, and the probe, with its high permeability, did not represent a hindrance. To keep changes in the saturation conditions around the probes as small as possible, the tubing connections between the probes and the stopcocks were made as short as possible. Thus, the smallest possible volume changes, resulting from pressure and temperature fluctuations, were achieved.

Based on a comparison of Equations (4.26) and (4.27), the tubing between the stopcock and the pressure transducer had to be made of steel to obtain a satisfactory response time for the pressure gage system. The tubing material that was used between the stopcocks and the probe holders could only be used for the connections between pieces of steel tubing elsewhere.



(a) Schematic



(b) Photograph

FIGURE 4.14. Prototype 5. Idea: The original concept of not using O-rings to obtain the smallest possible volume displacement had to be given up because of the unsatisfactory fluid seal. Result: A pumping effect was created with a far greater volume displacement than tolerable.

To evaluate the most favorable material for the tubing between the probe holders and the stopcocks, tubing of various materials was tested for fluid loss through diffusion and for volume change as a result of temperature and pressure changes.

The specific fluid loss through diffusion was determined in the laboratory using water. To ensure that the observed fluid loss was only a result of diffusion, the measurement of loss by diffusion was done with different tube lengths. Figure 4.20 shows the arrangement of the experiment. To compensate for evaporation from the open end of the tubing, one reference capillary was read off in addition to each measuring capillary. The difference between the

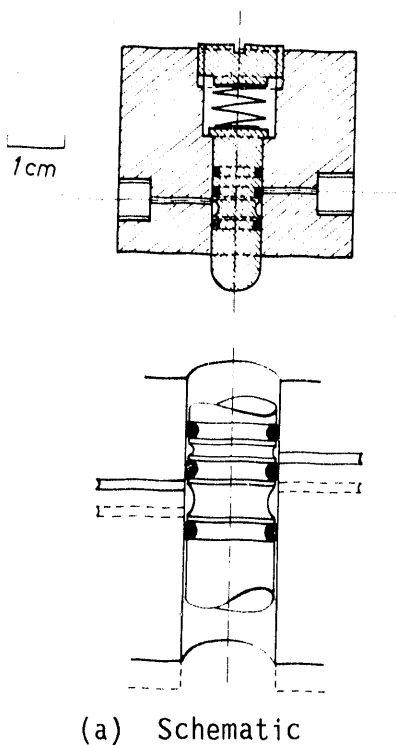
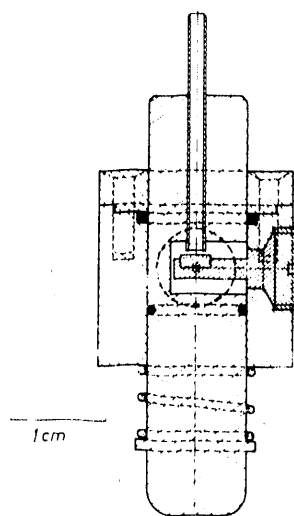


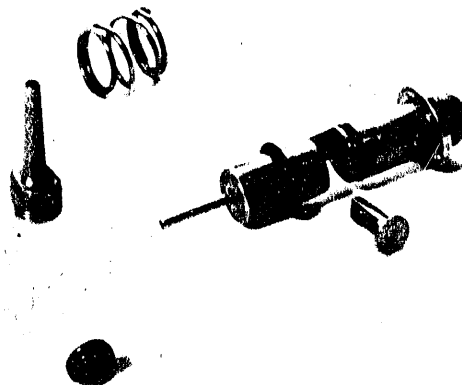
FIGURE 4.15. Prototype 6. Idea: O-rings should be located on shaft. Result: Probably smaller volume displacement despite greater pumping effect because of torsion on the O-rings.

meniscus subsidence in the measuring capillary and that in the reference capillary was designated as net subsidence, a .

Because of hysteresis of the contact angle at the water-air interface, it was ensured that the direction of meniscus movement did not change with time, and above all, that the drainage form of the initial meniscus was maintained. Otherwise, the hysteresis effect could have resulted in a significant error in the measurement. This type of error was amplified because the smallest possible capillaries were chosen so that the relatively small volume changes could be more exactly determined. The drainage form of the water meniscus was required because diffusion implies a fluid loss and thus, with respect to air, the retreat of the wetting fluid meniscus.



(a) Schematic



(b) Photograph

FIGURE 4.16. Prototype 7. Idea: Pumping effect should be eliminated because of the smaller axial displacement of the O-rings resulting from the placement of the sharp tube edges on a pad. Result: Pumping effect and volume displacement were still present. This must result from the nonconstant volume of the O-rings and also from their minimal displacement in the direction of their common axis.

The results of the experiments for three tubing materials (plastic, rubber, and Vibon) are reported separately. The evaporation volume was simply a fraction of the diffusion volume for each chosen hose length and capillary diameter. The specific diffusion volume, V_D (based on hose length and time) with the dimensions (L^2T^{-1}) or cm^2/sec is determined as

$$V_D = \frac{a\pi(\phi_K/2)^2}{l \cdot t} \quad (4.7)$$

where ϕ_K = diameter of the capillary

a = subsidence

l = tubing length (cm)

t = time (sec).

The hose lengths (l_1 to l_5) of the experiment using plastic tubing are listed in Table 4.2. The diffusion volume was expected to be linearly

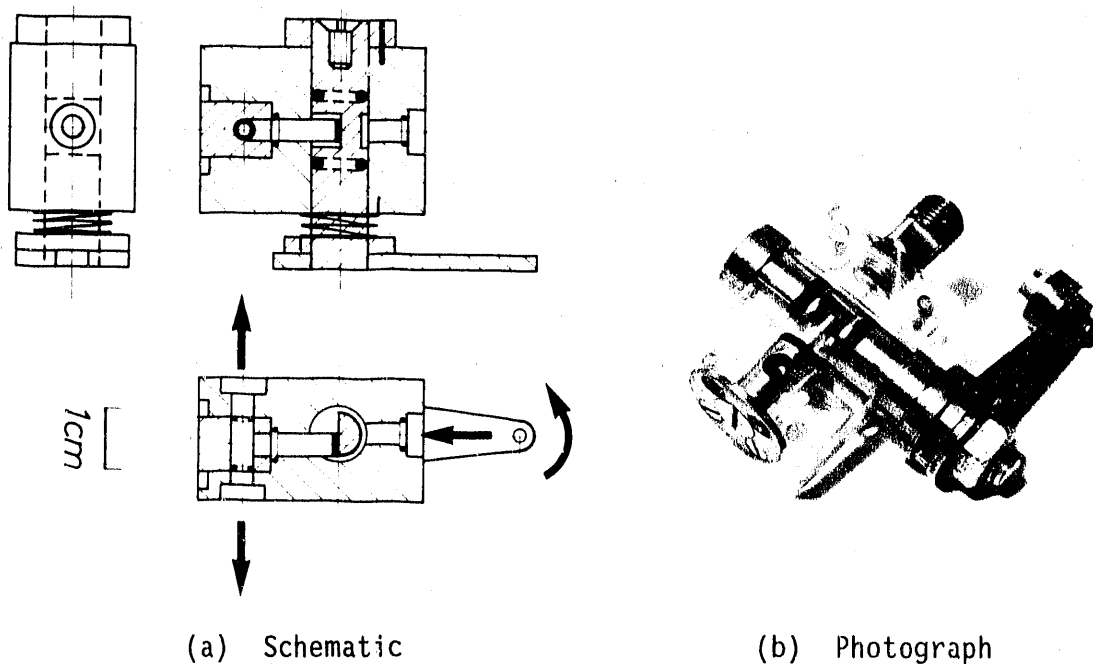


FIGURE 4.17. Prototype 8. Idea: O-rings should be rotated only on their common axis. Result: Volume displacement per closing or opening and fluid loss at 150 cm H₂O during 24 h are smaller than 10 mm. (The measurement of the volume displacement and the fluid loss from the stopcock occurred by observing the movement of a meniscus in a capillary with 0.2-mm inside diameter by using a magnifying lens.)

TABLE 4.2. Specific Diffusion Volumes for Plastic Tubing ($\phi_K = 0.9$ mm)

	1	2	4	5	3
l (cm)	49.5	61.0	86.5	99.0	193.0
V (mm ³ /138 h)	36.5	43.2	61.6	65.1	114.6
V_D (cm ² /sec)	$1.48 \cdot 10^{-9}$	$1.43 \cdot 10^{-9}$	$1.43 \cdot 10^{-9}$	$1.32 \cdot 10^{-9}$	$1.20 \cdot 10^{-9}$

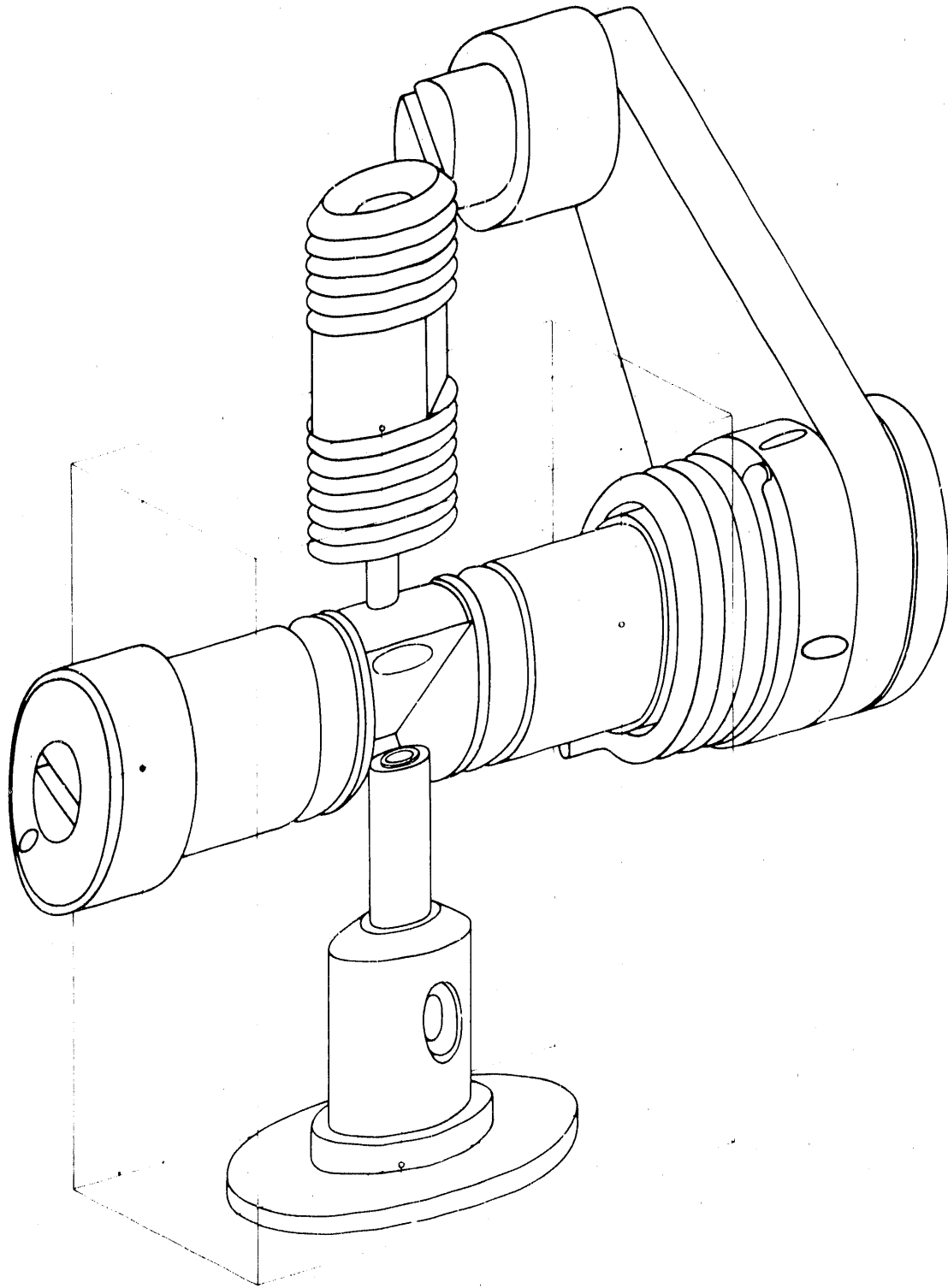


FIGURE 4.18. Three-Dimensional Drawing of Prototype 8

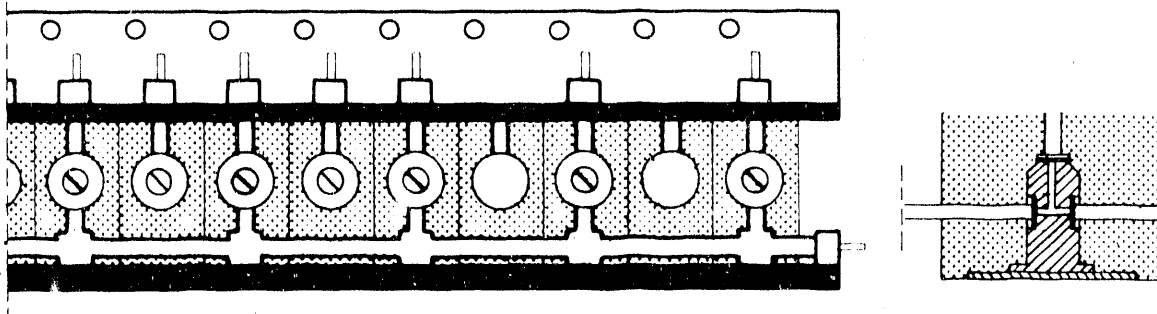


FIGURE 4.19. Sketch and Photograph of a Stopcock Manifold Composed of Prototype 8 Stopcocks

proportional to the length (Figure 4.21). Therefore, the average specific diffusion volume for the plastic tubing was calculated from the five experiments as

$$V_D_{Plastik} = 1,4 \cdot 10^{-9} \text{ cm}^3 / (\text{cm} \cdot \text{sec}) \quad (4.8)$$

Similarly, the diffusion volumes for the rubber and Vibon were experimentally determined. Figure 4.22 shows the net subsidence versus time for a 1-m length of tubing for each of the three different materials--plastic, rubber, and Vibon. The Vibon tubing showed the smallest diffusion. Its specific diffusion volume was

$$V_D_{Vibon} = 2,5 \cdot 10^{-10} \{ \text{cm}^3 / (\text{cm} \cdot \text{sec}) \} \quad (4.9)$$

Thus, Vibon was selected as the tubing material.

The volume change as a function of pressure change was determined with the experimental setup shown in Figure 4.23. As expected, proportionality

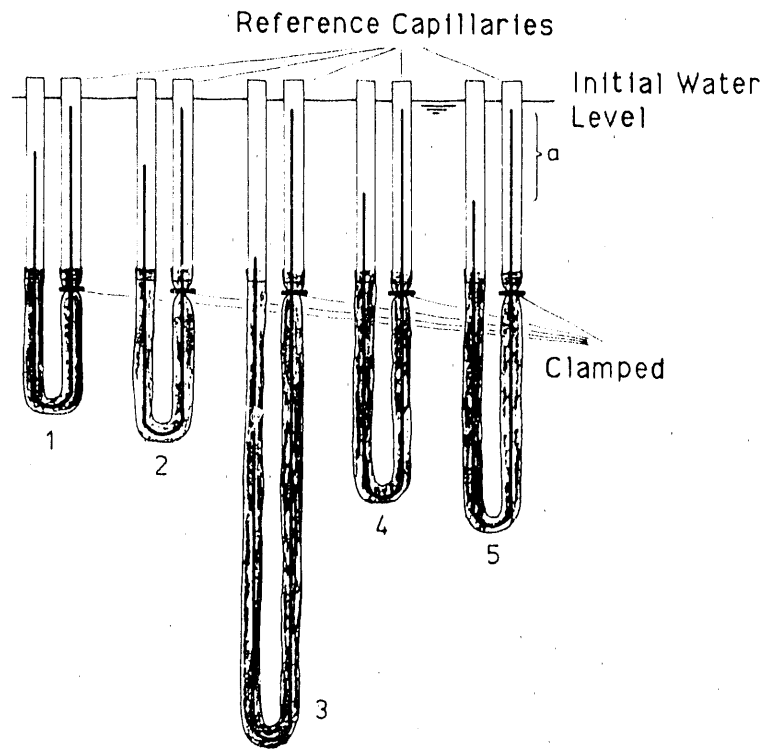


FIGURE 4.20. Sketch of the Apparatus for the Determination of the Fluid Loss Resulting from Diffusion Through the Tubing Walls.

existed between the pressure change and the enlargement of the Vibron hose, which is a linear function of the change in radius. This is confirmed by the somewhat parabolic relationship, $x = \lambda(\Delta p)^2$, that existed between pressure change and the oil drop displacement; that is, a quadratic function of the change in radius. According to Figure 4.24, λ is

$$\lambda = x/(\Delta p)^2 = 5/(10)^2 = 1/20$$

The specific volume change caused by pressure change, V_p , is

$$V_p = \frac{\pi \cdot \left(\frac{\phi_K}{2}\right)^2 \cdot x}{l \cdot (\Delta p)^2} \quad (4.10)$$

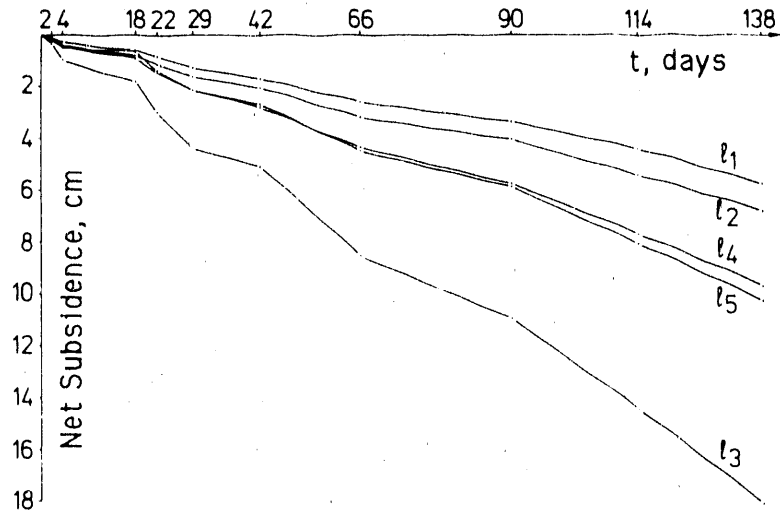


FIGURE 4.21. Net Subsidence, a , as a Function of Time Resulting from Diffusion Through the Walls of Different Lengths of Plastic Tubing

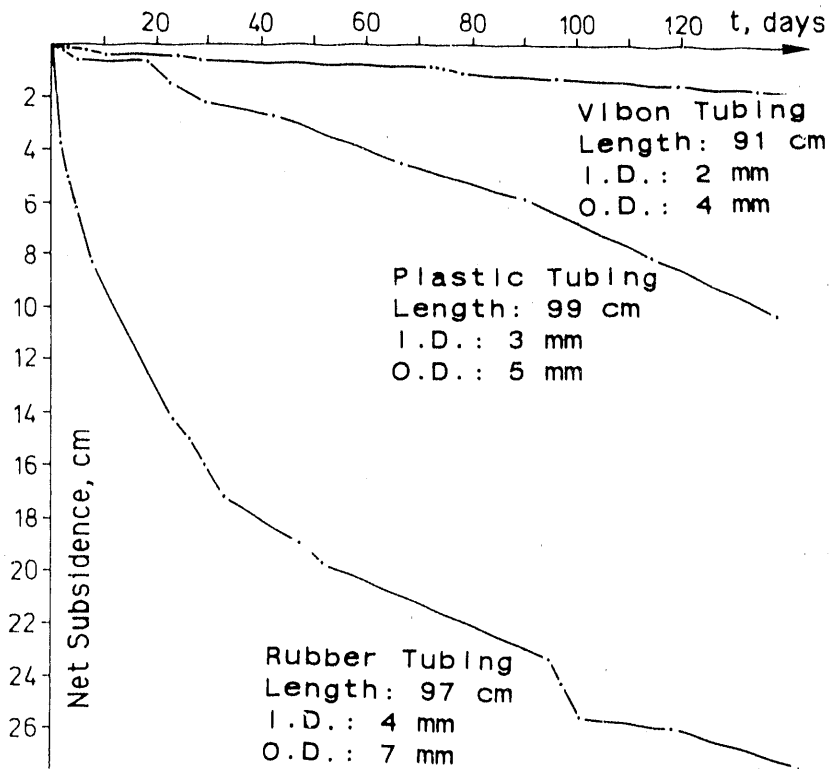


FIGURE 4.22. Time Function of Diffusion through the Wall of 1-m-Long Tubes of Plastic, Rubber, and Vibron

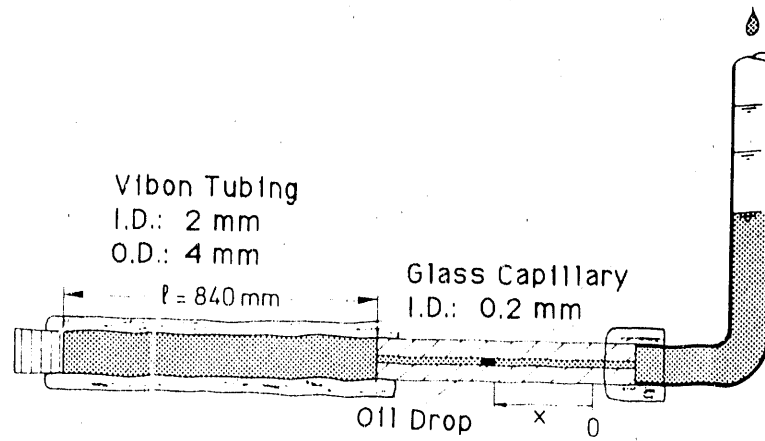


FIGURE 4.23. Apparatus for the Determination of the Volume Change of Vibron Hose Resulting from a Pressure Change

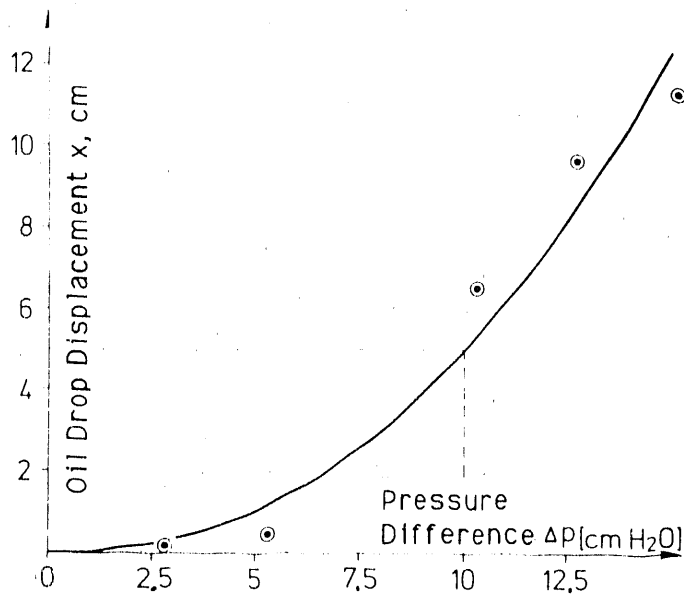


FIGURE 4.24. Oil Drop Displacement as a Function of the Pressure Change in Vibron Hose

where ϕ_K = diameter of the capillary
 x = displacement of the oil drop
 l = hose length
 Δp = pressure difference in cm H₂O.

All the parameters have the dimension of length. With $x = 1/20 (\Delta p)^2$, V_p for the Vibon is

$$V_{PVibon} = \frac{\pi \left(\frac{\phi_K}{2}\right)^2 (V20)}{l} = \frac{\pi \cdot 10^{-4}}{20 \cdot 84} = 1,9 \cdot 10^{-7} \text{ \{cm}^3 / (\text{cm} \cdot \text{cm}^2_{H_2O}) \} \quad (4.11)$$

To determine the volume change as a function of the temperature change, the experiment shown in Figure 4.25 was done. To evenly distribute the warm air introduced from a heat gun, baffles were installed in the insulated box. The change in volume versus time caused by different sudden temperature changes in the range around 20°C is shown in Figure 4.26 for an 80-cm-long Vibon tube.

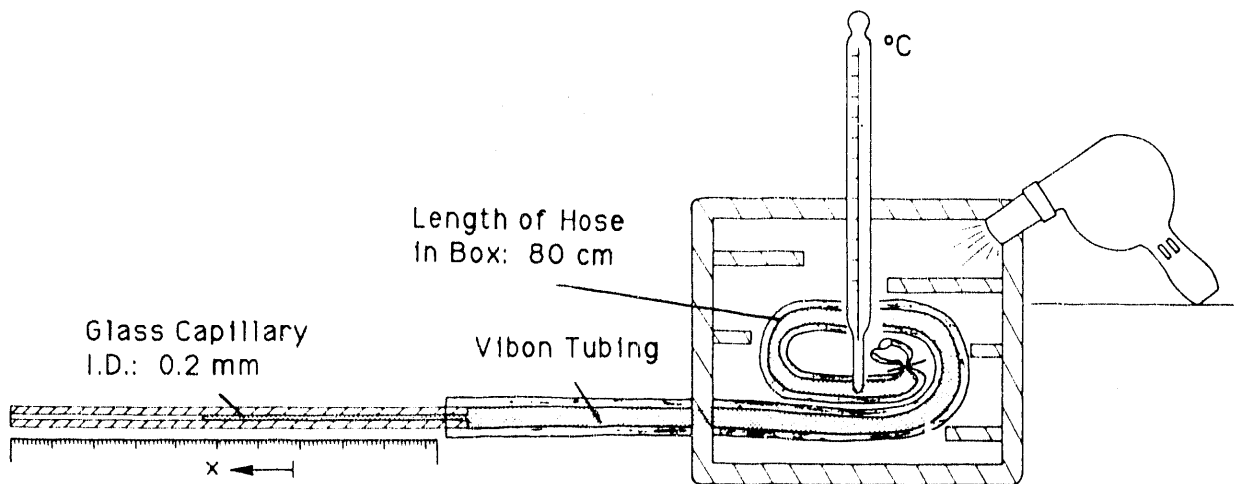


FIGURE 4.25. Experiment Setup for the Determination of the Volume Change in Vibon Hose as a Function of the Temperature Change

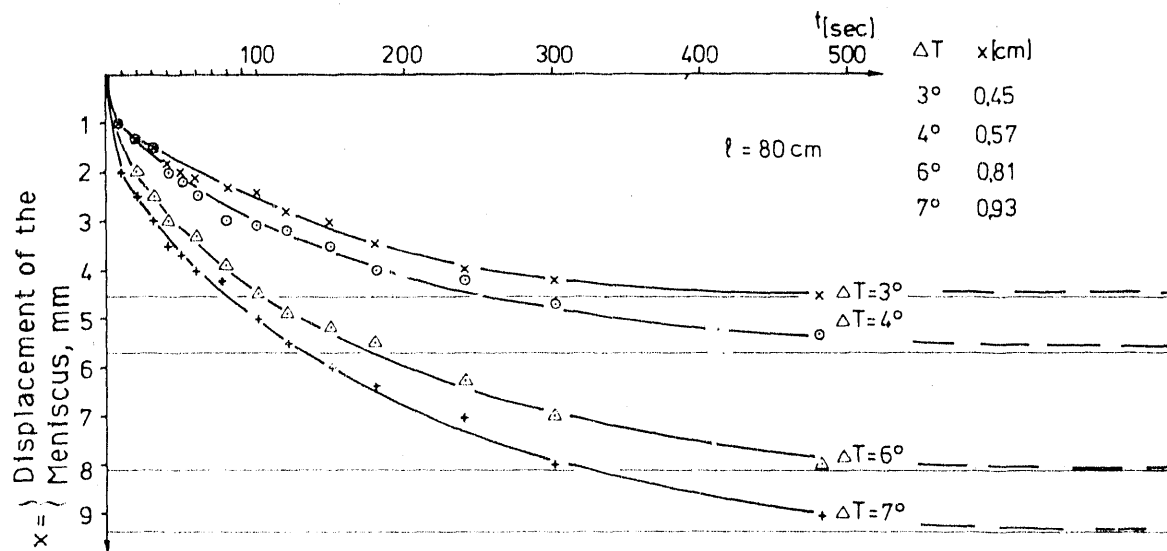


FIGURE 4.26. Meniscus Displacement Resulting from Volume Change in an 80-cm Vibron Hose Caused by Rapid Temperature Changes, ΔT

Based on the linearity between x and ΔT , the end value of the specific volume change, V_T , resulting from a temperature change, ΔT can be defined as

$$V_T = \frac{\pi \left(\frac{\Delta K}{\Delta T}\right)^2 x}{2 \cdot \Delta l} \quad (4.12)$$

According to Equation (4.12) and Figure 4.27, V_T for Vibron tubing equals

$$V_{T \text{ Vibron}} = \frac{\pi \cdot 10^{-4} \cdot 0,7}{80 \cdot 5} = 5,5 \cdot 10^{-7} \text{ (cm}^3 \text{ / (cm} \cdot \text{°C))} \quad (4.13)$$

This low value and the fairly constant temperature in the laboratory (see Section 3.3.2) allowed us to abandon plans to insulate the tubing system. We also assumed that the lab personnel would avoid touching the tubing. Insulation by wrapping or applying a two-component foaming material would have resulted in an enlargement of the hose diameter and thus reduced the area available for visual observation of the migration experiment.

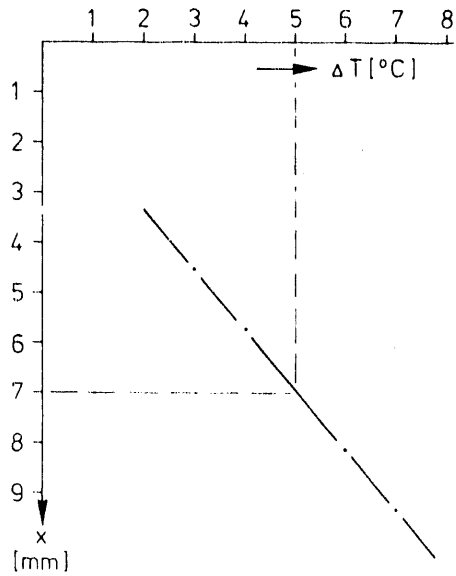


FIGURE 4.27. End Value of the Meniscus Displacement Resulting from the Volume Change in an 80-cm Vibron Tube as a Function of Rapid Temperature Changes

4.2.5 Response Time of the Pressure Gage System

To fulfill the initial requirements of the pressure gage system being developed, the accuracy of the pressure measurement as a function of the measuring time had to be clarified. An estimate of the response time between the pressure sensed at the probes and that detected by the pressure transducer was calculated based on the fact that the total specific volume change, V_{tot} , can only be displaced gradually because of the hydraulic resistance of the porous plate. In practice, the probes produced the only resistance or pressure drop. The pressure drop in the tubing system was insignificant. The smaller the fluid displacement, V_{tot} , and the more permeable the probe, the smaller the response time of the pressure gage system will be. Therefore, the response time is determined by hydraulic and not by electrical factors. The pressure gage system is presented schematically in Figure 4.28.

By opening the stopcock at time $t=0$, the pressure, p_H , initially derived from another probe site, suddenly changes in the transducer tubing (assuming that the pressure p_i to be determined differs from p_H). To detect p_i , the

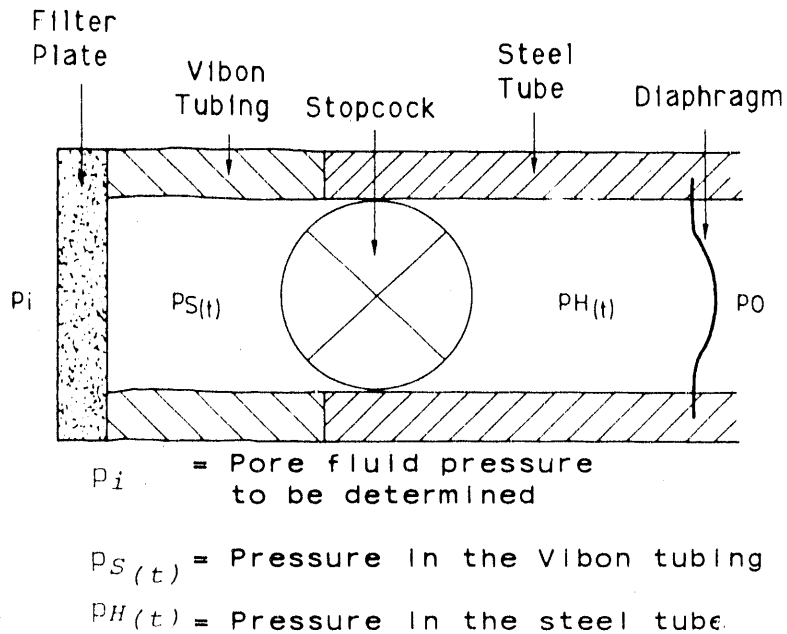


FIGURE 4.28. Schematic Illustration of Pressure Gage System

diaphragm deflection must change. Thus, the fluid volume equal to the difference in the diaphragm deflection must pass through the probe. Because of the hydraulic resistance of the probe, which opposes the transfer of this fluid volume, the pressure inside the pressure gage system will only gradually approach the pressure sensed at the probe. This can be shown graphically by assuming an exponential pressure response (Figure 4.29). Thus, the pressure in the transducer tubing as a function of time can be described by

$$P_H(t) = P_H(t=0) \cdot e^{-\lambda \cdot t} \quad (4.14)$$

Therefore, the response time, T , can be defined as the time for the measured pressure $P_H(t)$ to approach its final value, P_i , within $1/e$ of its initial value $P_H(t=0)$. This statement can be formulated mathematically as

$$P_H(t=0) \cdot e^{-\lambda \cdot T} = \frac{1}{e} \cdot P_H(t=0) = P_H(t=0) \cdot e^{-1} \quad (4.15)$$

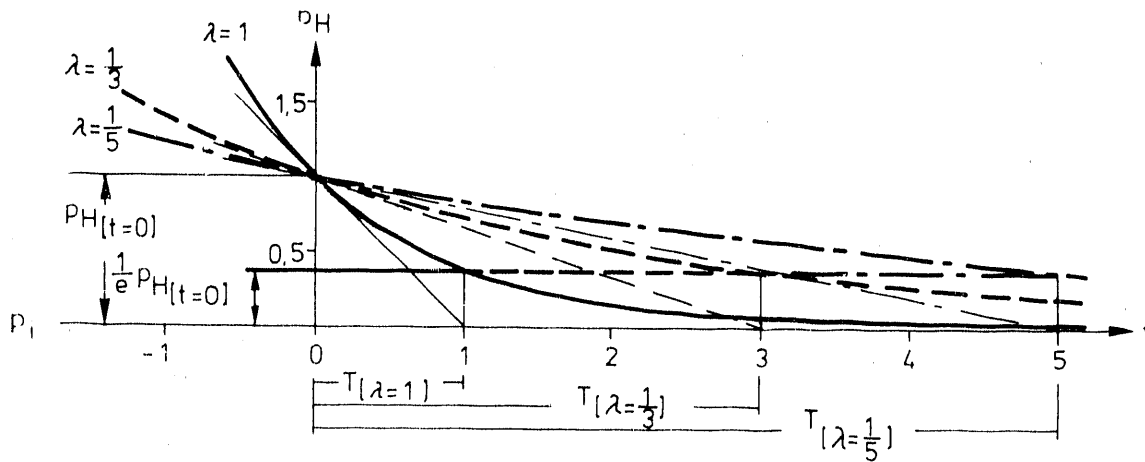


FIGURE 4.29. Diagram of the Experimental Progression of Pressure Detected by the Pressure Transducer After Switching to a Lower Pressure

where $e^{-\lambda T} = e^{-1}$, from which it follows that the reciprocal value of the response time is

$$\lambda = \frac{1}{T} \quad (4.16)$$

Thus, Equation (4.14) as a function of the response time can be written as

$$p_H(t) = p_H(t=0) \cdot e^{-\frac{t}{T}} \quad (4.17)$$

As shown in Figure 4.29, the response time can be determined graphically as the intersection point on the abscissa of the tangent passing through the ordinate at $t=0$. This can be confirmed by determining the slope of this tangent; that is, the time derivative of the function $p_H(t)$, which is

$$\frac{\partial}{\partial t} p_H(t) = \frac{\partial}{\partial t} (p_H(t=0) \cdot e^{-\frac{t}{T}}) = p_H(t=0) \cdot e^{-\frac{t}{T}} \cdot -\frac{1}{T} = -\frac{1}{T} p_H(t) \quad (4.18)$$

which for $t=0$, gives

$$p_H(t=0) = \frac{1}{L} \cdot \frac{\partial V_{tot}}{\partial t} = \frac{1}{L} \cdot \frac{\partial V_{tot}}{\partial t} \quad (4.19)$$

According to the expanded Darcy's Law, the flow rate dV/dt , or Q , equals the product of the cross-sectional flow area A , the relative and hydraulic permeability $k^r k$, and the potential gradients $(\Delta p/\Delta \zeta)$. The quotient $(Ak^r k/\Delta \zeta)$ can be assumed constant for a probe type, and together with Figure 4.4 can be designated as its conductance, L . The term $\Delta p(t)$ can be set equal to the instantaneous value of the function $p_H(t)$. Given these definitions, the following relation results:

$$L \cdot p_H(t) = - \frac{\partial V_{tot}}{\partial t} \quad (4.20)$$

The negative sign implies a decrease in flow.

The total necessary fluid exchange, V_{tot} , is theoretically the same as the sum of the volume changes resulting from diffusion in the tubing system, pressure and temperature changes in the tubing system, the change in the diaphragm deflection, and the fluid exchange in the stopcocks. The fluid exchange in the stopcocks was insignificant (see comments in Figure 4.17). Because the minimum value of the measuring time was later determined by Equation (4.29) as 1 sec, the volume changes caused by diffusion and temperature change were also insignificant. Thus, V_{tot} was reduced to the sum of the fluid exchange caused by the pressure change and to the change in diaphragm deflection.

The fluid exchange caused by pressure change was determined from Equation (4.10) as the product of $V_{pl}(\Delta p)^2$. The fluid exchange caused by diaphragm deflection was calculated theoretically from Equation (4.5). The value, $\pi(1-\mu^2)R^6/(16Ed^3)$, was designated as V_M . In both cases, they are dependent on the pressure difference, Δp . The term Δp is the same as the pressure difference between the pressure in the main channel, $p_H(t)$, and the pressure, p_i , sensed at the probe. If p_i is assumed to be the reference for the pressure measurement (Figure 4.29), then $\Delta p(t) = p_H(t)$, whereby

$$V_{tot} = V_P \cdot \ell \cdot p_H(t)^2 + V_M \cdot p_H(t) \quad (4.21)$$

If Equation (4.21) is inserted in Equation (4.20), then

$$L \cdot p_H(t) = -(V_P \cdot \ell \cdot \frac{\partial p_H(t)^2}{\partial t} + V_M \cdot \frac{\partial p_H(t)}{\partial t}) \quad (4.22)$$

If $\partial p_H(t)/\partial t$ is replaced by Equation (4.18) as follows:

$$\begin{aligned} \frac{\partial}{\partial t} p_H(t)^2 &= \frac{\partial}{\partial t} (p_{H(t=0)} e^{-\frac{t}{T}})^2 = p_{H(t=0)}^2 \frac{\partial}{\partial t} e^{-\frac{2}{T}t} = p_{H(t=0)}^2 e^{-\frac{2}{T}t} \cdot -\frac{2}{T} \\ &= (p_{H(t=0)} \cdot e^{-\frac{t}{T}})^2 \cdot -\frac{2}{T} = -\frac{2}{T} p_H(t)^2 \end{aligned} \quad (4.22a)$$

then

$$L \cdot p_H(t) = \frac{\{V_P \cdot \ell \cdot 2 \cdot p_H(t) + V_M\}}{T} \cdot p_H(t) \quad (4.23)$$

For $t = T$, according to Equation (4.17), the value $p_H(t) = p_{H(t=0)}/e$ can be applied. Thus the response time, T , in an explicit representation of Equation (4.23), can be given as

$$T = \frac{(2 \cdot \ell \cdot p_{H(t=0)} / e) V_P + V_M}{L} \quad (4.24)$$

In the pressure gage system, mostly steel tubing was used between the stopcocks and pressure transducers. If for steel tubing $V_P \approx 0$, then the response time for the pressure gage system can be reduced to

$$T \approx V_M / L \quad (4.25)$$

Thus, to determine the response time, only the specific volume change caused by the diaphragm deflection, V_M , played a role. According to Equation (4.5), V_M is theoretically determined as $\pi (1 - \mu^2) R^6 / (16Ed^3)$. From the specifications of the pressure transducer Type CEC-4-327 (Section 4.2.2), the experimentally measured volume difference for the diaphragm deflection at 2 m H₂O came to 0.143 mm³. Thus, V_M was calculated to be $1.43 \cdot 10^{-4} / 200 = 7 \cdot 10^{-7}$ cm². The conductance, L , of the probes was $8 \cdot 10^{-6}$ cm²/sec (Figure 4.4a). If these values are inserted into Equation (4.25), then the response time of the system is

$$t = \frac{7 \cdot 10^{-7} \text{ cm}^2}{8 \cdot 10^{-6} \text{ cm}^2/\text{sec}} \approx \frac{1}{10} \text{ sec} \quad (4.26)$$

To confirm the suitability of using steel tubing between the stopcocks and the pressure transducers, the response time for a system with tubing connections of different materials between the stopcock and pressure transducer was also calculated. The tubing connections were a minimum of 20 cm in length on the average. The specific volume displacement caused by pressure change was determined as $1.9 \cdot 10^{-7}$ for Vibon tubing according to Equation (4.11). If at time zero an actual average pressure difference, $p_H(t=0)$, of 15 cm is assumed, then according to Equation (4.24), the response time is

$$t = \frac{(2 \cdot 20 \cdot 15 / 2,72) 1,9 \cdot 10^{-7} + 7 \cdot 10^{-7}}{8 \cdot 10^{-6}} > 5 \text{ sec} \quad (4.27)$$

A comparison of Equations (4.26) and (4.27) shows that the response time for a pressure gage system using a minimum length of Vibon tubing between the stopcocks and pressure transducers was more than 50 times greater than that for a system with steel tubing.

4.2.6 Minimum Measuring Time

According to Equation (4.17), the measured pressure, $p_H(t)$, approaches its final value asymptotically, which, for $t \rightarrow \infty$, is the same as the pressure sensed by the probe, p_i . The minimum time required for a pressure measurement, Δt_{\min} , was defined by the time required for the measured pressure,

$p_H(t)$, to approach the final pressure p_i within half of the total tolerable pressure gage error, m_p , which was specified earlier as $\pm 0.5 \text{ mm H}_2\text{O}$. The most unfavorable (longest) minimum measuring time, which is for the maximum $p_H(t=0)$, can be calculated as

$$p_H(t=0) \cdot e^{-\frac{\Delta t_{min}}{T}} = p_i \quad (4.28)$$

from which it follows that

$$\Delta t_{min} = T \cdot \ln\left(\frac{p_H(t=0)}{m_p/2}\right)$$

If $p_H(t=0)$ is assumed to be $50 \text{ cm H}_2\text{O}$, then the minimum measuring time for the pressure gage system is

$$\Delta t_{min} = 0,1 \text{ sec} \cdot \ln\left(\frac{50 \text{ cm}}{0,025 \text{ cm}}\right) \approx 1 \text{ sec} \quad (4.29)$$

5.0 SATURATION MEASUREMENT APPARATUS

In this chapter, the apparatus for the determination of water, oil, and air saturations in a 15-cm-thick homogenous and isotropic porous medium of quartz sand is briefly described. The theory and development of the saturation measurement method is presented in greater detail in Chapter 6.0.

5.1 MEASUREMENT APPARATUS

The two-dimensional propagation experiments occurred along the plane delineated by the longitudinal x-axis and the vertical z-axis of the flume. In the horizontal y-axis normal to the plane, homogeneity was assumed. The saturation measurement method was based on the attenuation of collimated, monochromatic, and radioactive radiation in the y-direction.

Figure 5.1 is a schematic diagram and Figure 5.2 is a photograph of the source-detector pair used as the measuring apparatus.

An isotope produced the monochromatic radiation. An isotope is a radiation source and must be surrounded by a shield because of radiation safety considerations. A source collimator was used to obtain a beam of radiation. A detector collimator was used to minimize the scattered radiation reaching

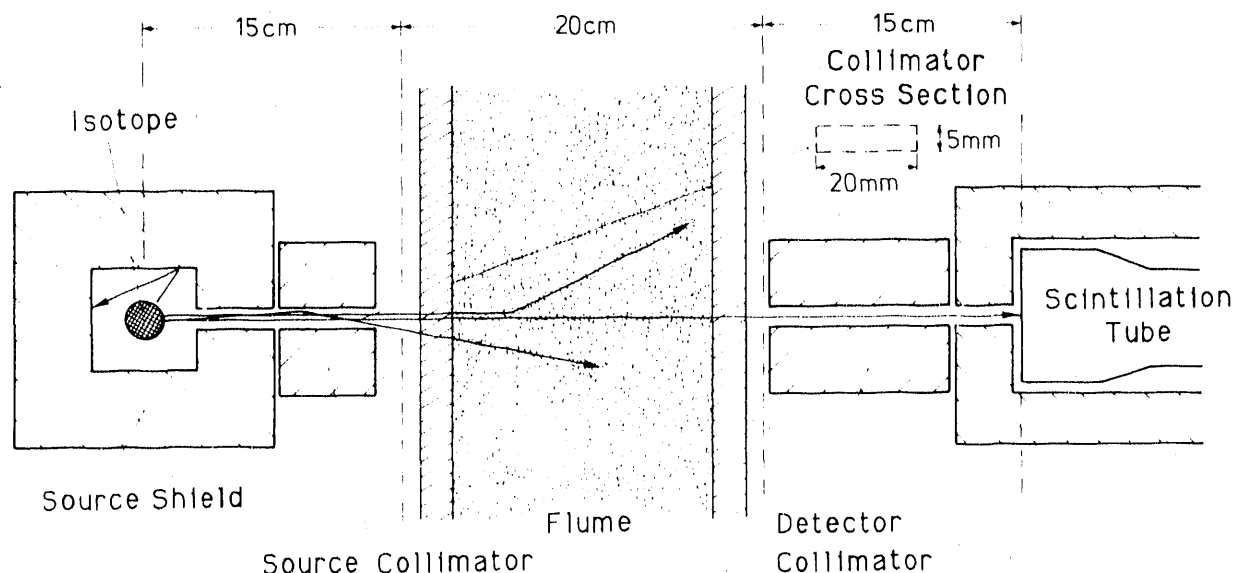


FIGURE 5.1. Schematic Diagram of the Source-Detector Pair

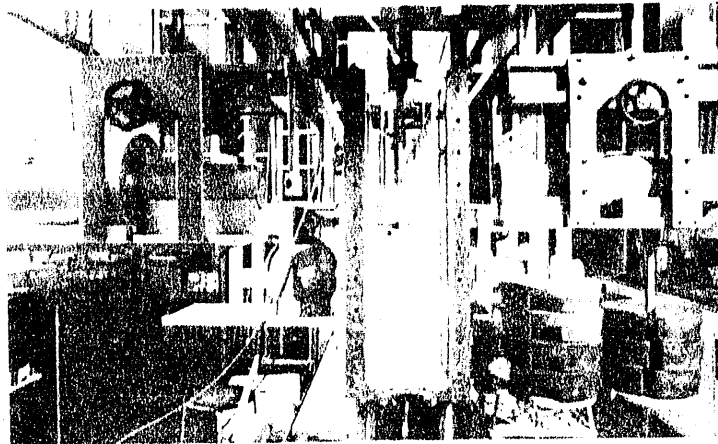


FIGURE 5.2. Photograph of Measurement Apparatus

the detector. The detector shield also served the same purpose. The detector consisted of scintillation crystals and photomultiplier tubes.

5.2 SOURCE SHIELDS

The isotopes Cs-137 and Tm-170 were used as the radiation sources for the saturation measurement method (see Chapter 6.0).

A source shield was required for radiation protection. The basic fundamentals of radiation protection are presented in the Radiation Protection Regulation (SSVO 1976). For occasional work with radioactive materials by dosimeter-equipped personnel, our tolerated dosage rate of 1.5 rem/yr is less than one-third of the annual radiation amount permitted by Article 32 of the SSVO for radiation workers. 1.5 rem/yr over 45 work weeks at 44 h per week equals a dosage rate of 0.75 mrem/h. According to article 70 of the SSVO, the protective container of a sealed radiation source must be constructed in such a way that at a 1-m distance from its surface, a dosage rate of 10 mrem/h is never exceeded. During transportation of radioactive sources within the working area, Article 101 requires that the dosage rate at the surface never exceeds 200 mrem/h.

A roentgen, R, and a milliroentgen, mR, are units of dosage. The dosage is the effective energy per mass expressed as erg/g. The dosage rate means

the dosage per unit time. To work with smaller numbers, the rad (100 erg/g) was introduced. Thus, the rad describes a dosage in energy per unit mass, whereas the roentgen is determined from a dosage determination based on ionization measurements. For quantum energies higher than 100 keV, the roentgen and the rad can be assumed equal for muscle and fat tissues (Glocker and Macherauch 1965, p. 231). The rem (Rad Equivalent Man), a biological effective dosage, is equal to the product of the relative biological activity, RBW, and the rads. The RBW factor should be considered during the administration of allowable high doses because for the same dosage measured in rads, the biological effect is different according to the type of rays (see Quality Factors in the appendix of the SSV0 1976).

The activity of the Tm-170 source was 2000 Ci (see Chapter 6.0). Despite the high activity of the Tm-170 source, a mercury jacket of only a few millimeters was enough to shield the emitted 84-keV gamma radiation. The attenuation property of mercury is high for 84-keV radiation because the electron K-shell of mercury lies at 83.1 keV (Strominger et al. 1958). Thus, for the attenuation of 84-keV radiation, the mass attenuation coefficient of the K-border can be assumed to equal the K-shell peak. The attenuation properties of lead and thallium can be extrapolated to estimate the mass attenuation coefficient for the mercury K-shell peak. According to Grodstein (1957), the mass attenuation coefficient of the K-shell of lead (atomic number 82) is 7.63 cm²/g and for thallium (atomic number 81) it is 7.93 cm²/g. Based on these values, mercury, with atomic number 80, has a mass attenuation coefficient for the K-shell of at least 8 cm²/g. The half-value thickness of mercury is determined for 84-keV radiation by solving for x in the attenuation law for radioactive radiation.

$$\frac{J}{J_0} = \exp\left\{-\left(\frac{\mu}{\rho}\right) \cdot x \cdot \rho\right\} \quad (5.1)$$

where J_0 is the initial radiation intensity (impulse count rate), J is the attenuated impulse count rate, (μ/ρ) is the mass attenuation coefficient, x is the irradiation path length, and ρ is the density of the irradiated material (see Equation [6.5]). Therefore, the required thickness for $J/J_0 = 0.5$ must be

$$\underline{x_{Hg} \left\{ J = \frac{1}{2} J_0 (84 \text{ keV}) \right\}} = \frac{\ln 0,5}{-\left(\frac{\mu}{\rho}\right)_{Hg(84 \text{ keV})} \cdot \rho_{Hg}} = \frac{-0,693}{-8 \cdot 13,6} \approx \underline{6,4 \cdot 10^{-3} \text{ cm}} \quad (5.2) \text{ (a)}$$

One millimeter of mercury will attenuate an initial impulse count rate with a quantum energy of 84 keV by a factor of $2 \cdot 10^{-5}$. On the other hand, a 1-cm thickness will attenuate the same initial impulse count rate by a factor of $6 \cdot 10^{-48}$.

The thickness of the shielding for the Tm-170 source was determined not by the quantitatively dominant radiation below 90 keV, but rather by the undesired radiation above 90 keV emitted by the superrefined aluminum vial used to contain the Tm-170 oxide powder. The radiation below 90 keV was relatively weak and thus less important from a radiation protection perspective. In spite of the high degree of purity of the vial material, its impurities were activated by the long and intense radiation during the Tm-170 production process. Because of the >90 keV radiation, a greater radiation-protection shield mass was needed. For information on the purity of the vial material, the radiation conditions, and the impossibility of obtaining another Tm-170 source, see Chapter 6.0. Lead was shown to be most suitable to shield the high-energy radiation spectrum. To fulfill the radiation protection requirements, the shield thickness had to be 10 cm.

For the 84-keV radiation of the thulium source, lead (compared to mercury) is probably a poorer shielding material because the electron K-shell of lead lies just above 84 keV, while that of mercury lies just below 84 keV. However, the mass attenuation coefficient of lead at 84 keV is about $1.4 \text{ cm}^2/\text{g}$ (see Chapter 6.0). Thus, the 10-cm thickness of lead was capable of weakening the 84-keV gamma radiation of the Tm-170 source by a factor of $\exp [-(\mu/\rho) \times \rho] = \exp [(-1.4)(10)(11.3)] = 2 \cdot 10^{-69}$.

In addition to gamma radiation at 84 keV, Tm-170 also emits beta radiation with energies at 880 keV and 970 keV. Beta radiation is a particle radiation with the particles being electrons.

(a) Equations were taken directly from the German text and, in some cases, use a different notation. For example, 0,01 = 1/100, whereas in this text, 1/100 would be shown as 0.01. Multiplication is indicated by a dot in the equations and in the text.

According to Glocker and Macherauch (1965, from p. 63 and on), while electrons pass through a material, the three fundamental processes of scattering, deceleration by collision, and deceleration by radiation emission are discernible. Scattering means essentially a deviation in the path of the electrons, but practically no energy loss. Energy loss, on the other hand, implies deceleration. During deceleration by collision, the energy is exchanged with an electron of the atomic shell; during deceleration by radiation emission, the energy is exchanged in the area of the nucleus.

Deceleration by collision leads to the stimulation and ionization of the atoms; deceleration by radiation emission leads to the emission of x-rays. X-rays are generated when fast electrons in the area of atomic nuclei undergo a quick deceleration. Upon deceleration, the kinetic energy of these electrons is changed into electromagnetic radiation energy. Deceleration by radiation emission only occurs at electron energies clearly greater than 1 MeV (Glocker and Macherauch 1965, pp. 66, 423).

During deceleration by collision, a fast electron gives off a portion of its energy to an electron in the atomic shell while simultaneously changing direction. If large amounts of energy are transferred, an electron will separate from the atomic shell and accept a certain amount of kinetic energy so that it can in turn cause the ionization and stimulation by impact of other atoms. If the amount of transmitted energy is not enough to eject an electron from the atomic shell (ionization), then only a stimulation results. The electron in question is raised to an outer unoccupied shell, raising the potential energy of the atom. This excess of energy is given up when the electron returns to its original state, which for gases produces an emission of light. Radiation produced as a result of deceleration by collision can consequently not be higher than the highest characteristic radiation. Of all the elements, lead has the highest characteristic radiation with which emitted beta radiation can be produced by mutual energy exchange, which is 88 keV.

Based on the above, deceleration by radiation emission could be ignored because the beta energies lie below 1 MeV. Furthermore, the highest possible radiation energy due to deceleration by collision is 88 keV. However, the experimentally determined Tm-170 spectrum revealed radiation above 90 keV that

was a product of the 880-keV and 970-keV beta emissions (Heath 1964). Thus, in the present case, deceleration by radiation emission must have been occurring when the electron energies were slightly below 1 MeV.

To prevent the beta radiation (emitting from the Tm-source as a result of deceleration by collision) from stimulating the characteristic radiation of lead, we tried to weaken the beta radiation to below 88 keV before it could reach the lead shield. This stimulation could occur because the characteristic radiation of lead (88 keV) is slightly higher than the 84-keV radiation from the Tm-170 source to be used for the saturation measurement. Such an attenuation of the beta radiation must be done with a material whose characteristic radiation lies somewhat lower, thus a material with a lower atomic number.

The mass deceleration capacity describes the density-specific deceleration capacity of a material for electrons. From the Bethe-Bloch deceleration formula (Glocker and Macherauch 1965, p. 67), the mass deceleration capacity is approximately proportionate to the quotient, Z/A , where Z is the atomic number and A is the atomic weight. This quotient is 0.5 for most low atomic weight elements and decreases to about 0.4 for elements with higher atomic numbers. Hydrogen has a deceleration capacity twice that of the other light atomic elements because $Z/A = 1$. Thus, plastic was chosen to be the Tm-170 source inner shield to weaken the beta radiation. Plastic, a hydrocarbon compound, has a high hydrogen fraction and is a light, easily worked material. Because of the high activity and the heating of the source environment caused by the radiation, a plastic with a sufficiently high melting point had to be selected.

In the photograph shown in Figure 5.3, the discoloration of the PVC ring at locations of larger radiation intensity is clearly recognized. The discoloration is caused by strong heating from the 2000-Ci Tm-170 source.

The necessary thickness of the plastic shielding was determined by estimating the maximum range of 1-MeV beta radiation in plastic. A practical range of 1-MeV beta particles in aluminum is about 400 mg/cm^2 (Glocker and Macherauch 1965, p. 71). Because the practical range of 6-MeV beta radiation is the same in aluminum and water (Glocker and Macherauch 1965, p. 72,

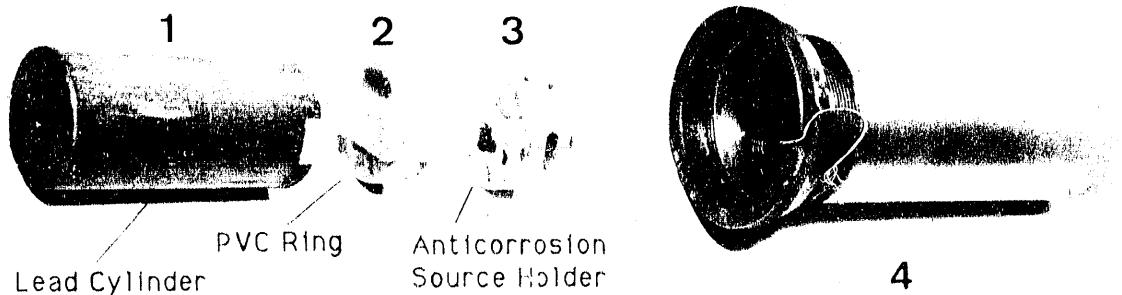


FIGURE 5.3. Components of the Thulium Source Shield

Table 3.8), 400 mg/cm^2 can be used as a first approximation for the practical range of 1 MeV beta radiation in plastic. This can be converted to a thickness by dividing by the average density of plastic, which is about 800 mg/cm^3 . Thus, an average practical range of 1-MeV beta radiation in plastic is 0.5 cm. This shows that the 2-cm-thick PVC source shield (Figure 5.4) effectively stops the emission of beta radiation.

To minimize the weight of an enveloping 10-cm-thick lead shield, a sphere with a minimum radius was chosen. A sphere with an inside radius of 6 cm and an outside radius of 16 cm was selected, considering the maximum distance between the surface of the PVC shield and the center of the source. The weight of such a lead sphere was determined as

$$G_{Tm-Absch.} = \frac{4}{3} \cdot \pi (R^3 - r^3) \rho_{Pb} = \frac{4}{3} \cdot \pi (16^3 - 6^3) 11.3 = 184 \text{ kg} \quad (5.3)$$

According to Section 6.8, the minimum required activity of the Cs-137 source was 0.2 Ci. A 1-Ci source was used for the experiments. A lead cylinder was constructed to shield the 1-Ci cesium source. Its thickness was determined from the dosage constant for Cs-137 (Stablein 1966). According to Marth (1966), this value is $3.5 \text{ R cm}^2/[(h)(\text{mCi})]$. This value is equivalent to a dosage rate of 3500 R/h 1 cm from the 1-Ci source.

The shielding was selected so that a person could work 15 cm away from the source for long periods. The dosage rate 15 cm away from an unshielded 1-Ci source is $(1/15^2) (3500 \text{ R/h}) = 15.6 \text{ R/h}$. Because the RBW factor = 1 for

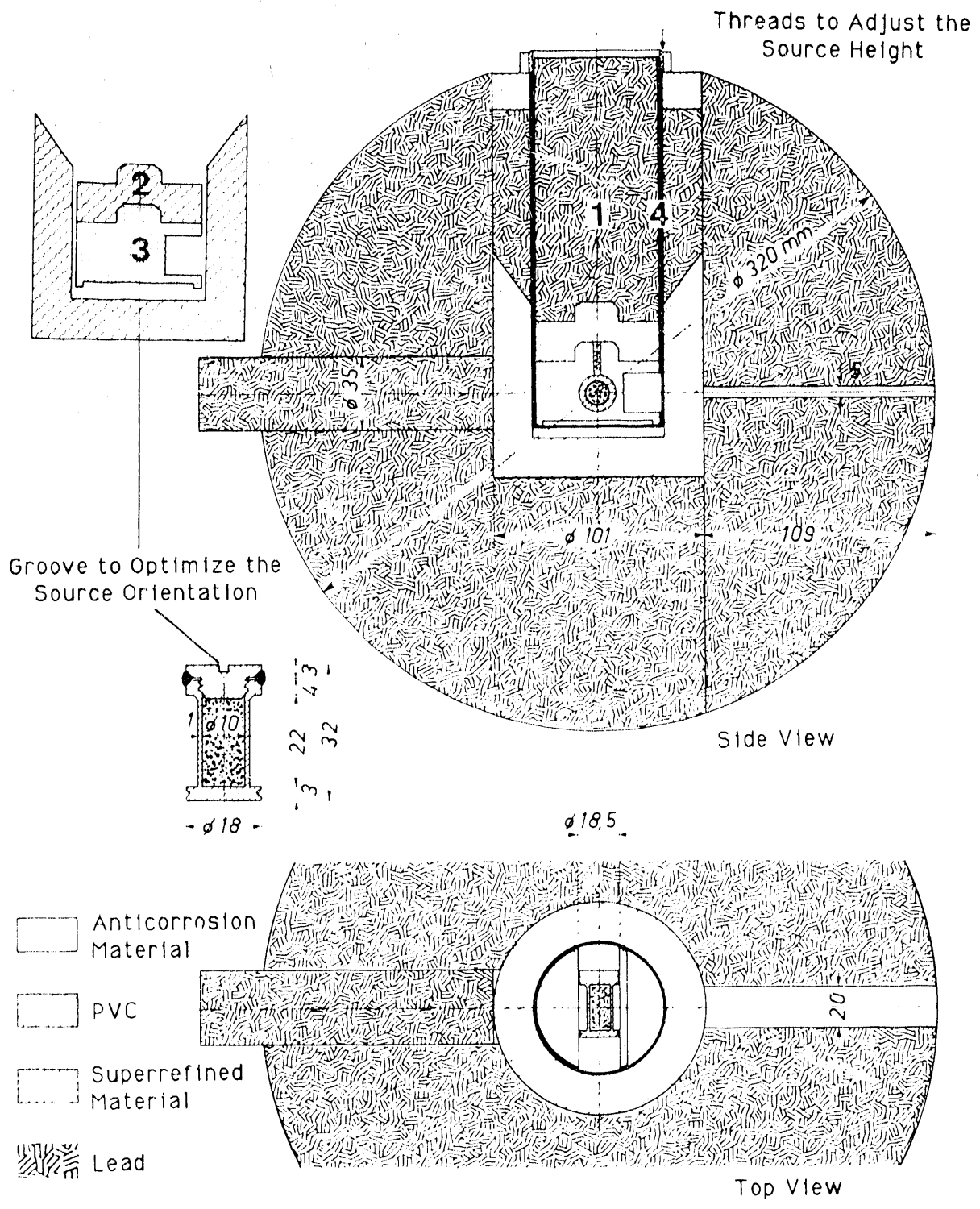


FIGURE 5.4. Schematic Diagram of the Thulium Source Shield

Cs-137 gamma radiation energy at 662 keV, the rad = R, and 15.6 R/h = 15.6 rem/h. So as to not exceed the 0.75-mrem/h value specified in Section 5.2, the lead shield must yield a $(15600/0.75) \approx 20000$ -fold weakening of the radiation. According to Equation (5.1), the minimum thickness of the lead shield is $x = \ln(20000)/[(\mu/\rho)_{\text{Pb}}, 662 \text{ keV} (\rho_{\text{Pb}})] = 9.9/[(0.1)(11.3)] = 8.8 \text{ cm}$. The thickness of the lead shield for the Cs-137 source was chosen as 10 cm.

As shown in Figure 5.5, the shield for the cesium source consisted of three lead cylinders, each with a 12-cm radius and an 8-cm height, plus a smaller cylinder with a 7-cm radius and a 5-cm height.

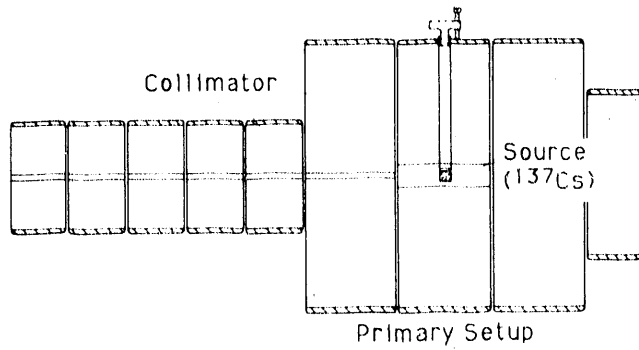
The weight of the lead shield was

$$G_{\text{Cs-Absch.}} = 3,14 \cdot 11,3 \{3 \cdot (12)^2 \cdot 8 + 7^2 \cdot 5\} = 132 \text{ kg} \quad (5.4)$$

5.3 COLLIMATION

The emission of radioactive radiation from an isotope occurs strongly in all directions. Collimation is used to obtain a limited cross section of radiation for measuring purposes and to absorb the remaining radiation. A collimator can thus be said to be an aperture for radioactive radiation. Collimators for both the 84-keV radiation of Tm-170 and also for the 662-keV radiation of Cs-137 were prepared from easy-to-form lead, a material with a high atomic number.

The cross-sectional geometry of the collimated beam should be chosen as large as possible to obtain a high impulse count rate, and thus a small standard deviation. On the other hand, the cross section of the collimated beam should extend only over a sampling area of a size for which an averaging of the true saturation values is sensible. Considering the available facts, the cross-sectional width of the collimated beam was chosen to be 5 mm. To obtain higher impulse count rates, and thus smaller errors, at locations with small spatial saturation gradients and larger attenuation, the geometry of the collimator slot was chosen to be 5 mm • 20 mm. The 90° rotation of one of two such collimators around their common axis could produce a collimated beam with a minimum cross-sectional area of 5 mm • 5 mm. To manufacture the collimators, lead was poured into a 5-cm-high, 9.8-cm-diameter steel tube in which a



Screw to Adjust
the Source
Height

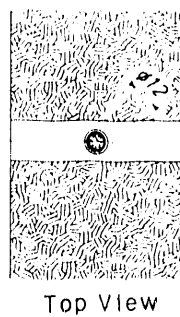
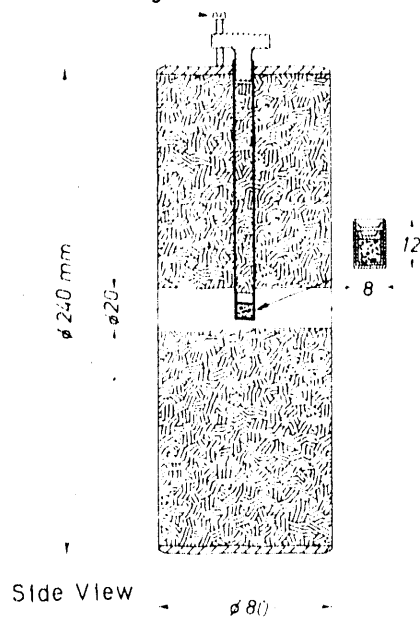


FIGURE 5.5. Schematic Diagram of the Cesium Source Shield

steel rod with a cross section of 5 mm • 20 mm was placed along the tube axis. The rod was removed after the lead cooled.

For high accuracy with short measuring times, the counting capacity of the detectors must be completely utilized. For a detector not to be uselessly loaded with scattered radiation, methods to minimize the amount of scattered radiation must be investigated. Once minimized, the remaining scattered radiation can be electronically filtered by discriminators. To minimize scattered radiation, the source radioactive beam must be collimated as much as possible by the source collimators before it strikes the sample being measured. In addition, the detector collimators are used to ensure that only a minimum of the scattered radiation exiting the sample strikes the detector.

The influence of different collimator configurations along the irradiation path and the influence of different source and detector distances was determined experimentally for Cs-137 (Figure 5.6). The different spatial arrangements of the collimators in relation to the detector and the source were characterized by the integral A of the impulse count rates between 530 and 760 keV divided by the integral B of the impulse count rates at energies lower than 530 keV (Figure 5.7). Figure 5.8 shows that the collimation length must be chosen as about 20 cm and that larger collimation lengths produced only a small improvement. Figure 5.8 also shows that neither the spatial arrangement of the collimators, the distance between source and detector, or the attenuation through a sand sample had a significant influence on the A/B ratio. Lastly, Figure 5.9 shows the collimator setup chosen for the Cs-137 and Tm-170 source-detector pairs.

5.4 DETECTOR

Scintillation counters were used as detectors. A quantum striking the detector is changed into an electrical impulse, whose magnitude is proportional to the energy of the quantum.

A scintillation counter consists of a crystal and a photomultiplier tube. Normally, the crystal is made of thallium-activated sodium iodide. When radioactive radiation strikes the crystal, fluorescent light is produced. Then, the fluorescent light travels to the photocathode installed in a vacuum tube.

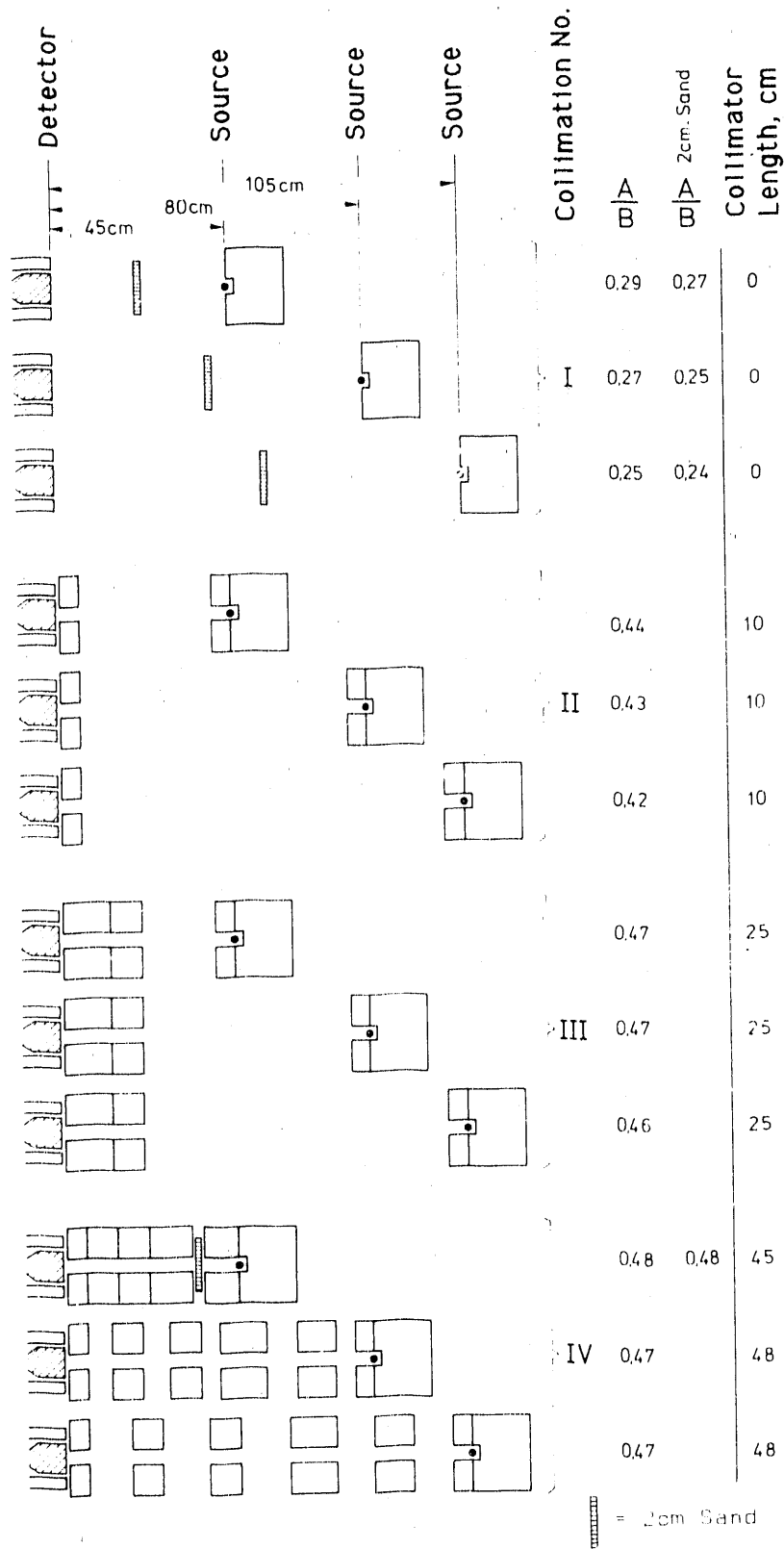


FIGURE 5.6. Influence of Different Collimator Configurations on the A/B Ratio

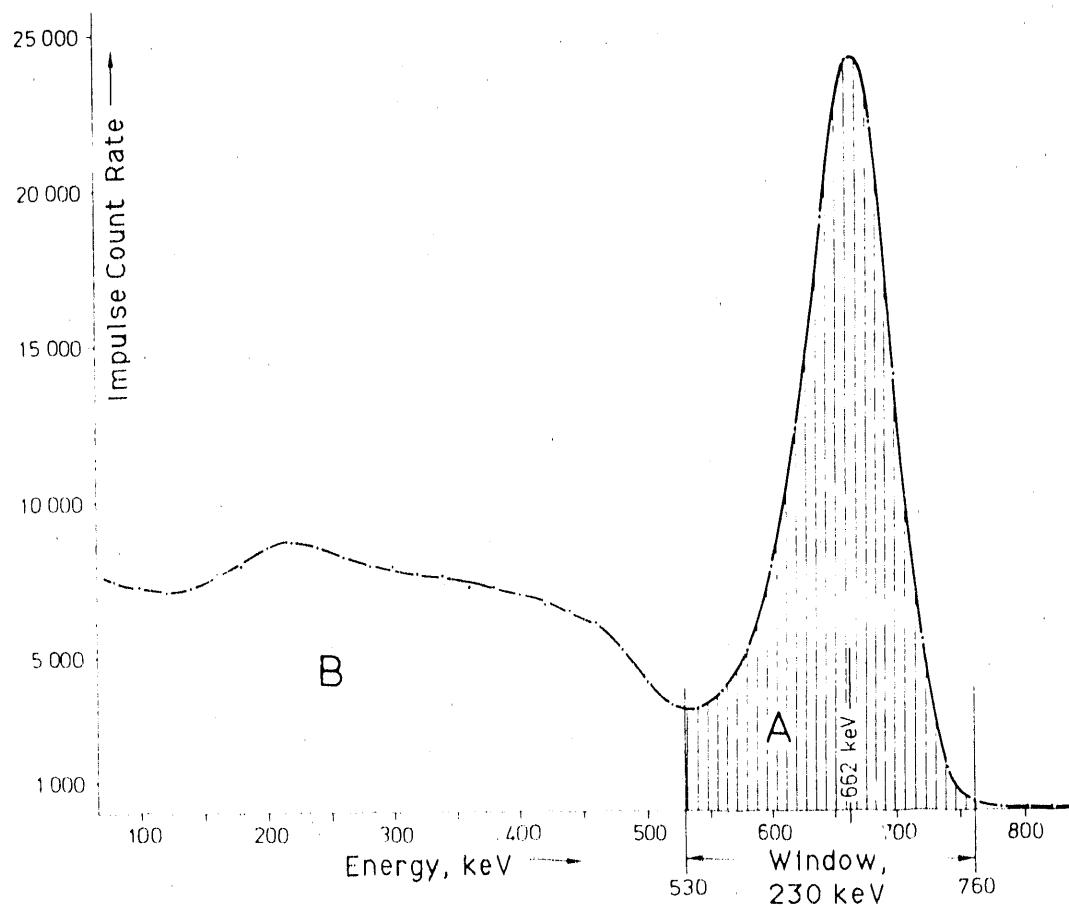


FIGURE 5.7. Impulse Count Rate Versus Energy (keV) Showing the Integral A and B

The surface of the photocathode is a light-sensitive cesium-antimony alloy. The light quanta cause electrons in the cesium-antimony alloy to be released, through the photoelectric effect. To enable the electrons to move away from the cathode, an electric field is applied. The field strength must be chosen so that, on impact with the anode, the accelerated electrons can cause the release of several more electrons. With a series of additional anodes, a multiplication of the number of electrons is produced by the applied electric field. Such a unit was designated as the "secondary electron multiplier" or photomultiplier. Figure 5.10 displays the components of the detector.

The working voltage of a photomultiplier tube lies between 1200 and 2000 V. The duration of the light impulse is 10^{-6} to 10^{-9} sec depending on

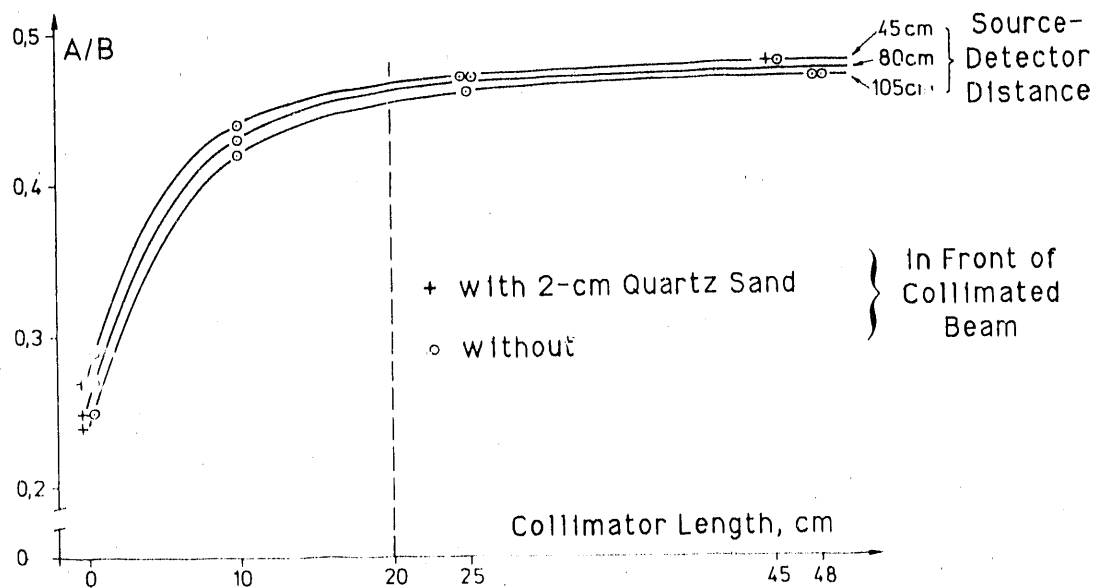


FIGURE 5.8. A/B Ratio Versus Collimation Length for Different Configurations

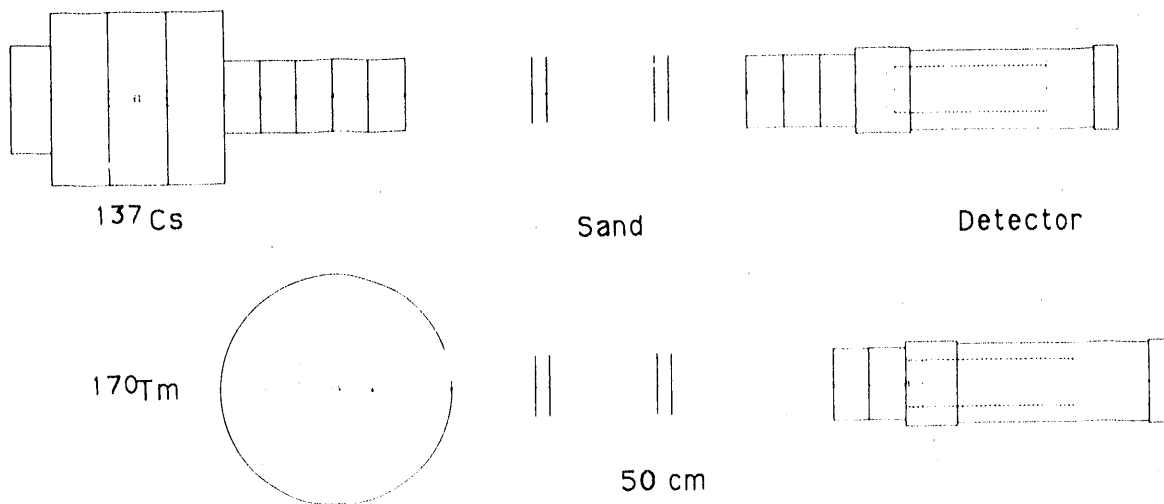


FIGURE 5.9. Selected Collimator Setup for the Cs-137 and Tm-170 Source-Detector Pairs

the scintillator substance (Glocker and Macherauch 1965, p. 180). The decay time for a NaI(Tl) crystal is $250 \cdot 10^{-9}$ sec. Thus, photomultipliers perform nearly instantaneously. The resolution of a scintillation counter is determined by its dead time (10^{-5} to 10^{-6} sec). The dead time is the duration of

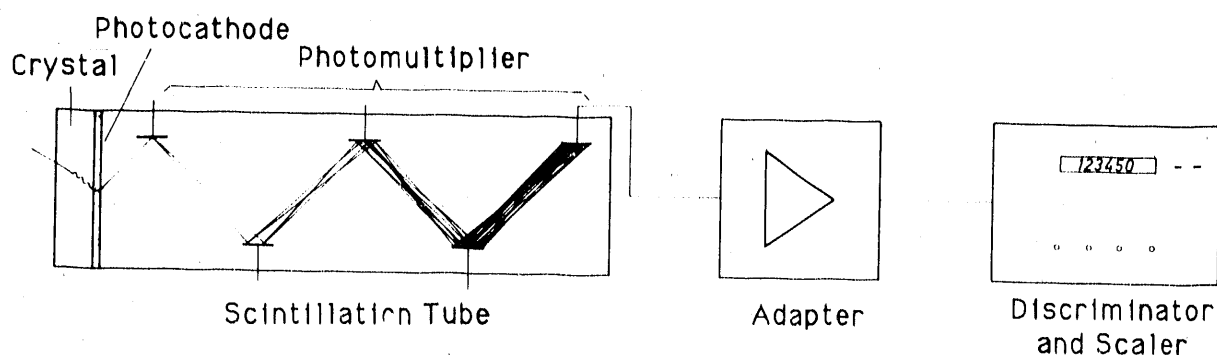


FIGURE 5.10. Schematic Diagram of the Detector Components

the recovery process after the registration of an impulse by the photomultiplier tube; in other words, the time until the next impulse can be registered with a correct impulse height. The dead time lowers the maximum order of magnitude of the quantum rate that can be registered by the scintillation counter to 10^4 impulses per second. Glocker and Macherauch (1965, p. 435) calculates that the loss of counts as a result of dead time can amount to several percent at quantum rates between 10^3 and 10^4 impulses/sec (Table 5.1).

Because of the restricted counting capacity of the scintillation counter, our goal was to count as many of the quanta of interest and as few of the other quanta as possible. For the scintillation counter to count only specific quanta, the probability of generating fluorescence must be high for the quanta with energies of interest and low for the quanta with other energies. This means that the incident radiation with the energies of interest must be absorbed as much as possible by the sodium iodide crystal, and that radiation of other energies may occur to any degree without exciting the crystal. This requirement can be partly met by selecting the thickness of the crystal so that the maximum number of quanta with the energies of interest are absorbed, while the quanta with higher energies have a smaller probability of interacting with the crystal.

TABLE 5.1. Percentage Count Loss Resulting from Dead Time as a Function of Quantum Rate

Quantum Rate (impulse/sec)	100	200	500	700	1000	2000	3000	4000	5000
Count Loss (%)	0.1	0.2	0.5	0.7	1	2	3.1	4.2	5.3

The most suitable crystal thickness for measuring the 662-keV radiation of Cs-137 and the 84-keV radiation of Tm-170 was calculated from the 99% probability of attenuation. Equation (5.5) shows the calculation of the crystal thickness. The mass attenuation coefficients of sodium iodide (NaI) for 662 keV and 84 keV are 0.075 and 2.2 cm²/g, respectively (see Chapter 6.0) and ρ_{NaI} is 3.67 g/cm³.

$$\begin{aligned} \left(\frac{J}{J_0}\right)_{\text{Cs-137}} &= \frac{1}{100} = e^{-\left(\frac{\mu}{\rho}\right)_{\text{NaI}; 0,662\text{MeV}} \cdot \rho_{\text{NaI}} \cdot x_{\text{Cs-137}}} \\ \rightarrow x_{\text{Cs-137}} &= \frac{\ln(10^{-2})}{-\left(\frac{\mu}{\rho}\right)_{\text{NaI}; 0,662\text{MeV}} \cdot \rho_{\text{NaI}}} = \frac{-4,6}{-0,075 \cdot 3,7} = 17 \text{ cm} \\ \left(\frac{J}{J_0}\right)_{\text{Tm-170}} &= \frac{1}{100} = e^{-\left(\frac{\mu}{\rho}\right)_{\text{NaI}; 0,084\text{MeV}} \cdot \rho_{\text{NaI}} \cdot x_{\text{Tm-170}}} \\ \rightarrow x_{\text{Tm-170}} &= \frac{\ln(10^{-2})}{-\left(\frac{\mu}{\rho}\right)_{\text{NaI}; 0,084\text{MeV}} \cdot \rho_{\text{NaI}}} = \frac{-4,6}{-2,2 \cdot 3,7} = 0,57 \text{ cm} \end{aligned} \tag{5.5}$$

NaI crystals are industrially manufactured. They are cultured and their price increases proportionally to their size. Because Cs-137 is an ideal source; that is, no radiation higher than 662 keV is emitted, there is no danger of an undesired loading of the photomultiplier tube by higher energy radiation. Thus, no reason existed to use an unbelievably large (17 cm) and correspondingly expensive NaI crystal for the Cs-137 measurement. Normally, to measure Cs-137 radiation, a crystal thickness on the order of 2 in. is needed, which has a attenuation probability of 80% (1 in. = 2.54 cm). Two-inch-thick crystals have a minimum diameter of 1.75 in. (4.5 cm), which is sufficient considering the 2-cm maximum width of the collimated ray. Thus, a 1.75-in. • 2-in. NaI(Tl) crystal was chosen for the Cs-137 measurement. To measure the 84-keV radiation of Tm-170, a crystal thickness of 5.7 mm was required (see Equation [5.5]). The NaI(Tl) crystal used had a 1.25-in. diameter and a 6-mm thickness.

5.5 IMPULSE HEIGHT ANALYZER

If the total energy of a gamma quantum is converted into electron energy in single or several stages within the scintillation crystal, and if the electron energy is completely released, then the intensity and thus the height of the resulting light-impulse is proportional to the gamma energy (Glocker and Macherauch 1965, p. 448). If a proportional electrical impulse forms in the photomultiplier tube as a product of the incidental light impulse, then the energy of the gamma quanta can be obtained by measuring the height of the impulse voltage provided by the scintillation counter. This measuring procedure is called impulse-height analysis, and the apparatus used is called an impulse-height analyzer. By using a discriminator, only the impulses whose impulse heights correspond to the energies of the quanta of interest are counted. The counts per unit time are thus equal to the quantum rates of interest.

The scaler used as an impulse height analyzer is a fully transistorized two-channel decade counter. The scaler contains a spectrometer and two decade counters, in addition to the timer. With this apparatus, the impulse counts for cesium and thulium at two different places could be counted simultaneously.

A high-voltage source was integrated with the scaler to operate the scintillation counter. The useful range of the scintillation counter is located within a plateau on a plot of the impulse count rate as a function of the high voltage. The experimentally determined plateaus of the cesium and thulium scintillation counters are shown graphically in Figure 5.11. The requirement for simultaneous measurement stipulated that the selected high voltage should be favorable for both scintillation counters. From this requirement, the value designated HV in Figure 5.11 was selected for the high voltage.

5.6 SOURCE-DETECTOR SCANNING SYSTEM

In principle, a saturation measurement should be possible at any location along the flume. To accomplish these measurements, the position of each of the two source-detector pairs had to be separately and arbitrarily variable

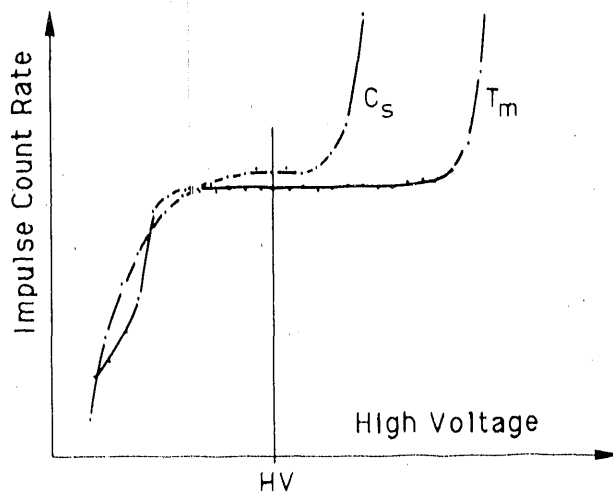


FIGURE 5.11. Plot of Impulse Count Rate Versus High Voltage Used to Select a Favorable High Voltage for the Scintillation Counters

relative to the position of the porous medium. We considered whether it was more appropriate to move the source-detector pairs relative to the porous medium, or to leave the source-detector pairs in a fixed position and to move the porous medium. A comparison of these two options showed that keeping the flume, with its water, oil, and pressure connections fixed, was easier and required less space. Nevertheless, the intermediate option of being able to move the flume vertically and the source-detector pairs horizontally still seemed plausible. However, this option was discarded because having one fixed and one movable system instead of two movable ones was more suitable. Above all, the deciding factor for movable source-detector pairs was the fact that each of the source-detector pairs could be moved independent of one another. The mechanism used to move the source-detector pairs was designated the source-detector scanning system.

The source-detector scanning system must allow fast and exact movement of the source-detector pair. The desired positional accuracy of ± 0.5 mm arose from the required resolution ability given large spatial saturation gradients. A vernier scale was used to determine the position of each source-detector pair, and thus of each collimated beam, versus the flume. The vernier scale was installed at the intersection of vertical and horizontal rulers. A

vertical ruler was affixed on each source-detector pair and a horizontal ruler was affixed on the flume (Figure 5.12).

We determined that, at any arbitrary position along the flume, the angular alignment error between the source collimator slit and the detector collimator slit should not be more than 10 angular seconds. The 10-angular-second value was calculated by assuming that the error from such a misalignment should be at most one-fourth the average error of a measured impulse count. At the maximum impulse counting rate of 10^4 counts/sec, a measuring time of 10 sec yields $\sqrt{10^5}$ counts. Thus, the average error is equal to $\sqrt{10^5}$, which equals 316 counts (see Section 6.5.2.1). One-fourth of 316 is approximately 80 counts, which is 0.08% of 10^5 . Finally, 0.08% of the cross-sectional width of the collimated beam of 5 mm or 20 mm is $4 \cdot 10^{-3}$ mm or $16 \cdot 10^{-3}$ mm, respectively. By assuming a distance of 50 cm between source and detector, the $4 \cdot 10^{-3}$ -mm and $16 \cdot 10^{-3}$ -mm misalignments correspond to a tolerated angle of 5 and 20 angular seconds, respectively.

Each source and its detector had to be moved simultaneously to maintain their precise angular alignment. Thus, the source and detector tables, on which the collimators were also placed, were connected to each other with a common cross beam (Figure 5.13). To hold the angle constant, the source and

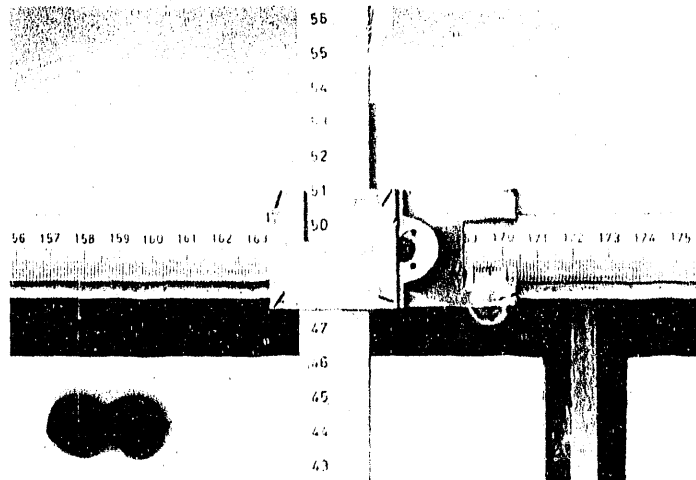


FIGURE 5.12. Vernier Scale Used to Determine the Position of Each Source-Detector Pair

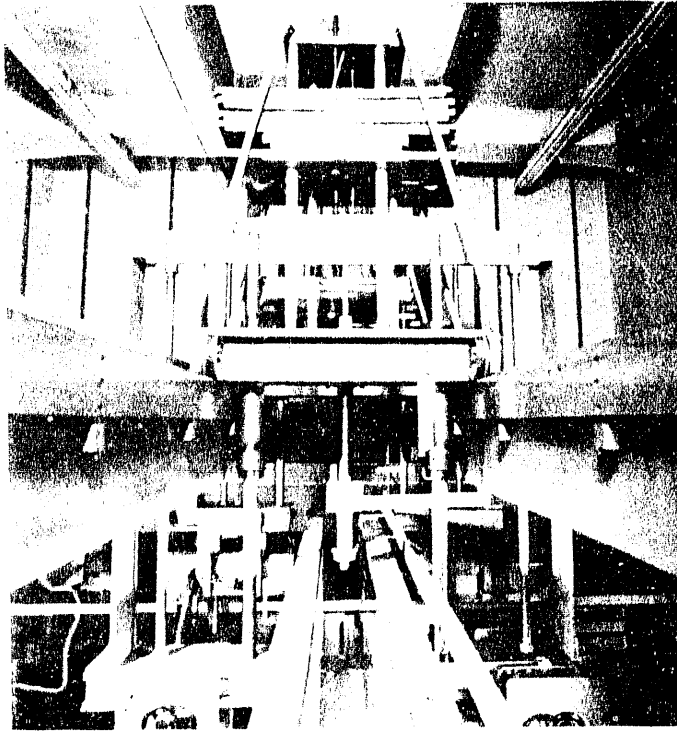


FIGURE 5.13. Bridge Connecting a Source Table and a Detector Table

detector tables were each suspended from a polished hardened-steel vertical shaft and held fixed by conical points opposite the shaft. Each of the two shafts were passed through two spherical precision bushings and were connected above to a massive crossbeam. For additional reinforcement, the rear of the tables were connected by plates to the crossbeam above.

The total weight of the thulium source table was approximately equal to the weight of the lead sphere, which served both as a shield and as a collimator of the thulium radiation. This was calculated in Equation (5.3) as more than 200 kg. The lead shield of the cesium source weighed 132 kg (Equation [5.4]). Together with the collimators, the cesium source table weighed 150 kg. To obtain an even load on the crossbeam, each detector table was loaded with compensatory weights until it stood in equilibrium with its

associated source table. Both source and detector tables could be moved horizontally normal to the experimental plane.

Because a simple, easy, and fast movement of the scanning system was desired, a counterbalance was necessary to allow each source-detector pair to be moved vertically by hand with little effort. The total weight of the thulium source-detector pair and the crossbeam was 425 kg, which consisted of two times 200 kg of lead and about 25 kg for the remaining material. Similarly, the weight of the cesium source-detector pair and crossbeam was calculated as $2(150) + 25 = 325$ kg. In the assembly of the counterbalance, these weights had to be compensated for by adding a corresponding counterweight. The objective of achieving vertical movement by hand directly over the counterbalance failed because of the great initial resistance to movement, and because of the impossibility of exactly determining the negative acceleration of the large weight. These factors would not allow the large weight to be brought to a standstill at exactly the desired position. Thus, a hand-operated oil-pressure pump had to be installed to provide the required displacement accuracy in the vertical direction.

For horizontal movement, the entire assembly used for the vertical movement (counterbalance, crossbeam, and source-detector pair) was reinforced and mounted on a cart. The cart could be moved along the length of the flume. The weight of the loaded cart used to move the thulium scanning system was $2(425)$ kg plus about 50 kg for a counterbalance frame, which totaled 900 kg. For the cesium scanning system, the loaded cart was $2(325)$ kg + 50 kg = 700 kg. Horizontal movement by hand was feasible and gave satisfactory accuracy.

A pair of rails was erected, completely independent of the flume, for the two carts to roll on. The placement of the rails onto the flume for reinforcement was excluded for several reasons. First, the extra-large weight would have necessitated a strengthening of the load supports of the flume. This would have restricted the open area available for the visual observation of the propagation processes. Second, the apparatus to incline the flume would have had to be more complicated compared to the use of independent rails, which would stay horizontal when the flume was inclined. Lastly, and

above all, we wanted to isolate the flume from vibrations to avoid changes in the porous medium due to settling. The cart rails could only be supported at their ends so that the collimated beams would have an unrestricted range of movement across the glass walls of the flume. Thus, the span of each rail was 480 cm.

Both cart rails consisted of channel beams for engineering strength. The moment of inertia of the rail was calculated from the following requirements. For the easiest and most accurate maneuverability of the cart, the least deflection, s , of the rails is required. Furthermore, the required positional accuracy of 0.5 mm implies a small change in the deflection ($\Delta\delta$) of the rails, and thus of the cart, as a function of the various location combinations of the two carts. Stated mathematically, this is

$$\Delta\delta = \delta_{max} - \delta_{min} < 0,5 \text{ mm} \quad (5.6)$$

To determine the maximum and minimum deflections in Equation (5.6), the moment of inertia (I) must be calculated. The calculation of the moment of inertia and of $\Delta\delta$ presents two problems: 1) the problem of determining the position of both carts so that the maximum vertical movement of a fixed cart due to the horizontal movement of the other cart can be calculated; and 2) the problem of making the calculation in a standard way.

Both carts and their loads were symmetrical. The bearing load on each of the four wheels was a fourth of the total weight. The total weight of the fully equipped thulium cart, P_{Tm} , was 900 kg, and the total weight of the cesium cart, P_{Cs} , was 700 kg. The length, L , of each beam serving as the cart rails was 480 cm. Because of symmetry, the load is partitioned equally on each beam. Thus, the analysis need only be done for one of the beams.

In Figure 5.14, x is the moving variable, and X defines the distance from the center of the cesium cart to the right beam support, B . a is the distance between the center of each cart. The minimum value of a , a_{min} , is 50 cm. The center of a cart can be pushed up to a minimum distance, a_0 , from the support, which is 64 cm. c_0 is the distance between the wheels and is 36 cm. The load

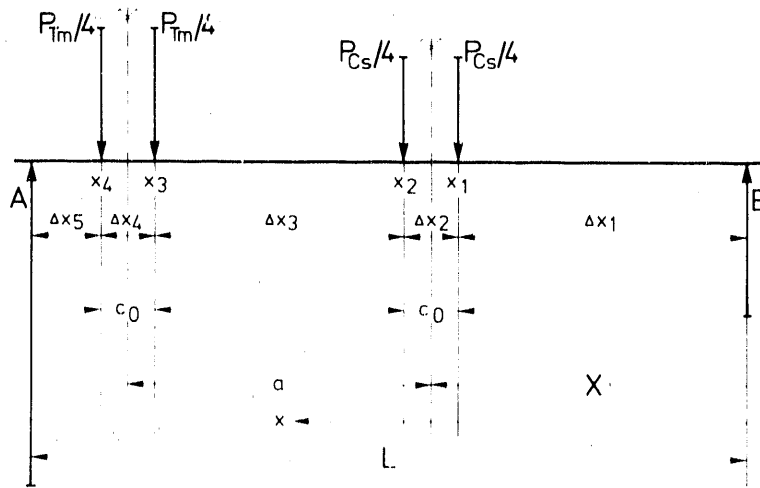


FIGURE 5.14. Stress Diagram on One of the Beams Carrying the Source-Detector Carts

on each wheel of the thulium cart is $1/4 (P_{Tm}) = 225$ kg, and the load on each wheel of the cesium cart is $1/4 (P_{Cs}) = 175$ kg. In summary,

$$\begin{array}{lll}
 P_{Tm}/4 = -225 \text{ kg} & c_0 = 36 \text{ cm} & L = 480 \text{ cm} \\
 P_{Cs}/4 = -175 \text{ kg} & a_{min} = 50 \text{ cm} & a_0 = 64 \text{ cm}
 \end{array} \quad (5.7)$$

The largest vertical deflection is certain to result when the lighter cesium cart is held at the location where the load resultant from both carts lies in the middle of the beam. The vertical deflection would decrease as the heavier thulium cart is pushed away from this location up to the minimum distance, a_0 , from support A. Based on this knowledge, X is a constant value, a must be equal to a_{min} for the determination of δ_{max} , and $a = L - X - a_0$ for the determination of δ_{min} . X is thus the single unknown in the equations describing the positions of the loads to calculate δ_{max} and δ_{min} .

The load on the middle of the beam yielding δ_{max} when the two carts are pushed together ($a = a_{min}$) is equal to the total resultant, $R = [2(P_{Tm}/4) + 2(P_{Cs}/4)]$. The distance X is determined by solving the moment balance between the total resultant and the individual loads for this load case:

$$R \cdot \frac{L}{2} = 2 \cdot (P_{Tm}/4) \cdot (X + a_{min}) + 2(P_{Cs}/4) \cdot X \quad (5.8a)$$

Thus,

$$= \frac{\{2(P_{Tm}/4) + 2(P_{Cs}/4)\} \frac{L}{2} - 2(P_{Tm}/4) a_{min}}{\{2(P_{Tm}/4) + 2(P_{Cs}/4)\}} = \frac{L}{2} - \frac{(P_{Tm}/4)}{(P_{Tm}/4 + P_{Cs}/4)} a_{min} \quad (5.8b)$$

Substituting the values summarized in Equation (5.7), Equation (5.8b) yields

$$X = \frac{480}{2} - \frac{-225}{-225 - 175} \cdot 50 = \underline{212 \text{ cm}} \quad (5.9)$$

The geometry of the force diagram for both load cases is determined by calculating δ_{max} and δ_{min} . δ_{max} is the deflection of the beam 212 cm from support B when the center of the cesium or thulium cart is 212 cm or 262 cm, respectively, from support B. δ_{min} is the deflection of the beam 212 cm from support B when the center of the thulium cart is 64 cm from support A, and the center of the cesium cart is 212 cm from support B.

The determination of a deflection (δ) at location x is made according to the principle of virtual work. The working equation for a deflection, δ , is

$$\delta = \int \frac{M \cdot M'}{E \cdot I} \cdot dx \quad (5.10a)$$

and for the case when EI is constant

$$= \frac{1}{E \cdot I} \cdot \int M \cdot M' \cdot dx \quad (5.10b)$$

where M is the bending moment at location x under the given load, and M' is the bending moment at location x because of the virtual load condition. The virtual load condition exists when a unit load is placed at the location and in the direction of the anticipated deflection.

The integration of Equation (5.10a) can be done graphically (Hofacker 1960, p. 21). Accordingly, the integral $MM'dx$ is the same as the sum of the

products of the M_i -areas and the corresponding length, y_{S_i} from the M' -area (Figure 5.15). The M -area is the moment area for the given load case. The M' -area is the moment area for the virtual load case.

The moment function for the effective load case is a variable function dependent on x , based on the load induced on the beam by the separate forces.

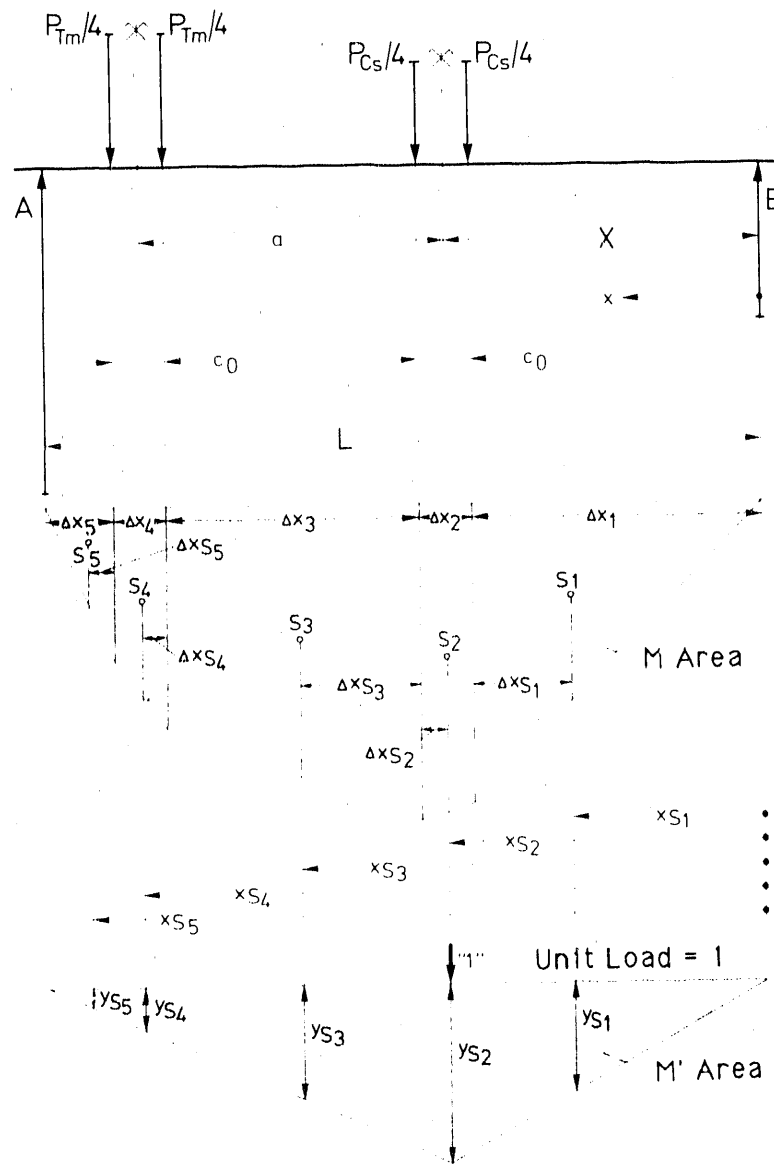


FIGURE 5.15. Graphic Integration to Calculate the Area Moment

The function is composed of straight lines with kinks at the application points of the forces. The graphic integration to be done is represented by $\sum M_i y_{S_i}$. M_i is the individual moment area between any two forces. y_{S_i} is the moment resulting from the virtual load condition at the location of the center of gravity, S_i , of the area, M_i , which is based on the effective load condition. The forces on each support must be determined to construct the moment area.

For each of the two given load cases, the force on support A is determined as a function of a by solving the moment balance at support B. The equation is

$$\begin{aligned}
 A &= \frac{-1}{L} \left\{ P_{Tm}/4 \cdot \left(\left(X+a+\frac{c_0}{2} \right) + \left(X+a-\frac{c_0}{2} \right) \right) + P_{Cs}/4 \cdot \left(\left(X+\frac{c_0}{2} \right) + \left(X-\frac{c_0}{2} \right) \right) \right\} \\
 &= \frac{-2}{L} \{ P_{Tm}/4 \cdot (X+a) + P_{Cs}/4 \cdot X \} \\
 &= \frac{-2}{480} \{ -225(212+a) - 175 \cdot 212 \} = 0,938 \cdot a + 353 \quad (\text{kg})
 \end{aligned} \tag{5.11}$$

By solving the force balance, the force on support B is

$$B = -\Sigma P - A = -2(P_{Tm}/4 + P_{Cs}/4) - A = 2(400) - A \quad (\text{kg}) \tag{5.12}$$

For the virtual load case with a unit load of -1 at the distance X from support B, the support load A' for a moment balance is

$$A' = \frac{-"1" \cdot X}{L} = \frac{212}{480} = 0,442 \tag{5.13a}$$

Because of the force balance,

$$B' = -"1" - A' = 1 - 0,442 = 0,558 \tag{5.13b}$$

With knowledge of the support forces, the moment area can be calculated by determining the moments at the load points, whose distances, Δx_i , are known. The shear forces are determined from the support and load forces. The moment at a load point is calculated as the sum of the products of the shear force and the distance between two applied forces (Table 5.2).

A partial moment area, M_i , from the M-area is calculated by using the formula for the area of a trapezoid. The arithmetic average of the two load point moments is multiplied by Δx_i or $(\Delta x_i/2)(M_{\text{left}} + M_{\text{right}})$.

The x_{S_i} 's must be known to determine the y_{S_i} -values in the M'-area. x_{S_i} is the distance between the center of gravity, S_i of a partial area and the right support B. Δx_{S_i} , the normal distance from the center of gravity of a trapezoid to its longest side, is determined by Bartsch (1968):

$$\Delta x_{S_i} = (\Delta x_i/3) \{ (M+2m)/(M+m) \} \quad (5.14)$$

In this case, m is the shorter side and M is the longer side of the parallel sides of the trapezoid, or the small and larger moments, respectively. The calculated Δx_{S_i} 's are shown in Table 5.2. Thus, the x_{S_i} 's are

$$\begin{aligned} x_{S_1} &= \Delta x_1 - \Delta x_{S_1} & x_{S_4} &= \Delta x_1 + \Delta x_2 + \Delta x_3 + \Delta x_{S_4} \\ x_{S_2} &= \Delta x_1 + \Delta x_2 - \Delta x_{S_2} & x_{S_5} &= L - 2\Delta x_{S_5} \\ x_{S_3} &= \Delta x_1 + \Delta x_2 + \Delta x_{S_3} \end{aligned} \quad (5.15)$$

The y_{S_i} -values are determined according to whether one is to the right or left of the virtual unit force by using one of the following relations:

$$\begin{aligned} y_{S_i} &= M'(X) \cdot \frac{x_{S_i}}{X} & \text{for } x_{S_i} < X \\ &= M'(X) \cdot \frac{(L-x_{S_i})}{(L-X)} & \text{for } x_{S_i} > X \end{aligned} \quad (5.16)$$

$M'(X)$, the fictitious moment at the application point of the virtual unit force, is determined by

TABLE 5.2. Calculation of Maximum and Minimum $\int MM' dx$

x (cm) Eq. (5.7) and (5.9)	Δx (cm)	(kg) Eq. (5.7)	ΣK	Q (Δx) (cm kg)	M (cm kg) $\Sigma (Q\Delta x)$	M_1 (cm ² kg) $\frac{\Delta x}{2} (M_1 + M_2)$	Δx Eq. (5.14)	x_s Eq. (5.15)	y_s Eq. (5.18)	$(MM' \Delta x)_{\max}$ (cm ³ kg) $M_1 (y_s)$
$x_B = 0$		+400			0					
$x_1 = 194$ ($=x - c_0/2$)	194	-175	+400	$+7.76 \cdot 10^4$	$7.76 \cdot 10^4$	$7.53 \cdot 10^6$	64.7	129	72.1	$5.43 \cdot 10^8$
$x_2 = 230$ ($=x + c_0/2$)	36	-175	+225	$+8.10 \cdot 10^3$	$8.57 \cdot 10^4$	$2.94 \cdot 10^6$	17.7	212	118.5	$3.48 \cdot 10^8$
$x_3 = 244$ ($=x + a - c_0/2$)	14	-225	+50	$+7.00 \cdot 10^2$	$8.4 \cdot 10^4$	$1.20 \cdot 10^6$	7.0	237	107.0	$1.28 \cdot 10^8$
$x_4 = 280$ ($=x + a - c_0/2$)	36	-225	-175	$-6.30 \cdot 10^3$	$8.01 \cdot 10^4$	$3.00 \cdot 10^6$	17.8	262	96.4	$2.89 \cdot 10^8$
$x_A = 480$	200	+400	-400	$-8.00 \cdot 10^4$		$8.01 \cdot 10^6$	66.7	347	58.8	$4.71 \cdot 10^8$
					0					
										$\int (MM' dx)_{\max} = \Sigma (MM' \Delta x)_{\max} = 1.77 \times 10^9 \text{ cm}^3 \text{ kg}$

$\int MM' dx$ at maximum deflection $a = 50$ cm; $A = 0.938(50) + 353 = 400$; $B = 800 - 400 = 400$

TABLE 5.2. (contd)

x (cm) Eq. (5.7) and (5.9)	Δx (cm)	(kg) Eq. (5.7)	Q (kg) ΣK	Q (Δx) (cm kg)	M (cm kg) $\Sigma (Q\Delta x)$	M_i (cm ² kg) $\frac{\Delta x}{2} (M_0 + M_i)$	Δx Eq. (5.14)	x_s Eq. (5.15)	y_s Eq. (5.18)	$(MM' \Delta x)_{\max}$ (cm ³ kg) $M_i (y_s)$
$x_B = 0$	194	+256	+256	+4.97 • 10 ⁴	0	4.82 • 10 ⁶	64.7	129	72.1	3.48 • 10 ⁸
$x_1 = 194$ ($=x - c_0/2$)	36	-175	+81	+2.92 • 10 ³	4.97 • 10 ⁴	1.84 • 10 ⁶	17.8	212	118.5	2.18 • 10 ⁸
$x_2 = 230$ ($=x + c_0/2$)	168	-175	-94	-1.58 • 10 ⁴	5.26 • 10 ⁴	7.51 • 10 ⁶	79.1	309	75.5	5.68 • 10 ⁸
$x_3 = 398$ ($=x + a - c_0/2$)	36	-225	-319	-1.15 • 10 ⁴	3.68 • 10 ⁴	1.12 • 10 ⁶	16.9	415	28.7	3.21 • 10 ⁷
$x_4 = 434$ ($=x + a - c_0/2$)	46	-225	-544	-2.50 • 10 ⁴	2.53 • 10 ⁴	5.82 • 10 ⁵	15.3	450	13.3	7.74 • 10 ⁷
$x_A = 480$		+544			0					

$\int MM' dx$ at minimum deflection $a = 204$ cm; $A = 0.938(204) + 353 = 544$; $B = 800 - 544 = 256$

$$\int (MM' dx)_{\min} = \Sigma (MM' \Delta x)_{\min} = 1.24 \times 10^9 \text{ cm}^3 \text{ kg}$$

$$M'(x) = A' \cdot (L-x) = B' \cdot x \quad (5.17)$$

With the support forces defined by Equation (5.13), and $X = 212$ cm, $M'(X)$ is 118.5 cm. If $M'(x) = 118.5$ cm, $X = 212$ cm, and $L = 480$ cm are inserted into Equation (5.16), then

$$\begin{aligned} y_{S_i} &= 0,559x_{S_i} && \text{for } x_{S_i} \leq 212, && \text{thus for } x_{S_1} && \text{and } x_{S_2} \\ &\text{or} && && && (5.18) \\ &= 0,442(480-x_{S_i}) && \text{for } x_{S_i} \geq 212, && \text{thus for } x_{S_2} && \text{through } x_{S_5} \end{aligned}$$

The calculation of the integral $\int MM'dx$ is shown in Table 5.2. For the load case with the maximum deflection, $a = a_{\min} = 50$ cm. For the load case with the minimum deflection, $a = (L-X-a_0) = (480-212-64) = 204$ cm.

In both investigated load cases, we are interested in the deflection at distance X , the distance between support B and the center of the stationary cesium cart. As mentioned, the maximum deflection, δ_{\max} , occurs when the thulium cart is next to the cesium cart, and their centers are separated by the minimum distance, a_{\min} . δ_{\min} occurs when the thulium cart is located next to support A; thus, the center of the cart is the distance a_0 from support A. With the integrals calculated in Table 5.2 substituted in Equation (5.10b), the equations to calculate the minimum and maximum deflections are

$$\begin{aligned} \delta_{\max(212)} &= \frac{1}{E \cdot I} \cdot 1,77 \cdot 10^9 \text{ cm}^3 \cdot \text{kg} && (5.19) \\ \delta_{\min(212)} &= \frac{1}{E \cdot I} \cdot 1,24 \cdot 10^9 \text{ cm}^3 \cdot \text{kg} \end{aligned}$$

If these values are inserted into Equation (5.6), then

$$\Delta\delta_{zul} = \frac{1}{E \cdot I} \cdot 0,53 \cdot 10^9 \text{ cm}^3 \cdot \text{kg} < 0,5 \text{ mm} \quad (5.20)$$

By assuming a value of $2.1 \cdot 10^6$ kg/cm² for the modulus of elasticity, E , of the building steel, the moment of inertia of the beam that satisfies Equation (5.20) is

$$I_{erf} \geq \frac{0,53 \cdot 10^9 \text{ cm}^3 \cdot \text{kg}}{2,1 \cdot 10^6 \text{ kg/cm} \cdot 5 \cdot 10^{-2} \text{ cm}} = 5,1 \cdot 10^3 \text{ cm}^4 \quad (5.21)$$

A commercially available beam with a higher moment of inertia is the beam designated UNP 28 with a moment of inertia, I_x , of 6280 cm^4 . With $I = 6280 \text{ cm}^4$ and $E = 2,1 \cdot 10^6 \text{ kg/cm}^2$, the maximum and minimum deflection of the beam for $X = 212 \text{ cm}$ is, according to Equation (5.19),

$$\begin{aligned} \delta_{max}(212) &= \frac{1,77 \cdot 10^9}{2,1 \cdot 10^6 \cdot 6,28 \cdot 10^3} = 0,134 \text{ cm} \\ \delta_{min}(212) &= \frac{1,24 \cdot 10^9}{2,1 \cdot 10^6 \cdot 6,28 \cdot 10^3} = 0,094 \text{ cm} \\ \Delta\delta &= 0,04 \text{ cm} \end{aligned} \quad (5.22)$$

Equation (5.22) reveals that the design of the beams fulfills the requirement stated in Equation (5.6).

To be able to adjust the elevation of the rails, they were mounted on the side of the beams instead of on the top (Figure 5.16), even though this

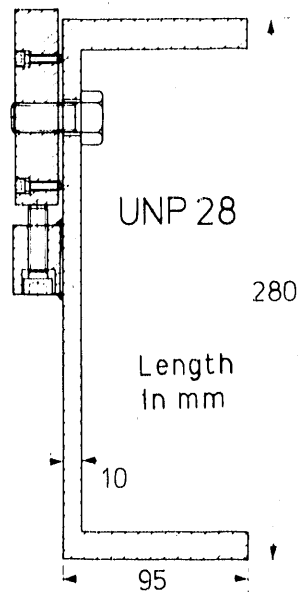


FIGURE 5.16. Schematic Diagram of Rail-Beam Assembly

produced torsion on the beam. Support blocks were welded to the side at evenly spaced intervals. Each support block had a tap screw used to adjust the elevation of the rail. Once set at the desired elevation, the rails were bolted to the beam. The elevation of the rails was adjusted to provide a horizontal track during an average deflection. In this way, the easy maneuverability of both carts in the horizontal direction was guaranteed, despite the average vertical deflection of the beam on the order of 1 mm, according to Equation (5.22).

6.0 DEVELOPMENT OF A METHOD FOR DETERMINING SATURATIONS DURING EXPERIMENTS ON THE DISPLACEMENT OF WATER, OIL, AND AIR IN POROUS MEDIA

6.1 THE DEFINITION OF SATURATION

Saturation, S (%), is the fluid volume with respect to the effective pore volume. The moisture content, θ (%) is the fluid volume with respect to the total volume. Consequently, the following relation exists between saturation and moisture content:

$$S = \theta/n \quad (6.1)$$

where n (%) is the porosity; that is, the effective pore volume with respect to the total volume.

6.2 REQUIREMENTS OF THE SATURATION MEASUREMENT METHOD

There were four requirements of a method for measuring saturation. The first requirement was that the method should permit simultaneous determination of the saturations of a petroleum derivative, water, and air over space and time in two-dimensional experiments performed in the physical model in the laboratory.

The second requirement was that the maximum standard deviation of the measured fluid saturation should not exceed $\pm 2\%$ saturation. This error tolerance limit results from the stipulation that the residual saturation of a petroleum derivative (which can be assumed to be about 4% saturation, according to laboratory experiments and practical experience) should be measurable within about a $\pm 50\%$ error.

The third requirement was that the porous medium (of at least 15 cm in cross-sectional width to be able to disregard the wall effect) should not be disturbed during a saturation measurement, so that the dynamic processes could occur unperturbed.

The fourth requirement was that the sample area over which the saturation was measured had to be large relative to a pore or grain diameter. This

macroscopic scale of observation is based on the continuum perspective, assumed in Darcy's equation. On the other hand, the sample area had to be small because the measured capillary rise curves in the quartz sand were likely to be relatively flat, representing large saturation changes with elevation for the assumed macroscopic observation.

6.3 PROPOSAL OF SOLUTIONS TO MEET THE STATED REQUIREMENTS

6.3.1 Alternative Methods

Various methods are available to determine the saturation of a fluid in a porous media, such as gravimetric methods, electrical resistance methods, and wave or particle radiation attenuation methods, particularly gamma or neutron radiation attenuation.

The gravimetric method was eliminated as an alternative for the determination of local saturations because the porous medium has to be disturbed, thus violating the condition of nondisturbance. The requirement for a locally limited measurement cannot be met by using electrical resistance. The attenuation of neutron radiation is often used to determine the saturation of water based on the high attenuation ability of hydrogen compared to that of other elements. However, because both water and petroleum derivatives (hydrocarbons) contain hydrogen, the measurement of neutron attenuation cannot serve to differentiate between the saturations of water and oil.

6.3.2 Attenuation of Gamma Radiation

Gamma radiation, in contrast to alpha or beta radiation, which refer to the flow of protons or electrons, respectively, is not particle radiation but rather wave radiation. To characterize wave radiation, first its wavelength or frequency must be known, and second, its intensity must be determined. Light rays, x-rays, and gamma rays are, like radio waves, electromagnetic waves, which can also be termed photon rays. This method of notation originates from Planck's quantum theory, according to which the emission and absorption of radiation energy by atoms cannot occur in arbitrary amounts, but only as integral multiples of determined values--the radiation quantum

(photons). The quantity of energy in one quantum of wave radiation of frequency ν , or of wavelength λ is

$$\epsilon = h \cdot \nu = \frac{h \cdot c}{\lambda} \quad (6.2)(a)$$

where h is Planck's constant and c is the velocity of light. For practical use, Equation (6.2) can be rewritten as

$$\epsilon = \frac{12,4}{\lambda} \quad (\text{KeV}) \quad (6.3)$$

if λ is specified in angstrom units (\AA). Thus, a quantum of wave radiation with a wavelength of 1.24 \AA has an energy of 10 KeV. The electron volt (eV) is an energy unit used frequently in atomic physics. It is

$$1\text{eV} = 1,6 \cdot 10^{-12} \text{erg} \quad (6.4)$$

The interaction of gamma radiation with matter is manifested as the deflection of individual quanta from their original trajectory. This interaction with matter leads to a reduction in the number of nondeflected quanta moving in their original direction. This effect is designated as matter attenuation. Because of this matter attenuation, the radiation intensity continually decreases as the radiation quanta traverse through more matter, thereby increasing the probability of interactions with the matter. The radiation intensity, J , is the radiation energy, in a unit of time, impinging on a unit cross-sectional area. The radiation energy equals the sum of the energies furnished by the separate quanta.

The decrease in the radiation intensity of monochromatic radiation, meaning radiation whose quanta all have the same energy, occurs according to the exponential decay law

(a) Equations were taken directly from the German text and, in some cases, use a different notation. For example, 0,01 = 1/100, whereas in this text, 1/100 would be shown as 0.01. Multiplication is indicated by a dot in the equations and in the text.

$$J = J_0 \cdot e^{-\left\{\left(\frac{\mu}{\rho}\right) \cdot x \cdot \rho\right\}} \quad (6.5)$$

where J_0 is the radiation intensity of a collimated, monochromatic beam before passing through matter, and J is the radiation intensity after passage. The term (μ/ρ) with the dimensions $(L^2 \cdot M^{-1})$ is the mass attenuation coefficient. It characterizes the attenuation characteristic of a specific matter for a radiation of specific energy. The mass attenuation coefficient is thus a property of the irradiated matter at the quantum energy of the monochromatic radiation. The mass attenuation coefficient will be discussed in Section 6.4.1 in greater detail. x , with the dimension (L) , is the thickness of the irradiated matter. ρ , with the dimensions $(M \cdot L^{-3})$, is the density.

Because of the assumed monochromatic radiation, the intensities J and J_0 can be interpreted as specific numbers of quanta. The term "specific" is, in this case, related to the time and the cross-sectional area. In detectors used to measure radiation intensity, each quantum detected yields an electrical impulse, whose value characterizes the energy of the quantum. So, instead of a quantum, one can speak of an impulse. For the current application, a quantum and an impulse are identical. This introduces the concept of the impulse count, which refers to the number of impulses generated by a collimated beam of a specified cross-sectional area during a suitable period of measurement. The period of measurement considered adequate was initially specified as 10 sec, which was later confirmed, and the cross-sectional area of the collimated beam was 1 cm^2 . Thus, J and J_0 in Equation (6.5) can be designated as impulse counts instead of intensities. For unspecified periods of measurements, J and J_0 are designated as impulse count rates.

The material irradiated in the experiments was composed of water (W), oil (O), air (L), and sand (S) as well as the glass (g) of the walls. Figure 6.1 is a realistic representation of a porous medium cross section. Figure 6.2 is a schematic representation of how the complex component geometry in Figure 6.1 can be translated into incremental path lengths of the various components.

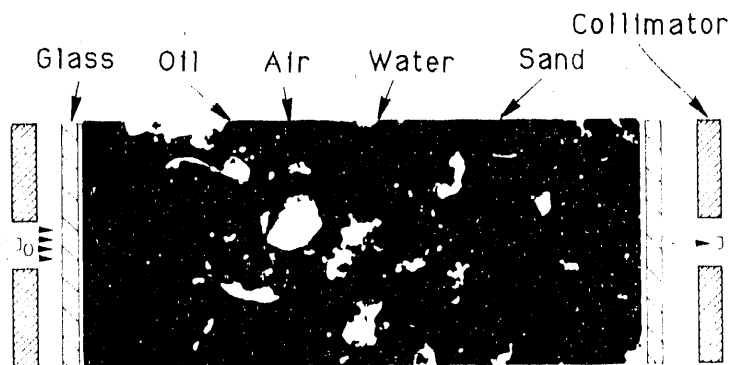


FIGURE 6.1. Realistic Representation of the Sand Porous Medium Filled with Water, Oil, and Air

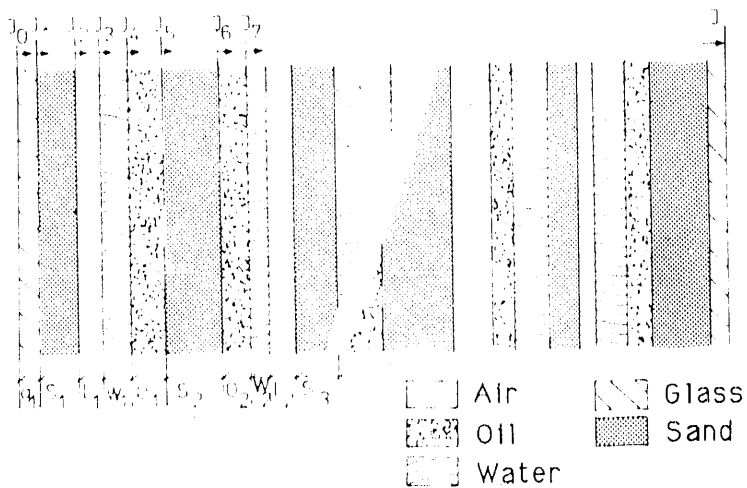


FIGURE 6.2. Schematic Representation of Incremental Path Lengths of the Various Components Traversed by the Radiation Beam

If Equation (6.5) were applied to each of the incremental path lengths (repeated in an arbitrary order) of the different materials in Figure 6.2, then

$$\begin{aligned}
J_1 &= J_0 \cdot e^{-\left\{ \left(\frac{\mu_g}{\rho_g} \right) g_1 \cdot \rho_g \right\}} \\
J_2 &= J_1 \cdot e^{-\left\{ \left(\frac{\mu_s}{\rho_s} \right) s_1 \cdot \rho_s \right\}} \\
J_3 &= J_2 \cdot e^{-\left\{ \left(\frac{\mu_l}{\rho_l} \right) l_1 \cdot \rho_l \right\}} \\
J_4 &= J_3 \cdot e^{-\left\{ \left(\frac{\mu_w}{\rho_w} \right) w_1 \cdot \rho_w \right\}} \\
J_5 &= J_4 \cdot e^{-\left\{ \left(\frac{\mu_o}{\rho_o} \right) o_1 \cdot \rho_o \right\}} \\
J_6 &= J_5 \cdot e^{-\left\{ \left(\frac{\mu_s}{\rho_s} \right) s_2 \cdot \rho_s \right\}} \\
J_7 &= J_6 \cdot e^{-\left\{ \left(\frac{\mu_o}{\rho_o} \right) o_2 \cdot \rho_o \right\}}
\end{aligned} \tag{6.6}$$

etc.

If J_n and J_{n+1} are calculated step by step, then the additive character of the attenuation relation (Equation [6.5]) is evident. If the exponents within the same medium are summed, then

$$J = J_0 \cdot e^{-\left\{ \left(\frac{\mu_g}{\rho_g} \right) \Sigma_g \cdot \rho_g + \left(\frac{\mu_s}{\rho_s} \right) \Sigma_s \cdot \rho_s + \left(\frac{\mu_w}{\rho_w} \right) \Sigma_w \cdot \rho_w + \left(\frac{\mu_o}{\rho_o} \right) \Sigma_o \cdot \rho_o + \left(\frac{\mu_l}{\rho_l} \right) \Sigma_l \cdot \rho_l \right\}}$$

and with $\Sigma_j = x_j$ (6.7)

$$= J_0 \cdot e^{-\left\{ \left(\frac{\mu_g}{\rho_g} \right) x_g \cdot \rho_g + \left(\frac{\mu_s}{\rho_s} \right) x_s \cdot \rho_s + \left(\frac{\mu_w}{\rho_w} \right) x_w \cdot \rho_w + \left(\frac{\mu_o}{\rho_o} \right) x_o \cdot \rho_o + \left(\frac{\mu_l}{\rho_l} \right) x_l \cdot \rho_l \right\}}$$

The various summations stated in Equation (6.7) are reproduced graphically by converting Figure 6.2 to 6.3.

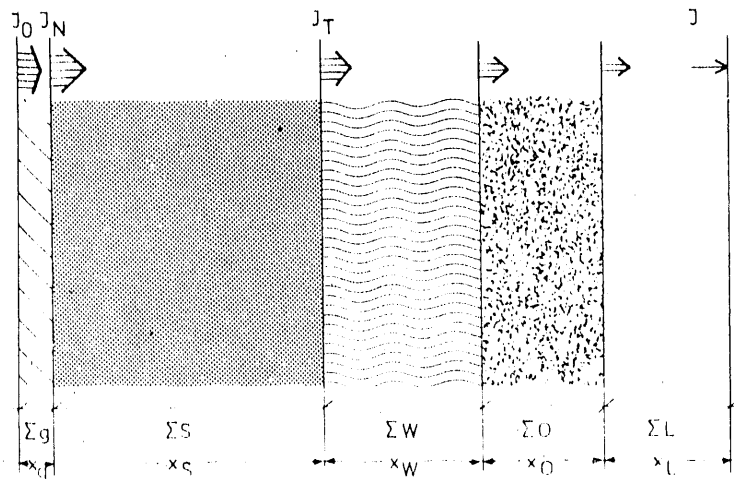


FIGURE 6.3. Schematic Representation of the Summation of Path Lengths of the Various Components Traversed by the Radiation Beam

Because the density of air is three orders of magnitude lower than that of water, oil, and sand, the attenuation effect of air (whose mass attenuation coefficient is of the same order of magnitude as that of the other materials; cross reference Figure 6.6) is small, and thus the last item in Equation (6.7) can be disregarded. Thus, Equation (6.7) is reduced to

$$J = J_0 \cdot e^{-\left\{ \left(\frac{\mu_g}{\rho_g} \right) x_g \cdot \rho_g + \left(\frac{\mu_s}{\rho_s} \right) x_s \cdot \rho_s + \left(\frac{\mu_w}{\rho_w} \right) x_w \cdot \rho_w + \left(\frac{\mu_o}{\rho_o} \right) x_o \cdot \rho_o \right\}} \quad (6.8)$$

As shown in Figures 6.1, 6.2, and 6.3, a collimated beam, which leaves the source with the impulse count rate J_0 , is always attenuated by the glass walls. Thus, the impulse count rate reduced by the glass walls is designated as the null impulse count rate, J_N . J_N is determined theoretically as

$$J_N = J_0 \cdot e^{-\left\{ \left(\frac{\mu_g}{\rho_g} \right) x_g \cdot \rho_g \right\}} \quad (6.9)$$

In practice, J_N was determined by making a null measurement by measuring the intensity of the radiation after it passed through the glass walls of the empty flume.

The irradiation widths, x , can be written as functions of the dimensionless porosity, n , and the thickness of the porous medium in the irradiation

direction, B (with the dimension of a length), as well as the dimensionless saturations of water and oil, S_W and S_O , respectively. Thus,

$$x_S = (1-n) \cdot B ; \quad x_W = n \cdot S_W \cdot B ; \quad x_O = n \cdot S_O \cdot B \quad (6.10)$$

With Equations (6.9) and (6.10), Equation (6.8) is reduced to

$$J = J_N \cdot e^{-B \left\{ \left(\frac{\mu_S}{\rho_S} \right) \cdot (1-n) \rho_S + \left(\frac{\mu_W}{\rho_W} \right) n \cdot S_W \cdot \rho_W + \left(\frac{\mu_O}{\rho_O} \right) n \cdot S_O \cdot \rho_O \right\}} \quad (6.11)$$

Before water or oil is introduced into the initially oven-dried porous medium, S_W and S_O , and thus the last two exponential terms in Equation (6.11), are zero. The dry impulse count rate, J_T , (that is, the null-impulse count rate through oven-dried sand filling) can be written as

$$J_T = J_N \cdot \exp \left(-B \left\{ \left(\frac{\mu_S}{\rho_S} \right) \cdot (1-n) \rho_S \right\} \right) \quad (6.12)$$

By knowing the irradiated thickness, B , the mass attenuation coefficient of sand, (μ_S/ρ_S) , the density of sand, ρ_S , as well as the measured null and dry impulse count rates, J_N and J_T , the porosity, n , can be determined experimentally by explicit representation from Equation (6.12)

$$n = 1 + \frac{\ln \left(\frac{J_T}{J_N} \right)}{B \left(\frac{\mu_S}{\rho_S} \right) \rho_S} \quad (6.13)$$

During the course of the two-dimensional experiments, not even the slightest change in the elevation of the sand surface could be documented. Thus, we concluded that the position of the separate grains within the unconsolidated sand filling was constant during an experiment. This permitted the dry impulse count rate, J_T , to be assumed constant and thus, J_T could be determined experimentally, according to Equation (6.12), at the beginning of an experiment. With J_T serving as the initial impulse count rate, Equation (6.11) can be reduced by inserting Equation (6.12) to

$$J = J_T \cdot e^{-n \cdot B \left\{ \left(\frac{\mu_W}{\rho_W} \right) S_W \cdot \rho_W + \left(\frac{\mu_O}{\rho_O} \right) S_O \cdot \rho_O \right\}} \quad (6.14)$$

Equation (6.14), the attenuation equation for gamma radiation passing through a mixture of water, oil, and air in an incompressible sand filling of porosity n and held together by two glass walls separated by the width B , is a relation with two unknowns: the saturation of water and the saturation of oil. The determination of both unknown saturations requires two independent relations to be solved simultaneously.

One way to obtain two independent equations is to observe the attenuation of gamma radiation at two different radiation energies. The pair of independent equations results from invoking Equation (6.14) for each of the two energies with presumably different mass attenuation coefficients. In this way, the independent equations have the general form of

$$m_I = a_I \cdot S_W + b_I \cdot S_O \quad ; \quad m_{II} = a_{II} \cdot S_W + b_{II} \cdot S_O$$

Assuming that the determinant $D = \begin{vmatrix} a_I & b_I \\ a_{II} & b_{II} \end{vmatrix} \neq 0$, the equation pair is clearly solvable. The solutions are

$$S_W = \frac{1}{D} \begin{vmatrix} m_I & b_I \\ m_{II} & b_{II} \end{vmatrix} \quad ; \quad S_O = \frac{1}{D} \begin{vmatrix} a_I & m_I \\ a_{II} & m_{II} \end{vmatrix}$$

Written out, the solutions are given as

$$\begin{vmatrix} m_I & b_I \\ m_{II} & b_{II} \end{vmatrix} = \ln\left(\frac{J}{J_T}\right)_I \cdot (-n \cdot B \left(\frac{\mu_O}{\rho_O}\right)_{II} \cdot \rho_O) - \ln\left(\frac{J}{J_T}\right)_{II} \cdot (-n \cdot B \left(\frac{\mu_O}{\rho_O}\right)_I \cdot \rho_O)$$

$$\begin{vmatrix} a_I & m_I \\ a_{II} & m_{II} \end{vmatrix} = (-n \cdot B \left(\frac{\mu_W}{\rho_W}\right)_I \cdot \rho_W) \cdot \ln\left(\frac{J}{J_T}\right)_{II} - (-n \cdot B \left(\frac{\mu_W}{\rho_W}\right)_{II} \cdot \rho_W) \cdot \ln\left(\frac{J}{J_T}\right)_I$$

$$D = n^2 B^2 \left\{ \left(\frac{\mu_W}{\rho_W}\right)_I \cdot \rho_W \left(\frac{\mu_O}{\rho_O}\right)_{II} \cdot \rho_O - \left(\frac{\mu_W}{\rho_W}\right)_{II} \cdot \rho_W \left(\frac{\mu_O}{\rho_O}\right)_I \cdot \rho_O \right\} \begin{vmatrix} \left(\frac{\mu_O}{\rho_O}\right)_I \left(\frac{\mu_O}{\rho_O}\right)_{II} \cdot \rho_O \\ \left(\frac{\mu_O}{\rho_O}\right)_I \left(\frac{\mu_O}{\rho_O}\right)_{II} \cdot \rho_O \end{vmatrix}$$

$$= n^2 B^2 \left(\frac{\mu_O}{\rho_O}\right)_I \cdot \left(\frac{\mu_O}{\rho_O}\right)_{II} \cdot \rho_O \cdot \rho_W \left\{ \frac{\left(\frac{\mu_W}{\rho_W}\right)_I}{\left(\frac{\mu_O}{\rho_O}\right)_I} - \frac{\left(\frac{\mu_W}{\rho_W}\right)_{II}}{\left(\frac{\mu_O}{\rho_O}\right)_{II}} \right\}$$

therefore,

$$S_W = \frac{\left(\frac{\mu_0}{\rho_0}\right)_I \cdot \ln\left(\frac{J}{J_I}\right)_{II} - \left(\frac{\mu_0}{\rho_0}\right)_{II} \cdot \ln\left(\frac{J}{J_I}\right)_I}{n \cdot B \cdot \rho_W \left(\frac{\mu_0}{\rho_0}\right)_I \left(\frac{\mu_0}{\rho_0}\right)_{II} \left\{ \frac{\left(\frac{\mu_W}{\rho_W}\right)_I}{\left(\frac{\mu_0}{\rho_0}\right)_I} - \frac{\left(\frac{\mu_W}{\rho_W}\right)_{II}}{\left(\frac{\mu_0}{\rho_0}\right)_{II}} \right\}} \quad (6.15)$$

$$S_0 = \frac{\left(\frac{\mu_W}{\rho_W}\right)_{II} \cdot \ln\left(\frac{J}{J_I}\right)_I - \left(\frac{\mu_W}{\rho_W}\right)_I \cdot \ln\left(\frac{J}{J_I}\right)_{II}}{n \cdot B \cdot \rho_0 \left(\frac{\mu_0}{\rho_0}\right)_I \left(\frac{\mu_0}{\rho_0}\right)_{II} \left\{ \frac{\left(\frac{\mu_W}{\rho_W}\right)_I}{\left(\frac{\mu_0}{\rho_0}\right)_I} - \frac{\left(\frac{\mu_W}{\rho_W}\right)_{II}}{\left(\frac{\mu_0}{\rho_0}\right)_{II}} \right\}}$$

Uniqueness of the solution, given that $D \neq 0$, requires that the expression in the curly brackets must be different from zero. This requires that the following inequality be valid:

$$\left\{ \frac{\left(\frac{\mu_W}{\rho_W}\right)_I}{\left(\frac{\mu_0}{\rho_0}\right)_I} \right\}_I \neq \left\{ \frac{\left(\frac{\mu_W}{\rho_W}\right)_{II}}{\left(\frac{\mu_0}{\rho_0}\right)_{II}} \right\}_{II} \quad (6.16)$$

Section 6.4 will deal further with the consequences of this condition.

6.3.3 Use of Radioactive Tracers

Another possible method of using attenuation of radiation, with an energy α , to measure fluid saturations nondestructively can be derived by rearranging Equation (6.14) as follows:

$$\left(\frac{J}{J_I}\right)_\alpha = e^{-n \cdot B \left\{ \left(\frac{\mu_W}{\rho_W}\right)_\alpha \cdot S_W \cdot \rho_W + \left(\frac{\mu_0}{\rho_0}\right)_\alpha \cdot S_0 \cdot \rho_0 \right\}} \quad (6.17)$$

The method consists of the radioactive labeling of one of the two fluids; that is, the use of radioactive tracers. Because the total amount of petroleum derivative in the physical model would be considerably smaller than that of water, radiolabeling the petroleum derivative is suitable from a radiation

safety standpoint. The petroleum derivative is also more adaptable to radiolabeling than water from a chemical viewpoint.

Various chemical compounds are available as oil-soluble isotope carriers. The suitability of a radioactive compound is determined by the extent to which it migrates from the petroleum derivative by diffusion, adsorption, and evaporation. White (1949) describes an oil-soluble carrier for the radioisotope Co-60. From a radiation safety viewpoint, it is advantageous if the half-life of the radionuclide used as a tracer lies within the order of magnitude of 10 to 100 days. For practical reasons, the half-life should not be shorter than 3 days, and the standard emitted energy should be larger than 0.5 MeV. Examples of isotopes that meet these criteria for radiolabeling the petroleum derivative and that are available commercially include Br-77 (57-h half-life; 0.24- and 0.52-MeV energy), I-124 (4.5 days; 0.60, 0.73, 1.72 MeV), Sb-122 (2.8 days; 0.56 MeV), Sb-124 (60 days; 0.6 MeV), and Fe-59 (45 days; 1.10 and 1.29 MeV). It is advisable to add bromine or iodine only to unsaturated hydrocarbons with relatively high boiling points, such as octane, decane, or dodecane, otherwise the volatility of the halogenated hydrocarbon would not be disregardably small. The use of antimony isotopes with unsaturated hydrocarbons produced a conversion into triphenylantimony, and the use of Fe-59 with unsaturated hydrocarbons produced a conversion into Fe(III) -tristearate or -acetalacetate, all of which would reduce the probability of adsorption.

The exiting impulse count rate, J , of monochromatic radiation with energy β generated by the isotope tracer can be determined from the schematic diagram in Figure 6.4.

The term dJ_p is the infinitesimal, internally produced impulse count rate. It is the product of the volume-specific, produced impulse count rate J_v and the infinitesimal section dx , corresponding to the oil saturation. The

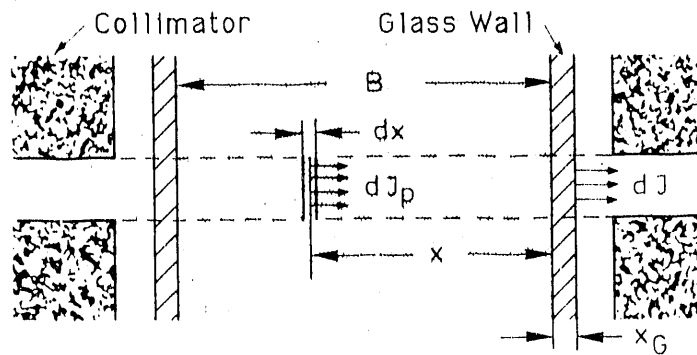


FIGURE 6.4. Generation of Infinitesimal Impulse Count Rate Reaching the Detector by the Tracer Method

attenuation of this infinitesimal, internally produced impulse count rate is determined by the following equation

$$dJ = dJ_p \cdot e^{-x \left\{ \left(\frac{\mu_S}{\rho_S} \right) \beta (1-n) \rho_S + \left(\frac{\mu_W}{\rho_W} \right) \beta \cdot n \cdot S_W \cdot \rho_W + \left(\frac{\mu_O}{\rho_O} \right) \beta \cdot n \cdot S_O \cdot \rho_O \right\}} \cdot e^{-\left(\frac{\mu_G}{\rho_G} \right) \beta \cdot \rho_G \cdot x_G} \quad (6.18)$$

$$= J_V \cdot n \cdot S_0 \cdot dx \cdot e^{-\left\{ \left(\frac{\mu_S}{\rho_S} \right) \beta (1-n) \rho_S + \left(\frac{\mu_W}{\rho_W} \right) \beta \cdot n \cdot S_W \cdot \rho_W + \left(\frac{\mu_O}{\rho_O} \right) \beta \cdot n \cdot S_O \cdot \rho_O \right\} x} \cdot e^{-\left(\frac{\mu_G}{\rho_G} \right) \beta \cdot \rho_G \cdot x_G}$$

which corresponds to Equation (6.11). Integrating over the width B gives for J the integral of the infinitesimal impulse count rate (as a function of the attenuating materials) based on the method of radioactive tracers

$$J = J_V \cdot n \cdot S_0 \cdot c_g \cdot \int_0^B e^{-\left\{ \left(\frac{\mu_S}{\rho_S} \right) \beta (1-n) \rho_S + \left(\frac{\mu_W}{\rho_W} \right) \beta \cdot n \cdot S_W \cdot \rho_W + \left(\frac{\mu_O}{\rho_O} \right) \beta \cdot n \cdot S_O \cdot \rho_O \right\} x} \cdot dx$$

$$= J_V \cdot n \cdot S_0 \cdot c_g \cdot \frac{1}{-\left\{ \left(\frac{\mu_S}{\rho_S} \right) \beta (1-n) \rho_S + \left(\frac{\mu_W}{\rho_W} \right) \beta \cdot n \cdot S_W \cdot \rho_W + \left(\frac{\mu_O}{\rho_O} \right) \beta \cdot n \cdot S_O \cdot \rho_O \right\}} \cdot e^{-\left\{ \left(\frac{\mu_S}{\rho_S} \right) \beta (1-n) \rho_S + \left(\frac{\mu_W}{\rho_W} \right) \beta \cdot n \cdot S_W \cdot \rho_W + \left(\frac{\mu_O}{\rho_O} \right) \beta \cdot n \cdot S_O \cdot \rho_O \right\} x} \Big|_0^B = J_V \cdot n \cdot S_0 \cdot c_g \cdot \frac{1}{-\left\{ \left(\frac{\mu_S}{\rho_S} \right) \beta (1-n) \rho_S + \left(\frac{\mu_W}{\rho_W} \right) \beta \cdot n \cdot S_W \cdot \rho_W + \left(\frac{\mu_O}{\rho_O} \right) \beta \cdot n \cdot S_O \cdot \rho_O \right\}} (e^{-\left\{ \left(\frac{\mu_S}{\rho_S} \right) \beta (1-n) \rho_S + \left(\frac{\mu_W}{\rho_W} \right) \beta \cdot n \cdot S_W \cdot \rho_W + \left(\frac{\mu_O}{\rho_O} \right) \beta \cdot n \cdot S_O \cdot \rho_O \right\} B} - 1)$$

$$= J_V \cdot n \cdot S_0 \cdot c_g \cdot \frac{(1 - e^{-B \left\{ \left(\frac{\mu_S}{\rho_S} \right) \beta (1-n) \rho_S + \left(\frac{\mu_W}{\rho_W} \right) \beta \cdot n \cdot S_W \cdot \rho_W + \left(\frac{\mu_O}{\rho_O} \right) \beta \cdot n \cdot S_O \cdot \rho_O \right\}})}{\left\{ \left(\frac{\mu_S}{\rho_S} \right) \beta (1-n) \rho_S + \left(\frac{\mu_W}{\rho_W} \right) \beta \cdot n \cdot S_W \cdot \rho_W + \left(\frac{\mu_O}{\rho_O} \right) \beta \cdot n \cdot S_O \cdot \rho_O \right\}} \quad (6.19)$$

By introducing the simplifying assumption that the tracer element and the integrated source are the same isotope, one can substitute the logarithm of Equation (6.17)

$$\frac{\ln\left(\frac{J}{J_T}\right)_{\alpha=\beta}}{-B} = \left\{ \left(\frac{\mu_W}{\rho_W}\right)_{\alpha=\beta} \cdot n \cdot S_W \cdot \rho_W + \left(\frac{\mu_O}{\rho_O}\right)_{\alpha=\beta} \cdot n \cdot S_O \cdot \rho_O \right\} \quad (6.20)$$

into Equation (6.19)

$$J = J_V \cdot n \cdot S_O \cdot c_g \cdot \frac{(1 - e^{-\{B\left(\frac{\mu_S}{\rho_S}\right) \cdot (1-n)\rho_S - \ln\left(\frac{J}{J_T}\right)\}})}{\left\{\left(\frac{\mu_S}{\rho_S}\right) \cdot (1-n)\rho_S - \left(\ln\left(\frac{J}{J_T}\right)\right)/B\right\}} \quad (6.21)$$

Solving Equation (6.21) for S_O yields

$$S_O = \frac{J \left\{ \left(\frac{\mu_S}{\rho_S}\right) \cdot (1-n)\rho_S - \left(\ln\left(\frac{J}{J_T}\right)\right)/B \right\}}{J_V \cdot n \cdot \exp\left(-\left(\frac{\mu_g}{\rho_g}\right)\rho_g \cdot x_g\right) \cdot \left(1 - \exp\left(-\left\{B\left(\frac{\mu_S}{\rho_S}\right) \cdot (1-n)\rho_S - \ln\left(\frac{J}{J_T}\right)\right\}\right)\right)} \quad (6.22)$$

An explicit representation for the water saturation is determined from Equation (6.20) and the oil saturation calculated from Equation (6.22) as

$$S_W = \frac{\ln\left(\frac{J}{J_T}\right) + B\left(\frac{\mu_O}{\rho_O}\right)n \cdot S_O \cdot \rho_O}{-B\left(\frac{\mu_W}{\rho_W}\right)n \cdot \rho_W} \quad (6.23)$$

From Equation (6.18), it can be seen that the infinitesimal impulse count rate reaching the detector decreases exponentially with increasing distance x from the boundary facing the detector. The practical significance of this is that the contribution to the integrated recorded impulse count rate is greater from quanta generated near the detector-side boundary than from quanta generated farther from this boundary. The contribution from remote quanta decreases very quickly with increasing distance from this wall, and soon becomes so small that it fails to influence the mean value of the infinitesimal impulse count rate from the first layers close to the wall. Observations made during the development of the method to fill the physical model with sand documented that at insular air saturation the oil preferentially stayed along the walls of the physical model. The phenomenon is clearly a consequence of

the larger pores along the walls (see Section 3.9.1 of Schiegg [1979]). This fact and the conclusion that tracers closest to the walls would dominate the radiation attenuation measurement, producing a nonrepresentative measurement, led to a final conclusion that a saturation measurement method relying on radioactive tracers would not be suitable for the planned model experiments. Furthermore, the type of radiation protection measures necessary while using the radioactive tracers and the complications arising from these measures were additional disadvantages. Thus, further consideration of the radioactive tracer method was abandoned.

6.3.4 Conclusion

Because of the decision to abandon the radioactive tracer method, the one method left for determining fluid saturations was the measurement of the attenuation of impulse count rates generated by two radiation sources having different monochromatic energies. With this method, the unknown oil and water saturations are determined according to the equation pair in Equation (6.15). The validity of the inequality in the ratios of the mass attenuation coefficients of oil and water (Equation [6.16]) is clearly necessary for the solution of Equation (6.15). The following section deals with the consequences resulting from the need for this inequality.

6.4 CONSEQUENCES FROM THE REQUIREMENT OF THE VALIDITY OF THE INEQUALITY STATED IN EQUATION (6.16)

To clarify the conditions for the validity of the inequality in Equation (6.16), which is required for a unique solution to Equation (6.15), we must first deal more closely with the nature of the mass attenuation coefficient and its dependence on the radiation energy.

6.4.1 Mass Attenuation Coefficient

The attenuation of a collimated monochromatic radiation beam through matter occurs according to

$$J = J_0 \cdot e^{-\mu \cdot x} \quad (6.24)$$

The term μ with the dimension (L^{-1}) is the attenuation coefficient. Because attenuation is a result of the interaction of quanta with the electrons of the atoms of the irradiated matter, the attenuation coefficient is dependent on the number of electrons in the atom, and thus on the atomic number, the atomic structure, and the density of the irradiated matter, as well as on the radiation energy. To eliminate the dependence on the density, the linear attenuation coefficient, μ (L^{-1}), is divided by the density ρ , ($M \cdot L^{-3}$), to yield the mass attenuation coefficient (μ/ρ) ($L^2 \cdot M^{-1}$), and the previous Equation (6.24) is converted into Equation (6.5).

The types of interactions of quanta with matter, and thus the different types of attenuation of radioactive radiation by matter, are shown schematically in Figure 6.5.

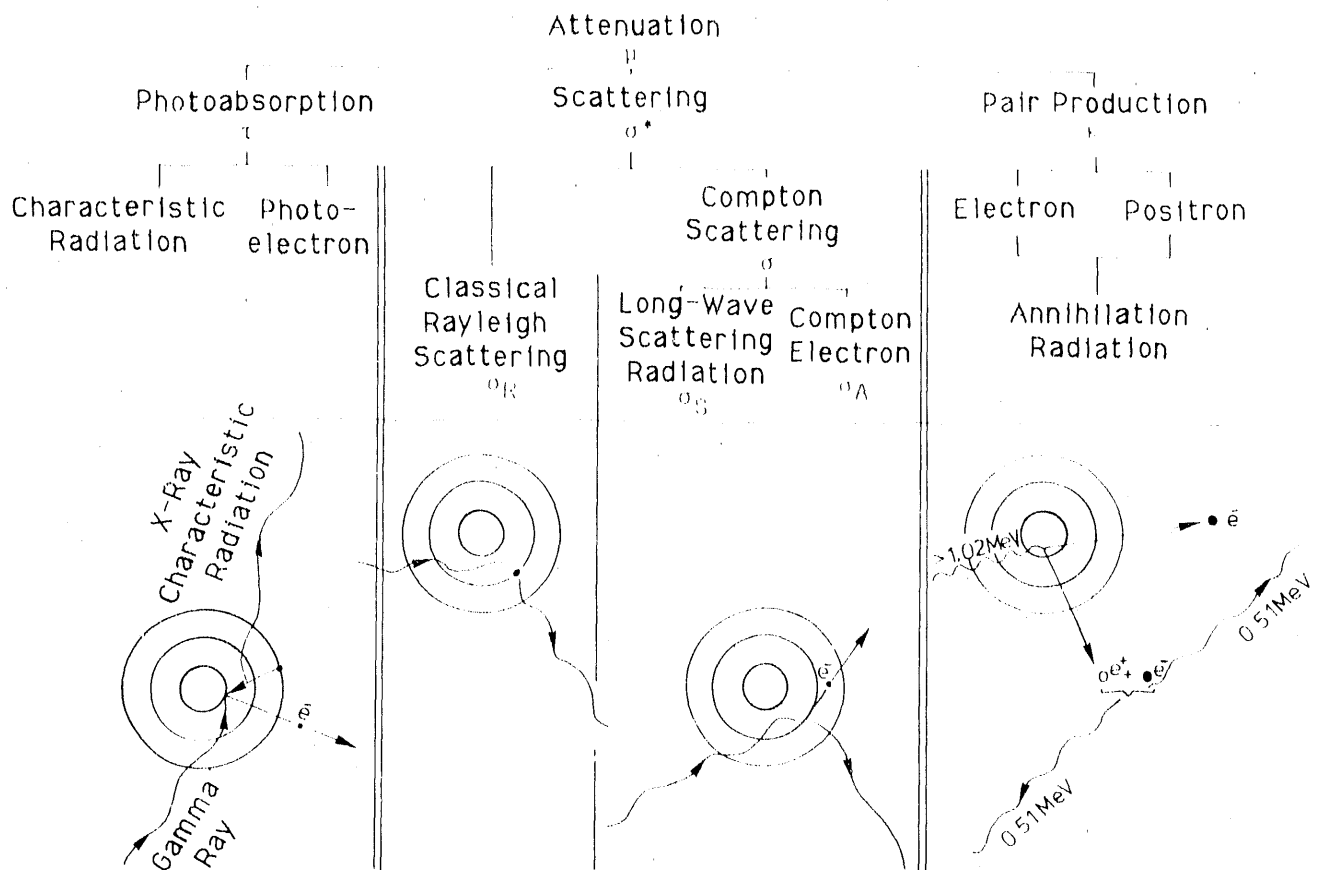


FIGURE 6.5. Schematic Representation of the Types of Attenuation

The attenuation coefficient, μ , is the sum of the attenuation effect from photoabsorption, τ , from scattering, σ^* , and from pair production, κ . All of these parameters have the dimension (L^{-1}).

$$\mu = \tau + \sigma^* + \kappa \quad (L^{-1}) \quad (6.25)$$

With respect to density, Equation (6.25) becomes

$$\frac{\mu}{\rho} = \frac{\tau}{\rho} + \frac{\sigma^*}{\rho} + \frac{\kappa}{\rho} \quad (L^2 \cdot M^{-1}) \quad (6.26)$$

The mass attenuation coefficient produced by photoabsorption, τ/ρ , can be approximated as, according to Glocker and Macherauch (1965, p. 118),

$$\frac{\tau}{\rho} = C \cdot \lambda^3 \cdot Z^3 \quad (6.27)$$

where λ is the wavelength, Z is the atomic number, and C is a universal constant dependent on the material. According to Marmier (1960, p. 45), the photoeffect is a function of the atomic number raised to the fourth to fifth power.

The mass attenuation coefficient produced by scattering, σ^*/ρ , includes the contribution from a mass attenuation coefficient describing the classical Rayleigh elastic scattering (σ_R/ρ), which refers only to the deviation of the primary radiation, and the contribution from a mass attenuation coefficient describing Compton scattering (σ/ρ). During Compton scattering, the energy of the deviated radiation is reduced, compared to that of the primary radiation, by the amount of energy associated with the emitted Compton electron and its total inertia. As a result, the deviated quantum displays a greater wavelength, compared to the primary quantum. The Compton scatter coefficient, σ , is composed of a component σ_S from inelastic collisions and a component σ_A from the emitted Compton electrons. According to Marmier (1960, p. 45), the Compton effect decreases monotonically with increasing energy for relatively high energies, and the Z -dependence is linear for relatively high energies.

The mass attenuation coefficient produced by pair (electron and positron) production, κ/ρ , increases above the $2 \cdot m_e \cdot c^2 = 1.02$ MeV (Glocker and Macherauch 1965, p. 130) static energy of the electron-positron pair, beginning with $\log(h \cdot \nu)$ according to Marmier (1960, p. 45). The term m_e is the resting mass of the electron, c is the velocity of light in a vacuum, h is Planck's constant, and ν is the velocity of light, c , divided by the wavelength, λ . The dependence of pair production on the atomic number is approximately quadratic.

The separate mass attenuation coefficients and their summation to yield one mass attenuation coefficient as a function of energy are shown in Figure 6.6a and b for water and lead, respectively, as examples.

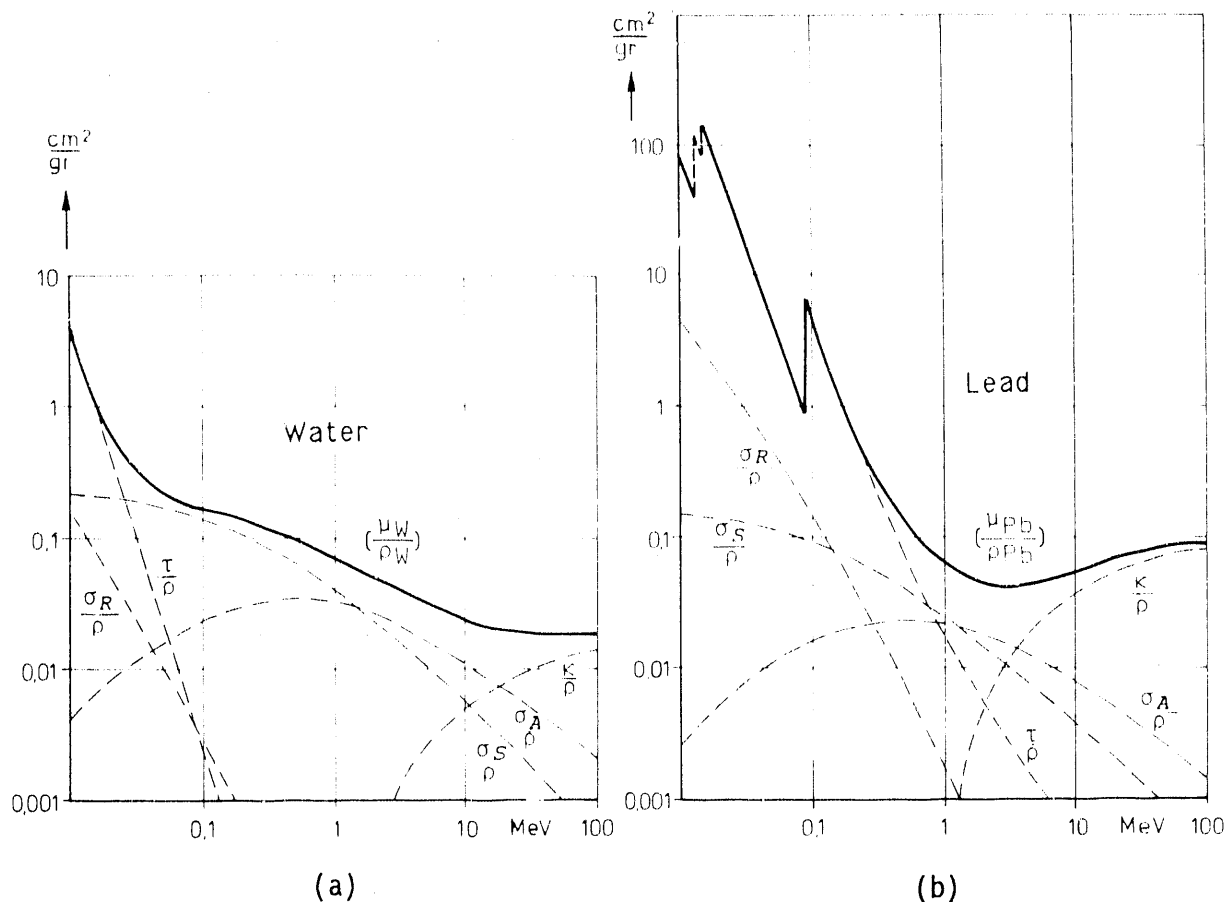


FIGURE 6.6. Values for the Separate Mass Attenuation Coefficients and Their Summation as a Function of Energy for a) Water and b) Lead

From Figure 6.6a and b, it can be seen that the photoeffect is associated with lower energies of the primary quantum, and that pair production is associated with higher energies of the primary quantum. The attenuation produced by scattering extends over the entire energy area, but is most significant in the middle energy range. The proportion of the three attenuation effects is dependent on the atomic structure; that is, on the atomic number of the attenuating matter. Figure 6.7 shows the isolines representing the atomic numbers at which the proportions of the photoeffect and Compton scattering and of Compton scattering and pair production are equal. Figure 6.7 shows the regions within which each attenuation effect predominates as a function of energy and the atomic number.

As stated in Equation (6.7), the exponent in the attenuation equation for a mixture of various materials is equal to the sum of individual exponents for each component.

$$\left(\frac{\mu_G}{\rho_G}\right) x_G \cdot \rho_G = \left(\frac{\mu_1}{\rho_1}\right) x_1 \cdot \rho_1 + \left(\frac{\mu_2}{\rho_2}\right) x_2 \cdot \rho_2 + \dots + \left(\frac{\mu_n}{\rho_n}\right) x_n \cdot \rho_n \quad (6.28)$$

Because the x_i s can be interpreted as area-specific volumes, the product $x_i \cdot \rho_i \cdot g$ represents area-specific weights, G_i , where g is acceleration of gravity. In particular, $x_G \cdot \rho_G \cdot g$ can be interpreted as the area-specific total weight, G_T . Thus, the quotient of G_i divided by G_T represents the weight fraction, g_i , of each component

$$g_i = \frac{G_i}{G_T} = \frac{x_i \cdot \rho_i \cdot g}{x_G \cdot \rho_G \cdot g} \quad (6.29)$$

With Equation (6.29), Equation (6.28) can be written as a determinative equation for the mass attenuation coefficient of a mixture

$$\left(\frac{\mu_G}{\rho_G}\right) = \left(\frac{\mu_1}{\rho_1}\right) g_1 + \left(\frac{\mu_2}{\rho_2}\right) g_2 + \dots + \left(\frac{\mu_n}{\rho_n}\right) g_n \quad (6.30)$$

A collection of similar molecules can be considered a mixture of the composite atoms. The weight fractions, g_i , of the separate elements are determined as quotients of the product of the atomic weight, A , times the

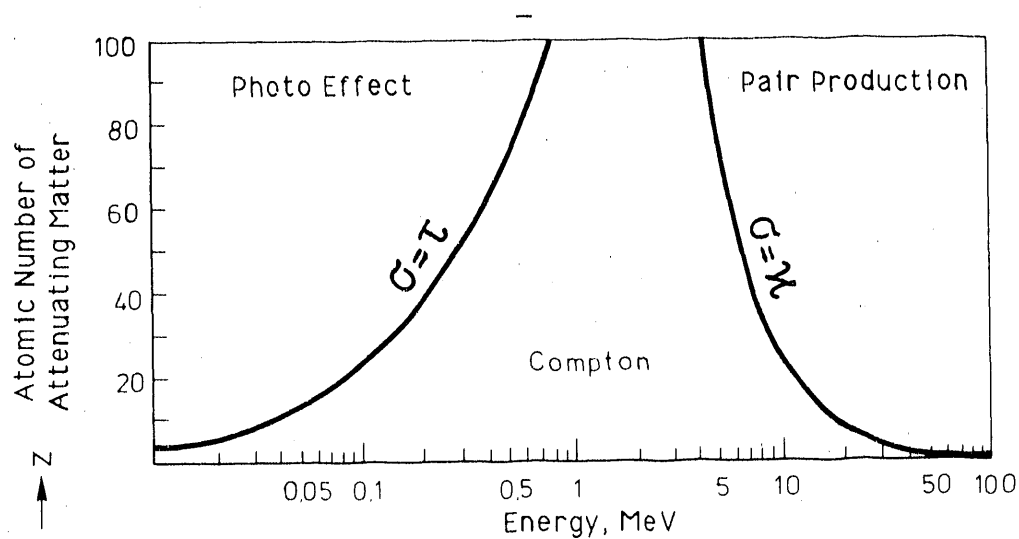


FIGURE 6.7. Isolines Representing the Atomic Numbers at Which the Proportion of τ and σ and of σ and κ are Equal

number of atoms, AA, of the pertinent element in the molecule divided by the molecular weight, M, of the chemical compound. Thus, the mass attenuation coefficient of a compound, μ_V/ρ_V , consisting of two elements, ϵ_1 and ϵ_2 , is

$$\left(\frac{\mu_V}{\rho_V}\right) = \left(\frac{\mu}{\rho}\right)_{\epsilon_1} \cdot \frac{\Lambda_{\epsilon_1} \cdot AA_{\epsilon_1}}{M} + \left(\frac{\mu}{\rho}\right)_{\epsilon_2} \cdot \frac{\Lambda_{\epsilon_2} \cdot AA_{\epsilon_2}}{M} \quad (6.31)$$

The mass attenuation coefficients of many of the elements of practical importance for the energy range between 0.01 to 100 MeV are given in Grodstein (1957). From these elemental values, the mass attenuation coefficients for the compounds of interest as a function of energy were calculated by using Equation (6.31). Table 6.1 lists the parameter values and the calculated mass attenuation coefficients for water (H_2O), quartz sand (SiO_2), and a representative petroleum derivative (C_8H_{18}).

Figure 6.8 shows graphically the calculated mass attenuation coefficients in Table 6.1, along with the mass attenuation coefficients for air, iron,

TABLE 6.1. Calculation of the Mass Attenuation Coefficients of Water, Quartz Sand, and Oil

Compound	Element	Atomic Weight	No. of Atoms Per Molecule	Weight Fraction In the Molecule $\frac{A_i Z_i^2}{\sum A_i Z_i^2}$	MeV	0,01	0,0151P	0,015	0,0159d	0,02	0,03
H ₂ O	H	1	2	0,111	84,6 $\frac{10P^2}{(9P^2)}$	0,045	41,9	1,500	135	0,041	0,039
	O	16	1	0,889		5,271				0,748	0,330
	M = 18 (Molecular Weight)					5,314				1,642	0,769
SiO ₂	Si	28	1	0,889	Calculated from Grodstein 1957	16,147	41,9	1,540	135	2,114	0,672
	O	16	2	0,111		3,162				0,449	0,198
	M = 60 (Molecular Weight)					19,309				5,907	2,563
C ₆ H ₁₄	C	12	6	0,857	$\frac{10P^2}{(9P^2)}$	1,920	41,9	0,060	135	0,361	0,212
	H	1	14	0,143		0,061				0,058	0,057
	M = 98 (Molecular Weight)					1,981				0,714	0,419

TABLE 6.1. (contd)

	0.04	0.05	0.06	0.08	0.10	0.15	0.20	0.30	0.40	0.50	0.60	0.70	0.80	0.90	1	1.5
	0.06	0.07	0.08	0.10	0.15	0.20	0.30	0.40	0.50	0.60	0.70	0.80	0.90	1	1.5	
	0.08	0.10	0.12	0.15	0.20	0.30	0.40	0.50	0.60	0.70	0.80	0.90	1	1.5		
	0.10	0.12	0.15	0.20	0.30	0.40	0.50	0.60	0.70	0.80	0.90	1	1.5			
	0.12	0.15	0.20	0.30	0.40	0.50	0.60	0.70	0.80	0.90	1	1.5				
	0.15	0.20	0.30	0.40	0.50	0.60	0.70	0.80	0.90	1	1.5					
	0.20	0.30	0.40	0.50	0.60	0.70	0.80	0.90	1	1.5						
	0.30	0.40	0.50	0.60	0.70	0.80	0.90	1	1.5							
	0.40	0.50	0.60	0.70	0.80	0.90	1	1.5								
	0.50	0.60	0.70	0.80	0.90	1	1.5									
	0.60	0.70	0.80	0.90	1	1.5										
	0.70	0.80	0.90	1	1.5											
	0.80	0.90	1	1.5												
	0.90	1	1.5													
	1	1.5														
	1.5															

TABLE 6.1. (contd)

	2	3	4	5	5	5	5	5	10	15	20	30	40	50	60	80	100
0,0460	0,0420	0,0401	0,0383	0,0365	0,0348	0,0332	0,0316	0,0300	0,0284	0,0268	0,0252	0,0236	0,0220	0,0204	0,0188	0,0172	0,0156
0,0007	0,0009	0,0010	0,0011	0,0012	0,0013	0,0014	0,0015	0,0016	0,0017	0,0018	0,0019	0,0020	0,0021	0,0022	0,0023	0,0024	0,0025
0,0030	0,0031	0,0032	0,0033	0,0034	0,0035	0,0036	0,0037	0,0038	0,0039	0,0040	0,0041	0,0042	0,0043	0,0044	0,0045	0,0046	0,0047
0,0000	0,0000	0,0000	0,0000	0,0000	0,0000	0,0000	0,0000	0,0000	0,0000	0,0000	0,0000	0,0000	0,0000	0,0000	0,0000	0,0000	0,0000
0,0000	0,0000	0,0000	0,0000	0,0000	0,0000	0,0000	0,0000	0,0000	0,0000	0,0000	0,0000	0,0000	0,0000	0,0000	0,0000	0,0000	0,0000
0,0000	0,0000	0,0000	0,0000	0,0000	0,0000	0,0000	0,0000	0,0000	0,0000	0,0000	0,0000	0,0000	0,0000	0,0000	0,0000	0,0000	0,0000
0,0000	0,0000	0,0000	0,0000	0,0000	0,0000	0,0000	0,0000	0,0000	0,0000	0,0000	0,0000	0,0000	0,0000	0,0000	0,0000	0,0000	0,0000
0,0000	0,0000	0,0000	0,0000	0,0000	0,0000	0,0000	0,0000	0,0000	0,0000	0,0000	0,0000	0,0000	0,0000	0,0000	0,0000	0,0000	0,0000
0,0000	0,0000	0,0000	0,0000	0,0000	0,0000	0,0000	0,0000	0,0000	0,0000	0,0000	0,0000	0,0000	0,0000	0,0000	0,0000	0,0000	0,0000
0,0000	0,0000	0,0000	0,0000	0,0000	0,0000	0,0000	0,0000	0,0000	0,0000	0,0000	0,0000	0,0000	0,0000	0,0000	0,0000	0,0000	0,0000
0,0000	0,0000	0,0000	0,0000	0,0000	0,0000	0,0000	0,0000	0,0000	0,0000	0,0000	0,0000	0,0000	0,0000	0,0000	0,0000	0,0000	0,0000

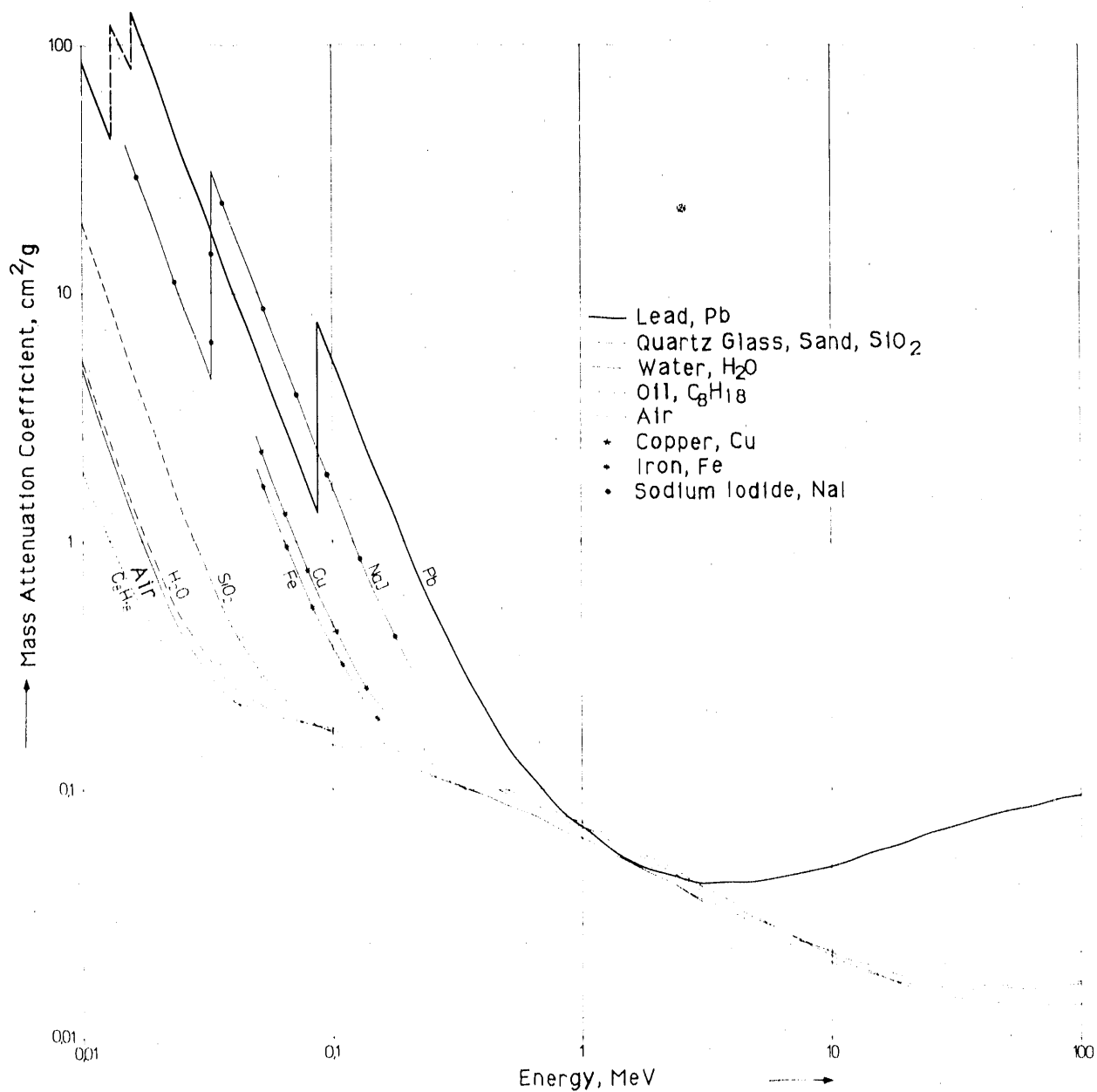


FIGURE 6.8. Mass Attenuation Coefficients as a Function of Energy for Lead, Water, Air, Quartz Sand, and a Representative Petroleum Derivative, as Well as Additional Elements or Compounds (after Grodstein 1957)

copper, sodium iodide, and lead. The mass attenuation coefficient of sodium iodide was used for the design of the radiation detector crystal.

The thickness of the scintillation crystal was chosen to optimize the scintillation counter for detecting radiation of a specific energy. The thickness of the crystal was selected to minimize the probability that radiation of higher energy that was not of interest would not interact with the crystal. Thus, it could pass through the detector without being counted. In this way, the undesired loading of the counting capacity of the photomultiplier tube could be avoided.

6.4.2 The Relationship Between the Mass Attenuation Coefficients of Water and Oil as a Function of Energy

For a unique solution of the equation pair in Equation (6.15), the inequality in Equation (6.16) must be made valid. Thus, the ratio of the mass attenuation coefficient of water to that of oil at each of the two selected radiation energies must be different. This implies that the ratio of the mass attenuation coefficient of water to that of oil is not constant as a function of energy. Considering this, we are interested in the quotient of the mass attenuation coefficient of water divided by the mass attenuation coefficient of oil as a function of energy. This quotient can be calculated from the values in Table 6.1, and is presented in Table 6.2.

TABLE 6.2. Ratio of the Mass Attenuation Coefficient of Water to That of Oil as a Function of Energy (calculated from Table 6.1)

$\frac{\mu_{H_2O}}{\rho_{H_2O}} = \frac{\mu_W}{\rho_W}$			$\frac{\mu_{C_8H_{18}}}{\rho_{C_8H_{18}}} = \frac{\mu_O}{\rho_O}$								
MeV			0,01	0,015	0,02	0,03	0,04	0,05	0,06	0,08	0,10
			2,682	2,300	1,883	1,372	1,158	1,062	1,041	1,000	0,977
0,15	0,2	0,3	0,4	0,5	0,6	0,8	1	1,5	2	3	4
0,974	0,965	0,960	0,964	0,956	0,960	0,962	0,959	0,960	0,963	0,968	0,977
5	6	8	10	15	20	30	40	50	60	80	100
0,980	0,993	1,008	1,023	1,061	1,093	1,137	1,164	1,175	1,191	1,222	1,235

The ratio of the mass attenuation coefficient of water to that of oil can likewise be obtained considering the following statements. Water and oil are compounds consisting of elements with atomic numbers ≤ 16 . Figure 6.7 illustrates that for atomic numbers ≤ 16 , the attenuation caused by scattering is dominant within the energy range of 0.1 to 10 MeV. Figure 6.6a shows that this attenuation consists entirely of Compton scattering. Attenuation by photoabsorption occurs only for energies < 0.1 MeV. Attenuation by pair production happens only with high-intensity particle radiation. Only during an attenuation effect caused by scattering is the ratio of two mass attenuation coefficients equal to the ratio of their corresponding atomic numbers within the order of magnitude that is characteristic for this attenuation effect. This is discussed in the remarks explaining Equation (6.26). Because the atomic numbers of oxygen and carbon are nearly equal and the Compton scattering, as mentioned, depends nearly linearly on the atomic number, the ratio of the mass attenuation coefficients of water and oil must be close to one, in the range between 0.1 to 10 MeV. This is confirmed in Figure 6.9.

According to Equation (6.27), photoabsorption decreases as a function of the atomic number by the third to fifth power. For atomic numbers ≤ 16 , the dominance of the photoeffect is limited to energies < 60 KeV, as shown in

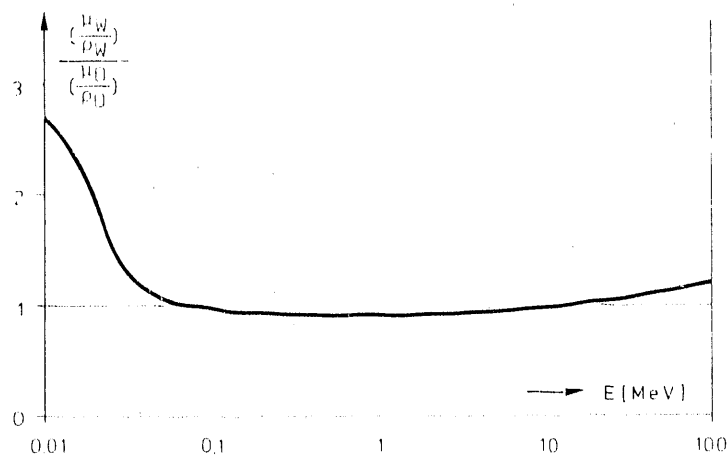


FIGURE 6.9. Plot of the Ratio of the Mass Attenuation Coefficient of Water to That of Oil as a Function of Energy

Figure 6.7. Thus, a definite divergence of the ratio of the mass attenuation coefficient of water to that of oil occurs first at energies <60 KeV (see Figure 6.9).

The simple quadratic dependence of the attenuation effect by pair production, whose dominant range for atomic numbers ≤ 16 is limited to energies >10 MeV, according to Figure 6.7, is capable of causing only a weak divergence in the ratio above 10 MeV (see Figure 6.9).

6.4.3 Possibilities Relating to the Selection of Radiation Sources

For the inequality in Equation (6.16) to be valid, the energies of each of the two radiation sources must be selected such that the ratios of the mass attenuation coefficients of water and oil (characteristic for each of the two source energies) are as different as possible. According to Figure 6.9, the energy of one source can lie between 0.1 to 10 MeV, but the energy of the other source must be outside of this range; that is, below 0.1 MeV or above 10 MeV.

6.4.3.1 Isotopes

Isotopes are sources of monochromatic radiation. An energy spectrum is the plot of the impulse count rate as a function of energy. The energy spectrum of the radiation from an isotope, after being attenuated by matter, is composed of the impulse count rate of the unattenuated quanta, which have discrete, isotope-specific energies, as well as the deceleration spectrum resulting from radiation generated during the interactions. The deceleration spectrum shows the distribution of the attenuated quanta as a function of their energy. The pertinent deceleration spectrum will also include the impulse count rates from any other unattenuated lower-energy radiation. Deceleration radiation and thus a deceleration spectrum can also be produced by the attenuation of particle radiation. The radiation attenuation equation (Equation [6.5]) on which the water and oil saturation equation (Equation [6.15]) is based, assumes monochromatic radiation. Equation (6.5) thus describes only the attenuation, caused by matter, of an energy-specific initial impulse count rate, but not a reduction in the deceleration spectrum,

nor any attenuation of lower-energy initial impulse count rates, which are masked by the scattered radiation.

An ideal isotope for determining saturations using the gamma-ray attenuation method must have its highest emitted quanta within the desired energy range, and it should not emit along with these quanta a higher-energy particle radiation. Furthermore, it should have a radiation half-life in the order of magnitude of at least the duration of the experiment. Finally, the required activity of the isotope must be producible.

A large number of possible isotopes exists as the first radiation source in the energy range between 0.1 and 10 MeV (Rakow 1962). The isotope Cs-137 emits a single gamma radiation energy of 0.662 MeV. It has a half-life of 30.1 yr, and can be produced with a large activity. However, it is the only isotope fulfilling the requirements of an ideal radiation source. Co-60 displays comparably suitable specifications. Yet, compared to Cs-137, the higher quanta energies of 1.17 MeV and 1.33 MeV for Co-60 necessitate greater amounts of protective shielding around the source. In addition, the half-life of 5.27 yr is about one-sixth that of cesium. These facts led us to prefer Cs-137 over Co-60.

More problematic is the selection of the second radiation source. The highest gamma radiation energies emitted from isotopes are of a few MeV. Ultra-high-energy gamma radiation, produced by particle accelerators (such as cyclotrons and betatrons) during the disintegration of elementary particles or appearing as cosmic-ray radiation, is not available as monochromatic radiation of suitable intensity. As shown in Figure 6.9, the ratio of the mass attenuation coefficients of water and oil is practically equal to one both for the ultra-high-energy gamma radiation and for the 0.662-MeV energy of Cs-137, the first radiation source. Thus, the suitable energy range for the highest emitted gamma energy of the second radiation source is limited to below 0.1 MeV.

In the first column of Table 6.3, only the isotopes whose highest energy does not exceed about 0.1 MeV and whose half-life is greater than 100 days are listed. The average duration of an experiment was estimated to be between weeks and months. It has been discussed why neither gamma nor particle

TABLE 6.3. Isotope Evaluation for Second Radiation Source

Radio-Isotope	Highest Emitted Gamma Energy	Half-Life	Probability of Emitting Quanta with the Energy Listed in Column II Per Nuclear Disintegration	Additional Gamma Peaks	Particle Radiation	Atomic Weight	Maximum Count Rate Theoretically Producing from Isotope	Maximum Material Attenuation Coefficient	Weight-Specific Impulse Count Rate Required to Obtain 10 ⁴ Imp/Sec Exiting Counts	Reason for Elimination
(keV)	(yr)	(yr)	(%)	(keV)	(α, β, γ, etc.)	(g)	(imp/sec-g)	(cm ² /g)	(imp/sec-g)	
Nuclide Table 61										
Equation (6.33) (1957) Grodstein Equation (6.52) Fig. 6.11										
Eu-155	0.483	4.76	0.0001	0.483	β ⁻	154.9226	1.5 × 10 ¹²	0.0001	1.5 × 10 ¹²	Neutron Source
Eu-156	0.483	0.42	0.0001	0.483	β ⁻	156.9254	1.5 × 10 ¹²	0.0001	1.5 × 10 ¹²	
Gd-153	0.483	1.3	0.0001	0.483	β ⁻	153.9202	1.5 × 10 ¹²	0.0001	1.5 × 10 ¹²	
Pr-143	0.483	13.5	0.0001	0.483	β ⁻	142.9054	1.5 × 10 ¹²	0.0001	1.5 × 10 ¹²	
Sm-147	0.483	106	0.0001	0.483	β ⁻	146.9150	1.5 × 10 ¹²	0.0001	1.5 × 10 ¹²	
Eu-151	0.483	5.21	0.0001	0.483	β ⁻	150.9196	1.5 × 10 ¹²	0.0001	1.5 × 10 ¹²	
Eu-152	0.483	13.2	0.0001	0.483	β ⁻	151.9242	1.5 × 10 ¹²	0.0001	1.5 × 10 ¹²	
Eu-154	0.483	8.59	0.0001	0.483	β ⁻	153.9288	1.5 × 10 ¹²	0.0001	1.5 × 10 ¹²	
Eu-155	0.483	4.76	0.0001	0.483	β ⁻	154.9334	1.5 × 10 ¹²	0.0001	1.5 × 10 ¹²	
Eu-156	0.483	0.42	0.0001	0.483	β ⁻	156.9380	1.5 × 10 ¹²	0.0001	1.5 × 10 ¹²	
Eu-157	0.483	1.53	0.0001	0.483	β ⁻	157.9426	1.5 × 10 ¹²	0.0001	1.5 × 10 ¹²	
Eu-158	0.483	0.33	0.0001	0.483	β ⁻	158.9472	1.5 × 10 ¹²	0.0001	1.5 × 10 ¹²	
Eu-159	0.483	0.17	0.0001	0.483	β ⁻	159.9518	1.5 × 10 ¹²	0.0001	1.5 × 10 ¹²	
Eu-160	0.483	0.07	0.0001	0.483	β ⁻	160.9564	1.5 × 10 ¹²	0.0001	1.5 × 10 ¹²	
Eu-161	0.483	0.03	0.0001	0.483	β ⁻	161.9610	1.5 × 10 ¹²	0.0001	1.5 × 10 ¹²	
Eu-162	0.483	0.01	0.0001	0.483	β ⁻	162.9656	1.5 × 10 ¹²	0.0001	1.5 × 10 ¹²	
Eu-163	0.483	0.00	0.0001	0.483	β ⁻	163.9702	1.5 × 10 ¹²	0.0001	1.5 × 10 ¹²	
Eu-164	0.483	0.00	0.0001	0.483	β ⁻	164.9748	1.5 × 10 ¹²	0.0001	1.5 × 10 ¹²	
Eu-165	0.483	0.00	0.0001	0.483	β ⁻	165.9794	1.5 × 10 ¹²	0.0001	1.5 × 10 ¹²	

(a) Mass attenuation coefficient of the specific element for its highest gamma energy estimated from an interpolation between the mass attenuation coefficient for these energies of two elements adjacent in atomic number, according to Grodstein (1957).

radiation with an energy higher than 0.1 MeV should be used for the second radiation source. Despite the multitude of existing isotopes, only a few fulfill these conditions. Within this reduced list of isotopes, however, most still do not qualify as the second radiation source for other reasons to be explained. Despite the likely presence of higher-energy particle radiation associated with these isotopes and inadequate knowledge of the deceleration spectrum of this particle radiation, the presence of particle radiation was initially not considered a reason for the elimination of an isotope from the evaluation process to identify the second radiation source. According to Table 6.3, the list of candidate isotopes can be narrowed by comparing the theoretical maximum producible activity, $J_{\text{prod}_{\text{max}}}$ (listed in column VIII), to the minimum required activity, $J_{\text{prod}_{\text{gef}}}$ (listed in column XI).

The weight-specific theoretical maximum activity, A_{max}^* , can be calculated as

$$A_{\text{max}}^* = \frac{L}{A} (-\ln 0.5) \frac{1}{T(\text{sec})} \cdot \frac{1}{3.7 \cdot 10^{10}} = 4.1 \cdot 10^{13} \cdot \frac{1}{A \cdot T(\text{sec})} \quad (\text{Ci/gr}) \quad (6.32)$$

where L is the Loschmidt's number, A is the atomic weight on a gram basis, T is the half-life assumed as known, and $3.7 \cdot 10^{10}$ disintegration/sec is the definition of the Curie (Radiochemical Manual 1966, p. 18). The weight-specific theoretical maximum producible activity, $J_{\text{prod}_{\text{max}}}$, of a given energy, from a pure radioisotope per unit of time, is obtained by multiplying A_{max}^* by $3.7 \cdot 10^{10}$ and the probability, p , of the formation of a quanta with the desired energy per nuclear disintegration.

$$J_{\text{prod}_{\text{max}}} = 3.7 \cdot 10^{10} \cdot A_{\text{max}}^* \cdot p = 4.1 \cdot 10^{23} \cdot \frac{p}{A \cdot T(\text{sec})} \quad \left(\frac{\text{Impulse}}{\text{sec} \cdot \text{gr}} \right) \quad (6.33)$$

The term $J_{\text{prod}_{\text{tot}}}$ is the infinitesimal volume-specific maximum impulse count of a given energy that is theoretically producible from a pure radioisotope per unit of time (Figure 6.10). As shown in Figure 6.10, only a fraction of $J_{\text{prod}_{\text{tot}}}$ reaches the radiation detector. The first reduction results from geometric attenuation because the quanta of energy are emitted radially and only a fraction have a path aimed toward the detector. Geometric

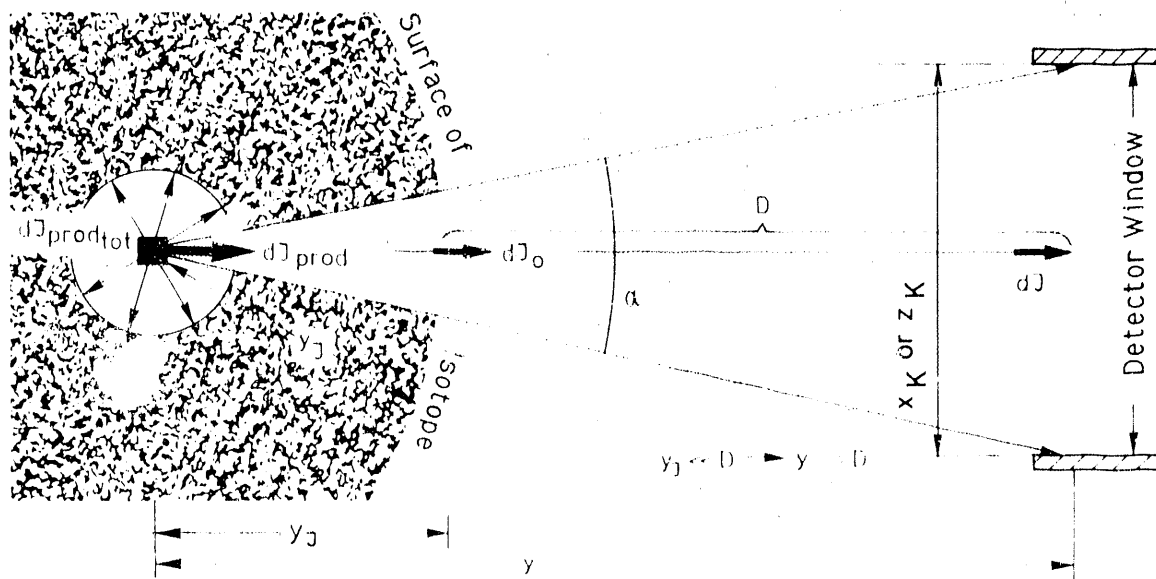


FIGURE 6.10. Schematic Explaining Geometric Attenuation and Self Absorption

attenuation differs from matter attenuation, which refers to the attenuation of radiation by matter between the isotope and the detector. The attenuation by the mass of the isotope itself is designated as self absorption.

Geometric attenuation is shown to reduce $dJ_{\text{prod}_{\text{tot}}}$ to dJ_{prod} . Because of self absorption, dJ_{prod} is reduced to the impulse rate dJ_0 , which is infinitesimally emitted as a collimated beam from the isotope. The matter attenuation of dJ_0 through glass, sand, water, and oil between the source and detector is described by Equation (6.8).

The geometric attenuation, σ_g , between the source and detector is equal to the ratio of the detector collimator cross-sectional area to the surface area of a sphere with a radius equal to the distance, y , between the infinitesimally small isotope and the detector. Because the distance, y_j , between the infinitesimal isotope volume and the surface of the isotope is minute in comparison to the distance, D , between the source and detector, the radius of the sphere can be set equal to D .

$$\sigma_g = \frac{\text{Detector cross-sectional area}}{4 \cdot \pi \cdot D^2} \quad (6.34)$$

In the two-dimensional, three-phase flow experiments described in Chapter 8.0, the cross-sectional area of the detector collimator was 1 cm^2 , and the distance between the source and detector was about 50 cm. Thus, the geometric attenuation is

$$\sigma_g = \frac{1 \text{ cm}^2}{4 \cdot \pi \cdot (50)^2} = 3.2 \cdot 10^{-5} \quad (6.35)$$

If an infinitesimal isotope volume is assumed inside an isotope, then its impulse count rate, dJ_{prod} , in the collimated beam is reduced by self absorption to an emitted impulse count rate, dJ_0 . This can be calculated by using an equation analogous to Equation (6.12)

$$\begin{aligned} dJ_0 &= dJ_{\text{prod}} \cdot e^{-\left(\frac{\mu}{\rho}\right)_J \cdot \gamma_J \cdot (1-n_J) \rho_J} \\ &= dJ_{\text{prod tot}} \cdot \sigma_g \cdot e^{-\left(\frac{\mu}{\rho}\right)_J \cdot \gamma_J \cdot (1-n_J) \rho_J} \end{aligned} \quad (6.36)$$

The matter attenuation of an isotope is generally determined according to Equation (6.30). The term ρ_J is the density of the isotope, and n_J is its porosity. Self absorption, σ_{SA} , is defined as the ratio of dJ_0 to dJ_{prod}

$$\sigma_{SA} = \frac{dJ_0}{dJ_{\text{prod}}} = \frac{dJ_0}{\sigma_g \cdot dJ_{\text{prod tot}}} = e^{-\left(\frac{\mu}{\rho}\right)_J \cdot \gamma_J \cdot (1-n_J) \rho_J} \quad (6.37)$$

To perform the integration of the infinitesimally emitted impulse count rate, dJ_0 , produced from the infinitesimal volume, dV , the total impulse count rate, $dJ_{\text{prod tot}}$, can be written as the product of the volume-specific produced impulse count rate, $J_{\text{prod}}^{\text{vol}}$ times dV . Thus, Equation (6.36) can be shown, after substituting Equation (6.37), to be

$$dJ_0 = J_{\text{prod}}^{\text{vol}} \cdot \sigma_g \cdot \sigma_{SA} \cdot dV \quad (6.38)$$

The impulse count rate J_0 emitted from the isotope as the collimated beam is equal to the integral of dJ_0 over the isotope volume V_J .

$$J_0 = \int_{V_J} (J_{prod}^{vol} \cdot \sigma_g \cdot \sigma_{SA}) dV \quad (6.39)$$

The isotope volume, V_J , is equal to the product of the width and height of the collimated beam, x_K and z_K , as well as the thickness, Y_J , of the isotope. The volume-specific produced impulse count rate, J_{prod}^{vol} , and the geometric attenuation factor, σ_g , can be set up as constants within the integral. On the other hand, σ_{SA} , according to Equation (6.37), is a function of y_J . Thus, by substituting $dV = dx \cdot dy \cdot dz$, Equation (6.39) can be written as

$$J_0 = J_{prod}^{vol} \cdot \sigma_g \cdot \int_0^{x_K} dx \cdot \int_0^{z_K} dz \cdot \int_0^{Y_J} \sigma_{SA} \cdot dy_J \quad (6.40)$$

By substituting the collimator factor $F_K = x_K \cdot z_K$ and Equation (6.37), Equation (6.40) becomes

$$J_0 = J_{prod}^{vol} \cdot \sigma_g \cdot F_K \cdot \int_0^{Y_J} \left\{ e^{-\left(\frac{\mu}{\rho}\right)_J \cdot y_J} \cdot (1 - n_J) \rho_J \right\} dy_J \quad (6.41)$$

The exponential dependence of self absorption over the distance y_J means that the contribution of an infinitesimal isotope volume to the integral of the impulse count rate, J_0 (emitted from the isotope), decreases exponentially over the distance y_J . Consequently, the integral yielding the impulse count rate approaches a maximum value as the isotope is expanded infinitely in the y -direction. Thus, because $\int e^{ax} dx = (1/a)e^{ax}$, the integral in Equation (6.41) is calculated as

$$\begin{aligned} \int_0^{\infty} \left(e^{-\left(\frac{\mu}{\rho}\right)_J \cdot y_J} \cdot (1 - n_J) \rho_J \right) dy_J &= \frac{1}{-\left(\frac{\mu}{\rho}\right)_J (1 - n_J) \rho_J} \cdot e^{-\left(\frac{\mu}{\rho}\right)_J \cdot y_J (1 - n_J) \rho_J} \Bigg|_0^{\infty} \\ &= \frac{1}{\left(\frac{\mu}{\rho}\right)_J (1 - n_J) \rho_J} \end{aligned} \quad (6.42)$$

A requirement that the extension of the isotope in the y -direction is selected to yield 99.9% of the maximum impulse count rate value can be met by using this y value, designated as $Y_{(99.9\%)}$, as the upper integration limit in Equation (6.42), thus yielding

$$\frac{1}{-(\frac{\mu}{\rho})_J(1-n_J)\rho_J} \cdot e^{-(\frac{\mu}{\rho})_J \cdot y_J \cdot (1-n_J)\rho_J} \Big|_{0}^{Y(99.9\%)} \\ = \frac{1}{-(\frac{\mu}{\rho})_J(1-n_J)\rho_J} \{ e^{-(\frac{\mu}{\rho})_J Y(99.9\%)(1-n_J)\rho_J} - 1 \} = 0.999 \cdot \frac{1}{(\frac{\mu}{\rho})_J(1-n_J)\rho_J} \quad (6.43)$$

$Y(99.9\%)$, (which will be substituted later into Equation [6.90]) is explicitly determined by rearranging terms in Equation (6.43) as

$$Y(99.9\%) = \frac{\ln(1-0.999)}{-(\frac{\mu}{\rho})_J(1-n_J)\rho_J} \cdot \frac{6.9}{(\frac{\mu}{\rho})_J(1-n_J)\rho_J} \quad (6.44)$$

Assuming that $Y_J = Y(99.9\%)$ and that

$$\int_0^{Y_J} e^{-(\frac{\mu}{\rho})_J \cdot y_J \cdot (1-n_J)\rho_J} dy_J = 1 / \{ (\frac{\mu}{\rho})_J(1-n_J)\rho_J \} \quad (6.45)$$

the calculation of the impulse count rate, emitted within the collimated beam from the isotope source, according to Equation (6.41) yields

$$J_U = J_{prod}^{vol} \cdot \sigma_R \cdot \int_0^{Y_J} e^{-(\frac{\mu}{\rho})_J(1-n_J)\rho_J} dy_J \quad (6.46)$$

The material attenuation, σ_m , is defined as the ratio of the impulse count rate, J , that exits the attenuating material to the initial impulse count rate, J_0 , that enters the attenuating material. With the attenuating materials used in the experiments, the maximum expected material attenuation, σ_m^{max} , is determined to be

$$\sigma_m^{max} = \frac{J}{J_0} = e^{-\{ (\frac{\mu}{\rho})_{SiO_2} \cdot x_{SiO_2} \cdot \rho_{SiO_2} + (\frac{\mu}{\rho})_W \cdot x_W \cdot \rho_W \}} \quad (6.47)$$

The mass attenuation coefficients can be taken from Table 6.1 or Figure 6.6. The term x_{SiO_2} is the sum of the two 2.2-cm-thick glass container walls and the irradiation path length, x_s , through pure quartz sand. x_s is calculated from the designated porous medium thickness, B , of 15 cm and a porosity, n , of

0.4 as $(B \cdot [1 - n] = 15 \text{ cm} \cdot 0.6)$, which is equal to 9 cm. The density of the glass plate and quartz sand was experimentally determined as 2.65 g/cm^3 . To estimate the maximum material attenuation, 100% water saturation was assumed. Thus, the irradiation path length through water, x_W , is calculated as $(B \cdot n = 15 \text{ cm} \cdot 0.4)$, which is equal to 6 cm. With these values specified for the experiments, the maximum expected material attenuation as a function of energy can be calculated according to Equation (6.47). The calculated values of σ_m^{max} are shown graphically in Figure 6.11.

The attenuated impulse count rate, J , obtained during maximum material attenuation as a function of gamma energy is given by combining Equations (6.46) and (6.47) as

$$J = J_0 \cdot \sigma_m^{\text{max}} = J_{\text{prod}}^{\text{vol}} \cdot \sigma_g \cdot \sigma_m^{\text{max}} \cdot F_K / \left\{ \left(\frac{\mu}{\rho} \right)_J (1 - n) \rho_J \right\} \quad (6.48)$$

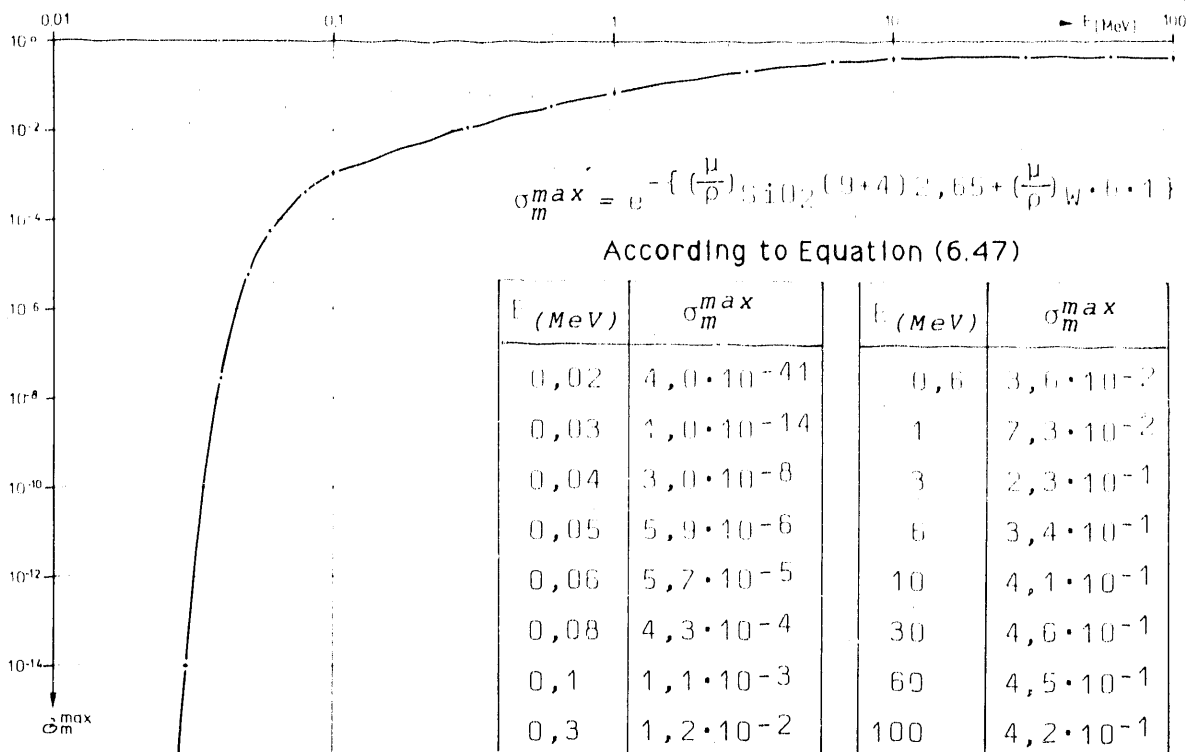


FIGURE 6.11. Expected Values of the Maximum Material Attenuation to be Observed During the Two-Dimensional Experiments

Because of the experimental objective of the shortest possible counting time with the maximum possible accuracy (i.e., maximizing the possible impulse count rate), the maximum impulse count rate detectable by the scintillation counter (10^4 counts/sec) should be fully utilized. Thus, the minimum for J is specified as 10^4 counts/sec. Therefore, the required volume-specific impulse count rate, $J_{prod_{gef}}^{vol}$, produced from the isotope can be determined, according to Equation (6.48), as

$$J_{prod_{gef}}^{vol} = \frac{10^4 \cdot \left(\frac{\mu}{\rho}\right)_J (1 - \rho_J) \rho_J}{\sigma_g \cdot \sigma_m^{max} \cdot FF} \quad (6.49)$$

To evaluate the candidate isotopes for the low-energy radiation source proposed in Table 6.3, the weight-specific, maximum impulse count rate, theoretically available from an isotope $J_{prod_{max}}$ [Equation (6.33)], should be compared with the weight-specific impulse count rate capable of being produced by the isotope $J_{prod_{gef}}^{gr}$. $J_{prod_{max}}$ is a function of the number of grams of pure isotope; that is, the number of grams of the pure radioactive element gr_{E1} . For comparison, $J_{prod_{gef}}^{gr}$ must also be related to gr_{E1} . Therefore, $J_{prod_{gef}}^{gr}$ should be more exactly written as $J_{E1_{prod_{gef}}}^{gr}$, which will be called the required impulse count rate.

The impulse count rate per gram of isotope J^{grJ} is calculated by dividing the volume-specific impulse count rate, J^{volJ} , by the density of the isotope, ρ_J . Because an isotope is generally a mixture of elements or a compound, the isotope molecular weight must be divided by the weight fraction of the radioactive element in the mixture or the compound ($g_{E1} = gr_{E1}/gr_G$). This gives the impulse count rate per gram of the radioactive element, J^{grE1} .

$$\left(J^{grE1} = \frac{Imp}{gr_{E1}} \right) = \left(J^{volJ} = \frac{Imp}{vol_J} \right) \cdot \frac{1}{\left(\rho_J = \frac{gr_J}{vol_J} \right)} \cdot \frac{1}{\left(g_{E1} = \frac{gr_{E1}}{gr_G} \right)} \quad (6.50)$$

Equation (6.49) is inserted into Equation (6.50), to obtain the required impulse count rate $J_{E1_{prod_{gef}}}^{gr}$. Thus,

$$J_{prod_{gef}}^{gr_{El}} = \frac{10^4 \cdot (\frac{\mu}{\rho})_J \cdot (1 - n_J)}{\sigma_g \cdot \sigma_m^{max} \cdot F_K \cdot g_{El}} \quad (6.51)$$

For the desired comparison of $J_{prod_{gef}}^{gr_{El}}$ to $J_{prod_{max}}$, it can simply be assumed that the isotope is a pure dense radionuclide. Thus, the mass attenuation coefficient of the isotope, $(\mu/\rho)_J$, can be assumed to be the mass attenuation coefficient of the radioactive element, $(\mu/\rho)_{El}$. Furthermore, the porosity of the isotope, n_J , can thus be assumed as zero, and the weight fraction of the radioactive element, g_{El} , in the isotope assumed to be one. For the experiments under consideration, σ_g is determined according to Equation (6.35), and the cross-sectional area of the collimated ray, F_K , is 1 cm^2 , assuming that x_K is 2 cm and z_K is 0.5 cm. Thus, Equation (6.51) can be written as

$$J_{prod_{gef}}^{gr_{El}} = \frac{10^4 \cdot (\frac{\mu}{\rho})_{El}}{3,2 \cdot 10^{-5} \cdot \sigma_m^{max}} = 3,1 \cdot 10^8 \cdot \frac{(\frac{\mu}{\rho})_{El}}{\sigma_m^{max}} \quad (6.52)$$

To obtain the optimum counting efficiency from the specific experimental design, the maximum counting capacity of the scintillation counter (10^4 count/sec) must be used. The required number of quanta (produced by each gram of the pure dense radioactive element per second) of the desired highest emitted gamma energy is determined by Equation (6.52). The results of the calculation of $J_{prod_{gef}}^{gr_{El}}$ for each radioisotope listed in column I of Table 6.3 are presented in column XI of Table 6.3. The maximum material attenuation to be expected for each gamma energy (specific to each isotope and listed in column II) is taken from Figure 6.11 and recorded in column X. The mass attenuation coefficient for the pure radioactive element was taken either directly from Grodstein (1957) or indirectly by interpolating between two elements of adjacent atomic number and is recorded in column IX.

A comparison of columns VIII and XI of Table 6.3 shows that for energies below 60 KeV, the required impulse count rate, $J_{prod_{gef}}^{gr_{El}}$, exceeds the theoretical impulse count rate, $J_{prod_{max}}$, by orders of magnitude. Above 60 KeV, this occurs only for Am-243 because of the relatively low theoretical impulse count rate caused by the high half-life. The fact that $J_{prod_{max}} \ll J_{prod_{gef}}^{gr_{El}}$ leads us to eliminate this isotope from further evaluation.

Tin (Sn-119) must be eliminated because the coefficient of internal atomic conversion of the 65-KeV gamma radiation is 100% (Amersham Catalog 1974/75). Internal atomic conversion is a direct mutual exchange between the stimulated nucleus and a bonded shell electron. The atomic nucleus transfers its stimulation energy to the electron shell, and in this way the energy is expelled from the atom (Marmier 1960, p. 235; see also Section 6.9). This process occurs concurrently to gamma emission. The conversion coefficient indicates the ratio of the probability of producing a conversion electron to that of a emitting quantum. If the conversion coefficient is 100%, as for the 65-KeV gamma-radiation of Sn-119, no 65-KeV radiation is emitted.

Californium (Cf-252) emits primarily fast neutrons (Amersham Catalog 1974/75). Based on the fact that fast neutrons are poorly shieldable and have a relative biological activity factor of 10 (Swiss Atomic Handbook 1963), Cf-252 was eliminated for radiation protection reasons, among others. Thus, the choice of candidate isotopes for the second radiation source was reduced to Eu-155, Cd-109, and Tm-170.

Eu-155 and Tm-170 emit higher-energy beta radiation in addition to gamma radiation. The attenuation of higher-energy beta radiation (the deceleration of electrons in the irradiated matter to below the energy of the initial beta radiation) produces a deceleration spectrum that extends over the entire energy spectrum. Thus, the peak gamma-energy radiation of Eu-155 and Tm-170 is superimposed on the deceleration spectrum, a fact that is undesirable and causes the elimination of these two isotopes, leaving Cd-109 as the only low-energy isotope under consideration as the second radiation source.

$J_{\text{prod,max}}$ determined by Equation (6.33) represents the theoretical maximum producible number of impulses per second per gram of the pure radioisotope. It is an open question whether this impulse count rate (that is, the activity) can be produced at all in practice. According to the Radiochemical Manual (1966), the production process of Cd-109 is



This means that the nuclide Ag-109 must be bombarded with protons or deuterons and that the Cd-109 is formed by expulsion of one or two neutrons, respectively. Proton or deuteron bombardment requires a particle accelerator, a cyclotron. The strongest obtainable Cd-109 source, at the time of these scoping calculations, had an activity of 10 mCi and a volume of $(\pi \cdot [0.42]^2 \cdot 0.0125)$ approximately $7 \cdot 10^{-3} \text{ cm}^3$. A weight-specific activity of about 0.1 Ci/g was calculated by assuming a specific weight of about 10 g/cm^3 . This activity corresponds (by multiplication with the impulse count rate defining the Curie of $3.7 \cdot 10^{10}$ disintegration/sec and with $p = 0.083$ from Table 6.3) to a practical maximum impulse count rate of about 10^8 impulses/(g \cdot sec). This value is several orders of magnitude smaller than that required as listed in column XI in Table 6.3. After making inquiries to Amersham, a radioisotope supplier, we quickly concluded that it was not practical to produce the theoretical weight-specific maximum producible activity of cadmium. In addition, even if practical, the costs would have exceeded U.S. \$10000/Ci (approximately 326 Ci of Cd-109 would be required). Thus Cd-109, the theoretically satisfactory isotope for the second radiation source, was found to be only practically producible at an activity several orders of magnitude lower than that desired.

Based on this knowledge, the two isotopes Eu-155 and Tm-170 had to be reconsidered, despite the deceleration spectra. We reconsidered these two isotopes with the hope that the deceleration spectrum produced by the decelerated particle radiation could be reduced to almost nothing by using an optimum collimator design, or if this failed, by using a simple analytical method to subtract out the deceleration spectrum. Tm-170 was selected over Eu-155 primarily because the gamma radiation energy of thulium (84 KeV) is lower than that of europium (102 KeV). An energy lower than 100 KeV (0.1 MeV) is a definite advantage, according to the discussion at the beginning of Section 6.4.3. Apart from this, Tm-170 is a commercially obtainable isotope that has relatively high activity, while Eu-155 was not obtainable from normal commercial suppliers (Amersham Catalog 1974/75).

Tm-170 is producible by a (n, τ) process. Neutron bombardment implies production in a reactor. Because of the impracticality of producing Cd-109 in

the desired activity, the possibility of producing Tm-170 in the required activity should be clarified. The weight-specific activity, A^* , produced by neutron radiation can be determined by the following relation (Glocker and Macherauch 1965, p. 417)

$$A^* = 1,63 \cdot 10^{-11} \cdot \frac{\Phi \cdot \sigma}{A} \cdot (1 - \exp\{-0,693 \cdot \frac{t}{T}\}) \quad (\text{Ci/gr}) \quad (6.54)$$

where Φ is the neutron flux, σ is the capture cross-section of the irradiated element for reactor neutrons, A is the atomic weight, T is the half-life of the nuclide produced, and t is the time of exposure to radiation. For Tm-170, $A = 169$ and $T = 127$ days. The capture cross section is 130 barn for the thulium oxide (Tm_2O_3) used as the target material (Radiochemical Manual 1966). Assuming that the isotope could be produced in the most efficient reactor in Europe (Mol, Belgium), with a neutron flux at the production source of $D = 5 \cdot 10^{14}$ (at that time, the Würenlinger reactors produced a flux of $2 \cdot 10^{13}$ and $3 \cdot 10^{13}$ for diorite and sapphire, respectively), and also assuming an irradiation time of 50 days, a weight-specific, producible activity is calculated from Equation (6.54) as

$$A^* = 1,63 \cdot 10^{-11} \cdot \frac{5 \cdot 10^{14} \cdot 130}{169} \cdot (1 - \exp\{-0,693 \cdot \frac{50\text{d}}{127\text{d}}\}) \quad (6.55)$$

$$= 1,5 \cdot 10^3 \quad (\text{Ci/gr})$$

The weight-specific maximum producible activity for a flux of $5 \cdot 10^{14}$, $A^*_{\text{max}}(5 \cdot 10^{14})$, is yielded by calculating the asymptotic value approached as $t \rightarrow \infty$

$$A^*_{\text{max}}(5 \cdot 10^{14}) = 1,63 \cdot 10^{-11} \cdot \frac{5 \cdot 10^{14} \cdot 130}{169} = 6,3 \cdot 10^3 \quad (\text{Ci/gr}) \quad (6.56)$$

The weight-specific theoretically maximum producible activity of the isotope is given from Equation (6.32) as

$$A^*_{\text{max}} = 1,1 \cdot 10^{13} \cdot \frac{1}{A \cdot T(\text{sec})} = 5,9 \cdot 10^3 \quad (\text{Ci/gr}) \quad (6.57)$$

A comparison of the results of Equations (6.56) and (6.57) shows that the maximum producible activity for Tm-170 at a flux of $5 \cdot 10^{14}$ for $t \rightarrow \infty$ is theoretically producible. Even if the activity practically producible in 50 days (Equation [6.55]) yields an impulse count rate at 84 KeV of approximately $5 \cdot 10^{12}$ (that is, $1.5 \cdot 10^3 \cdot 3.7 \cdot 10^{10} \cdot 0.085$), which is only one-fourth of the maximum producible in theory according to column VIII in Table 6.3, it is still larger than the required weight-specific impulse count rate, $J^{gr} E_{l, prod_{gef}}$, shown for Tm-170 in column XI of Table 6.3. Consequently, the discrepancy established for cadmium between the required and practically producible activity does not exist for thulium.

Based on the above observations, in principle, no problems seem to stand in the way of producing a thulium source with an activity in the required order of magnitude. The open question regarding the possible use of thulium, now the lone candidate for the second radiation source, is the eventual effectiveness of the efforts to design a collimator that will diminish the deceleration spectrum caused by particle radiation, or whether a simple mathematical method can be found for the subtraction of this deceleration spectrum to obtain an accurate count of the peak gamma energy. Given this uncertainty, the possibility of using x-rays as an alternative to isotopes as the low-energy second radiation is discussed in the following section.

6.4.3.2 X-Ray Tubes

An x-ray tube produces gamma radiation in the low to middle energy range; this gamma-radiation is termed x-ray radiation. An x-ray tube consists of an anode and a cathode. Voltage is applied to the cathode to accelerate electrons toward the anode, where the electrons are decelerated. The deceleration of electrons on the anode is a function of its geometry. This deceleration, a mutual exchange of particle radiation with the shell electrons of the anode material, ensues in one or probably several stages. The multitude of electrons striking the anode produces an entire energy spectrum of gamma radiation, as they decelerate. The exponential radiation attenuation equation (Equation [6.5], which serves as the basis for Equation [6.47]) is only valid for monochromatic radiation. The idea, then, in using an x-ray tube to generate low-energy gamma radiation is to take advantage of the high radiation

flux produced by an x-ray tube to yield an energy peak at the characteristic radiation of the target. This energy peak would serve as the monochromatic, low-energy gamma radiation.

The characteristic radiation of a target is a product of the photoeffect. When an impinging gamma quantum causes the emission of an electron (the so-called photoelectron) from an inner shell of the atomic shell, then the nascent electron position is filled at once by an electron from an outer shell, as shown schematically on the left of Figure 6.5. The energy difference between the energy of this electron in its original position and its energy in the new position is emitted as a characteristic radiation. The differences in energy between the separate electron shells are characteristic of each element in the periodic table and thus so is the emitted radiation. The energy of the characteristic radiation can reach 141.6 KeV, which lies in the range needed for the second radiation source, according to earlier observations. The characteristic radiation can be obtained from the tables in Strominger et al. (1958, p. 594). The discontinuity (peak) at about 0.1 MeV in the plot of the mass attenuation coefficient of lead as a function of energy (observable in Figure 6.6b) is the result of the ionization of electrons in the K-shell. When an electron in the outermost shell of lead replaces an electron that was emitted from the K-shell, characteristic radiation is emitted at about 88 KeV. Replacement of electrons emitted from an inner shell would produce a lower characteristic radiation. The mentioned discontinuity is designated as an absorption border, specifically as the K-border.

The following appraisal was made to clarify the applicability of using an x-ray tube with various targets to generate characteristic radiation that would adequately serve as the second source of weak monochromatic radiation. The electron flux emitted from the anode of the x-ray tube is linear with respect to the electric current applied at the anode. X-ray tubes can be used with optimum cooling of the anode at current intensities (I) of up to about 20 mA. The charge of an electron, e , is $1.6 \cdot 10^{-19}$ A \cdot sec, where $1 \text{ A} = 6.3 \cdot 10^{18}$ electrons/sec. The efficiency, η , with respect to the gamma radiation produced in the deceleration spectrum is about 1%, while about 99%

is removed in the form of heat, according to Glocker and Macherach (1965, pp. 91 and 113). Assuming that the cross-sectional area of the target is 1 cm^2 , and its distance from the anode of the x-ray tube is 30 cm, the result is a geometric attenuation between anode and target, $\sigma_g|_A^T$ (corresponding to Equation [6.34]) of $1/(4 \cdot \pi \cdot 30^2)$. The probability, p , that a quantum of the characteristic radiation will be produced during a deceleration within the anode was assumed to be 1%. The emission of activated characteristic radiation from a target occurs radially, just as for an isotope. Thus, the geometric attenuation between target and detector, $\sigma_g|_T^D$, is $3.2 \cdot 10^{-5}$, according to Equation (6.35). Assuming an element is selected as a target whose characteristic radiation is about 60 KeV, the material attenuation, σ_m , determined from Figure 6.11 would be about $6 \cdot 10^{-5}$. From these values for the different kinds of radiation attenuation, the impulse count rate, J , is calculated as

$$\begin{aligned}
 J_{(\text{x-ray tube})} &= \frac{I}{e} \cdot \eta \cdot \sigma_g|_A^T \cdot p \cdot \sigma_g|_T^D \cdot \sigma_m \\
 &= \frac{(20 \cdot 10^3) (6,3 \cdot 10^{18}) \cdot 10^{-2} \cdot 10^{-2} \cdot (3,2 \cdot 10^{-5}) (6 \cdot 10^{-5})}{(4 \cdot \pi \cdot 30^2)} \\
 &\approx 2 \qquad \qquad \qquad (6.58)
 \end{aligned}$$

If the required impulse count rate is assumed to be 10^4 , from the same basis as in Equation (6.49), then the resulting impulse count rate, $J_{(\text{x-ray tube})}$, is about four orders of magnitude too small. Use of an x-ray tube to yield activated characteristic radiation from a target was thus not adequate in terms of the proposed design to function as the second radiation source. The missing four orders of magnitude of radiation could possibly be generated by combining the target and anode into a single unit such that the desired characteristic radiation is produced directly from the anode. This combination would eliminate the geometric attenuation between anode and target, $\sigma_g|_A^T$, which for an anode-target distance of 30 cm reduced the radiation flux by a factor of 11310, or about 10^4 . The major assumption for a practical realization of this idea is that a metallic element can be found for use as an anode whose most intensive characteristic radiation has an energy of about 60 KeV and whose melting point is at least about 1000°C .

Wolfram, with a melting temperature of 3400°C, is an anode material often used in x-ray tubes. The highest characteristic radiation energy of Wolfram is at 59 KeV (Glocker and Macherauch 1965, Table 4.5). Other metallic elements with somewhat lower energies for the highest characteristic radiation energy and high melting points were lutetium with a melting point of 1652°C and thulium with a melting point of 1545°C. Both these rare-earth metals could be ordered in the purest possible form (>99.9%) as plates or wire from Johnson, Matthey and Co., Hatton Garden, London. The highest characteristic radiation energy of an element decreases as a function of the element's atomic number. Thus, for silver, copper, and aluminum, whose atomic numbers are 47, 29, and 13, respectively, the highest characteristic radiation energies are 25 KeV, 9 KeV, and 1.5 KeV, respectively. To decrease the danger of superheating the anode because of current intensity, these anodes would have to be bathed in oil or rotated.

The determining factor in uniting the target and anode, compared to having the target lying outside the x-ray tube, is the fact that with the combined anode and target the deceleration radiation of the anode is superimposed on the desired characteristic radiation of the target. The fundamental interest in the elimination or at least the decrease of such a deceleration spectrum was discussed in the previous section. The influence of the deceleration radiation, undesirably superimposed on the characteristic radiation, can be essentially reduced by creating a condition in which the gamma radiation is strongly attenuated on the short-wave side of an absorption border. To do this, a layer of an element whose K-border lies just above the characteristic radiation energy is brought in line as a selective filter within the radiation beam emitted by the x-ray tube. Figure 6.12 shows the selective filtering (shift of beta components to 17.5 KeV) of the characteristic radiation of a molybdenum anode by using zircon, whose K-border is at 18.2 KeV, as a filter. The energizing voltage and the filter material thickness must be optimized to meet the high requirements for the homogeneity of the radiation (Glocker and Macherauch 1965, p. 122).

The difficulties already described at the beginning of Section 6.4.3.1 are encountered again because of the likelihood that the enormous material

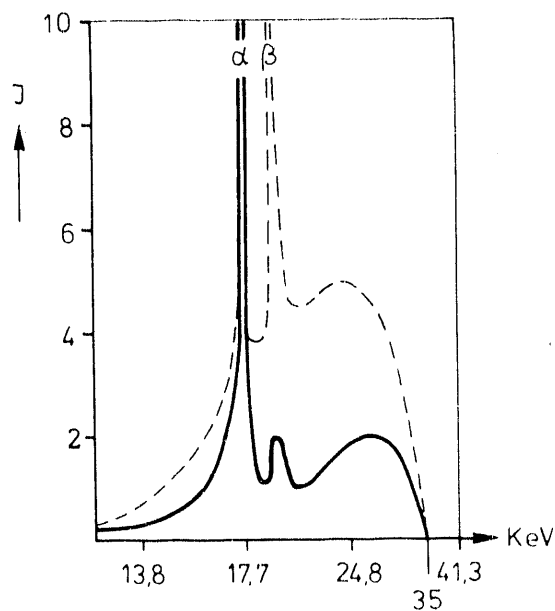


FIGURE 6.12. X-Ray Spectrum (Deceleration and Characteristic Radiation Spectrum) of a Molybdenum Anode at 35-kV Tube Voltage (dashed line). Attainment of homogeneous molybdenum K-border characteristic radiation by selective filtering with zircon (solid line) (Glocker and Macherauch 1965, p. 122).

attenuation (Figure 6.11) would produce a dominant deceleration spectrum, which cannot be ignored. A compromise between these two methods consisting of decreasing the interval between anode and target to a minimum seems promising.

6.4.4 Conclusions

For a unique solution to the equation pair in Equation (6.15), the inequality in Equation (6.16) must be valid. The validity of the inequality is more guaranteed the lower is the energy of the second radiation source. This is true if the energy of the first radiation source is assumed to be between 0.1 and 10 MeV.

In Section 6.4.3.1, only Tm-170 was identified as being a suitable isotope for the second radiation source. The gamma-radiation energy peak emitted by Tm-170 is at 84 KeV. By using an x-ray tube to activate the characteristic radiation of a target, a low-characteristic radiation energy can be selected depending on element used as the target. According to Figure 6.11, the

material attenuation below 100 KeV increases sharply with decreasing quanta energy. According to the observations summarized in Equation (6.58), the usefulness of the method of using an x-ray tube to activate the characteristic radiation energy of a target is limited to an anode and target setup that will produce a characteristic radiation energy no lower than 60 KeV.

From Figure 6.9, it can be seen that the ratio of the mass attenuation coefficient of water to that of oil at an energy of 60 KeV hardly differs from the ratio at 84 KeV. Furthermore, it is greater than the ratio within the energy range of 0.1 to 10 MeV, within which the first radiation source was selected. Thus, the options for the second radiation source have been narrowed, according to the stated criteria, to the selection of thulium as either an isotope (Tm-170) or a target whose characteristic radiation is activated by an x-ray tube. The suitability of thulium is still only marginally guaranteed given that the appraisal methods probably include various uncertainties.

Before further evaluating both methods in Section 6.7, it should be determined whether the stated $\pm 2\%$ saturation accuracy can be achieved. The standard error of the saturation measurement will be determined by considering the mass attenuation coefficients for both water and oil at the two energies, one at 0.662 MeV and the other between 0.06 and 0.084 MeV. The calculations will be performed by assuming that 1) the scintillation counter used as the detector will be operated at its maximum counting capacity of 10^4 impulses/sec, and 2) quantifying the dynamic flow of the oil in the flume requires a maximum measuring time of 10 sec, which together imply a count of 10^5 impulses per measurement.

6.5 CONSIDERATION OF THE STANDARD ERROR OF THE SATURATION MEASUREMENT

The goal of the following consideration of the standard error is to describe the dependence of the standard error of a specific oil saturation on the energy of the second radiation source, assuming that the first radiation source is Cs-137. The oil saturation, S_0 , is determined from the second equation of the equation pair in Equation (6.15) and is a function of each of the variables listed in Equation (6.59). The value of each variable will be measured and is thus affected by errors.

$$S_0 = S_0 \left\{ \left(\frac{\mu_W}{\rho_0} \right)_I, \left(\frac{\mu_W}{\rho_0} \right)_{II}, \left(\frac{\mu_W}{\rho_0} \right)_I, \left(\frac{\mu_W}{\rho_0} \right)_{II}, n, B, \rho_0, J_I, J_{II}, J_{T_I}, J_{T_{II}} \right\} \quad (6.59)$$

The square of the standard error at a specific value of S_0 is determined by using the simplifying assumption that each variable is independent. According to Gauss' Law of Probability, it thus can be written as

$$\begin{aligned} m_{S_0}^2 = & \left\{ \frac{\partial S_0}{\partial \left(\frac{\mu_W}{\rho_0} \right)_I} \right\}^2 \cdot m_{\left(\frac{\mu_W}{\rho_0} \right)_I}^2 + \left\{ \frac{\partial S_0}{\partial \left(\frac{\mu_W}{\rho_0} \right)_{II}} \right\}^2 \cdot m_{\left(\frac{\mu_W}{\rho_0} \right)_{II}}^2 + \left\{ \frac{\partial S_0}{\partial \left(\frac{\mu_0}{\rho_0} \right)_I} \right\}^2 \cdot m_{\left(\frac{\mu_0}{\rho_0} \right)_I}^2 \\ & + \left\{ \frac{\partial S_0}{\partial \left(\frac{\mu_0}{\rho_0} \right)_{II}} \right\}^2 \cdot m_{\left(\frac{\mu_0}{\rho_0} \right)_{II}}^2 + \left\{ \frac{\partial S_0}{\partial n} \right\}^2 \cdot m_n^2 + \left\{ \frac{\partial S_0}{\partial B} \right\}^2 \cdot m_B^2 + \left\{ \frac{\partial S_0}{\partial \rho_0} \right\}^2 \cdot m_{\rho_0}^2 \\ & + \left\{ \frac{\partial S_0}{\partial J_I} \right\}^2 \cdot m_{J_I}^2 + \left\{ \frac{\partial S_0}{\partial J_{II}} \right\}^2 \cdot m_{J_{II}}^2 + \left\{ \frac{\partial S_0}{\partial J_{T_I}} \right\}^2 \cdot m_{J_{T_I}}^2 + \left\{ \frac{\partial S_0}{\partial J_{T_{II}}} \right\}^2 \cdot m_{J_{T_{II}}}^2 \end{aligned} \quad (6.60)$$

Gauss' Law of Probability requires mutual independence of the separate variables. If two variables are correlated, their covariance must be considered in addition to the square of the derivatives developed above. Because covariances never dominate the sum of squares of the multiplicand and the multiplier, discounting the actual dependencies of the separate variables, and thus the covariance, will not change the size of the standard error in the first approximation. Thus, Equation (6.60) is adequate, as a first approximation, to estimate the size of the standard error of a specific oil saturation, even with mutual dependence of the variables.

6.5.1 Determination of the Separate Differential Quotients

According to the second equation in Equation (6.15) in Section 6.3, the oil saturation is determined as

$$S_0 = \frac{\left(\frac{\mu_W}{\rho_W}\right)_{II} \cdot \ln\left(\frac{J}{J_T}\right)_I - \left(\frac{\mu_W}{\rho_W}\right)_I \cdot \ln\left(\frac{J}{J_T}\right)_{II}}{n \cdot B \cdot \rho_0 \cdot \left(\frac{\mu_0}{\rho_0}\right)_I \cdot \left(\frac{\mu_0}{\rho_0}\right)_{II} \cdot \left\{ \frac{\left(\frac{\mu_W}{\rho_W}\right)_I}{\left(\frac{\mu_0}{\rho_0}\right)_I} - \frac{\left(\frac{\mu_W}{\rho_W}\right)_{II}}{\left(\frac{\mu_0}{\rho_0}\right)_{II}} \right\}} = \frac{Z}{N} = \frac{Z}{K \cdot \{ \}} \quad (6.61)$$

The differential quotients with respect to mass attenuation coefficients are determined as

$$\frac{\partial S_0}{\partial \left(\frac{\mu_W}{\rho_W}\right)_I} = \frac{\partial}{\partial x} \left(\frac{a-x \cdot b}{K \left\{ \frac{x}{c} - d \right\}} \right) = \frac{N(-b) - Z \left(\frac{K}{c} \right)}{N^2} = \frac{-\ln\left(\frac{J}{J_T}\right)_{II}}{N} - \frac{S_0}{\left(\frac{\mu_0}{\rho_0}\right)_I \{ \}}$$

$$\frac{\partial S_0}{\partial \left(\frac{\mu_W}{\rho_W}\right)_{II}} = \frac{\partial}{\partial x} \left(\frac{x \cdot a - b}{K \left\{ c - \frac{x}{d} \right\}} \right) = \frac{N \cdot a - Z \left(-\frac{K}{d} \right)}{N^2} = \frac{\ln\left(\frac{J}{J_T}\right)_I}{N} + \frac{S_0}{\left(\frac{\mu_0}{\rho_0}\right)_{II} \{ \}}$$

$$\begin{aligned} \frac{\partial S_0}{\partial \left(\frac{\mu_0}{\rho_0}\right)_I} &= \frac{\partial}{\partial x} \left(\frac{Z}{a \cdot x \left\{ \frac{b}{x} - c \right\}} \right) = \frac{\partial}{\partial x} \left(\frac{Z}{a} (b - c \cdot x)^{-1} \right) = \frac{-Z}{a} (b - c \cdot x)^{-2} (-c) \\ &= \frac{Z \cdot c \cdot a}{a^2 \left(x \left\{ \frac{b}{x} - c \right\} \right)^2} = \frac{Z \cdot a \cdot c}{N^2} = S_0 \cdot \frac{n \cdot B \cdot \rho_0 \left(\frac{\mu_W}{\rho_W}\right)_{II}}{N} \end{aligned}$$

$$\begin{aligned} \frac{\partial S_0}{\partial \left(\frac{\mu_0}{\rho_0}\right)_{II}} &= \frac{\partial}{\partial x} \left(\frac{Z}{a \cdot x \left\{ b - \frac{c}{x} \right\}} \right) = \frac{\partial}{\partial x} \left(\frac{Z}{a} (b \cdot x - c)^{-1} \right) = \frac{-Z}{a} (b \cdot x - c)^{-2} \cdot b \\ &= \frac{-Z \cdot b \cdot a}{a^2 \left(x \left\{ b - \frac{c}{x} \right\} \right)^2} = \frac{-Z \cdot a \cdot b}{N^2} = -S_0 \cdot \frac{n \cdot B \cdot \rho_0 \left(\frac{\mu_W}{\rho_W}\right)_I}{N} \end{aligned}$$

(6.62a)

and the remaining differential quotients are calculated as

$$\begin{aligned} \frac{\partial S_0}{\partial n} &= \frac{\partial}{\partial x} \left(\frac{Z}{x \cdot a\{\}} \right) = \frac{-Z}{x^2 \cdot a\{\}} = -\frac{S_0}{n} \\ \frac{\partial S_0}{\partial B} &= \frac{\partial}{\partial x} \left(\frac{Z}{x \cdot a\{\}} \right) = \frac{-Z}{x^2 \cdot a\{\}} = -\frac{S_0}{B} \\ \frac{\partial S_0}{\partial \rho_0} &= \frac{\partial}{\partial x} \left(\frac{Z}{x \cdot a\{\}} \right) = \frac{-Z}{x^2 \cdot a\{\}} = -\frac{S_0}{\rho_0} \\ \frac{\partial S_0}{\partial J_I} &= \frac{\partial}{\partial x} \left(\frac{a(\ln x - b) - c}{N} \right) = \frac{a}{N \cdot x} = \frac{\left(\frac{\mu_W}{\rho_W}\right)_{II}}{N \cdot J_I} \\ \frac{\partial S_0}{\partial J_{II}} &= \frac{\partial}{\partial x} \left(\frac{a - b(\ln x - c)}{N} \right) = \frac{-b}{N \cdot x} = -\frac{\left(\frac{\mu_W}{\rho_W}\right)_I}{N \cdot J_{II}} \\ \frac{\partial S_0}{\partial J_{TI}} &= \frac{\partial}{\partial x} \left(\frac{a(b - \ln x) - c}{N} \right) = \frac{-a}{N \cdot x} = -\frac{\left(\frac{\mu_W}{\rho_W}\right)_{II}}{N \cdot J_{TI}} \\ \frac{\partial S_0}{\partial J_{TII}} &= \frac{\partial}{\partial x} \left(\frac{a - b(c - \ln x)}{N} \right) = \frac{b}{N \cdot x} = \frac{\left(\frac{\mu_W}{\rho_W}\right)_I}{N \cdot J_{TII}} \end{aligned} \tag{6.62b}$$

6.5.2 Estimate of the Values and Standard Errors of the Separate Variables

To apply Gauss' Law of Probability to a special case, the approximate values of the separate variables must be known or estimated to determine the differential quotients.

Most of the variables shown in Equation (6.59) are indirect observations. Indirect observations can be functions of direct as well as other indirect observations. The standard error of an indirect observation is a function of the standard error of the direct observation, used to define the indirect observation. Thus, Gauss' Law of Probability must be also applied to determine the standard error of the indirectly observed variables, which will be inserted in Equation (6.60). This approach is valid for the estimate of the standard error of the indirect observations and also for later direct observations, such as the mass attenuation coefficients and the porosity. The standard error based on the arithmetic mean is given as $\pm\sqrt{[\Sigma(vv)]/\{n(n-1)\}}$. Here $\Sigma(vv)$ is the sum of the squares of the differences from the arithmetic mean value of n-measurements.

6.5.2.1 Values and Standard Errors of the Impulse Count Rates

The values of the impulse count rates (described conceptually in connection with Equation [6.5]) are specified by the fact that 1) the scintillation counter used as a detector had a maximum counting capacity of 10^4 to 10^5 impulses/sec, and 2) from experience, a measurement time of 10 sec should not be exceeded if one hopes to quantify fluid saturations during a relatively fast fluid displacement process. Because we are interested in counting the highest possible number of impulses to minimize the standard error of the observed impulse counts, a minimum measured exiting impulse count on the order of 10^5 was selected. This exiting impulse count would also be almost 10 times greater than the maximum possible material attenuation factor (10^4) in the energy range of interest. The value of the entering impulse count rate, J_0 , required to maximize the counting capacity of the detector (i.e., to obtain 10^5 counts in 10 sec) depends on the thickness and chemical nature of the matter to be irradiated and the energy of the radiation. J_0 is calculated in Equation (6.8).

The following discussion shows that the standard error of the impulse count rate is equal to its square root. This is explicitly stated subsequently in equation (6.68).

It is known that radioactive decomposition processes are statistical processes for which the assumptions of a Poisson distribution are fulfilled (Glocker and Macherauch 1965, p. 439). Thus, an impulse count rate J_0 emitted from an isotope is not constant, but rather is a random variable that fluctuates statistically around a probable value, termed the expected value, E_J . To not bias the continuing evaluation between an isotope and an x-ray tube as the second radiation source (discussed in Section 6.7), it was assumed that this mathematical interrelationship is also valid for the characteristic radiation emitted by an activated target within an x-ray tube.

The variability around the expected value was assumed to be a normal distribution described by Gauss' bell-shaped curve. The normal distribution is binomial during a random experiment with only two complementary possibilities of occurrence: a positive occurrence with the probability p and a negative occurrence with the probability q . For the case of a larger number of observations, n , this binomial distribution can be replaced by a normal distribution (Heinhold and Gaede 1964, p. 160). If, in addition, as $n \rightarrow \infty$, simultaneously $p \rightarrow 0$, then the result is the Poisson distribution. A quantitative measure for the magnitude of the variation around the expected value (i.e., a characterization of the distribution) is given by the data scatter or the variance. The square root of the variance is designated as the standard deviation, σ , or the standard error, m . For a Poisson distribution, the expected value, E , and the variance, m^2 , are equally large. With a binomial distribution, the expected value is $E = n \cdot p$ and the variance is $m^2 = n \cdot p \cdot (1 - p)$.

According to the discussion in Section 6.4.4, the energy of the second radiation source must lie between 0.06 and 0.084 MeV. Given this energy range and the design of the saturation measurement apparatus, the material attenuation is expected to be on the order of 10^4 , according to Figure 6.11. The process of material attenuation is stochastic in nature with an initially unknown variance. Thus, the question that must be posed concerns the error

distribution or standard deviation, σ_J , of the impulse count rate, J , after passing through the material. σ_J is dependent on σ_{J_0} , the standard deviation of the Poisson distribution of the impulse count rate J_0 before passing through the material, and on the initially unknown variance of the material attenuation.

If a gamma-quantum interacts with an electron of the irradiated material, then it must occur as a function of the quantum energy of one of the processes shown in Figure 6.3. The quantum is deflected and generally undergoes an attenuation of its energy, and thus the quantum is said to undergo a negative action. If a quantum does not interact with the material, then the quantum is said to undergo a positive action. Thus, only either a positive or a negative action can happen to a quantum. Consequently, the sum of the number of positive and negative actions must equal the total number of actions, and thus must equal the number of occurring quanta. Simplified, the conceptual model describing the spatial attenuation of collimated radiation can be reduced to that of a simple plate, impenetrable by gamma radiation, with randomly distributed holes. The probability p of the passage of a ray from a radiation bundle distributed, on the average, homogeneously over the plate, is equal to the ratio of the cross-sectional area of the ray to that of the plate. The probability q of the negative action; that is, not passing through the plate is $q = 1 - p$.

Until now, the concept of the term "action" referred to the outcome of the test with respect to the passage of a single quantum through the plate. In the following discussion, the term "action" will refer to the outcome of a test with respect to the passage of specified number of quanta (i.e., the impulse count rate, J_0 , through the material). We are interested in the variance or the standard error of the exiting impulse count rate, J , detected by the scintillation counter. According to Equation (6.24), J is the impulse count rate after the initial, or entering, impulse count rate, J_0 , has been reduced by material attenuation.

Previously it was assumed that the entering impulse count rate, J_0 , was constant. If the attenuation process was a definite action (where the

p -portion of J_0 exits from the material as unattenuated quanta, thus $J = p \cdot J_0$, then the variance or the standard error of the exiting impulse count rate would be zero. However, because the attenuation process is stochastic, J_0 is not reduced with certainty to the p -portion, but only by the probability of p occurring; that is, the probability of the collision-free passage of a single quantum. Most likely, $p \cdot J_0$ is the most probable value or the expected value, E_J ; that is:

$$E_J = p \cdot J_0 \quad (6.63)$$

The stochastic nature of the attenuation process indicates that the impulse count rate exiting unattenuated from the irradiated material is binomially distributed around the expected value, as in the plausible conceptual model of a plate with holes (Heinhold and Gaede 1964, p. 175). The mean variation of a binomial distribution is, by definition,

$$\sigma_J = \sqrt{q \cdot E_J} = \sqrt{q \cdot p \cdot J_0} \quad (6.64)$$

Figure 6.13 is a graphical representation of the above formula. The entering impulse count rate, J_0 , is plotted on the x-axis. Given the preliminary assumption that J_0 is constant, J_0 can be replaced by the constant entering impulse count rate, J_K . The exiting impulse count rate is plotted on the y-axis. By means of the straight lines, whose slopes represent the probability of p occurring, the linear, most probable reduction of J_0 according to Equation (6.63) can be shown graphically. The expected value of the unattenuated exiting impulse count rate is accordingly equal to the p -portion of J_0 . Because of the stochastic nature of the attenuation process, one can distinguish between the impulse count rate resulting from an event versus that resulting from the expected value. The larger the deviation of the impulse count rate from its expected value, the less likely this count rate will occur again. If the frequency of the entering impulse count rate is plotted in the z-direction, while each exiting impulse count rate is plotted on the y-axis to record its frequency, a binomial distribution, $f(J)$, is produced from the

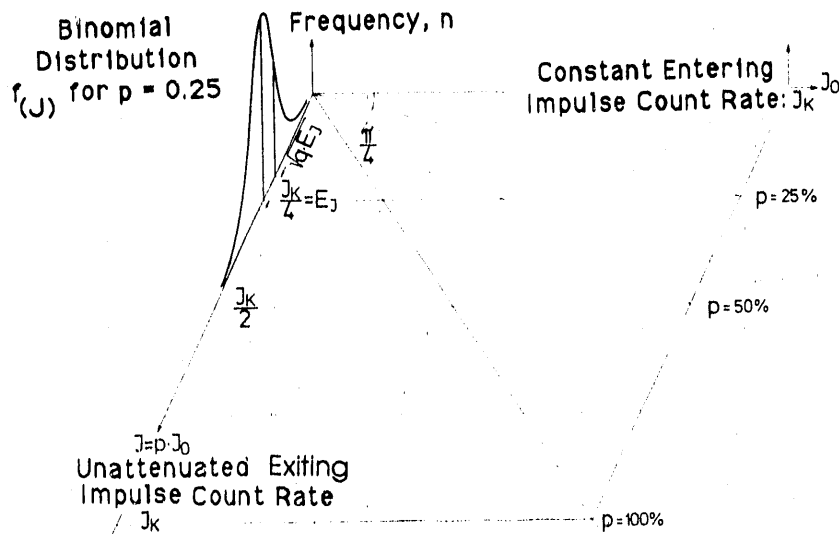


FIGURE 6.13. Binomial Distribution of the Exiting Impulse Count Rate, J Assuming a Constant Entering Impulse Count Rate, J_k

frequency curve of the above observation for a very large number of events; that is, for a multitude of impulse count rates exiting under the same conditions.

Contrary to the previous preliminary assumption, the entering impulse count rate, J_0 , is not constant, because of the stochastic nature of radioactive decay, but is rather a statistical variable, described by a Poisson distribution. Consequently, a large number of entering impulse count rates are distributed according to the Poisson distribution, $f(J_0)$, shown in Figure 6.14. Each entering impulse count rate, with a frequency depending on J_0 according to $f(J_0)$, will emerge from the irradiated material distributed binomially as $f(J, J_0)$, based on the discussion of Figure 6.13. Given the assumption that there are a large number of exiting unattenuated impulse count rates, their distribution will obey the marginal distribution $f_2(J, J_0)$. The marginal distribution $f_2(J, J_0)$ is derived from the projection and superposition of the various binomial distributions on π_2 . The expected value of an unattenuated exiting impulse count rate is equal to

$$EJ = p \cdot EJ_0 \quad (6.65)$$

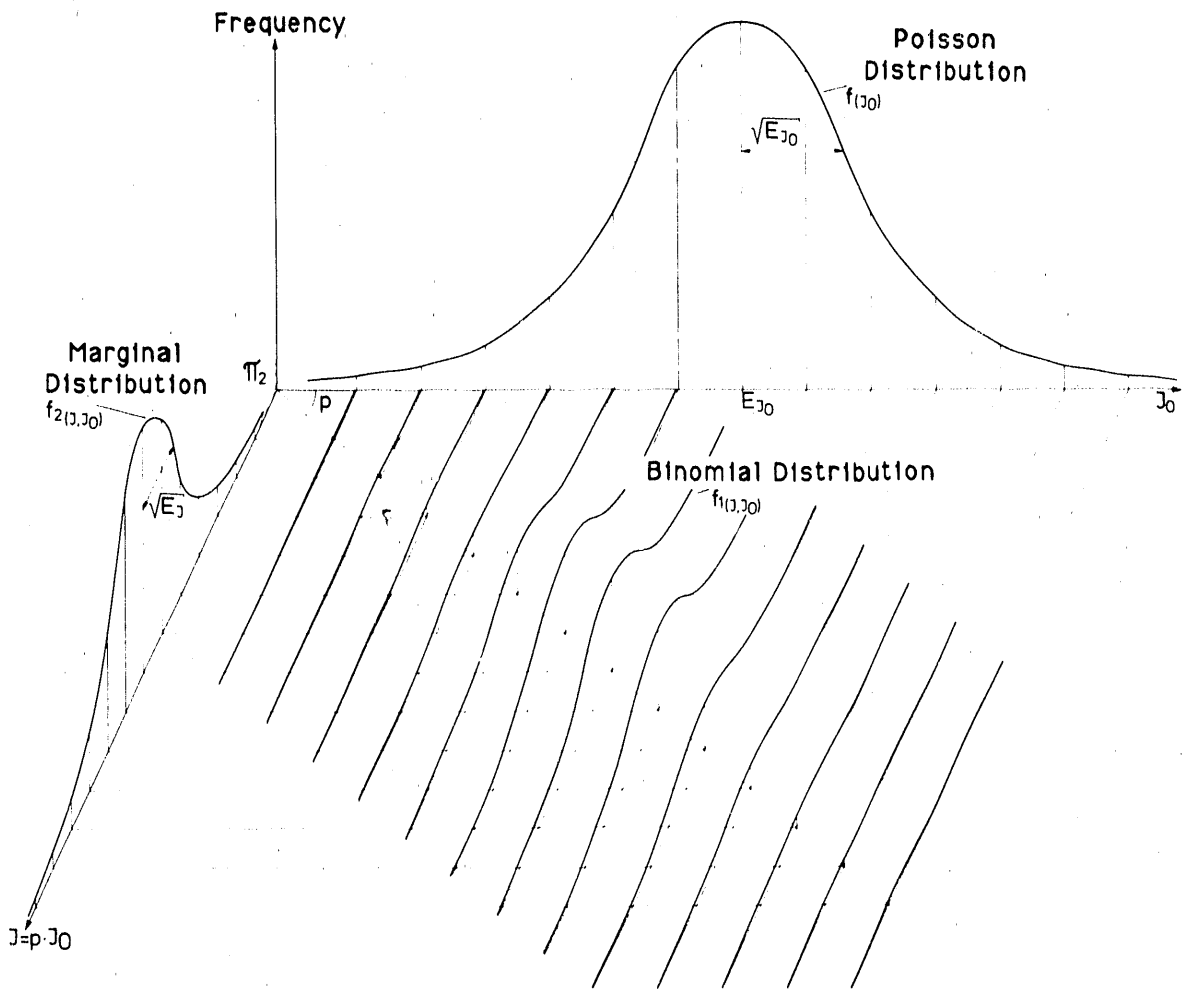


FIGURE 6.14. Marginal Distribution of the Exiting Impulse Count Rates for an Entering Impulse Count Rate That Satisfies a Poisson Distribution

Analytically, the marginal distribution $f_2(J, J_0)$ is obtained by the integral

$$f_2(J, J_0) = \int_{-\infty}^{+\infty} f(J_0) \cdot f_1(J, J_0) \cdot dJ_0 \quad (6.66)$$

The question posed initially is synonymous to the question about the variation of the marginal distribution. To determine the marginal distribution (under the simplified assumption of a normal distribution of both the Poisson

distribution and the binomial distribution), Equation (6.66) was solved using the Monte-Carlo method on a computer as follows (the computer program was written by M. Jensen, ETH):

- random generation of n J_0 -values), which obey a normal distribution, and thus have E_{J_0} as the expected value
- for each J_0 , a random generation of a J , which obeys a normal distribution
- determination of the distribution function $f_2(J, J_0)$ of these n J -values
- repetition of these procedures for various p -probabilities; that is, large and small attenuations.

The following was obtained as the variance of the marginal distribution for each p , and thus the variance is independent of the attenuation

$$\sigma_J = \sqrt{E_J} \quad (6.67)$$

From this result, one can conclude that the standard error m_J of each attenuated arbitrary impulse count rate J is equal to its square root. Thus, independent of material attenuation, the following is valid:

$$m_J = \sqrt{J} \quad (6.68)$$

For very high attenuation, such as produced by a material attenuation on the order of magnitude of 10^4 , Equation (6.68) can be developed directly from the following considerations; that is, without using a computer. For a large probability of attenuation (that is, a very small p), with a constant emerging impulse count rate and thus a constant expected value E_J , the expected value of the entering impulse count rate E_{J_0} must be correspondingly large, according to Equation (6.65). The larger the expected value E_{J_0} of a Poisson distribution is, the more insignificant the standard deviation (the square root of the expected value) will be. Thus, the representation shown in Figure 6.14 will be transformed into the representation shown in Figure 6.13, and therefore the marginal distribution will become a binomial distribution. The variance, given in Equation (6.64), of a binomial distribution for a large

attenuation and thus very small p (thereby, q must be about 1) transforms into the square root of the expected value--the statement made in Equation (6.68).

6.5.2.2 Values of the Standard Error of the Densities of the Fluids and the Sand

The densities of the fluids, water and fuel oil, are plotted as a function of temperature in Figure 6.15. The function $\rho_W = \rho_W(T)$ was taken from the Radiochemical Manual (1966). The function $\rho_O = \rho_O(T)$ was determined experimentally using a pycnometer and scale.

The value of the density of water was assumed as 1 g/cm^3 , and that of fuel oil as 0.85 g/cm^3 . The experimental determination of the density of quartz sand yielded 2.65 g/cm^3 --the value for SiO_2 .

The assumed standard error of the fluid densities are not a result of measurement inaccuracies, but rather it originates more from density changes caused by temperature fluctuations in the laboratory of at most, a few degrees

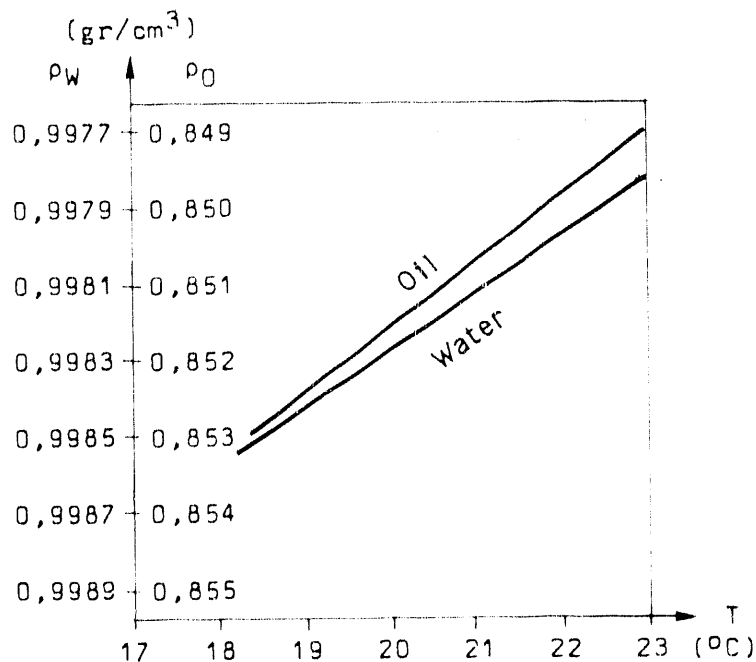


FIGURE 6.15. Fluid Densities as a Function of Temperature

Celsius. The experimental determination of the sand density led, by repetition, to an average standard error of 0.005 g/cm^3 . Thus, the values and standard errors of the fluid and sand densities are:

$$\rho_W = 1 \pm 10^{-3} \text{ gr/cm}^3; \quad \rho_0 = 0,85 \pm 3 \cdot 10^{-3} \text{ gr/cm}^3; \quad (6.69)$$

$$\rho_{SiO_2} = 2,65 \pm 5 \cdot 10^{-3} \text{ gr/cm}^3$$

6.5.2.3 Values and Standard Error of the Irradiation or Flume Width B

The flume constructed for the two-dimensional physical simulations of three-phase flow had a bottom consisting of the upper flange of an I-beam (DIN-20), which was inclinable to vary the slope of the flume, and had two vertical glass walls separated by a distance B equal to 15 cm.

$$B = 15 \text{ cm} \quad (6.70)$$

The irradiation or flume cross-sectional width B was not constant, primarily because of the somewhat variable glass thickness but also because of the deflection of the glass walls. Because the deflection occurred only when the flume was filled with sand, the best estimate of the value and standard error of B was not determinable with the empty flume. The flume width varied from measuring point to measuring point in small amounts and consequently had to be determined individually at each point. The quantification of the irradiation or flume cross-sectional width was made by measuring the glass thicknesses, d_1 and d_2 , at the irradiation measurement point before filling with sand, as well as by measuring the distances b_1 and b_2 to the external reference planes, E_1 and E_2 , before and after filling the flume with sand. According to Figure 6.16, B is equal to

$$m_B = \sqrt{5(5 \cdot 10^{-3})^2} \approx \pm 10^{-2} \text{ cm} \quad (6.71)$$

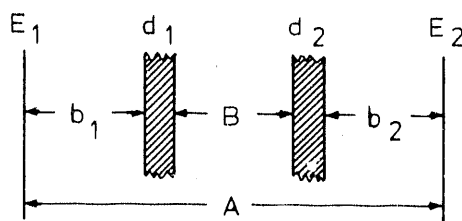


FIGURE 6.16. Determination of the Irradiation or Flume Width B

The standard error of B is yielded by using Gauss' Law of Probability and assuming that each of the five distances in Equation (6.71) were determined with dial gauges exactly to $\pm 5 \cdot 10^{-3}$ cm.

$$B = A - (b_1 + b_2 + d_1 + d_2) \quad (6.72)$$

6.5.2.4 Values and Standard Errors of the Mass Attenuation Coefficients

The approximate values of the mass attenuation coefficients can be taken from Figure 6.8. Because the petroleum derivative used in the experiments was not necessarily identical to C_8H_{18} , and the water was not necessarily identical to pure H_2O , the mass attenuation coefficients of both fluids were determined experimentally. This determination was made by irradiating each of the two fluids with each of the two radiation sources in a calibration vessel with a known inside diameter D. The following equation yields the explicit representation of the mass attenuation coefficient from Equation (6.5)

$$\left(\frac{\mu}{\rho}\right) = \frac{-\ln\left(\frac{J}{J_L}\right)}{D \cdot \rho} \quad (6.73)$$

J_L is the entering impulse count rate; that is, the impulse count rate measured through the empty calibration vessel. J is the exiting impulse count rate; that is, the impulse count rate reduced by the filled calibration vessel. The mass attenuation coefficient is thus an indirect observation, a function of both direct and indirect observations. The standard error of the mass attenuation coefficients of each fluid is yielded by applying Gauss' Law of Probability to Equation (6.73)

$$m\left(\frac{\mu}{\rho}\right) = \sqrt{\left\{\frac{\partial\left(\frac{\mu}{\rho}\right)}{\partial J}\right\}^2 \cdot m_J^2 + \left\{\frac{\partial\left(\frac{\mu}{\rho}\right)}{\partial J_L}\right\}^2 \cdot m_{J_L}^2 + \left\{\frac{\partial\left(\frac{\mu}{\rho}\right)}{\partial D}\right\}^2 \cdot m_D^2 + \left\{\frac{\partial\left(\frac{\mu}{\rho}\right)}{\partial \rho}\right\}^2 \cdot m_\rho^2} \quad (6.74)$$

The differential quotients are calculated from a modified form of Equation (6.73), $(\mu/\rho) = (\ln J_L - \ln J)/D \cdot \rho$, as

$$\frac{\partial\left(\frac{\mu}{\rho}\right)}{\partial J} = \frac{-1}{D \cdot \rho \cdot J}; \quad \frac{\partial\left(\frac{\mu}{\rho}\right)}{\partial J_L} = \frac{1}{D \cdot \rho \cdot J_L}; \quad \frac{\partial\left(\frac{\mu}{\rho}\right)}{\partial D} = \frac{\ln\left(\frac{J}{J_L}\right)}{D^2 \cdot \rho}; \quad \frac{\partial\left(\frac{\mu}{\rho}\right)}{\partial \rho} = \frac{\ln\left(\frac{J}{J_L}\right)}{D \cdot \rho^2} \quad (6.75)$$

The mass attenuation coefficient of the quartz sand used was also determined experimentally, because the sand was not necessarily identical to pure silicon dioxide. After applying Gauss' Law of Probability to the explicit representation of (μ_S/ρ_S) from Equation (6.12), whereby

$$\left(\frac{\mu_S}{\rho_S}\right) = \frac{\ln\left(\frac{J}{J_L}\right)}{(n-1) \cdot D \cdot \rho_S}, \quad (6.76)$$

the standard error of (μ_S/ρ_S) can be written as

$$m\left(\frac{\mu_S}{\rho_S}\right) = \sqrt{\left\{\frac{\partial\left(\frac{\mu_S}{\rho_S}\right)}{\partial J}\right\}^2 m_J^2 + \left\{\frac{\partial\left(\frac{\mu_S}{\rho_S}\right)}{\partial J_L}\right\}^2 m_{J_L}^2 + \left\{\frac{\partial\left(\frac{\mu_S}{\rho_S}\right)}{\partial n}\right\}^2 m_n^2 + \left\{\frac{\partial\left(\frac{\mu_S}{\rho_S}\right)}{\partial D}\right\}^2 m_D^2 + \left\{\frac{\partial\left(\frac{\mu_S}{\rho_S}\right)}{\partial \rho_S}\right\}^2 m_{\rho_S}^2} \quad (6.77)$$

The differential quotients are calculated from Equation (6.76) as

$$\frac{\partial\left(\frac{\mu_S}{\rho_S}\right)}{\partial J} = \frac{-1}{(n-1) \cdot D \cdot \rho_S \cdot J}; \quad \frac{\partial\left(\frac{\mu_S}{\rho_S}\right)}{\partial J_L} = \frac{1}{(n-1) \cdot D \cdot \rho_S \cdot J_L} \quad (6.78)$$

$$\frac{\partial\left(\frac{\mu_S}{\rho_S}\right)}{\partial n} = \frac{-\ln\left(\frac{J}{J_L}\right)}{(n-1)^2 \cdot D \cdot \rho_S}; \quad \frac{\partial\left(\frac{\mu_S}{\rho_S}\right)}{\partial D} = \frac{-\ln\left(\frac{J}{J_L}\right)}{(n-1) \cdot D^2 \cdot \rho_S}; \quad \frac{\partial\left(\frac{\mu_S}{\rho_S}\right)}{\partial \rho_S} = \frac{-\ln\left(\frac{J}{J_L}\right)}{(n-1) \cdot D \cdot \rho_S^2}$$

The inside diameter, D , of the calibration vessel was 10 cm. This vessel was used to determine experimentally the mass attenuation coefficient of the petroleum derivative, the water, and the quartz sand. The standard error of the diameter measurement came to $\pm 5 \cdot 10^{-3}$ cm. The measuring time and distance between source and detector were selected so that the number of impulses per second impinging on the detector was about equal to its capacity of 10^4 . Thus, in 10 sec a total of 10^5 impulses were recorded. In all three calibration cases, the exiting impulse count J was assumed to be 10^5 impulses. The optimal entering impulse count J_L is a function of the (μ/ρ) values of the fluids according to Equation (6.5)

$$J_L = 10^5 \cdot e^{+(\frac{\mu}{\rho}) \cdot D \cdot \rho} \quad (6.79)$$

The calculation of the standard error of the experimentally determined mass attenuation coefficients of the fluids, based on Equations (6.74) and (6.75), for different energies is compiled on Table 6.4. In this case, J_L was determined according to Equation (6.79), which implies J equaled 10^5 . According to Equation (6.68), the standard error of the impulse count rate is equal to its square root. D was assumed to be 10 ± 0.005 cm. The densities and their standard error are given by Equation (6.69).

To calculate the standard error of the mass attenuation coefficient of SiO_2 (whose value can be taken from Figure 6.8), the porosity n and its standard error based on gravimetric measurements, 0.428 ± 0.0005 , is used. Assuming that $J = 10^5$, J_L is determined according to Equation (6.12) as

$$J_L = 10^5 \cdot e^{+D(\frac{\mu_S}{\rho_S})(1-n)\rho_S} \quad (6.80)$$

Table 6.5 presents the values for the components of the standard error of the mass attenuation coefficient for SiO_2 , according to Equations (6.77) and (6.78), for the example radiation energy $E_I = 0.662$ MeV, for which $(\mu_S/\rho_S) = 0.076$ and $J_L = 3.16 \cdot 10^5$.

TABLE 6.4. Calculation of the Expected Standard Error of the Mass Attenuation Coefficients (to be determined experimentally) of the Fluids

MeV	$\left(\frac{\mu}{\rho}\right)$ Table 6.1	J_L Eq. 6.79	$\ln\left(\frac{J=105}{J_L}\right)$	$\left(\frac{1}{D \cdot \rho \cdot J_L}\right)^2 \cdot m_{JL}^2$	$\frac{\ln\left(\frac{J}{J_L}\right)^2}{D^2 \cdot \rho} \cdot m_D^2$	$\frac{\ln\left(\frac{J}{J_L}\right)^2}{D \cdot \rho^2} \cdot m_p^2$	$m \frac{\mu}{\rho} = \sqrt{\Sigma}$
Water $\rho = 1$; $\left(\frac{-1}{D \cdot \rho \cdot J}\right)^2 \cdot m_J^2 = 1,00 \cdot 10^{-7}$							
100	0,0166	1,18 · 10 ⁵	-1,66 · 10 ⁻¹	8,47 · 10 ⁻⁸	6,69 · 10 ⁻¹¹	2,76 · 10 ⁻¹⁰	4,30 · 10 ⁻⁴
50	0,0161	1,19 · 10 ⁵	-1,61 · 10 ⁻¹	8,51 · 10 ⁻⁸	6,48 · 10 ⁻¹¹	2,59 · 10 ⁻¹⁰	4,31 · 10 ⁻⁴
30	0,0166	1,18 · 10 ⁵	-1,66 · 10 ⁻¹	8,47 · 10 ⁻⁸	6,89 · 10 ⁻¹¹	2,76 · 10 ⁻¹⁰	4,30 · 10 ⁻⁴
10	0,0219	1,24 · 10 ⁵	-2,15 · 10 ⁻¹	8,03 · 10 ⁻⁸	1,20 · 10 ⁻¹⁰	4,80 · 10 ⁻¹⁰	4,25 · 10 ⁻⁴
6	0,0275	1,32 · 10 ⁵	-2,78 · 10 ⁻¹	7,60 · 10 ⁻⁸	1,89 · 10 ⁻¹⁰	7,56 · 10 ⁻¹⁰	4,21 · 10 ⁻⁴
EI	0,0858	2,36 · 10 ⁵	-8,58 · 10 ⁻¹	4,24 · 10 ⁻⁸	1,64 · 10 ⁻⁹	7,35 · 10 ⁻⁹	3,89 · 10 ⁻⁴
0,1	0,171	5,53 · 10 ⁵	-1,71 · 10 ⁰	1,81 · 10 ⁻⁸	7,31 · 10 ⁻⁹	2,92 · 10 ⁻⁸	3,93 · 10 ⁻⁴
0,06	0,204	7,69 · 10 ⁵	-2,04 · 10 ⁰	1,30 · 10 ⁻⁸	1,04 · 10 ⁻⁸	4,16 · 10 ⁻⁸	4,06 · 10 ⁻⁴
0,03	0,370	4,04 · 10 ⁶	-3,70 · 10 ⁰	2,47 · 10 ⁻⁹	3,42 · 10 ⁻⁸	1,37 · 10 ⁻⁷	5,23 · 10 ⁻⁴
0,01	5,31	1,15 · 10 ²⁸	-5,30 · 10 ¹	8,69 · 10 ⁻³¹	7,05 · 10 ⁻⁶	2,82 · 10 ⁻⁵	5,95 · 10 ⁻³
Petroleum Derivative $\rho = 0,85$; $\left(\frac{-1}{D \cdot \rho \cdot J}\right)^2 \cdot m_J^2 = 1,38 \cdot 10^{-7}$							
100	0,0136	1,12 · 10 ⁵	-1,13 · 10 ⁻¹	1,23 · 10 ⁻⁷	4,62 · 10 ⁻¹¹	2,30 · 10 ⁻⁹	5,14 · 10 ⁻⁴
60	0,0136	1,12 · 10 ⁵	-1,13 · 10 ⁻¹	1,23 · 10 ⁻⁷	4,62 · 10 ⁻¹¹	2,30 · 10 ⁻⁹	5,14 · 10 ⁻⁴
30	0,0146	1,13 · 10 ⁵	-1,22 · 10 ⁻¹	1,22 · 10 ⁻⁷	5,33 · 10 ⁻¹¹	2,65 · 10 ⁻⁹	5,13 · 10 ⁻⁴
10	0,0214	1,20 · 10 ⁵	-1,82 · 10 ⁻¹	1,15 · 10 ⁻⁷	1,14 · 10 ⁻¹⁰	5,70 · 10 ⁻⁹	5,09 · 10 ⁻⁴
6	0,0277	1,27 · 10 ⁵	-2,39 · 10 ⁻¹	1,09 · 10 ⁻⁷	1,92 · 10 ⁻¹⁰	9,56 · 10 ⁻⁹	5,07 · 10 ⁻⁴
EI	0,0891	2,13 · 10 ⁵	-7,56 · 10 ⁻¹	6,49 · 10 ⁻⁸	1,99 · 10 ⁻⁹	9,89 · 10 ⁻⁸	5,52 · 10 ⁻⁴
0,1	0,175	4,43 · 10 ⁵	-1,49 · 10 ⁰	3,13 · 10 ⁻⁸	7,66 · 10 ⁻⁹	3,81 · 10 ⁻⁷	7,48 · 10 ⁻⁴
0,06	0,198	5,38 · 10 ⁵	-1,68 · 10 ⁰	2,57 · 10 ⁻⁸	9,80 · 10 ⁻⁹	4,68 · 10 ⁻⁷	8,14 · 10 ⁻⁴
0,03	0,269	9,84 · 10 ⁵	-2,29 · 10 ⁰	1,41 · 10 ⁻⁸	1,81 · 10 ⁻⁸	9,01 · 10 ⁻⁷	1,04 · 10 ⁻³
0,01	1,981	2,06 · 10 ¹²	-1,68 · 10 ¹	6,73 · 10 ⁻¹⁵	9,81 · 10 ⁻⁷	4,89 · 10 ⁻⁵	7,07 · 10 ⁻³

TABLE 6.5. Calculation of the Expected Standard Error of the Mass Attenuation Coefficients (to be determined experimentally) for SiO₂ or Quartz Sand or Glass (E_I = 0.662 MeV)

$\left(\frac{1}{(n-1)D \cdot \rho_S \cdot J}\right)^2 \cdot m_J^2$	$\left(\frac{-1}{(n-1)D \cdot \rho_S \cdot J_L}\right)^2 \cdot m_{J_L}^2$	$\left(\frac{-\ln\left(\frac{J}{J_L}\right)}{(n-1)^2 D \cdot \rho_S}\right)^2 \cdot m_n^2$
4,35 · 10 ⁻⁸	1,38 · 10 ⁻⁸	4,40 · 10 ⁻⁹
$\left(\frac{-\ln\left(\frac{J}{J_L}\right)}{(n-1)D^2 \rho_S}\right)^2 \cdot m_D^2$	$\left(\frac{-\ln\left(\frac{J}{J_L}\right)}{(n-1)D \cdot \rho_S^2}\right)^2 \cdot m_{\rho_S}^2$	$m\left(\frac{\mu_S}{\rho_S}\right) = \sqrt{\Sigma}$
1,44 · 10 ⁻⁹	2,05 · 10 ⁻⁸	2,9 · 10 ⁻⁴

6.5.2.5 Value and Standard Error of the Porosity

The value of the porosity of the unconsolidated quartz-sand filling used for the experimental simulations is yielded from gravimetric determinations as

$$n = 0,428 \quad (6.81)$$

The standard error of the porosity, if the porosity were determined according to Equation (6.13) instead of gravimetrically, is calculated based on Gauss' Law of Probability as

$$m_n^2 = \left(\frac{\partial n}{\partial J_T}\right)^2 \cdot m_{J_T}^2 + \left(\frac{\partial n}{\partial J_N}\right)^2 \cdot m_{J_N}^2 + \left(\frac{\partial n}{\partial B}\right)^2 \cdot m_B^2 + \left(\frac{\partial n}{\partial\left(\frac{\mu_S}{\rho_S}\right)}\right)^2 \cdot m_{\left(\frac{\mu_S}{\rho_S}\right)}^2 + \left(\frac{\partial n}{\partial(\rho_S)}\right)^2 \cdot m_{\rho_S}^2 \quad (6.82)$$

From Equation (6.13), the differential quotients are

$$\frac{\partial n}{\partial J_T} = \frac{1}{B\left(\frac{\mu_S}{\rho_S}\right)\rho_S \cdot J_T}; \quad \frac{\partial n}{\partial J_N} = \frac{-1}{B\left(\frac{\mu_S}{\rho_S}\right)\rho_S \cdot J_N}; \quad \frac{\partial n}{\partial B} = \frac{-\ln\left(\frac{J_T}{J_N}\right)}{B^2\left(\frac{\mu_S}{\rho_S}\right)\rho_S}; \quad (6.83)$$

$$\frac{\partial n}{\partial\left(\frac{\mu_S}{\rho_S}\right)} = \frac{-\ln\left(\frac{J_T}{J_N}\right)}{B\left(\frac{\mu_S}{\rho_S}\right)^2 \rho_S}; \quad \frac{\partial n}{\partial \rho_S} = \frac{-\ln\left(\frac{J_T}{J_N}\right)}{B\left(\frac{\mu_S}{\rho_S}\right)\rho_S^2}$$

With $J_T = 10^5$, $J_N = [10^5 \cdot \exp(+B\{(\mu_S/\rho_S)(1-n)\rho_S\})]$, and the parameter values for 0.662 MeV used in the previous section, the standard error of the porosity is given by

$$m_n = \sqrt{1,1 \cdot 10^{-6} + 1,9 \cdot 10^{-7} + 1,4 \cdot 10^{-7} + 4,8 \cdot 10^{-6} + 1,2 \cdot 10^{-6}} \\ = \pm 2,7 \cdot 10^{-3} \quad (6.84)$$

The standard error of gravimetrically determined porosities is probably five times smaller. Nevertheless, the nondestructive examination of the homogeneity of the sand filling can only be done by gamma radiation attenuation. The expected standard error (calculated in Equation [6.84]) of a scant 0.3%; however, provided sufficient accuracy to verify experimentally that the homogeneity of the sand filling was within 0.5% of a pore volume (see, e.g., Section 8.2).

6.5.2.6 Standard Error of the Oil Saturation, m_{S_0} , as a Function of the Energy of the Second Radiation Source

The calculation of the standard error, m_{S_0} , (according to Equation [6.60]), as a function of the energy of the second radiation source, E_{II} , as well as of the oil saturation, S_0 , is shown in Table 6.6. S_0 is determined from the second equation in Equation (6.15) with Cs-137 as the high-energy radiation source and a second radiation source whose monochromatic quanta energy is less than 60 KeV. Figure 6.17 is the graphical representation of the results from Table 6.6.

According to Section 6.4.3.3, none of the proposed saturation determination methods can use an energy lower than 60 KeV for the second radiation source. Figure 6.17 shows that the standard error of an oil saturation is not adequate because m_{S_0} is more than 10% saturation greater than the stipulated 2% oil saturation measurement accuracy (see Section 6.2).

6.6 RAISING THE MASS ATTENUATION COEFFICIENT OF THE PETROLEUM DERIVATIVE WITH AN ELEMENT WITH A HIGHER ATOMIC NUMBER

The failure of the oil saturation measurement methods proposed in Section 6.4.3 to measure the oil saturation to meet the accuracy specified in Section 6.2 is clearly a result of the two ratios in Equation (6.16) being too

TABLE 6.6. Standard Error at 4%, 20%, and 70% Oil Saturation, According to Equation (6.60), as a Function of the Energy of the Second Radiation Source, E_{II}, with Cs-137 as the First Radiation Source

Compilation of Original Data

E _I =E _{Cs-137} =0,662MeV		ρ ₀ =0,85gr/cm ³		J=105		S ₀ =0,04= 4% S _W =0,76=76% S _L =0,20=20%		S ₀ =0,20=20% S _W =0,60=60% S _L =0,20=20%		S ₀ =0,70=70% S _W =0,10=10% S _L =0,20=20%	
n=0,43		B=15cm		J=105		JT		JT		JT	
E _{II} ($\frac{W}{P_W}$) ($\frac{U_0}{P_0}$)		K ()		N		JT		JT		JT	
MeV	cm ² /gr	For Designations, See Equation (6.61)									
100	0,0166	6,64·10 ⁻³	2,58·10 ⁻¹	1,72·10 ⁻³	1,09·10 ⁵	6,90·10 ⁻⁵	1,06·10 ⁵	3,43·10 ⁻⁴	1,06·10 ⁵	1,20·10 ⁻³	1,06·10 ⁵
60	0,0161	6,64·10 ⁻³	2,21·10 ⁻¹	1,47·10 ⁻³	1,09·10 ⁵	5,91·10 ⁻⁵	1,06·10 ⁵	2,94·10 ⁻⁴	1,06·10 ⁵	1,03·10 ⁻³	1,06·10 ⁵
30	0,0166	7,13·10 ⁻³	1,75·10 ⁻¹	1,25·10 ⁻³	1,09·10 ⁵	5,01·10 ⁻⁵	1,08·10 ⁵	2,49·10 ⁻⁴	1,07·10 ⁵	8,71·10 ⁻⁴	1,07·10 ⁵
10	0,0219	1,05·10 ⁻²	6,10·10 ⁻²	6,37·10 ⁻⁴	1,12·10 ⁵	2,51·10 ⁻⁵	1,11·10 ⁵	1,27·10 ⁻⁴	1,10·10 ⁵	4,46·10 ⁻⁴	1,10·10 ⁵
6	0,0275	1,35·10 ⁻²	3,04·10 ⁻²	4,11·10 ⁻⁴	1,15·10 ⁵	1,62·10 ⁻⁵	1,15·10 ⁵	8,20·10 ⁻⁵	1,13·10 ⁵	2,88·10 ⁻⁴	1,13·10 ⁵
E _I	0,0858	0,0891			1,55·10 ⁵		1,54·10 ⁵		1,49·10 ⁵		1,49·10 ⁵
0,1	0,171	8,55·10 ⁻²	1,47·10 ⁻²	1,26·10 ⁻³	2,40·10 ⁵	5,05·10 ⁻⁵	2,35·10 ⁵	2,52·10 ⁻⁴	2,19·10 ⁵	8,82·10 ⁻⁴	2,19·10 ⁵
0,06	0,204	9,67·10 ⁻²	6,79·10 ⁻²	6,57·10 ⁻³	2,84·10 ⁵	2,63·10 ⁻⁴	2,74·10 ⁵	1,31·10 ⁻³	2,44·10 ⁵	4,60·10 ⁻³	2,44·10 ⁵
0,03	0,370	1,31·10 ⁻¹	4,13·10 ⁻¹	5,43·10 ⁻²	6,51·10 ⁵	2,17·10 ⁻³	5,62·10 ⁵	1,09·10 ⁻²	3,56·10 ⁵	3,80·10 ⁻²	3,56·10 ⁵
0,01	5,31	9,68·10 ⁻¹	1,72·10 ⁰	1,66·10 ⁰	3,11·10 ¹⁶	6,65·10 ⁻²	7,38·10 ¹⁴	3,33·10 ⁻¹	6,15·10 ⁹	1,16·10 ⁰	6,15·10 ⁹

TABLE 6.6. (contd)

EI = ECs-137=0,662MeV							Compilation of the Standard Error According to Section 6.5.2	
EI MeV	$m(\frac{\mu W}{\rho W})$	$m(\frac{\mu D}{\rho D})$	m_{JTI}	m_{JTI}	m_{JTI}			
			$S_0=4\%$	$S_0=20\%$	$S_0=70\%$			
100	$4,30 \cdot 10^{-4}$	$5,14 \cdot 10^{-4}$	329,9	329,0	326,3	$m_n = \pm 4 \cdot 10^{-3}$		
60	$4,31 \cdot 10^{-4}$	$5,14 \cdot 10^{-4}$	329,4	328,7	326,3	$m_B = \pm 10^{-2}$		
30	$4,30 \cdot 10^{-4}$	$5,3 \cdot 10^{-4}$	329,9	329,2	327,0	$m_{\rho D} = \pm 5 \cdot 10^{-3}$		
10	$4,25 \cdot 10^{-4}$	$5,10 \cdot 10^{-4}$	334,5	333,8	331,8	$m_J = \pm 316,2$		
6	$4,21 \cdot 10^{-4}$	$5,07 \cdot 10^{-4}$	339,3	338,6	336,5			
EI	$3,89 \cdot 10^{-4}$	$5,52 \cdot 10^{-4}$						
0,1	$3,93 \cdot 10^{-4}$	$7,48 \cdot 10^{-4}$	490,2	484,6	467,5	$m_{JTI} \begin{cases} (S_0=4\%) = \pm 394,0 \\ (S_0=20\%) = \pm 392,0 \\ (S_0=70\%) = \pm 385,7 \end{cases}$		
0,06	$4,06 \cdot 10^{-4}$	$8,14 \cdot 10^{-4}$	532,8	523,1	493,8			
0,03	$5,23 \cdot 10^{-4}$	$1,04 \cdot 10^{-3}$	806,6	749,9	597,0			
0,01	$5,95 \cdot 10^{-3}$	$7,07 \cdot 10^{-3}$	$1,76 \cdot 10^8$	$2,72 \cdot 10^7$	$7,85 \cdot 10^4$			

EI = ECs-137=0,662MeV									Calculation of the Partial Derivatives According to Section 6.5.1	
EI MeV	$\frac{\partial SO}{\partial(\frac{\mu W}{\rho W})_I}$	$\frac{\partial SO}{\partial(\frac{\mu W}{\rho W})_{II}}$	$\frac{\partial SO}{\partial(\frac{\mu D}{\rho D})_I}$	$\frac{\partial SO}{\partial(\frac{\mu D}{\rho D})_{II}}$	$\frac{\partial SO}{\partial J_I}$	$\frac{\partial SO}{\partial J_{II}}$	$\frac{\partial SO}{\partial J_{TI}}$	$\frac{\partial SO}{\partial J_{TII}}$		
$S_0=0,04=4\%$			$S_W=0,76=76\%$			$S_L=0,20=20\%$				
$\frac{\partial SO}{\partial n} = -9,30 \cdot 10^{-2}$			$\frac{\partial SO}{\partial B} = -2,67 \cdot 10^{-3}$			$\frac{\partial SO}{\partial \rho D} = -4,71 \cdot 10^{-2}$				
100	$-4,74 \cdot 10^1$	$2,45 \cdot 10^2$	$-1,74 \cdot 10^0$	$1,14 \cdot 10^1$	$-9,68 \cdot 10^{-5}$	$-5,00 \cdot 10^{-4}$	$6,23 \cdot 10^{-5}$	$-4,59 \cdot 10^{-4}$		
60	$-5,37 \cdot 10^1$	$2,86 \cdot 10^2$	$-2,03 \cdot 10^0$	$1,33 \cdot 10^1$	$-1,09 \cdot 10^{-4}$	$-5,83 \cdot 10^{-4}$	$7,05 \cdot 10^{-5}$	$-5,37 \cdot 10^{-4}$		
30	$-6,54 \cdot 10^1$	$3,38 \cdot 10^2$	$-2,57 \cdot 10^0$	$1,57 \cdot 10^1$	$-1,33 \cdot 10^{-4}$	$-6,89 \cdot 10^{-4}$	$8,59 \cdot 10^{-5}$	$-6,33 \cdot 10^{-4}$		
10	$-1,68 \cdot 10^2$	$6,60 \cdot 10^2$	$-7,36 \cdot 10^0$	$3,07 \cdot 10^1$	$-3,44 \cdot 10^{-4}$	$-1,35 \cdot 10^{-3}$	$2,21 \cdot 10^{-4}$	$-1,20 \cdot 10^{-3}$		
6	$-3,28 \cdot 10^2$	$1,02 \cdot 10^3$	$-1,48 \cdot 10^1$	$4,75 \cdot 10^1$	$-6,69 \cdot 10^{-4}$	$-2,09 \cdot 10^{-3}$	$4,31 \cdot 10^{-4}$	$-1,81 \cdot 10^{-3}$		
0,1	$-6,65 \cdot 10^2$	$3,34 \cdot 10^2$	$-3,05 \cdot 10^1$	$1,55 \cdot 10^1$	$-1,36 \cdot 10^{-3}$	$-6,80 \cdot 10^{-4}$	$8,47 \cdot 10^{-4}$	$-2,83 \cdot 10^{-4}$		
0,06	$-1,52 \cdot 10^2$	$6,40 \cdot 10^1$	$-6,61 \cdot 10^0$	$2,98 \cdot 10^0$	$-3,11 \cdot 10^{-4}$	$-1,31 \cdot 10^{-4}$	$2,00 \cdot 10^{-4}$	$-4,60 \cdot 10^{-5}$		
0,03	$-3,34 \cdot 10^1$	$7,74 \cdot 10^0$	$-1,09 \cdot 10^0$	$3,60 \cdot 10^{-1}$	$-6,82 \cdot 10^{-5}$	$-1,58 \cdot 10^{-5}$	$4,39 \cdot 10^{-5}$	$-2,43 \cdot 10^{-6}$		
0,01	$-1,57 \cdot 10^1$	$2,53 \cdot 10^{-1}$	$-2,61 \cdot 10^{-1}$	$1,18 \cdot 10^{-2}$	$-3,19 \cdot 10^{-5}$	$-5,16 \cdot 10^{-7}$	$2,06 \cdot 10^{-5}$	$-1,66 \cdot 10^{-8}$		
$S_0=0,20=20\%$			$S_W=0,60=60\%$			$S_L=0,20=20\%$				
$\frac{\partial SO}{\partial n} = -4,65 \cdot 10^{-1}$			$\frac{\partial SO}{\partial B} = -1,33 \cdot 10^{-2}$			$\frac{\partial SO}{\partial \rho D} = -2,35 \cdot 10^{-1}$				
100	$-3,75 \cdot 10^1$	$1,93 \cdot 10^2$	$-8,69 \cdot 10^0$	$5,70 \cdot 10^1$	$-9,68 \cdot 10^{-5}$	$-5,00 \cdot 10^{-4}$	$6,30 \cdot 10^{-5}$	$-4,62 \cdot 10^{-4}$		
60	$-4,24 \cdot 10^1$	$2,26 \cdot 10^2$	$-1,01 \cdot 10^1$	$6,64 \cdot 10^1$	$-1,09 \cdot 10^{-4}$	$-5,83 \cdot 10^{-4}$	$7,12 \cdot 10^{-5}$	$-5,40 \cdot 10^{-4}$		
30	$-5,16 \cdot 10^1$	$2,67 \cdot 10^2$	$-1,29 \cdot 10^1$	$7,85 \cdot 10^1$	$-1,33 \cdot 10^{-4}$	$-6,89 \cdot 10^{-4}$	$8,68 \cdot 10^{-5}$	$-6,36 \cdot 10^{-4}$		
10	$-1,33 \cdot 10^2$	$5,21 \cdot 10^2$	$-3,68 \cdot 10^1$	$1,53 \cdot 10^2$	$-3,44 \cdot 10^{-4}$	$-1,35 \cdot 10^{-3}$	$2,24 \cdot 10^{-4}$	$-1,21 \cdot 10^{-3}$		
6	$-2,59 \cdot 10^2$	$8,07 \cdot 10^2$	$-7,39 \cdot 10^1$	$2,38 \cdot 10^2$	$-6,69 \cdot 10^{-4}$	$-2,09 \cdot 10^{-3}$	$4,35 \cdot 10^{-4}$	$-1,82 \cdot 10^{-3}$		
0,1	$-5,25 \cdot 10^2$	$2,63 \cdot 10^2$	$-1,52 \cdot 10^2$	$7,75 \cdot 10^1$	$-1,36 \cdot 10^{-3}$	$-6,80 \cdot 10^{-4}$	$8,83 \cdot 10^{-4}$	$-2,90 \cdot 10^{-4}$		
0,06	$-1,20 \cdot 10^2$	$5,05 \cdot 10^1$	$-3,31 \cdot 10^1$	$1,49 \cdot 10^1$	$-3,11 \cdot 10^{-4}$	$-1,31 \cdot 10^{-4}$	$2,02 \cdot 10^{-4}$	$-4,77 \cdot 10^{-5}$		
0,03	$-2,64 \cdot 10^1$	$6,11 \cdot 10^0$	$-5,43 \cdot 10^0$	$1,80 \cdot 10^0$	$-6,82 \cdot 10^{-5}$	$-1,58 \cdot 10^{-5}$	$4,44 \cdot 10^{-5}$	$-2,81 \cdot 10^{-6}$		
0,01	$-1,24 \cdot 10^1$	$2,00 \cdot 10^{-1}$	$-1,31 \cdot 10^0$	$5,88 \cdot 10^{-2}$	$-3,19 \cdot 10^{-5}$	$-5,16 \cdot 10^{-7}$	$2,08 \cdot 10^{-5}$	$-6,99 \cdot 10^{-8}$		
$S_0=0,70=70\%$			$S_W=0,10=10\%$			$S_L=0,20=20\%$				
$\frac{\partial SO}{\partial n} = -1,63 \cdot 10^0$			$\frac{\partial SO}{\partial B} = -4,67 \cdot 10^{-2}$			$\frac{\partial SO}{\partial \rho D} = -8,24 \cdot 10^{-1}$				
100	$-6,24 \cdot 10^0$	$3,22 \cdot 10^1$	$-3,04 \cdot 10^1$	$1,99 \cdot 10^2$	$-9,68 \cdot 10^{-5}$	$-5,00 \cdot 10^{-4}$	$6,51 \cdot 10^{-5}$	$-4,69 \cdot 10^{-4}$		
60	$-7,06 \cdot 10^0$	$3,76 \cdot 10^1$	$-3,55 \cdot 10^1$	$2,32 \cdot 10^2$	$-1,09 \cdot 10^{-4}$	$-5,83 \cdot 10^{-4}$	$7,36 \cdot 10^{-5}$	$-5,48 \cdot 10^{-4}$		
30	$-8,60 \cdot 10^0$	$4,44 \cdot 10^1$	$-4,50 \cdot 10^1$	$2,75 \cdot 10^2$	$-1,33 \cdot 10^{-4}$	$-6,89 \cdot 10^{-4}$	$8,96 \cdot 10^{-5}$	$-6,44 \cdot 10^{-4}$		
10	$-2,22 \cdot 10^1$	$8,68 \cdot 10^1$	$-1,29 \cdot 10^2$	$5,37 \cdot 10^2$	$-3,44 \cdot 10^{-4}$	$-1,35 \cdot 10^{-3}$	$2,31 \cdot 10^{-4}$	$-1,22 \cdot 10^{-3}$		
6	$-4,31 \cdot 10^1$	$1,35 \cdot 10^2$	$-2,59 \cdot 10^2$	$8,32 \cdot 10^2$	$-6,69 \cdot 10^{-4}$	$-2,09 \cdot 10^{-3}$	$4,50 \cdot 10^{-4}$	$-1,84 \cdot 10^{-3}$		
0,1	$-8,75 \cdot 10^1$	$4,39 \cdot 10^1$	$-5,33 \cdot 10^2$	$2,71 \cdot 10^2$	$-1,36 \cdot 10^{-3}$	$-6,80 \cdot 10^{-4}$	$9,12 \cdot 10^{-4}$	$-3,11 \cdot 10^{-4}$		
0,06	$-2,00 \cdot 10^1$	$8,42 \cdot 10^0$	$-1,16 \cdot 10^2$	$5,21 \cdot 10^1$	$-3,11 \cdot 10^{-4}$	$-1,31 \cdot 10^{-4}$	$2,09 \cdot 10^{-4}$	$-5,35 \cdot 10^{-5}$		
0,03	$-4,40 \cdot 10^0$	$1,02 \cdot 10^0$	$-1,90 \cdot 10^1$	$6,30 \cdot 10^0$	$-6,82 \cdot 10^{-5}$	$-1,58 \cdot 10^{-5}$	$4,58 \cdot 10^{-5}$	$-4,43 \cdot 10^{-6}$		
0,01	$-2,06 \cdot 10^0$	$3,33 \cdot 10^{-2}$	$-4,57 \cdot 10^0$	$2,06 \cdot 10^{-1}$	$-3,19 \cdot 10^{-5}$	$-5,16 \cdot 10^{-7}$	$2,15 \cdot 10^{-5}$	$-8,38 \cdot 10^{-8}$		

TABLE 6.6. (contd)

$\frac{\partial^2 E_{SO}}{\partial t^2} = 0.5527 \text{ s}^{-1}$ $\frac{\partial^2 E_{SO}}{\partial t^2}$ $\frac{\partial^2 E_{SO}}{\partial t^2}$ $\frac{\partial^2 E_{SO}}{\partial t^2}$ $\frac{\partial^2 E_{SO}}{\partial t^2}$		Products of the Squared Derivatives and the Variances, Yielding the Standard Error of the Oil Saturation Measurement m_{SO}									
$\frac{\partial^2 E_{SO}}{\partial t^2} = 0.5527 \text{ s}^{-1}$											
$\frac{\partial^2 E_{SO}}{\partial t^2} = 0.5527 \text{ s}^{-1}$											
$\frac{\partial^2 E_{SO}}{\partial t^2} = 0.5527 \text{ s}^{-1}$											
1.5410	2.2710	3.2610	4.4710	5.8610	7.4710	9.2510	11.1610	13.1710	15.2610	17.4210	19.6510
1.5410	2.2710	3.2610	4.4710	5.8610	7.4710	9.2510	11.1610	13.1710	15.2610	17.4210	19.6510
1.5410	2.2710	3.2610	4.4710	5.8610	7.4710	9.2510	11.1610	13.1710	15.2610	17.4210	19.6510
1.5410	2.2710	3.2610	4.4710	5.8610	7.4710	9.2510	11.1610	13.1710	15.2610	17.4210	19.6510
1.5410	2.2710	3.2610	4.4710	5.8610	7.4710	9.2510	11.1610	13.1710	15.2610	17.4210	19.6510
1.5410	2.2710	3.2610	4.4710	5.8610	7.4710	9.2510	11.1610	13.1710	15.2610	17.4210	19.6510
1.5410	2.2710	3.2610	4.4710	5.8610	7.4710	9.2510	11.1610	13.1710	15.2610	17.4210	19.6510
1.5410	2.2710	3.2610	4.4710	5.8610	7.4710	9.2510	11.1610	13.1710	15.2610	17.4210	19.6510
1.5410	2.2710	3.2610	4.4710	5.8610	7.4710	9.2510	11.1610	13.1710	15.2610	17.4210	19.6510
1.5410	2.2710	3.2610	4.4710	5.8610	7.4710	9.2510	11.1610	13.1710	15.2610	17.4210	19.6510

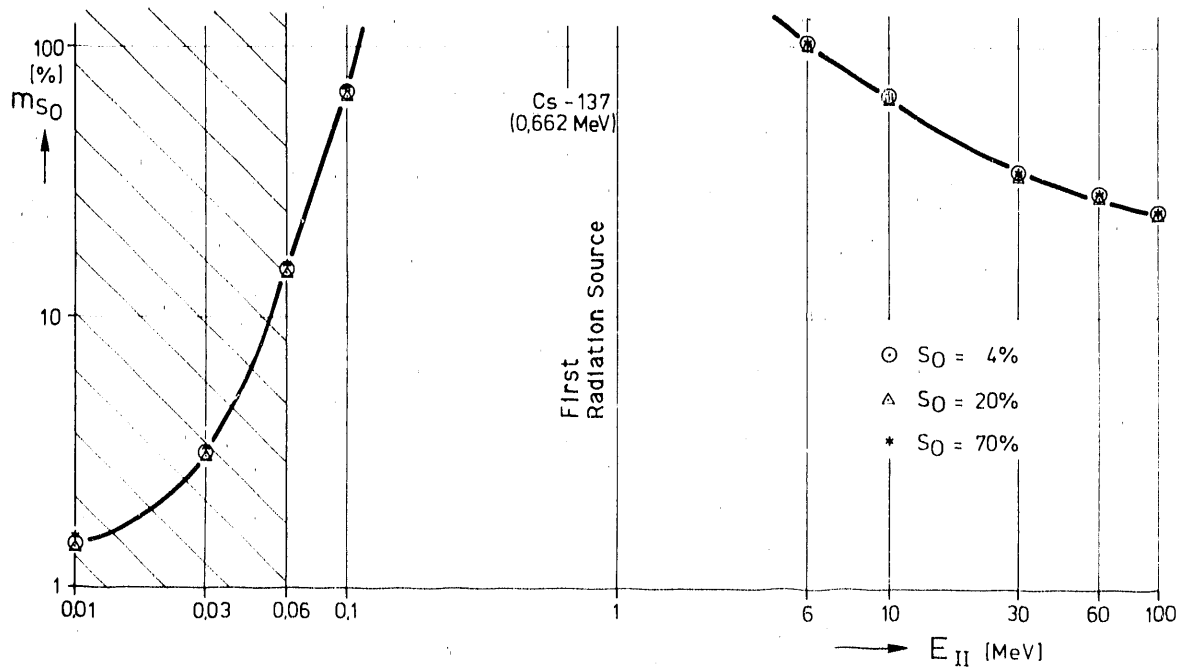


FIGURE 6.17. $m_{S_0} = m_{S_0}(E_{II}S_0)$

close to equal. The difference between the ratios of the mass attenuation coefficient of water to that of oil at the two assumed radiation energies of 0.66 MeV and 0.06 MeV is too small. The proposal described in Section 6.3 to develop an oil saturation measurement method can only yield satisfactory results by enlarging the difference between the ratios of the mass attenuation coefficients at the two radiation energies of 0.66 MeV and 0.06 MeV.

Figure 6.8 shows that at 0.66 MeV (the energy of the first radiation source, Cs-137), the mass attenuation coefficients for elements with low atomic numbers or for their compounds (such as water or oil), differ only slightly from the mass attenuation coefficients of elements with higher atomic numbers (such as lead). On the other hand, at energies below 0.10 MeV (the energy range of the second radiation source) a much larger difference is seen between the mass attenuation coefficients of low atomic number elements and their compounds and the mass attenuation coefficients of higher atomic number elements. In Section 6.4.1, this larger difference is explained as being a

result of the photoabsorption being a third to fifth power function of the atomic number of the attenuating matter.

From these observations, it was concluded that the problem of low measurement accuracy might be solved by adding an element with a higher atomic number to either the water or oil, forming a stable compound. Assuming that this stable compound could be found, a further constraint was that the radiation source should possess an energy that lies as little as possible above the K-shell boundary energy of the higher atomic number element. To test whether adding a high atomic number element would provide a sufficiently large difference between the ratios of the mass attenuation coefficients to attain the required oil saturation measurement accuracy of $\pm 2\%$ of the pore volume, another analysis of the standard error of the observation was performed. To be practical, a compound substituted for either the oil or the water must have chemical and physical characteristics (such as viscosity, density, interfacial tension, and contact angle) that do not fundamentally alter the propagation process, at the required concentration of the higher atomic number element. In addition, the element with the higher atomic number should remain in the compound and not diffuse out.

From a chemical standpoint, it is clear that only a petroleum derivative can form a stable compound with an element of higher atomic number. Because engine fuel generally contains lead, one can conclude that no systematic difficulties stand in the way of producing a hydrocarbon-lead compound. Thus, for the new analysis of the standard error of an observation, lead was chosen to represent an element with a higher atomic number that would be used to dope the petroleum derivative.

Before more closely evaluating the most satisfactory combination of doping element and second radiation source, we should determine the order of magnitude of the required element concentration in the petroleum derivative necessary to determine the oil saturation within $\pm 2\%$, according to the second equation in Equation (6.15).

The mass attenuation coefficient of a hydrocarbon-lead compound (designated KWB) can be determined according to Equation (6.30) by knowing the weight fraction, g_j , of each component, and by using the mass attenuation

coefficients for oil and lead shown in Figure 6.8. To calculate the standard error of an oil-lead compound saturation as a function of the energy of the second radiation source, the procedure described in Section 6.5 was repeated for an oil saturation of 4% with three different weight fractions of 1%, 5%, and 10% lead in oil. The results of these calculations are presented in Table 6.7. The graphical representation of these results is shown in Figure 6.18.

Figure 6.9 shows that theoretically the oil saturation can be determined within the required accuracy of $\pm 2\%$ of the pore volume. This can be attained by selecting the energy of the second radiation source at about 100 KeV when the weight fraction in the hydrocarbon-lead compound is about 3%.

To experimentally confirm these theoretical estimates, the experiment shown schematically in Figure 6.19 was performed. A mixture of either lead naphenate, lead oleate, or lead octoate with a light petroleum derivative was considered as the hydrocarbon-lead compound. These alternatives to lead tetra-ethyl or -methyl, commonly added to engine fuel, were considered because lead tetra-ethyl or -methyl decompose in contact with water and are also toxic. In the selection of the lead compound, toxicity considerations were decisive, especially regarding the highest possible lead concentration. Thus, lead octoate, with 38% lead weight fraction and a density of 1.46 g/cm^3 was the most suitable hydrocarbon-lead compound. The metal content is expressed as a constant weight fraction of the organic compound because the volumes occupied by each separate element in a compound are not known.

For this confirmation experiment, a hydrocarbon-lead compound was prepared to yield a 4% lead weight fraction. The K-boundary of lead lies at 88.001 KeV (Strominger et al. 1958 or Figure 6.6). Table 6.3 lists the radio-nuclide Eu-155 as one of two isotopes with a gamma radiation energy peak of slightly more than 88 KeV. In this experiment, the customary commercially available isotopes Cd-109 or Tm-170 could not be used as radiation sources because their respective gamma radiation energy peaks of 87 KeV and 84 KeV lie below the 88 KeV of the K-boundary of lead. To efficiently use one of these isotopes, a doping element other than lead, one with a lower atomic number and consequently a lower K-boundary, would have to be used instead. The

TABLE 6.7. Standard Error of a 4% Hydrocarbon-Lead Compound Saturation with 1%, 5%, or 10% Lead Concentration as a Function of the Energy of the Second Radiation Source, Given Cs-137 as the First Radiation Source

a) Determination of the Mass Attenuation Coefficients for the Carbon-Hydrogen-Lead Compound According to Equation (6.30)

E _I =E _{Cs-137} =0,662MeV						
		Lead Concentration		1%	5%	10%
		Weight Fraction of Oil		0,99	0,95	0,90
		Weight Fraction of Lead		0,01	0,05	0,10
E MeV	$\frac{\mu_W}{\rho_W}$	$\frac{\mu_O}{\rho_O}$	$\frac{\mu_{Pb}}{\rho_{Pb}}$	$\frac{\mu_{KWB}}{\rho_{KWB}}$	$\frac{\mu_{KWB}}{\rho_{KWB}}$	$\frac{\mu_{KWB}}{\rho_{KWB}}$
100	0,0166	0,0136	0,0939	0,0144	0,0176	0,0216
60	0,0161	0,0136	0,0843	0,0143	0,0171	0,0207
30	0,0166	0,0146	0,0697	0,0152	0,0174	0,0201
10	0,0219	0,0214	0,0489	0,0217	0,0228	0,0242
6	0,0275	0,0277	0,0436	0,0279	0,0285	0,0293
E _I	0,0858	0,0891	0,104	0,0893	0,0899	0,0906
0,1	0,171	0,175	5,47	0,2280	0,4398	0,7045
0,06	0,204	0,198	3,55	0,2315	0,3656	0,5332
0,03	0,370	0,269	23,5	0,5013	1,4306	2,5921
0,01	5,31	1,981	84,6	2,8072	6,1120	10,2429

c) Compilation of the Standard Error

E _I =E _{Cs-137} =0,662MeV							
S _{KWB} =0,04=4%; S _W =0,76=76%; S _L =0,20=20%							
m _n =±4·10 ⁻³ ; m _B =±10 ⁻² ; m _{ρ_{KWB}} =±5·10 ⁻³ ; m _J =±316,2; m _{J_{II}} =±334,0							
(Calculation of the μ/ρ-values; see the following subtable b)							
E MeV	m($\frac{\mu_W}{\rho_W}$)	m($\frac{\mu_{KWB}}{\rho_{KWB}}$)	m _{J_{II}}	m($\frac{\mu_{KWB}}{\rho_{KWB}}$)	m _{J_{II}}	m($\frac{\mu_{KWB}}{\rho_{KWB}}$)	m _{J_{II}}
		Lead conc. = 1%		Lead conc. = 5%		Lead conc. = 10%	
100	4,30·10 ⁻⁴	6,45·10 ⁻⁴	329,9	6,69·10 ⁻⁴	330,0	6,97·10 ⁻⁴	330,1
60	4,31·10 ⁻⁴	6,45·10 ⁻⁴	329,5	6,66·10 ⁻⁴	329,6	6,81·10 ⁻⁴	329,7
30	4,30·10 ⁻⁴	6,51·10 ⁻⁴	329,9	6,67·10 ⁻⁴	330,0	6,87·10 ⁻⁴	330,1
10	4,25·10 ⁻⁴	6,97·10 ⁻⁴	334,5	7,05·10 ⁻⁴	334,5	7,14·10 ⁻⁴	334,6
6	4,21·10 ⁻⁴	7,39·10 ⁻⁴	339,3	7,43·10 ⁻⁴	339,3	7,48·10 ⁻⁴	339,4
E _I	3,89·10 ⁻⁴	5,52·10 ⁻⁴		5,53·10 ⁻⁴		5,54·10 ⁻⁴	
0,1	3,93·10 ⁻⁴	1,61·10 ⁻³	493,0	2,20·10 ⁻³	504,6	2,78·10 ⁻³	519,5
0,06	4,06·10 ⁻⁴	1,62·10 ⁻³	534,8	2,01·10 ⁻³	542,7	2,42·10 ⁻³	552,8
0,03	5,23·10 ⁻⁴	2,35·10 ⁻³	827,4	3,98·10 ⁻³	916,2	5,41·10 ⁻³	1040,6
0,01	5,95·10 ⁻³	5,59·10 ⁻³	1,93·10 ⁸	8,61·10 ⁻³	2,78·10 ⁸	1,16·10 ⁻²	4,37·10 ⁸

TABLE 6.7. (contd)

b) Compilation of the Original Values

E _I =E _{Cs-137} =0,662MeV		n=0,43		B=15cm		ρ _{KWB} =0,85gr/cm ³		J=10 ⁵	
				S _{KWB} =0,04=4%		S _W =0,76=76%		S _L =0,20=20%	
EII	($\frac{\mu_W}{\rho_W}$)	($\frac{\mu_{KWB}}{\rho_{KWB}}$)	J _T	K	{ }	N	Z		
MeV	cm ² /gr								
J _T =10 ⁵ ·e ⁿ ·B{($\frac{\mu}{\rho}$) _W ·S _W ·ρ _W +($\frac{\mu}{\rho}$) _{KWB} ·S _{KWB} ·ρ _{KWB} }									
Lead concentration = 1%									
100	0,0166	0,0144	1,09·10 ⁵	7,05·10 ⁻³	-1,92·10 ⁻¹	-1,35·10 ⁻³	-5,38·10 ⁻⁵		
60	0,0161	0,0143	1,09·10 ⁵	7,00·10 ⁻³	-1,65·10 ⁻¹	-1,15·10 ⁻³	-4,61·10 ⁻⁵		
30	0,0166	0,0152	1,09·10 ⁵	7,41·10 ⁻³	-1,35·10 ⁻¹	-1,00·10 ⁻³	-3,97·10 ⁻⁵		
10	0,0219	0,0217	1,12·10 ⁵	1,06·10 ⁻²	-4,96·10 ⁻²	-5,26·10 ⁻⁴	-2,12·10 ⁻⁵		
6	0,0275	0,0279	1,15·10 ⁵	1,36·10 ⁻²	-2,63·10 ⁻²	-3,59·10 ⁻⁴	-1,41·10 ⁻⁵		
E _I	0,0858	0,0893	1,55·10 ⁵						
0,1	0,171	0,228	2,43·10 ⁵	1,12·10 ⁻¹	+2,11·10 ⁻¹	+2,35·10 ⁻²	+9,40·10 ⁻⁴		
0,06	0,204	0,232	2,86·10 ⁵	1,13·10 ⁻¹	+7,97·10 ⁻²	+9,02·10 ⁻³	+3,61·10 ⁻⁴		
0,03	0,370	0,501	6,85·10 ⁵	2,45·10 ⁻¹	+2,23·10 ⁻¹	+5,46·10 ⁻²	+2,19·10 ⁻³		
0,01	5,31	2,807	3,73·10 ¹⁶	1,37·10 ⁰	-9,31·10 ⁻¹	-1,28·10 ⁰	-5,11·10 ⁻²		
Lead concentration = 5%									
100	0,0166	0,0176	1,09·10 ⁵	8,68·10 ⁻³	+1,20·10 ⁻²	+1,04·10 ⁻⁴	+3,89·10 ⁻⁶		
60	0,0161	0,0171	1,09·10 ⁵	8,44·10 ⁻³	+1,48·10 ⁻²	+1,25·10 ⁻⁴	+4,73·10 ⁻⁶		
30	0,0166	0,0174	1,09·10 ⁵	8,55·10 ⁻³	-2,08·10 ⁻³	-1,77·10 ⁻⁵	-8,34·10 ⁻⁷		
10	0,0219	0,0228	1,12·10 ⁵	1,12·10 ⁻²	-7,16·10 ⁻³	-8,03·10 ⁻⁵	-3,35·10 ⁻⁶		
6	0,0275	0,0285	1,15·10 ⁵	1,40·10 ⁻²	-1,07·10 ⁻²	-1,50·10 ⁻⁴	-5,67·10 ⁻⁶		
E _I	0,0858	0,0899	1,55·10 ⁵						
0,1	0,171	0,440	2,55·10 ⁵	2,17·10 ⁻¹	+5,66·10 ⁻¹	+1,23·10 ⁻¹	+4,90·10 ⁻³		
0,06	0,204	0,366	2,95·10 ⁵	1,80·10 ⁻¹	+3,96·10 ⁻¹	+2,14·10 ⁻²	+2,86·10 ⁻³		
0,03	0,370	1,431	6,39·10 ⁵	2,65·10 ⁻¹	+6,96·10 ⁻¹	+4,90·10 ⁻¹	+1,96·10 ⁻²		
0,01	5,31	6,112	7,70·10 ¹⁶	3,01·10 ⁰	+8,56·10 ⁻²	+2,58·10 ⁻¹	+1,03·10 ⁻²		
Lead concentration = 10%									
100	0,0166	0,0216	1,09·10 ⁵	1,07·10 ⁻²	1,79·10 ⁻¹	1,92·10 ⁻³	7,67·10 ⁻⁵		
60	0,0161	0,0207	1,09·10 ⁵	1,03·10 ⁻²	1,68·10 ⁻¹	1,72·10 ⁻³	6,91·10 ⁻⁵		
30	0,0166	0,0201	1,09·10 ⁵	1,00·10 ⁻²	1,21·10 ⁻¹	1,21·10 ⁻³	4,83·10 ⁻⁵		
10	0,0219	0,0242	1,12·10 ⁵	1,20·10 ⁻²	3,97·10 ⁻²	4,77·10 ⁻⁴	1,99·10 ⁻⁴		
6	0,0275	0,0293	1,15·10 ⁵	1,45·10 ⁻²	7,69·10 ⁻³	1,12·10 ⁻⁴	4,60·10 ⁻⁶		
E _I	0,0858	0,0906	1,55·10 ⁵						
0,1	0,171	0,705	2,70·10 ⁵	3,50·10 ⁻¹	7,04·10 ⁻¹	2,46·10 ⁻¹	9,85·10 ⁻³		
0,06	0,204	0,533	3,06·10 ⁵	2,65·10 ⁻¹	5,64·10 ⁻¹	1,49·10 ⁻¹	5,97·10 ⁻³		
0,03	0,370	2,592	1,08·10 ⁶	1,29·10 ⁰	8,04·10 ⁻¹	1,03·10 ⁰	4,14·10 ⁻²		
0,01	5,31	10,243	1,91·10 ¹⁷	5,09·10 ⁰	4,28·10 ⁻¹	2,18·10 ⁰	8,21·10 ⁻²		

TABLE 6.7. (contd)

d) Calculation of the Standard Error of the Experimentally Determined Mass Attenuation Coefficients

E II MeV	$\left(\frac{\mu}{\rho}\right)$	$\left(\frac{-1}{(D \cdot \rho \cdot J)}\right)^2 \cdot m_p^2$	$\left(\frac{1}{(D \cdot \rho \cdot J)}\right)^2 \cdot m_p^2$	$\left(\frac{-10 \left(\frac{J}{J_1}\right)}{(0.2 \cdot 6)}\right)^2 \cdot m_p^2$	$\left(\frac{-10 \left(\frac{J}{J_1}\right)}{(0 \cdot \rho^2)}\right)^2 \cdot m_p^2$	$m_p \left(\frac{\mu}{\rho}\right) = \sqrt{\Sigma}$
Water						
100	0,0166	$1,00 \cdot 10^{-7}$	$8,47 \cdot 10^{-8}$	$6,89 \cdot 10^{-11}$	$2,76 \cdot 10^{-10}$	$4,30 \cdot 10^{-4}$
60	0,0161	"	$8,51 \cdot 10^{-8}$	$6,48 \cdot 10^{-11}$	$2,59 \cdot 10^{-10}$	$4,31 \cdot 10^{-4}$
30	0,0166	"	$8,47 \cdot 10^{-8}$	$6,89 \cdot 10^{-11}$	$2,76 \cdot 10^{-10}$	$4,30 \cdot 10^{-4}$
10	0,0219	"	$8,03 \cdot 10^{-8}$	$1,20 \cdot 10^{-10}$	$4,80 \cdot 10^{-10}$	$4,25 \cdot 10^{-4}$
6	0,0275	"	$7,60 \cdot 10^{-8}$	$1,89 \cdot 10^{-10}$	$7,56 \cdot 10^{-10}$	$4,21 \cdot 10^{-4}$
EI	0,0858	"	$4,24 \cdot 10^{-8}$	$1,84 \cdot 10^{-9}$	$7,35 \cdot 10^{-9}$	$3,89 \cdot 10^{-4}$
0,1	0,171	"	$1,81 \cdot 10^{-8}$	$7,31 \cdot 10^{-9}$	$2,92 \cdot 10^{-8}$	$3,93 \cdot 10^{-4}$
0,06	0,204	"	$1,30 \cdot 10^{-8}$	$1,04 \cdot 10^{-8}$	$4,16 \cdot 10^{-8}$	$4,06 \cdot 10^{-4}$
0,03	0,379	"	$2,47 \cdot 10^{-9}$	$3,42 \cdot 10^{-8}$	$1,37 \cdot 10^{-7}$	$5,23 \cdot 10^{-4}$
0,01	5,31	"	$8,69 \cdot 10^{-11}$	$7,5 \cdot 10^{-6}$	$2,82 \cdot 10^{-5}$	$5,95 \cdot 10^{-3}$
Carbon - Hydrogen - Lead Compound (KWB)						
Lead concentration = 1%						
100	0,0144	$1,38 \cdot 10^{-7}$	$1,22 \cdot 10^{-7}$	$3,75 \cdot 10^{-11}$	$1,53 \cdot 10^{-7}$	$6,46 \cdot 10^{-4}$
60	0,0143	"	$1,23 \cdot 10^{-7}$	$3,70 \cdot 10^{-11}$	$1,52 \cdot 10^{-7}$	$6,45 \cdot 10^{-4}$
30	0,0152	"	$1,22 \cdot 10^{-7}$	$4,15 \cdot 10^{-11}$	$1,60 \cdot 10^{-7}$	$6,51 \cdot 10^{-4}$
10	0,0217	"	$1,15 \cdot 10^{-7}$	$8,49 \cdot 10^{-11}$	$2,30 \cdot 10^{-7}$	$6,92 \cdot 10^{-4}$
6	0,0279	"	$1,09 \cdot 10^{-7}$	$1,40 \cdot 10^{-10}$	$2,95 \cdot 10^{-7}$	$7,39 \cdot 10^{-4}$
EI	0,0893	"	$6,48 \cdot 10^{-8}$	$1,99 \cdot 10^{-9}$	$9,92 \cdot 10^{-8}$	$5,52 \cdot 10^{-4}$
0,1	0,228	"	$1,99 \cdot 10^{-8}$	$9,39 \cdot 10^{-9}$	$2,41 \cdot 10^{-5}$	$1,61 \cdot 10^{-3}$
0,06	0,232	"	$1,93 \cdot 10^{-8}$	$9,68 \cdot 10^{-9}$	$2,45 \cdot 10^{-5}$	$1,62 \cdot 10^{-3}$
0,03	0,501	"	$1,95 \cdot 10^{-9}$	$4,54 \cdot 10^{-8}$	$5,31 \cdot 10^{-5}$	$2,35 \cdot 10^{-3}$
0,01	2,807	"	$6,00 \cdot 10^{-18}$	$1,42 \cdot 10^{-6}$	$2,97 \cdot 10^{-5}$	$5,59 \cdot 10^{-3}$
Lead concentration = 5%						
100	0,0126	$1,38 \cdot 10^{-7}$	$1,19 \cdot 10^{-7}$	$7,76 \cdot 10^{-11}$	$1,87 \cdot 10^{-7}$	$6,69 \cdot 10^{-4}$
60	0,0171	"	$1,20 \cdot 10^{-7}$	$7,34 \cdot 10^{-11}$	$1,81 \cdot 10^{-7}$	$6,60 \cdot 10^{-4}$
30	0,0174	"	$1,18 \cdot 10^{-7}$	$7,53 \cdot 10^{-11}$	$1,84 \cdot 10^{-7}$	$6,62 \cdot 10^{-4}$
10	0,0278	"	$1,14 \cdot 10^{-7}$	$1,30 \cdot 10^{-10}$	$2,41 \cdot 10^{-7}$	$7,05 \cdot 10^{-4}$
6	0,0285	"	$1,09 \cdot 10^{-7}$	$2,03 \cdot 10^{-10}$	$3,02 \cdot 10^{-7}$	$7,41 \cdot 10^{-4}$
EI	0,0898	"	$6,45 \cdot 10^{-8}$	$2,02 \cdot 10^{-9}$	$1,01 \cdot 10^{-7}$	$5,53 \cdot 10^{-4}$
0,1	0,440	"	$3,39 \cdot 10^{-9}$	$4,64 \cdot 10^{-8}$	$4,66 \cdot 10^{-5}$	$2,70 \cdot 10^{-3}$
0,06	0,366	"	$6,19 \cdot 10^{-9}$	$3,34 \cdot 10^{-8}$	$3,87 \cdot 10^{-5}$	$2,01 \cdot 10^{-3}$
0,03	1,431	"	$2,25 \cdot 10^{-13}$	$5,12 \cdot 10^{-7}$	$1,51 \cdot 10^{-5}$	$3,98 \cdot 10^{-3}$
0,01	6,112	"	$3,29 \cdot 10^{-30}$	$9,34 \cdot 10^{-6}$	$6,47 \cdot 10^{-5}$	$8,11 \cdot 10^{-3}$
Lead concentration = 10%						
100	0,0216	$1,38 \cdot 10^{-7}$	$1,15 \cdot 10^{-7}$	$1,17 \cdot 10^{-10}$	$2,29 \cdot 10^{-7}$	$6,92 \cdot 10^{-4}$
60	0,0207	"	$1,16 \cdot 10^{-7}$	$1,07 \cdot 10^{-10}$	$2,19 \cdot 10^{-7}$	$6,91 \cdot 10^{-4}$
30	0,0201	"	$1,17 \cdot 10^{-7}$	$1,01 \cdot 10^{-10}$	$2,13 \cdot 10^{-7}$	$6,82 \cdot 10^{-4}$
10	0,0242	"	$1,13 \cdot 10^{-7}$	$1,46 \cdot 10^{-10}$	$2,56 \cdot 10^{-7}$	$7,14 \cdot 10^{-4}$
6	0,0293	"	$1,08 \cdot 10^{-7}$	$2,14 \cdot 10^{-10}$	$3,10 \cdot 10^{-7}$	$7,48 \cdot 10^{-4}$
EI	0,0905	"	$6,41 \cdot 10^{-8}$	$2,05 \cdot 10^{-9}$	$1,02 \cdot 10^{-7}$	$5,54 \cdot 10^{-4}$
0,1	0,705	"	$3,47 \cdot 10^{-10}$	$1,24 \cdot 10^{-7}$	$7,46 \cdot 10^{-6}$	$2,76 \cdot 10^{-3}$
0,06	0,533	"	$1,49 \cdot 10^{-9}$	$7,11 \cdot 10^{-8}$	$5,65 \cdot 10^{-6}$	$2,42 \cdot 10^{-3}$
0,03	2,592	"	$3,74 \cdot 10^{-17}$	$1,68 \cdot 10^{-6}$	$2,74 \cdot 10^{-5}$	$5,41 \cdot 10^{-3}$
0,01	10,243	"	$2,14 \cdot 10^{-45}$	$2,62 \cdot 10^{-5}$	$1,08 \cdot 10^{-4}$	$1,16 \cdot 10^{-2}$

TABLE 6.7. (contd)

e) Calculation of the Partial Derivatives

E _I = E _{Cs} - 13.7 = 0,662 MeV					S _{KWB} = 0,04 = 4%		S _W = 0,76 = 76%		S _L = 0,20 = 20%	
$\frac{\partial S_{KWB}}{\partial n} = -9,30 \cdot 10^{-2}$			$\frac{\partial S_{KWB}}{\partial B} = -2,67 \cdot 10^{-3}$			$\frac{\partial S_{KWB}}{\partial \rho_{KWB}} = -4,71 \cdot 10^{-2}$				
E _{II} MeV	$\frac{\partial S_{KWB}}{(\frac{\mu W}{\rho W})_I}$	$\frac{\partial S_{KWB}}{(\frac{\mu W}{\rho W})_{II}}$	$\frac{\partial S_{KWB}}{(\frac{\mu_{KWB}}{\rho_{KWB}})_I}$	$\frac{\partial S_{KWB}}{(\frac{\mu_{KWB}}{\rho_{KWB}})_{II}}$	$\frac{\partial S_{KWB}}{\partial J_I}$	$\frac{\partial S_{KWB}}{\partial J_{II}}$	$\frac{\partial S_{KWB}}{\partial J_{TI}}$	$\frac{\partial S_{KWB}}{\partial J_{TII}}$		
Lead concentration = 1%										
100	-6,02 · 10 ¹	+3,11 · 10 ²	-2,34 · 10 ⁰	+1,45 · 10 ¹	-1,23 · 10 ⁻⁴	-6,35 · 10 ⁻⁴	+7,91 · 10 ⁻⁵	-5,63 · 10 ⁻⁴		
60	-6,85 · 10 ¹	+3,65 · 10 ²	-2,72 · 10 ⁰	+1,70 · 10 ¹	-1,40 · 10 ⁻⁴	-7,44 · 10 ⁻⁴	+9,00 · 10 ⁻⁵	-6,86 · 10 ⁻⁴		
30	-8,14 · 10 ¹	+4,20 · 10 ²	-3,32 · 10 ⁰	+1,96 · 10 ¹	-1,66 · 10 ⁻⁴	-8,58 · 10 ⁻⁴	+1,07 · 10 ⁻⁴	-7,88 · 10 ⁻⁴		
10	-2,04 · 10 ²	+7,99 · 10 ²	-9,04 · 10 ⁰	+3,72 · 10 ¹	-4,16 · 10 ⁻⁴	-1,63 · 10 ⁻³	+2,68 · 10 ⁻⁴	-1,46 · 10 ⁻³		
6	-3,76 · 10 ²	+1,17 · 10 ³	-1,70 · 10 ¹	+5,46 · 10 ¹	-7,67 · 10 ⁻⁴	-2,39 · 10 ⁻³	+4,94 · 10 ⁻⁴	-2,08 · 10 ⁻³		
0,1	+3,57 · 10 ¹	-1,79 · 10 ¹	+2,13 · 10 ⁰	-6,33 · 10 ⁻¹	+7,28 · 10 ⁻⁵	+3,65 · 10 ⁻⁵	-4,69 · 10 ⁻⁵	+1,50 · 10 ⁻⁵		
0,06	+1,11 · 10 ²	-4,66 · 10 ¹	+5,63 · 10 ⁰	-2,17 · 10 ⁰	+2,26 · 10 ⁻⁴	+9,50 · 10 ⁻⁵	-1,46 · 10 ⁻⁴	+3,32 · 10 ⁻⁵		
0,03	+3,32 · 10 ¹	-7,69 · 10 ⁰	+2,01 · 10 ⁰	-3,58 · 10 ⁻¹	+6,77 · 10 ⁻⁵	+1,57 · 10 ⁻⁵	-4,36 · 10 ⁻⁵	+2,29 · 10 ⁻⁶		
0,01	-2,04 · 10 ¹	+3,29 · 10 ⁻¹	-4,82 · 10 ⁻¹	+1,53 · 10 ⁻²	-4,15 · 10 ⁻⁵	-6,71 · 10 ⁻⁷	+2,68 · 10 ⁻⁵	-1,80 · 10 ⁻¹⁸		
Lead concentration = 5%										
100	+7,79 · 10 ²	-4,02 · 10 ³	+3,70 · 10 ¹	-1,89 · 10 ²	+1,53 · 10 ⁻³	+6,21 · 10 ⁻³	-1,02 · 10 ⁻³	+7,54 · 10 ⁻³		
60	+6,31 · 10 ²	-3,36 · 10 ³	+3,00 · 10 ¹	-1,57 · 10 ²	+1,29 · 10 ⁻³	+6,85 · 10 ⁻³	-8,29 · 10 ⁻⁴	+6,31 · 10 ⁻³		
30	-4,93 · 10 ³	+2,37 · 10 ⁴	-2,15 · 10 ²	+1,11 · 10 ³	-9,38 · 10 ⁻³	-4,83 · 10 ⁻²	+6,03 · 10 ⁻³	-4,44 · 10 ⁻²		
10	-1,34 · 10 ³	+5,23 · 10 ³	-6,22 · 10 ¹	+2,45 · 10 ²	-2,73 · 10 ⁻³	-1,07 · 10 ⁻²	+1,76 · 10 ⁻³	-9,54 · 10 ⁻³		
6	-9,01 · 10 ²	+2,81 · 10 ³	-4,18 · 10 ¹	+1,32 · 10 ²	-1,84 · 10 ⁻³	-5,73 · 10 ⁻³	+1,18 · 10 ⁻³	-4,98 · 10 ⁻³		
0,1	+6,84 · 10 ⁰	-3,43 · 10 ⁰	+7,87 · 10 ⁻¹	-1,61 · 10 ⁻¹	+1,40 · 10 ⁻⁵	+7,00 · 10 ⁻⁶	-8,99 · 10 ⁻⁶	+2,75 · 10 ⁻⁶		
0,06	+1,48 · 10 ¹	-5,69 · 10 ⁰	+1,12 · 10 ⁰	-2,76 · 10 ⁻¹	+2,86 · 10 ⁻⁵	+1,20 · 10 ⁻⁵	-1,84 · 10 ⁻⁵	+4,08 · 10 ⁻⁶		
0,03	+3,70 · 10 ⁰	-8,57 · 10 ⁻¹	+6,40 · 10 ⁻¹	-4,02 · 10 ⁻²	+7,55 · 10 ⁻⁶	+1,75 · 10 ⁻⁶	-4,86 · 10 ⁻⁶	+2,05 · 10 ⁻⁷		
0,01	+1,01 · 10 ²	-1,63 · 10 ⁰	+5,20 · 10 ⁰	-7,64 · 10 ⁻²	+2,06 · 10 ⁻⁴	+3,33 · 10 ⁻⁶	-1,33 · 10 ⁻⁴	+4,32 · 10 ⁻¹⁸		
Lead concentration = 10%										
100	4,23 · 10 ¹	-2,18 · 10 ⁻²	2,47 · 10 ⁰	1,03 · 10 ¹	8,63 · 10 ⁻⁵	4,46 · 10 ⁻⁴	5,55 · 10 ⁻⁵	4,09 · 10 ⁻⁴		
60	4,59 · 10 ¹	-2,44 · 10 ⁻²	2,63 · 10 ⁰	1,15 · 10 ¹	9,35 · 10 ⁻⁵	4,99 · 10 ⁻⁴	6,02 · 10 ⁻⁵	4,56 · 10 ⁻⁴		
30	6,73 · 10 ¹	-3,47 · 10 ⁻²	3,65 · 10 ⁰	1,54 · 10 ¹	1,37 · 10 ⁻⁴	7,09 · 10 ⁻⁴	8,84 · 10 ⁻⁵	6,51 · 10 ⁻⁴		
10	2,25 · 10 ²	-9,82 · 10 ⁻²	1,11 · 10 ¹	4,17 · 10 ¹	4,59 · 10 ⁻⁴	1,80 · 10 ⁻³	2,96 · 10 ⁻⁴	1,61 · 10 ⁻³		
6	1,21 · 10 ³	-3,76 · 10 ⁻³	5,75 · 10 ¹	1,78 · 10 ²	2,46 · 10 ⁻³	7,67 · 10 ⁻³	1,58 · 10 ⁻³	6,66 · 10 ⁻³		
0,1	3,40 · 10 ⁰	-1,71 · 10 ⁰	6,27 · 10 ⁻¹	8,07 · 10 ⁻²	6,94 · 10 ⁻⁶	3,43 · 10 ⁻⁶	4,47 · 10 ⁻⁶	1,29 · 10 ⁻⁶		
0,06	6,70 · 10 ⁰	-2,81 · 10 ⁰	7,83 · 10 ⁻¹	1,33 · 10 ⁻¹	1,37 · 10 ⁻⁵	5,74 · 10 ⁻⁶	8,80 · 10 ⁻⁶	1,88 · 10 ⁻⁶		
0,03	1,75 · 10 ⁰	-4,06 · 10 ⁻¹	5,49 · 10 ⁻¹	1,92 · 10 ⁻²	3,58 · 10 ⁻⁶	8,29 · 10 ⁻⁷	2,30 · 10 ⁻⁶	7,65 · 10 ⁻⁸		
0,01	1,20 · 10 ¹	-1,93 · 10 ⁻¹	1,03 · 10 ⁰	9,12 · 10 ⁻³	2,44 · 10 ⁻⁵	3,94 · 10 ⁻⁷	1,57 · 10 ⁻⁵	2,07 · 10 ⁻¹⁹		

TABLE 6.7. (contd)

f) Products of the Squared Derivatives and the Variances, Yielding the Standard Error of the Oil (Doped with Lead) Saturation Measurement m_{SO}

$EI = ECs = 137 = 0.662MeV$		$SKWB = 0.04 = 4\%$		$SW = 0.76 = 76\%$		$SL = 0.20 = 20\%$		
$(\frac{2SKWB}{8c})^2 \cdot m_{SO}^2 = 1.55 \cdot 10^{-7}$		$(\frac{2SKWB}{8c})^2 \cdot m_{SO}^2 = 7.11 \cdot 10^{-10}$		$(\frac{2SKWB}{8c})^2 \cdot m_{SO}^2 = 6.54 \cdot 10^{-8}$		$(\frac{2SKWB}{8c})^2 \cdot m_{SO}^2 = 6.54 \cdot 10^{-8}$		
$EI = ECs$ $YE = 3/2 \cdot X$	$\frac{2SKWB}{8c}$ $\frac{2SKWB}{8c}$	$\frac{2SKWB}{8c}$ $\frac{2SKWB}{8c}$	$\frac{2SKWB}{8c}$ $\frac{2SKWB}{8c}$	$\frac{2SKWB}{8c}$ $\frac{2SKWB}{8c}$	$\frac{2SKWB}{8c}$ $\frac{2SKWB}{8c}$	$\frac{2SKWB}{8c}$ $\frac{2SKWB}{8c}$	$\frac{2SKWB}{8c}$ $\frac{2SKWB}{8c}$	
Lead concentration = 1%								
100	5.50·10 ⁻⁴	1.79·10 ⁻²	1.65·10 ⁻⁶	6.74·10 ⁻⁵	1.51·10 ⁻³	14.03·10 ⁻³	3.70·10 ⁻²	3.14·10 ⁻¹
50	7.12·10 ⁻⁴	2.27·10 ⁻²	2.26·10 ⁻⁶	1.20·10 ⁻⁴	1.95·10 ⁻³	5.54·10 ⁻³	5.11·10 ⁻²	3.66·10 ⁻¹
30	1.00·10 ⁻³	3.27·10 ⁻²	3.35·10 ⁻⁶	1.52·10 ⁻⁴	2.73·10 ⁻³	7.58·10 ⁻³	6.76·10 ⁻²	4.84·10 ⁻¹
10	6.52·10 ⁻³	1.76·10 ⁻¹	2.49·10 ⁻⁵	6.74·10 ⁻⁴	1.23·10 ⁻²	2.66·10 ⁻²	2.36·10 ⁻¹	6.09·10 ⁻¹
5	2.14·10 ⁻²	2.43·10 ⁻¹	6.62·10 ⁻⁵	1.53·10 ⁻³	3.66·10 ⁻²	5.71·10 ⁻²	4.95·10 ⁻¹	1.29·10 ⁰
0.1	1.93·10 ⁻⁴	4.95·10 ⁻³	1.38·10 ⁻⁶	1.79·10 ⁻⁶	3.93·10 ⁻⁴	1.53·10 ⁻³	5.48·10 ⁻⁵	3.51·10 ⁻²
0.05	1.56·10 ⁻³	3.55·10 ⁻²	9.63·10 ⁻⁶	1.23·10 ⁻⁵	5.11·10 ⁻³	8.03·10 ⁻³	3.16·10 ⁻⁴	1.09·10 ⁻¹
0.03	1.67·10 ⁻⁴	1.62·10 ⁻³	1.23·10 ⁻⁶	7.06·10 ⁻⁷	4.59·10 ⁻⁴	2.46·10 ⁻³	3.60·10 ⁻⁶	3.11·10 ⁻²
0.01	6.28·10 ⁻⁵	3.82·10 ⁻⁶	7.00·10 ⁻⁶	7.33·10 ⁻⁹	1.72·10 ⁻⁴	14.49·10 ⁻³	1.21·10 ⁻¹⁹	1.87·10 ⁻²
Lead concentration = 5%								
100	9.19·10 ⁻²	2.99·10 ⁰	4.15·10 ⁻⁴	1.59·10 ⁻²	3.21·10 ⁻¹	6.73·10 ⁰	6.13·10 ⁰	4.05·10 ⁰
50	6.03·10 ⁻²	2.09·10 ⁰	2.75·10 ⁻⁴	1.10·10 ⁻²	1.66·10 ⁻¹	4.70·10 ⁰	4.32·10 ⁰	3.52·10 ⁰
30	3.19·10 ⁰	1.04·10 ²	1.50·10 ⁻²	5.49·10 ⁻¹	6.73·10 ⁰	2.34·10 ²	2.15·10 ²	2.39·10 ¹
10	2.71·10 ⁻¹	4.86·10 ⁰	1.18·10 ⁻³	2.99·10 ⁻²	3.43·10 ⁻¹	1.11·10 ⁰	1.02·10 ¹	5.89·10 ⁰
5	1.23·10 ⁻¹	1.40·10 ⁰	5.31·10 ⁻⁴	1.58·10 ⁻²	1.39·10 ⁻¹	5.26·10 ⁻¹	2.55·10 ⁰	2.67·10 ⁰
0.1	7.10·10 ⁻⁶	1.30·10 ⁻⁶	1.89·10 ⁻⁷	1.35·10 ⁻⁷	1.39·10 ⁻⁶	1.90·10 ⁻⁶	1.92·10 ⁻⁶	6.64·10 ⁻⁵
0.05	2.96·10 ⁻⁶	5.21·10 ⁻⁶	9.64·10 ⁻⁷	3.03·10 ⁻⁷	3.28·10 ⁻⁶	3.49·10 ⁻⁶	4.96·10 ⁻⁶	1.38·10 ⁻²
0.03	2.07·10 ⁻⁶	2.01·10 ⁻⁶	1.25·10 ⁻⁷	2.55·10 ⁻⁶	2.73·10 ⁻⁶	3.33·10 ⁻⁶	3.61·10 ⁻⁶	3.31·10 ⁻³
0.01	1.55·10 ⁻⁶	9.40·10 ⁻⁶	6.23·10 ⁻⁶	4.55·10 ⁻⁷	4.43·10 ⁻⁶	1.11·10 ⁻⁵	1.44·10 ⁻¹⁶	9.29·10 ⁻²
Lead concentration = 10%								
100	2.71·10 ⁻¹	6.63·10 ⁻³	1.56·10 ⁻⁵	5.16·10 ⁻⁵	0.43·10 ⁻¹	1.95·10 ⁻³	1.62·10 ⁻²	2.20·10 ⁻¹
50	3.19·10 ⁻⁴	1.11·10 ⁻³	2.13·10 ⁻⁶	9.35·10 ⁻⁶	9.73·10 ⁻³	2.49·10 ⁻³	2.26·10 ⁻²	2.46·10 ⁻¹
30	6.66·10 ⁻⁴	2.23·10 ⁻³	4.08·10 ⁻⁶	1.27·10 ⁻⁴	1.19·10 ⁻³	5.03·10 ⁻³	4.61·10 ⁻²	3.50·10 ⁻¹
10	7.69·10 ⁻³	1.41·10 ⁻¹	3.79·10 ⁻⁵	5.99·10 ⁻⁴	2.11·10 ⁻²	1.22·10 ⁻¹	2.66·10 ⁻¹	6.93·10 ⁻¹
5	2.20·10 ⁻¹	2.50·10 ⁰	1.01·10 ⁻⁵	1.77·10 ⁻²	6.01·10 ⁻¹	3.66·10 ⁰	5.11·10 ⁰	3.64·10 ⁰
0.1	1.76·10 ⁻⁶	4.51·10 ⁻⁶	1.21·10 ⁻⁷	5.05·10 ⁻⁶	4.10·10 ⁻⁶	1.21·10 ⁻⁵	4.45·10 ⁻⁷	3.49·10 ⁻³
0.05	6.60·10 ⁻⁶	1.91·10 ⁻⁶	1.68·10 ⁻⁷	1.04·10 ⁻⁷	1.55·10 ⁻⁶	3.53·10 ⁻⁶	1.06·10 ⁻⁶	6.61·10 ⁻³
0.03	4.66·10 ⁻⁶	1.31·10 ⁻⁶	9.26·10 ⁻⁸	1.06·10 ⁻⁶	1.28·10 ⁻⁶	5.86·10 ⁻⁶	6.34·10 ⁻⁹	1.73·10 ⁻³
0.01	2.17·10 ⁻⁶	1.15·10 ⁻⁶	9.26·10 ⁻⁷	1.12·10 ⁻⁶	5.94·10 ⁻⁶	1.54·10 ⁻⁵	8.13·10 ⁻²¹	1.10·10 ⁻²

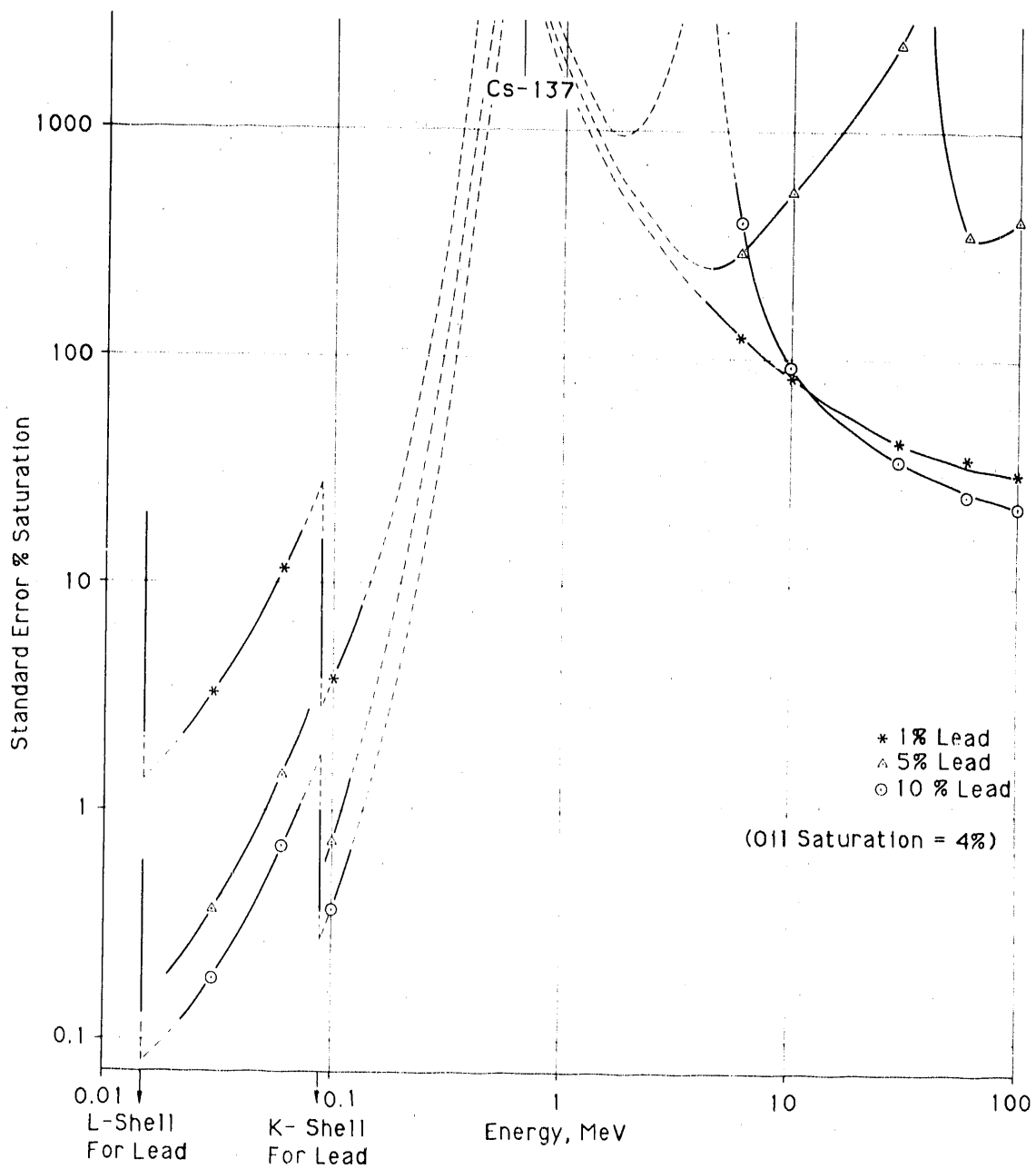


FIGURE 6.18. Standard Error of 4% Oil Saturation, S_{KWB} , as a Function of the Energy of the Second Radiation Source, E_{II} , with Lead Weight Fractions, g_{pb} , of 1%, 5%, or 10% in the Oil

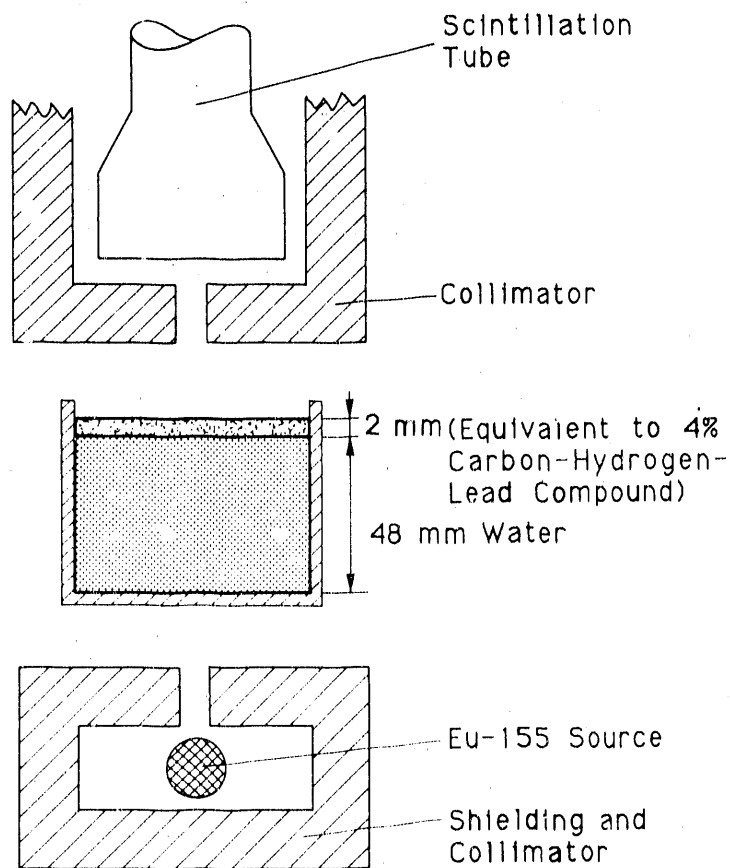


FIGURE 6.19. Schematic Diagram of the Equipment Used to Experimentally Verify Theoretical Standard Error Estimates Shown in Figure 6.18

difficulties in producing a stable chemical compound from some other doping element and a petroleum derivative appeared greater than having the likely commercially unavailable Eu-155 produced for us. After several attempts, the Swiss Federal Institute for Reactor Research (E.I.R) at Würenlingen was finally able to produce a Eu-155 source with an activity of about 3 mCi.

Because preliminary experiments proved that making the attenuation measurement with or without sand had no influence on the determination of the accuracy of the individual fluid saturation measurements, sand was not used in this experiment. Thus, the impulse count rate, within a counting window around the peak 102-KeV energy of Europium, measured across the empty vessel was interpreted as J_0 in the equation for the determination of S_0 (the second equation of Equation [6.15]). The measured impulse counts were

$$\begin{aligned}
 J_{TCs} &= 109'384 & J_{TEu} &= 107'996 \\
 J_{Cs} &= 72'971 & J_{Eu} &= 45'718
 \end{aligned}
 \tag{6.85}$$

If these measured impulse counts and the experimentally determined parameter values summarized in Table 6.8 are inserted into the equation for calculating S_0 , then S_0 is equal to 4.06%.

The deviation of the measured saturation value of 4.06% from the theoretical value of 4% is 0.06% and thus lies far below the tolerated deviation of 2% saturation. The density and viscosity of the hydrocarbon-lead compound corresponded to the densities and viscosities of petroleum derivatives. The equal capillary rise of a fuel and the hydrocarbon-lead compound in a quartz-glass capillary showed that their surface tensions and contact angles cannot be very different.

Based on these results, it was concluded that in principal, the addition of a higher atomic number element to a petroleum derivative makes it possible to exactly determine (within $\pm 2\%$ saturation) the water and oil saturations (based on Equation [6.15]) by using two monochromatic gamma radiation sources with energy peaks greater than 60 KeV.

6.7 SELECTION OF Tm-170 AS A SECOND RADIATION SOURCE AND MERCURY AS AN ELEMENT WITH HIGHER ATOMIC NUMBER FOR DOPING THE PETROLEUM DERIVATIVE

By doping the petroleum derivative with an element with a higher atomic number, the requirement that the second radiation source have the lowest possible energy changes to require that the energy of the second radiation source lie just slightly above the K-boundary of the doping element. Because the

TABLE 6.8. Experimental Determination of a 4% Oil Saturation with 4% Lead Content According to Equation (6.15). Cs-137 was the first radiation source and Eu-155 was the second, lower-energy radiation source.

$\left(\frac{\mu_W}{\rho_W}\right)_{Cs}$	$\left(\frac{\mu_W}{\rho_W}\right)_{Eu}$	$\left(\frac{\mu_{KWB}}{\rho_{KWB}}\right)_{Cs}$	$\left(\frac{\mu_{KWB}}{\rho_{KWB}}\right)_{Eu}$	$\ln\left(\frac{J}{J_T}\right)_{Cs}$	$\ln\left(\frac{J}{J_T}\right)_{Eu}$	n	B	ρ_{KWB}	S_0
0,0857	0,171	0,0867	0,476	-0,4048	-0,8596	1	5	0,85	4,06%

energy of the second radiation source must no longer be as low as possible but rather only slightly above the characteristic K-boundary radiation of the doping element, one should now select as high as possible an energy of the second radiation source. The higher the energy of the second radiation source is, the lower the material attenuation. Consequently, it is more likely that the theoretically required activity (based on obtaining the highest impulse count in a 10-sec counting time to minimize the standard error of the measurement) of the second radiation will be producible in practice.

The energy of an element's K-boundary is a function of its atomic number: the larger the atomic number, the higher the energy. The elements with the largest atomic numbers are unstable. Understandably, only stable elements could be considered as doping elements, and of these, bismuth has the largest atomic number. Lead has the second largest atomic number of the stable elements. According to Strominger et al. (1958), the K-boundaries of bismuth and lead are at 90.521 KeV and 88.001 KeV, respectively.

In Section 6.4.3.2, a target activated by an x-ray tube to its characteristic radiation was proposed as a possible second radiation source. By adopting lead, whose K-boundary lies at 88 KeV, as the element for doping the petroleum derivative and using bismuth, whose characteristic K-boundary radiation is 90.5 KeV, as the target element for the x-ray, then the smallest maximum material attenuation, $\sigma_m^{\max} = 7.5 \cdot 10^{-4}$, is achieved (Figure 6.11). Thus, one of the smallest impulse count rates would be required from the second radiation source. Given the further favorable assumption that the target could be placed only 5 cm away from the anode, the calculation of the maximum exiting impulse count rate observed at the detector (Equation [6.58]) was repeated. The result was

$$\text{max. J (x-rays)} = \frac{(20 \cdot 10^{-3})(6,3 \cdot 10^{18})(0,01)^2(3,2 \cdot 10^{-5})(7,5 \cdot 10^{-4})}{(4 \cdot \pi \cdot 5^2)} = 962 \quad (6.86)$$

The calculated maximum exiting impulse count rate of about 10^3 , according to Equation (6.86), still lies one order of magnitude below the stipulated impulse count rate of 10^4 , which is the maximum number of impulses that can be processed in 1 sec by the detector in the scintillation counter. Because of

this inadequacy, adopting a target activated by an x-ray tube to its characteristic radiation as the second radiation source was discarded as an option.

Based on the facts in Section 6.4.3.1, Tm-170 emerged as the only isotope suitable as the second radiation source. Thus, a hydrocarbon compound that includes a doping element with a higher atomic number had to be found that was suitable for use with Tm-170. Because a suitable doping element must have a K-boundary with an energy that lies just below the gamma radiation emitted by the isotope, lead and its hydrocarbon compounds were eliminated because the K-boundary of lead at 88 KeV lies above the Tm-170 energy of 84 KeV. According to Strominger et al. (1958), the elements that have K-boundaries just below 84 KeV are mercury (83.1 KeV), gold (80.7 KeV), and platinum (78.4 KeV). Mercury is the most suitable of the three elements because its K-boundary energy is nearest to 84 KeV and because it can form a stable compound with hydrocarbons. Beilstein (1929), Eichler (1879), Marvel and Calvery (1923), and Gilman and Brown (1929, 1930) present various data on the preparation of hydrocarbon-mercury compounds. An important criterion is that the hydrocarbon-mercury compound be insoluble in water. Dimethyl mercury (C_2H_6Hg), diethyl mercury ($C_4H_{10}Hg$), and dipropyl mercury ($C_6H_{14}Hg$) are relatively insoluble in water. Di-n-octyl mercury ($C_{16}H_{34}Hg$) was designated as insoluble in water.

Under license by Hüls America (Piscataway, New Jersey) to sell mercury fungicides, the Borchers Brothers Company (Goslar, Federal Republic of Germany) had a commercial mercury-hydrocarbon compound, which saved us the effort of preparing our own mercury-hydrocarbon compound. Super-ad-It, the commercial compound, is diphenyl mercuric dodecenyloxy-succinate in an organic solvent. Its mercury content is 10% by weight. To transform the viscosity and density of the Super-Ad-It (which are similar to those of edible vegetable oil) to those of an extra-light fuel oil (the representative petroleum derivative for the two-dimensional propagation experiments with $\rho = 0.85 \text{ g/cm}^3$ and $\mu = 3 \text{ cp}$), the Super-Ad-It was diluted with an extra-light petroleum fraction. This petroleum fraction, which was as clear as water, was a hydrocarbon with a density of 0.74 g/cm^3 , a viscosity below that of water, and a particularly high boiling point of 110 to 140°C , especially for a petroleum derivative. We

were interested in a high boiling point because of the associated relatively low volatility at room temperature, and consequently the reduced danger of combustion and toxicity. By mixing Super-Ad-It and the petroleum fraction on the basis of the desired viscosity, a mixture could be obtained that was more analogous to extra-light fuel oil than to gasoline. This mixture was designated as SAI for short. To confirm that the product of the surface tension and the cosine of the contact angle with respect to quartz was not very different between the SAI and a light petroleum derivative, comparisons of capillary rise in glass capillaries were made. SAI, with similar density and viscosity, was found to have a similar rise in glass capillaries.

6.8 PRODUCTION OF Cs-137 AND Tm-170

To calculate the required activity of the first radiation source, Cs-137, the radiation source can be assumed to be a point source because of the negligible small self absorption, whereby $\sigma_{SA} \sim 1$. The geometric attenuation coefficient, σ_g , is equal to $3.2 \cdot 10^{-5}$ according to Equation (6.35). The maximum material attenuation, σ_m^{\max} , to be expected from the designed experiments given the Cs-137 energy at 662 KeV, can be inferred to be equal to $4.4 \cdot 10^{-2}$ from Figure 6.11. For Cs-137, the probability, p , of the formation of a quantum with the energy of 0.662 MeV per nuclear disintegration is 92% (Rakow 1962, n. 45). Given these values and the specified exiting impulse count rate, J , of 10^4 impulses/sec, the number of nuclear disintegrations per second, A_K , required to be produced by the Cs-137 isotope is calculated as

$$A_K(\text{Cs-137}) = J / (\sigma_m^{\max} \cdot \sigma_g \cdot \sigma_{SA} \cdot p) = 10^4 / (4.4 \cdot 10^{-2} \cdot 3.2 \cdot 10^{-5} \cdot 0.92) \quad (6.87)$$

$$= 7.7 \cdot 10^9 \text{ disintegrations/sec}$$

The conversion of disintegrations per second into Curies (division by $3.7 \cdot 10^{10}$) yields the required activity of the Cs-137 source, $A_{(\text{Cs-137})}$

$$A_{(\text{Cs-137})} = \frac{A_K(\text{Cs-137})}{3.7 \cdot 10^{10}} = 0.2 \text{ Ci} \quad (6.88)$$

Cs-137 sources up to activities of several Curies can be bought commercially in various forms.

The required activity per unit weight of the Tm-170 source, $A^*(\text{Tm-170})$, is determined based on the weight-specific required impulse count rate $J_{\text{prodgef}}^{\text{grE1}}$ (Column XI of Table 6.3) being $3 \cdot 10^{12}$ and p (Column IV) being 0.085, thus

$$A^*(\text{Tm-170}) = \frac{J_{\text{prodgef}}^{\text{grE1}}}{p \cdot 3,7 \cdot 10^{10}} = 954 \cdot (\text{Ci/gr}) \quad (6.89)$$

The weight-specific activity producible by a neutron flux of $5 \cdot 10^{14}$ in 50 days was determined in Equation (6.55) as 1500 Ci/g. By including a production error margin and by considering the short Tm-170 half-life of 127 days, compared to the projected experimental application period of about 1.5 yr, one can see that neither an irradiation time shorter than 50 days nor a neutron flux lower than $5 \cdot 10^4$ could be considered for the production of Tm-170. In practice, this meant that producing the isotope in Würenlingen was excluded; that is, either in the sapphire core with a neutron flux of $3 \cdot 10^{13}$ at the time, or in the diorite core with a neutron flux of $2 \cdot 10^{13}$ at the time. Consequently, we had to produce the isotope in the most powerful reactor in Europe, which at the time was located in Mol, Belgium. This reactor had a neutron flux of $5 \cdot 10^{14}$, and was one of the few reactors that could accommodate the relatively long irradiation time of 50 days.

The possibility of producing the isotope in the United States was rejected on the basis of the relatively short half-life period. Very strict protective shielding requirements are enforced by the airlines, and the transport time by ocean freighter is too long. As it turned out, significantly more protective shielding (and thus higher transportation costs) than was estimated was required to absorb the unexpected higher-energy radiation generated by impurities in the irradiated vial containing the thulium-oxide powder.

The thulium being irradiated had to be as pure as possible because the intense irradiation over a long period could activate the slightest impurities to such an extent to compromise the protective shielding. More important, the radiation generated by the activated impurities would distort the energy spectrum of the collimated measuring beam. The thulium oxide sold by Research

spectrum of the collimated measuring beam. The thulium oxide sold by Research Chemicals, Phoenix, Arizona, was certified to be more pure than the elemental thulium offered by Johnson-Matthew, London, in platelet or wire form. The impurities in the thulium oxide consisted of ytterbium (0.005%), erbium (0.002%), yttrium (0.001%), and calcium, magnesium, and silicon (below 0.001%). On the other hand, elemental thulium was more compact with a density of 9.33 g/cm^3 . Thus, more thulium atoms would be within the area of a collimated beam. The density of the concentrated white thulium-oxide powder was 3.6 g/cm^3 . The weight fraction of thulium in the thulium oxide, g_{Tm} , is determined from the ratio of atomic weight of two thulium atoms to the atomic weight of the thulium oxide as

$$g_{\text{Tm}} = \frac{2 \cdot 169}{2 \cdot 169 + 3 \cdot 16} = 0,88 \quad (6.90)$$

The radiation of the activated oxygen with a half-life of only seconds (see Nuklidkarte 1963) is inconsequential and is not disadvantageous relative to the characteristics of irradiated elemental thulium.

To confirm the previous discussion regarding the preparation and use of Tm-170 as the second radiation source, a test source with an activity of about 1 Ci was prepared at the E.I.R. in Würenlingen. Despite the extreme care exercised during the transfer of the irradiated thulium-oxide powder from its irradiated container into a nonirradiated container, particles of radioactive thulium-oxide powder were dispersed by the slightest air turbulence, resulting in the contamination of the hot cell within which the transfer was performed. Therefore, the E.I.R. declined to undertake a second loading of irradiated thulium-oxide powder. This meant that a container had to be found that could serve as the container both during and after irradiation. This container had to be made of very pure material, with purity standards as high as those for the thulium oxide.

Aluminum or silicon dioxide (glass) are the only commonly available materials that are only relatively weakly activated when irradiated. In previous discussions with radiation experts, pure quartz glass was established as the most satisfactory material for the permanent container. After determining a

method to produce the container from glass and manufacturing a test glass container, the option of glass as the container material was abandoned because glass provided very little protective shielding from the radioactive thulium oxide. Thus, the container had to be made out of the purest aluminum. Very pure aluminum was obtained from the research division of Swiss Aluminum Inc. (Neuhausen-am-Rheinfall) in a superrefined form with impurities of less than 0.001% consisting mainly of iron, silicon, and copper.

Because of radiation-shielding design considerations, we were forced to select an isotope no larger in size than absolutely necessary. Striving for a maximum possible emitted impulse count rate, the physical dimension of the thulium source should be equal to the cross-sectional dimensions of the collimated beam; that is, equal to 0.5 by 2 cm. The source dimension in the y-direction was set equal to $Y_{Tm_2O_3(99.9\%)}$; that is, a distance such that 99.9% of the theoretical activity yielded from an infinite y-dimension was reached. $Y_{Tm_2O_3(99.9\%)}$ is determined from Equation (6.44). The self mass attenuation coefficient of the isotope compound, $(\mu/\rho)_J$, is determined from Equation (6.30) as

$$\left(\frac{\mu}{\rho}\right)_J = \left(\frac{\mu}{\rho}\right)_{Tm} \cdot g_{Tm} + \left(\frac{\mu}{\rho}\right)_O \cdot g_O \quad (6.91)$$

According to Column IX of Table 6.3, the self-mass attenuation coefficient of the element thulium can be set to about $5 \text{ cm}^2/\text{g}$ for the gamma emission energy of 84 KeV. According to Grodstein (1957), the self mass attenuation coefficient for oxygen at 84 KeV is about $0.17 \text{ cm}^2/\text{g}$. With g_{Tm} calculated in Equation (6.90) as 0.88, it follows that $g_O = 0.12$, and thus $(\mu/\rho)_J$ according to Equation (6.91) is

$$\left(\frac{\mu}{\rho}\right)_J = 5 \cdot 0.88 + 0.17 \cdot 0.12 = 4.42 \quad (\text{cm}^2/\text{gr}) \quad (6.92)$$

Because $(1 - n_J) \cdot \rho_J$ represents the unit weight of the isotope, which for thulium oxide was determined as 3.6 g/cm^3 , then according to Equation (6.44), $Y_{Tm_2O_3(99.9\%)}$ is

$$Y_{Tm_2O_3(99.9\%)} = \frac{6.9}{4.42 \cdot 3.6} = 0.43 \text{ cm} \quad (6.93)$$

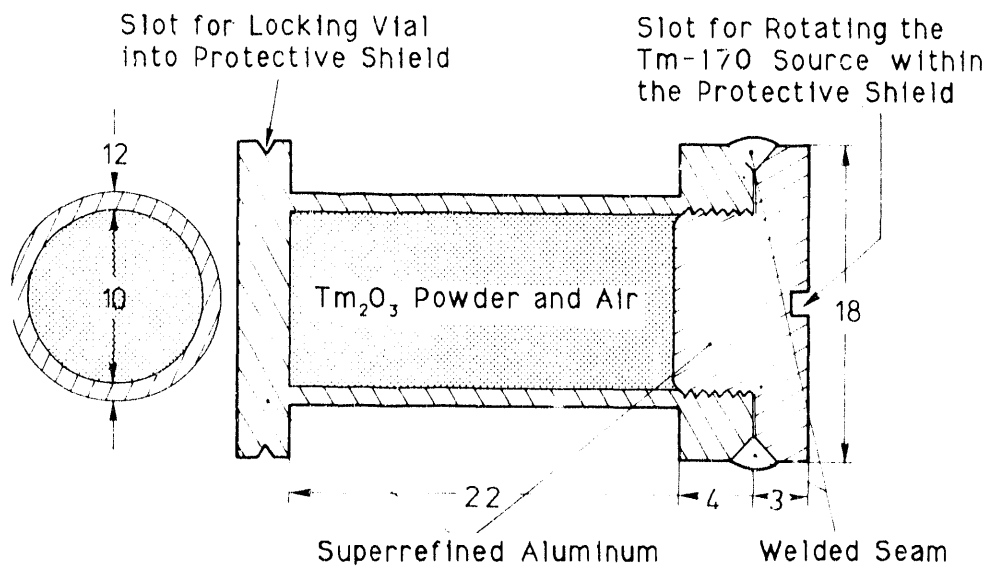
Thus, the minimum dimensions of a thulium source were specified as 0.5 · 2.0 · 0.5 cm.

The design of the superrefined aluminum vial for the Tm-170 source is shown in Figure 6.20. Aluminum of such purity is very soft and poses certain problems in its machining.

The total activity, A_{tot} , produced from a thulium isotope of such dimensions, and with $(1-n_j)\rho_j = 3.6 \text{ g/cm}^3$, $g_{Tm} = 0.88$ (Equation [6.90]), and $A^* = 1500 \text{ Ci/g}$ (Equation [6.55]), equals

$$A_{tot} = V_j(1-n_j)\rho_j \cdot g_{Tm} \cdot A^* = \pi \cdot 0,5^2 \cdot 2,2 \cdot 3,6 \cdot 0,88 \cdot 1500 = 8211 \text{ Ci} \quad (6.94)$$

Because of self absorption, however, the activity emitted from the source, A_{emitt} , will be only a fraction of this total produced activity of 8211 Ci. The desired A_{emitt} was specified to the manufacturer in Mol, Belgium, as 2000 Ci.



Dimensions in mm

FIGURE 6.20. Schematic Diagram of the Tm-170 Source Vial

6.9 Tm-170 SPECTRA

The energy spectrum emitted from Tm-170 as determined by a silicon semiconductor detector is shown in Figure 6.21. An NaI(Tl) scintillation counter is probably easier to handle than a semiconductor detector but has, however, a poorer resolution. This is obvious from the unattenuated Tm-170 energy spectrum shown in Figure 6.22, which was recorded with a NaI(Tl) scintillation photomultiplier. The energy-specific impulse count rate determination was performed with a double-channel, high-frequency impulse analyzer by using 5-KeV-window increments.

In Figure 6.21, the impulse count rate maxima lying between 50 to 60 KeV are a result of electron capture, whose probability for Tm-170 is equal to 0.2% (Amersham Catalog 1974/75). Electron capture is one of the possible types of radioactive decomposition. This type of decomposition results when an electron is captured from its orbit by an activated nucleus that has lost a positron. Just as the Compton scattering is the mutual exchange between

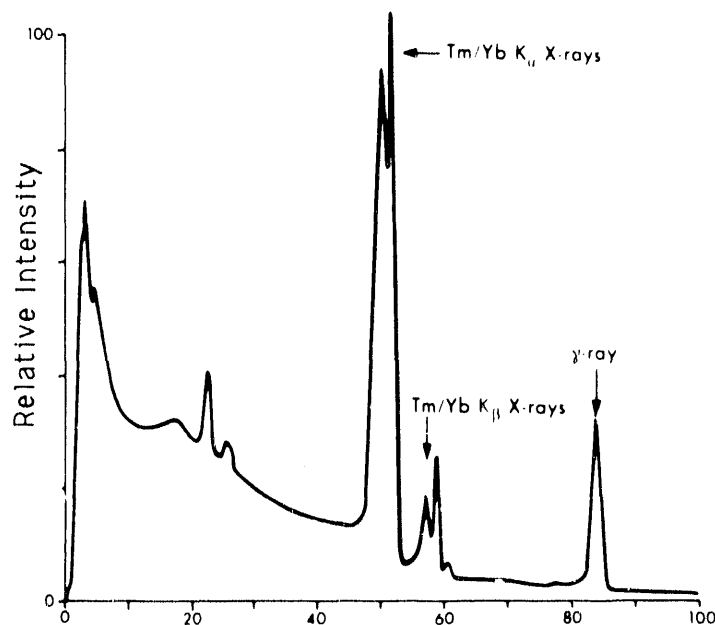


FIGURE 6.21. Unattenuated Tm-170 Energy Spectrum Determined by Using a Silicon Semiconductor Detector (Technical Bulletin 72/6, Radiochemical Center, Amersham Nuclear)

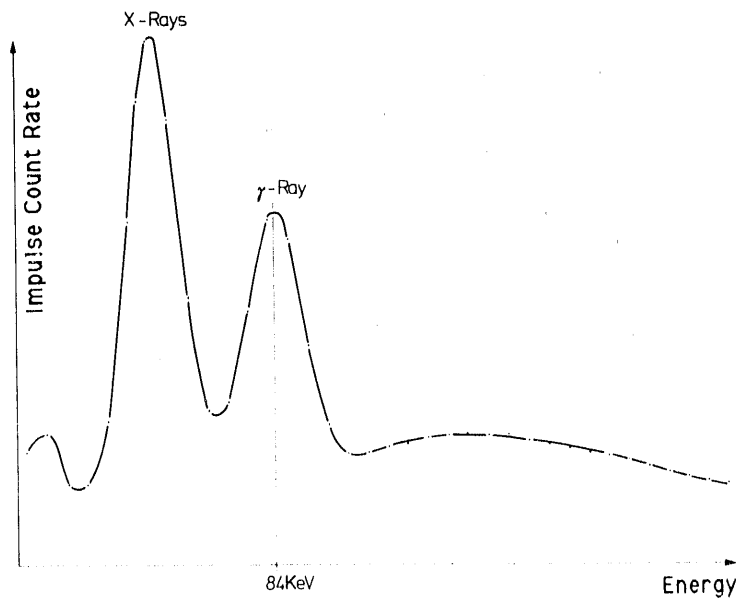


FIGURE 6.22. Unattenuated Tm-170 Energy Spectrum Emitted by the 2000-Ci Source Manufactured at Mol, as Determined by NaI(Tl) Scintillation Counting

radiation and material (i.e., inner conversion), this decomposition event results in the occupation of the vacant electron site by an electron from another shell. In the process, the differential electron shell energy is released as an emission of a characteristic radiation, which, because of the decrease of the atomic number by one caused by the electron capture, is that of the daughter element (Glocker and Macherauch 1965, p. 471) and also as an emission of a so-called Auger electron. The daughter element of thulium is ytterbium.

As mentioned in the conclusion of Section 6.4.3.1, the applicability of Tm-170 as the second radiation source depended on to what extent the deceleration radiation of the 0.97- and 0.88-MeV particle radiation can be diminished by conditioning the emitted spectrum with metal plate filters or to what extent the deceleration spectrum exiting the irradiated material can be described by a mathematical method and then subtracted from the emitted spectrum. To clarify the answer to this important question before the irradiation of the 2000-Ci source in Mol, Belgium, a test source of about 1 Ci of thulium oxide, described in Section 6.8, was commissioned to the E.I.R. in

Würenlingen. The spectra shown in Figure 6.23 were the result of test experiments with the 1-Ci source for various levels of attenuation. The material attenuation coefficients, σ_m , were determined for both lower curves, that is, for attenuation caused by 2.5-cm or 5-cm sand, by using an equation analogous to Equation (6.47). Given a mass attenuation coefficient for sand (SiO_2) of about $0.2 \text{ cm}^2/\text{g}$ (according to Table 6.1), $x_{\text{SiO}_2} = (1-n) \cdot x_{\text{sand}}$; that is, $0.6 \cdot 2.5 \text{ cm} = 1.5 \text{ cm}$, or $0.6 \cdot 5.0 \text{ cm} = 3.0 \text{ cm}$, and finally with $\rho_{\text{SiO}_2} = 2.65 \text{ g/cm}^3$, the result is

$$\begin{aligned} \sigma_m(2,5 \text{ cm}) &= \exp\{-0,2 \cdot 1,5 \cdot 2,65\} = 0,45 \\ \sigma_m(5,0 \text{ cm}) &= \exp\{-0,2 \cdot 3,0 \cdot 2,65\} = 0,20 \end{aligned} \quad (6.95)$$

The area between the unattenuated spectrum and the open circles shown in Figure 6.23 represents the entering impulse count rate J_0 ; the area between the attenuated spectra and the open circles represents the exiting impulse count rates, J . The σ_m values determined in Equation (6.95) are confirmed in Figure 6.23 by calculating J/J_0 ratios from the areas determined with a planimeter, which yielded 0.42 and 0.22 for 2.5 and 5.0 cm of sand, respectively.

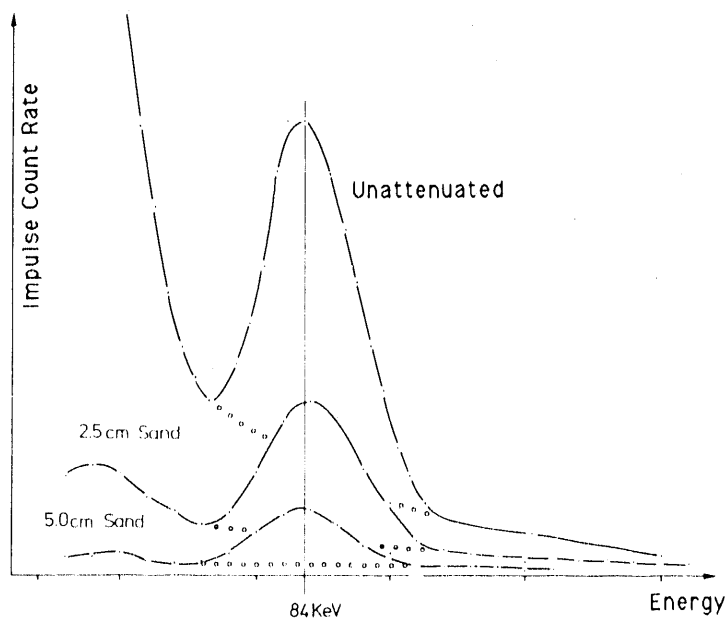


FIGURE 6.23. Tm-170 Spectra Obtained for Various Levels of Attenuation with the 1-Ci Test Source

By comparing the unattenuated 2000-Ci Tm-170 source spectra shown in Figure 6.22 to that for the 1-Ci Tm 170-source in Figure 6.23, it can be seen that the deceleration spectra lying above 84 KeV are not the same. Figure 6.24 shows that the deceleration spectrum associated with the 2000-Ci source was more pronounced, even dominant, with increasing levels of attenuation. To ensure that the undesired deceleration spectrum did not consist mainly of reflected radiation, the specially constructed lead sphere serving as the shielding container for the 2000-Ci source was completely bored out along the axis of the collimated ray. In addition, to prove that the deceleration spectrum was in no way influenced by the lead shield, the source was lifted out of the lead sphere under the necessary safety precautions, and then the spectra shown in Figure 6.24 were measured.

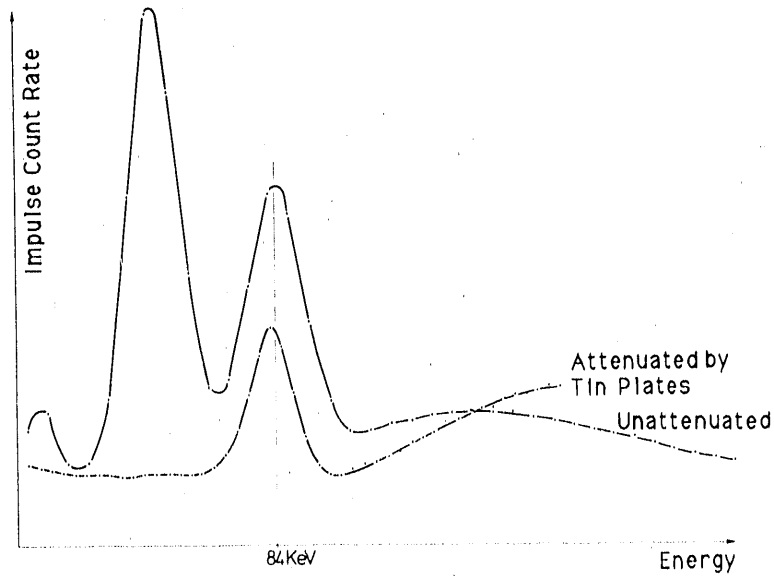
It must be concluded from Figures 6.23 and 6.24 that the disturbing extent of the deceleration spectrum was associated to a much smaller degree with the 1-Ci source compared to the 2000-Ci source. The greater undesired deceleration spectrum undoubtedly stems from the impurities in the super-refined aluminum vial activated during irradiation. Only the 1-Ci Tm-170 source could be feasibly transferred into a nonradioactive vial.

Unloading the isotope from the vial was out of the question because of the potential dispersion of radioactive particles during transfer. Repeating the irradiation of thulium oxide in a new source container was also impossible. Therefore, we had to consider how the undesired deceleration spectrum could be reduced or eliminated.

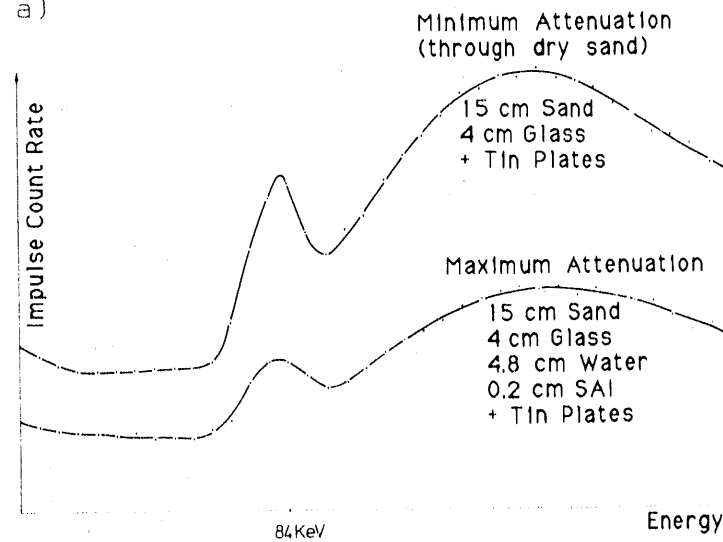
6.10 MEASURES FOR THE ELIMINATION OF THE DECELERATION SPECTRUM

Figure 6.24 shows several spectra obtained from the 2000-Ci source. The disturbing deceleration spectrum is clearly obvious in these spectra. The deceleration spectrum is the undesired spectrum of the scattered, decelerated radiation. The desired spectrum, superimposed on the deceleration spectrum during the impulse counting, is that of unattenuated 84-KeV radiation.

The energy spectra were measured with a NaI(Tl) scintillation tube. Naturally, the ratio of unattenuated 84-KeV radiation to the deceleration radiation could be improved by using radiation detectors with better resolution,



a)



b)

FIGURE 6.24. Unshielded 2000-Ci Tm-170 Spectra a) Unattenuated and with Tin Conditioning Filters and b) with Tin Conditioning Filters and Various Levels of Attenuation by Materials Used in the Experiments

such as a semiconductor detector. However, with a semiconductor detector, the deceleration spectrum within the energy window to detect the unattenuated 84-KeV radiation would not have been disregardably small compared to its integral. Therefore, the considerably greater expense of a semiconductor detector was not considered worth the better resolution.

Knowing that the estimation of the deceleration spectrum could not be abandoned, an attempt was made to simulate the shape of the deceleration spectrum below the 84-KeV radiation by using various mathematical functions. The success of subtracting the deceleration spectrum by using a mathematical function was tested by experimentally measuring the mass attenuation coefficients at 84 KeV of water (representative of compounds or elements with low atomic numbers) and lead (representative of compounds or elements with high atomic numbers). These measured values were then compared with the theoretical mass attenuation coefficients of water and lead at 84 KeV shown in Figure 6.8.

6.10.1 Elimination of the Characteristic Radiation

In an effort to give the spectrum a satisfactory shape for applying a mathematical function to describe the deceleration spectrum; that is, a spectrum without the 84-KeV gamma radiation of Tm-170, we first tried to eliminate the impulse count rate peak between 50 and 60 KeV caused by electron capture.

The desired conditioning of a spectrum within the energy range of soft radiation can be accomplished by filtering with elements whose K-electron-shell boundary lies in the energy range of interest. Thus, by combining various elements into distinct thin layers so that minimal attenuation of the spectrum in the remaining energy range results, especially the 84-KeV radiation, it is possible to distort a spectrum so that it is conditioned into a desired form. Figure 6.24 shows how the undesired characteristic radiation in the Tm-170 spectrum can be filtered out with tin plates.

6.10.2 Mathematical Function to Describe the Deceleration Radiation Spectrum

In principle, the mathematical function should be defined by the smallest number of points needed to adequately describe the shape of the deceleration spectrum. Furthermore, the function should be independent of the attenuation volume of the fluids.

The shape of the deceleration spectrum was assumed to be that of the dashed line in Figure 6.25. Given the further assumption that the dashed line can be represented by a conic section with its apex at point S, and the tangent at S is horizontal, the fit of a conic section only requires the additional point P. To apply the conic section function to correct the impulse

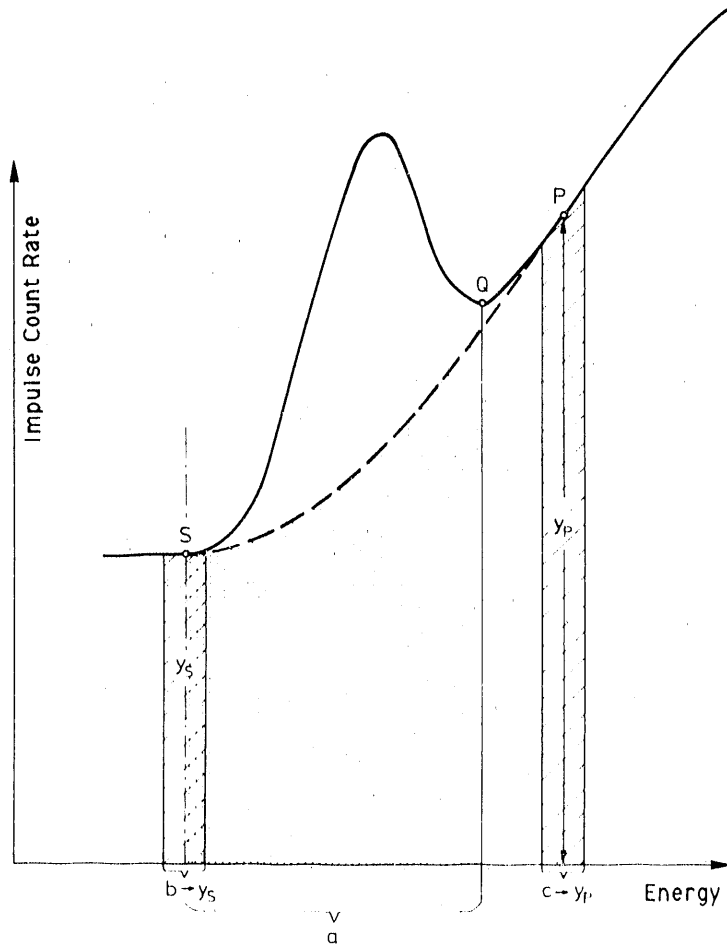


FIGURE 6.25. Use of Conic Section as Mathematical Function to Describe Deceleration Spectrum

count rate measured within the "a" window, the impulse count rate must also be measured within the "b" and "c" windows to determine points S and P of the conic section. By means of these two additional measurements, the shape of the deceleration radiation can be determined analytically, and thus the area under the deceleration radiation spectrum within window "a" can be calculated. If this area under the deceleration radiation spectrum within window "a" is subtracted from the observed spectrum (solid line in Figure 6.25), the impulse count rate of the unattenuated 84-KeV radiation is yielded, which is the impulse count rate of ultimate interest.

The accuracy with which this conic section correction yielded the mass attenuation coefficients of water and lead (a comparison with the theoretical

mass attenuation coefficients shown in Figure 6.8 was the test of the mathematical correction) was shown to be unsatisfactory compared to the tolerated standard error of the mass attenuation coefficients calculated in Table 6.4.

With an exponential function as the mathematical function (shown in Figure 6.26), somewhat improved accuracies could be obtained at only very slight attenuation levels compared to a conic section; generally, however, the accuracies were poorer. Moreover, the determination of the position and orientation of the exponential function, and of the parameter λ in the exponential function requires a larger effort because the slope of tangent "m" must be determined; the tangent line "m" serves as the abscissa for the exponential function. Because the slope of "m" is calculated by using y_{p1} , y_{p2} , and Δx_p , a definite inaccuracy is implied by the relatively small value of Δx_p .

A better approach to fitting the exponential function is illustrated in Figure 6.27. The tangent of the practically linearly ascending deceleration spectrum above 84 KeV intersects y_S , the ordinate passing through point S, at point D. The height of point D is approximately equal to about one third of y_S over the range of possible attenuation levels, m_{max} and m_{min} . This fact has two advantages. First, the slope of tangent "m" can be determined with more certainty. Second, the effort involved with fitting the exponential function can be reduced. This improved determination of the slope of tangent "m" yields a more acceptable accuracy in the determination of the mass attenuation coefficients.

In addition, Figure 6.27 shows that x_S and x_Q are independent of the amount of attenuation. Thus, to symbolize their constancy, they can be written as

$$x_S = x_{S_{max}} = x_{S_{min}} ; \quad x_Q = x_{Q_{max}} = x_{Q_{min}} \quad (6.96)$$

The experimentally determined mass attenuation coefficients that were closest to the theoretical values were calculated by approximating the underlying deceleration spectrum with the Descartes function.

In Figure 6.28, both an X-Y Cartesian coordinate system and an x-y coordinate system are shown. The tangent m^0 has a slope defined by the angle

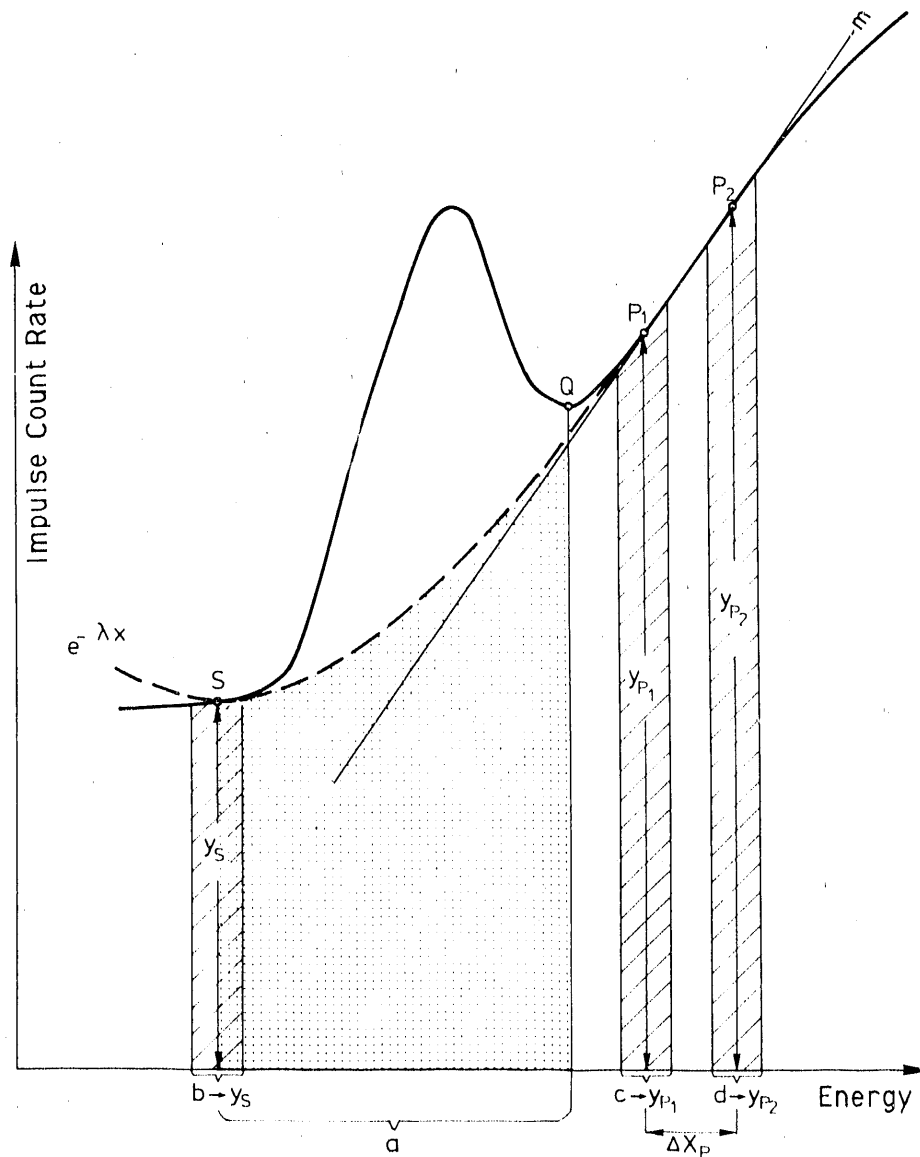


FIGURE 6.26. Use of Exponential Function as Mathematical Function to Describe Deceleration Spectrum Associated with Maximum and Minimum Attenuation

$\pi/4$ relative to the X- and Y-axes. In general, the tangent of the deceleration spectrum, as it ascends, is practically linear and has a slope defined by an arbitrary angle α relative to the abscissa x . Thus, Figure 6.28 represents a refined illustration of the observed spectrum, where the x -axis is rotated

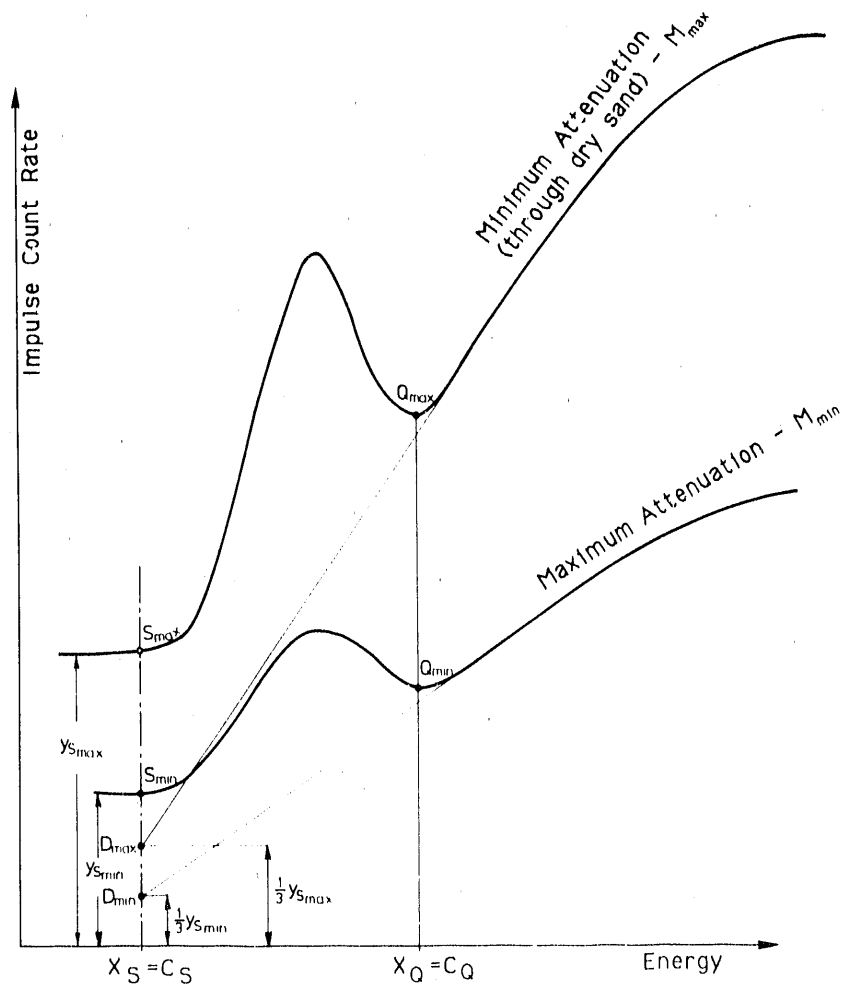


FIGURE 6.27. Plot of Deceleration Spectrum Showing the Tangent, m , Intersecting at the Third Point, D (x_S and x_Q are Constants c_S and c_Q)

such that α equaled 45° , and the X - and Y -axes of the Cartesian system are rotated 90° relative to the x - y coordinate system. The illustration includes the conversion

$$\operatorname{tg} \alpha = \frac{\Delta y}{\Delta x} \rightarrow \operatorname{tg}(\pi/4) = 1 = \frac{\Delta y}{\Delta x^0} \quad (6.97)$$

where x^0 is the rotated x -axis, and tg indicates the tangent function. With $\Delta x^0 = \Delta y = \Delta x \cdot \operatorname{tg} \alpha$, or $x^0 = y = x \cdot \operatorname{tg} \alpha$, the following equation is used to convert from x - y coordinates to X - Y coordinates

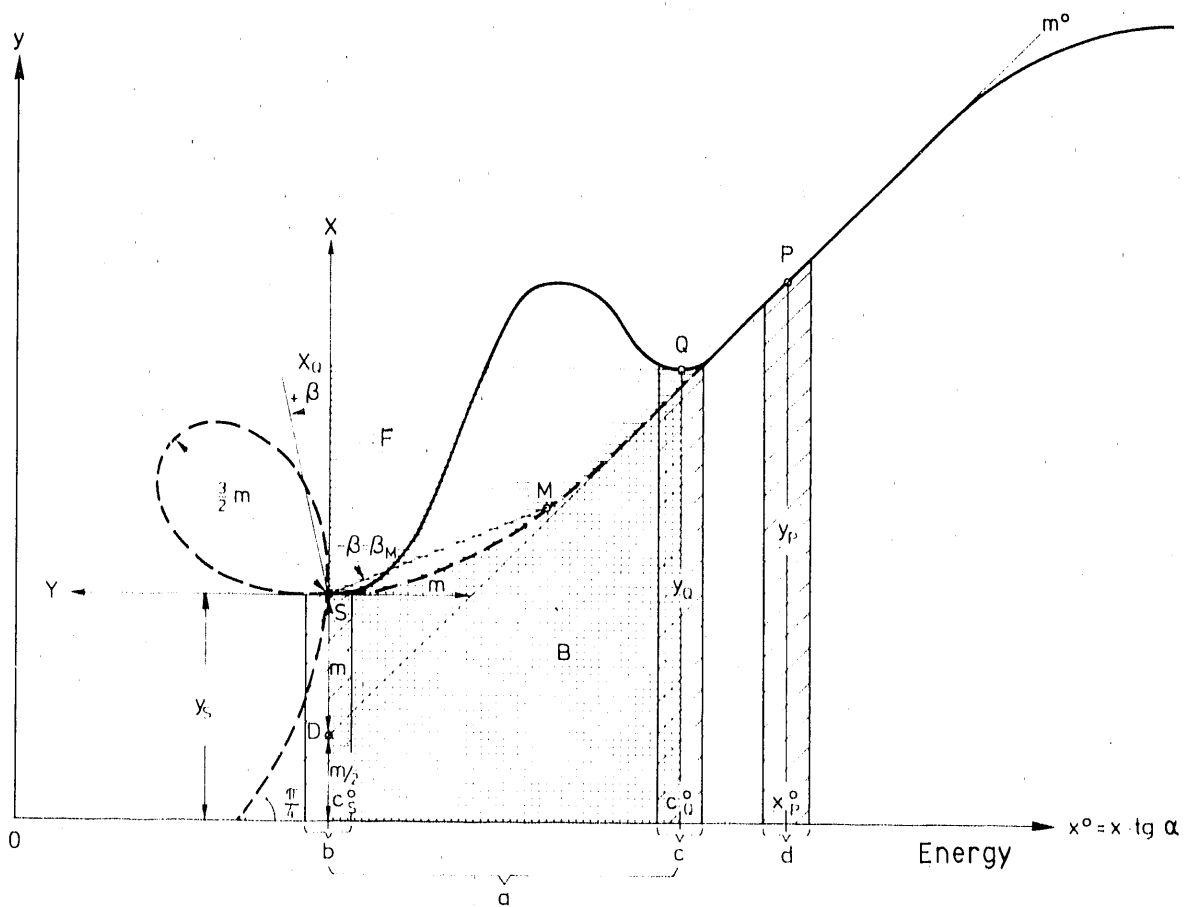


FIGURE 6.28. Use of Descartes Function as Mathematical Function to Describe Deceleration Spectrum

$$X = y - y_0 ; \quad Y = -(x^0 - c_0^0) = -(x - c_0) \operatorname{tg} \alpha \quad (6.98)$$

According to Bronstein and Semendjajew (1968, p. 84), the Descartes function is given in implicit form as

$$X^3 + Y^3 - 3mXY = 0 \quad (6.99)$$

in parameter form as

$$X = \frac{3m \cdot \operatorname{tg} \beta}{1 + \operatorname{tg}^3 \beta} ; \quad Y = \frac{3m \cdot \operatorname{tg}^2 \beta}{1 + \operatorname{tg}^3 \beta}$$

and in polar coordinates as

$$r = \frac{3m \cdot \sin\beta \cdot \cos\beta}{\sin^3\beta + \cos^3\beta}$$

Equation (6.99) must be integrated between $X = 0$ and $X = X_Q$ to determine the area F, shaded with horizontal lines in Figure 6.28. This is then used to calculate area B, shaded with dots, below the deceleration spectrum. Based on the parameter form of Equation (6.99), the integral can be written by substituting t for $\text{tg } \beta$, such that

$$X = \frac{3m \cdot t}{1+t^3} \quad \text{and} \quad \frac{dX}{dt} = \frac{(1+t^3)3m - 3mt \cdot 3t^2}{(1+t^3)^2}$$

then

$$\begin{aligned} F &= \int_0^{X_Q} Y \cdot dX = \int_{\text{tg}(-\pi/2)=-\infty}^{\text{tg}\beta_Q} \frac{3m \cdot t^2}{(1+t^3)} \cdot \frac{3m\{(1+t^3) - 3t^3\}}{(1+t^3)^2} \cdot dt \\ &= 9m^2 \left\{ \int \frac{t^2}{(1+t^3)^2} \cdot dt - 3 \int \frac{t^5}{(1+t^3)^3} \cdot dt \right\} \end{aligned} \quad (6.100)$$

Substituting

$$t^3 = \tau, \quad t = \tau^{\frac{1}{3}}, \quad \frac{dt}{d\tau} = \frac{1}{3} \tau^{-\frac{2}{3}}$$

the integral becomes

$$F = 3m^2 \left\{ \int \frac{1}{(1+\tau)^2} \cdot d\tau - 3 \int \frac{\tau}{(1+\tau)^3} \cdot d\tau \right\} \quad (6.101)$$

After separating the second integral into

$$\int \frac{\tau}{(1+\tau)^3} \cdot d\tau = \int \frac{d\tau}{(1+\tau)^2} - \int \frac{d\tau}{(1+\tau)^3}$$

the result is

$$F = 3m^2 \left\{ 3 \int_{\tau_1}^{\tau_2} \frac{d\tau}{(1+\tau)^3} - 2 \int_{\tau_1}^{\tau_2} \frac{d\tau}{(1+\tau)^2} \right\} \quad (6.102)$$

By substituting $(1 + \tau) = n$, $\tau = n-1$, $d\tau/dn = 1$, it follows from the integration that

$$F = 3m^2 \left\{ -\frac{3}{2} \frac{1}{(1+\tau)^2} \Big|_{\tau_1}^{\tau_2} + c_1 + 2 \frac{1}{(1+\tau)} \Big|_{\tau_1}^{\tau_2} + c_2 \right\} \quad (6.103)$$

and additionally, with $\tau_1 = \text{tg}^3 \beta_0 = -\infty$ and $\tau_2 = \text{tg}^3 \beta_Q$

$$\begin{aligned} F &= 3m^2 \left\{ 2 \left(\frac{1}{(1+\text{tg}^3 \beta_Q)} - \frac{1}{(1-\infty)} \right) - \frac{3}{2} \left(\frac{1}{(1+\text{tg}^3 \beta_Q)^2} - \frac{1}{(1-\infty)^2} + c \right) \right\} \\ &= 3m^2 \left\{ \frac{2}{(1+\text{tg}^3 \beta_Q)} - \frac{3}{2} \left(\frac{1}{(1+\text{tg}^3 \beta_Q)^2} \right) + c \right\} \end{aligned} \quad (6.104)$$

For $\text{tg} \beta_Q = \text{tg}(-\pi/2) = -\infty$, then $F = 0$. Thus, $c = 0$. F is given as

$$F = 3m^2 \left\{ \frac{2}{(1+\text{tg}^3 \beta_Q)} - \frac{3}{2} \frac{1}{(1+\text{tg}^3 \beta_Q)^2} \right\} \quad (6.105)$$

The impulse count rate J of final interest; that is, the impulse count rate of the unattenuated 84-KeV radiation, is now determined based on the impulse count rate J_a measured within window "a"

$$J = J_{a-B} = J_a - \{ (c_Q^0 - c_S^0) y_Q + F \} \quad (6.106)$$

The positive sign in front of F in Equation (6.106) results from the fact that F in Equation (6.105) lies in the fourth quadrant of the X-Y coordinate system and thus has a negative sign. Based on Equation (6.97), Equation (6.106) can be written as a function of the original x-y coordinate system of the measured spectrum

$$J = J_a - \{(c_Q - c_S) \operatorname{tg} \alpha \cdot y_Q + 3m^2 \left(\frac{2}{(1 + \operatorname{tg}^3 \beta_Q)} - \frac{3}{2(1 + \operatorname{tg}^3 \beta_Q)} \right)\} \quad (6.107)$$

With

$$m = \frac{2}{3} \cdot y_S$$

$$\operatorname{tg} \alpha = (y_P - y_S/3) / (x_P - c_S)$$

$$\operatorname{tg} \beta_Q = Y_Q / X_Q = -\operatorname{tg} \alpha \{(c_Q - c_S) / (y_Q - y_S)\} \quad (6.108)$$

the desired unattenuated 84-KeV impulse count rate J in Equation (6.107) can be determined by experimentally obtaining four impulse count rates: J_a , J_S , J_Q , and J_p , within counting windows a, b, c, and d, respectively, shown in Figure 6.28. This determination can be made provided y_i is replaced by J_i/i ; that is, the quotient of the measured impulse count rate J_i divided by the window width, i. The constant values on the abscissa, according to Equation (6.96), were assumed as known. These constants could be taken from the spectra shown in Figure 6.24b, which can be considered as known for each experiment. The term $\operatorname{tg} \beta_Q$ is a negative value according to the above definition. Its range of validity is

$$-\infty \leq \operatorname{tg} \beta_Q < -1 \quad (6.109)$$

The proposed mathematical method to deduct the deceleration spectrum suffered from the fact that, although the experimentally determined mass attenuation coefficients agreed mostly quite well with theoretical values, they occasionally fluctuated arbitrarily and erratically. The error distribution function did not have a static character; it was periodically very different, and consequently we had to acknowledge an inherent system error caused by relying on a mathematical method to compensate for the undesired deceleration

spectrum. This inherent system error was probably caused by electronic instabilities. In turn, these instabilities probably caused the impulse count rates, determined within the narrow windows of the steep portion of the spectrum (e.g., the determination of y_p), to vary sharply. In spite of the fact that electronic instabilities led to the abandonment of the proposed methods to deduct the undesired deceleration spectrum, the various methods and their confirming experiments were documented. Should future improvements in the electronics of scintillation counting systems reduce the electronic instabilities, the mathematical methods could then be used.

6.10.3 Consequences of Unreliable Impulse Count Rate Determinations on Steep Portions of the Deceleration Spectrum

Impulse count rate determinations on steep portions of the deceleration spectrum were deemed unreliable because possible instabilities in the electronics could lead to definite fluctuations in the settings that defined a counting window. The steeper the portion of the spectrum was, then the greater the impulse count rate variation was because of this fluctuation. Therefore, we attempted to flatten the deceleration spectrum to achieve a spectrum that was close to parallel with the abscissa.

The requirement of a deceleration spectrum close to parallel with the abscissa means that the deceleration spectrum must be flattened above 84 KeV. This conditioning can be accomplished by means analogous to the method used to eliminate the characteristic radiation of thulium between 50 and 60 KeV by using tin plates. In this method, discussed in Section 6.10.1, combinations of thin plates of elements, whose K-shell boundaries lie in the energy area where the conditioning is desired, were used as filters. The element combinations, as well as the thicknesses of the separate thin plates, must be selected experimentally in such a way that the total attenuation is minimal. Figure 6.29 shows the conditioning obtained by using only a thin plate and by using a combination of tin, thallium, lead, and bismuth plates. To simplify the determination of the deceleration spectrum to be deducted, and consequently, to reduce the effort to apply the deduction method, the desired conditioning provided by the filter plates should be, if possible, equally high below and above the unattenuated 84-KeV radiation peak. Furthermore, the

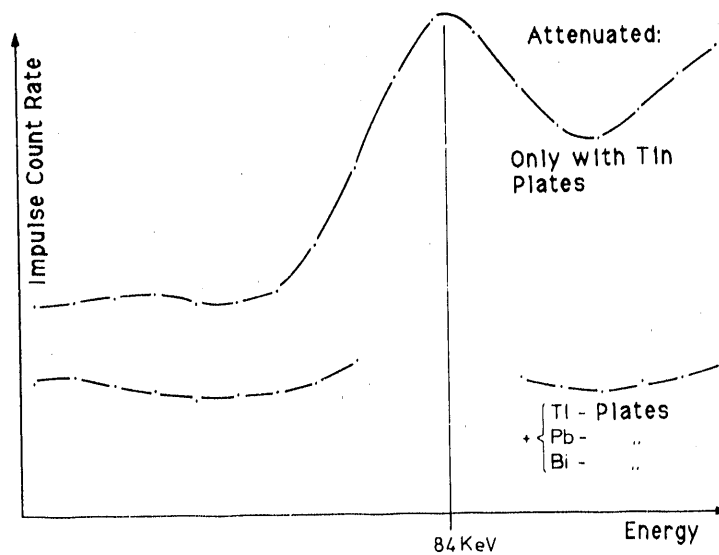


FIGURE 6.29. Flattening of the Deceleration Spectrum Obtained by Using a Zinc Plate and a Combination of Thallium, Lead, and Bismuth Plates

conditioning should be independent of the range of attenuation levels encountered by irradiating the flume.

If the spectrum on both sides of the unattenuated 84-KeV radiation is flattened, the determination of the deceleration spectrum component can be easily simplified by assuming that the deceleration spectrum is horizontal throughout the entire range of energy, as shown in Figure 6.30. Thus, in addition to measuring the impulse count rate J_a within the "a" counting window, only one more separate measurement is necessary--that of determining the constant height, y_i , of the deceleration spectrum within the "a" counting window. Unfortunately when tested experimentally, this method also did not yield a measurement accuracy of $\pm 2\%$ fluid saturation.

6.10.4 Final Observations on the Radiation Attenuation Method Used to Measure Fluid Saturations

Experimentally, it was shown that none of the mathematical or physical methods proposed to correct for the deceleration spectrum, together or separately, could satisfy the required measurement accuracy of $\pm 2\%$ fluid

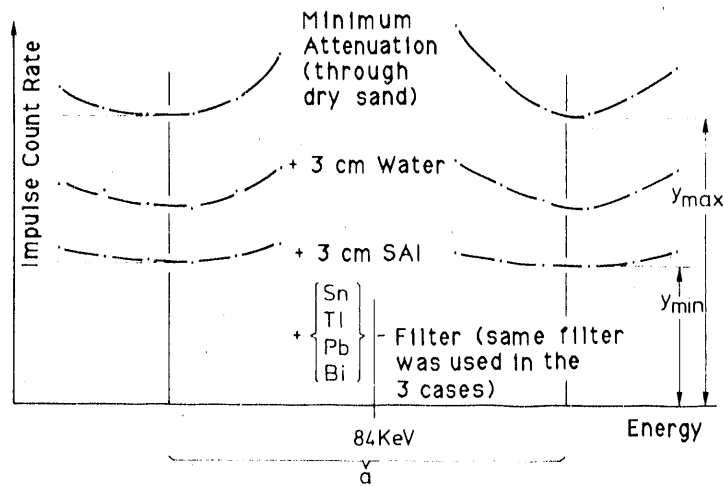


FIGURE 6.30. Flattening of the Deceleration Spectrum Shown to be Independent of Attenuation Levels (Vertical lines signify the experimentally determined fitting points.)

saturation specified in Section 6.2. Therefore, the possibility of determining the saturations of water and oil according to Equation (6.15) had to be abandoned.

The single remaining option for a trouble-free determination of the saturations of water and oil using the gamma radiation attenuation consisted of interpolating unknown saturation values from a nomograph calibrated to known fluid saturation combinations. This nomograph had to be plotted at the beginning of each experiment.

6.11 SEMIGRAPHIC DETERMINATION OF THE FLUID SATURATIONS

The plotting of a nomograph for the semigraphic determination of the fluid saturations began by experimentally determining the thulium impulse count rates for various known attenuation cases, which covered the range of possible combinations of water and oil saturations. Water and oil saturations were specified in centimeters, that is, in irradiation path lengths x_W and x_O , respectively. Next, the measured impulse counts were plotted as a function of the irradiation path length of oil, x_O , in a parametric representation of the irradiation path length of water, x_W , as shown in Figure 6.31. On the basis

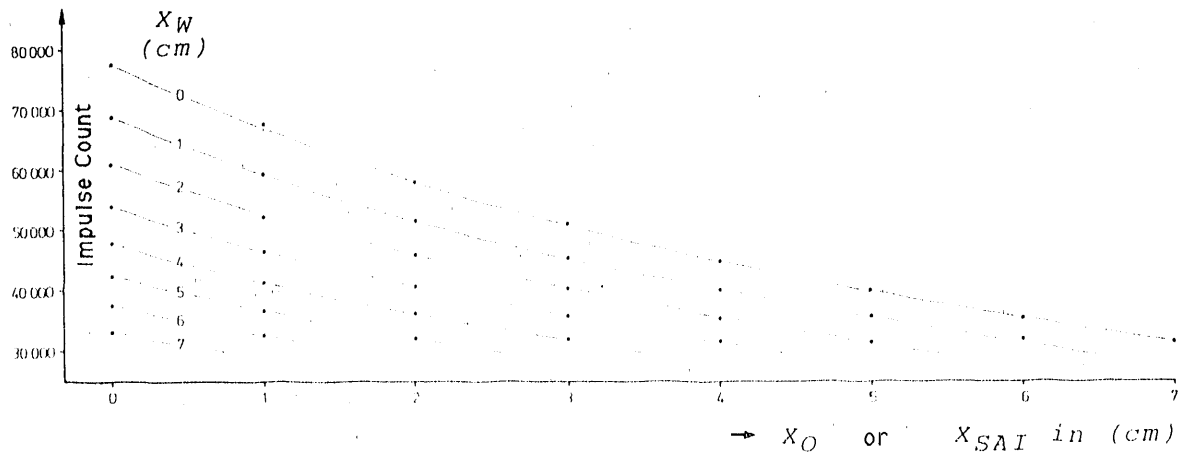


FIGURE 6.31. Auxiliary Diagram for Plotting the Nomograph Used to Determine Fluid Saturations

of this auxiliary diagram, the nomograph was then plotted with x_0 or x_{SAI} as the abscissa and x_W as the ordinate, and the lines of equal impulse counts were plotted (Figure 6.32).

The determination of an unknown water and oil saturation combination was made by means of the specific, experimentally determined cesium and thulium impulse counts and the nomograph in Figure 6.32 as described in the following. From Section 6.3, if Equation (6.10) is inserted into Equation (6.14) and the natural logarithm taken, then the following is yielded to describe, for example, the attenuation of the Cs-137 radiation

$$\ln\left(\frac{J}{J_T}\right)_{Cs} = -\left\{\left(\frac{\mu_W}{\rho_W}\right)_{Cs} \cdot \rho_W \cdot x_W + \left(\frac{\mu_{SAI}}{\rho_{SAI}}\right)_{Cs} \cdot \rho_{SAI} \cdot x_{SAI}\right\} \quad (6.10)$$

The explicit representation of x_W from Equation (6.110) yields

$$\begin{aligned} x_W &= -\frac{\left(\frac{\mu_{SAI}}{\rho_{SAI}}\right)_{Cs} \cdot \rho_{SAI}}{\left(\frac{\mu_W}{\rho_W}\right)_{Cs} \cdot \rho_W} \cdot x_{SAI} - \frac{\ln\left(\frac{J}{J_T}\right)_{Cs}}{\left(\frac{\mu_W}{\rho_W}\right)_{Cs} \cdot \rho_W} \\ &= -C1 \cdot x_{SAI} + C2 \end{aligned} \quad (6.111)$$

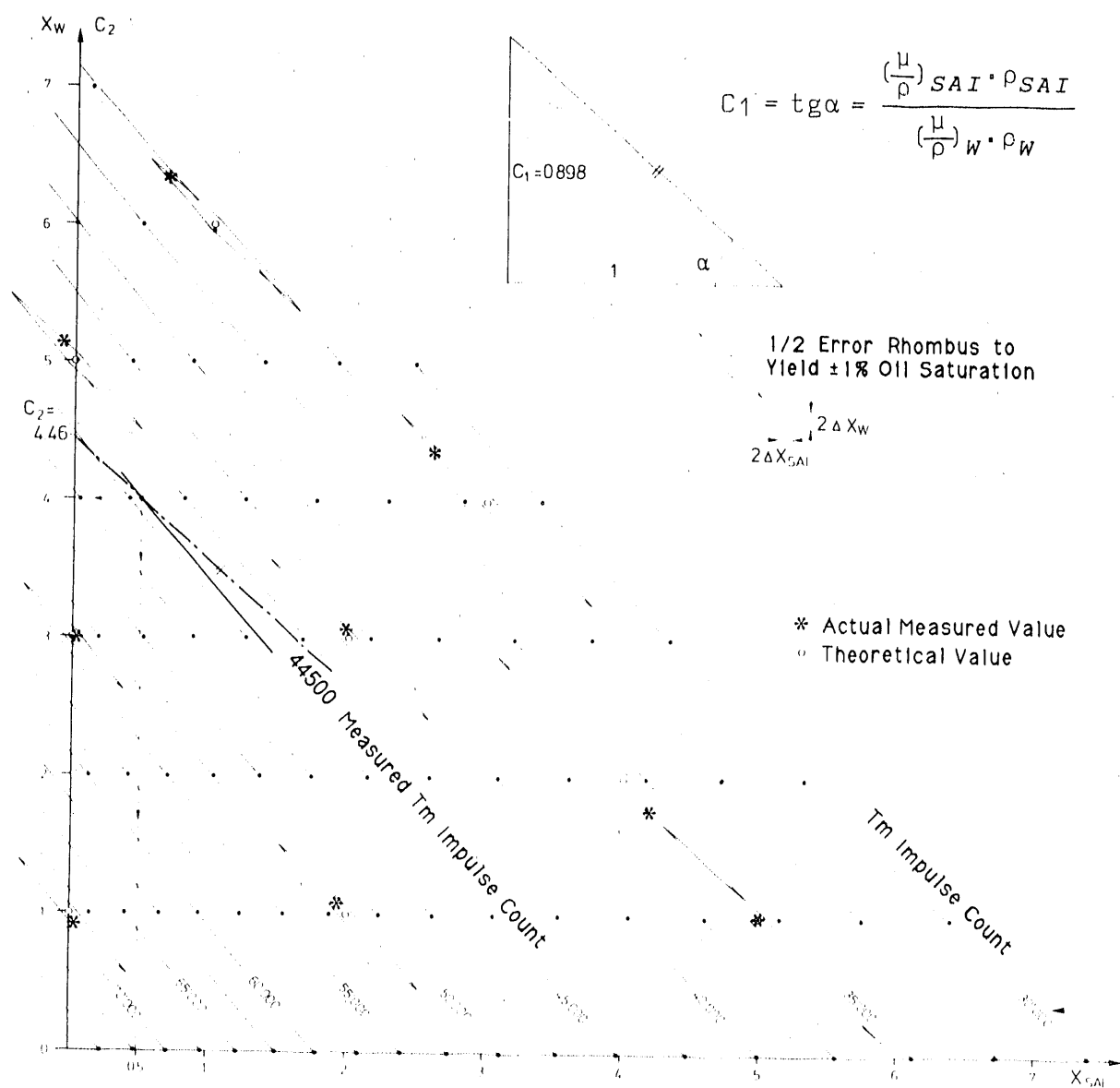


FIGURE 6.32. Nomograph for the Semigraphic Determination of Fluid Saturations

The line defined by Equation (6.111) is the geometric position of x_W . The location of this line is calculated from the slope c_1 and the intercept c_2 , relative to the origin, and is plotted in the nomograph shown in Figure 6.32 as _____. The values for x_W and x_{SAI} were determined by the coordinates of the intersection of this line and a line representing the interpolation of the measured thulium impulse count (_____ in Figure 6.32). An example is shown in Figure 6.32 for $J_{TM} = 44481$ and $(J/J_T)_{CS} = 0.6820$. With $(\mu/\rho)_W = 0.0858 \text{ cm}^2/\text{g}$

and $(\mu/\rho)_{SAI} = 0.0906 \text{ cm}^2/\text{g}$ for the gamma energy of Cs-137 (according to Table 6.7a), and with $\rho_W = 1 \text{ g/cm}^3$ and $\rho_{SAI} = 0.85 \text{ g/cm}^3$, c_1 and c_2 are calculated as 0.898 and 4.46, respectively. The lines intersect at the point where $x_W = 4 \text{ cm}$ and $x_{SAI} = 0.5 \text{ cm}$. The saturations S_W and S_0 or S_{SAI} are calculated from the irradiation path lengths x_W and x_0 or x_{SAI} according to Equation (6.10).

The accuracy of the semigraphic saturation determination satisfies the required accuracy of $\pm 2\%$ saturation, as specified in Section 6.2. This is shown by the fact that all the actual measured values (identified in Figure 6.32 with the asterisk) for each attenuation case lie within the one-half-error rhomboids that were plotted for the theoretical values (identified with the open circle). The one-half-error rhomboids are the areas of tolerated deviations for a standard error that is equal to half of the maximum tolerated error of $\pm 2\%$ fluid saturation, that is, $\pm 1\%$. For a porosity of 0.4 and a total irradiation path length B of 15 cm, the intervals between the sides of the rhomboid, across its center and parallel to the x- and y-axes (Δx_{SAI} or Δx_W), are equivalent to an irradiation path length equal to $(n \cdot B) \cdot 1\% = 0.4 \cdot 15 \cdot 0.01 = 0.6 \text{ mm}$.

A nomograph as shown in Figure 6.32 had to be replotted every other day because of the Tm-170 half-life of 127 days. Even if the attenuation measurements in dry sand changed only slightly with position along the two-dimensional flume, and thus had to be determined individually, the nomograph nevertheless was assumed as generally valid, that is, independent of the position. By using this assumption, the thulium impulse count rates were corrected according to the cesium measurements in dry sand.

7.0 CAPILLARY PRESSURE HEAD CURVES MEASURED IN A ONE-DIMENSIONAL COLUMN

7.1 CAPILLARY PRESSURE HEAD CURVES

To create a saturation diagram, the capillary rise curves of the three fluid combinations must be known: those between water and air, ACWL, between oil and air, ACOL, and between water and oil, ACWO. In statics, the capillary pressure head curve is equivalent to the capillary rise curve; thus, HCWL = ACWL, HCOL = ACOL, and HCWO = ACWO. Because of hysteresis, one must distinguish between an imbibition, IM, curve and a drainage, DR, curve. To shorten the nomenclature, the AC and HC have been omitted, and thus WLIM, WLDR, OLIM, OLDR, WOIM, and WODR are used to distinguish the curves.

According to the contamination concept of Schiegg (1979, p. 78) for water and air, a virgin (jfrl) and contaminated (befl) capillary pressure head saturation curve can be specified. Virgin (jfrl) implies pure water-air menisci. Contaminated (befl), on the other hand, refers to impure water-air menisci; actually double menisci consisting of water-oil and oil-air menisci. Thus, according to Schiegg (1979, p. 82), $HCWL_{befl}$ can be theoretically determined by using the oil-air and water-oil curves

$$HCWL_{befl} = \rho_o \cdot HCOL + (1 - \rho_o) HCWO \quad (7.1)$$

where ρ_o is the density of oil.

The difference ($HCWL_{jfrl} - HCWL_{befl}$) was designated as the capillary pressure head reduction, Δh_c . For the quartz sand with the grain distribution curve shown in Figure 3.1a, Δh_c is calculated from Figure 7.1 as

$$\begin{aligned} \Delta h_c(\text{Imbibition}) &\approx +3 \text{ cm} \\ \Delta h_c(\text{Drainage}) &\approx +4 \text{ cm} \end{aligned} \quad (7.2)$$

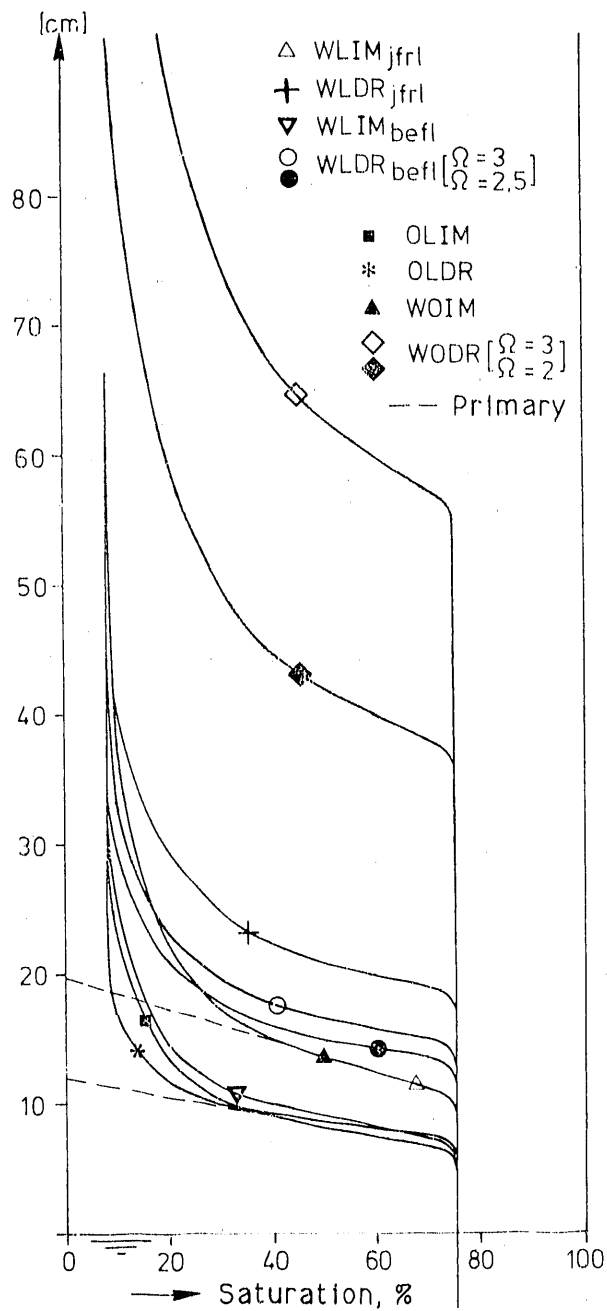


FIGURE 7.1. Theoretical Capillary Pressure Head Curves for Oil as Well as for the Contaminated Water Based on the Experimentally Determined Virgin Water Curves and the Scaling Parameter, Ω

where the independence of Δh_c from saturation is a simplification. It is understood that the $HCWL_{befl}$ curve resulting from Equation (7.1) is not the curve measured when the water-air level remains static, but rather, when a virgin HCWL curve becomes contaminated and the water-air level remains stationary, the resulting curve equals the $HCWL_{befl}$ curve and $\Delta h_c(IM) \sim 0$ (see Schiegg 1979, p. 81). $\Delta h_c(DR)$, on the other hand, remains + 4 cm.

The capillary pressure is a function of the porous medium according to the La Place equation of capillarity. The capillary pressures across the pure and contaminated menisci are independent of each other. Thus, capillary pressure across a contaminated meniscus for both drainage and imbibition can be greater or less than the capillary pressure across the pure meniscus. However, change during contamination (i.e., a reduction of the capillary pressure or the capillary rise, whose difference was explained in connection with Equation [2.8]), is only possible if 1) during drainage, the capillary pressure across the contaminated meniscus is smaller than the capillary pressure across the pure meniscus, or 2) during imbibition, the capillary pressure across the contaminated meniscus is larger than the capillary pressure across the pure meniscus. Because a drained pure meniscus can only decrease in pressure and an imbibed pure meniscus can only increase in pressure, this statement assumes that the air-water level is constant or its change is not dominant, and that the pressure change is not greater than the hysteresis range. This also implies that when the capillary pressure across the contaminated meniscus is larger during drainage or is smaller during imbibition than the capillary pressure across the pure meniscus, then the position of the meniscus cannot be changed by contamination.

According to Schiegg (1979, p. 52), as a first approximation, the HCOL and HCWO curves could be interpreted as approximate copies of the $HCWL_{jfrl}$ curve. Thus, they can be obtained theoretically by multiplying the $HCWL_{jfrl}$ curve by their respective scaling parameter, Ω , values

$$\begin{aligned} HCWL_{jfrl} &= HCOL / \Omega \Big|_O^L \\ &= HCWO / \Omega \Big|_W^O \end{aligned} \tag{7.3}$$

The Ω -values are functions of the assumed wetting angle and the radius of curvature. According to Schiegg (1979, p. 45):

$$\begin{aligned}\Omega |_{\overset{L}{O}(IM)} &= (0,6) \\ \Omega |_{\overset{L}{O}(DR)} &= 0,4 \\ \Omega |_{\overset{O}{W}(IM)} &\approx 1 \\ \Omega |_{\overset{O}{W}(DR)} &= 2:3\end{aligned}\tag{7.4}(a)$$

From Equation (7.3) and the relationships presented in Equation (7.4), the theoretical capillary pressure head curves for oil can be determined from the experimentally determined pure capillary pressure head curves for water. The contaminated curves can, in turn, be calculated according to Equation (7.1). All of these curves are shown in Figure 7.1.

A capillary pressure head curve is designated as primary if no residual saturation of the displaced fluid is present. A capillary pressure head curve is considered fully developed if it is the same as one of the two curves delineating the hysteresis area, which means that all parts of the curve move simultaneously with the transient fluid level.

7.2 SERIES A AND B SATURATION DIAGRAMS

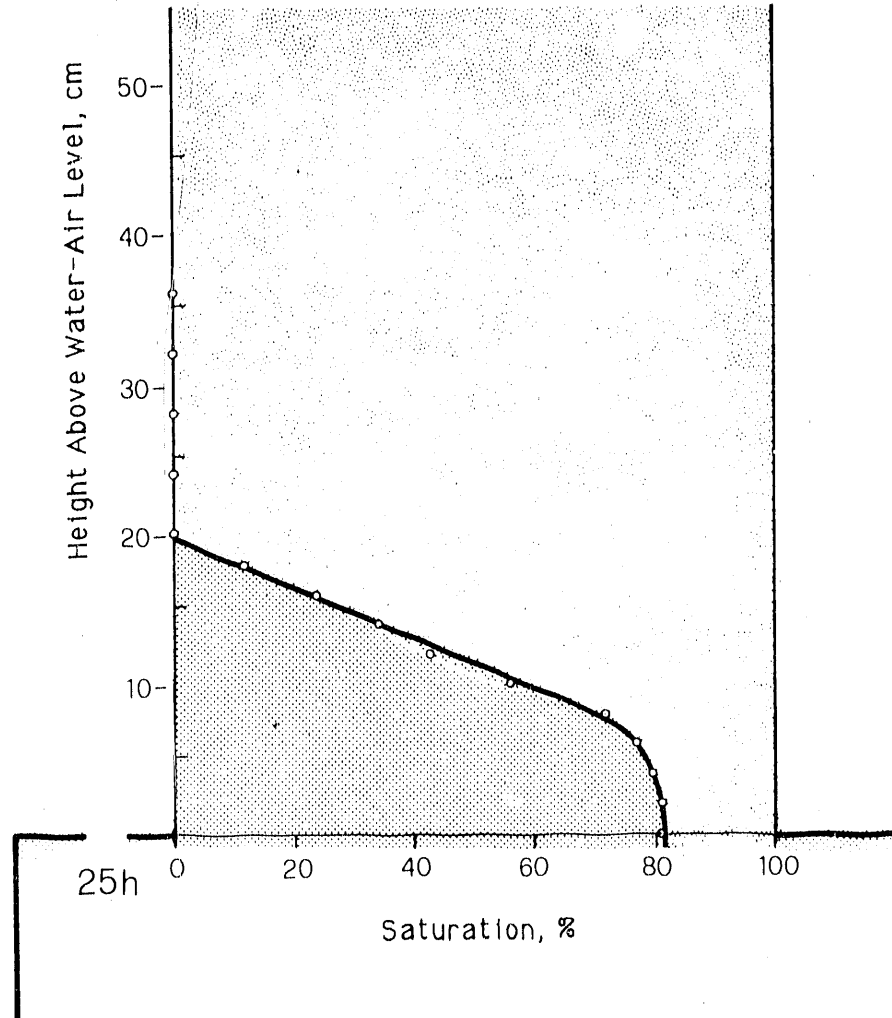
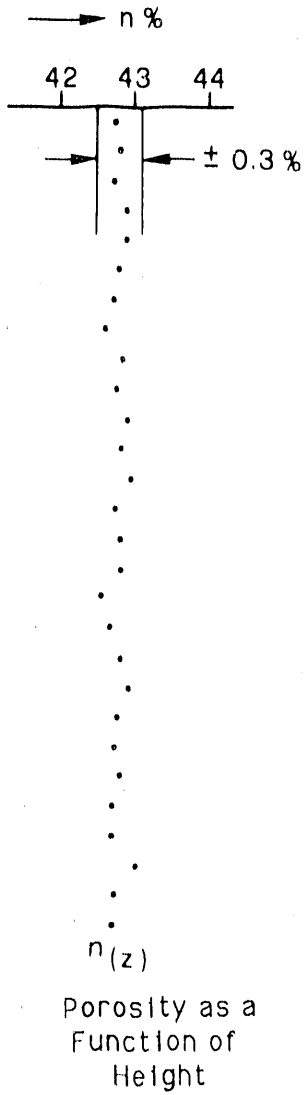
The saturation diagrams presented in the following section show the actual saturation distribution within the measurement range depicted in Figure 3.3. The saturations are presented along the horizontal axis, and the height above the assumed level of the free-fluid pairs is plotted along the vertical axis.

A saturation diagram depends on the three potential distributions in water, oil, and air. Because of hysteresis, the saturation diagram is dependent on the development of these potential differences.

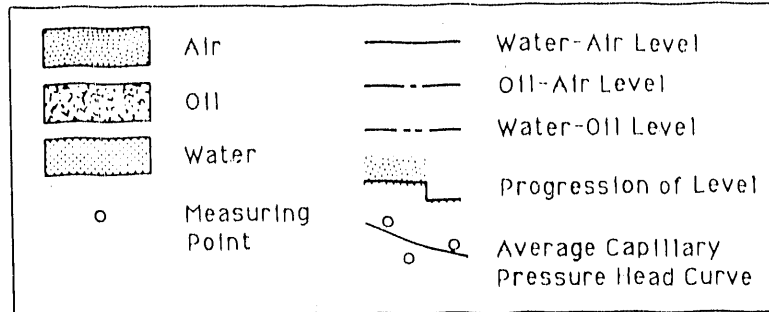
-
- (a) Equations were taken directly from the German text and, in some cases, use a different notation. For example, 0,01 = 1/100, whereas in this text, 1/100 would be shown as 0.01. Multiplication is indicated by a dot in the equations and in the text. The notation ÷ signifies a range, as in 2 to 3.

In general, the following saturation diagrams are static saturation diagrams. Statics implies spatially constant potentials and that the capillary rise curves can be described by the capillary pressure head curves (see remarks associated with Equation [2.8]). From statics, one can conclude whether the discharge of the displaced fluid is complete. Static saturation diagrams can be constructed by superpositioning the capillary pressure head curves (Figure 2.2) with similar drainage or imbibition histories. To superposition the curves the free-fluid level must be calculated according to Equation (2.9). From these levels the relative potential, ϕ^r , can be determined, where ϕ^r is the oil potential relative to the water-air level (Schiegg 1979, p. 95) and has the units (erg/cm^3).

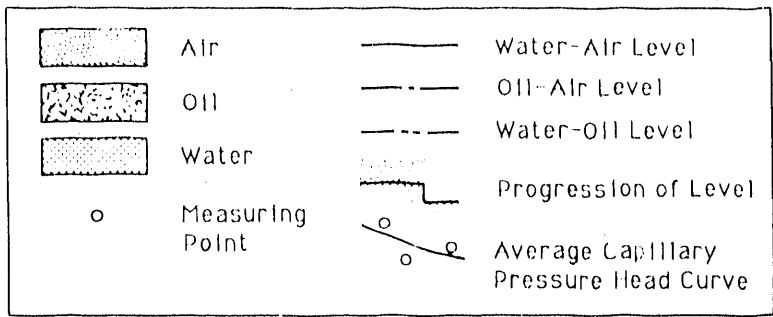
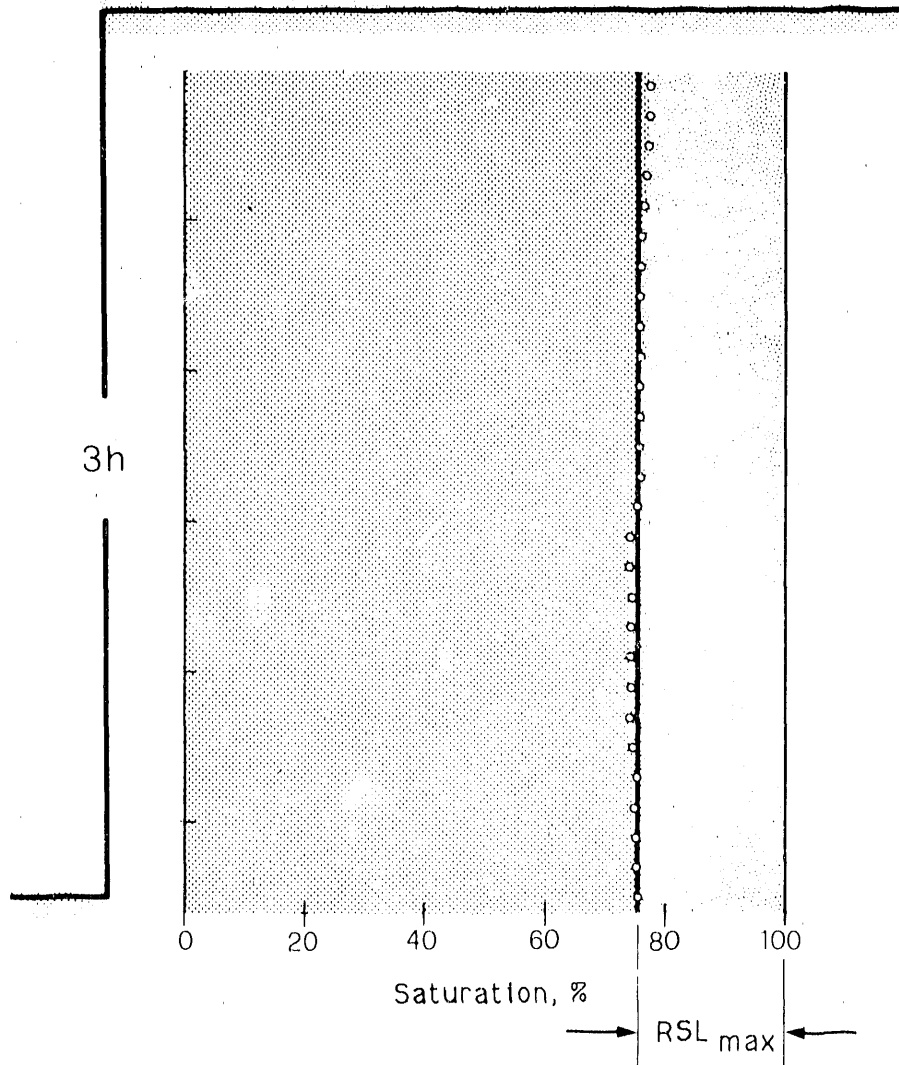
These measured saturation diagrams are given in Section 7.3. The 33 saturation diagrams in experimental series A are accompanied by comments beginning on p. 7.39. The eight saturation diagrams in experimental series B begin on p. 7.52, with the associated commentary starting on p. 7.60.



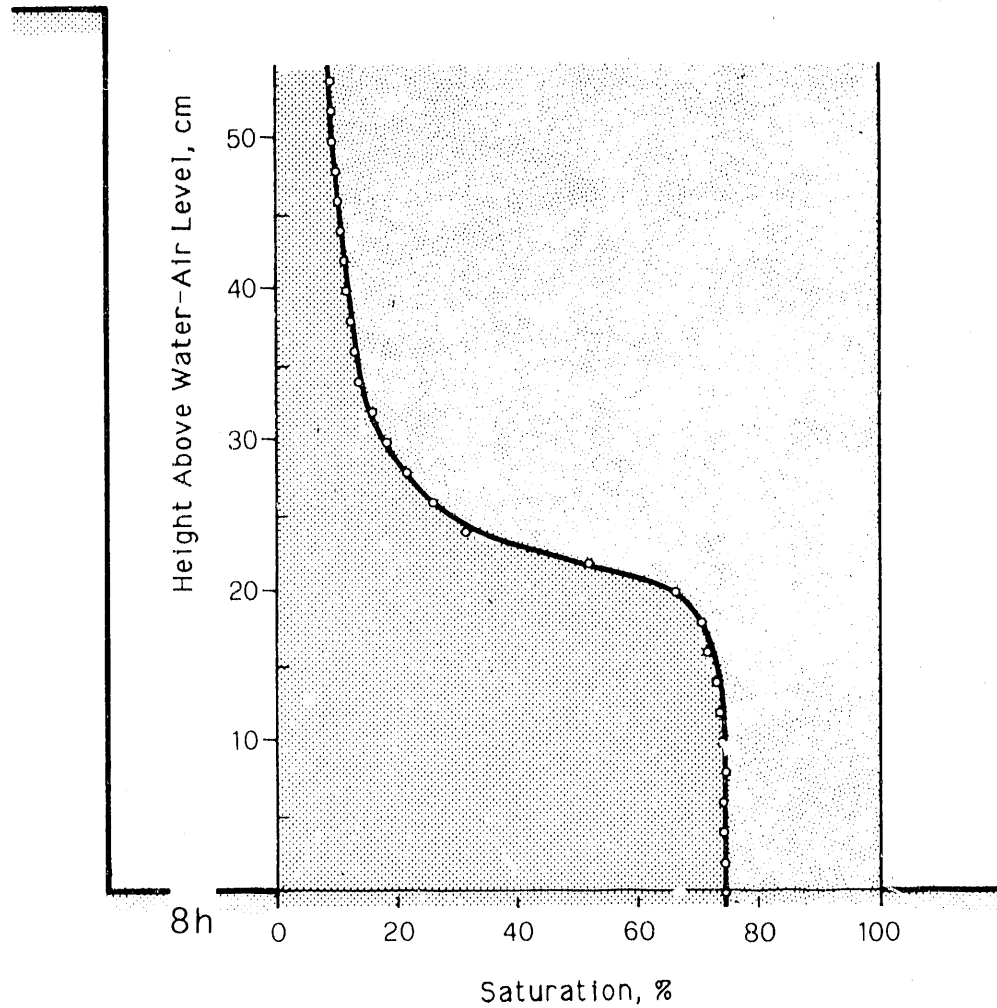
Primary WLIM j_{fr1}



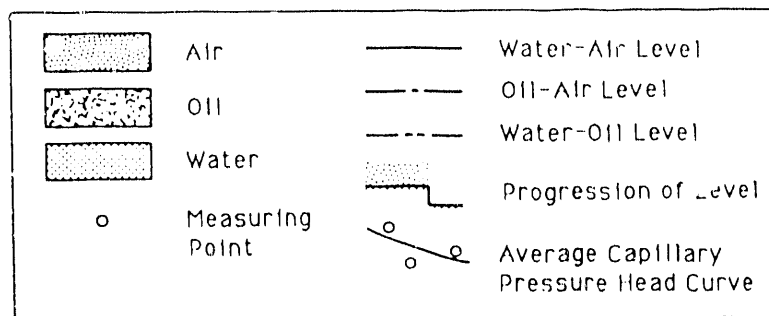
Experimental Series A: Diagram A1



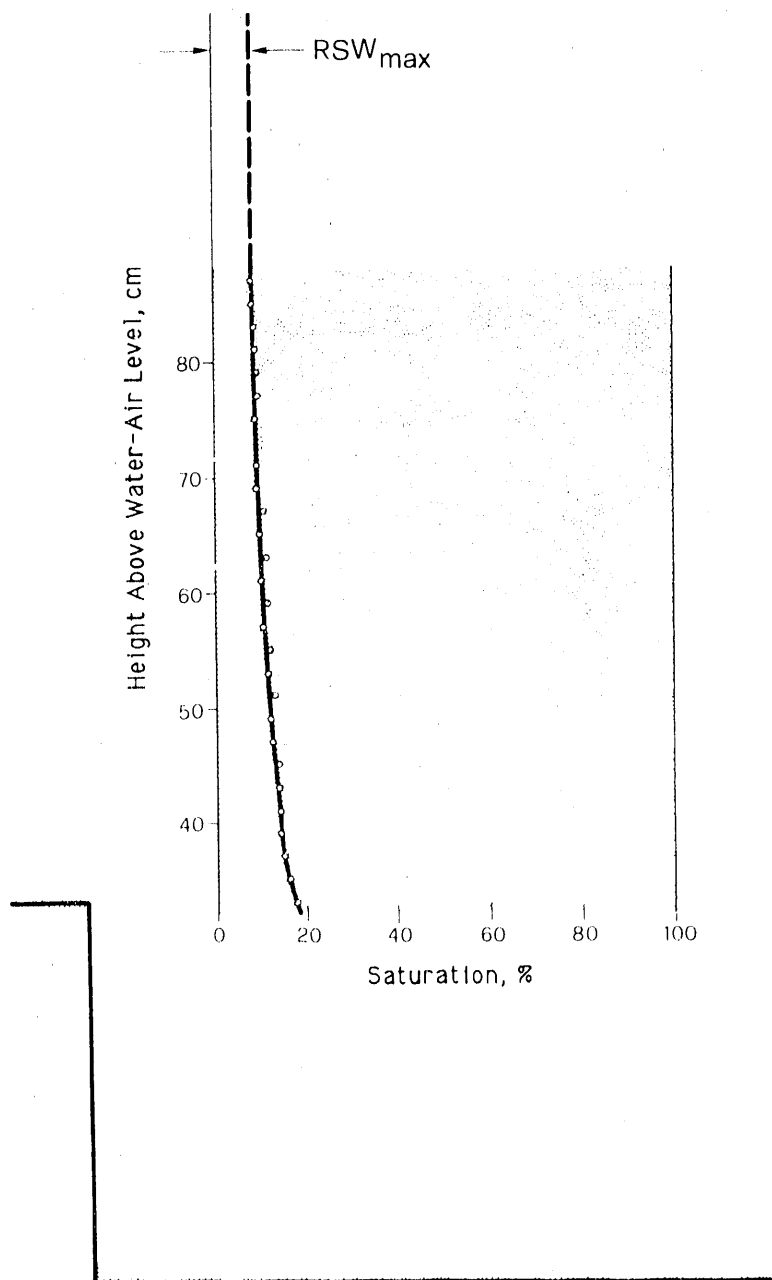
Experimental Series A: Diagram A2



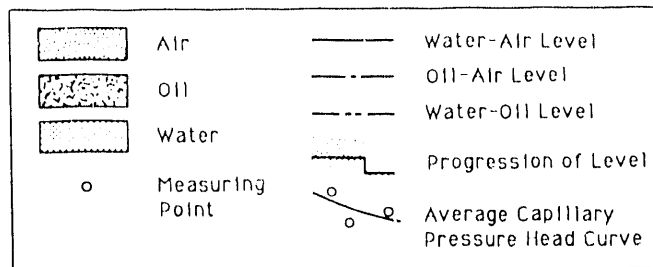
WLDR jfrl



Experimental Series A: Diagram A3



6h

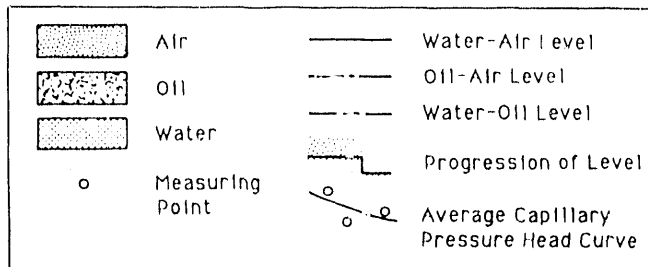
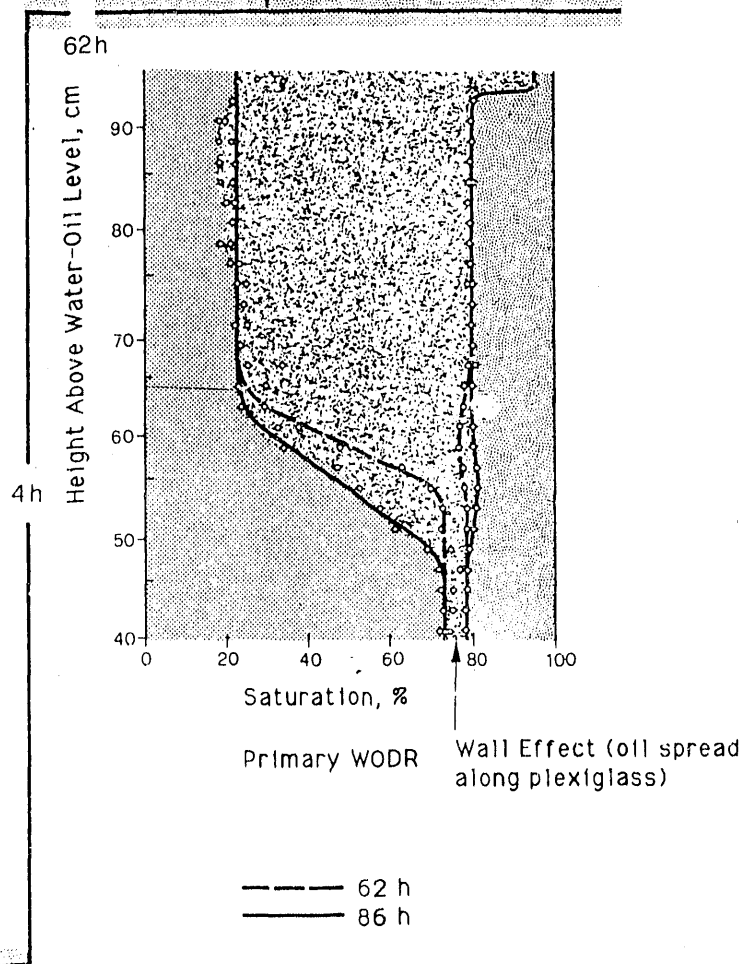


Experimental Series A: Diagram A4

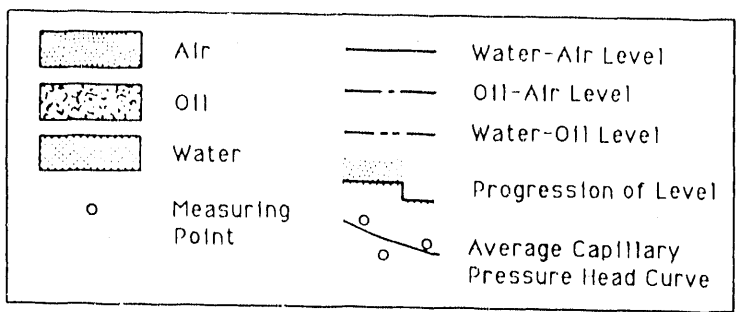
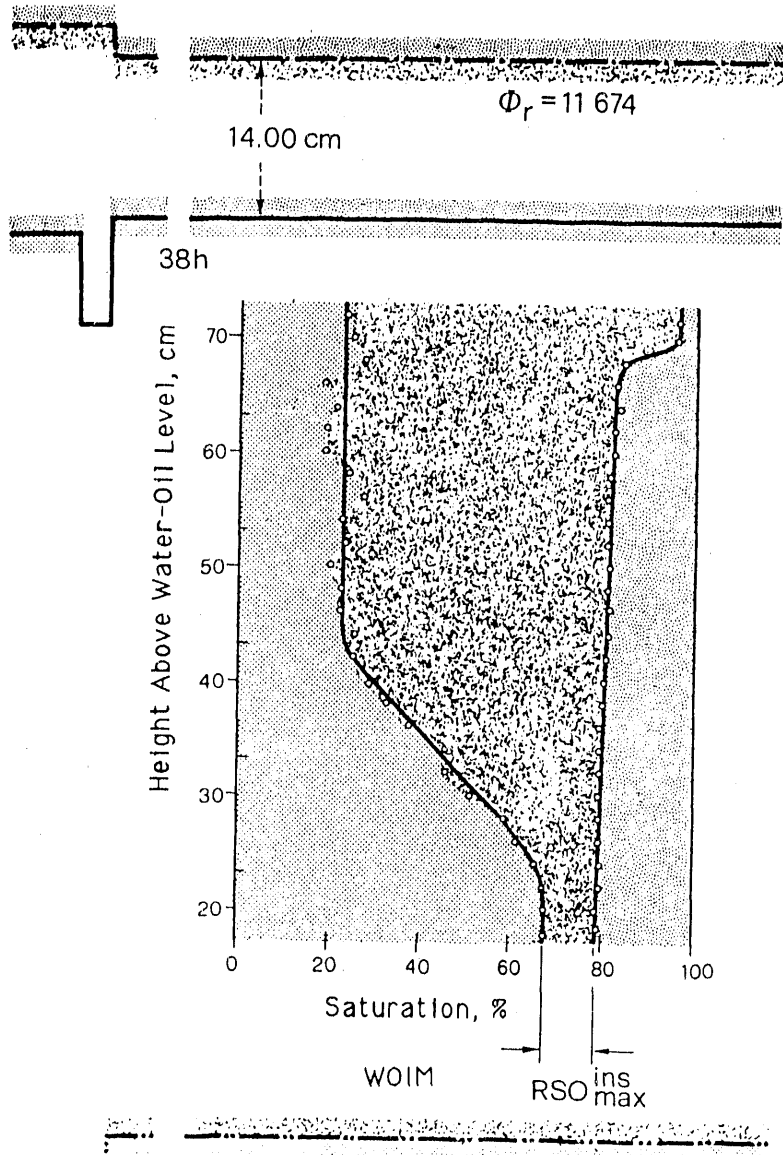


17.75 cm

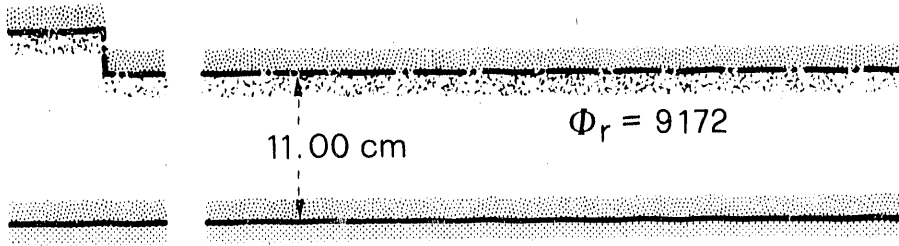
$$\begin{aligned} \Phi^r &= \rho_o \cdot g \cdot \Delta h \\ &= 0.85 \cdot 981 \cdot 17.75 \\ &= 14\ 800 \end{aligned}$$



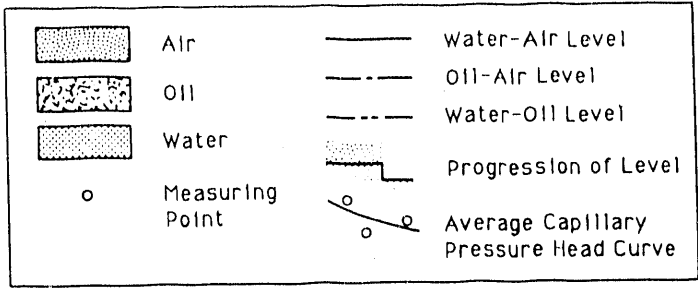
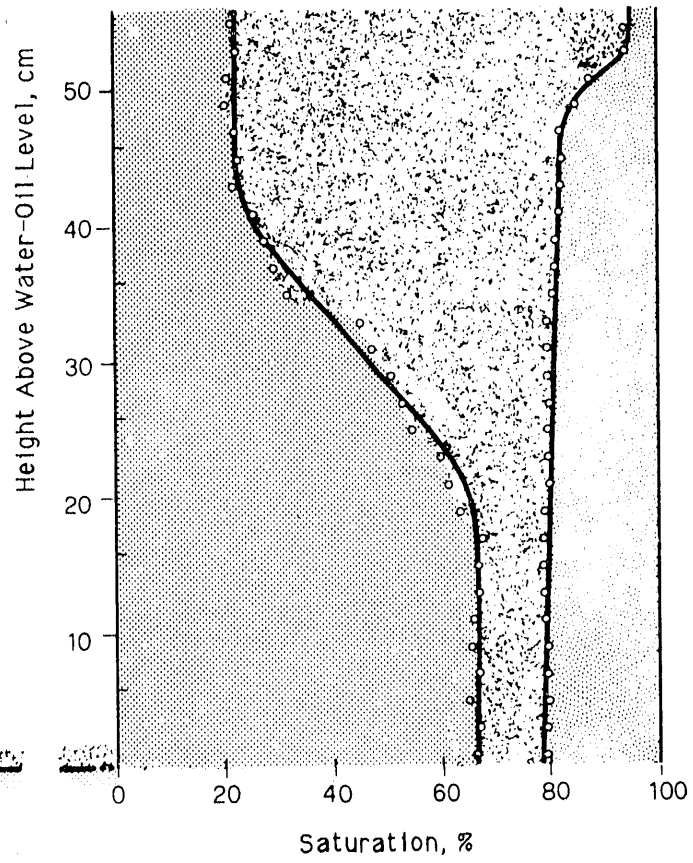
Experimental Series A: Diagram A5



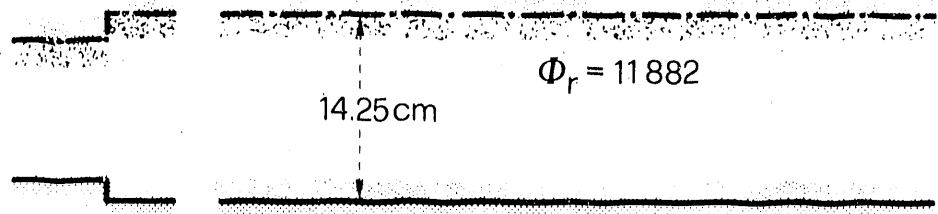
Experimental Series A: Diagram A6



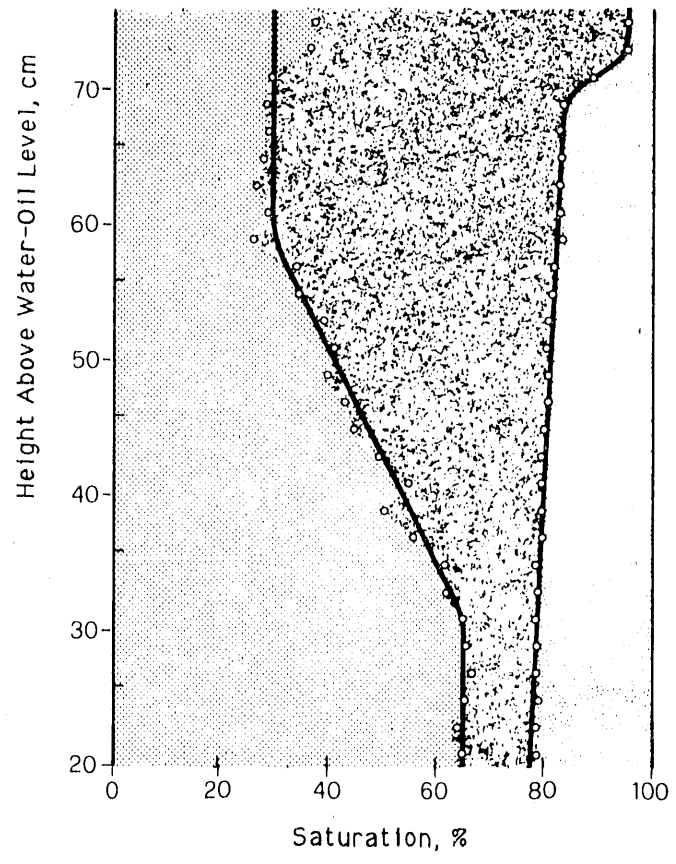
16h



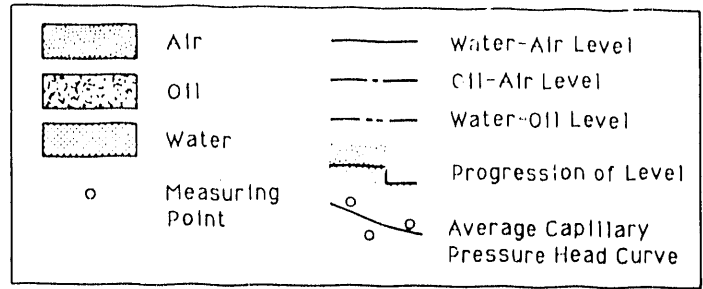
Experimental Series A: Diagram A7



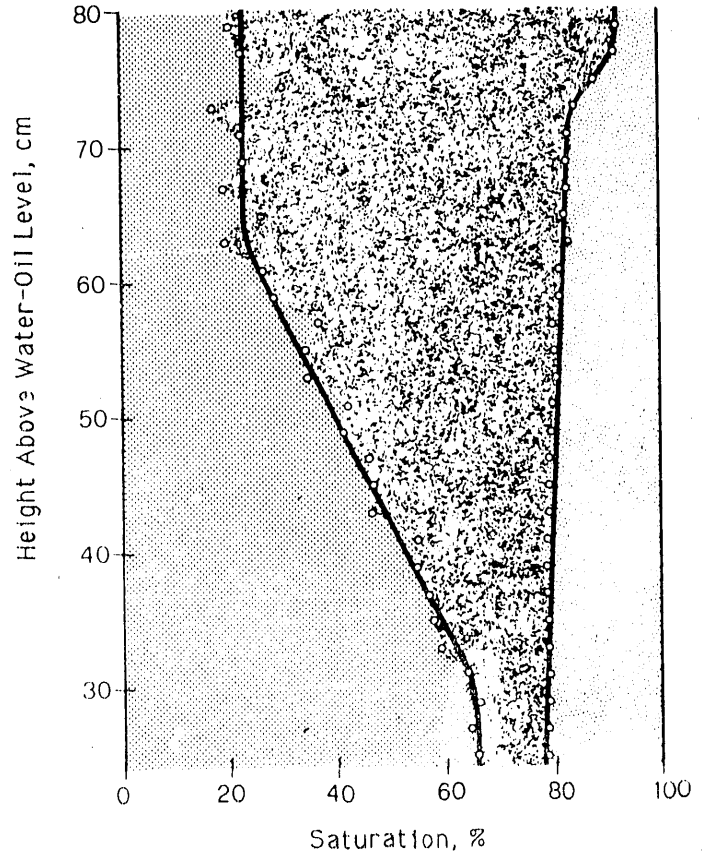
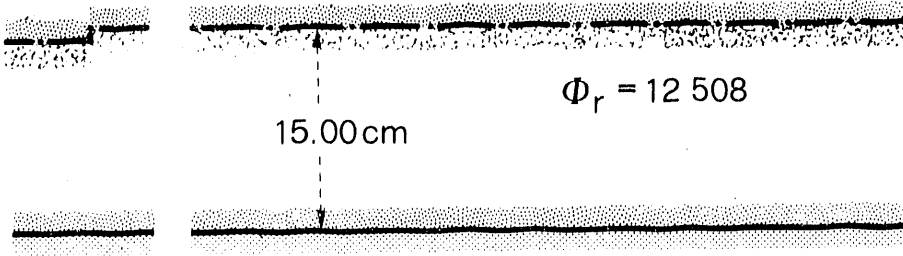
64h



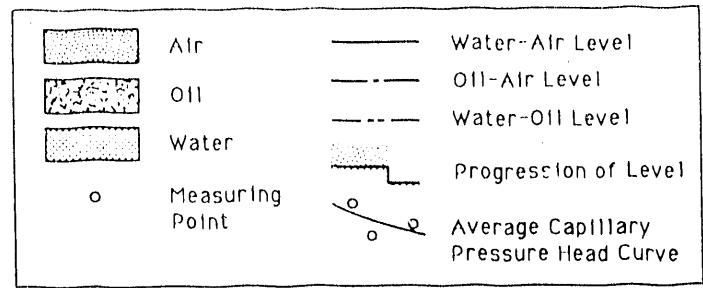
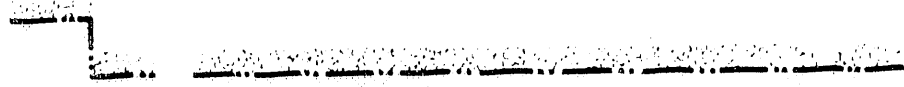
WODR



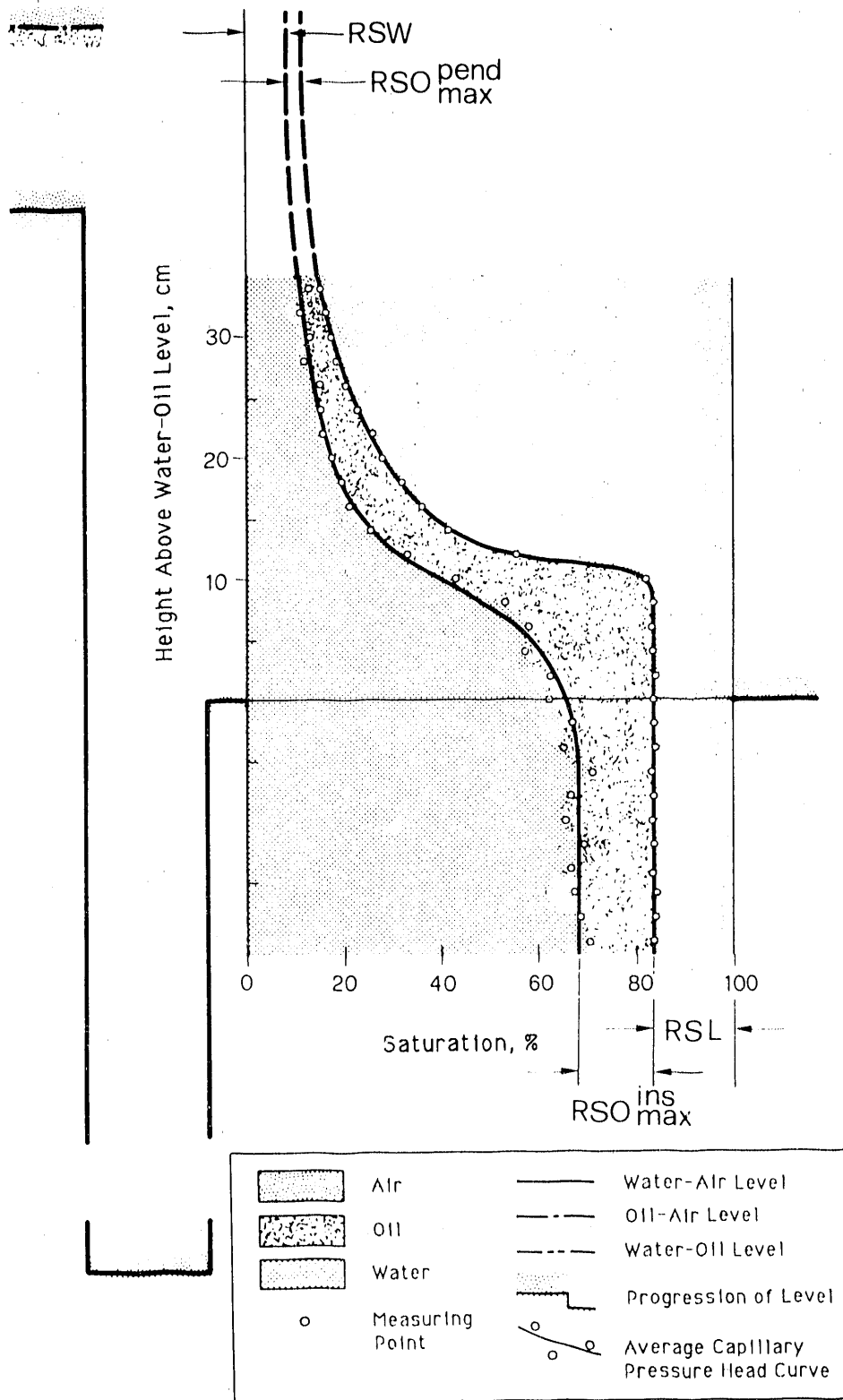
Experimental Series A: Diagram A8



WODR

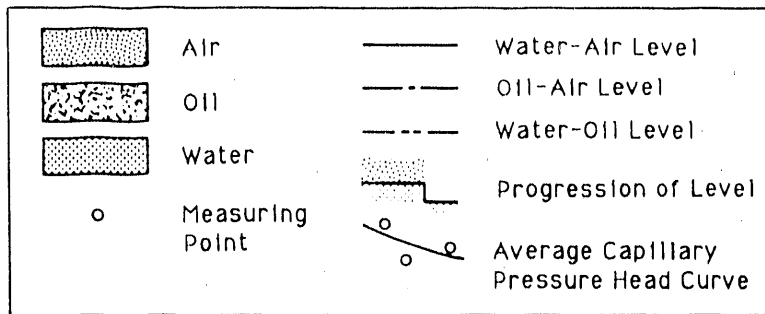
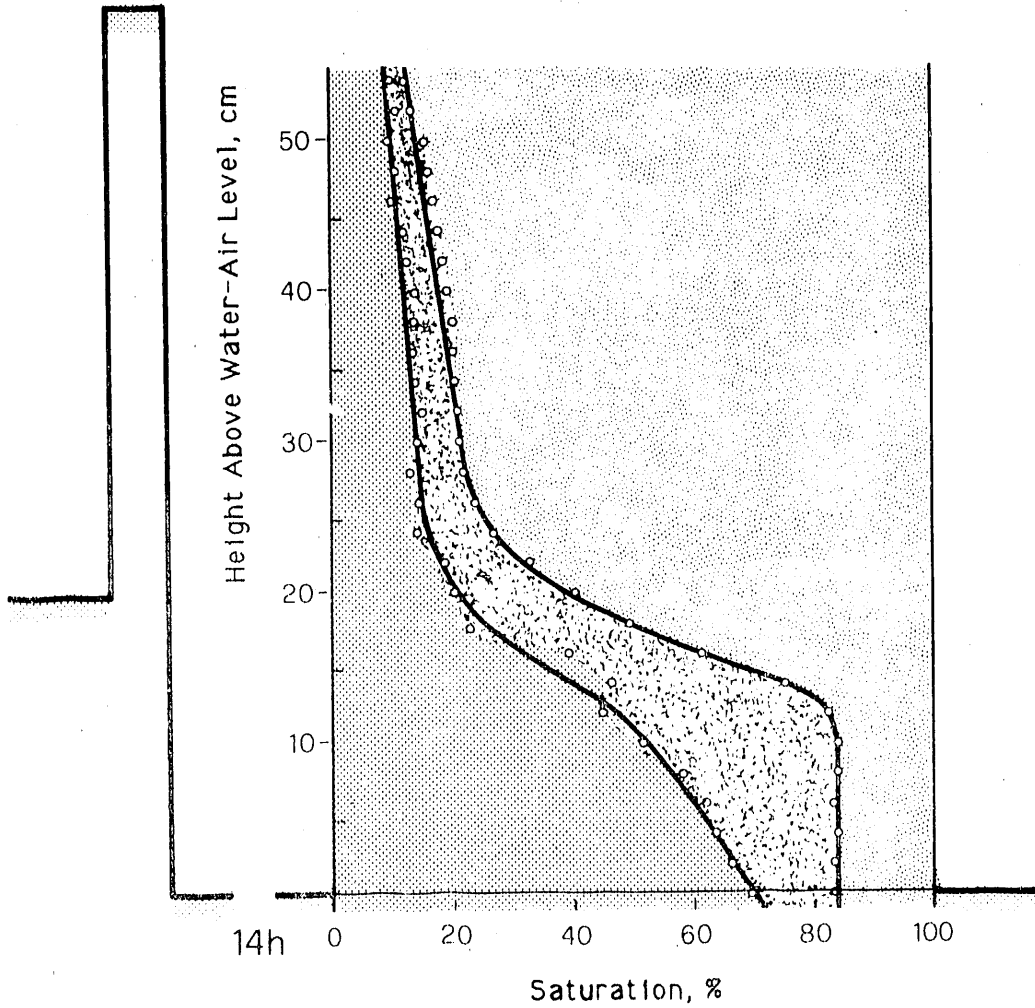


Experimental Series A: Diagram A9



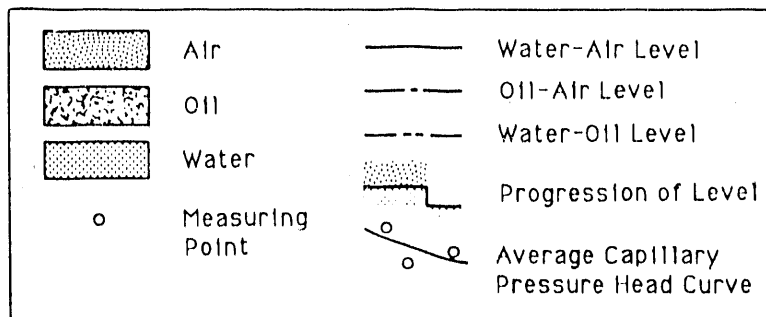
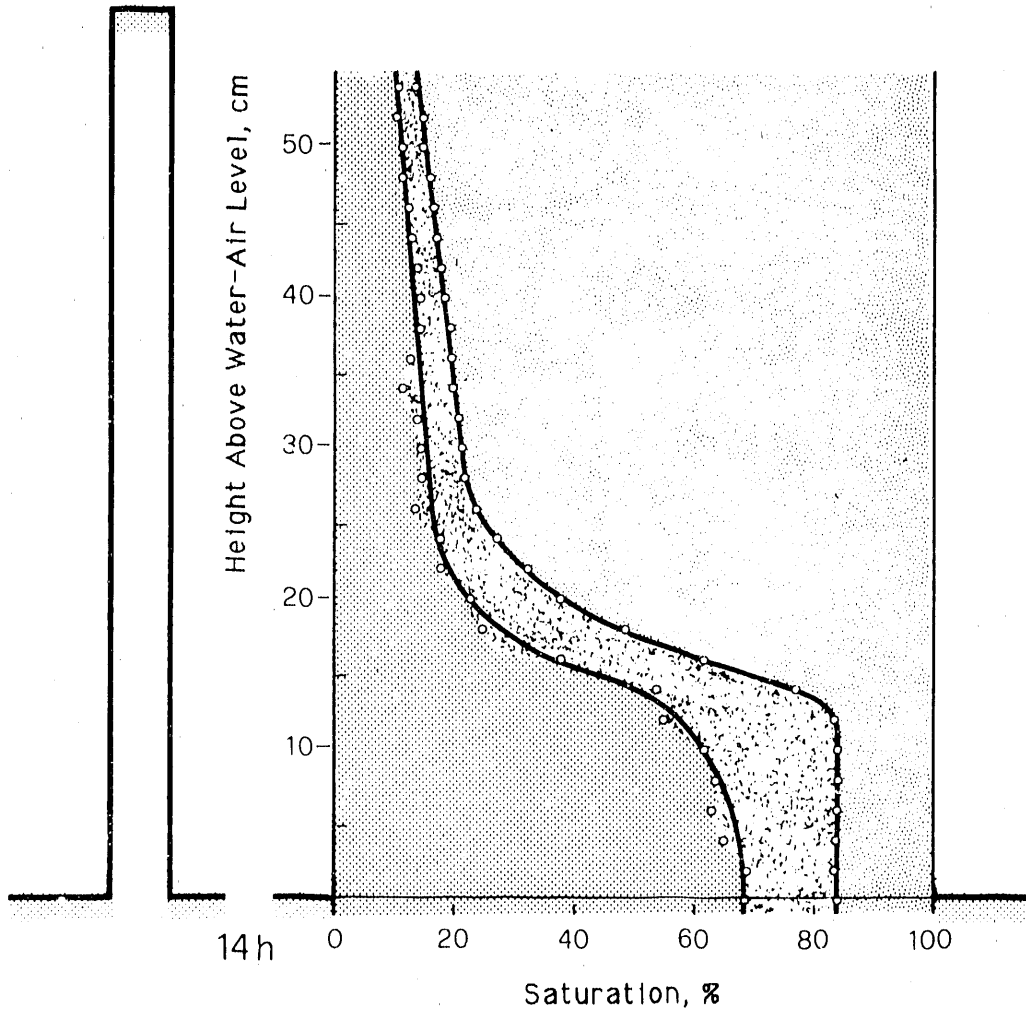
Experimental Series A: Diagram A10

~1 dL Oil Drained
from Column



Experimental Series A: Diagram A11

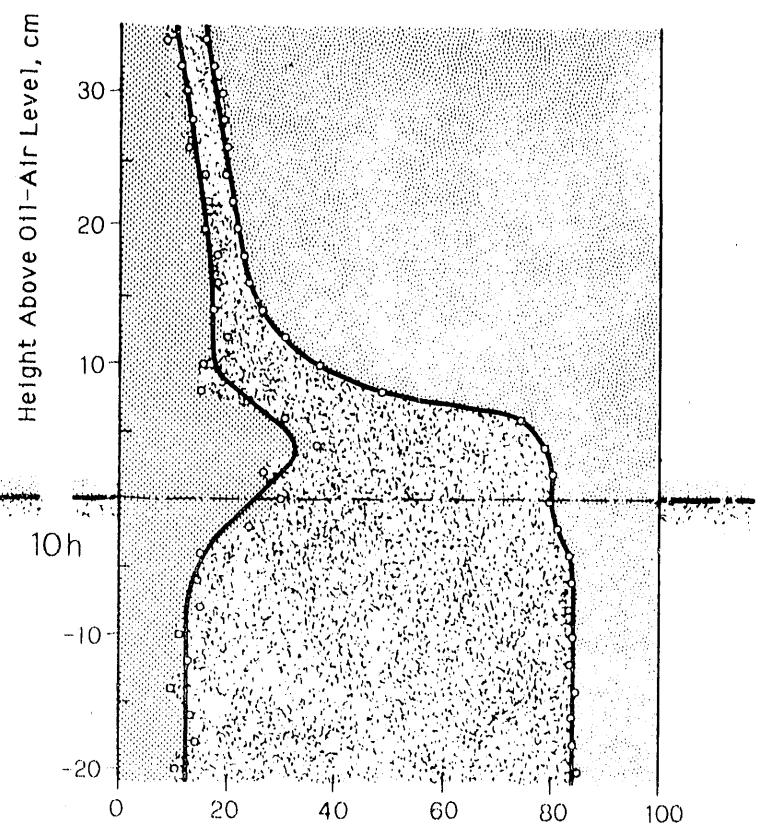
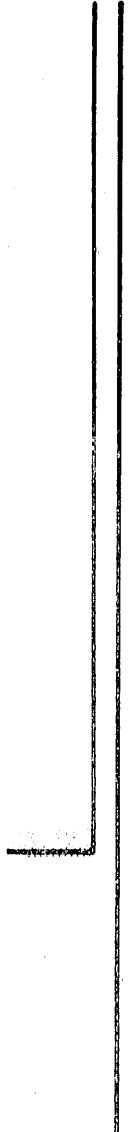
~1 dL Oil Drained
from Column



Experimental Series A: Diagram A12

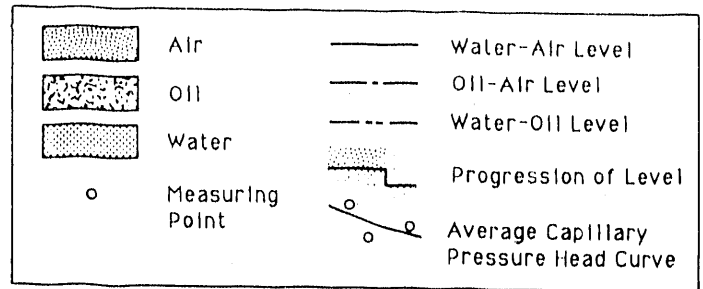


Water flowed upward at $\Delta\Phi \gg 1$
for 2.5 h. Some oil still drained.

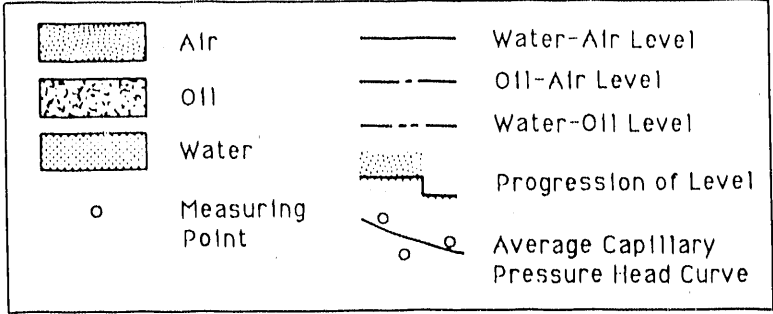
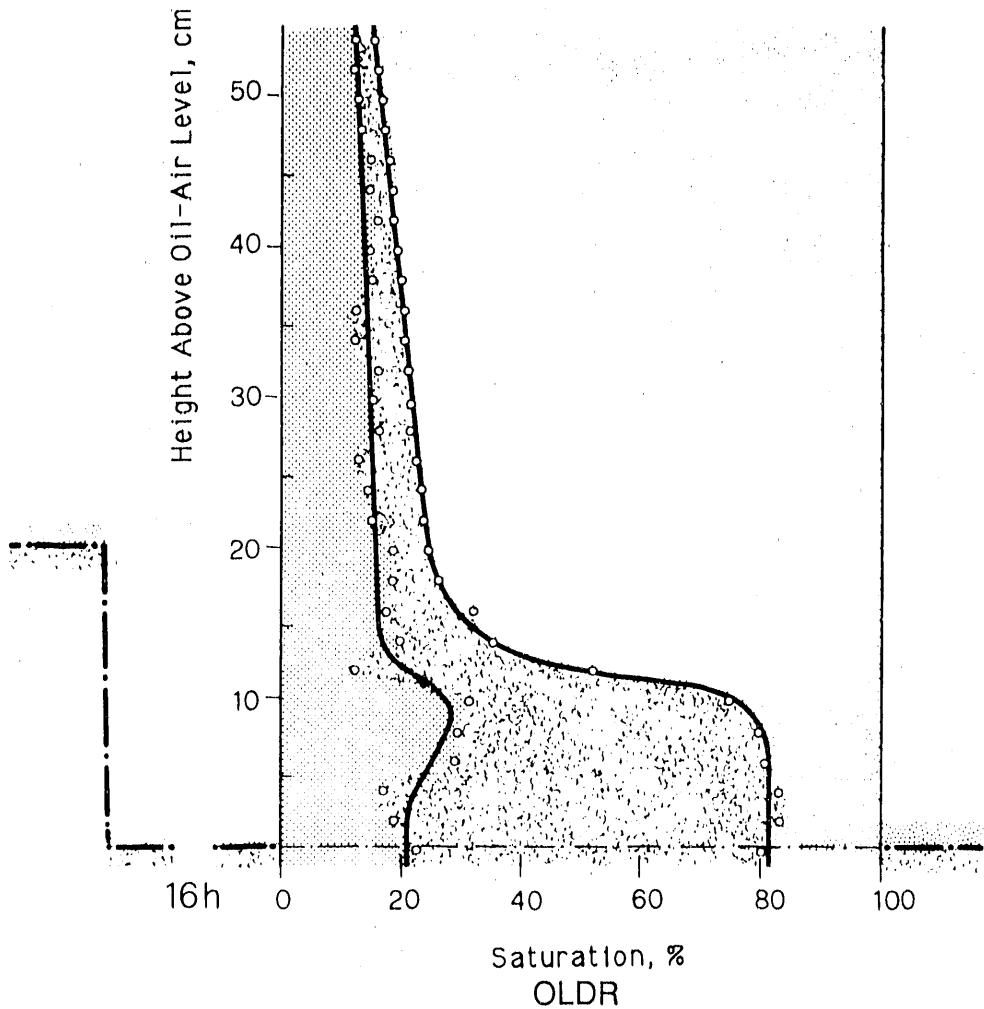


Saturation, %

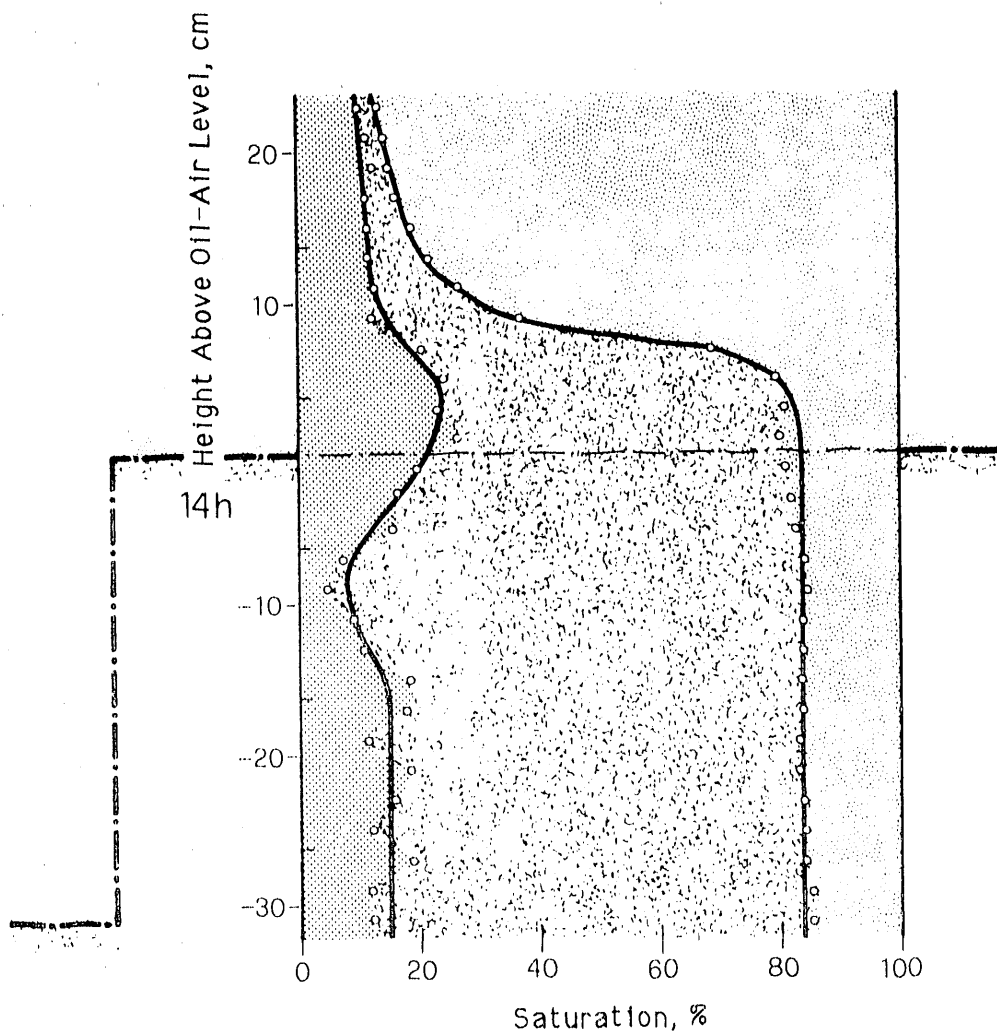
OLIM



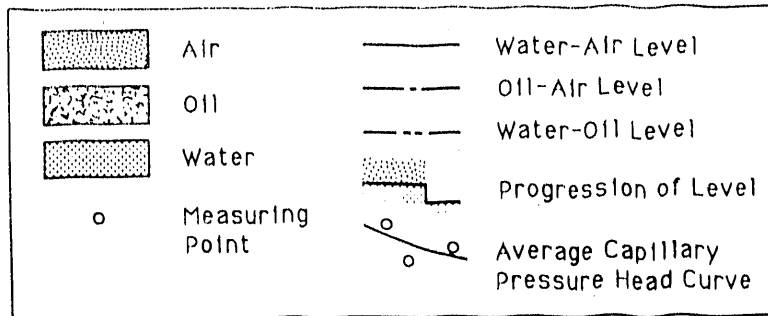
Experimental Series A: Diagram A13



Experimental Series A: Diagram A14

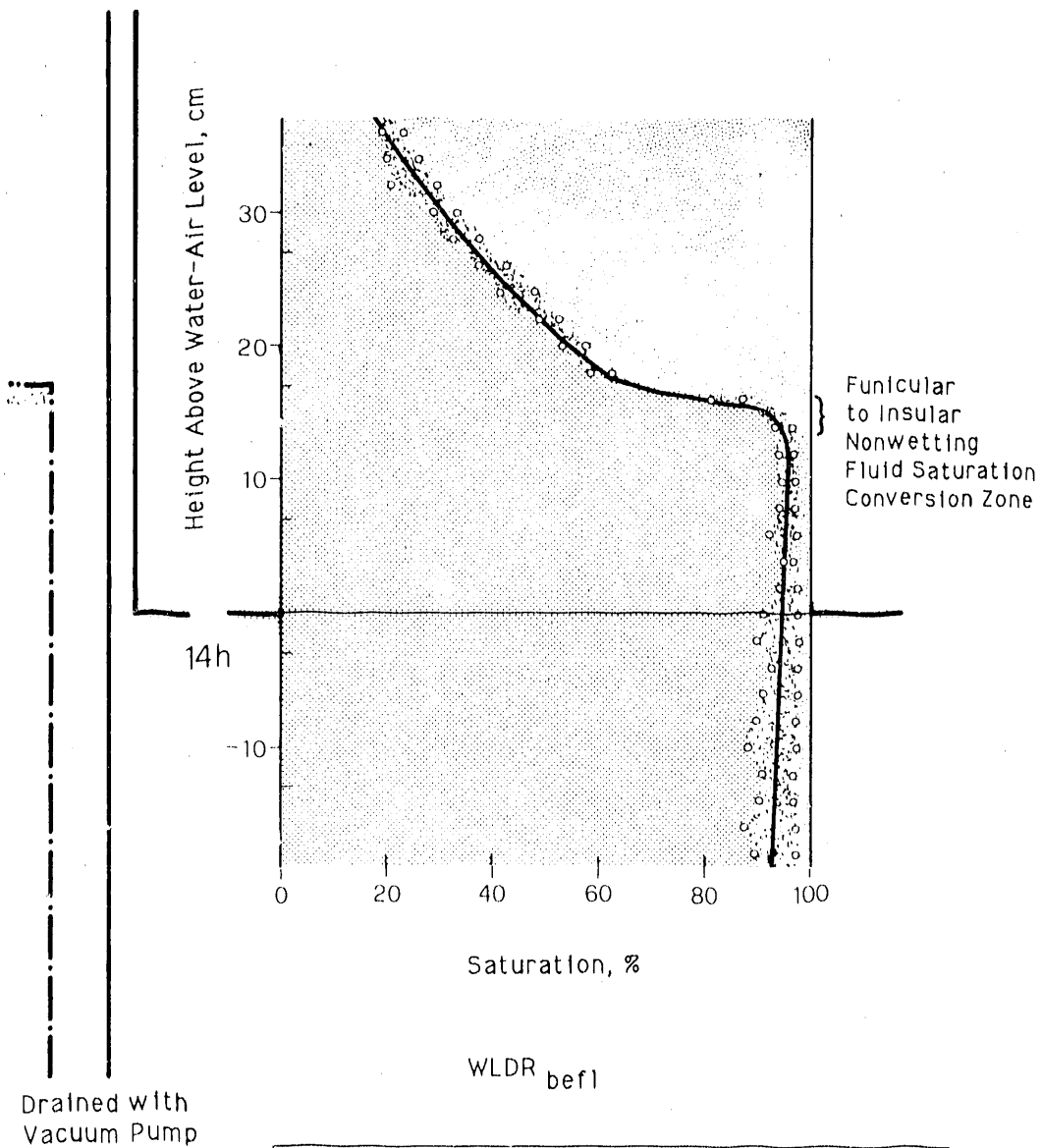


OLIM

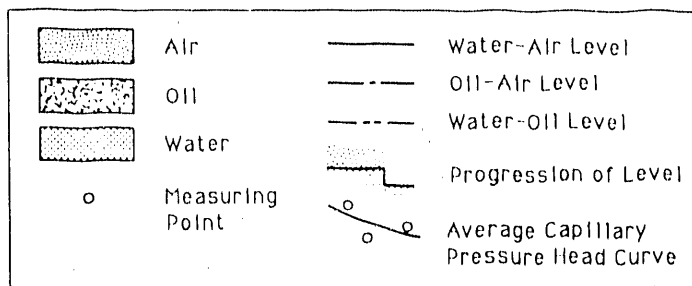


Experimental Series A: Diagram A15

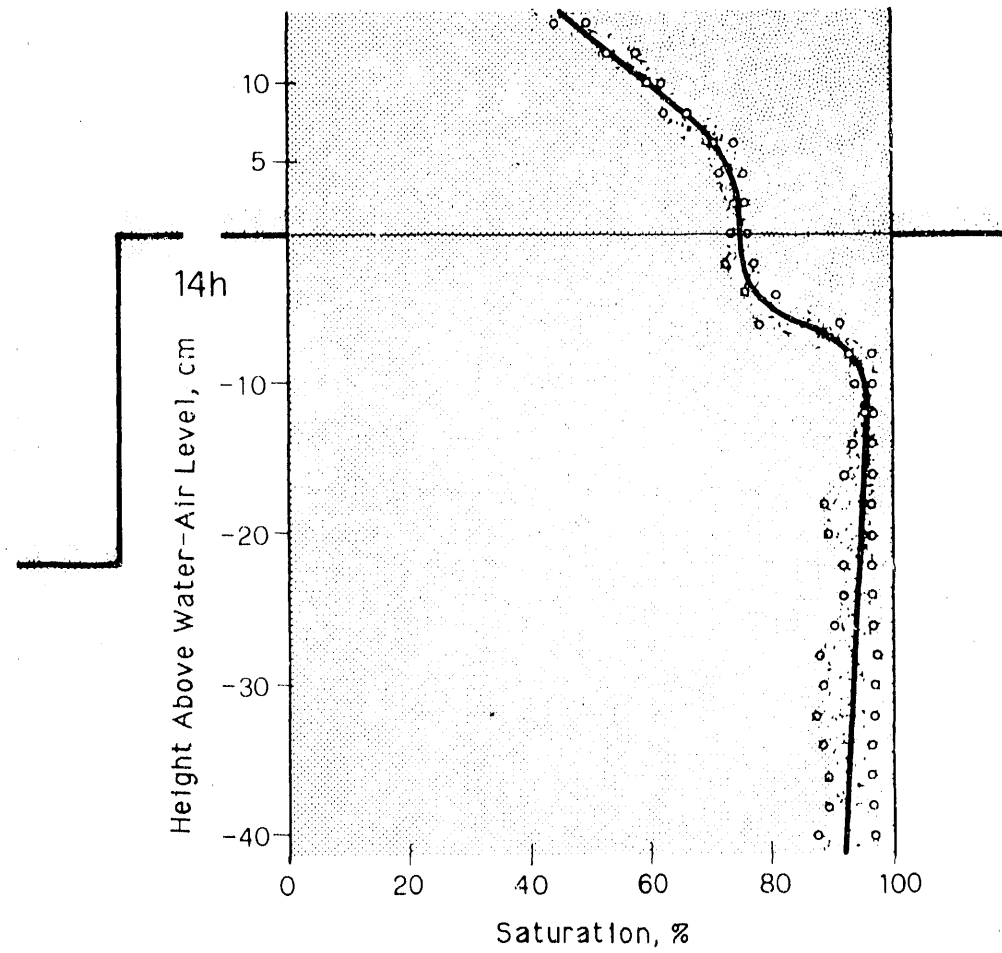
Water flowed upward at $\Delta\Phi \gg 1$
for 72 h. The oil was washed out.



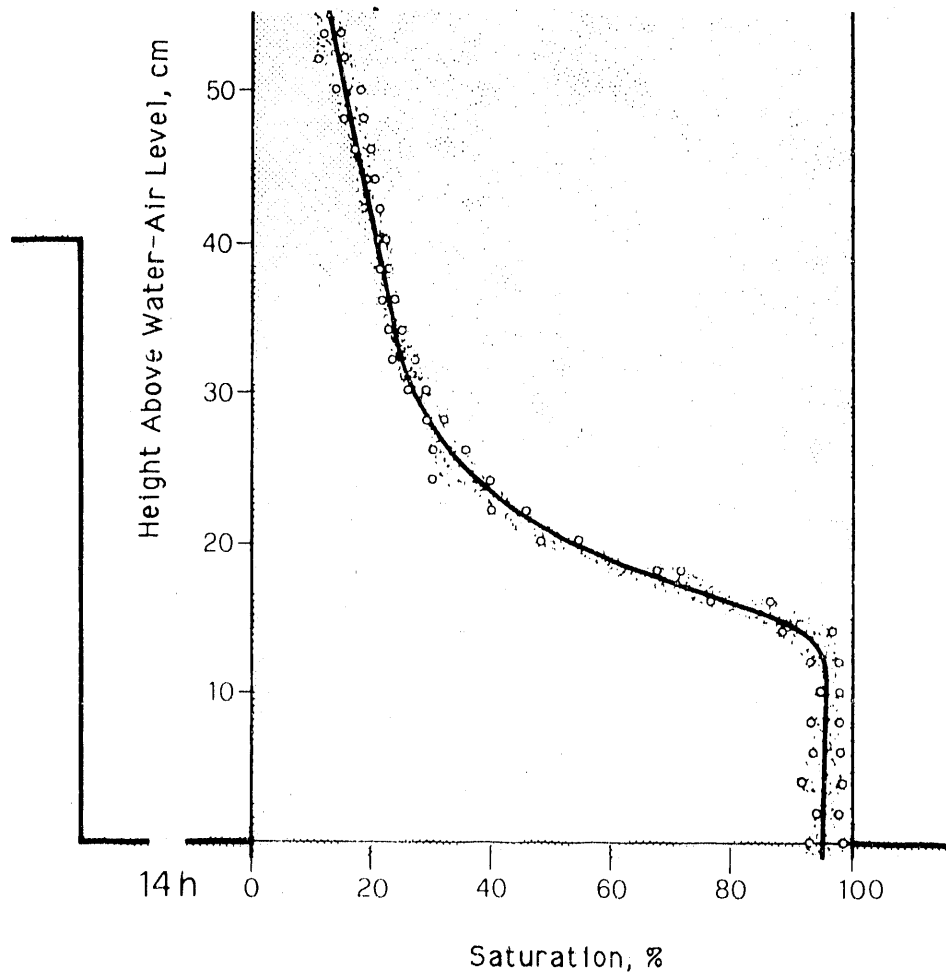
WLDR bef1



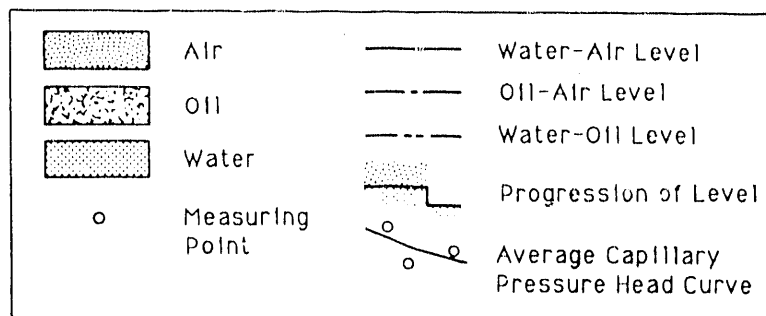
Experimental Series A: Diagram A16



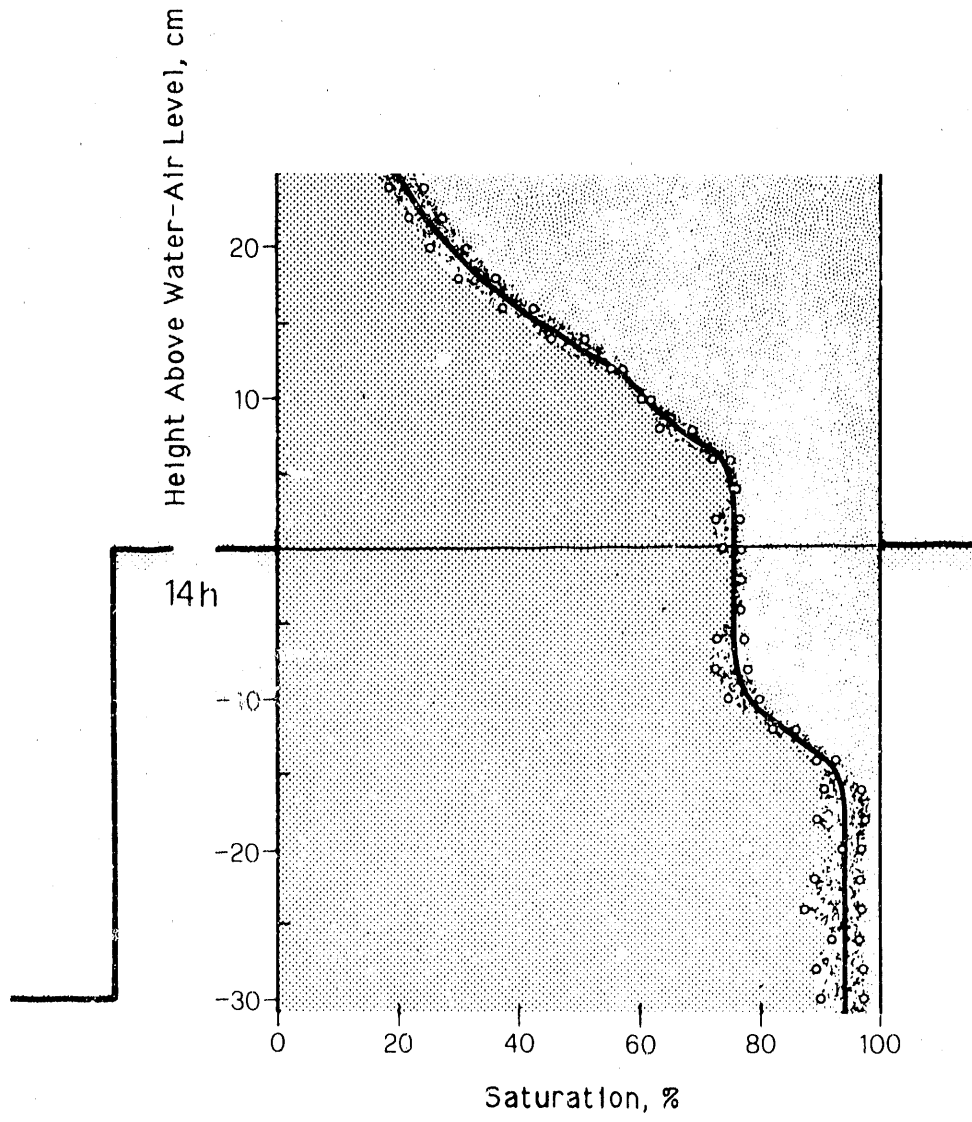
Experimental Series A: Diagram A17



WLDR_{befl}

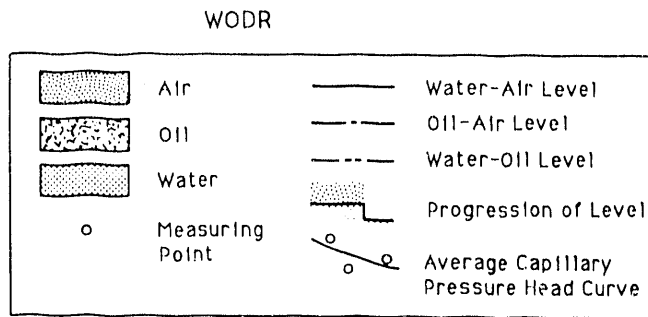
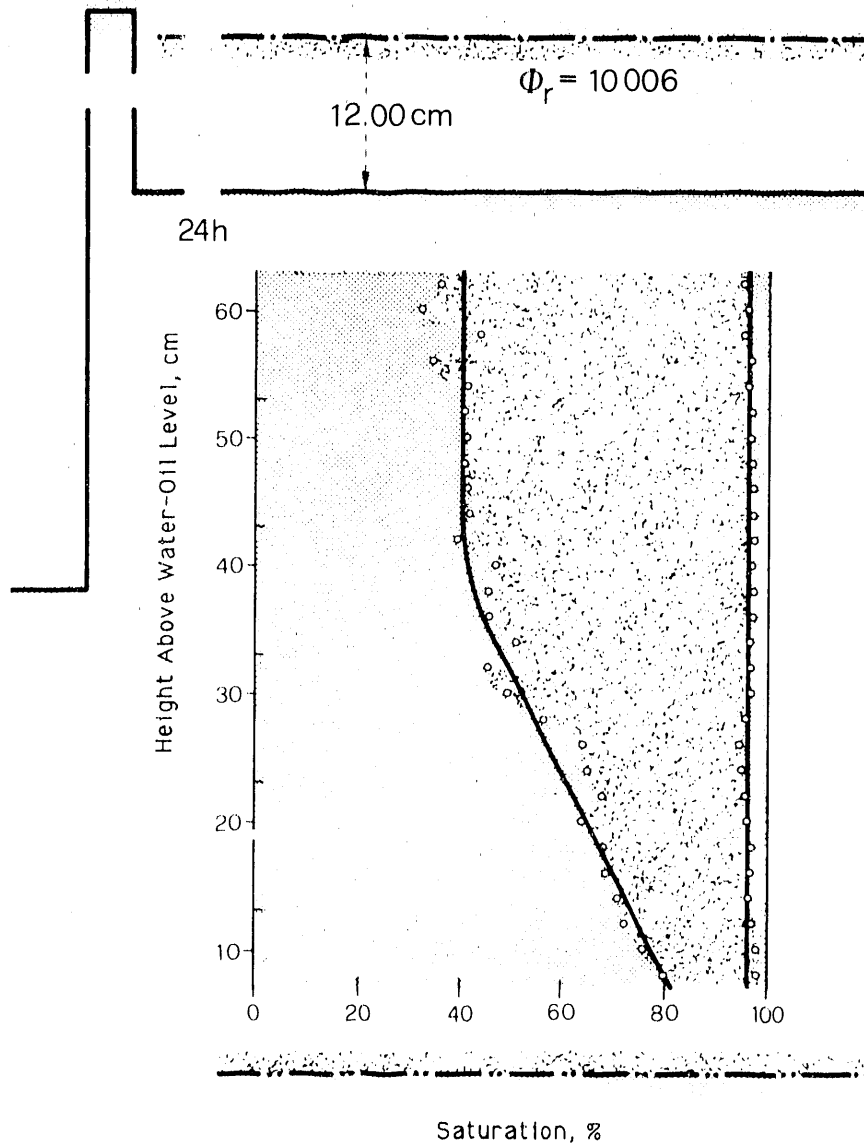


Experimental Series A: Diagram A18

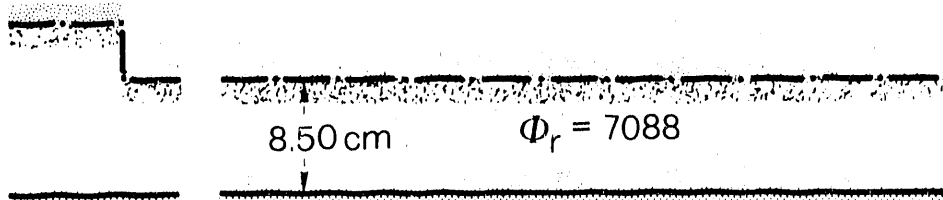


Experimental Series A: Diagram A19

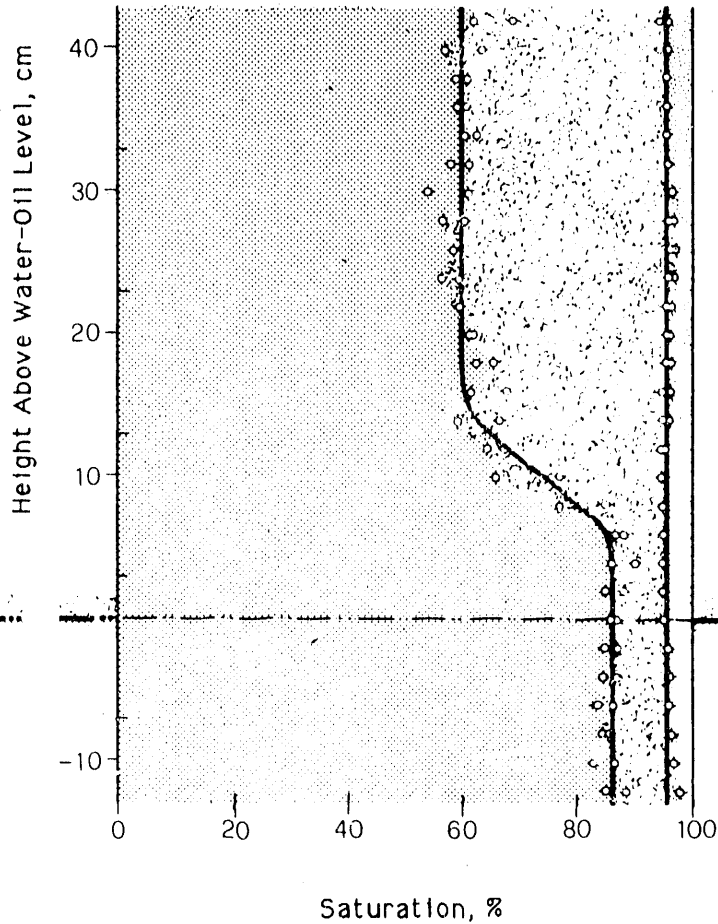
Water flowed upward at $\Delta\Phi \gg 1$
for 26 h.



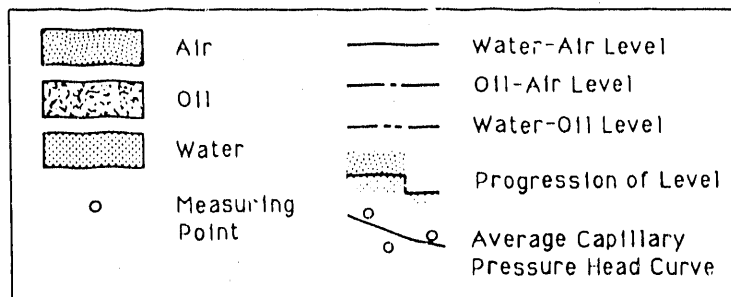
Experimental Series A: Diagram A20



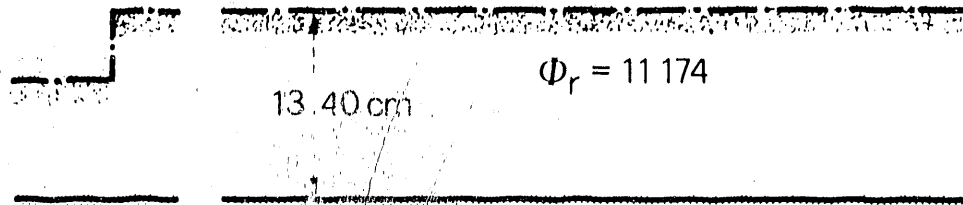
60h



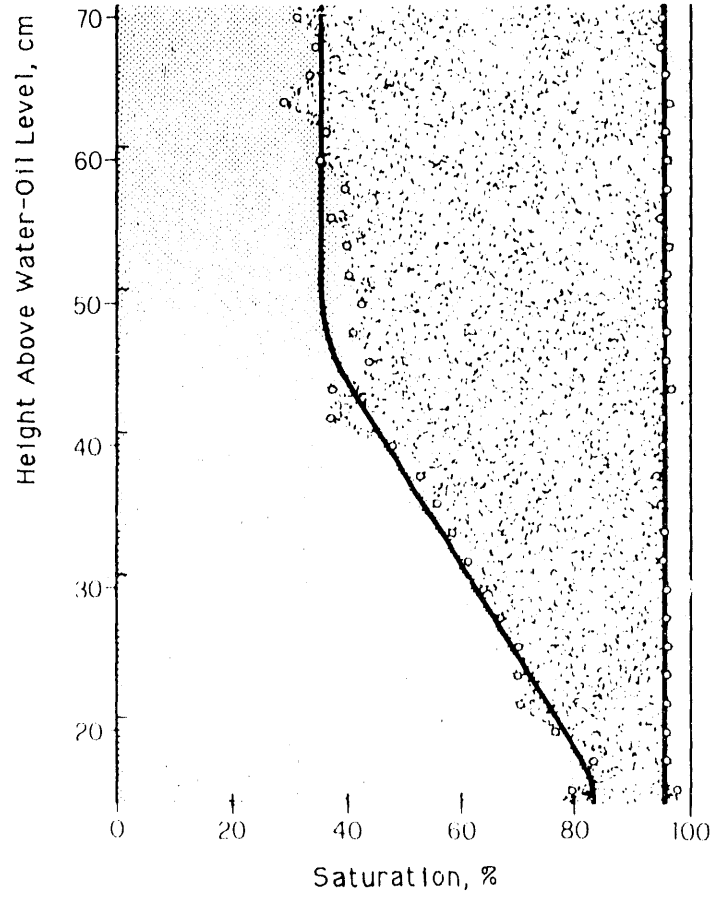
WOIM



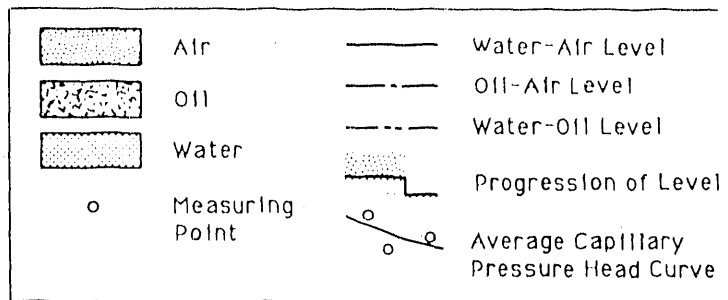
Experimental Series A: Diagram A21



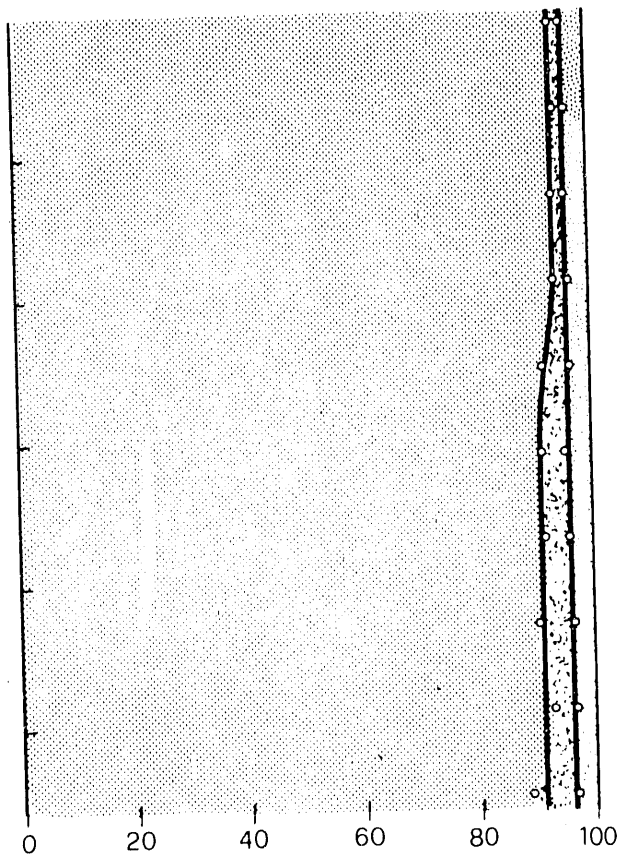
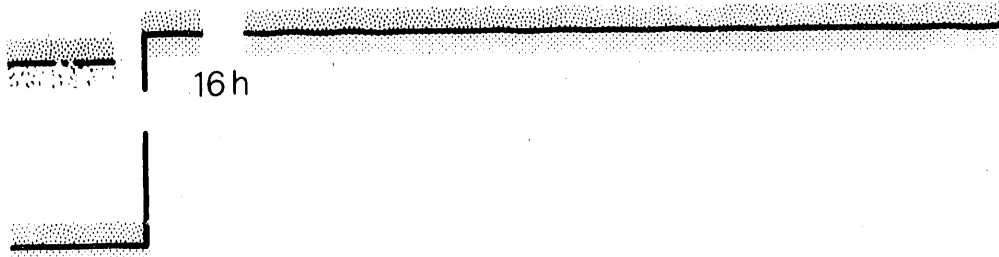
16 h



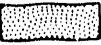






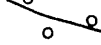
WODR



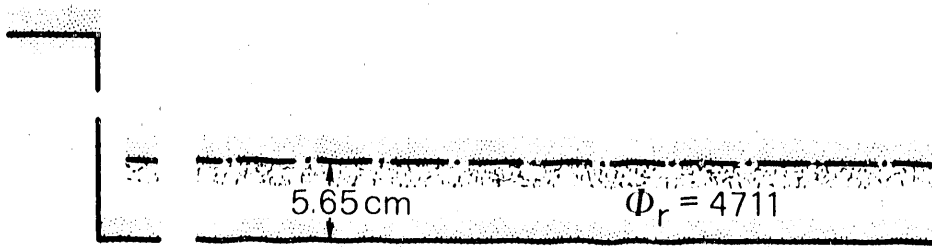
Experimental Series A: Diagram A22



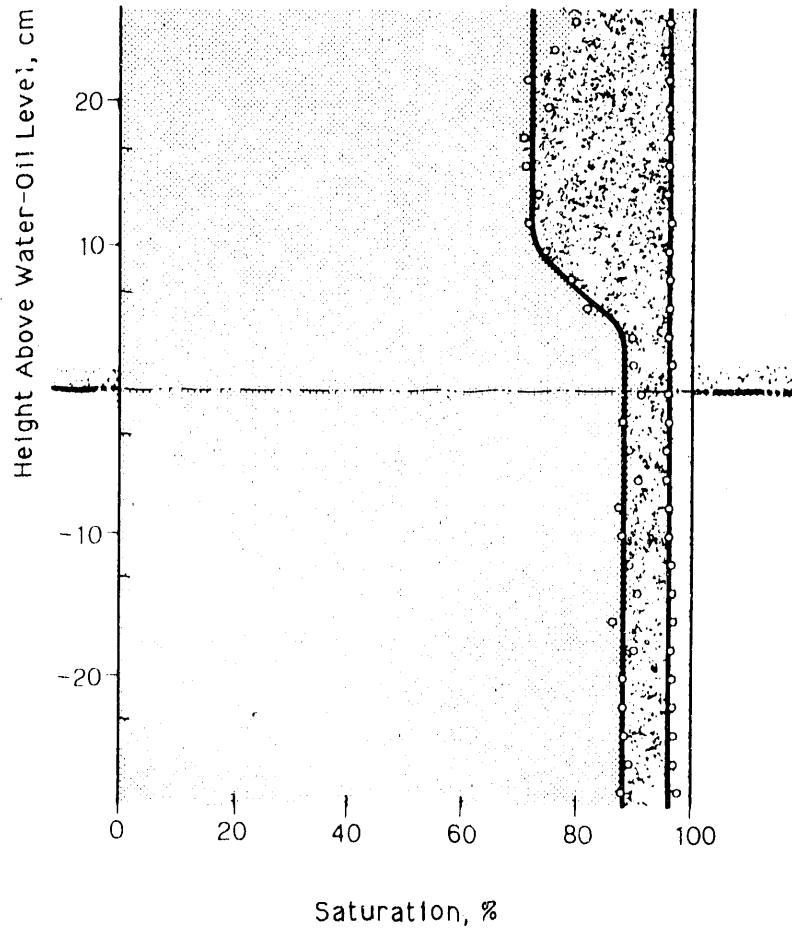
Saturation, %

	Air		Water-Air Level
	Oil		Oil-Air Level
	Water		Water-Oil Level
o	Measuring Point		Progression of Level
			Average Capillary Pressure Head Curve

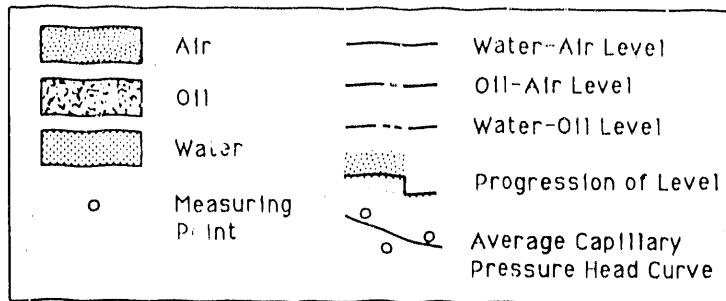
Experimental Series A: Diagram A23



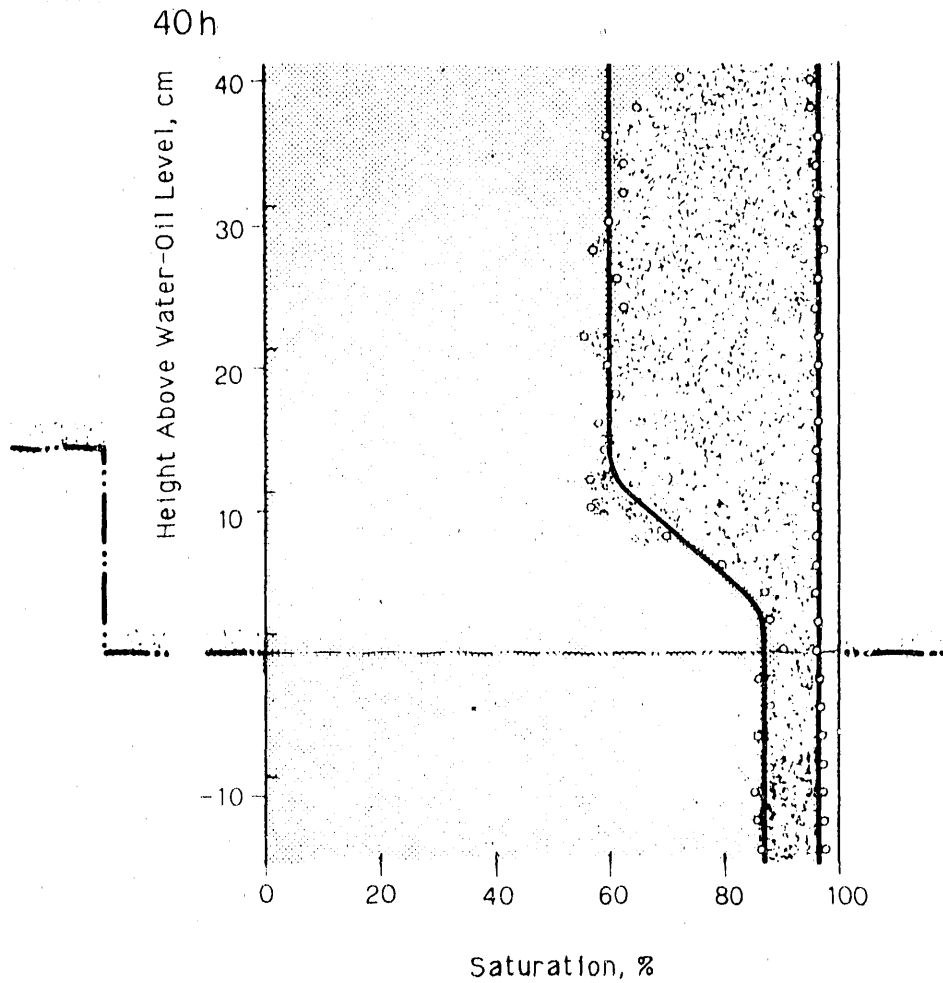
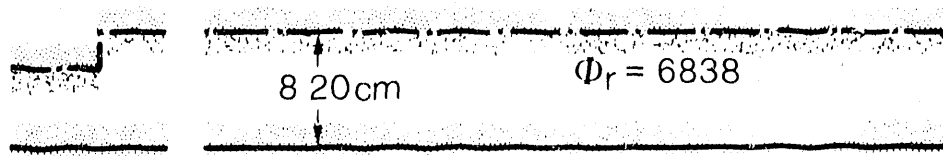
40h



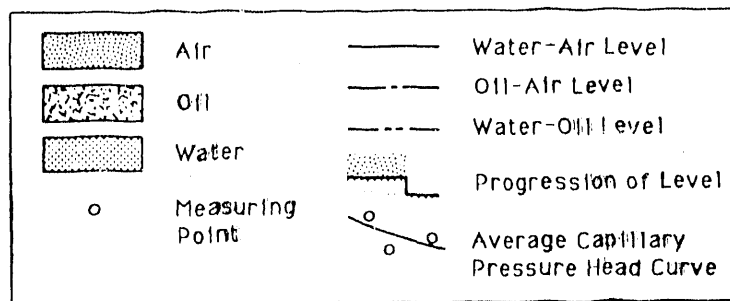
WODR



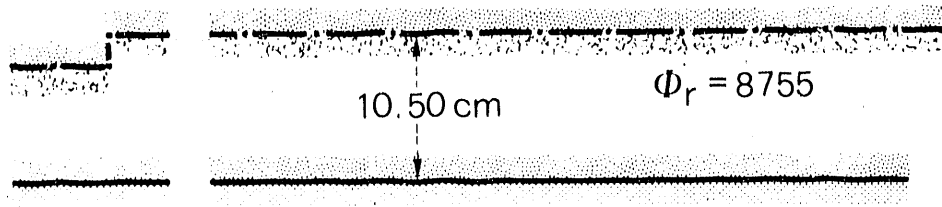
Experimental Series A: Diagram A24



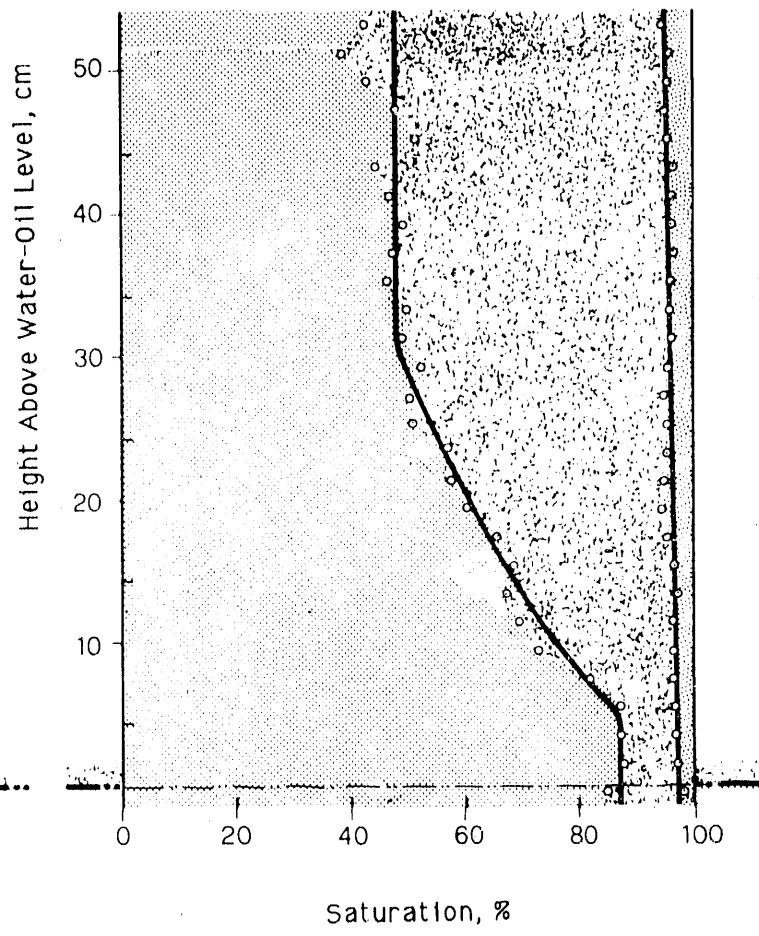
WODR



Experimental Series A: Diagram A25

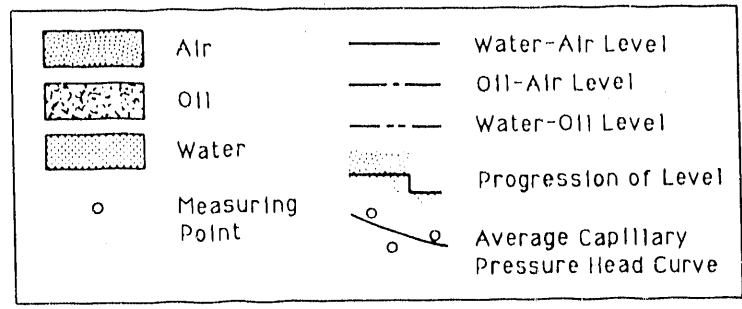


40h

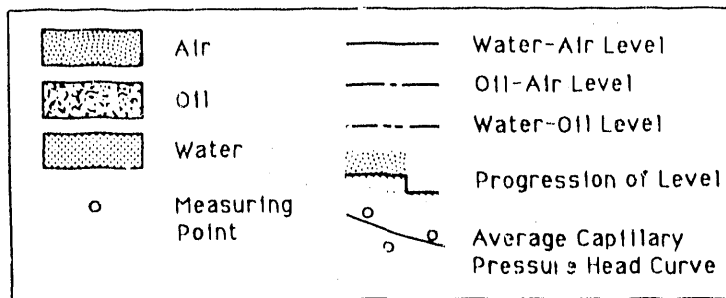
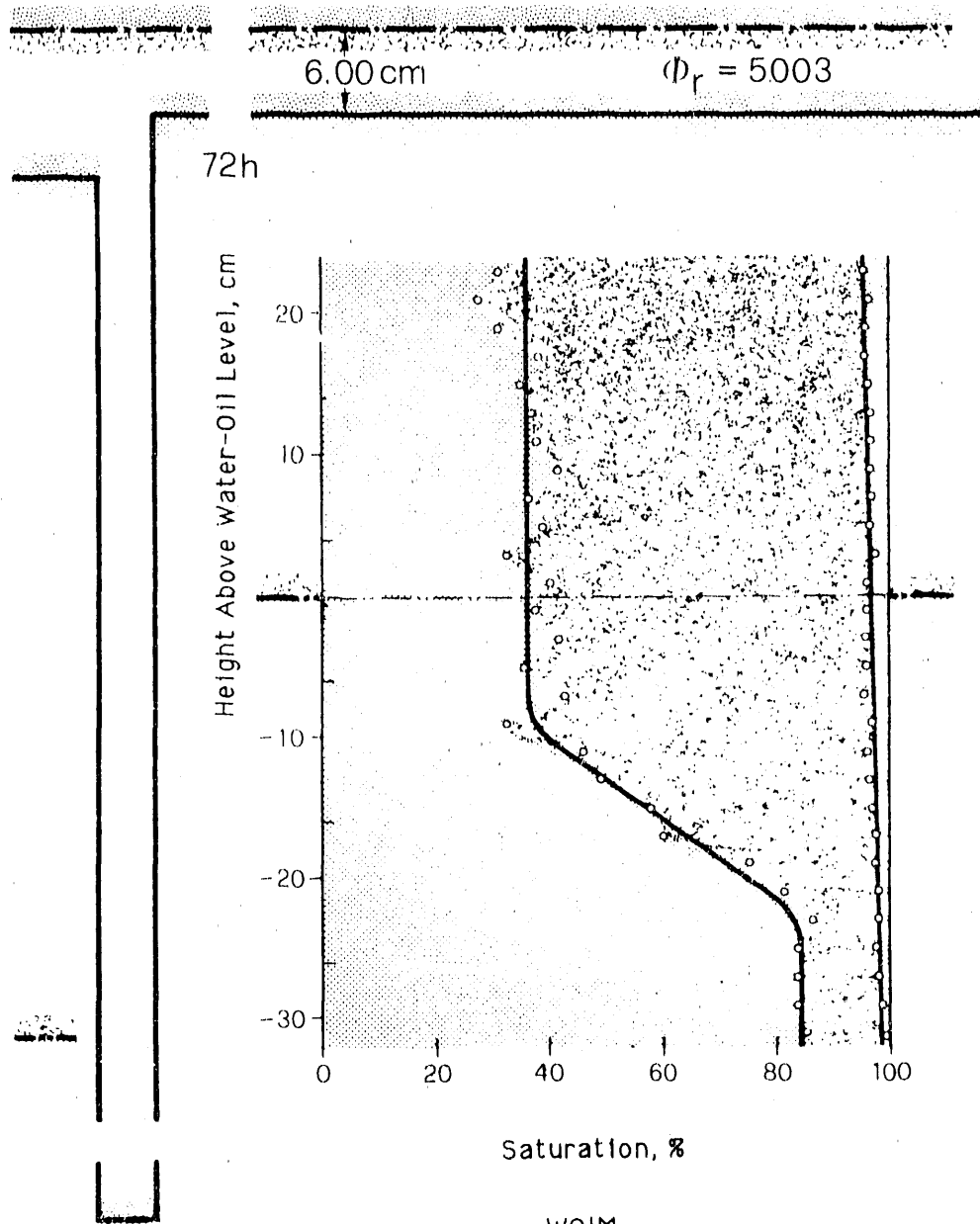


Saturation, %

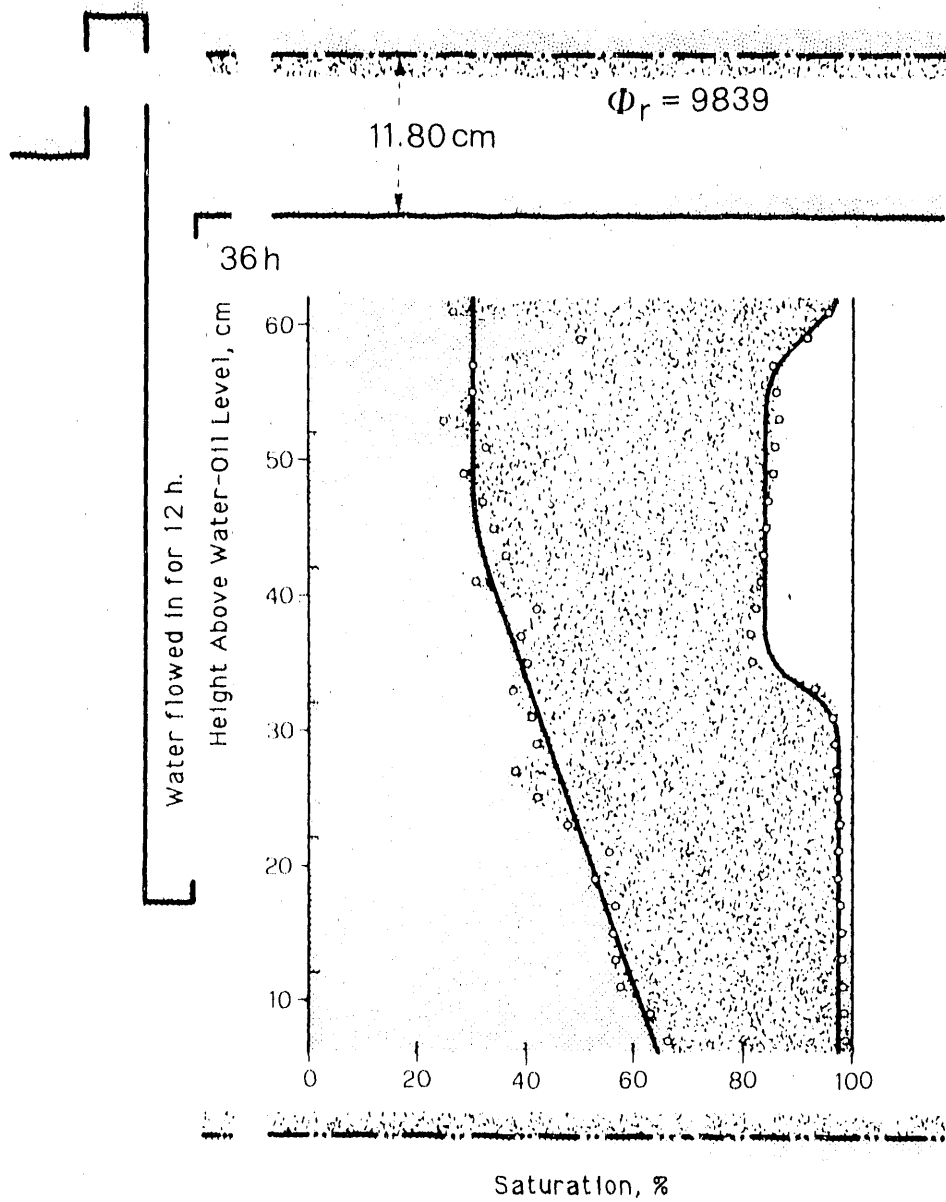
WODR



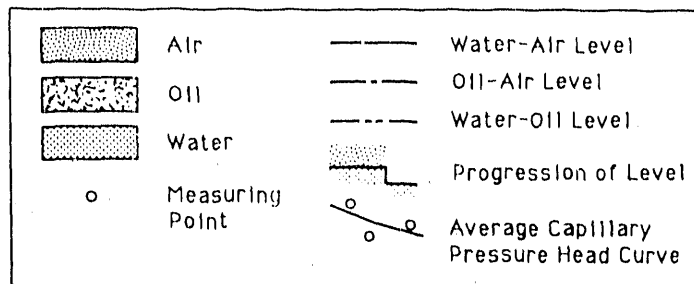
Experimental Series A: Diagram A26



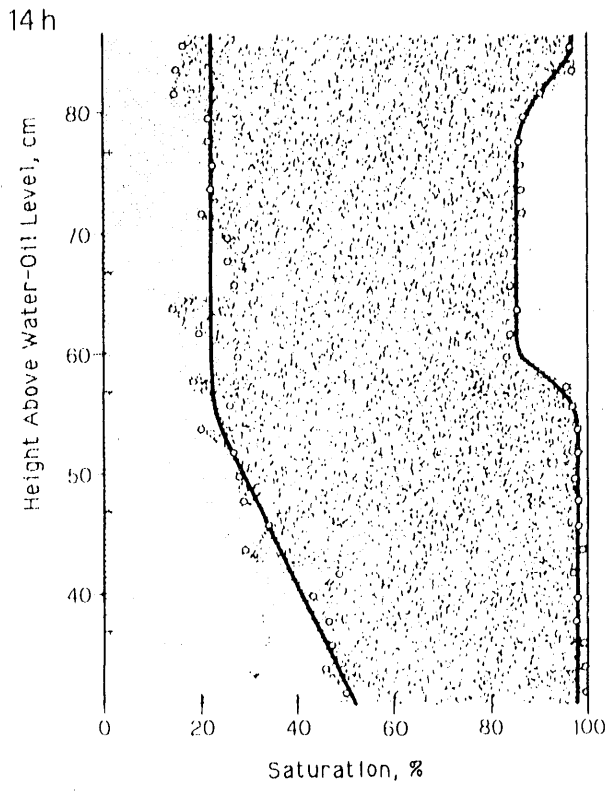
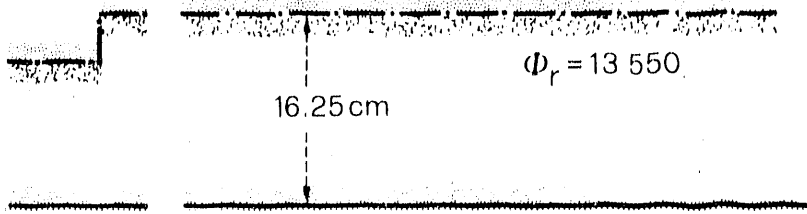
Experimental Series A: Diagram A27



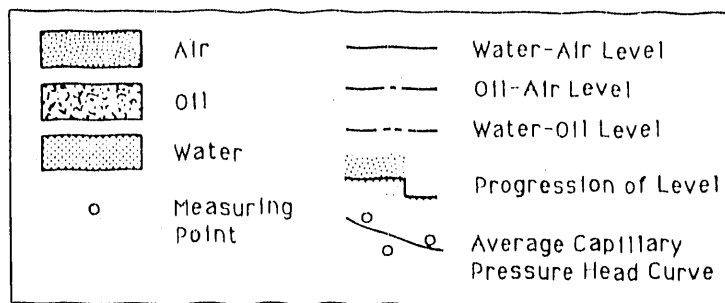
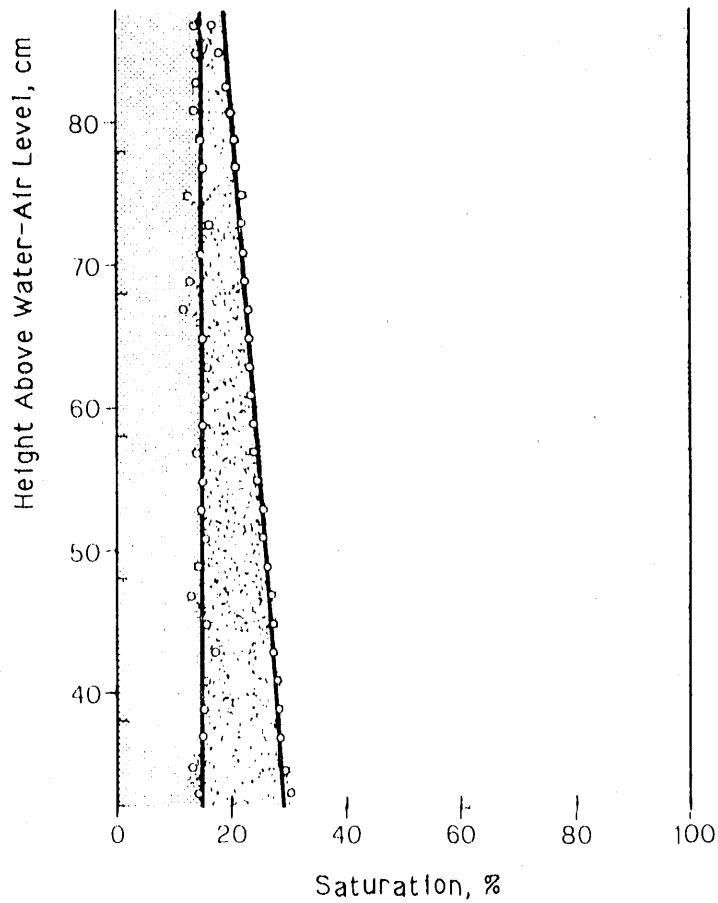
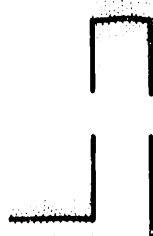
WODR



Experimental Series A: Diagram A28

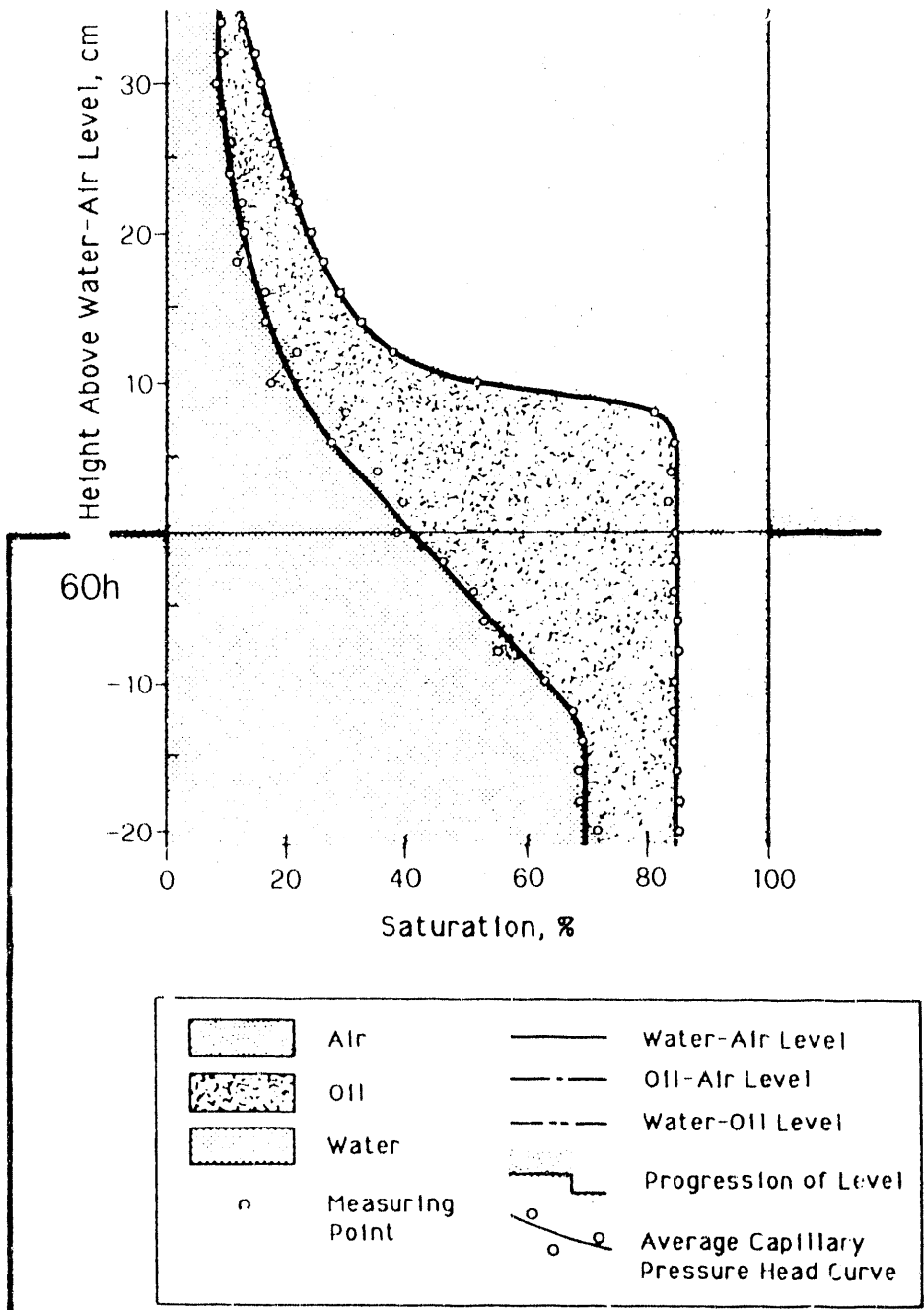


Experimental Series A: Diagram A29

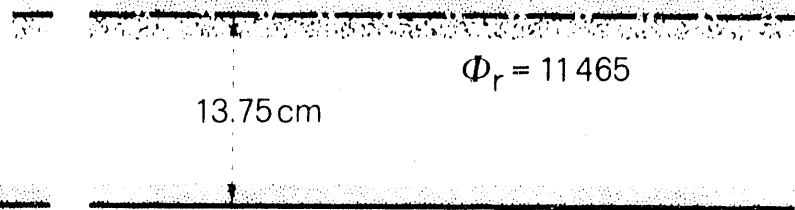


14 h

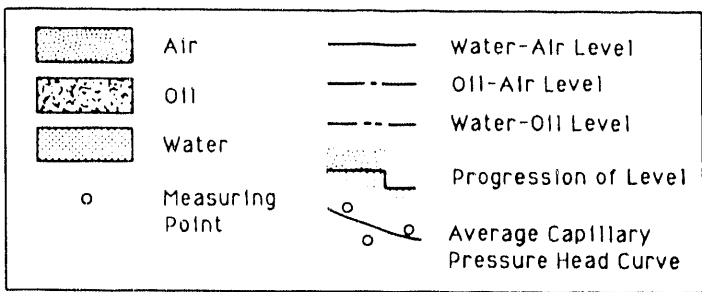
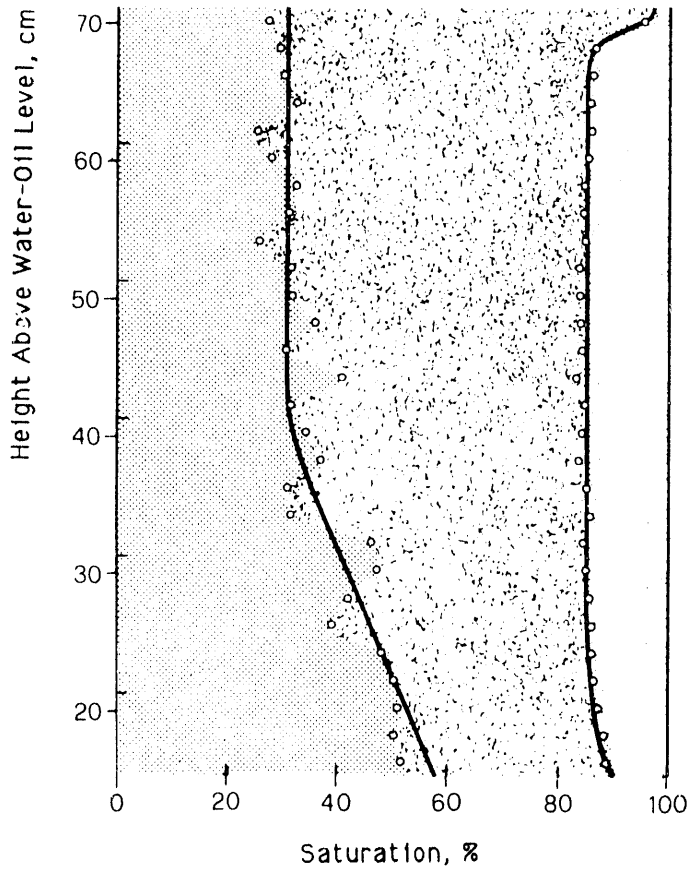
Experimental Series A: Diagram A30



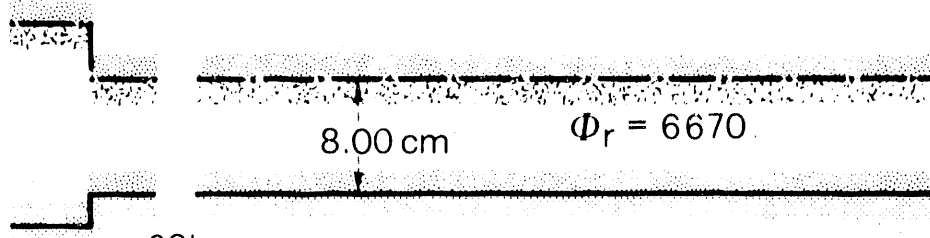
Experimental Series A: Diagram A31



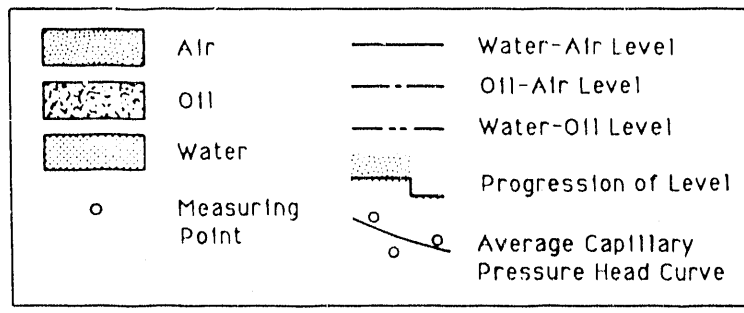
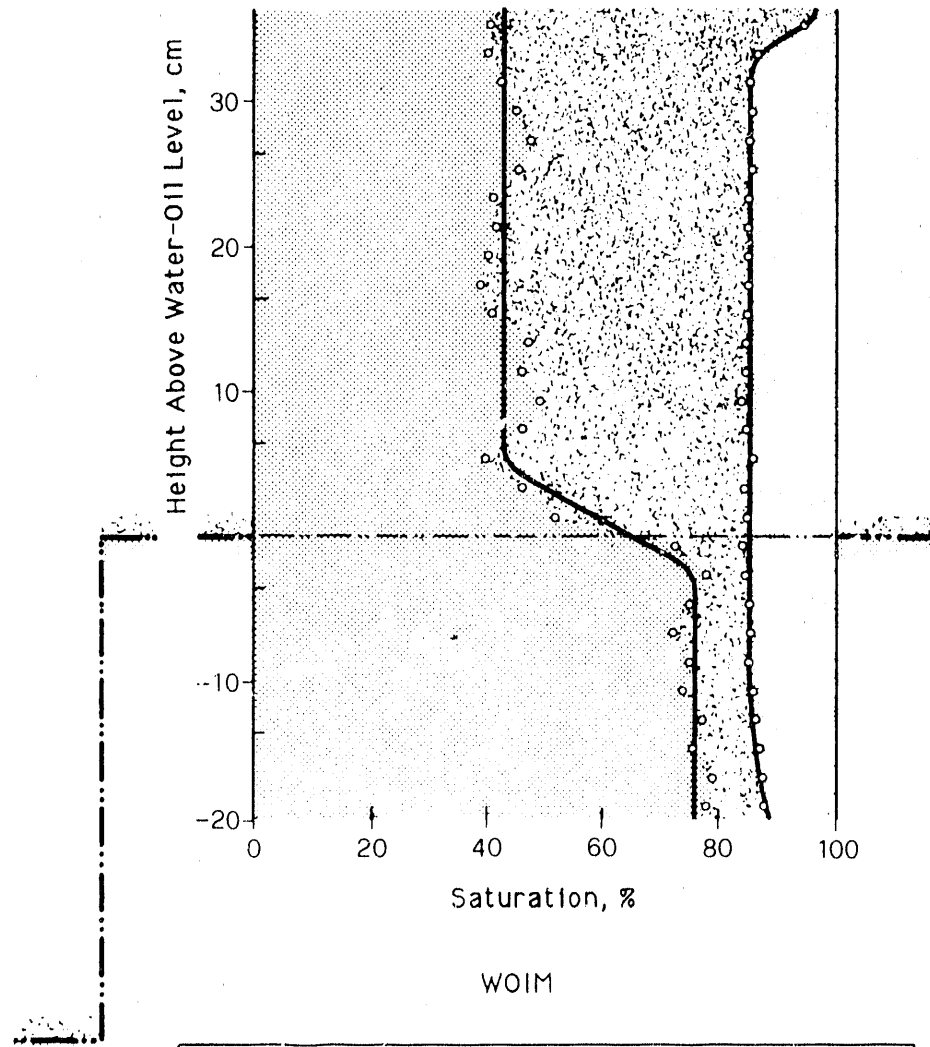
72 h



Experimental Series A: Diagram A32



62h



Experimental Series A: Diagram A33

7.3 COMMENTS ON EXPERIMENTAL SERIES A

Saturation diagrams from experimental series A are shown in the previous section. Comments on each diagram are given here.

A1. The measured primary $WLIM_{jfr1}$ curve lies lower than the theoretical primary $WLIM_{jfr1}$ curve shown in Figure 7.1.

A2. By slowly raising the water-air level over the course of 3 h, the air in the porous medium was slowly displaced. This procedure yielded the maximum residual air saturation, RSL_{max} . An RSL_{max} of about 25% confirms an earlier result.

A3. After lowering the water-air level to the bottom of the measuring area, the pure drainage curve reached equilibrium in less than 8 h.

A4. By lowering the water-air level below the bottom of the porous medium, the medium drained up to the maximum residual saturation of water, RSW_{max} , except at the area of discharge, where the saturation was higher because of an end effect. The end effect phenomenon refers to the retention of the wetting fluid during drainage at the boundary of the porous medium (Collins 1961, p. 141). The lower sand boundary was 34 cm below the lowest measuring point, and the continuation of the WLDR curve, as in Figure 7.1, is still recognizable. The water saturation asymptotically approaches the maximum residual saturation of water, RSW_{max} . According to previous results, RSW_{max} is 8% to 12%.

A5. The completely drained porous medium was resaturated with water over 4 h, and an approximate maximum residual air saturation was again reached. The water-air level was 17.75 cm from the soil surface. Oil was then infiltrated from the top into the water-saturated porous medium at maximum residual air saturation, thereby displacing the water. The first saturation measurements were made after 62 h. After 86 h, the displacement of water by the oil was considered complete because outflow of the displaced water had ceased.

The displacement of residual air by oil in the uppermost area of A5 could be the result of diffusion of the trapped air, as described by Adam and Corey (1968). This displacement occurred despite the fact that displacement of a residual fluid as a result of potential gradients is not possible because the

relative permeability is zero by definition. The 8% air saturation after 62 h, the 5% air saturation after 86 h at the uppermost measuring site, and the decrease from 20% to 4% at the second highest measuring point during the next 38 h (shown in diagram A6) give a measure of the time function for the diffusion effect.

The relatively long stability of the fluid levels (62 h and 86 h) is also one reason why the oil spread along the plexiglass wall against gravity. The adjusted oil saturation was in reality probably smaller.

A6. A small subsidence of the water-air level, with an oil-air level held constant, created a funicular oil saturation, even at the lowest measuring point. By the corresponding raising of the water-air level and lowering of the oil-water level, the oil was reduced at the lowest measuring point to insular residual saturation. Because the raising of the water-air level occurred slowly, the maximum insular residual oil saturation, RSO_{\max}^{ins} , was obtained. RSO_{\max}^{ins} has values of 6% to 12% according to other experiments. This range is confirmed in A6 (compare commentary B6).

A7. Sixteen hours after reducing the relative oil potential by lowering the oil-air level and maintaining the same water-air level, thereby increasing the water-oil level, the WOIM curve was still not fully developed. Equilibrium was not reached because a small drop-by-drop oil discharge could be observed. From this, one concludes that the WOIM curve of A7 was gradually approaching the lower WOIM curve of A6, as seen in Figure 7.2.

A8. Equilibrium was reached after lowering the water-oil level 20 cm. The static WOIM curve was obtained within 64 h. The funicular range (i.e., the range of nonconstant water saturation in the WO curves of A8) was displaced (compared to that of A7) its entire length. From this, one concludes that the subsidence of 20 cm was sufficient to allow the fully developed WOIM curve in A7 to be transformed into the fully developed WODR curve of A8. Therefore, the hysteresis range between nonprimary WODR and WOIM curves must nowhere be larger than 20 cm (compare Figure 7.2 to Figure 7.3).

A9. The WODR curves in A8 and A9 have almost the same shape (Figure 7.3). The two curves differ in position because of the 43-mm subsidence of the

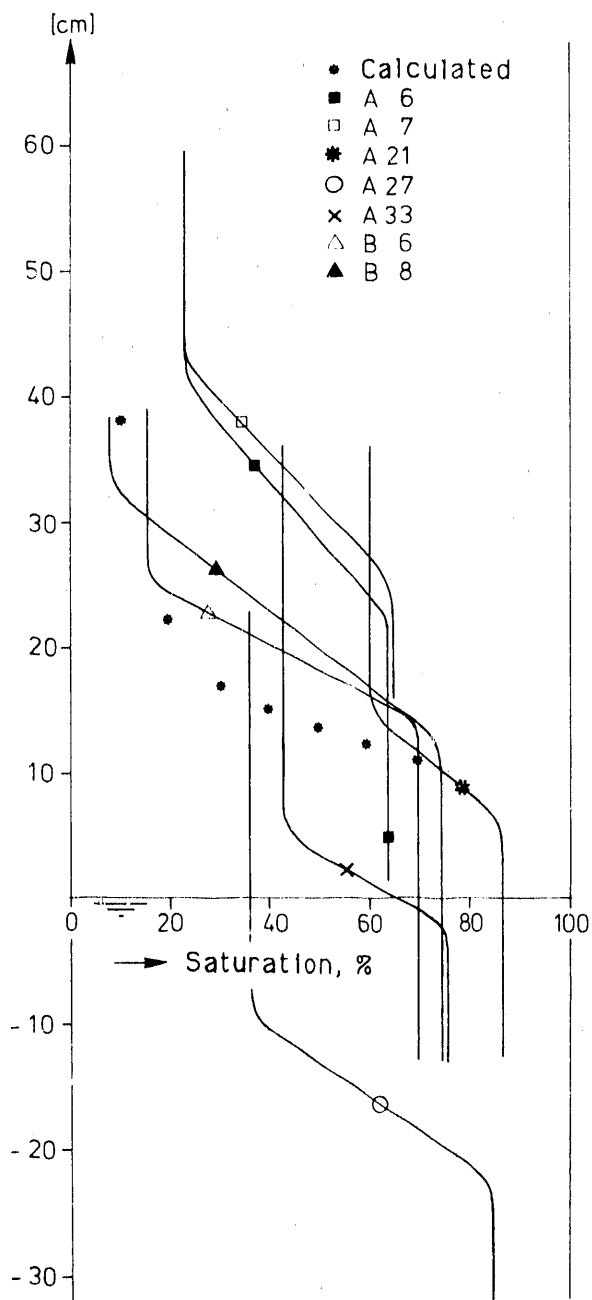


FIGURE 7.2. Measured and Calculated Saturation Diagram, WOIM

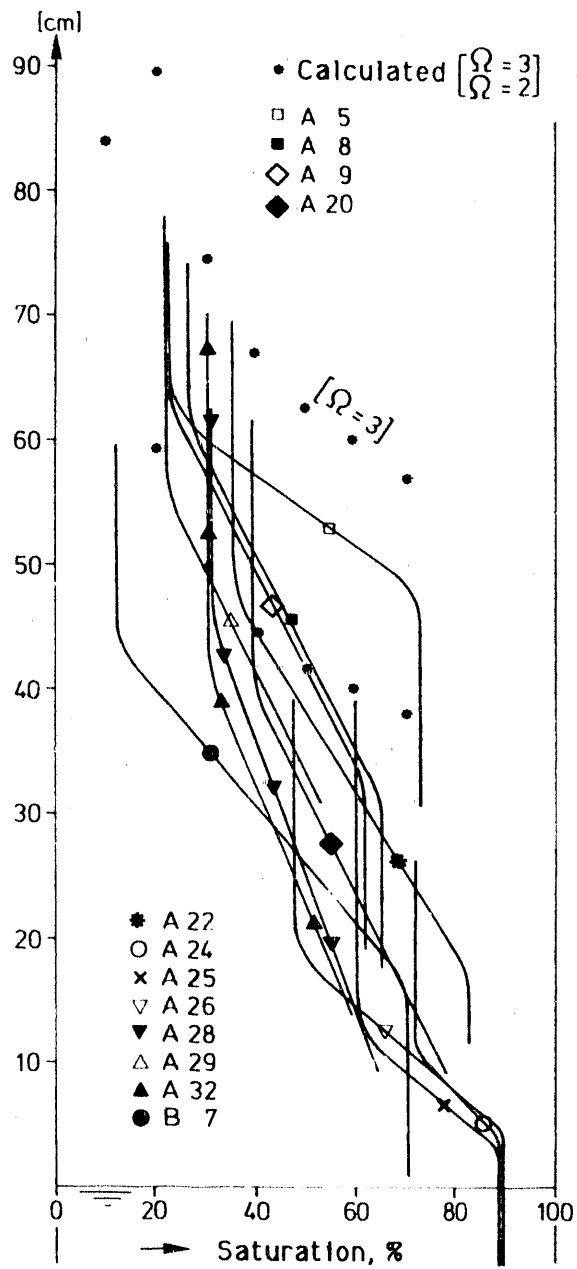


FIGURE 7.3. Measured and Calculated Saturation Diagram, WODR

water-oil level produced by raising the oil-air level 7.5 mm $[(7.5 \text{ mm})\rho_o / (1-\rho_o) = 43 \text{ mm}]$. Therefore, this confirms that the WODR curve in A8 or A9 is the fully developed curve.

A10. To obtain saturation diagram A10, the oil discharge was interrupted, the water-air level lowered below the sand bottom, and the porous medium exposed to air. The result was a porous medium drained of both water and oil. Next, the water-air level was slowly raised to just below the middle of the measuring range. In this manner, the approximate maximum residual saturations of air and insular oil was obtained.

During the oil and water drainage between A9 and A10, the oil saturation was not reduced to the residual oil saturation over the entire length of the column and thus did not reach pendular oil saturation because of the end effect that occurred between the oil and air. If RSO_{\max}^{pend} had been reached over the entire range, then RSO_{\max}^{ins} (in A10) had to be nearly twice as large as RSO_{\max}^{ins} , which is in agreement with Equation (2.1). Furthermore, the funicular oil above the constant water-air level showed that oil was still draining from the area above.

The form of the OLIM curve is identical to the theoretical curve in Figure 7.1. To what extent their positions (i.e., their heights above the oil-air level) agree cannot be said because the oil potential was not measured, and thus the position of the oil-air level is not known.

A11. Over 2-1/2 h, the column was filled with water by raising the water-air level above the top of the sand. During this time, nearly 1 dL of oil flowed out. The water-air level was then lowered almost to the lower border of the measuring range. After 24 h, the A11 saturation diagram was produced. Despite the outflow of the deciliter of oil, the oil saturation was still in the funicular range just above the water-air level.

A12. After once more raising the water-air level above the top of the porous medium along with a weak water flow from bottom to top for nearly an hour, an additional 1.1 dL of oil flowed out. Fourteen hours after lowering the water-air level to the height shown in A11 yielded, the saturation diagram in A12 was measured. The area representing the oil in A12 is smaller than in A11, and the difference accounts for the 1.1-dL loss, as shown by the following

calculation. Using a porosity of 43% (see A1), an oil content of 547 cm³ in A11 and 433 cm³ in A12 was calculated for the first 30 cm above the water-air level in the plexicolumn (see Figure 3.3), whose cross-sectional area is 25 cm². The difference was 114 cm³ and corresponds to the 1.1-dL oil outflow.

The saturation diagrams shown are somewhat misleading compared to a field-scale situation because during three-dimensional propagation in the field, equilibrium is only reached when the oil has disintegrated to residual saturation. This oil disintegration occurs in such a way that the funicular oil spreads out along the propagation surface. Because of gravity, funicular oil flows from above to the propagation surface until pendular residual oil saturation is attained above, and funicular oil flows from below to the propagation surface until insular residual saturation is attained below. Pendular residual oil saturation is located to the right of the stationary contaminated capillary rise curve between water and air, and the insular residual oil saturation is located to the left of this stationary curve, as shown in Figure 7.4. Within the funicular range, the model of Schiegg (1979) places the stationary curve in the middle of the residual oil at the expense of not tracing portions of the water and air curves. The transition between these three ranges is continuous. Figure 7.4 helps to explain A12.

Finally, the column was filled with water and a strong flow was induced from bottom to top. As was to be expected from the analysis of A12, only a small amount of oil could be flushed out this way.

A13. After draining the porous medium of both water and oil, the column was filled slowly (but not drop-by-drop) with oil until the oil-air level was 20 cm above the bottom of the measuring range, where it was held constant. In this way, an OLIM curve was formed. This curve was fully developed in less than 10 h. It is identical to the calculated OLIM curve (Figure 7.5). That the residual air saturation did not equal the maximum value of nearly 25% can be due to the fact that the raising of the oil-air level probably did not occur slowly enough; that is, drop-by-drop.

A clearly recognizable hallux, or bulge, formed in the curve between water and oil. According to Schiegg (see Appendix B), a hallux is an encroachment of the function between saturation and capillary pressure head

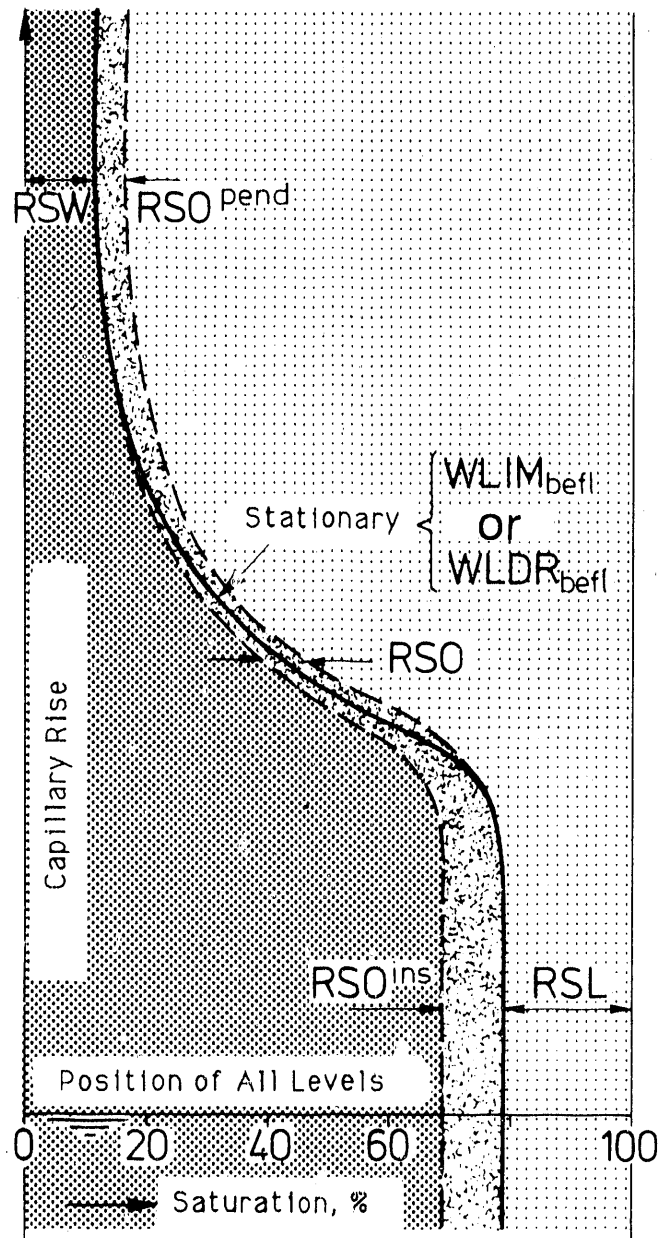


FIGURE 7.4. Distribution of the Residual Oil in the Water-Air Capillary Fringe

into the range of insular nonwetting fluid saturation within the transition zone between the funicular to insular saturation region. The hallux phenomenon is the result of the nonformation of insular nonwetting fluid saturation. This phenomenon is explainable at the microscopic pore level and not from a macroscopic view. At the funicular to insular transition zone elevation, during a shift from drainage to imbibition in pore bodies, the

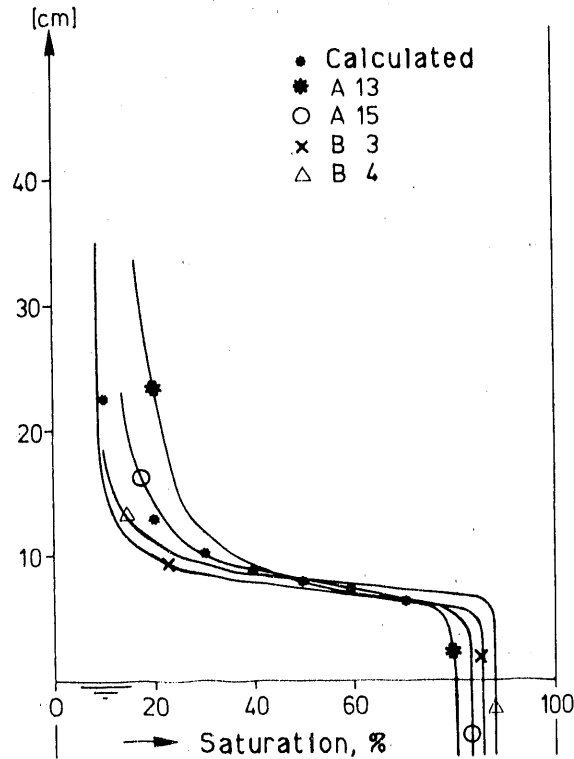


FIGURE 7.5. Measured and Calculated Saturation Diagram, OLIM

nonwetting fluid can more readily escape before pinching at the pore throats occurs. The water-oil hallow observed in A13 can be explained by the slow drainage of the still funicular water above the oil-air level, which yielded a WODR curve.

A14. Lowering the oil-air level about 20 cm created an OLDOR curve. The measured OLDOR curve in A14 lies somewhat higher than the calculated curve (Figure 7.6). The shapes of the calculated and measured OLDOR curves agree very well. A too-short equilibration time does not explain the higher position of the calculated OLDOR curve versus the measured one (even after moving both curves to obtain the same residual air saturation), because the measured OLDOR curve was expected to be fully developed after the 16-h equilibration time (see commentary B5).

A15. Slowly raising the oil-air level created an OLIM curve. The OLIM curve was fully developed in less than 14 h. It agrees very well with the calculated OLIM curve (Figure 7.5).

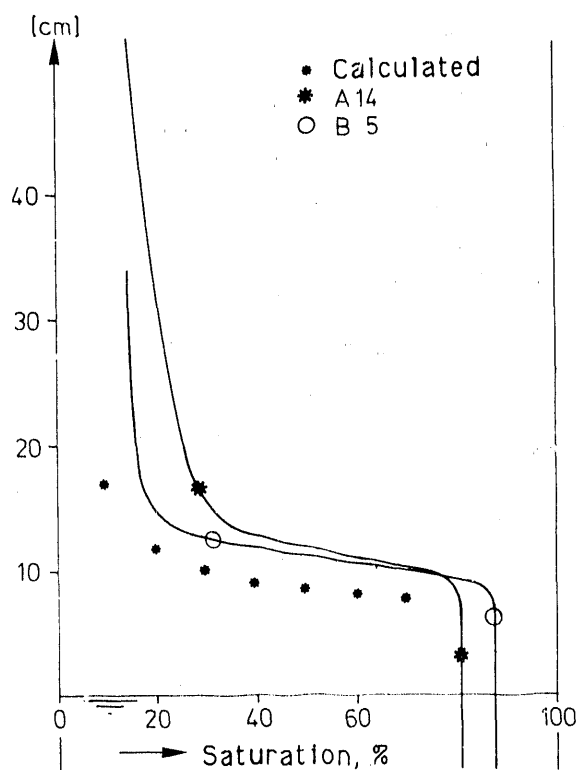


FIGURE 7.6. Measured and Calculated Saturation Diagram, OLDR

Next, the column was completely drained, then completely filled with water, and finally a strong water flow was induced from bottom to top for 72 h. In this way, the oil was flushed out to its residual saturation. Considering the end effect (see commentary A4) and the fact that the capillary rise was important relative to the height of the column, complete drainage required an extraction of the fluids with a vacuum pump.

A16. 14 h after lowering the water-air level to about 20 cm above the bottom of the measuring range, the contaminated WLDR curve was established. From A16, it is clear that by using the strong water flow to flush the porous medium, the existing insular oil saturation was reduced below its maximum value of 12%. The residual oil saturation was reduced to the maximum value of pendular residual oil saturation (~4-6%) only in the upper portion of the porous medium despite the strong and long water flow (see commentary A23). This is confirmed by the fact that no funicular oil collected by drainage in the funicular to insular nonwetting saturation conversion zone after lowering

the water-oil level. Above the capillary fringe, this would have resulted in the conversion of the insular oil saturation to a pendular oil saturation that was about half as much.

The $WLDR_{befl}$ curve of A16 is identical in form and position with the theoretical curve shown in Figure 7.7 after moving it to obtain the same residual air saturation. The minimum residual air saturation in the lower portion of A16 is a result of the long and strong water flow used to flush the porous medium.

A17. After raising the water-air level about 22 cm, the fully developed WLIM curve was established in less than 14 h. The position of the conversion from funicular to insular is identical to the calculated one (see Figure 7.8). The funicular range in the measured curve is steeper than in the calculated one.

The S shape of the funicular to insular conversion can be explained by the slow raising of the water-air level. The newly formed residual air saturation is the same as its maximum value of about 25%, whereas the residual air

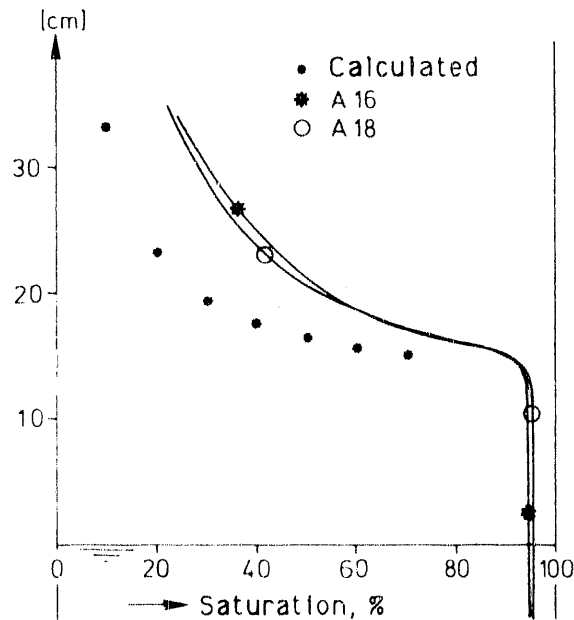


FIGURE 7.7. Measured and Calculated Saturation Diagram, $WLDR_{befl}$

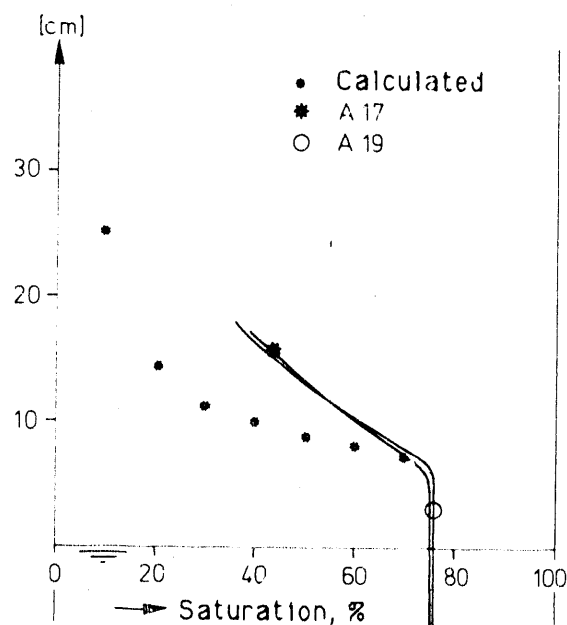


FIGURE 7.8. Measured and Calculated Saturation Diagram, $WLIM_{bef1}$

saturation, already present in A16, is much smaller. Thus, the old conversion from funicular to insular oil saturation in A16 was preserved next to the newly formed one. This led to the S-shaped curve.

A18. The contaminated WLDR curves created by lowering the water-air level about 40 cm are identical to that of A16 (also see Figure 7.7).

A19. After once more raising the water-air level about 30 cm, the $WLIM_{bef1}$ curve was established. According to Figure 7.8, it is identical to the $WLIM_{bef1}$ curve of A17 (a commentary on the S-shaped curve development was already presented).

A20 to A33. A strong upward flow of water for 26 h reduced the residual air saturation to a minimum. Next, oil was introduced. Then, WO curves were established for various values and different developments of the relative potential, ϕ^r . The relative potential is the oil potential relative to the water-air level.

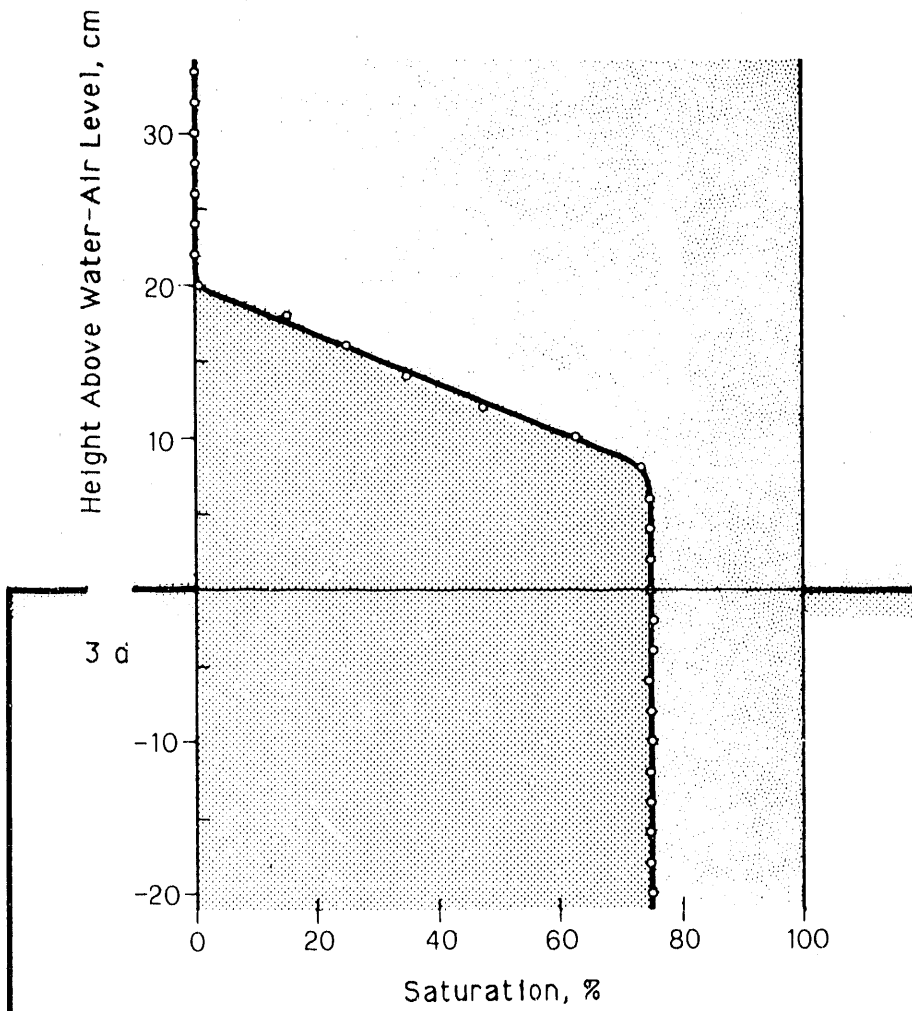
The extreme free-fluid level positions among the separate saturation diagrams were used to regenerate the porous medium. For example, to obtain A23, a strong water flow for 16 h produced residual saturation values for oil

and air. From the shape of the reduced insular oil saturation in A23, one can conclude that reducing the insular residual oil saturation by flushing (as described by Schiegg; see Appendix C) seems to be more probable closer to the discharge site. A23 was probably similar to the curve from which A16 originated.

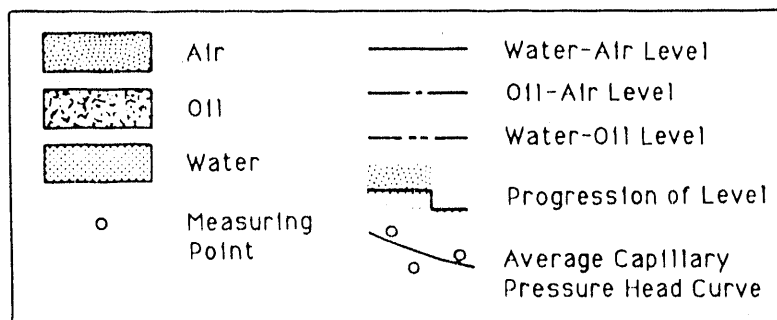
A27 resulted from the rapid subsidence and raising of the water-air level with a constantly held oil-air level. To obtain A28, the column was filled with water after interrupting the oil feed, and thus the oil was displaced to insular saturation. Next, the upper portion of the column was drained of water. A contaminated WLDR curve analogous to A16 was established. Its funicular to insular conversion can still be detected below the middle of the measuring range of A28. These steps produced a larger residual air saturation of more than 15% because of the drop-by-drop addition and correspondingly slow rise of the water-air level, as opposed to the fast raising of the level in A27. Finally, large portions of funicular water were displaced by a newly established oil-air level with a relative potential of about 10000 erg/cm^3 . However, the residual air saturation, varying over the height, could not be influenced by this potential. The small air saturation at the top of the sand can be explained by diffusion (see A5). The distribution of the residual air was not influenced by a change in the oil potential between A28 and A29.

The interruption of the oil feed associated with A29, and the short rise and subsequent subsidence of the water-air level to the bottom of the sand produced extensive drainage of both water and oil (A30). As the water-air level slowly rose, the funicular oil that existed because of the end effect also rose. This produced the saturation diagram A31, which stabilized in less than 60 h. The OLIM curve agrees with curves A13 and A15. Because the oil potential in A31 was not measured, the position of the oil-air level is not known, and thus a verification of the position of the OLIM curve in A31 is not possible. The same situation exists for the WO curve.

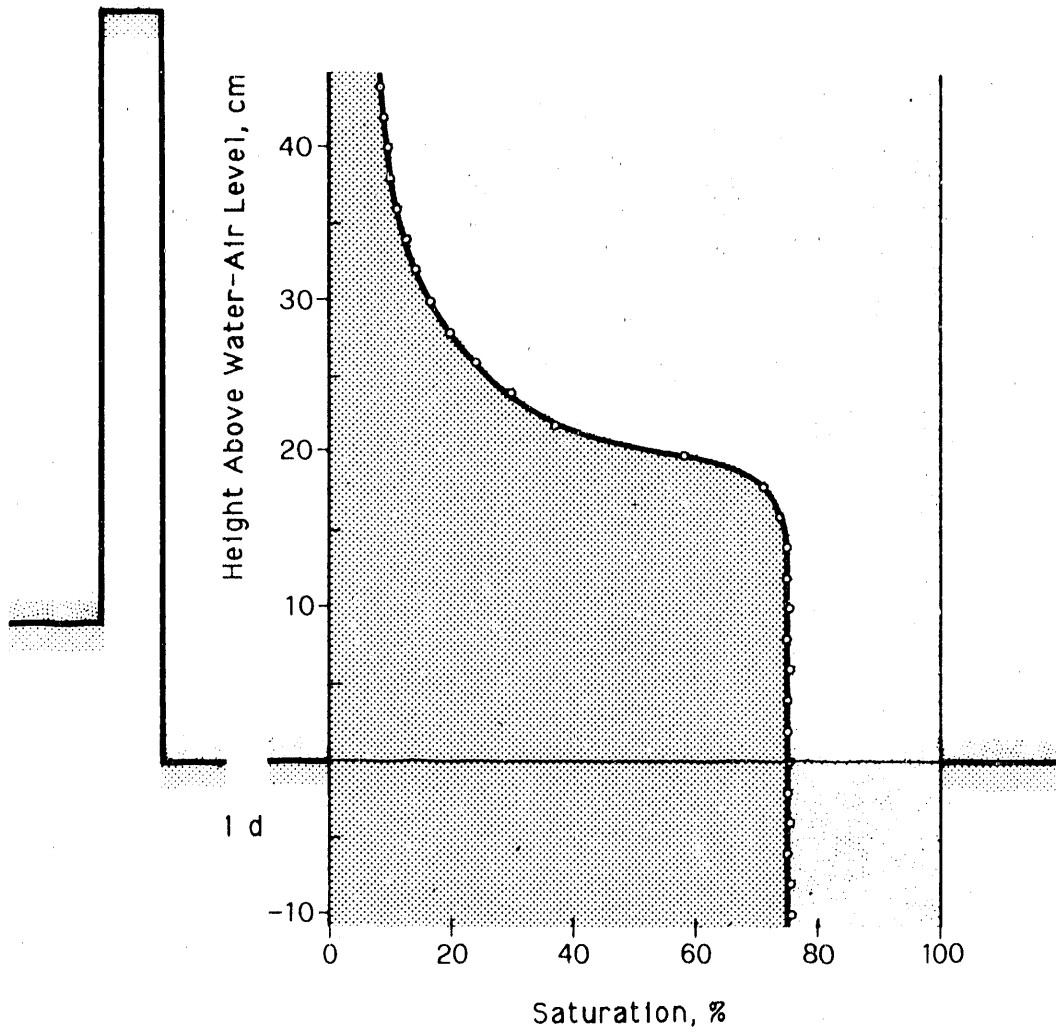
Continuing the slow raising of the water-air level to above the porous medium yielded a maximum residual air saturation for the entire measuring range neglecting the diffusion effect at the top of the sand already mentioned in A5. The maximum residual air saturation was maintained in the saturation



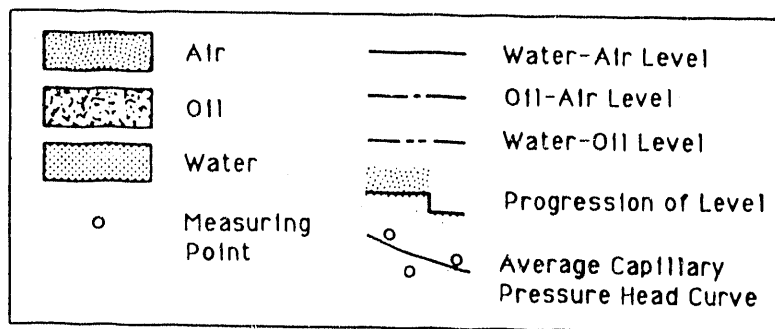
Primary WLIM jfr1



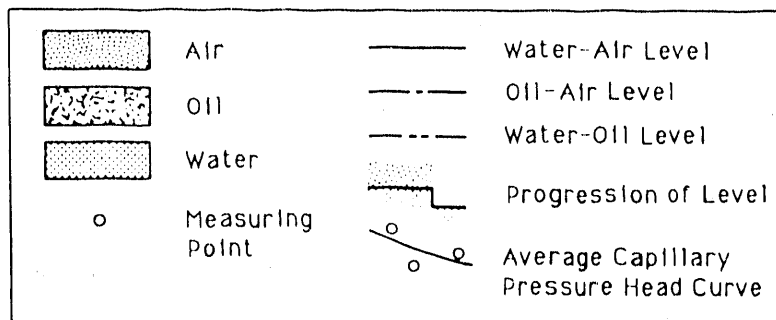
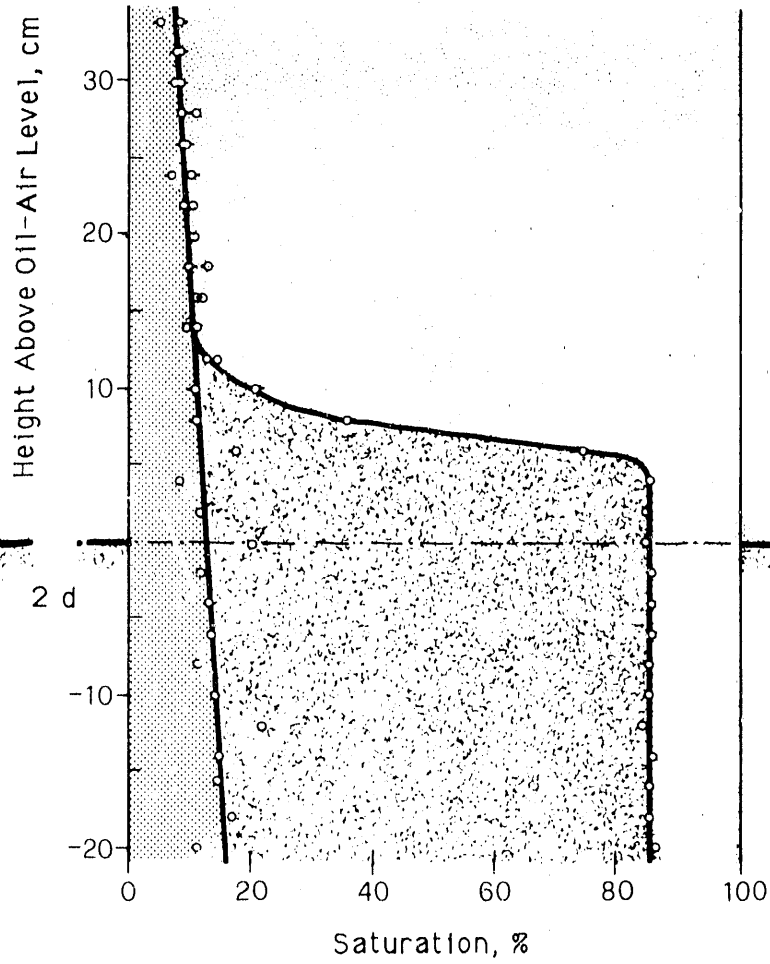
Experimental Series B: Diagram B1



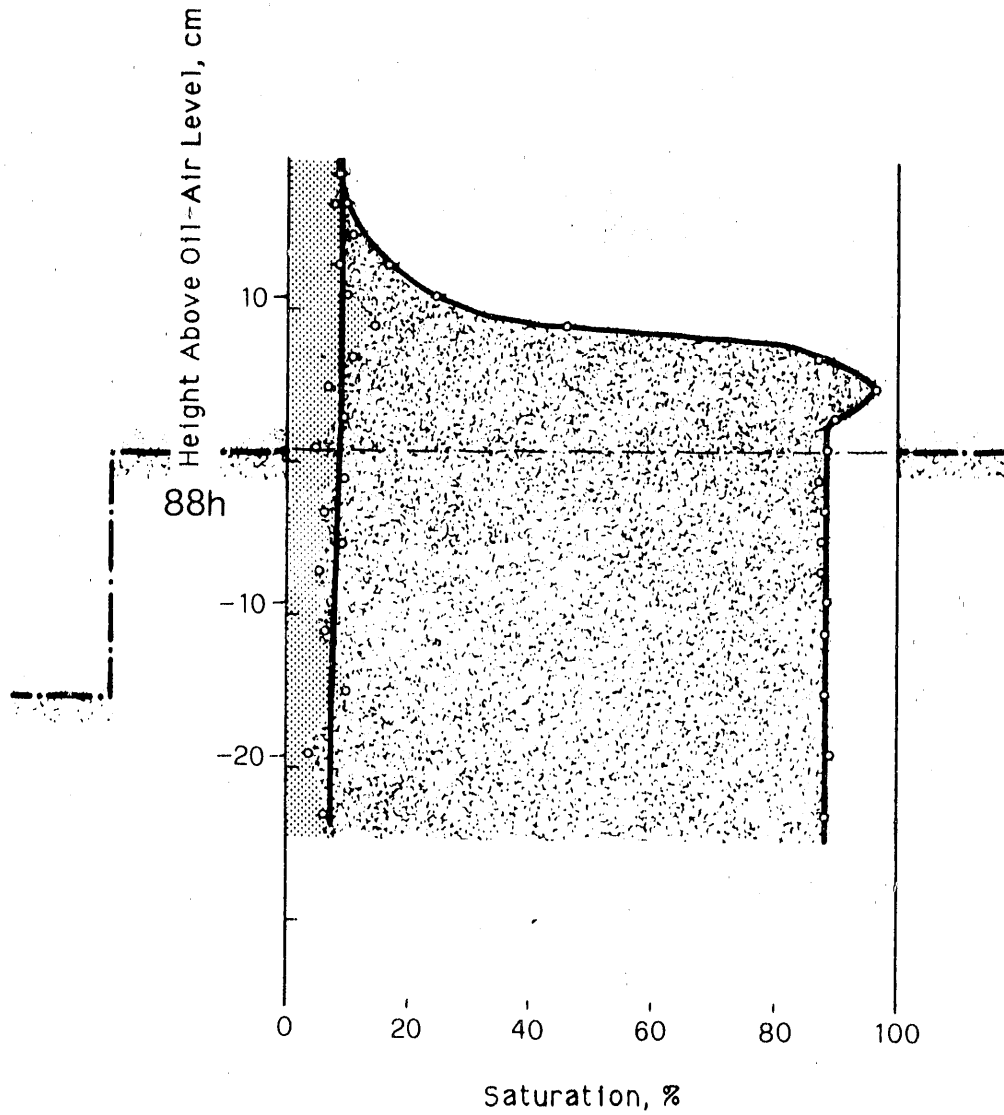
WLDRjfrl



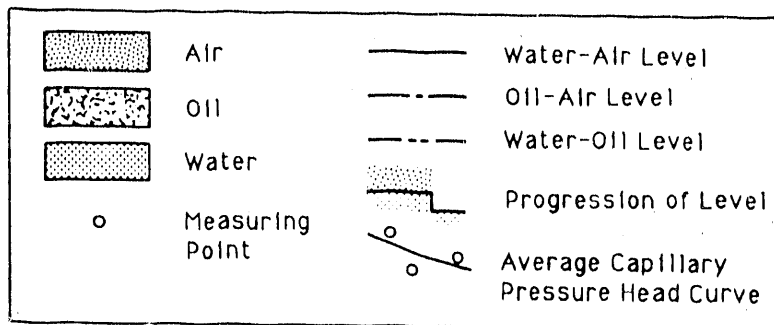
Experimental Series B: Diagram B2



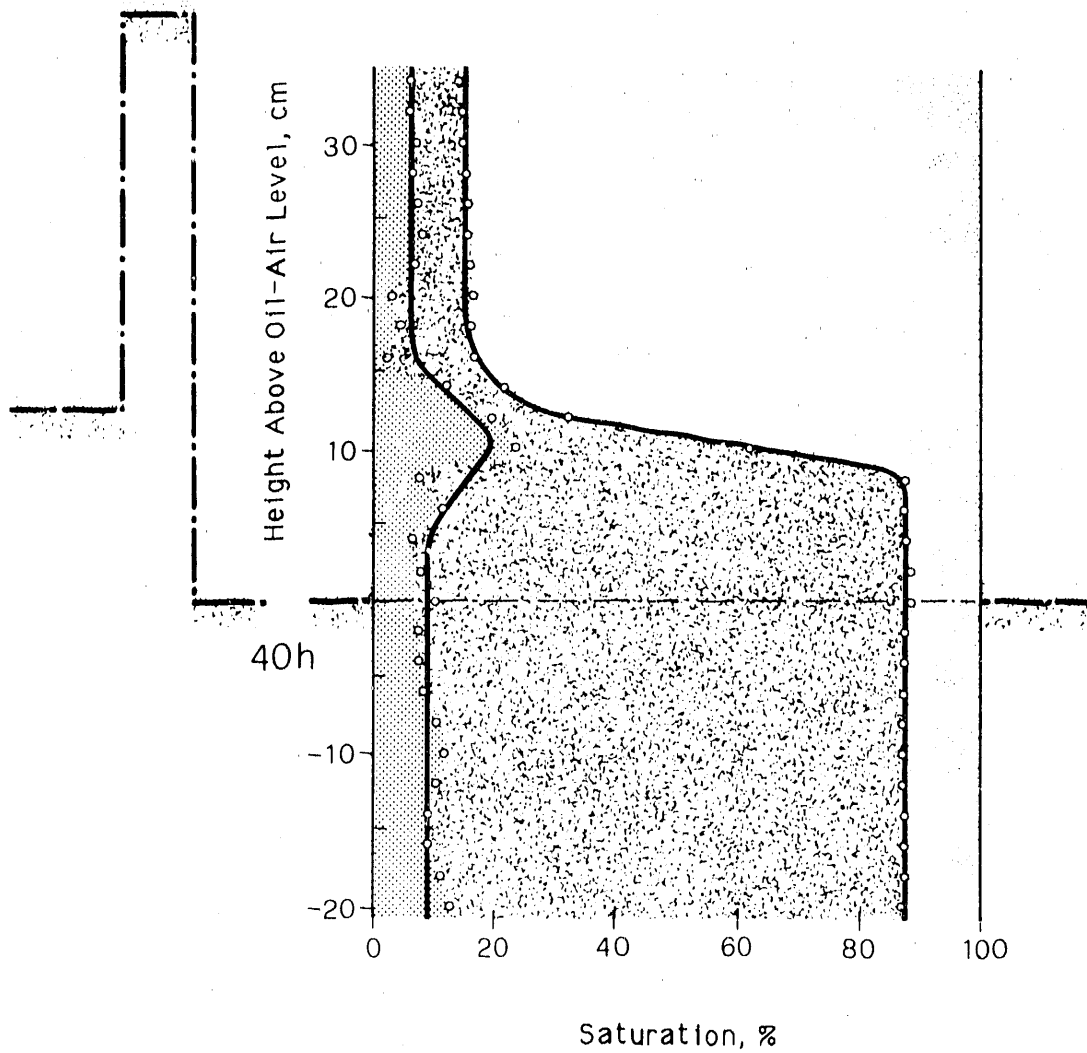
Experimental Series B: Diagram B3



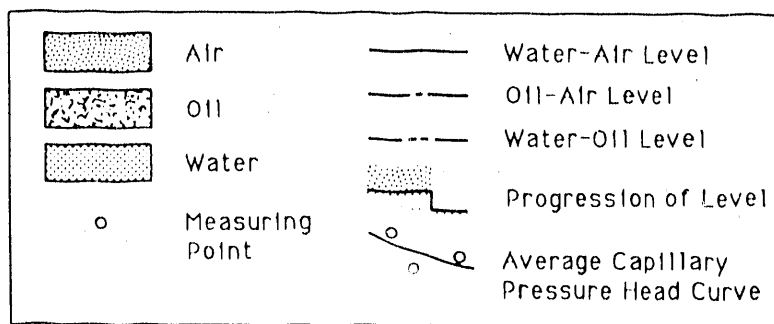
Primary OLIM



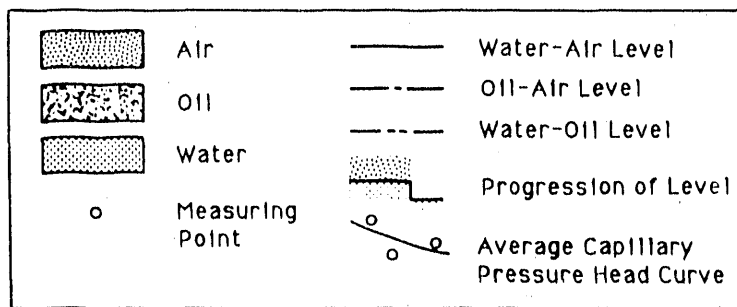
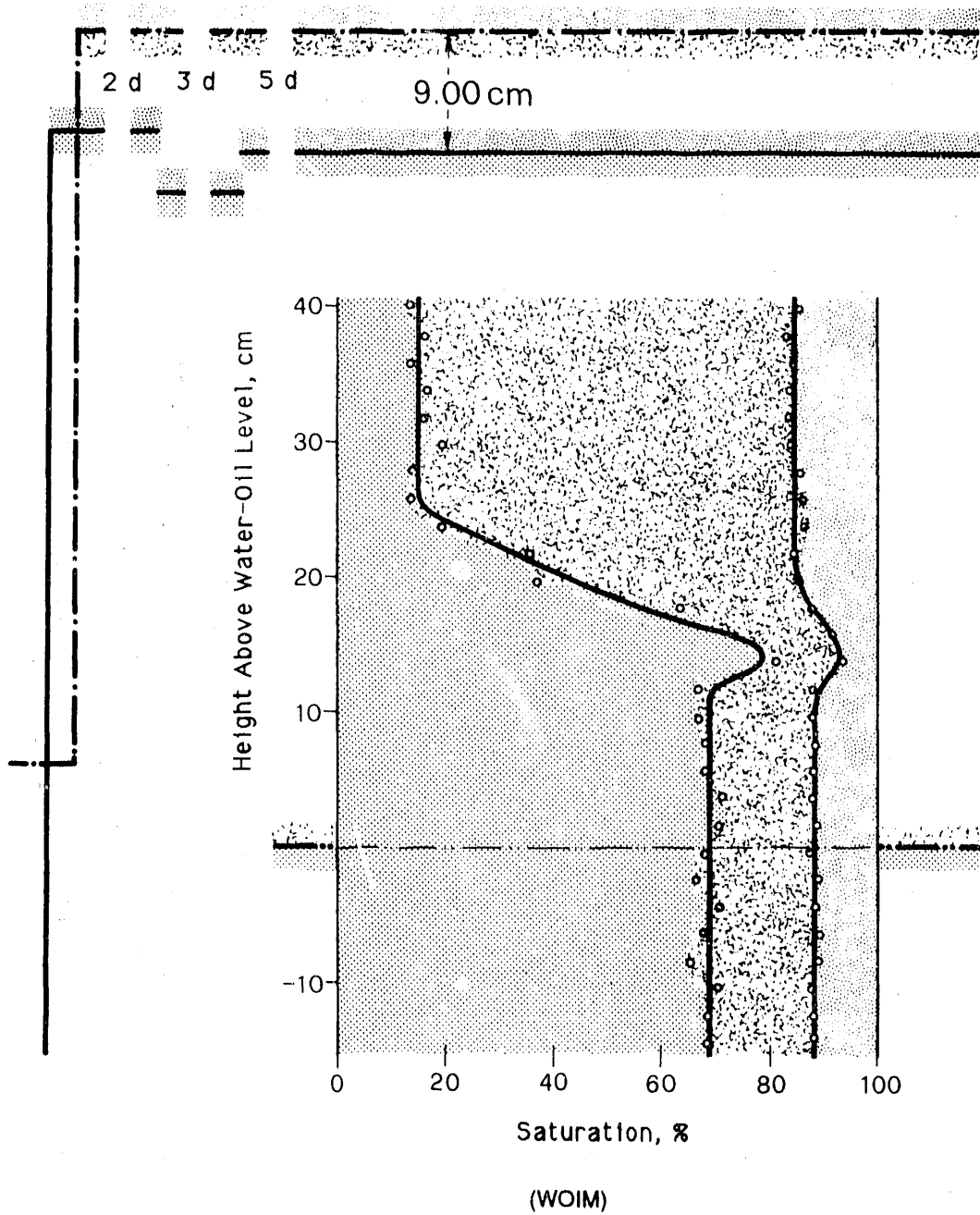
Experimental Series B: Diagram B4



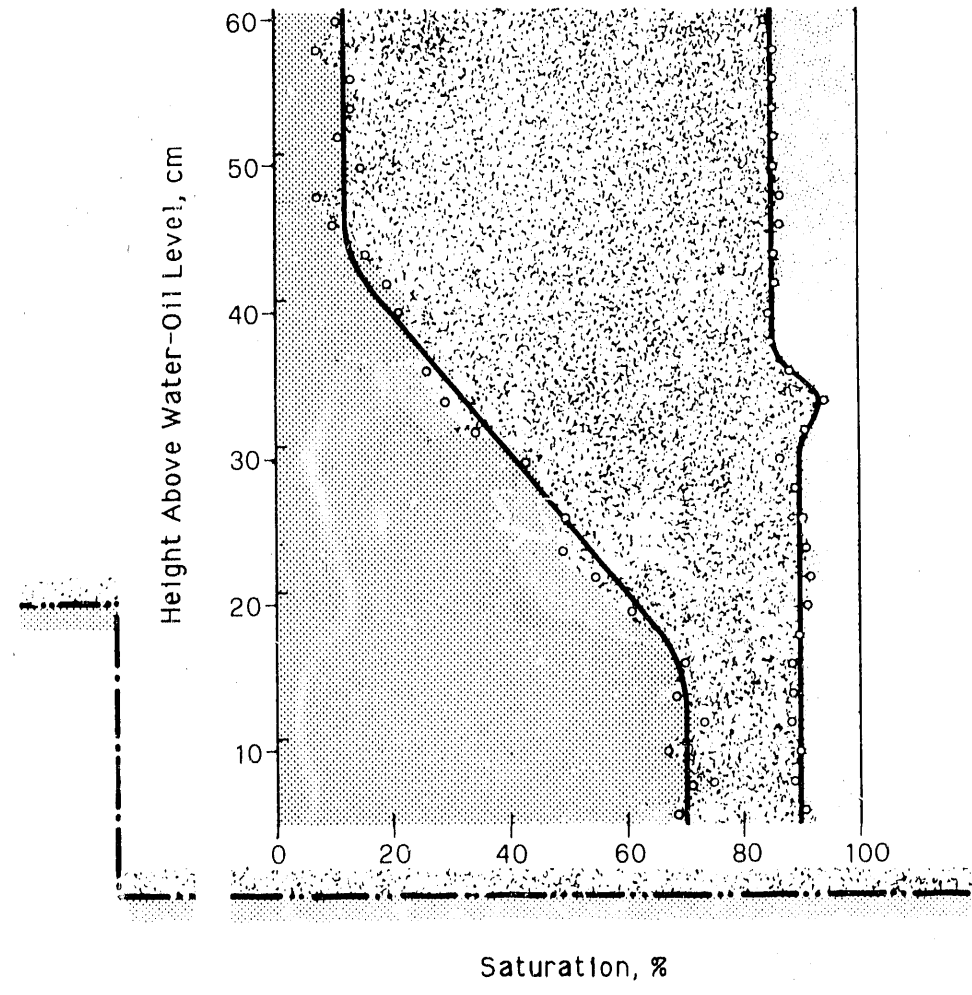
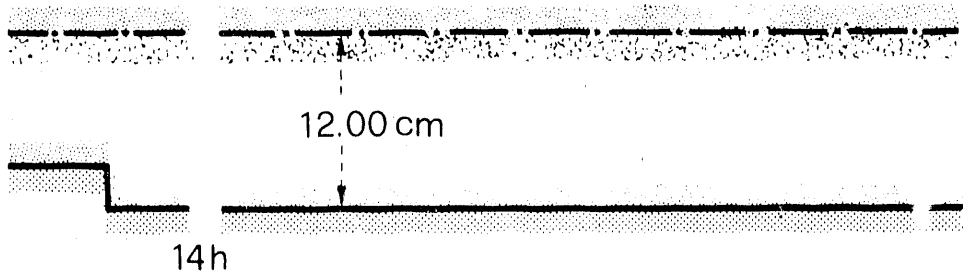
OLDR



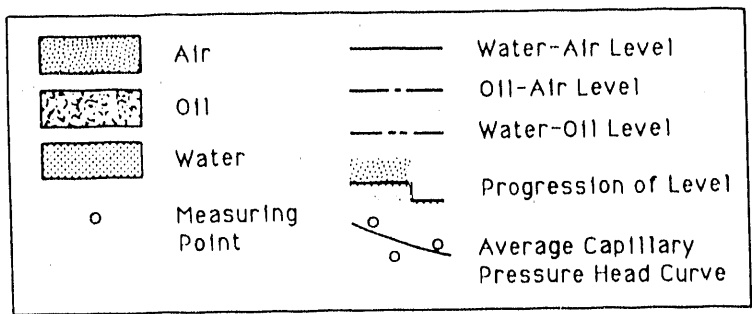
Experimental Series B: Diagram B5



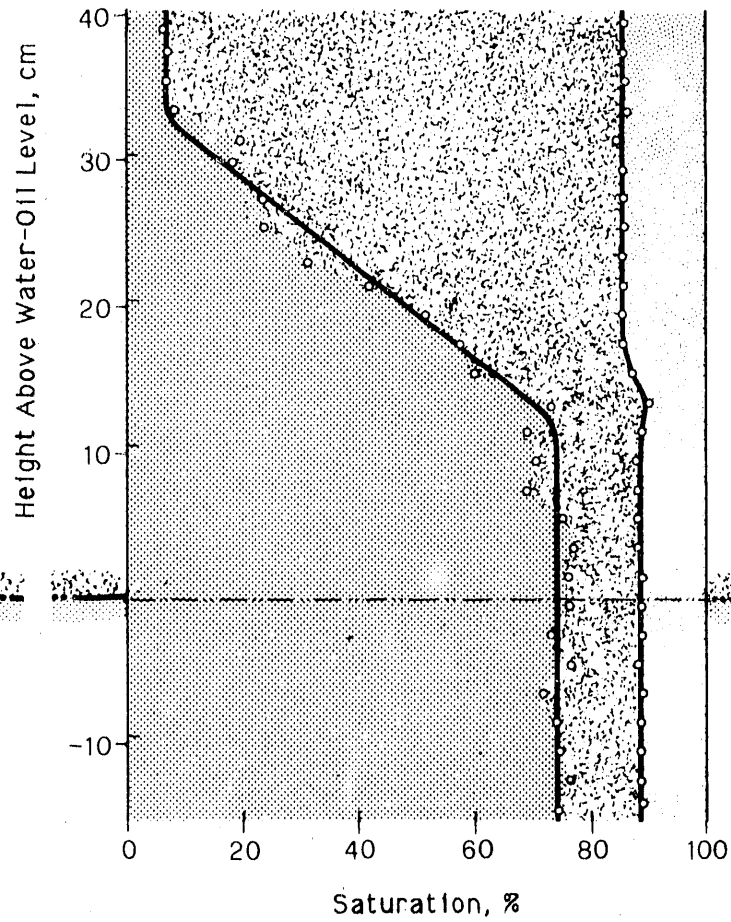
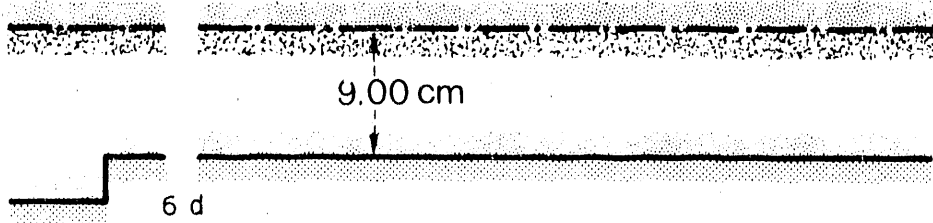
Experimental Series B: Diagram B6



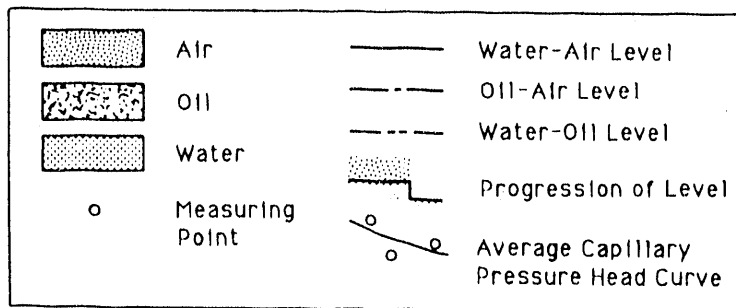
(WODR)



Experimental Series B: Diagram B7



WOIM



Experimental Series B: Diagram B8

diagrams of A32 and A33 during the establishment of an oil potential of 11465 erg/cm^3 (A32) and 6670 erg/cm^3 (A33).

7.4 COMMENTS ON EXPERIMENTAL SERIES B

B1. The primary virgin WLIM curve of experimental series B, measured 3 days after the water-air level was established in the oven-dried porous medium, is identical to the curve of experimental series A and similarly lies lower than the nonprimary curve (Figure 7.9).

B2. After a slow raising of the water-air level to above the porous medium and subsequent subsidence, the fully developed virgin WLDR curve was

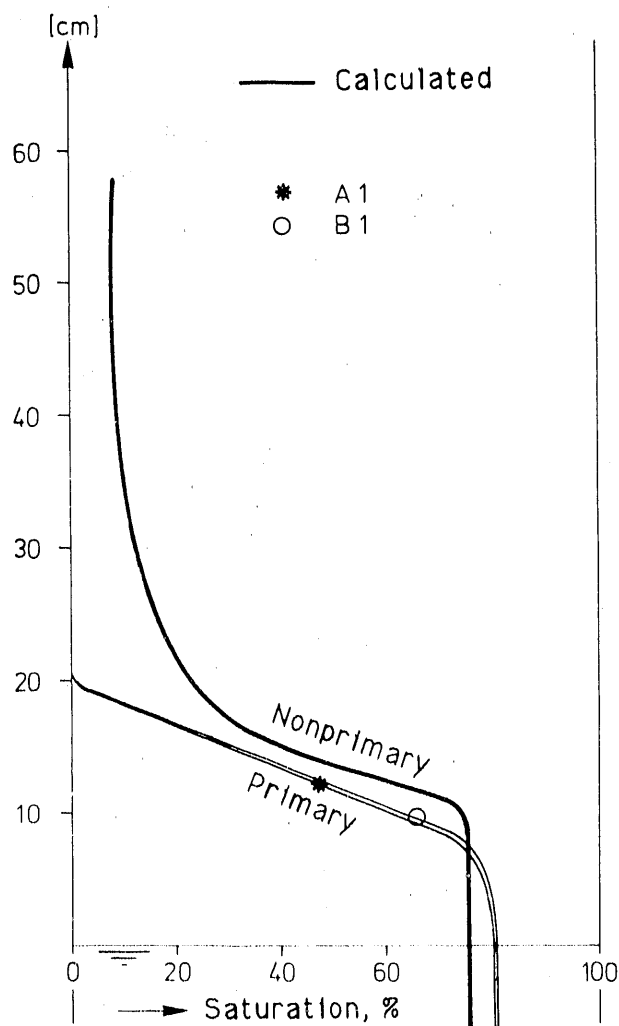


FIGURE 7.9. Measured Saturation Diagram for WLIM_{jfr1}

established in less than 1 day. This curve coincides with that of A3 and is identical with the mean measured reference curve (Figure 7.10).

B3. First, the water-air level was lowered below the porous medium, and the bottom was exposed to air for 18 h. In this way, the porous medium was drained and a $WLDR_{jfr1}$ curve was constructed at the lower boundary because of the end effect. With height, the WLDR curve decreases in saturation toward the asymptote at residual water saturation. Subsequently, the porous medium was filled with oil from below to obtain the primary OLIM shown. The oil level was raised over about 1 h, which was relatively slow, as was proved by the high residual air saturation.

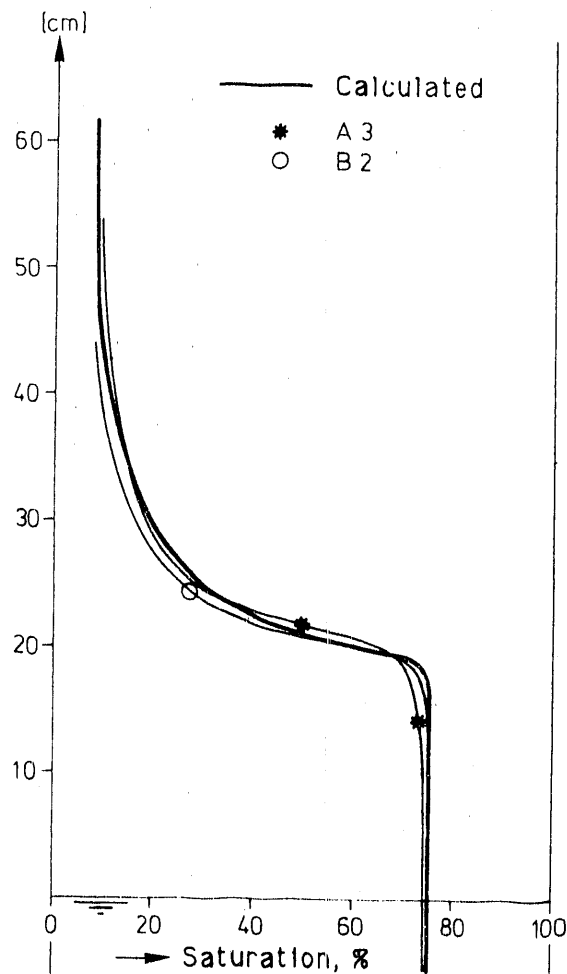


FIGURE 7.10. Measured Saturation Diagram for $WLDR_{jfr1}$

B4. After further increasing the oil-air level by about 16 cm, another primary OLIM curve was established. Apart from the unexpectedly smaller residual air saturation, this OLIM curve is also identical to the earlier curves (Figure 7.5).

After 88 h at constant level, the development of a hallux was clearly discernible. This hallux did not exist at 48 h (see comments on A13 for a possible explanation of the hallux development).

B5. The oil-air level was raised above the porous medium, and the medium was saturated with oil. Then, the oil-air level was lowered to its height in B3, which created an OLDR curve. After 40 h the 9% oil saturation above the oil-air level was probably still not quite pendular (see end of commentary associated with B6). This OLDR curve and the OLDR curve of A14 lies above the calculated OLDR curve (Figure 7.6). Based on the similarity of the measured OLDR curves, one can conclude that the value of 0.4 for $\alpha|_{O(DR)}^L$ given in Equation (7.4) must be too low.

B6. The water-air level was raised 12 cm above the porous medium, thereby displacing the oil. Subsequently, the oil-air level was set above the water-air level, and oil infiltrated from above into the water-saturated porous medium. After 2 days, the water-air level was lowered 4 cm, and 3 days later it was raised about 3 cm. Theoretically, an incompletely developed WOIM curve was produced (given that the WODR curve was fully developed before lowering the water-air level) because the hysteresis range (i.e., the difference between imbibition and drainage curves) is larger than 3 cm (Figure 7.1). Because the curve is not fully developed, its designation, WOIM, was set in parentheses.

A comparison of curve B6 to curve B8 in Figure 7.2 shows that, as expected, the funicular to insular boundary kept its fully developed form because there the hysteresis range is the smallest. Because the funicular-insular boundary of the incompletely developed WOIM curve of B6 coincides with that of the fully developed WOIM curve of B8, one must conclude that the hysteresis range there cannot be greater than 3 cm. Thus, the hysteresis range between measured WODR and WOIM curves must be smaller than between the calculated WODR and WOIM curves shown in Figure 7.1.

After 6 days at constant fluid levels, the development of halluxes occurred between oil and air and between water and oil. The insular oil saturation of about 18%, obtained after about 9 days, is larger than RSO_{max}^{ins} shown in A6. Given this measured value, RSO_{max}^{pend} of about 9% is calculated from Equation (2.1) (see B5).

B7. Lowering the water-air level about 3 cm relative to the constant oil-air level led to a WODR curve that was probably not fully developed after 14 h because of the relatively slow displacement caused by the unfavorable viscosity ratios for water and oil, and for the liquids and air. Thus, the designation WODR is set in parentheses. Note that the oil-air hallux is still present.

B8. Raising the water-air level 3 cm to its previous level and maintaining the oil-air level created a WOIM curve (see B6 for further discussion).

7.5 COMPARISON OF THE CAPILLARY PRESSURE HEAD CURVES

In the following illustrations, experimentally determined capillary pressure head curves were compared among themselves and to the theoretical curves shown in Figure 7.1.

As can be seen in Figures 7.9 and 7.10, the virgin water-air curves of experimental series A and B correspond to the mean value curves of earlier experiments (see Figure 8.2). Nonprimary WLIM curves lie somewhat higher than primary ones. RSL_{max} is confirmed to be about 25%, and RSW_{max} is confirmed to be about 8%.

Figures 7.7 and 7.8 show that the contaminated water-air curves from the experiment agree well with the curves in Figure 7.1, determined with the capillary pressure head reduction equation (Equation [7.2]), except for a known difference at lower water saturations. During imbibition, agreement occurs at the funicular-insular boundary. During drainage, agreement among residual air saturations occurs after compensating for different air-water levels. The maximum value of residual air saturation is about 25%, which also holds for the contaminated cases.

According to Figure 7.5, the measured OLIM curves also correspond very well with the curves calculated by using Equation (7.3), when the various

residual saturations of air were adjusted relative to the oil-air level. With OLIM curves, the experimentally determined maximum air saturation seems to be about 15% at a slow imbibition rate.

For an explanation of the higher position of the experimental OLDR curve in Figure 7.6 compared to the calculated curve shown in Figure 7.1, refer to commentary B5 in Section 7.4.

A comparison of the WODR curves in Figure 7.3 shows that the primary WODR curve (i.e., in A5 or in a porous medium without residual oil already present) agrees both in form and position with the calculated curve in Figure 7.1, provided that a Ω -value between 2 and 3, or $\Omega = 2.5$, is assumed as recommended. For nonprimary WODR curves with residual oil present, the lower WODR curves (and thus, corresponding smaller capillary rise) could be explained by a smaller contact angle than during primary drainage. Referring to the shape, a steep funicular portion means, in principle, a less-uniform pore-size distribution.

Comparison of the WOIM curves in Figure 7.2 shows a still more arbitrary behavior than is shown for WODR curves. In contrast to the WODR curves, stable WOIM curves lie partly or completely below the free-fluid level, whereby reverse wetting must be concluded. This arbitrary behavior is not surprising if one considers that Wolf (1957, p. 207) disputed the existence of one imbibition value for the contact angle. This opinion was supported by the observations of Bartell and Wooley (1933), as well as McCaffery and Mungan (1970). According to their experimental experience, the wetting angle of a fluid is essentially dependent on the purity of the surface of the solid, which must be determined ahead of time. This means that the contact angle hysteresis is only an apparent phenomenon, dependent on the contamination of the surface of the solid. Only the receding angle (i.e., the contact angle during drainage) can be designated as characteristic for a combination of two fluids and one solid.

From the large variability in position and form of the WO curves, in spite of a very homogenous porous medium (see porosity distribution in A1), one can see that funicular saturation distributions between water and oil are often quite unstable. Thus, with a small potential change, a WO curve could

suddenly change erratically in form and position, although the curve had scarcely moved previously with a larger potential change.

This arbitrary behavior of the interface between water and oil does not only occur with macroscopic observations. It is also observed with microscopic observations, such as the menisci in quartz glass tubes. This behavior exists because a water-oil meniscus can remain under the free-fluid level (shown in Figure 7.11) even though quartz glass is clearly more wetted by water than by oil. Another example of the randomness of the capillary rise is the fact that extreme cases of capillary rise can be produced in a capillary with an average diameter. Also, one can easily observe that the water-oil menisci in cylindrical quartz glass capillaries with the same diameter are not displaced simultaneously, but in a nonrepeatable, erratic sequence. The instability of the interfacial meniscus, which probably is a result of approximately monomolecular contamination, is confirmed by the unsteady

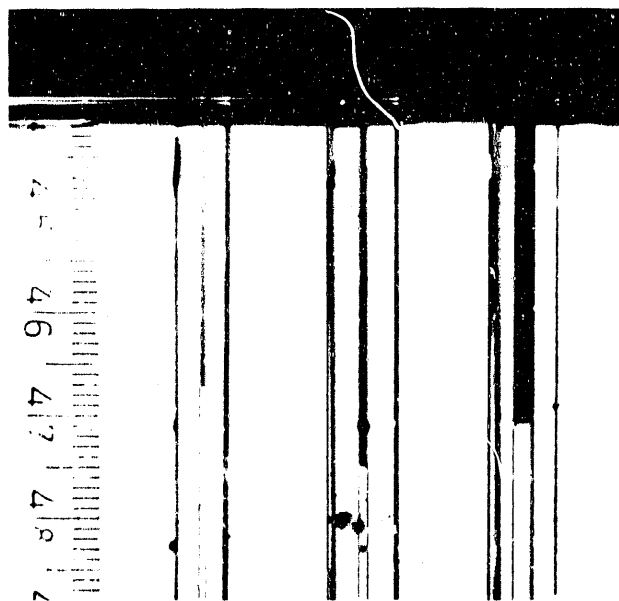


FIGURE 7.11. Photograph of WO Imbibition in Three Quartz Glass Capillaries

(within a certain range), arbitrary position of the interface between water and oil, as well as by macroscopic observations. Only an overextended contact angle can explain the lower imbibition curves during imbibition.

It is interesting to observe the various constant water saturations above the capillary fringe between water and oil, S_w^C , observed in experimental series A and B. If the average water saturation of this range is plotted as a function of the relative potential, then the diagram shown in Figure 7.12 is produced.

No.	A5	A6	A7	A8	A9	A20	A21	A22	A24	A25
Curve	DR	IM	IM	DR	DR	DR	IM	DR	DR	DR
$\Phi^r/10^3$	14,8	11,7	9,2	11,9	12,5	10,0	7,0	11,2	4,7	6,8
S_w^C (%)	22	22	22	28	22	49	60	35	72	60

No.	A26	A27	A28	A29	A32	A33	B6	B7	B8
Curve	DR	IM	DR	DR	DR	IM	IM	DR	IM
$\Phi^r/10^3$	8,8	5,0	9,8	13,6	11,5	6,7	7,5	10,0	7,5
S_w^C (%)	48	37	30	22	31	43	15	12	8

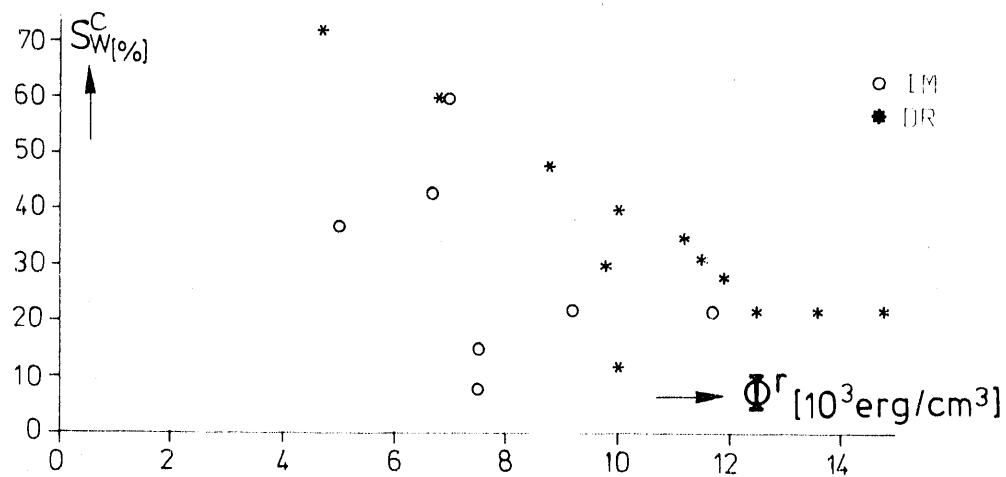


FIGURE 7.12. $S_w^C = f(\Phi^r)$

7.6 ACCURACY OF THE SATURATION MEASUREMENT

The curve and porosity distribution with height in A1 in Section 7.3 and the experimentally determined measuring point series in B1 and B2 of Section 7.4 show the homogeneity of the porous medium as well as the accuracy of the air and liquid saturation measurement based on the gamma attenuation method using only the Cs-137 source.

A measure of the accuracy of the anticipated less exact dual-gamma radiation method of determining the saturation of water, oil, and air in a porous medium by using a nomogram, which uses inputs from Cs-137 and Tm-170 gamma attenuation measurements (see Chapter 6.0), can be estimated from the upper portion of B3, an OLIM curve. Above the oil-air capillary fringe, the oil saturation naturally should be zero and thus the Cs-137 and Tm-170 measurements must always coincide. Their small differences confirm the order of magnitude of the relatively small error, less than 2%, in the saturation measurement methods (see Chapter 6.0). Additionally, one can conclude that the variations in the saturation distribution between water and oil were predominantly of an arbitrary nature, and thus resulted from a measurement error.

7.7 MAXIMUM RESIDUAL SATURATIONS (for sand at $n = 43\%$, Figure 2.1)

On the basis of the saturation diagrams of experimental series A and B in Sections 7.2 through 7.5, the experimental observations of the mean value of the maximum residual saturations are confirmed.

In summary, these are:

$$15\% \leq RSI_{\max} \leq 25\%$$

$$8\% \leq RSW_{\max} \leq 12\% \text{ (uncertain for residual air; see Figure 7.12)}$$

$$6\% \leq RSO_{\max}^{\text{ins}} \leq 12\% \text{ (eventually also higher)}$$

$$3\% \leq RSO_{\max}^{\text{pend}} \leq 6\%$$

8.0 TWO-DIMENSIONAL PROPAGATION EXPERIMENTS

The mathematical simulation of the processes involved in the displacement of three immiscible fluids (air, oil, and water) in a porous medium is performed by using the differential form of the system of equations defined in Schiegg (1979) by Equations (2) and (3) in Section 2.4 (pp. 18 and 19). As explained in Schiegg (1979), Section 2.6 (pp. 21-26), integration of the differential equations must generally be done numerically. Numerical solutions always imply definite simplifications. Thus, to verify numerical simulations, data from experiments are necessary. In addition, the experimental results should not only confirm the general course of the displacement processes, but they should also help to explain details of the processes. In this chapter, results are presented from a series of laboratory experiments on the two-dimensional propagation of a petroleum derivative in a homogenous, isotropic, and unconsolidated porous medium (quartz sand) filled with air and water.

8.1 PARAMETERS TO BE MEASURED

The system of equations defined by Equations (2) and (3) in Section 2.4 of Schiegg (1979, pp. 18 and 19) shows which parameters influence the displacement processes of air, oil, and water in a porous medium. Yet, the needed saturations of the three fluids and the needed potentials of water and oil are usually unknown. For simplification, the potential of air was assumed as constant and equal to zero in this experimental series. In addition, material characteristics, such as density, viscosity, porosity, and the relative permeability, were assumed known. The relative permeabilities of oil and water are functions of the saturations. The relationship between the saturations and the potentials is given by the capillary pressure curves or by the static saturation diagram (see Schiegg 1979, Chapter 3). The capillary pressure curves and the relative permeability curves must be known or experimentally determined. To determine these relationships experimentally, specific initial and boundary conditions must be used.

These considerations show that the displacement processes are determined by the distribution of liquid potentials over space and time. Thus, the liquid potentials are among those parameters that must be measured during displacement experiments involving three immiscible fluids.

The fluid saturations can theoretically be obtained from the potentials by using the capillary pressure curves or the static saturation diagrams. Because such a determination of the fluid saturation incorporates various simplifying assumptions, the fluid saturations were measured along with the potentials as a function of space and time for quality control purposes and as a backup in case of unexplainable results.

8.2 CAPILLARY PRESSURE HEAD CURVES AND POROUS MEDIUM

According to experimental results, the smallest inhomogeneities in porosity can have a definite influence on the propagation process. Thus, the tolerated inhomogeneity was stipulated as smaller than $\pm 0.5\%$ of the measured porosity (0.428). Obtaining such a highly uniform porous medium in a flume 260 cm • 55 cm • 15 cm required the use of an electrically controlled mechanical filling device because the required homogeneity could not be attained by filling the flume manually.

The grain-size distribution curve of the quartz sand used in the series of experiments is shown in Figure 8.1.

Figure 8.2 shows the experimentally determined capillary pressure head curves. The capillary pressure head curves for oil can be estimated from the water-air curves by using the Ω scaling factor (see Schiegg 1979, Equation [2] of Section 3.2.1 [p. 52] and Table 1 of Section 3.1.6 [p. 45]). The capillary pressure head reduction, that is, the difference between the $HCWLDR_{(bef)}$ curve and the $HCWLDR_{(jfr)}$ curve, is found to be constant over the entire saturation range in spite of the dependence of Equation (6) of Section 3.4 (in Schiegg 1979, p. 79) on the reciprocal of R , the effective pore radius. With $h_{c|W}^L(jfr, DR, 1-RRSL) = 18$ cm, according to Equation (3) of Section 3.9.4 (in Schiegg 1979, p. 112), and $h_{c|W}^L(bef, DR, 1-RRSL) = h_{c|W}^L(DR, DR, 1-RRSL) = 14$ cm for $\Omega|_W^0 = 3$, according to Equation (6) of Section 3.9.4 in Schiegg (1979, p. 112), the capillary pressure head reduction, according to

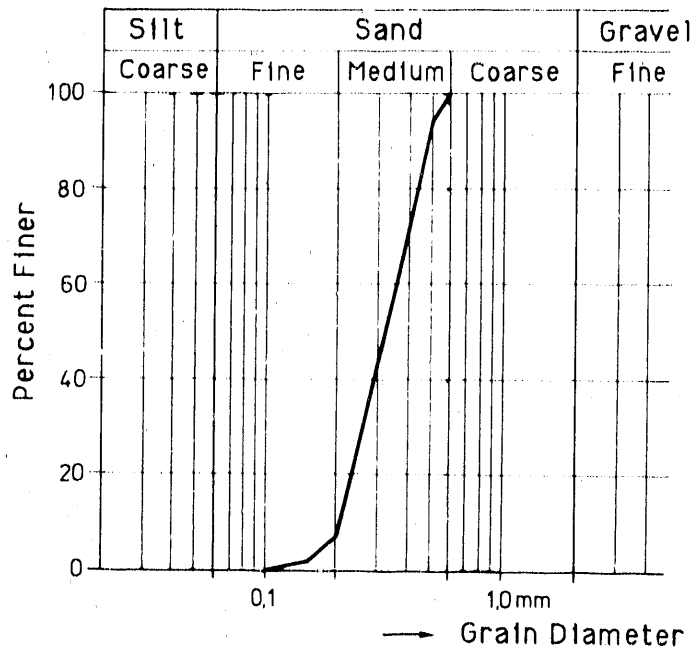


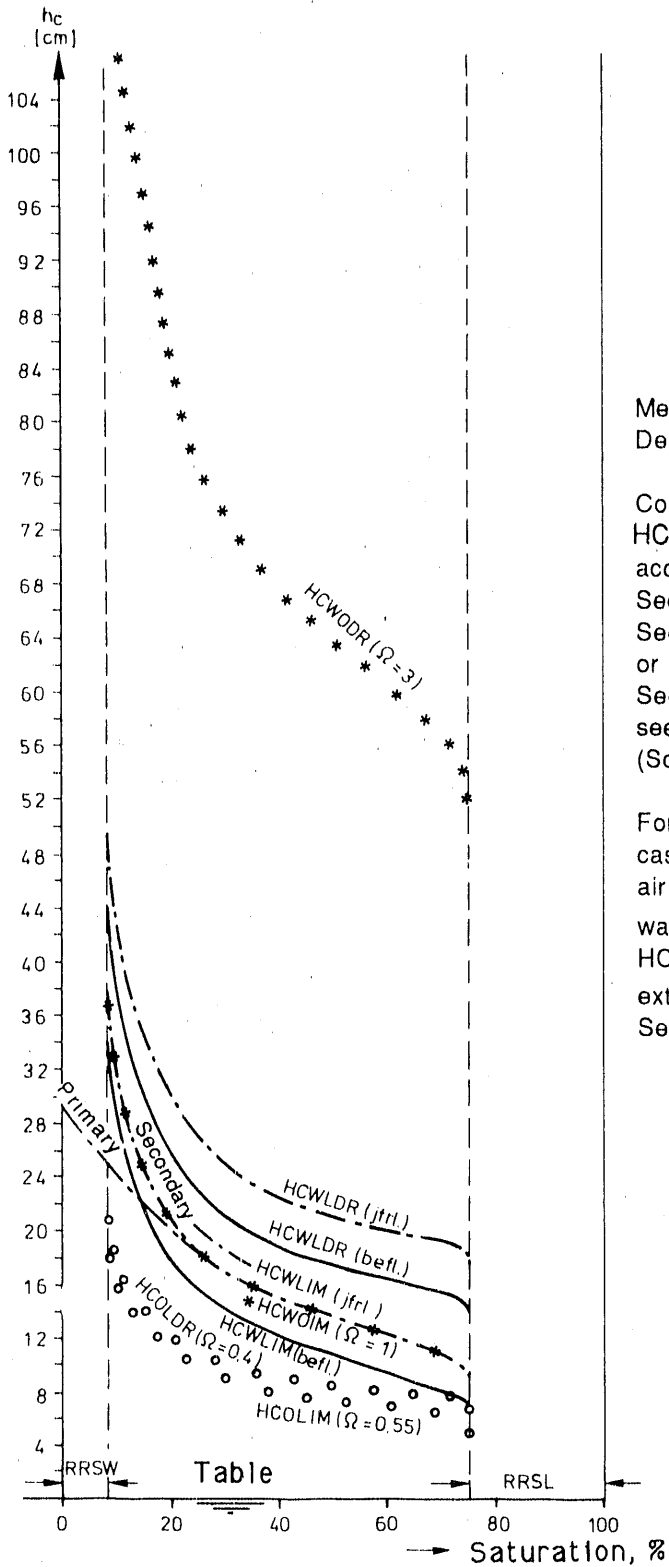
FIGURE 8.1. Grain-Size Distribution Curve

Equation (5) of Section 3.4 in Schiegg (1979, p. 79), is (see also the conclusion of Section 3.9.5, Schiegg 1979)

$$\Delta h_c = h_c \left| \frac{L}{W} (jfr1, DR, 1-RRSL) \right| - h_c \left| \frac{L}{W} (DR, DR, 1-RRSL) \right| = 4 \text{ cm} \quad (8.1)$$

The influence of the capillary pressure head reduction on the eventual residual oil saturation is considered and explained in Section 3.5 of Schiegg (1979, pp. 83 through 87).

During the experiments, whose results are summarized in Tables α , β , and δ (in the envelope included with this report), the distribution of potentials with height was almost always constant when the saturation diagrams were measured, which can be seen by examining the potential histograms adjacent to the saturation diagrams. Almost constant potentials imply practically static gradients. Thus, the changes in the saturation diagrams were always a product of very slow processes.



Mean Value Experimental Determinations

Control: Determination of oil-HCSB from the HCWL was according to Equation (2), Section 3.2.1 with Table 1 of Section 3.1.6, Schiegg (1979) or compare with values in Section 3.9.4 for (1-RSSL); see conclusion of Section 3.3 (Schiegg 1979).

For the static contamination case with the imbibed water-air interface, the $HCWLIM_{(befl)}$ was described by the $HCWLIM_{(jfrl)}$ _____, not by the extended curve -.-.-; see Section 3.9.5, Schiegg (1979).

FIGURE 8.2. Capillary Pressure Head Curves

For these reasons, the independently measured static saturation diagrams could be used to verify the saturation diagrams from the two-dimensional experiments. A static saturation diagram equivalent to the static capillary rise curve (ACSB) is identical to the capillary pressure head curve (HCSB). Thus, the knowledge that the capillary pressure head curves can be superimposed onto the static saturation diagram provides an adequate tool to estimate the fluid saturation distribution over space.

For the porous medium used in the two-dimensional experiments, the product of the saturated hydraulic conductivity and the relative permeability at residual air saturation (79% water saturation) was measured as $1.9 \cdot 10^{-2}$ cm/sec (see Schiegg 1979, Section 3.2.3.1, pp. 61-68).

8.3 MEASUREMENT METHODS

The potentials were measured by using probes having porous tips made of fritted glass. The nonwetting fluid-entry pressure of the porous tips was greater than the nonwetting fluid-entry pressure of the porous medium. SiO₂ as glass or quartz sand is more wettable by water than by air or oil. This property rendered the fritted glass tip suitable for the water potential measurement. To determine the oil potential, the porous fritted glass tips were treated with silicon, which rendered the glass surfaces oleophilous, or hydrophobic.

The liquid pressure present at the probe tip was transferred mechanically through a conducting system of Vibon tubing and stainless steel tubes to a CEC-pressure transducer. Because of cost considerations, several liquid pressure probes had to be connected to the same CEC-pressure transducer by using a switching valve, which had to meet the specification of a small liquid exchange volume. When the only commercially available switching valve proved to be susceptible to clogging because of mercury precipitation from the mercury-containing SAI (see Section 6.7), a battery of stopcocks had to be fabricated at ETH.

The tolerated volume exchange per switching process must be specified small because the induced error in the measured pressure or potential, and thus the estimated saturation (even for a flat capillary pressure curve), must

be clearly less than the tolerated standard error of the potential measurement. For the same reason, the influence of changes in liquid pressure and temperature on the volume of tubing between probe and transducer must be correspondingly small. Finally, the change in volume resulting from the deflection of the diaphragm in the pressure transducer at the maximum pressure difference encountered must be of the same magnitude as the tolerated volume exchange of the stopcocks. The electrical signal from the pressure transducer was recorded with a chart recorder.

A pressure transducer measured the static pressure head between the transducer and a liquid pressure probe plus the liquid pressure in the porous medium sensed at the probe. Thus, the total gravitational potential was measured and recorded.

The reference datum, or zero line, for the recorded data was determined for both water and oil by using either the water-air level or the oil-air level outside the flume adjusted to the transient height of the water table in the flume. The graphical representation of the electronically recorded potentials used the lowest water table during an experiment as the datum, which was superimposed on the vertical time axis of the measurement profile. For potential measurements taken when the water table level was situated higher than the datum, the value $\rho_W g \Delta h_S|_W^L = \Delta h_S|_W^L \cdot 10^3$ was added to the electronically recorded water potentials, and the value $\rho_O g \Delta h_S|_W^L \approx 0.85(\Delta h_S|_W^L \cdot 10^3)$ was added to the oil potentials. $\Delta h_S|_W^L$ is the difference between the transient position of the water table and the lowest position of the water table used as the datum during an experiment. Thus, the graphical representation of potentials is equivalent to the representation of potentials relative to the stationary position of an external water-air level reference set at the lowest position of the internal water table during an experiment. The relative oil potential is calculated by using, in Schiegg (1979, p. 95), Equation (1) of Section 3.7.2, Equation (8) of Section 3.7.1 (p. 91), and Equation (2) of Section 3.1.6 (p. 44) with $\phi_L \approx \rho_L \approx 0$ and $\rho_W \approx 1$:

$$\phi^R = \phi_U - \phi^{tR} = \phi_U - \rho_U \cdot g \cdot h_S \left| \frac{L}{W} \right. = \phi_U - \rho_U \cdot \phi_W \quad (8.2) \text{ (a)}$$

Thus, ϕ_W is the water potential relative to the lowest water table, provided the potentials are referenced to a datum not corresponding to this lowest water table; otherwise, ϕ_W is zero.

The measurement locations can be seen from the photographs, which are next to the tables for Experiments A, B, and D (in envelope). The potential and saturation measurements occurred in various vertical measurement profiles. The liquid potential profile underneath where the oil was applied was designated the application site profile. The water and oil potential measurements were taken simultaneously at the same height. The vertical distance between pressure probes was 4 cm. The liquid pressure probes of varied lengths were thrust horizontally into the oven-dried porous medium to various depths. The locations at which the potential measurements were taken can be seen on the photographs where the tubing connects to the stopcock battery, which consists of a number of separate stopcocks assembled to provide the number of desired switching locations in a potential measurement profile. A stopcock battery for each of the two liquids is mounted onto a vertical rail and is connected to a pressure transducer with tubing. This tubing transfers the pressure sensed at a probe to the CEC-pressure transducer when the associated stopcock is opened.

The determination of fluid saturations used three counting times in which the attenuation of a collimated beam (0.5 cm high and 2.0 cm wide) of gamma radiation from Cs-137 and Tm-170 was measured. The semigraphical method described in Section 6.11 was used to interpret the attenuation data. Details of the experiment setup were presented in Chapters 3.0 through 6.0.

(a) Equations were taken directly from the German text and, in some cases, use a different notation. For example, 0,01 = 1/100, whereas in this text, 1/100 would be shown as 0.01. Multiplication is indicated by a dot in the equations and in the text.

8.4 OIL APPLICATION AND BOUNDARY CONDITIONS

Oil was applied in a 2-cm-wide trench in the uncovered sand surface. The trench was perpendicular to the two-dimensional propagation. The oil application was quantified by either the infiltration rate or the application potential. For simplification, the value of the specified parameter was held constant for the duration of the oil application.

In all of the photographs taken during an experiment (see, for example, tables in envelope), the position of the water table within the flume was indicated by a black line with the standard water table symbol. The position of this line was determined by drawing a horizontal line between the water levels in the two overflow vessels on each side of the flume. The capillary fringe above the water table can be seen in the photographs as an extension of the dull color below the water table. Because of hysteresis, the height of the capillary fringe is dependent on the history of the water table position, and this information is given as an initial condition.

According to Figure 3 of Section 3.2.3.1 in Schiegg (1979, p. 67), the displacement of air by a liquid with potential gradients of about $|1|$, unit gradient, is observed to be piston-like, at least in the quartz sand used. Muskat (1934) shows that the temporal progression of piston-like displacement during constant infiltration is clearly dominated by geometric effects if capillarity is neglected for the sake of radial and spherical symmetry; that is, the effect of the viscosity difference is very slight. This observation implies that the temporal progression for such a displacement process can be described by an analytical solution for the corresponding flow of one fluid. Accordingly, this observation also means that the boundary conditions are satisfied naturally, regardless of those along the advancing infiltration front. In Appendix E, Schiegg experimentally shows (because it is not analytically possible as a result of the nonlinear boundary condition at the wetting front; see Equation (8) of Section 2.5 in Schiegg 1979, p. 21) that even with a relatively slight capillary effect, the above statements are also valid when the effect of gravity is incorporated. This fact implies that path and flow lines are identical, and thus a constant flow pattern also exists during a displacement process with constant infiltration. Thus, the



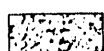
potentials must be constant, independent of the transient position of the infiltration front, before the oil front reaches the propagation surface near the capillary fringe. These assertions, derived from the mentioned experiments, could also be proven directly by experiment.

In reality, the size of the infiltration front (as described in Schiegg 1979, Section 3.2.3, p. 58) for gradients of about $|1|$ is, in general, relatively small compared to the horizontal propagation of the oil or compared to the vertical distance between the application site and the propagation surface in the vicinity of the capillary fringe. However, during the two-dimensional experiments, these relationships were not valid because the capillary fringe in the flume was the same as at the field scale, whereas the infiltration rate and the interval between the infiltration site and the propagation surface were not at the field scale. Thus, in the flume, the rate of infiltration front advance was not small compared to the duration of the first propagation phase (i.e., before the oil front reaches the propagation surface). This experimental artifact explains why the potentials were not constant during the first propagation phase in spite of a constant infiltration rate. Therefore, it is open to question to what extent Schiegg's (1975) proposed semi-empirical analytical model of displacement processes incorporating a characteristic capillarity (a rectangular approximation of the capillary pressure head curve) agrees with the experimentally observed nonpiston-like displacement.

Furthermore, in the series of two-dimensional experiments, the forms of oil propagation could not be verified by using Schiegg's (1977a) proposed methods for evaluating the first propagation phase because the height of the funicular region in the dynamic capillary rise curves and the size of the oil front with a gradient of about $|1|$ were not small compared to the dimensions of the propagation process. This statement applies even though the development and form of the oil propagation in the two-dimensional laboratory experiments agree in principle with common conceptual representations discussed and illustrated later in this chapter.

8.5 LEGEND FOR THE SATURATION AND POTENTIAL TIMELINE FOR EXPERIMENTS A THROUGH E

Figure 8.3 shows the saturation diagram and Figure 8.4 the potential histogram and timeline for Experiments A through E. In Figures 8.3 and 8.4, the vertical axis is the time. The shaded areas and the measuring points are

-  air
-  water (only for potentials associated with funicular saturation)
-  oil

- Potentials associated with residual saturation = unreliable values
- Potentials associated with funicular saturation = reliable values

The profile on the right lies 62 cm to the right of the profile underneath the oil application site.

Figure 8.3 is the graphical representation of the measured instantaneous saturation distribution of water and oil. One is presented for the profile underneath the application site and another is presented for the profile 62 cm to the right. The elapsed time for a saturation diagram is indicated below the water-air level. The profiles are planes normal to the two-dimensional propagation experiments. Within a potential histogram (Figure 8.4), the

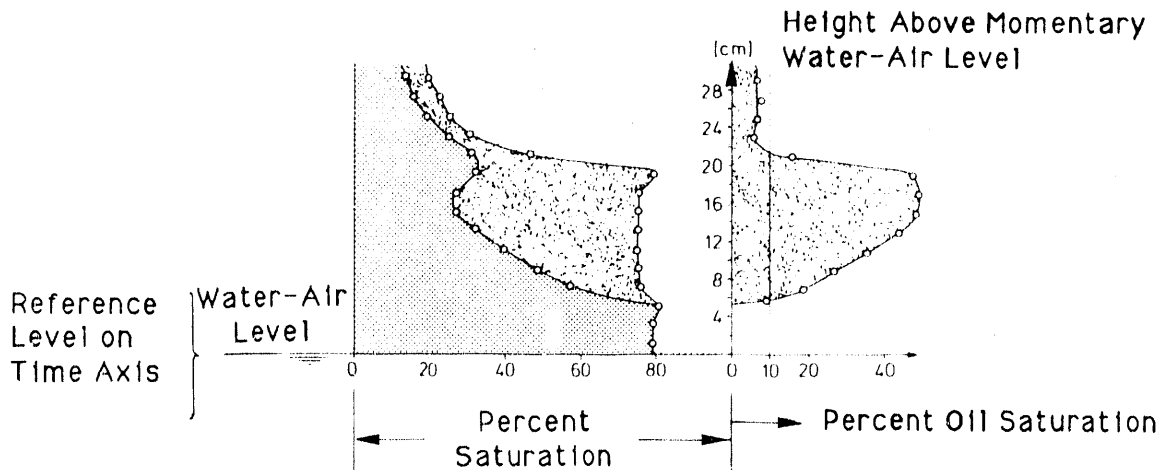


FIGURE 8.3. Saturation Diagram for Experiments A Through E

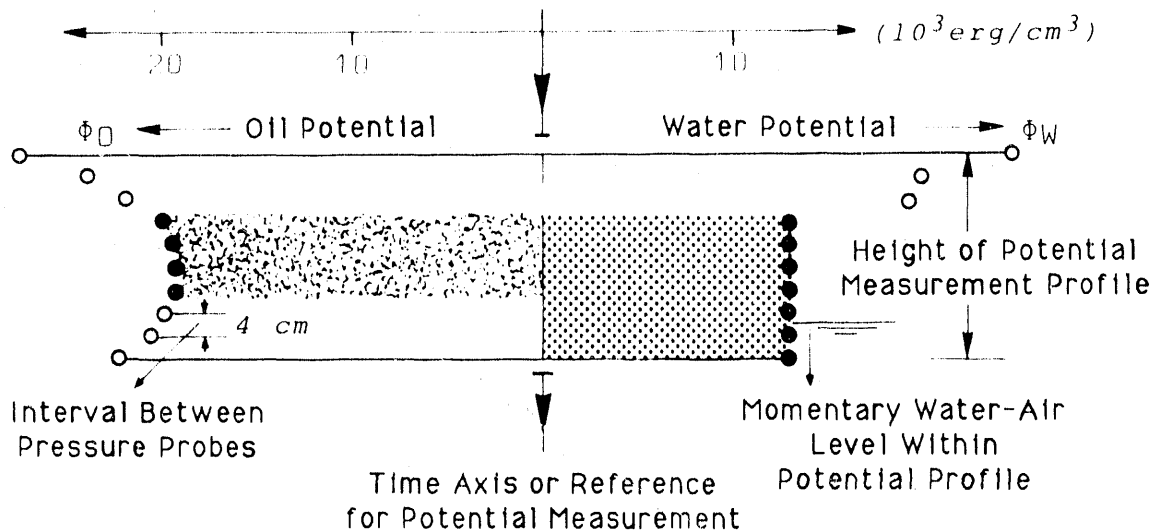


FIGURE 8.4. Potential Histogram and Timeline for Experiments A Through E

vertical axis denotes the height in the profile. The measurement points with the highest gravitational potentials are presented first on the time axis, and the points with the lowest gravitational potentials are presented last on the time axis. In between lie the remaining measuring points, which have a constant vertical interval of 4 cm. The water potential is plotted to the right of the vertical, and the oil potential is plotted to the left. The reference for the potential measurements is the lowest water-table level at which potential measurements were made during an experiment. The units erg/cm^3 , with the dimension of pressure ($\text{ML}^{-1}\text{T}^{-2}$), can be interpreted as a volume-specific potential area. A fluid column height is calculated by dividing by the specific weight, ρg , ($\text{ML}^{-2}\text{T}^{-2}$). Thus for water ($\rho_{\text{W}}g \approx 10^3$), 10^3 erg/cm^3 corresponds to a 1-cm water-column height, and for oil ($\rho_{\text{O}}g \approx 0.85 \cdot 10^3$) 10^3 erg/cm^3 corresponds to a 1.16-cm oil-column height.

8.5.1 Selected Characteristics for Experiments A Through E

Petroleum derivative:	Super-Ad-It in organic solvent + extra light petroleum fraction (see Section 6.7) (designated as oil or SAI)
Grain-size distribution curve:	Figure 8.1
Porosity:	$n = 0.43$

Capillary pressure head curves: Figure 8.2

Initial and boundary conditions: Table 8.1

8.6 EXPERIMENT A

The liquid potential and fluid saturation measurements at various times during Experiment A are shown graphically next to the photographs of the flume in Table α (in envelope). Time is represented on the vertical axis, where "1'" means after 1 min, "1h" means after 1 h, and "1T" means after 1 day (i.e., 24 h into the experiment), thus the second day of the experiment. The liquid potentials are plotted perpendicular to the time axis with the water potentials plotted to the right and the oil potentials to the left. The specifics of Experiment A are presented in Table 8.1.

A potential measurement location is where the water and oil potentials were measured. As in Figure 8.4, the oil potentials were plotted to the left, and the water potentials were plotted to the right of a vertical reference. The value 10^3 erg/cm^3 corresponds to 1 cm water. A histogram is produced by compiling the measured potentials over a cross section. A new vertical reference was established for each additional measurement profile (see Experiment B, because in Experiment A, data were collected only for the profile below the oil application site). Measured potentials represented by solid circles indicate that these potentials are associated with oil or water in the funicular saturation state, whereas open circles indicate those potentials associated with oil and water in the residual saturation state. The area below the solid circles is shaded a different pattern for oil and water. The decision of whether a potential value should be indicated by a solid or open circle was based primarily on whether an immediate and well-defined shift of the pen on the plot recorder was observed as the measured value was recorded. In addition, whether a potential was associated with funicular or residual saturation relied on an interpretation of the saturation diagrams, the photographs, and the experimental results.

The instantaneous saturation values for the measurement profile are presented as in Figure 8.3, in which the water saturation is plotted on the left, the oil saturation is plotted in the middle, and the air saturation is

plotted on the right versus their height above the transient water table. In addition, the actual oil saturation with height was plotted separately to the right of the 100% saturation value for the three-fluid saturation diagram. The time from the start of the experiment and the location of the water table are indicated on the individual saturation diagrams in the tables found in the envelope.

The measured saturation diagrams can be independently estimated by using the measured potentials, as discussed in Section 3.5 of Schiegg (1979, p. 83). The fluid saturations associated with an oil and water potential pair can be determined by first calculating the theoretical positions of the oil-air, water-oil, and water-air levels, then superimposing the oil-air, water-oil, and water-air capillary pressure head curves at the position of the respective fluid levels, and, finally, reading the saturation values corresponding to the measured potentials from the drainage or imbibition capillary pressure curves, depending on the saturation history. In a transient experiment, this procedure must be repeated for each potential measurement pair. If the experiment is approaching static equilibrium, and thus a constant potential with height, the method is simplified because the distribution of fluid saturations with height for various potential measurement pairs can be estimated from only one superposition of the three static capillary pressure curves. For example, Figure 8.5 presents a saturation diagram estimated from the measured potentials about 1 day after the start of Experiment A. This diagram corresponds very closely to the second saturation diagram shown in Table α (in envelope).

Twenty-three hours after the beginning of the experiment, the potentials of both water and oil with height were almost constant. Thus, the criterion for static equilibrium was fulfilled. The water potential was measured as $13 \cdot 10^3$ erg/cm³, and the oil potential was between $19.5 \cdot 10^3$ and $20 \cdot 10^3$ erg/cm³. The potential of atmospheric air is zero. With these potentials, the elevations of the air-water, air-oil, and oil-water tables, given an oil density of 0.85 g/cm³, are determined with Equation (2) of Section 3.1.6 in Schiegg (1979, p. 44) as

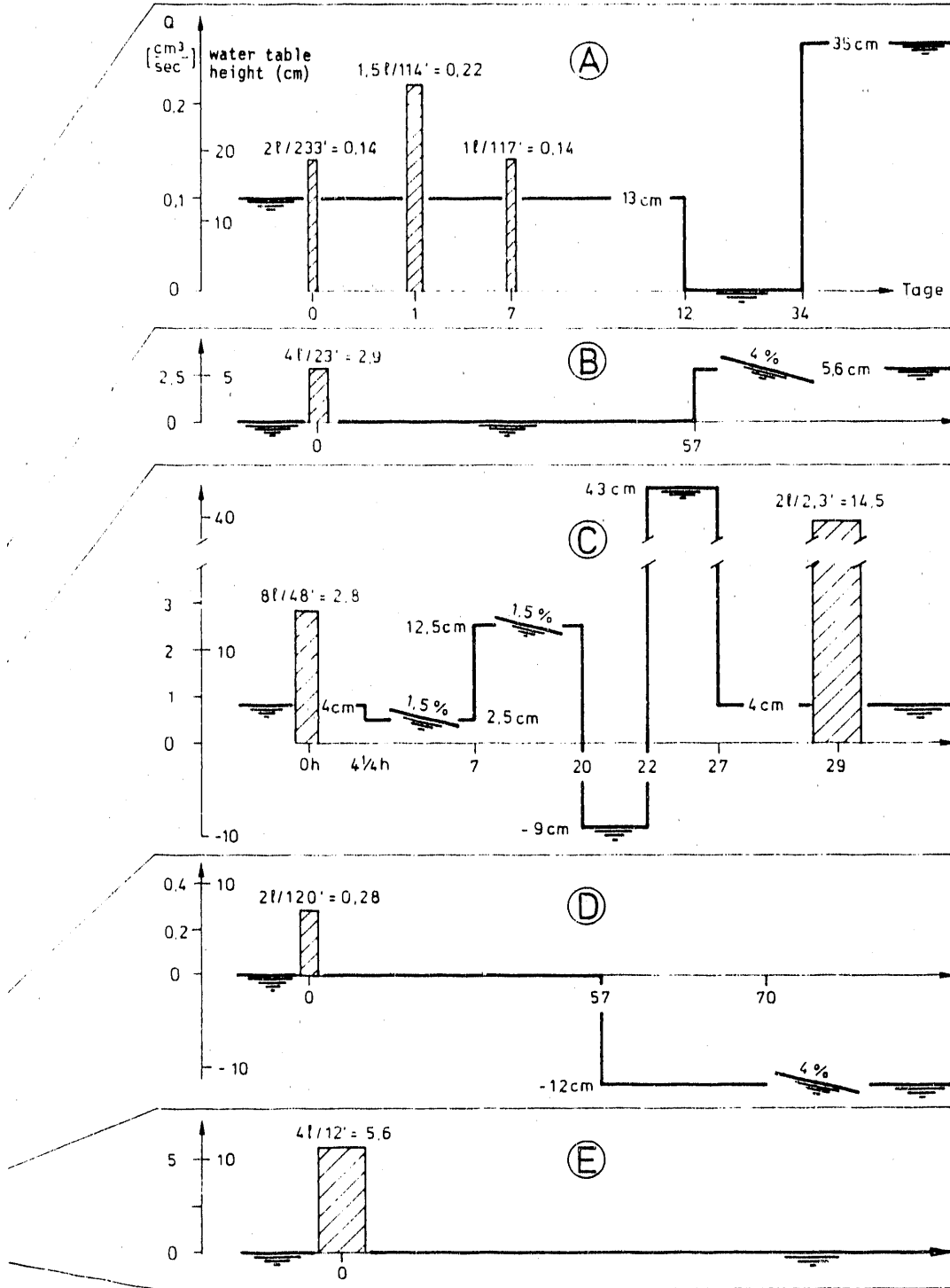
$$\begin{aligned}
 h_g \Big|_W^L &= (0 - 13 \cdot 10^3) / \{(0 - 1, 0) \cdot 10^3\} = +13 \text{ cm} \\
 h_g \Big|_O^L &= (0 - 20 \cdot 10^3) / \{(0 - 0,85) \cdot 10^3\} = +24 \text{ cm} \\
 h_g \Big|_W^O &= (19,5 \cdot 10^3 - 13 \cdot 10^3) / \{(0,85 - 1, 0) \cdot 10^3\} = -43 \text{ cm}
 \end{aligned}
 \tag{8.3}$$

TABLE 8.1. Initial and Boundary Conditions, Experiment A-E

Exp.	Oil Application			Water-Air Level				Chronology
	Type of Initial Capillary Fringe Established	Height Above Propagation Surface	Oil Volume Per Time = Q	Initial Relative to Reference for Measurement	Lowest	Slope	Δh	
A	WLDR	22 cm	Constant Infiltration Rate	$2\frac{1}{2}/233'$	+13 cm	0 cm		
				$= 0.14 \frac{\text{cm}^3}{\text{sec}}$			0%;	0 cm
				$1.5\frac{1}{2}/114'$				0 d
				$= 0.22 \frac{\text{cm}^3}{\text{sec}}$				0 d
				$1\frac{1}{2}/117'$				7 d
				$= 0.14 \frac{\text{cm}^3}{\text{sec}}$			0%;	-13 cm
							0%;	+35 cm
B	WLDR	10 cm	Constant Potential	$4\frac{1}{2}/23'$	0 cm	0 cm	0%;	0 cm
				$= 2.9 \frac{\text{cm}^3}{\text{sec}}$ *			0%;	0 cm
							0%;	+5.6 cm
C	WLDR	18 cm	Constant Potential	$8\frac{1}{2}/48'$	+4 cm	-9 cm	0%;	0 cm
				$= 2.8 \frac{\text{cm}^3}{\text{sec}}$ *			1.5%;	-1.5 cm
							1.5%;	+10 cm
							0%;	-21.5 cm
							0%;	+52 cm
							0%;	-39 cm
				$2\frac{1}{2}/2.3'$				
				$= 14.5 \frac{\text{cm}^3}{\text{sec}}$			= Initial Water Table Level	29 d
D	Primary WLIM	30 cm	Constant Infiltration Rate	$2\frac{1}{2}/120'$	0 cm	-12 cm	0%;	0 cm
				$= 0.28 \frac{\text{cm}^3}{\text{sec}}$			0%;	-12 cm
							4%;	Flume Sloped
E	Primary WLIM	15 cm	Constant Potential	$4\frac{1}{2}/12'$	0 cm	0 cm	0%;	0 cm
				$= 5.6 \frac{\text{cm}^3}{\text{sec}}$				0 d

* See Section 8.4 concerning the constancy of the infiltration rate at constant application potential.

TABLE 8.1. (contd)



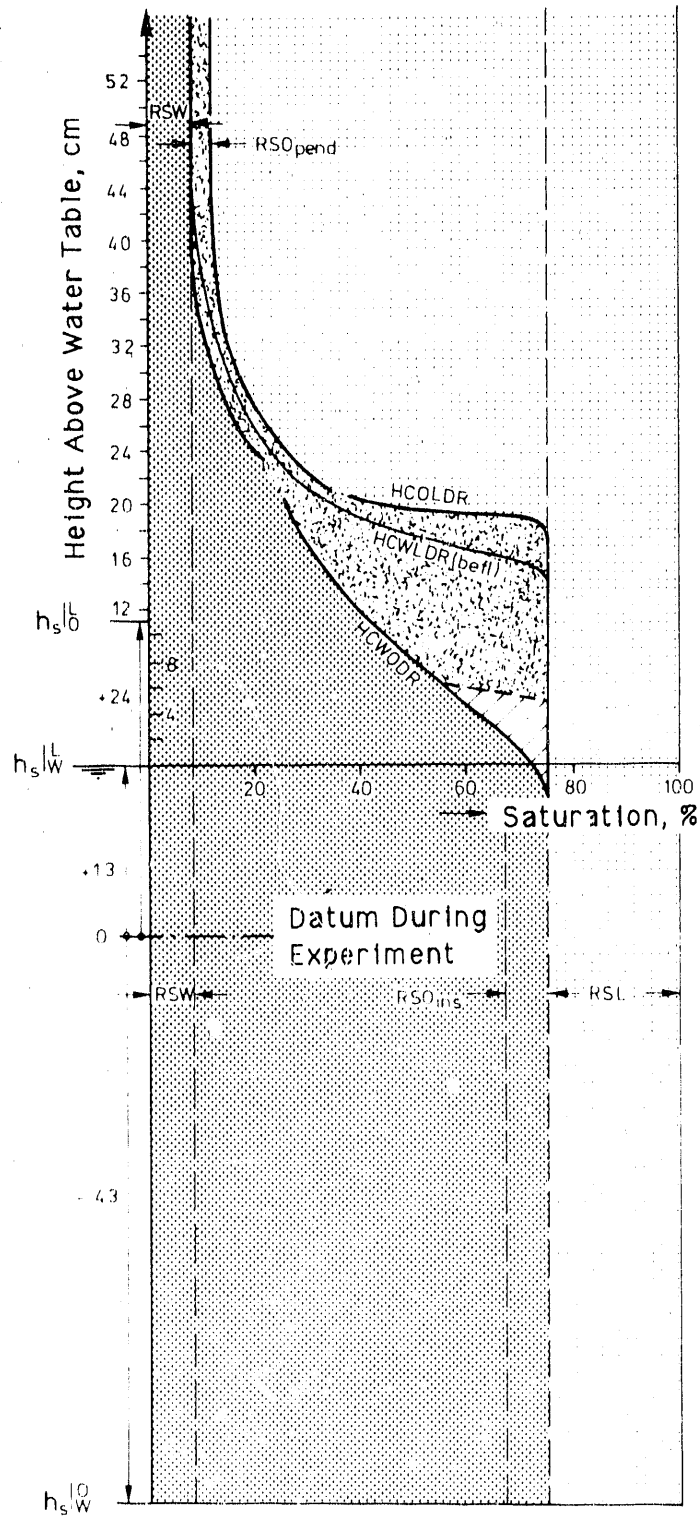


FIGURE 8.5. Estimated Static Saturation Diagram 1 Day After the Beginning of Experiment A

The relative oil potential is calculated, according to Equation 8.2, as

$$\phi^r = \phi_0 - \rho_0 \cdot g \cdot h_S \left| \frac{L}{W} \right. = (19,5 \div 20) 10^3 - 11 \cdot 10^3 = 8500 \div 9000 \text{ erg/cm}^3 \quad (8.4)(a)$$

To reflect the capillary pressure head reduction in the water-air capillary pressure curve resulting from contamination by oil, and because the water in the measurement profile is in a drainage state, the HCWLDR_(befl) curve is the appropriate curve to superimpose on the water-air level. About 120 min after the start of the experiment, the oil front met the water-air capillary fringe, whose menisci were in a drainage state. From 120 min until the end of the oil infiltration at 234 min, the oil potential at the fourth to seventh measurement location starting from the top increased to between 22400 and 21000 erg/cm³. The increase was caused by the damming effect of the capillary fringe, over which the oil later propagated horizontally. According to Equation (8.2), the observed increase in the oil potential is equivalent to a relative potential of between 10300 and 9500 erg/cm³ at water potentials of between 14200 and 13500 erg/cm³, respectively. After stopping the infiltration of oil, the relative oil potential decreased to between 9000 and 8500 erg/cm³ (Equation [8.4]) 23 h into the experiment. The resulting form and development of the flattest oil meniscus during Experiment A is displayed graphically on the nomograph in Figure 8.6, which is based on Figure 1 of Section 3.9.4 in Schiegg (1979), p. 113). In Figure 1 in Schiegg (1979), the starting point is Corner #3 of the hysteresis rhomboid because the oil front encountered water-air menisci in the drainage state at the water capillary fringe.

The nomograph in Figure 8.6 reveals that the HCOLDR curve can be quite satisfactorily superimposed on the oil-air level to construct the fluid saturation diagram 23 h into the experiment. In addition, the dashed line in Figure 8.6 indicates that the conversion of the water-oil drainage curve to the water-oil imbibition curve was theoretically only one-sixth complete 23 h after the beginning of the experiment because $a/b = 5/1$. The dashed line in Figure 8.7 shows the likely shape of the water-oil capillary pressure head

(a) The notation \div signifies a range, as in 8500 to 9000.

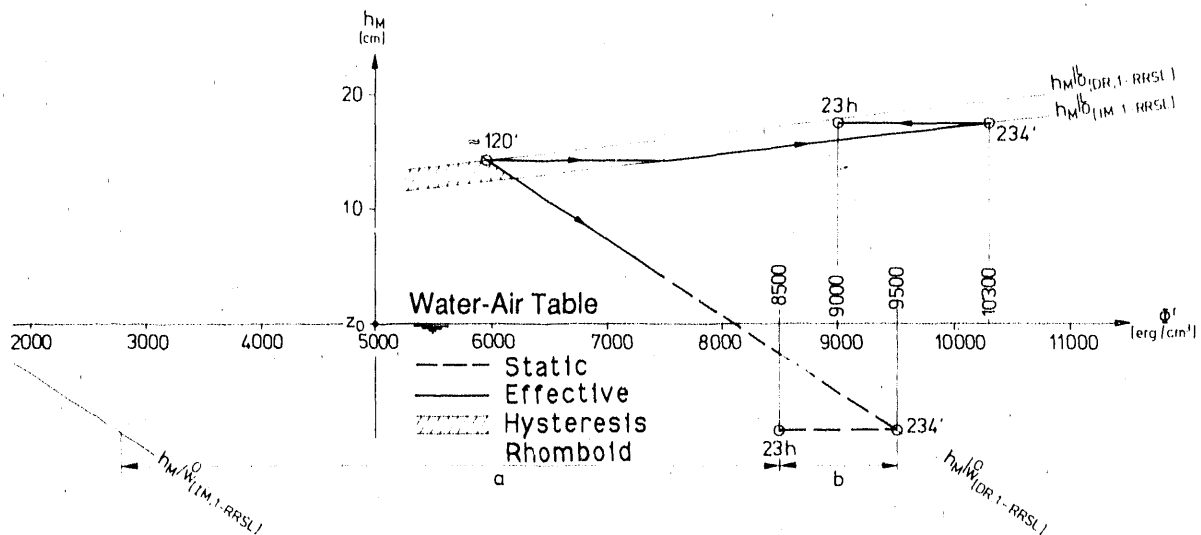


FIGURE 8.6. Nomograph Displaying the Development of the Form and Position of the Flattest Oil-Air Meniscus up to the Second Saturation Diagram of Experiment A

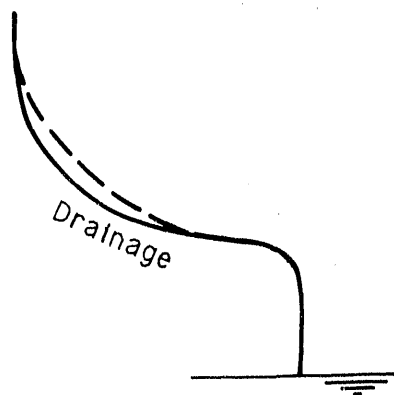


FIGURE 8.7. Conversion from the Drainage to the Imbibition Capillary Pressure Head Curve

curve when the conversion from drainage to imbibition is about one-sixth complete. This estimate, which is based on the experimental results presented in Figure 2b of Section 3.2.2, in Schiegg (1979, p. 55) shows that at this stage of the conversion, the drainage curve is generally still valid. To estimate the second saturation diagram of Experiment A at 23 h, the HCWODR curve was superimposed on the water-oil level because, in reality, the water-oil menisci were still in the drainage form. This conclusion follows from the

information contained in Figure 8.6 and from the visual location of the oil front above the water table (refer to the photographs in Table α , in envelope), which suggests that the flattest menisci were still above the water table. Thus, the decision to use the HCWODR curve was well supported.

Figure 8.5 shows the estimate of the second saturation diagram of Experiment A from the measured potentials by superpositioning the appropriate static oil-air, water-oil, and water-air capillary pressure curves from Figure 8.2 according to the method presented Section 3.3 of Schiegg (1979).

The estimated saturation diagram in Figure 8.5 compares well with the second measured saturation diagram in Table α , both in the pertinent form and position relative to the water table. The principal difference between the measured and estimated saturation diagrams is shown by the area indicated with the diagonal lines.

Displacement processes between oil and water occur rather slowly compared to those between air and oil as a result of the orders-of-magnitude greater viscosity and density of water versus that of air. Thus, a measured potential combination must remain constant over a definite time period before the water-oil capillary rise curve becomes fully developed. Because the magnitude of the potential gradients during this final stage before equilibrium is often smaller than the resolution of the instrument used to measure the potentials, a static equilibrium is indicated even though the menisci are clearly not in their static position. Another reason for the often-observed difference between the measured static capillary rise curve and the one assumed at equilibrium is the highly variable contact angle of the slow-moving menisci under certain conditions. Thus, the effective position of the water-oil menisci will often not correspond completely to their static position despite practically constant potentials. For this reason, there are often differences between the assumed static equilibrium form and position and the effective form and position of the water-oil menisci.

During the second infiltration of oil (1.5 L in 2 h), the higher potentials enabled the flattest water-oil meniscus to be displaced slightly below the propagation surface. At the end of the second oil infiltration, the potentials were not much different than those at the end of the first oil

infiltration. The increased volume of oil below the propagation surface due to the additional displacement produced by the second oil infiltration is clearly visible in the saturation diagram for Day 6 (see Table α , in envelope).

The propagation surface must lie 14 cm above the water table. According to Figure 8.2, the flattest virgin water-air menisci must be 18 cm above the water table, and the drainage menisci must be 4 cm beneath this because of the capillary pressure height reduction (Equation [8.1]). The capillary pressure height of the propagation surface is defined as $h_c |_{W(DR,DR,1-RRSL)}^L$ in Equation (6) of Section 3.9.4 in Schiegg (1979, p. 112). However, the effective height of the propagation surface, as defined in Figure 1 of Section 3.8 (in Schiegg 1979, p. 96) is the zone of the most intense redness and is about 3 cm higher. This gives an effective height of the propagation surface above the water table of 17 cm. This is confirmed by the photos and the saturation diagrams.

The first photograph in Table α (in envelope), taken 28 min after the beginning of the first application of oil (2 L in 233 min), shows the radial propagation of the infiltrating oil produced by the application pressure or the capillary suction. The second photograph, taken after 77 min, shows the conversion from the radial to the vertical propagation stage resulting from gravity. At the moment the third photograph was taken (161 min into the experiment), the oil front had just reached the propagation surface, and the propagation parallel to the water table began along the propagation surface. The photograph taken after 234 min shows the form of the oil plume at the moment oil infiltration ceased at the sand surface.

These propagation forms correspond in principle to the two-dimensional version of the conceptual representation of the three-dimensional propagation process reproduced in Figure 8.8. In Figure 8.8 $a_c^- |_{W}^L$ is the average capillary rise representing capillarity, t_U is the point in time when the source is shut off, t_A is the moment at which the oil front reaches the propagation surface, M_0 is the thickness of the oil pool, and E is the point source.

Comparing Figure 8.2 and the first saturation diagram in Table α (in envelope) reveals that the capillary curve in the flume lies a little above the water-air drainage capillary curve. Thus, the capillary curve in the

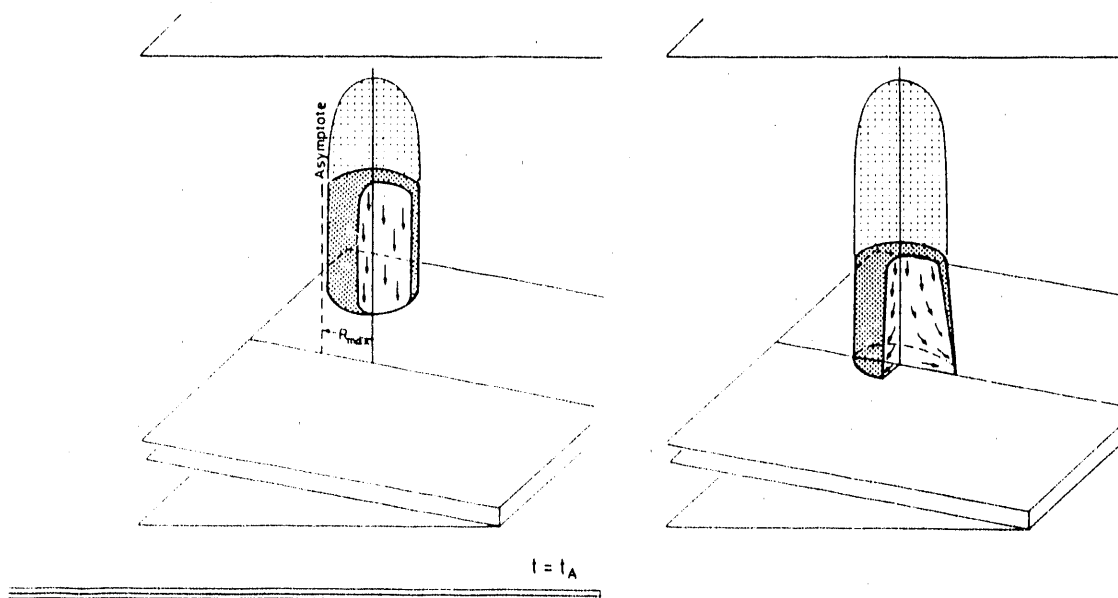
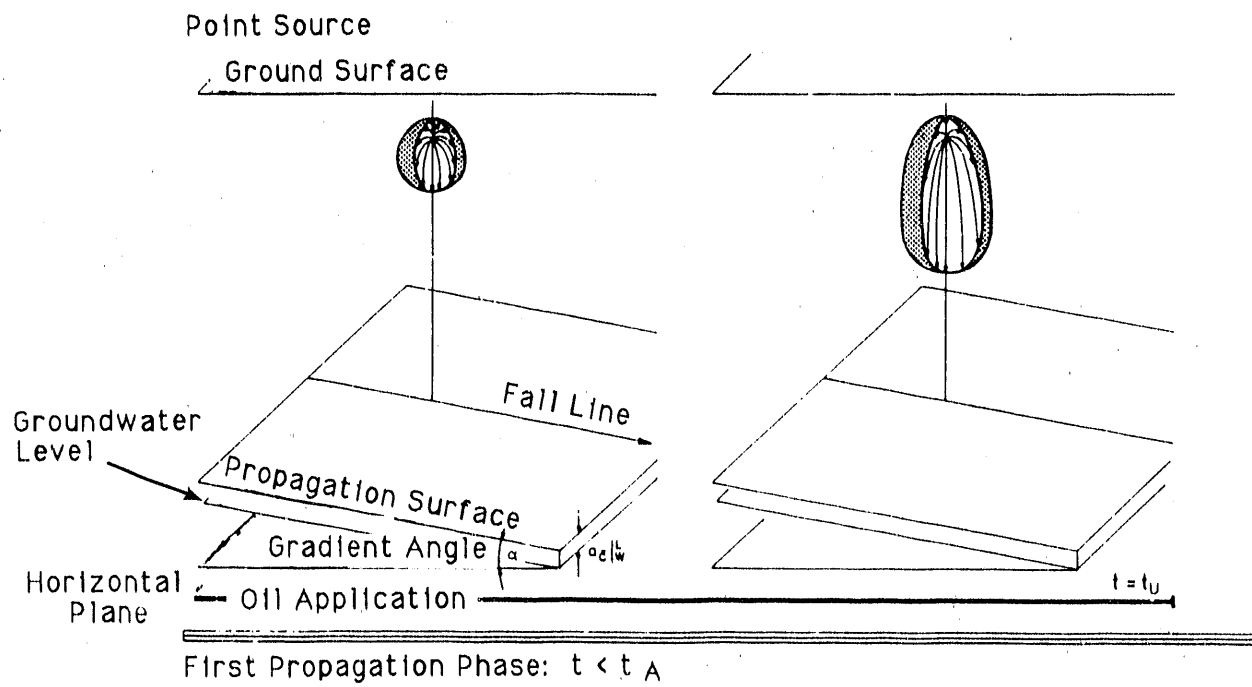
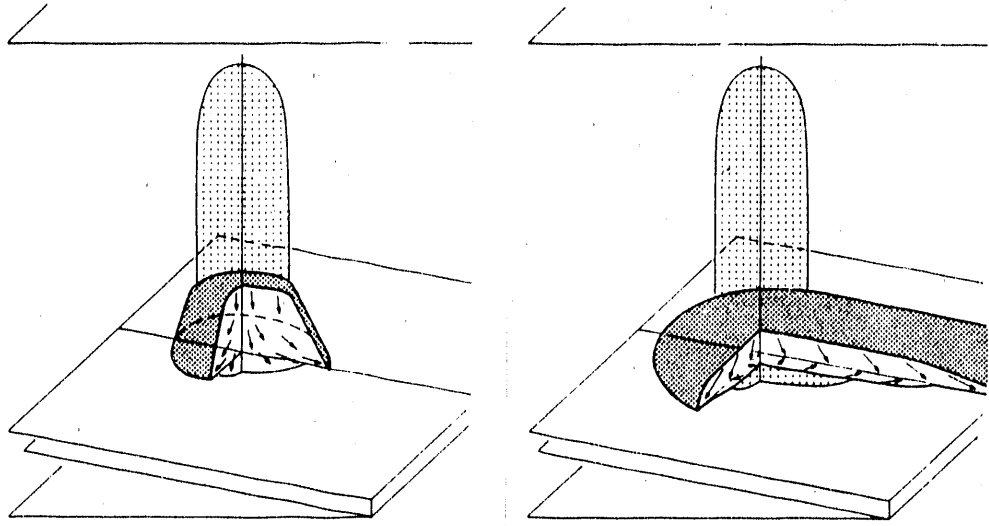
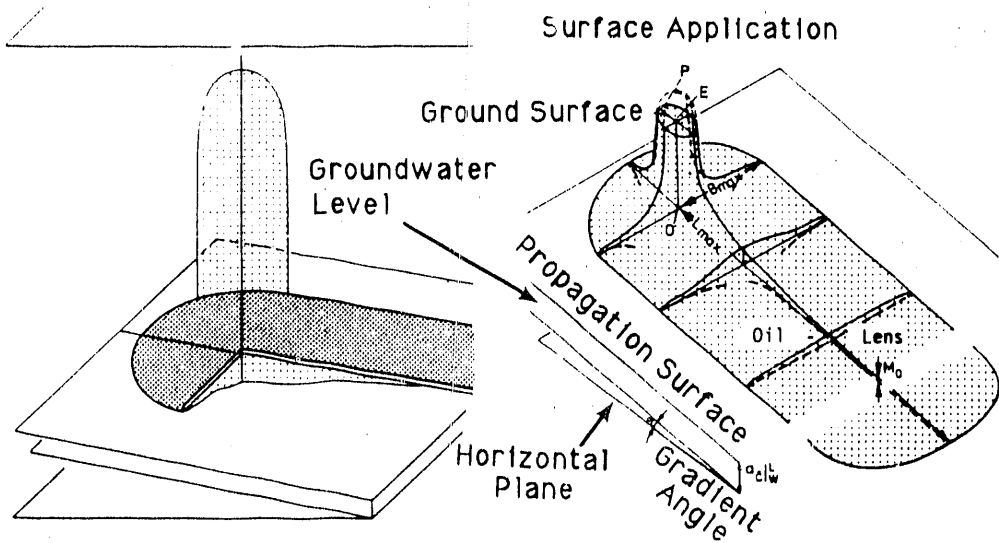


FIGURE 8.8. Conceptual Representation of a Three-Dimensional Oil Propagation Process



Second Propagation Phase: $t > t_A$



End of Propagation

residual
 Funicular

FIGURE 8.8. (contd)

flume is not yet fully formed. This is because only a short time had elapsed since the water table in the flume was lowered to its indicated position.

The first water potential histogram indicates that the water potential is constant with height. The water potential value of $13 \cdot 10^3$ erg/cm³ means that the reference or datum for the potential measurements is 13 cm below the initial water table level. This reference was determined as the elevation of the lowest water table level during an experiment, as discussed in Section 8.3.

Because the interval between potential measurement pairs is about 4 cm and the potential measurement pair highest in elevation is about 36 cm above the initial water table, one can conclude from the first saturation diagram that the water, at the beginning, was in a funicular state over the entire measurement area. Thus, the area under the entire initial water potential data points was shaded in. In contrast, at the same time, the area under the oil potential data points must naturally be left blank. The oil potential values shown represent the potentials based on the random average curvature of the oil menisci in the outermost pores of the hydrophobic probes inserted in the water-wet quartz sand. The pressures and thus also the potentials in the residual fluid fraction generally change simultaneously with the pressure or potential changes in the surrounding funicular fluid if the average curvature of the menisci does not change. For residual oil below the water table, this can be verified by examining the data when the water table rose toward the end of the experiment. It is also widely confirmed by the water potentials measured at residual water saturation.

The first potential histogram after the start of oil infiltration is identical to the potential histogram describing the initial conditions. Within 30 min into the experiment, the oil front reached the first potential measurement pair, and because the oil saturation at the highest measuring point was funicular, the oil potential increased. A partial obstruction during infiltration caused a slight instability in the assumed constant potential and is evidenced by the decrease in the funicular oil potential between the 15- and 30-min potential measurements. As discussed earlier, the oil front reached the propagation surface about 120 min after the beginning of

infiltration. Given that the interval between potential measuring pairs was 4 cm, the potential histograms in Table α (in envelope) confirm the expected oil potential gradient of a little above |1| before the oil front reached the propagation surface.

After the oil front reached the propagation surface, the oil dammed up in the vicinity of the propagation surface, and thus a lens of funicular oil was formed (refer to the conceptual representation in Figure 8.8). The ensuing buildup of oil pressure can produce water displacement in the vertical direction (i.e., the oil pressures can depress the propagation surface). From this point in time, the further vertical propagation of oil proceeded relatively slowly, as mentioned in the discussion of water-oil menisci. However, the horizontal propagation of oil along the propagation surface was faster due to the pressure within the oil lens. The relatively faster horizontal propagation was due to the relatively low viscosity and density of the air being displaced. Thus, oil flow within this lens occurred mainly in a horizontal direction. In the vertical direction, oil flow or the oil potential gradient was relatively small compared to that in the horizontal direction. The existence of this transient oil lens, as well as its thickness, is documented in the oil potential histogram by the presence of the small vertical potential gradients at $t > t_A = 120$ min, which are much less than the potential gradients above the oil lens. From the oil potential histogram for $t > 120$, one can conclude that the top of the oil lens must have lain at the fourth from the top potential measurement location (refer to the photographs in Table α). Indeed, the oil potential at the top of the oil lens tended to increase from this time forward until the end of oil infiltration because more oil was entering the flume. However, this increase in potential was small because the oil infiltration was practically in equilibrium with the spread of the oil lens in the other directions.

After interrupting the application of oil, the oil potentials decreased. The decrease implies that the oil was draining at a constant air potential and residual water saturation. According to the second saturation diagram and the fifth photograph in Table α , the oil saturation above the oil lens decreased to approximately the residual saturation in less than 1 day. The vertical

potential gradients within the lens of funicular oil dissipated to almost nothing within 13 h. Consequently, further dissipation of the oil potentials occurred from oil flowing along the propagation surface.

According to Equation (8.1), the capillary pressure reduction of the elevation at which the transition from insular to the funicular nonwetting fluid saturation occurs is about 4 cm. Because of the dependency of the capillary pressure reduction on the reciprocal of R , the effective capillary radius (Equation [6] of Section 3.4 in Schiegg 1979), the capillary pressure reduction must increase with decreasing water saturation or increasing capillary pressure head, and thus smaller menisci radii. Thus, at the beginning of oil propagation, the water saturations at the highest three potential measurement locations decreased not because of the pressure of the infiltrating oil (the oil moves practically by gravitational flow) but more so because of the capillary pressure-reduction produced by the conversion from funicular water saturation to pendular residual water saturation. Thus, the area under the measured water potentials was left blank in the potential histograms.

The other funicular water potentials remained almost constant with respect to elevation and time, even during the oil application. One must conclude from the small water potential gradients, and thus a slight water flow in the downward vertical direction, that the infiltrating oil primarily displaced air and not water. Moreover, the small vertical water flow could also have been partly a product of drainage initiated by the capillary pressure reduction.

On the second day of the experiment, a second application of oil was made; 1.5 L of oil were added in 114 min. The first oil potential histogram after the beginning of the second oil infiltration illustrates the physical significance of the residual saturation state. As long as no connection exists between the new infiltrating oil and the funicular oil present from the first infiltration (i.e., as long as the second oil infiltration front does not reach the top of the funicular oil lens produced by the first oil infiltration, or as long as an area of residual oil saturation exists between them), the potential of the upper funicular oil cannot be transferred to the lower funicular oil. Thus, flow in the lower funicular oil cannot be

influenced. The fourth liquid potential histogram after the beginning of the second oil infiltration was measured shortly after the moment when the second oil front reached the funicular oil lens from the first oil infiltration. Only at this moment did the potentials of the already present funicular oil and water fractions begin to increase in response to the arrival of the second oil infiltration.

The new influx of oil into the existing oil lens was larger than the immediate outflux from the oil lens. Consequently, the height of the upper oil lens surface increased from the fourth to the third from the top potential measurement location (see the oil potential histogram 2 h after the start of the second oil infiltration). Because of the recently increased oil potentials, an accelerated propagation occurred both downward and horizontally. The vertical potential gradient and thus the downward oil flux increased, but naturally only within the oil lens. As expected, the oil potential gradients above the oil lens remained constant and equal to about $|1|$ because of gravity flow (i.e., about $[4 \text{ cm}] \cdot [0.85 \text{ g/cm}^3] = 3400 \text{ erg/cm}^3$) between two oil potential measurement locations. At the beginning of the infiltration, the potential gradient is greater than $|1|$ because of the capillary suction along the advancing oil front, which is equivalent to an applied pressure.

The somewhat higher oil potential within the oil lens at the end of the second infiltration, compared to the oil potential at the end of the first infiltration, caused additional water displacement in the vicinity of the water table (as already mentioned in the discussion of the difference in the estimated and observed saturation diagram presented in Figure 8.5). This observation is corroborated by the changes observed in the saturation diagrams after 1 and 6 days, and by the photographs taken after 20 h and after 4 days.

The larger water potential gradients toward the end of the second oil infiltration (versus the water potential gradients at the end of the first oil infiltration) could be the result of a possibly stronger downward oil flow produced by the approximately 1.5-times greater oil infiltration rate. They could also be the result of the smaller relative water permeability associated with the higher oil saturations in the vicinity of the oil lens.

The two photographs taken after 4 and 7 days show that little oil propagation occurred during this time interval. This observation is confirmed by the only slight decrease in the relative oil potential of about 400 erg/cm^3 during this time interval. The exponential decrease in the relative oil potential given constant boundary conditions is clear.

After 7 days, oil was infiltrated for the third time (1 L in 117 min). During the third oil infiltration, the vertical potential gradients within the oil lens were smaller than those during the second oil infiltration. In addition to the fact that the third infiltration rate was only two-thirds of the second, the smaller vertical potential gradients could be a product of both the higher oil relative permeability and the small water displacement. The higher oil relative permeability at the beginning of the third infiltration was a result of the clearly higher oil saturations at the beginning of the third infiltration compared to those at the beginning of the second oil infiltration, as shown by the saturation diagrams after 1 and 6 days.

The similar saturation diagrams after 6 and 8 days confirm that practically no displacement of water occurred in the profile under the application site during the third oil infiltration. The potential nomograph in Figure 8.9 provides the information to explain this observation. The nomograph in Figure 8.9 is the continuation of the nomograph in Figure 8.2 and accounts for the potentials measured for the flattest oil menisci near the water-oil level during the second and third oil infiltration. The information in Figure 8.9 restates that the oil potential at the end of the second oil infiltration easily exceeds that at the end of the first oil infiltration. As previously mentioned, the increase in the oil saturation observed in the saturation diagrams is clearly responsible for the greater oil potential. Nevertheless, the displacement of water up to 18 cm below the water-air capillary fringe theoretically (i.e., based on the static water-oil capillary pressure drainage curve) induced by the relative oil potential of 10900 erg/cm^3 cannot be confirmed experimentally. In the experiment, the saturation diagrams after 1 and 6 days show that the water-oil level moved downward from 14 to 15 cm below the water-air capillary fringe. Possible reasons for this observation were presented in the discussion of Figure 8.5. The observation that the

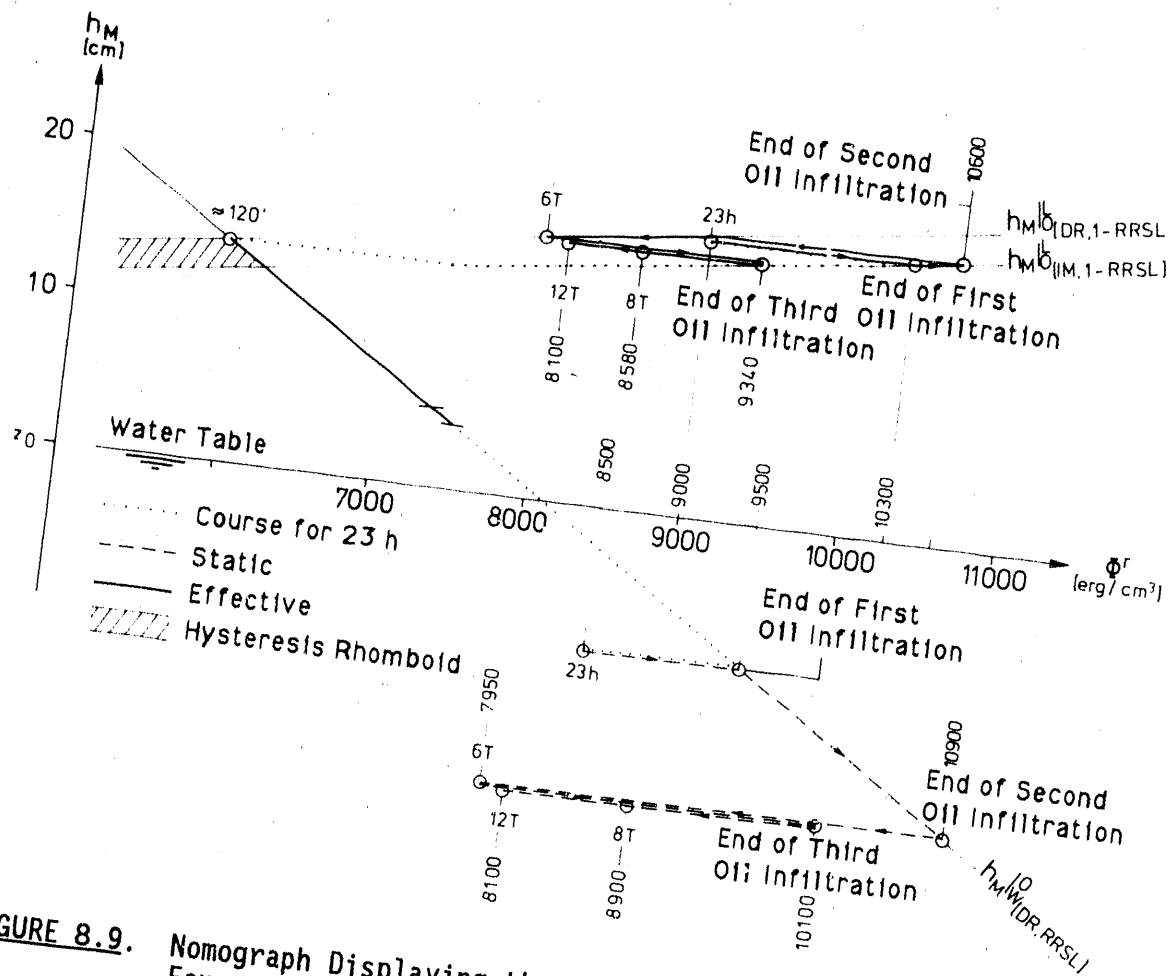


FIGURE 8.9. Nomograph Displaying the Complete Development of the Form and Position of the Flattest Oil Menisci Between 23 Hours and 12 Days Since the Start of Experiment A (T = days)

third oil infiltration did not produce a change in measured fluid saturations is confirmed in Figure 8.9, in which one can see that the flattest oil menisci (i.e., both the oil-air and the water-oil menisci) between 6 and 8 days do not leave their hysteresis area, and thus change only their shape but not their position. A comparison of the photographs after 7 and 12 days reveals that such constancy in the oil saturation, during the third oil infiltration, within the profile underneath the application site is a reflection of the definite horizontal propagation of the oil lens.

The multiple oil applications show the differences between secondary and primary oil infiltrations with similar infiltration rates. During the first

oil infiltration, the oil front reaches the fourth potential measurement location in 80 min. During the third oil infiltration, with practically the same infiltration rate as the first, the fourth potential measurement location was reached in 60 min. During the second infiltration, with a 1.5-times greater infiltration rate than the first, the fourth potential measurement location was reached in 45 min. From a comparison of these durations, it follows that the velocity of the oil front increases with increasing infiltration rate or larger application pressure, and that the oil front during primary infiltration progresses more slowly than during secondary infiltration. The explanation for this last conclusion is that the unoccupied funicular range (ΔS) during secondary infiltrations is smaller than during the primary infiltration because of the already existing pendular oil saturation. The effect of the unoccupied funicular range is given in Schiegg (1979, p. 59) by Equations (1) and (2) of Section 3.2.3, which state that the average pore-liquid velocity during infiltration is inversely proportional to the unoccupied funicular saturation range. (The experimental proof of this can be seen by comparing the last two parts of Figure 2 in Appendix E).

The data in Experiment B confirm that liquid potentials decrease exponentially as a function of time. Yet, the decrease in the potentials in Experiment A occurred extremely slowly compared to the other experiments. In spite of the only slight decrease in the relative oil potential of about 700 erg/cm^3 between 8 and 12 days after the beginning of the experiment, a comparison of the saturation diagrams after 8 and 11 days shows very clearly the tendency for the water-oil drainage capillary curve (shown in Figure 8.7) to distort as a result of its conversion to the imbibition curve. This conversion is caused by the lower relative oil potential, which permits water to displace the oil.

After 12 days, the water table was lowered 13 cm in one step to just above the outlets on the bottom of the flume. The propagation surface subsided the same distance, as can be seen by comparing the photographs taken after 12 and 22 days. If the water-air capillary fringe had been formed by imbibition before lowering the water table, then the subsidence of the propagation surface would have been smaller than that observed for the capillary fringe formed by drainage. In the present case, the position of the flattest

contaminated menisci (and thus the position of the propagation surface) is given both before and after subsidence by $h_c \frac{L}{W} (DR, DR, 1-RRSL)$. The elevation of the contaminated water-air capillary fringe was 14 cm, according to Equation (6) of Section 3.9.4 in Schiegg (1979, p. 112).

From the water potential measurements presented in Table α (in envelope), one can see that the vertical water potential gradient was larger above the propagation surface than below. The upper potential gradient was smaller than $|1|$, indicating a dammed-up water discharge, which was probably due to the smaller water saturations and thus smaller relative water permeabilities above the propagation surface. The propagation surface fell simultaneously with the lowering of the water table. The volume of funicular oil was decreased by a volume equivalent to the volume of pendular residual oil retained in the subsidence zone. A comparison of the photographs and the saturation diagrams before and after the lowering of the water table reveals a small intrusion of the oil below the propagation surface. An explanation for this oil intrusion is that the oil potential at the second and third lowest potential measurement locations were lower after lowering the water table than the oil potentials measured at the end of the second oil infiltration, when the maximum penetration of oil below the water-air capillary fringe was recorded.

Between the first and twentieth day after lowering the water table, the relative oil potential falls from about 9500 erg/cm^3 to 6800 erg/cm^3 . The water potential gradients dissipated to practically zero within 1 day. A comparison of the photographs taken after 12 and 22 days shows that during the first 10 days after lowering the water table, an advance of still funicular oil occurred along the propagation surface. However, between the time photographs were taken on Day 22 and Day 32, practically no propagation of the oil is discernible.

Thirty-four days after the beginning of Experiment A, the water-air level outside the flume was raised 35 cm in one step by raising the reservoirs on either side of the flume. The water-air level outside the flume had corresponded up to this point with the water table within the flume. As expected, the raising of the external water-air level caused an upward flow of water and the funicular oil that was still present in the flume, as evidenced

by the upward oil and water potential gradients. The rate at which the water table rose decreased with time as the potential gradient dissipated. In addition, the dependence of the potential gradients on the saturation, which varied with height, can be seen from the beginning.

After 6 h, only a very low potential gradient of about 200 erg/cm^3 was discernable within the 36-cm height in which liquid potential measurements were made. Within 22.5 h, the water potential increased 400 erg/cm^3 to reach its end value of 35000 erg/cm^3 .

As the water table rose, the relative oil potential in the funicular oil still present was reduced. The rate at which the water table rose was very fast compared to the very small tendency for the oil to move, which was the case before the external water-air level was raised. Therefore, the moment the external water-air level was raised, Case V of Table 1 in Section 3.9.1 in Schiegg (1979, p. 103) is valid, and according to Figure 1 of Section 3.9.4 in Schiegg (1979, p. 113), the relative oil potential theoretically dissipates to the value of 460 erg/cm^3 (Point 1) before the oil becomes residual. The conversion to insular residual oil saturation, caused by the rising water table, occurred in such a way that the value of insular residual oil saturation is twice as large as the value of pendular residual oil saturation (a first approximation given by Equation (2) of Section 3.3 in Schiegg 1979, p. 71).

Potential differences were present in the oil as it became insular (see the last potential histograms from Experiment A), similar to those seen earlier in the pendular oil and residual water. For these potential differences to be preserved in spite of the statics of the surrounding funicular fluid, they must be systematically controlled. A residual state is defined as the existence of disconnected fluid fractions unable to balance potential differences between them. Alternatively, potential differences will not induce flow between the disconnected fractions. The conversion from funicular to residual saturation is defined by a characteristic capillary pressure; that is, by a characteristic pressure difference between the wetting and nonwetting fluids. Compared to the pressure in the surrounding fluid, the pressure in a

residual fluid differs from the capillary pressure that determines the conversion to residual saturation. The pressure in the residual fluid is changed simultaneously and equally with the pressure in the surrounding funicular fluid. Thus, the pressure difference between residual fluid fractions is equal to the pressure change over space in the surrounding funicular fluid. If the densities of the two fluids are not equal, then the pressure difference between residual fluid fractions is not equal to the static pressure distribution in the funicular fluid. For a lighter-than-water residual fluid, such as oil in funicular water, the potential in the residual fluid during statics increases linearly with increasing depth (see the last oil potential histogram of Experiment A). For residual water in a funicular lighter-than-water oil, the potentials would decrease linearly.

The photograph from the last day of Experiment A shows the area of insular residual oil 7 days after raising the external water-air level. Based on the observable disturbances, one can conclude from this photograph that the new position of the propagation surface was about 9 to 10 cm above the raised water table. A first theoretical approximation given by Equation (7) of Section 3.9.4 in Schiegg (1979, p. 112) is 6 cm; however, the effective height of the propagation surface above the water table is about 3 to 4 cm greater, as mentioned in Section 3.6 in Schiegg (1979).

The drainage of oil above the propagation surface is independent of whether drainage is induced by lowering the water table or by primary or secondary oil infiltration and occurs equally as fast in both cases. In 1 day, the oil saturation was reduced to about 6% to 7% of the pore volume as a result of gravity flow (refer to the saturation diagrams after 1 and 13 days). After 2 days the oil saturation was still about 5% (refer to the saturation diagram after 14 days). Within 5 days, the oil saturation had already dissipated to its maximum insular residual value of about 4%.

8.7 EXPERIMENTS B, C, AND D

Experiments B and C differ from Experiment D, and also from the previously described Experiment A, in that, a constant application potential was used first instead of a constant infiltration rate as the oil application

boundary condition; and second, the application site and the propagation surface lie closer together. Section 8.4 dealt with the relationship between a constant application potential and the infiltration rate in displacement processes supported by experimental results. The magnitude of the application potential was such that the average infiltration rates during Experiments B and C were about 10 times larger than for Experiment D and 10 to 20 times larger than for Experiment A. During Experiment B, the application site was only 8 to 10 cm above the propagation surface. During Experiment C, the distance from the application site to the propagation surface of about 21 cm was clearly larger than in Experiment B, yet only a little smaller than in Experiment A with a distance of about 22 cm. For all three experiments (A, B, and C), a drainage water-air capillary fringe was established as an initial condition.

Experiment D differs from Experiments A, B, and C in that a primary imbibition water-air capillary fringe was established as an initial condition. Also, the distance of 28 to 30 cm from the application site to the propagation surface is larger than in all other experiments. And lastly, the infiltration of oil occurred with a constant infiltration rate.

Figure 8.10 shows the sequence of the oil propagation process expected from the conceptual model represented in Figure 8.5 compared to photographs from the actual experiments. Refer to the last paragraph of Section 8.4 for a discussion of the limitations of applying the analytical model to estimate the development of oil propagation in the flume.

8.7.1 Experiment B

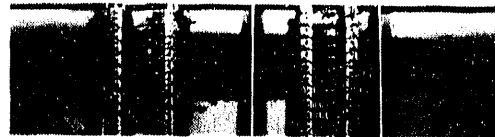
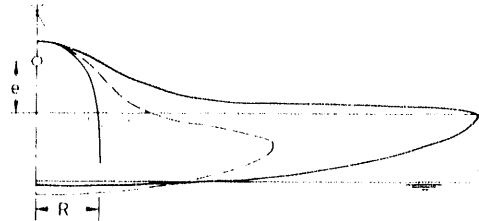
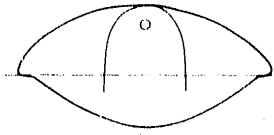
Table β (in envelope) presents the results of Experiment B, in which 4 L of oil were infiltrated in 23 min.

During Experiment B, the saturation diagrams after 12 days did not correspond to theory, which was somewhat surprising. In the saturation range where the conversion of funicular air to residual air is expected, the air was unexpectedly completely displaced by the liquids over time. The resulting protuberance into the zone of residual air saturation was designated as a

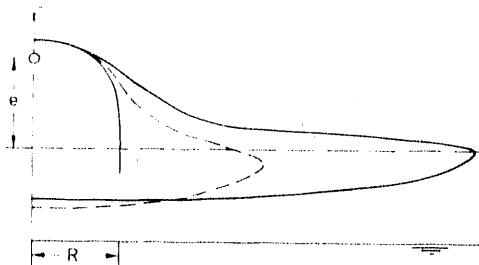
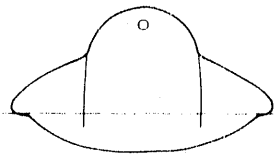
After Oil Front
Has Reached
Propagation Surface

Maximum Observed
Oil Propagation

Rudimentary Form:
Experiment B



Intermediate Form:
Experiment C



Developed Form:
Experiment D

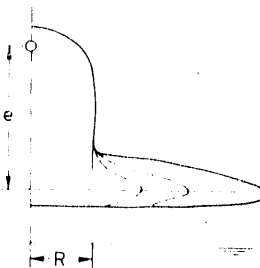
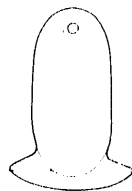


FIGURE 8.10. Oil Propagation Forms for Experiments B, C, and D

hallux. In addition to this oil-air hallux, an water-oil hallux formed almost simultaneously and initially at the same elevation above the water table.

The water-oil hallux seemed driven to hold its elevation. Its elevation was equal to the pressure head for the conversion of the contaminated water-air curve to insular air (i.e., equal to $h_{c|W}^L(DR,DR,1-RRSL) = 14$ cm) for the quartz sand and fluids used in these experiments. On the other hand, the peak of the oil-air hallux fell below this value with time. The subsidence of the oil-air hallux peak below $h_{c|W}^L(DR,DR,1-RRSL)$ is designated as the hallux depression, which had a value of about 2 cm in Experiment B.

The formation of a hallux is not a phenomenon limited to a three-fluid flow system nor due to a systematic error in the semi-graphic method used to obtain the fluid saturations from the Cs-137 and Tm-170 gamma attenuation counts. This is supported by the fact that the hallux phenomenon can also be observed in a quartz sand column with the two-fluid combination of water and air even when a gravimetric sectioning method is used to determine the fluid saturations (see Figures 2b and 2c of Section 3.2.2 in Schiegg 1979, pp. 55-56).

The hallux phenomenon is not explainable hydromechanically because the residual saturation fractions could only decrease by being flushed out or by molecular diffusion. If molecular diffusion is the explanation of the hallux phenomenon, it is surprising that the phenomenon is limited to such a narrow pressure head range and does not manifest itself continuously toward the water table, even to a decreasing extent. Another interesting observation is that although the zone for the conversion from funicular to insular air is displaced within the porous medium when the water table is raised, the elevation of the hallux remains constant, as can be seen from Figure 2c in Section 3.2.2 in Schiegg (1979, p. 56). Must the water-oil hallux be explained as a product of the oil-air hallux because of continuity? Another question is why the hallux phenomenon can occur with such strong differences in appearance. According to experimental results, a hallux can be present more or less distinctly one time, while another time it can practically be missing. It is open to question whether the indentation in the liquid saturation profile that normally appears at the site of the conversion of the flattest menisci from their

drainage to their imbibition form is related to the hallux phenomenon. An example of the indentation is seen on the first saturation diagram of Table β (the fact that the indentation lies at the elevation of the water table in Experiment B is coincidental). The explanation for the hallux phenomenon is given in Appendix B.

The theory presented in Section 3.5 in Schiegg (1979) on the construction of the saturation diagrams from measured potentials does not consider the hallux phenomenon. However, if this were taken into consideration (i.e., if hallux-deformed curves are superimposed), then the saturation diagrams in Experiment B, although unusual in form, correspond to a great extent to the smooth form of the saturation diagram, as shown in Figure 8.11.

The oil infiltration rate in Experiment B is almost 20 times larger than in Experiment A, which caused a distinct displacement of water and thus a clearly recognizable vertical water potential gradient that was barely present in Experiment A. According to the schematic diagram in Figure 8.12, the vertical displacement of water must produce a horizontal flow of water and even a rise in the water table in the vicinity of the oil plume. The slight rise in the water table causes a definite upward flow component. This observation is confirmed in the water potential histogram for the right-hand profile (62 cm to the right of the oil application site), where the water potential gradient was in the upward direction during the application of oil.

After ending the application of oil, the oil potential decreased exponentially with time. The displacement of water by oil decreased correspondingly fast, stopped, and then reversed as the water in turn displaced the oil. As the depressed water table underneath the oil plume rebounded, the previously observed rise in the water table in the vicinity of the oil plume ceased and the water table level began to subside, as is shown by the dashed lines in Figure 8.12. However, the fact that the water potential gradients in the application site profile did not change their direction after the end of the oil application indicates that only the upper dashed arrow, directed toward the left, in Figure 8.12 can be valid.

Because of the about 20-times-greater (than in Experiment A) infiltration rate and the small distance from the oil application site to the propagation

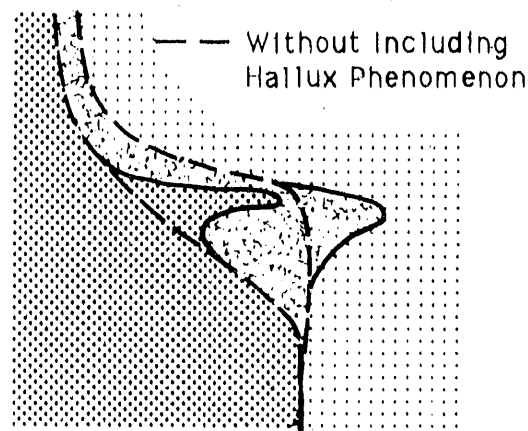


FIGURE 8.11. Saturation Diagram Including the Hallux Phenomenon

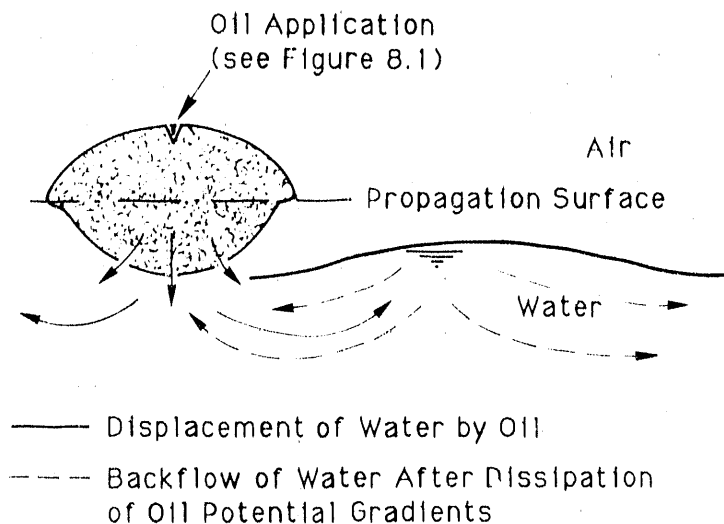


FIGURE 8.12. Diagram of Water Displacement by Oil Infiltration

surface, the oil front reached the propagation surface after 2 min, where it dammed up. This damming of the oil front is shown in the oil potential histogram as a reduction of the oil potential gradient to below $|1|$. The early damming of the oil front increases the spreading of the top of the oil lens shortly after the start of oil infiltration at the application site. This behavior creates the propagation form described as rudimentary in Figure 8.10 for small distances between the application site and the propagation surface. The relative oil potential during application was 25500 erg/cm^3 .

Before the end of the oil application, the water potential in the right-hand potential profile is more than 1000 erg/cm^3 lower than in the potential profile under the application site. This means that water was flowing outward from the application profile, which corresponds to the schematic representation in Figure 8.12. As a consequence of the outward flow, a definite return flow appeared after the end of the oil infiltration. The return flow of water must have been almost horizontal as a result of the lack of an upward component. This is confirmed by the larger water potentials (several 100 erg/cm^3) after about 50 min in the right-hand profile compared to those in the application profile.

Eighteen hours into Experiment B, the water potentials had already dissipated to yield the initial static potential gradients of zero. In addition, the oil potentials had already become practically static with no vertical gradients. Thus, vertical flows could no longer be detected. The oil potential beneath the application site was about 8000 erg/cm^3 , and the oil potential in the right-hand profile was about 1000 erg/cm^3 less. This indicated a significant horizontal flow of oil along the propagation surface. The saturation diagrams show that this horizontal oil flow must have still existed several days later even when a horizontal oil potential gradient could no longer be detected. Thus, the difference in oil potential over the 62-cm distance between the right-hand profile and the application site profile was smaller than 50 erg/cm^3 , or the potential gradient was less than 1 erg/cm^3 . This small potential gradient implies that the flow of oil along the propagation surface probably became very slow early in the experiment. However, the oil potential beneath the application site did dissipate from about 8000 erg/cm^3 after 18 h to 2800 erg/cm^3 within 57 days.

After 57 days, the slope of the water table was adjusted to approximately 4%. The exact slope was calculated as 4.35% by using the observed water potential difference of 2700 erg/cm^3 (or $2.7 \text{ cm H}_2\text{O}$) over the 62-cm distance between the two potential profiles. More important, the slope adjustment caused a rise in the water table in both the application site potential profile and the right-hand potential profile. The rise in the water table was

determined as 5.6 cm based on the resulting 5600 erg/cm^3 increase in the water potential underneath the oil application site.

Given such a development history during the 59 days since the start of Experiment B, the hysteresis cycle for the flattest menisci is presented in Figure 8.13, which is based on the nomograph in Figure 1 of Section 3.9.4 in Schiegg (1979, p. 113).

Figure 8.13 reveals that the flattest oil-air menisci subsided below the flattest contaminated water-air menisci, probably because of the hallux depression. This occurred contrary to the theory calling for the eventual existence of hysteresis-caused oil pools (see comments for Cases VII and VIII of Table 1 in Section 3.9.1 in Schiegg 1979, p. 103). This observation is only explainable by the fact that the relative oil potential during oil infiltration exceeded the approximately 6000 erg/cm^3 of corner point 3 in the hysteresis rhomboid of Figure 1 in Section 3.9.4 (Schiegg 1979, p. 113) for the (DR,DR) menisci. After 57 days, the relative oil potential dissipated to 2800 erg/cm^3 . During static equilibrium, a relative oil potential of 2800 erg/cm^3 means that the flattest oil-air menisci are located just 11 cm above the water table. The saturation diagram at 56 days shows that the effective position of the flattest oil-air meniscus was a little above 12 cm. The estimated elevation (11 cm) of the flattest oil-air menisci helps to explain why the observed elevation (12 cm) of the propagation surface in Experiment B (as evidenced by the saturation diagrams and the photographs in Table β , in envelope) is not approximately 4 cm lower (the value for the static capillary rise reduction from Equation [8.1]), but about 6 cm lower than the flattest pure water-air drainage menisci, which were 18 cm above the water table.

From the moment the water table began to rise in response to the changing water table slope, the movement of the water table dominated the subsequent form and position of the oil menisci. This would also have been true even if the relative oil potential had not increased during the first 20 min, as was observed in Experiment B. This dominance of the rising water table meant that the flattest oil-air menisci, which were in their drainage form while static, tended toward their imbibition form relative to the porous matrix. Such a

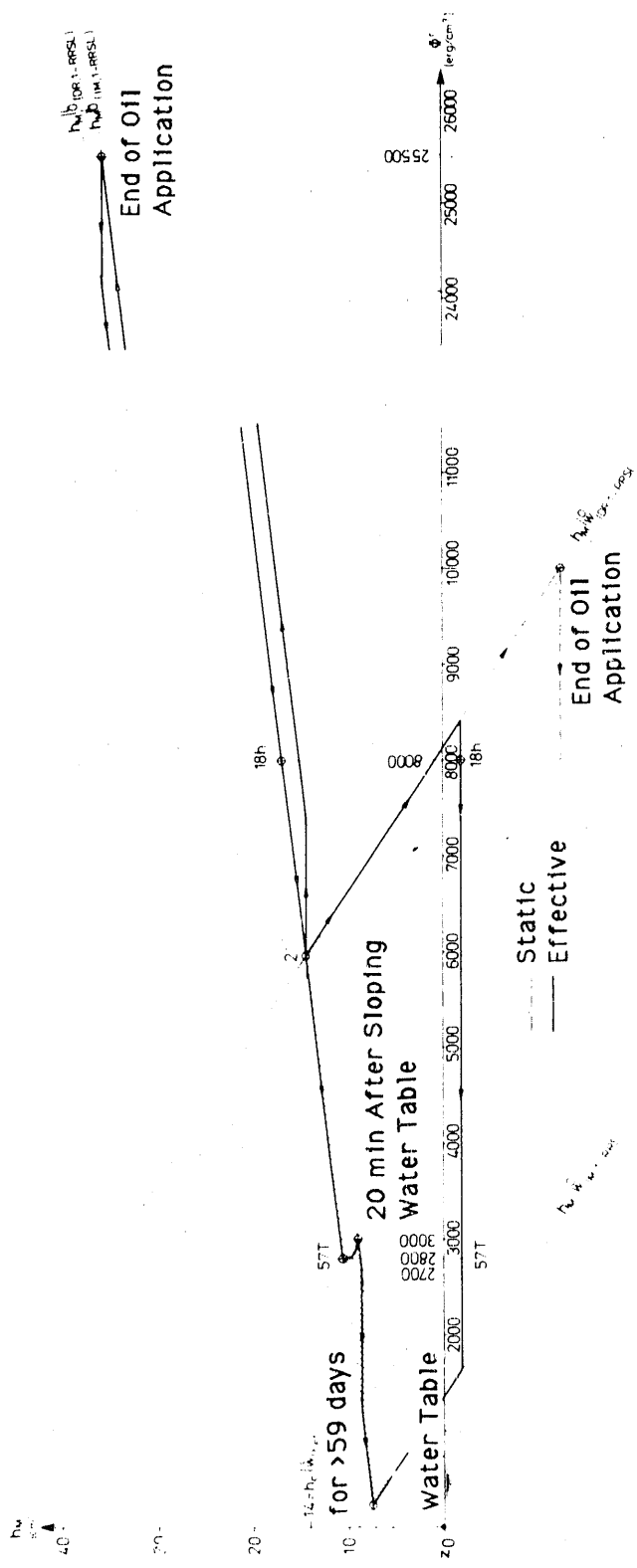


FIGURE 8.13. Nomograph Displaying the Development of the Form and Position of the Flattest Oil Menisci in the Oil Application Profile During Experiment B (T = days)

shift caused the relative oil potential to increase, which is reflected by the line curving to the right in the hysteresis rhomboid shown in Figure 8.13. If a constant relative oil potential had been maintained, the line would have proceeded vertically downward, and if the relative oil potential had decreased, the line would have curved to the left.

Twenty minutes after readjusting the slope of the water table, the water potential in the funicular oil area was a little above 2000 erg/cm^3 . Thus, up to this time, the water table had risen a little more than 2 cm ($\Delta h_S|_W^L$). The hysteresis, $\Delta H_C|_O^L(1-RRSL)$, in the flattest oil-air menisci is determined from Equation (4) of Section 3.9.4 in Schiegg (1979, p. 112) as

$$\begin{aligned} \Delta H_C|_O^L(1-RRSL) &= h_C|_O^L(DR, 1-RRSL) - h_C|_O^L(IM, 1-RRSL) \\ &= 7,2\text{cm} - 5,4\text{cm} = 1,8\text{cm} \end{aligned} \quad (8.5)$$

By comparing $\Delta H_C|_O^L$ and $\Delta h_S|_W^L$, one can conclude that the flattest oil-air menisci just reach their imbibition form. For $\Delta H_C|_O^L > \Delta h_S|_W^L$ after 20 min, the conversion point for the development of the oil potential would not lie directly on the $h_M|_O^L(IM)$ line (such as in Figure 8.13) but would lie within the hysteresis loop. Nevertheless, the observed oil potential is still called the conversion point because the relative oil potential (calculated from Equation [8.2]) begins to fall again after 20 min.

Because of the change in the water potential, for about 1 h, the rising water table predominantly determined the position and form of the flattest oil-air menisci. Thus, the oil-air menisci rose simultaneously with the water table until about 70 min after readjusting the slope in spite of the decreasing relative oil potential. This behavior caused the oil-air menisci to take on their imbibition form. They directly followed the $h_M|_O^L(IM)$ line in the hysteresis rhomboid during their conversion, at the relative oil potentials observed until 70 min after readjusting the slope of the water table. After 70 min, the relative oil potential had dissipated to about 2700 erg/cm^3 . Then, the decrease in the relative oil potential began to once again dominate over the rising water table in influencing the form and position of the oil menisci. This means that during a falling relative oil potential, during a

falling oil-air level, and during a slow rise of the water table, the oil-air menisci maintain their position relative to the porous matrix and thus tend to take on their drainage form. If the oil-air menisci reach this drainage form, then they follow the $h_{M|O}^L(DR)(\phi^r)$ line until their union with the flattest water-oil menisci.

The rise of the water table during the first 70 min induced an imbibition process in the water-oil menisci. This is confirmed by the accelerated disintegration of the funicular oil, which was still present below the propagation surface, to insular residual saturation. This is evident from the comparison of the saturation diagrams.

Because the oil-air menisci were in a drainage form, and the water-oil menisci were in an imbibition form, both oil menisci were at Point 4 of the hysteresis rhomboid of Figure 1 in Section 3.9.4 in Schiegg (1979, p. 113). Thus, they had the smallest possible transitional relative oil potential, (i.e., 230 erg/cm^3). The merging of both oil menisci and the associated potential reduction up to 230 erg/cm^3 , which was confirmed by the potential measurements, was only possible because the water table was still rising (imbibing). If the water table were stationary, then Case VIII in Table 1 of Section 3.9.1 in Schiegg (1979) would have existed. Naturally, the coincidence of both oil menisci producing the contaminated water-air menisci assumes a microscopic point of view. However, the merging of both oil menisci is incompatible with the development of the potential within the hysteresis rhomboid. From a macroscopic viewpoint, this merging of the flattest oil menisci in the propagation surface reflects the conversion from funicular to residual oil saturation.

Two days after readjusting the slope of the water table, the relative oil potential had already dissipated to about 230 erg/cm^3 . The funicular oil remained in the vicinity of the fourth (counting down) oil potential measurement location for about 10 more days. By then, the oil had lost its funicular characteristic and had become residual. Thus, contaminated DR,IM-menisci associated with residual oil remained behind. The capillary pressure head or static capillary rise of these menisci was about 7.5 cm according to Equation (8) of Section 3.9.4 in Schiegg (1979, p. 112). This is confirmed by the

fact that the conversion to insular air in the application site profile was found to be about 8 cm above the water table in the last saturation diagrams.

In Experiment B, the last saturation diagram before readjusting the slope of the water table confirms that the propagation surface or the flattest contaminated water-air menisci (as discussed previously) lay only about 12.7 cm above the water table instead of 14 cm. Because the observed 9.3-cm rise of the water table in the right-hand profile is greater (based on the potential measurements) than the hysteresis area of ΔH_c , ($[h_c^L|_W(IM,DR,1-RRSL) = 12.7 \text{ cm}] - [h_c^L|_W(IM,IM,1-RRSL) = 6 \text{ cm}]$) = 6.7 cm, the elevation above the water table for the conversion to insular air saturation must be equal to the minimum contaminated capillary pressure head $h_c^L|_W(IM,IM,I-RRSL) = 6 \text{ cm}$. In the last saturation diagram of the right-hand profile at 8 days, the elevation for the conversion lies somewhat lower.

Finally, it should be noted that the observed pendular residual oil saturations in the application site profile are higher and less uniform than observed in Experiment A. It is open to question whether this observation is a result of a residual oil constriction caused by the decrease in the elevation of the oil-air hallow coupled with the constant water-oil hallow elevation.

8.7.2 Experiment C

In Experiment C, 8 L of oil were infiltrated in 48 min, at a constant application potential, into the quartz sand in which a drainage water-air capillary fringe had been established. After 4 h and 15 min, the slope of the water table was adjusted to 1.5%. After 7 days, the sloped water table was raised about 10 cm. The saturation diagrams in Figure 8.14 represent the application site profile after 8, 17, and 19 days. Figure 8.15 presents photographs taken of the oil propagation during the 7 days since the beginning of Experiment C. After 20 days, the water table was leveled off to a 0.0% slope and was simultaneously lowered 21.5 cm. The saturation diagram after 21 days is shown in Figure 8.16.

The third saturation diagram in Figure 8.14 reveals that the insular residual oil saturation is about 8%. This is a confirmation of the relation

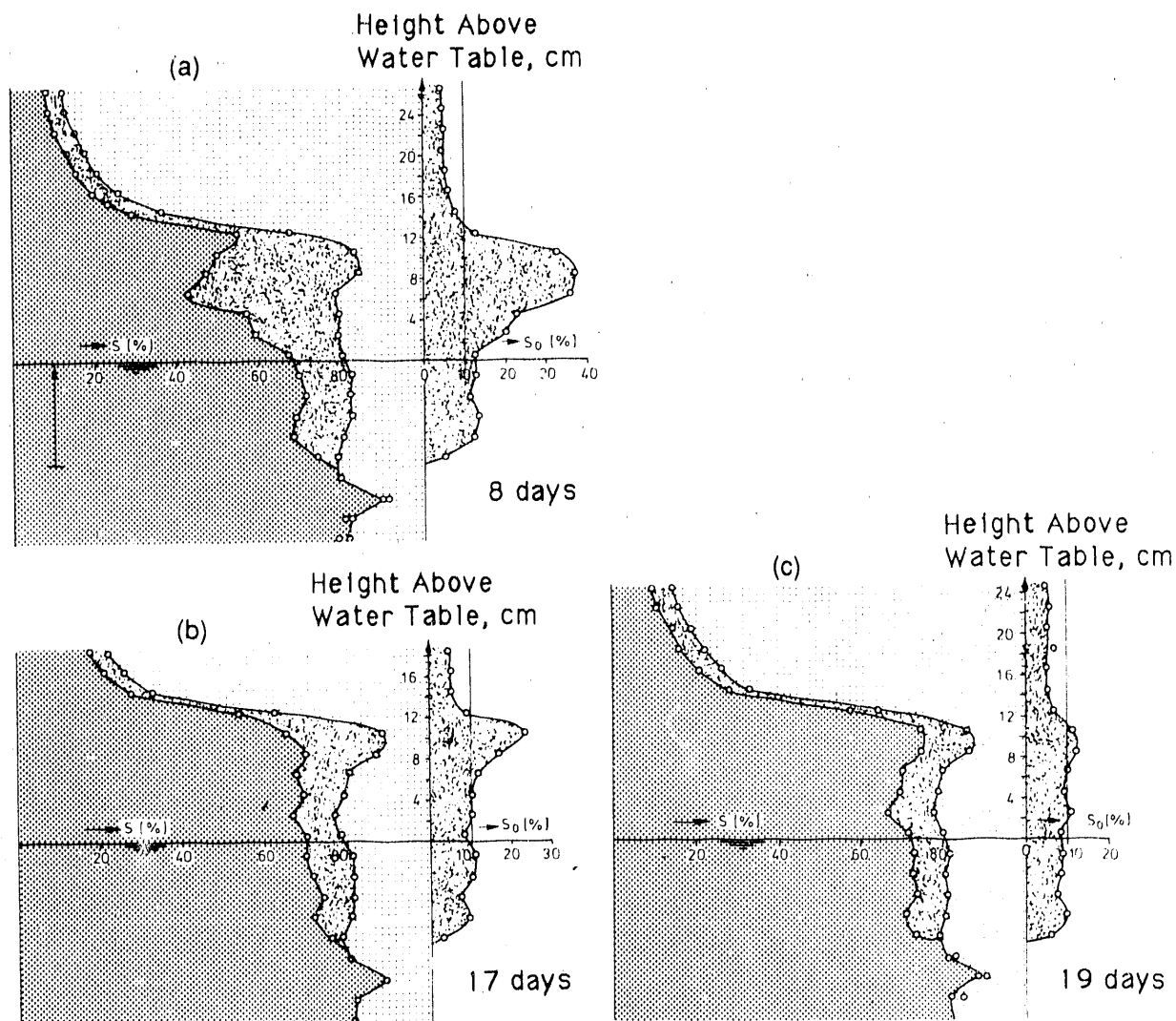


FIGURE 8.14. Saturation Diagrams for the Oil Application Profile (a) 8, (b) 17, and (c) 19 Days into Experiment C

given by Equation (2) of Section 3.3 in Schiegg (1979, p. 71), which states that the insular saturation is about twice as large as the pendular saturation. The conversion from the third saturation diagram in Figure 8.14 to that in Figure 8.16 is experimental proof of the explanation given at the end of Section 3.9.1 in Schiegg (1979, pp. 102-108), which states that the conversion from insular to pendular residual oil saturation, resulting from lowering of the water table, must occur through a funicular oil region.

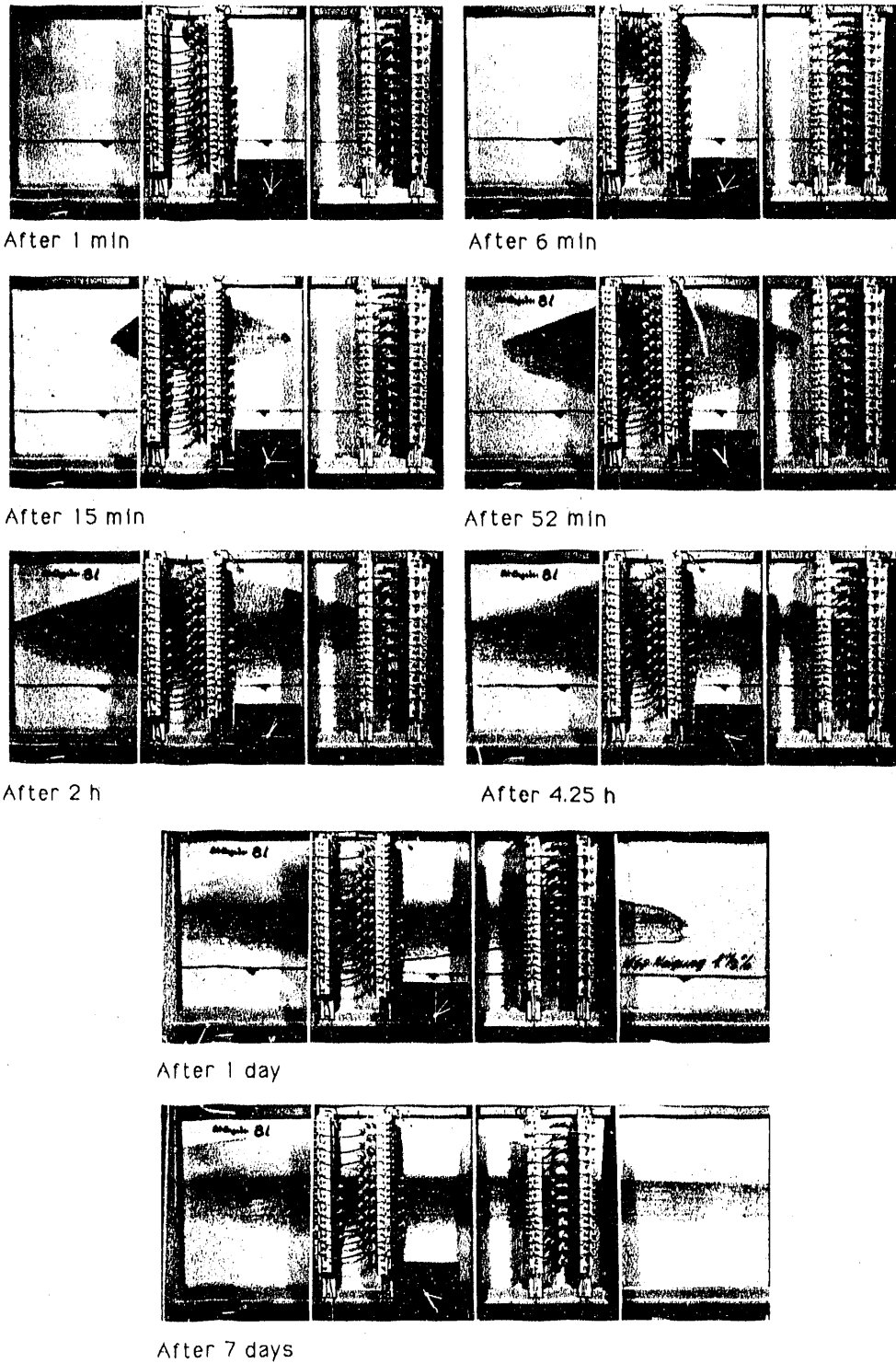


FIGURE 8.15. Photographs Taken During the First 7 Days of Experiment C

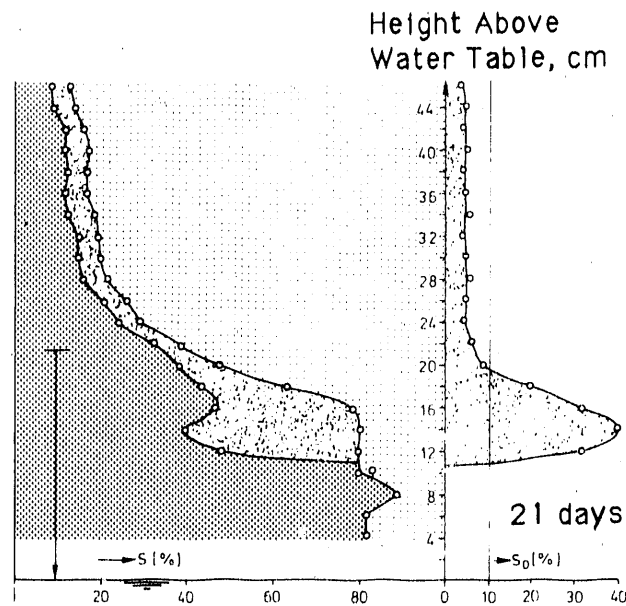


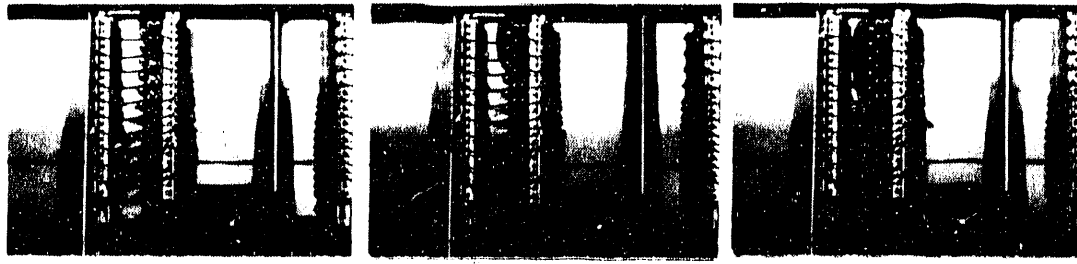
FIGURE 8.16. Saturation Diagram 1 Day After Lowering the Water Table in Experiment C

8.7.3 Experiment D

Experiment D was performed with the predominant goal of studying the propagation of oil along the propagation surface. To accomplish this goal, fluid saturations were obtained at nine profiles. The results of Experiment D are presented in Table 8 (in envelope).

During Experiment D, 2 L of oil were applied at a constant infiltration rate into the quartz sand in which a primary imbibition water-air capillary fringe had been established for 2 h. After 57 days, the water table was lowered about 12 cm, and after 68 days the slope of the water table was adjusted to 4%. Figure 8.17 is a compilation of the photographs taken during Experiment D.

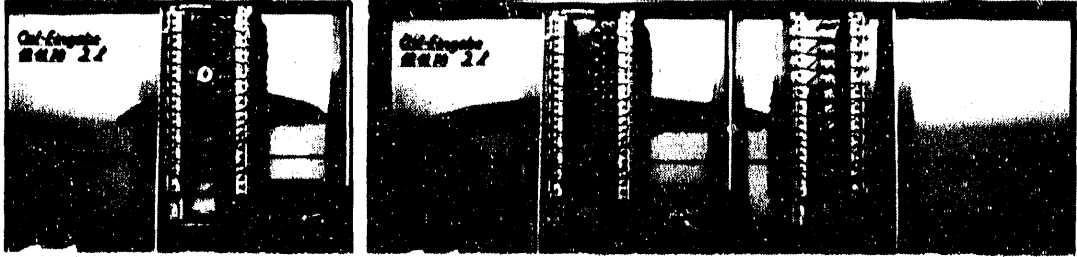
The photographs in Figure 8.17 clearly reveal the upper and lower boundaries of the funicular water zone for the imbibed, virgin water-air capillary fringe. Because the vertical distance between the separate potential measurement locations is 4 cm, the elevation of these boundaries agrees with the lower boundary of 9 cm and the upper boundary of 23 cm above the water table



After 21 min, 40 sec

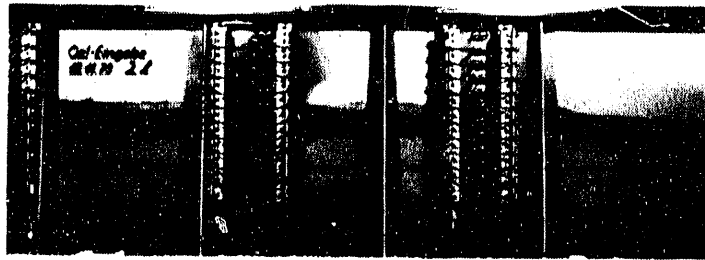
After 41.5 min

After 1 h, 19 min

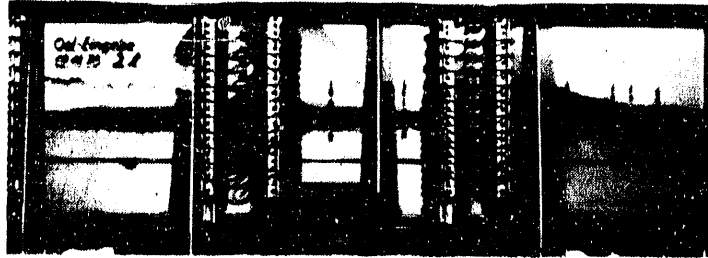


After 2 h

After 3 h, 24 min



After 3 days



After 29 days



After 67 days

FIGURE 8.17. Photographs of Oil Propagation During Experiment D

found in the first saturation diagram of Table 6. As the 2-h-old primary imbibition water-air capillary fringe further matured during the first days of Experiment D, its upper boundary rose from 23 cm to 28-30 cm. This latter value for the upper boundary of funicular water is in agreement with the pure, primary HCWLIM curve of Figure 8.2 and can be observed in the saturation diagrams, as well as in the photograph taken on Day 29 (Figure 8.17).

The liquid potential measurements show that during the application of oil at an infiltration rate twice as large as in Experiment A and 10 times smaller than in Experiments B and C, the water potentials increased to only a couple of hundred erg/cm^3 . The oil potential measurements confirm the expected gravity flow in the zone of the upper five potential measurement locations. By following the evolution of the liquid potentials during the application of oil, one can monitor the formation of the lateral funicular oil lens as the oil reaches the propagation surface. By the end of the oil application, the oil lens had built up until its top was just below the fifth (counting from the top) potential measurement location. From the photographs and the known 4-cm interval between potential measurement locations, the top of the oil lens can be defined as being approximately 16 cm above the water table. This value is confirmed by the fact that the observed relative oil potential (Equation [8.2]) at the fifth potential measurement location (about 8500 erg/cm^3) corresponds to an elevation for the flattest imbibed oil-air menisci of 15.5 cm above the water table, according to Figure 1 of Section 3.9.4 in Schiegg (1979, p. 113). The relative oil potential at the bottom of the oil lens, which is in the vicinity of the seventh (counting from the top) potential measurement location, reached a maximum value of 7830 erg/cm^3 after 150 min.

After ceasing the application of oil, the relative oil potential fell even while the elevation of the water table stayed constant. This means that the oil-air menisci were changing from their imbibition form to their drainage form, that the water-oil menisci were changing from their drainage form to their imbibition form, and that the oil-air and water-oil menisci were finally beginning to approach each other or the propagation surface. After 1 day, the relative oil potential, which was already almost constant with elevation, was

still 5500 erg/cm³. After 22 days, the relative oil potential had dissipated to 3800 erg/cm³. A value of 3800 erg/cm³ corresponds to an elevation of about 12 cm above the water table for the flattest drainage oil-air menisci. The saturation diagram of the application site profile after 22 days confirms this. According to the potential measurements taken 30 and 56 days after the start of Experiment D, the relative oil potential had dissipated to 3300 and 2600 erg/cm³, respectively, and thus had approached its minimum possible value of 1500 erg/cm³ for $h_{c|W}^L(\text{bef}1) = 9$ cm, as depicted in the potential nomograph presented in Figure 8.18 (the minimum possible value is valid for an initially pure imbibition curve formed over a stationary water table for which the contaminated $h_{c|W}^L$ equals 9 cm, according to Section 3.9.5 in Schiegg (1979) or Figure 8.2; these conditions are defined by Case VII of Table 1 in Section 3.9.1 in Schiegg 1979, p. 103).

At static equilibrium, an oil potential of 7830 erg/cm³ corresponds to an elevation of the water-oil menisci 2 cm above the water table. According to Figure 8.18, the threshold potential of 6750 erg/cm³, which is the potential that must be overcome for the water-oil menisci to push below the propagation surface (i.e., for oil to displace water at the imbibition water-air capillary fringe), was exceeded by about 1000 erg/cm³ for only a few hours. Thus, the oil was able to effectively displace the water just a few centimeters below the propagation surface. The elevation of the propagation surface above the water table is, in the first approximation, equal to $h_{c|W}^L(\text{bef}1,1\text{-RRSL}) = 9$ cm, according to Section 3.6 in Schiegg (1979). In the photographs taken from the front of the flume, this penetration was only 2 to 3 cm; and in the photographs taken from the back of the flume, it was only 1 cm. The saturation diagrams within the application site profile confirm these observations, because the flattest water-oil menisci are shown to lie 7 to 8 cm above the water table. Away from the application site profile, the relative oil potential did not exceed the threshold value of 6750 erg/cm³, and, consequently, the oil could not push below the propagation surface.

Experiment D shows, among other things, the experimental proof of the statement in Case IV of Table 1 in Section 3.9.1 in Schiegg (1979, p. 103). Consequently, with water-oil menisci that lie below Corner 2 of the

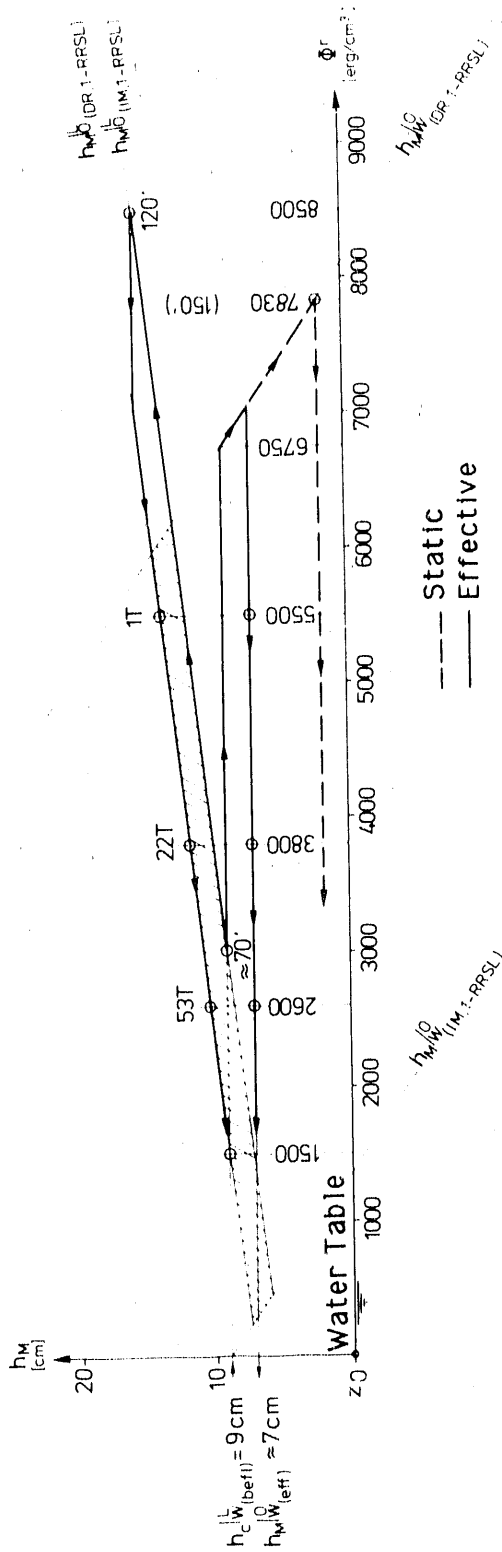


FIGURE 8.18. Nomograph Showing the Development of the Form and Position of the Flattest Oil Menisci During the First 53 Days of Experiment D (T = days)

hysteresis rhomboid of Figure 1 in Section 3.9.4 in Schiegg (1979), drainage (which would naturally induce the drainage form of the water-oil meniscus) is not possible as long as the relative oil potential exceeds the threshold value Φ_{IV}^r . Based on the remarks in the brackets of Table 1 in Section 3.9.1 in Schiegg (1979), Φ_{IV}^r was 6750 erg/cm^3 . The minimum value Φ_{IV}^r is equal to the transition oil potential in the porous matrix for Corner 2 (i.e., it is equal to $\Phi_{(IM,DR)}^{rtM}$), determined as 6200 erg/cm^3 according to Equation (9) of Section 3.9.4 in Schiegg (1979, p. 114). The lower the water-oil meniscus lies below Corner 2 of the hysteresis rhomboid, the larger is the threshold value of Φ_{IV}^r .

A comparison of the photographs taken at the end of Experiment D (in envelope) and at the end of the primarily analogous Experiment E (Figure 8.19) indicates that the penetration of oil below the propagation surface and the subsequent shape of the oil lens depends on whether the relative oil potential exceeds the threshold value Φ_{IV}^r at a definite time or by a definite amount. During Experiment E, a stationary imbibition water-air capillary fringe was also established before applying the oil. The porous matrix had the same characteristics as the one used in Experiments A through D. As in Experiment D, the propagation surface in Experiment E was 9 cm above the water table, and the threshold value Φ_{IV}^r was the same with a value of 6750 erg/cm^3 . At the end of the oil application during Experiment E, the relative oil potential at the propagation surface below the application site reached a maximum value of 17000 erg/cm^3 and thus exceeded the threshold Φ_{IV}^r value of 6750 erg/cm^3 by 10000 erg/cm^3 , whereas in Experiment D the maximum value was 7830 erg/cm^3 , which exceeded the threshold Φ_{IV}^r value by only 1000 erg/cm^3 .

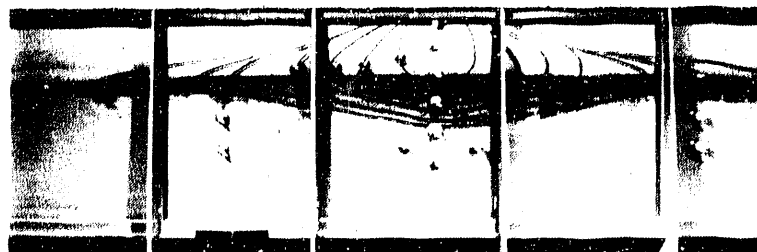


FIGURE 8.19. Final Extent of Oil Propagation in Experiment E

In contrast to the water-oil menisci, one does not need to differentiate between the static and effective position of the oil-air menisci. In contrast to the slow displacement of water by oil, the faster (because of density) displacement of air by oil allows the oil-air menisci to reach their static equilibrium position while subject to a constant potential or potential gradients for only a short time. This was confirmed in Experiment E by the fact that the oil-air menisci in the oil lens rises to 15.5 cm in less than 50 min, which corresponds to 500 erg/cm^3 .

Lowering the water table by 12 cm after 57 days induced a change in the form of the water-air menisci from the earlier imbibition form to the drainage form while not affecting their position relative to the porous matrix. Hysteresis in the flattest contaminated water-air menisci is, according to Equation (5) of Section 3.9.5 in Schiegg (1979, p. 117),

$$\Delta H_c \left| \frac{L}{W}(\text{Defl}, I-RRSL) \right| = \left| \frac{L}{W}(\text{Defl}, DR, I-RRSL) \right| = \left| \frac{L}{W}(\text{Defl}, IM, I-RRSL) \right| \quad (8.6)$$

Thus, the constant position of the contaminated water-air menisci (while changing their form) is valid while lowering the water table the first 5 cm. For the remaining 7 cm of the 12-cm subsidence, the flattest contaminated drainage water-air menisci move simultaneously with the water table. In this manner, the interval between the water table and the propagation surface is enlarged from 9 cm to $(9 + 5) \text{ cm} = 14 \text{ cm}$.

A 7-cm subsidence of the propagation surface implies that the funicular oil fraction also subsided 7 cm. On the other hand, the residual oil cannot follow the subsiding propagation surface and thus remains at its original location in the porous matrix. Consequently, the distance between the original pendular oil and the new water table is increased by the total distance the water table was lowered, or 12 cm. The correctness of this analysis is evidenced by comparing the separate plots of the oil saturation distribution with elevation before and after the lowering of the water table. These plots are adjacent to the total liquid saturation diagrams and use the 100% total liquid saturation vertical line as their zero oil saturation ordinate. The

average distance between the pendular oil fraction and the water table increased from about 12 cm to about 24 cm after the lowering the water table.

From the oil saturation diagrams presented on the left of the application site profile of Table 8, one can see that the above concept is also applicable to the residual oil fraction occurring along the oil front along the propagation surface. Likewise, these oil saturation diagrams confirm that the greater the volume of funicular oil, the more the funicular oil can follow the subsiding propagation surface; that is, until the available funicular oil has been distributed residually with elevation. This development is illustrated by the decrease in the elevation of the flattest water-oil meniscus in the oil saturation diagrams from the profile farthest to the left (farthest from the application site) to the profile farthest to the right (underneath the application site). Finally, if the funicular oil fraction is large enough to maintain a funicular state over the entire distance that the water table subsides, then the oil will flow to the lowest possible elevation and thus create a new propagation surface. In practice, after subsidence has induced the flattest menisci to take on their drainage forms, the new propagation surface must be a little more than 14 cm above the water table. This is confirmed by the oil saturation diagram for the application site profile and by the last photograph in Figure 8.17.

Because the position of the residual oil fraction occurring along the oil front along the propagation surface is practically constant, the drainage of water caused by lowering the water table produces the illusion in the saturation diagrams that the residual oil is displaced along the contaminated water-air pressure curve. This observation explains the formation of the seemingly incompatible saturation diagrams in the profile farthest to the left after the lowering of the water table. In fact, these observed saturation diagrams are not incompatible with the theory used to estimate the saturation diagrams presented in Section 3.5 in Schiegg (1979, p. 87). It is accidental that the residual oil fractions are visually displaced to the zone where funicular water is converting to residual water. The location of the residual oil fraction was determined by the extent to which the propagation surface subsided in the experiment. With a smaller subsidence, the residual oil

fractions would have remained well within the funicular water zone, whereas with a larger subsidence, the residual oil fractions would have been displaced to within the residual water saturation zone.

The propagation surface subsided by 7 cm beneath the application site after lowering the water table 12 cm. Consequently, its distance to the water table increased by only about 5 cm. This is surprising because the saturation diagrams of the farthest-left profile reveal scarcely any subsidence of the propagation surface, as evidenced by the distance to the water table increasing the full 12 cm. Currently, the only explanation for this behavior is that the desired 12-cm lowering of the water table, which was achieved through the piezometer connections inserted in the bottom of the flume, only occurred in the vicinity of the application site, whereas on the two sides of the flume, the initial water table elevation could apparently be maintained by clogged outlets. This explanation is compatible with the effect of the observed gradient (between the farthest-left profile and the application site profile), caused by lowering the water table, on the form and location of the oil lens.

Between the time the photographs (Figure 8.17) at 3 h and 24 min and at 3 days into Experiment D were taken, a second oil propagation surface had formed about 28 cm above the water table. This somewhat unexpected phenomenon is a product of the immature primary imbibition water-air capillary fringe. According to the first saturation diagram in Table 8 (in envelope), the quartz sand 28 cm above the water table was still oven dry, which indicates that hygroscopic water had not yet formed by condensation. Consequently, there was an interface between the oven-dry sand and the water-wet sand. When the oil front reached the water-wet sand at 28 cm, the oil spreading pressure induced oil to preferentially move along the water at this interface and thus a second propagation surface was observed. After 66 and 67 days, the saturation diagrams of the profile adjacent to the application site profile show that the oil saturation in the vicinity of this second propagation surface was smaller than the maximum pendular residual oil saturation. Therefore, one must conclude that the observed oil propagation along the second propagation surface could not be a product of funicular oil flow. The cloud-like and diffuse film observed in the photographs above the clearly darker outline of the oil

propagating horizontally is only a manifestation of the wall effects. This film was also observed in the other experiments, although less distinctly. Finally, it should be noted that the subsidence of the tip of the oil front seen at the far left in the photograph at the bottom of Table 8 is an edge effect produced by a vertically sliding side wall used while filling the flume, but since removed.

The good reproducibility of the saturation diagrams is evidence of the high accuracy of the cesium-thulium gamma-ray attenuation instrument used to measure the fluid saturations.

Experiment D yields more observations on the hallux phenomenon. During the experiment up to Day 57, it is interesting to note that only small oil-air halluces formed, and that a hallux formed between water and air just below the oil lens in the outer saturation profiles (where the oil lens is thinnest), whereas such a water-air hallux is not seen beneath where the oil lens is thicker. The water-air hallux disappears completely during the lowering of the water table. This occurs even though the propagation surface hardly subsided at the outer saturation profile because of reasons already discussed.

The last few saturation diagrams of the application site profile confirm that the value of the pendular residual oil saturation is 4% of the pore volume, which was also observed on Day 19 of Experiment C (Figure 8.12). Thus, according to Equation (2) of Section 3.3 in Schiegg (1979, p. 71), RSO_{\max}^{ins} is calculated as about 8% saturation.

With increasing time, the lens of funicular oil becomes flatter because of continuity. The funicular oil spreads along the propagation surface, and eventually changes into the oil pool described in the conceptual model presented in Figure 8.8. In Section 3.8 of Schiegg (1979), a method was proposed for determining the minimum thickness of the oil pool by using a macroscopic viewpoint and disregarding hysteresis. According to Figure 1 of Section 3.8 in Schiegg (1979, p. 96), the method uses superimposed ACOL and ACWO curves. The ACOL curve is displaced perpendicular to the water table until the horizontal distance between the ACOL curve and the ACWO curve (i.e., the oil saturation) is equal to RSO_{\max}^{ins} . The consideration of hysteresis is absolutely necessary in the experimental proof of this method to estimate the oil-pool

thickness. First assume that the water table is stationary and thus the development of the oil potential controls the movement of the oil menisci. The ACOL curve must then be set equal to the ACOLIM curve, and the ACWO curve must be set equal to the ACWODR curve. When the oil menisci move very slowly (as usually occurs during the propagation of the oil after oil infiltration has ceased), the capillary rise curves, ACSB, can be approximated by their static functions and thus by the capillary pressure head curves, HCSB (shown in Figure 8.2). From the plot of the capillary pressure-head curves in Figure 8.20, the minimum oil-pool thickness (M_0) is estimated for the porous media used in the experiments. Translating the area between the ACOLIM curve and the ACWODR curve into a rectangle with a length equal to RSO_{max}^{ins} yields a value of M_{red} of about 3 cm.

According to Equation (1) of Section 3.8 in Schiegg (1979, p. 97), M_{red} can also be determined as $M_{red} = \kappa_M(a_c^-|_W^L)$. If, to account for hysteresis, the average static contaminated water-air capillary fringe is defined by $a_c^-|_W^L$, then $a_c^-|_W^L$ is the arithmetic average of the inflection capillary pressure head values on the ACWLDR_(befl) curve and the ACWLIM_(befl) curve. From Figure 8.2, the inflection points can be estimated as 16.6 cm and 12.8 cm, and thus, the value of $a_c^-|_W^L$ is 14.7 cm. With $a_c^-|_W^L$ equal to 14.7 and M_{red} equal to 3 cm, κ_M is calculated as 0.2.

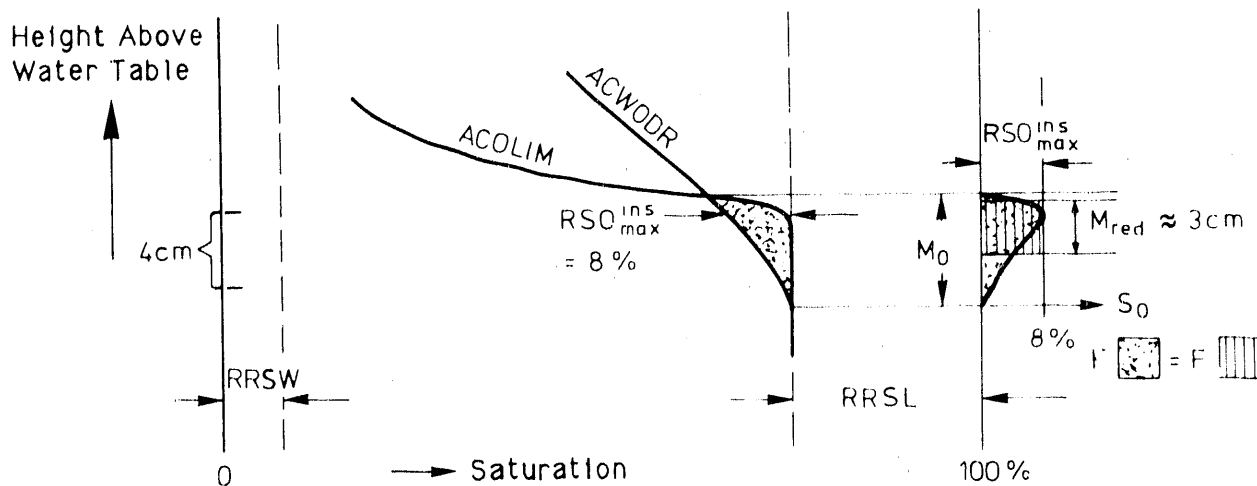


FIGURE 8.20. Minimum Oil-Pool Thickness Estimated with the ACOLIM Curve and the ACWODR Curve

As Figure 8.18 shows, the relative oil potential of the flattest water-oil menisci does not go above 6750 erg/cm^3 when the oil front encounters a stationary imbibition water-air capillary fringe such as the one established in Experiment D. On the other hand, the radius of curvature of the oil-air menisci will increase because of the increase in the relative oil potential. This means that for the estimation of the minimum thickness of the oil-contaminated area, the ACOL curve and the ACWO curve must not be displaced against each other as depicted in Figure 8.20 (because the ACWO curve changes only its form but not its position), but rather the ACOL curve must be displaced above the ACWL curve until the horizontal distance between them corresponds to $RSO_{\text{max}}^{\text{ins}} = 8\%$ saturation. The ACOLIM curve is the appropriate curve for the ACOL curve, and the HCWLIM_(jfr1) curve, equal to the static ACWLIM_(jfr1) curve for which the capillary rise reduction is zero during imbibition, is the appropriate curve for the ACWL curve encountered by the oil front. By using the corresponding capillary pressure head curves in Figure 8.2, the saturation diagram presented in Figure 8.21 is obtained. The form and position of the oil saturation distribution in Figure 8.21 correspond very well with all the measured saturation diagrams of Experiment D in Table 8, except the saturation diagrams of the profile to the far right, which are distorted by the distinct formation of a hallux.

With a stationary drainage water-air capillary fringe, only the ACWODR curve moves, corresponding to case III of Table 1 in Section 3.9.1 in Schiegg (1979, p. 103). Thus, to determine the minimum oil pool thickness according to Section 3.8 (Schiegg 1979), the ACWODR curve and the ACWLDR_(bef1) curve must be vertically displaced against each other, which is shown in Figure 8.22.

According to Figure 8.21, M_{red} is about 2 cm, while according to Figure 8.20 it is about 3.5 cm. Thus, by using Equation (1) of Section 3.8 in Schiegg (1979, p. 97) and assuming $a_c^L/W = 14.7 \text{ cm}$, the value of κ_M is 0.14 and 0.25, respectively. The κ_M value of 0.2 calculated from Figure 8.20 lies between these. These experimental values show that the value for κ_M of 0.6, proposed in Section 3.8 in Schiegg (1979), is not very satisfactory. A 3 to 5 times larger κ_M value would result in a calculated oil pool area 3 to

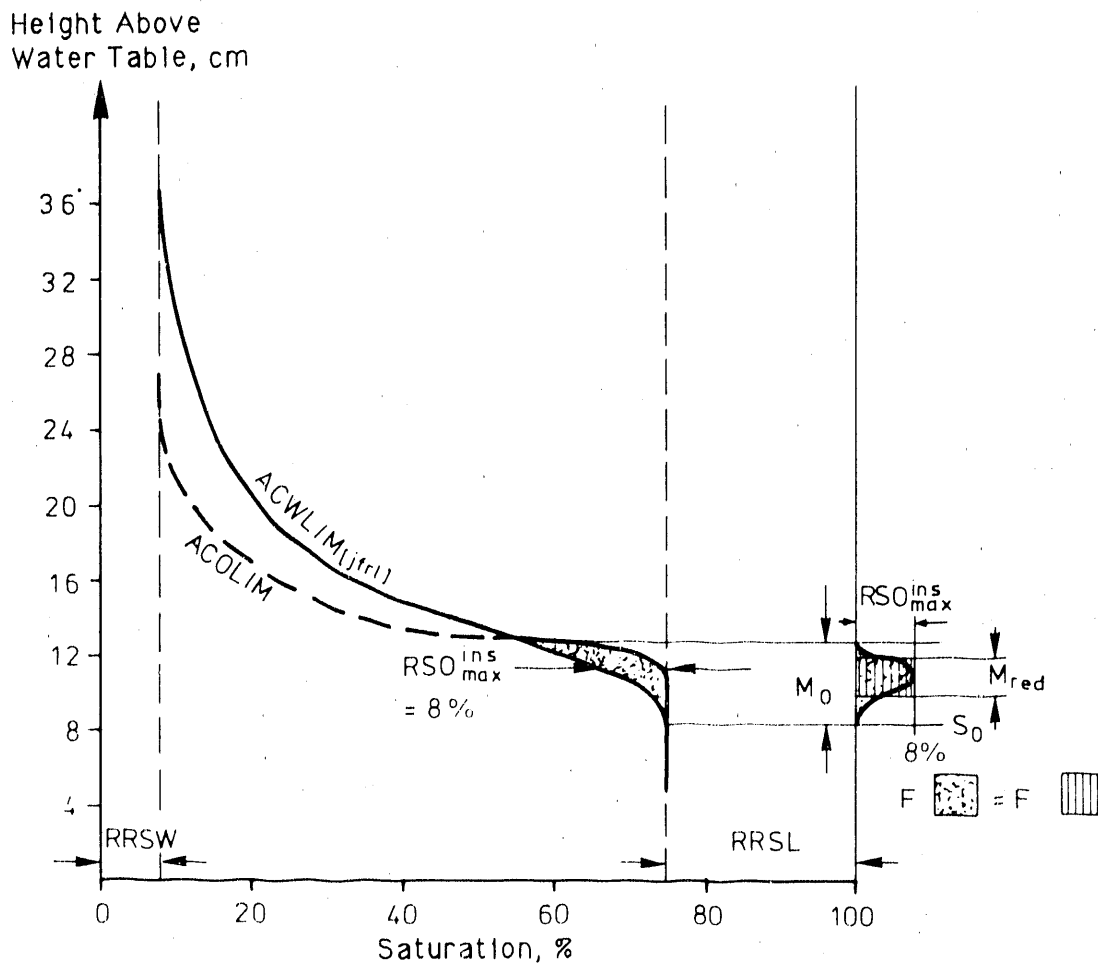


FIGURE 8.21. Oil-Pool Thickness in Experiment D

5 times smaller. Thus, the calculated size of the oil propagation area would be too small when used to assess the extent of oil contamination after a spill. Theoretically, this conclusion is probably true. Yet, for practical problems, a larger κ_M -value may not be unreasonable because local inhomogeneities and water table fluctuations, which often exist in the field as mentioned in Section 3.8 in Schiegg (1979), both tend to produce a larger minimum oil-pool thickness.

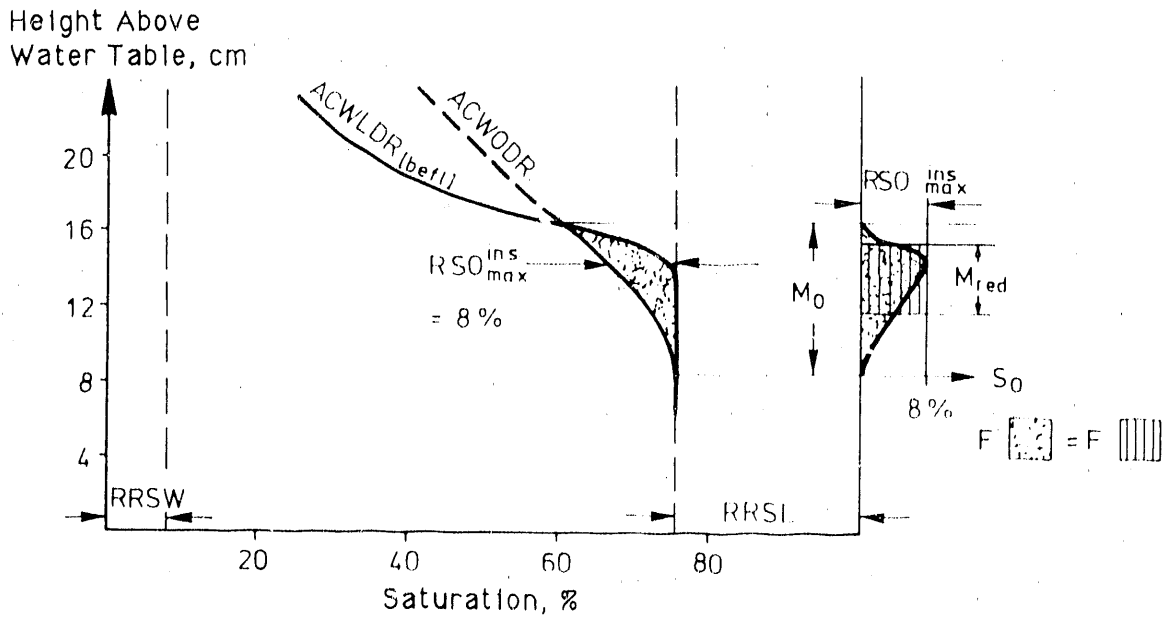


FIGURE 8.22. Minimum Oil-Pool Thickness Estimated with the ACWODR Curve and the ACWLDR_(befl) Curve

9.0 SUMMARY OF REMAINING TWO-DIMENSIONAL PROPAGATION EXPERIMENTS

The measurement series presented in this chapter are results of more two-dimensional propagation experiments. These were carried out in the flume described in Section 3.3.2.

The measurement series are part of a larger experimental program, whose results were discussed in detail in Chapter 8.0, where three experiment series, analogous to the corresponding measurement series included in this chapter, were discussed extensively and supported by interpretive theories. Because a detailed discussion would be in many respects a repetition, the measurement series described in this chapter will be briefly characterized only in comparison, and should confirm, supplement, and expand the experimental results discussed in the previous chapter. The initial and boundary conditions and the remaining characteristics will be discussed in Sections 9.2 and 9.3.

9.1 COMPARISON OF THE DIFFERENT EXPERIMENTS

For all experiments except Experiment 8, oil was applied starting at a constant potential. A small trough was dug in the sand surface and a constant oil-air level was maintained. The potential during application was determined from the difference in the oil-air level and the water-air level at the application site (see Appendix E for information on the approximately constant infiltration rates associated with multidimensional applications and constant potential applications). For Experiment 8, a constant infiltration rate was provided.

Experiments 1 and 2 differ because in Experiment 1 oil infiltrated into a fully developed water-air drainage capillary fringe, whereas in Experiment 2 oil infiltrated into a fully developed nonprimary imbibition capillary fringe. In both cases, the application site was about 28 cm above the constantly held water table.

According to the model of Schiegg (1979, p. 96) and the capillary pressure head curves in Figures 7.3 to 7.10, the propagation surface lies about 3 cm above the funicular-insular nonwetting fluid saturation boundary of the

contaminated water-air capillary pressure head curves. Thus, the position of the propagation surface above the water table can be calculated for the different experiments:

$$\text{Drainage (see Figure 7.7): } 14 \text{ cm} + 3 \text{ cm} = 17 \text{ cm} \\ \text{(Experiments 1, 4, 6, and 8)} \quad (9.1)$$

$$\text{Imbibition (see Figure 7.8): } 7 \text{ cm} + 3 \text{ cm} = 10 \text{ cm}$$

Or for the present experiments, in which the imbibition water table has remained in constant position since contamination (see text after Equation 7.2):

$$\text{Imbibition (see Figure 7.9): } 8 \text{ cm} + 0 \text{ cm} = 8 \text{ cm (for primary} \\ \text{imbibition, Experiment 9)} \quad (9.2)$$

$$\text{Imbibition (see Figure 7.9): } 9 \text{ cm} + 0 \text{ cm} = 9 \text{ cm (for nonprimary} \\ \text{imbibition, Experiments 2 and 3)}$$

A confirmation of these values is given in the photographs of the experiments in Section 9.5, remembering that the vertical distance between pressure probe parts is 4 cm.

Experiments 3 and 4 show the reproducibility of these representative experiments. Experiment 3 is a repetition of Experiment 2. Experiment 4 is a repetition of Experiment 1. Results and photographs of the replicate experiments generally show good agreement. In Experiment 3, the halved infiltration rate and thus double infiltration time was the result of an unexpected lower permeability in the area of the application site. However, the difference in infiltration rate had no influence on subsequent propagation processes.

Experiment 6 differs from Experiments 1 through 4 in that the interval between the application site and the propagation surface, e (see Figure 8.10), was 11 cm greater because the water table was 39 cm below the application site. In addition, the water table during the course of the experiment was inclined, raised, and lowered, and oil was applied a second time after 29 days.

Experiment 8 integrates the influence of as many boundary conditions as possible. For example, during the course of Experiment 8, water was sprinkled at the surface to remove the residual oil (see Appendix C). On day 59, an interesting detail, which is still unresolved, appeared: within 15 days after changing the flume conditions, the residual air saturation had completely disappeared. On day 75, these flume conditions were repeated, and the results from before were confirmed.

During Experiment 9, oil was applied at constant pressure into a primary imbibition saturation distribution. The water table was 37 cm below the application site. Because the propagation surface of a primary imbibition saturation distribution lies 8 cm above the water table according to Equation (9.2), then $e = 29$ cm. In Experiment 9, the potentials and saturations were not measured; only photographs were taken.

According to Figure 8.10, the small interval between application site and propagation surface (i.e., a small value of e) signifies a rudimentary propagation form (see Experiments 1 and 4). If e is greater than the radial propagation caused by the application pressure, then the intermediate propagation form appears (see Experiments 2, 3, 6, 8). When e is much larger than the radial propagation, then the fully developed form is produced (see Experiment 9). With the fully developed form, the model described in Figure 8.8 can clearly distinguish a first and second propagation phase.

9.2 INITIAL AND BOUNDARY CONDITIONS

Table 9.1 shows the initial and boundary conditions for Experiments 1, 2, 3, 4, 6, and 8.

TABLE 9.1. Initial and Boundary Conditions, Experiments 1-8

Exp.	Type of Initial Capillary Funge Established	Oil Application		Water-Air Level			Chronology	
		type	Oil Volume Per Time = $Q \approx \text{const.}$ (Schlegg 19/5)	Initial Measurement	Lowest Relative to Reference for Potential	Slope		Δh
1	WLDR	Constant potential	$(4\text{ l}/4\text{ l})/25'$	0 cm	0 cm	0%	0 d	
			$= 2.8 \frac{\text{cm}^3}{\text{sec}}$					
			$(1\ 1/2\text{ l})/5'$			0%	6 d	
			$= 5.0 \frac{\text{cm}^3}{\text{sec}}$					
2	Non-primary WLIM	Constant potential	$4\text{ l}/11'$	0 cm	0 cm	0%	0 d	
			$= 6.0 \frac{\text{cm}^3}{\text{sec}}$					
3	Non-primary WLIM	Constant potential	$4\text{ l}/25'$	0 cm	0 cm	4 1/2%	0 d	
			$= 2.7 \frac{\text{cm}^3}{\text{sec}}$					
4	WLDR	Constant potential	$4\text{ l}/22'$	0 cm	0 cm	0%	0 d	
			$= 3.0 \frac{\text{cm}^3}{\text{sec}}$					
6	WLDR	Constant potential	$8\text{ l}/48'$	+4 cm	-9 cm	0%	0 h	
			$= 2.8 \frac{\text{cm}^3}{\text{sec}}$					
			$2\text{ l}/2.5'$			1 1/2%	-1.5 cm	4 1/4 h
			$= 14.5 \frac{\text{cm}^3}{\text{sec}}$			1 1/2%	+10 cm	7 d
						0%	-21.5 cm	20 d
						0%	+52 cm	22 d
						0%	-39 cm	27 d
						= Initial Water - Air Level		29 d

TABLE 9.1. (contd)

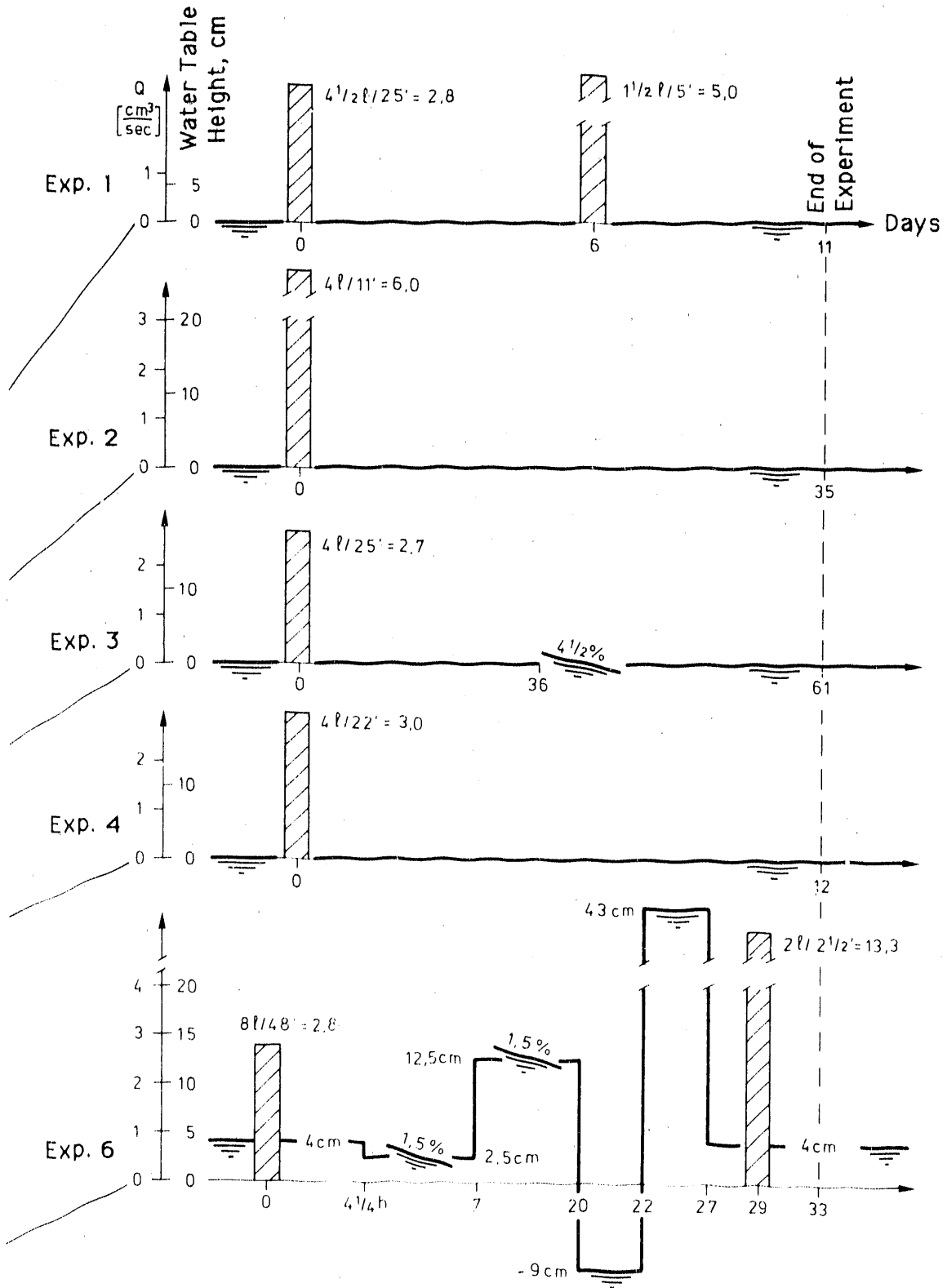
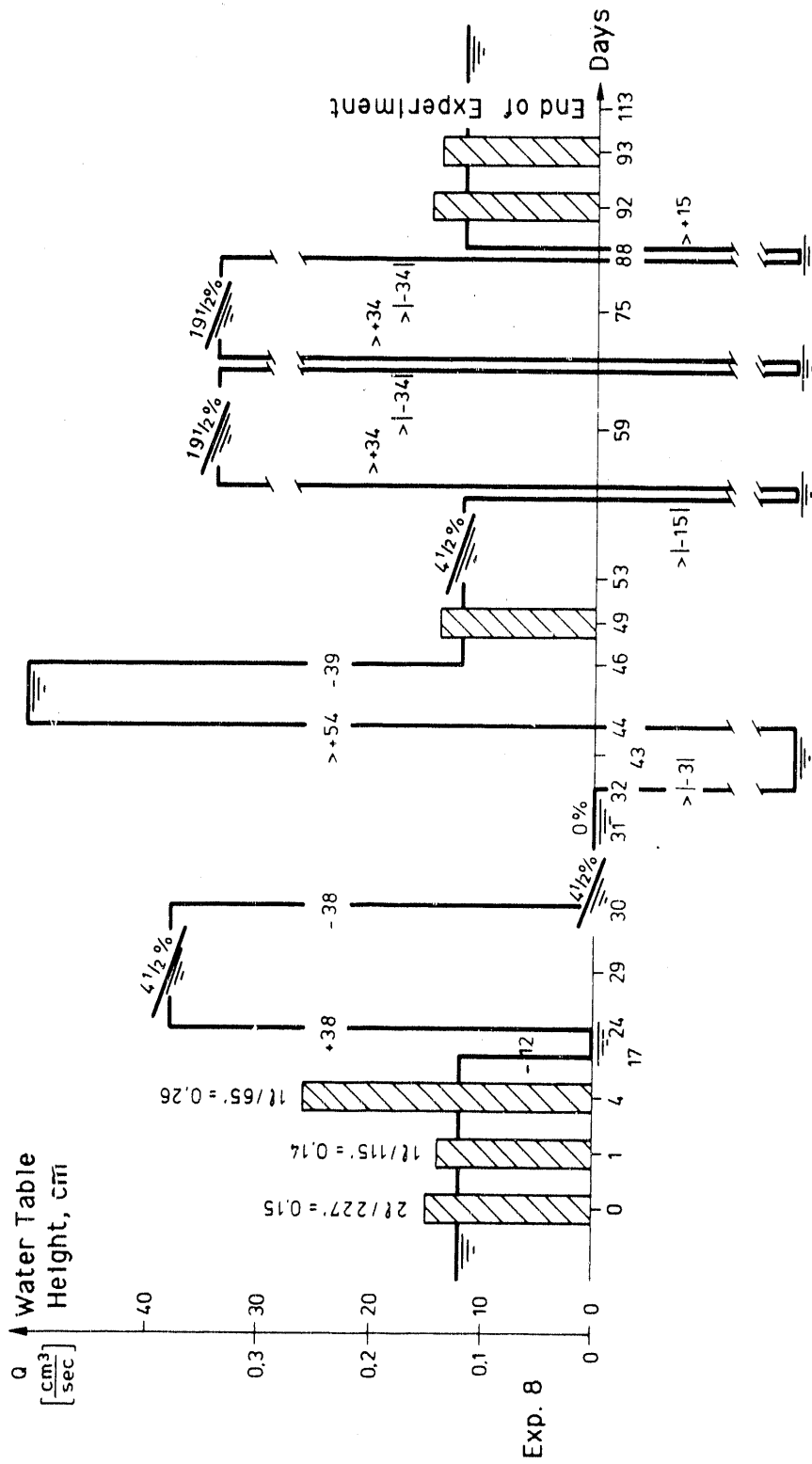


TABLE 9.1. (contd)

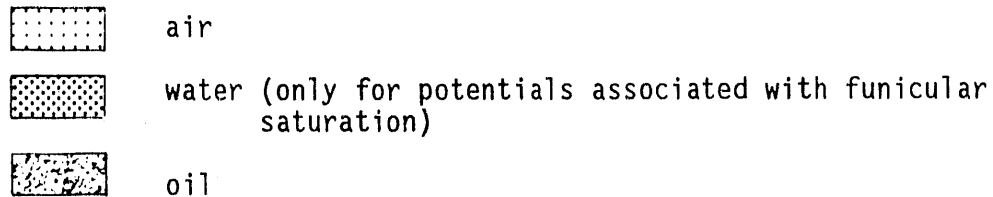
Exp.	Type of Initial Capillary Fringe Established	Oil Application		Water-Air Level			Chronology	
		type	Oil Volume Per Time = Q	Initial	Lowest	Slope		Δh
8	WLDR	Constant	2l/227'	+12 cm	0 cm	0%		0-16 d
		Infiltration rate	= 0.15 $\frac{\text{cm}^3}{\text{sec}}$					
			1l/115' = 0.14 $\frac{\text{cm}^3}{\text{sec}}$					
			1l/65' = 0.26 $\frac{\text{cm}^3}{\text{sec}}$					
						0%	-12	17 d
						0%	+38	24 d
						4 1/2%	0	29 d
						4 1/2%	-38	30 d
						0%	0	31 d
						0% at least	-3	32 d
						0%	0	43 d
						0% at least	+54	44 d
						0%	-39	46 d
						0%	0	49 d
						4 1/2%	0	53 d
						19 1/2% at least	-15	59 d
							at least +34	
						19 1/2% at least	-34	75 d
							at least +34	
						0%	at least -34	88 d
							at least +15	
			2l/227'			0%	0	92 d
			0.15 $\frac{\text{cm}^3}{\text{sec}}$					
			1l/115' = 0.14 $\frac{\text{cm}^3}{\text{sec}}$			0%	0	93 d

TABLE 9.1. (contd)



9.3 LEGEND FOR THE SATURATION AND POTENTIAL TIMELINE FOR EXPERIMENTS 1 THROUGH 8

Figure 9.1 shows the saturation diagram and Figure 9.2 the potential histogram and timeline for Experiments 1 through 8. In Figures 9.1 and 9.2, the vertical axis is the time. The shaded areas and the measuring points are



- Potentials associated with residual saturation = unreliable values
- Potentials associated with funicular saturation = reliable values

The profile on the right lies 62 cm to the right of the profile underneath the oil application site.

Figure 9.1 is the graphical representation of the measured instantaneous saturation distribution of water, oil, and air underneath the oil application site and 62 cm to the right. These profiles are planes normal to the two-dimensional propagation experiments. The elapsed time for a saturation diagram is indicated below the water-air level.

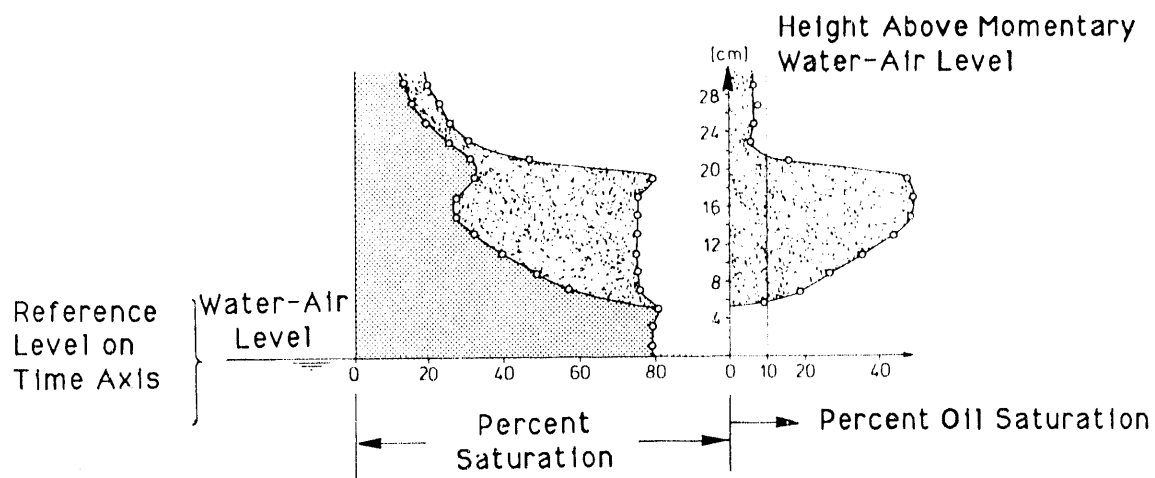


FIGURE 9.1. Saturation Diagram for Experiments 1 Through 8

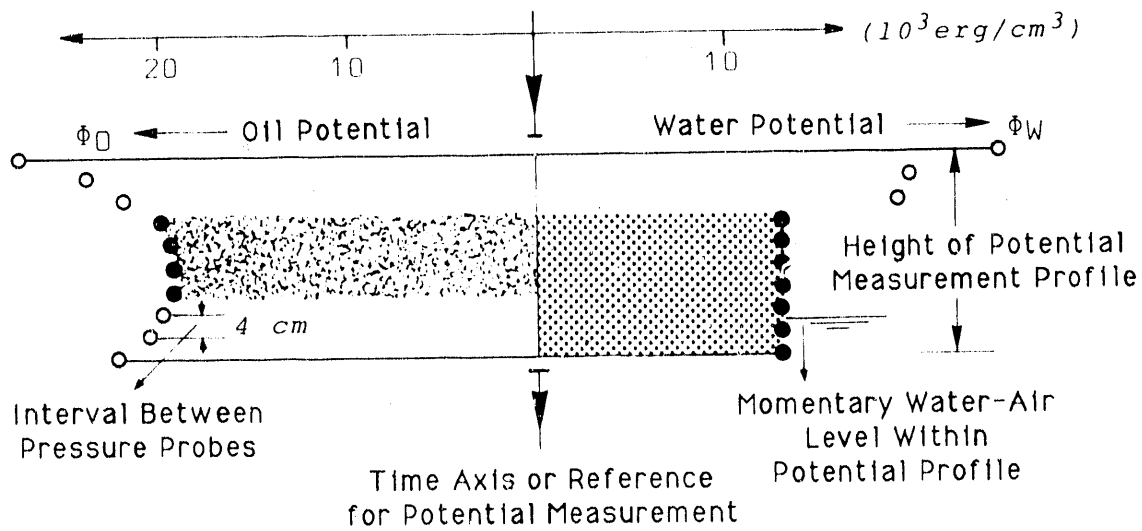


FIGURE 9.2. Potential Histogram and Timeline for Experiments 1 Through 8

The potential histogram (Figure 9.2) is the graphical representation of the measured instantaneous potential distributions of water and oil. One is presented for the profile underneath the application site and another is presented for the profile 62 cm to the right. The profiles are planes normal to the two-dimensional propagation experiments. Within a potential histogram, the vertical axis denotes the height in the profile. The measurement points with the highest potentials are presented first on the time axis, and the points with the lowest potentials are presented last on the time axis. In between lie the remaining measuring points, which have a constant vertical interval of 4 cm. The water potential is plotted to the right of the vertical, and the oil potential is plotted to the left. The reference for the potential measurements is the deepest water-air level at which potential measurements were made during an experiment. The units erg/cm^3 , with the dimension of pressure ($\text{ML}^{-1}\text{T}^{-2}$), can be interpreted as a volume-specific potential area. A fluid column height is calculated by dividing by the specific weight, ρg , ($\text{ML}^{-2}\text{T}^{-2}$). Thus for water ($\rho_w g \approx 10^3$), $10^3 \text{ erg}/\text{cm}^3$ corresponds to a 1-cm water-column height, and for oil ($\rho_o g \approx 0.85 \cdot 10^3$) $10^3 \text{ erg}/\text{cm}^3$ corresponds to a 1.16-cm oil-column height.

9.3.1 Selected Characteristics for Experiments 1 Through 8

Experiments 1, 2, 3, 4, 6, and 8 had the following characteristics:

Petroleum derivative: Super-Ad-It in organic solvent + extra light petroleum fraction (see Section 6.7) (designated as oil or SAI)

$$\rho_{SAI} = 0.85 \text{ g/cm}^3$$

$$\mu_{SAI} \approx 0.7 \text{ cp}$$

Water-SAI interfacial tension = 27.0 dyn/cm

SAI-air interfacial tension = 23.3 dyn/cm

Grain-size distribution curve: see Figure 3.1a and Figure 8.1

Porosity: $n = 0.43$ (see diagram A1 in Section 7.2)

Capillary pressure head curve: see Figure 7.1, Figures 7.3 through 7.10, or Figure 8.2

9.4 PHOTOGRAPHS OF EXPERIMENT 9

Saturation and potential timelines for Experiments 1 through 8 are shown in the plates found in the envelope with this report.

9.5 SATURATION AND POTENTIAL TIMELINE FOR EXPERIMENTS 1 THROUGH 8

Figure 9.3 is a photograph of Experiment 9.

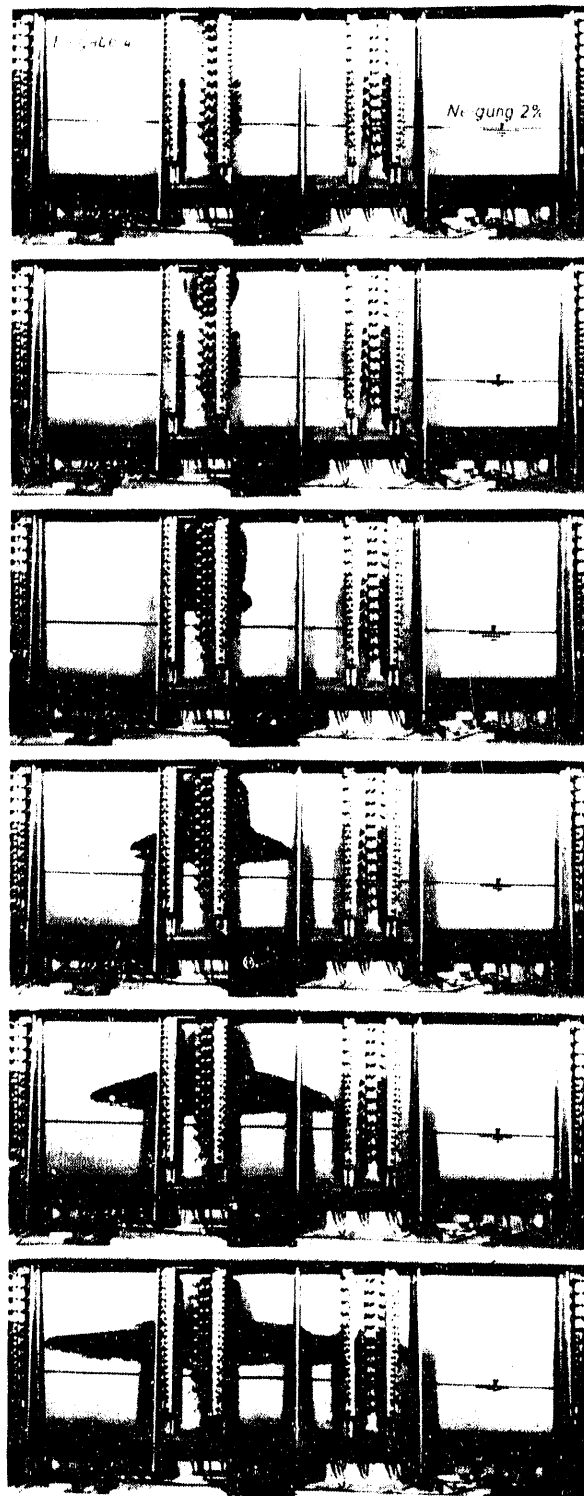


FIGURE 9.3. Photographs of Experiment 9

10.0 REFERENCES AND BIBLIOGRAPHY

10.1 REFERENCES

- Abriola, L. M. 1984. Multiphase Migration of Organic Compounds in a Porous Medium: A Mathematical Model. Lecture Notes in Engineering, 8, Springer-Verlag, Berlin.
- Abriola, L. M., and G. F. Pinder. 1985a. "A Multiphase Approach to the Modeling of Porous Media Contamination by Organic Compounds, 1. Equation Development." Water Resour. Res. 21:11-18.
- Abriola, L. M., and G. F. Pinder. 1985b. "A Multiphase Approach to the Modeling of Porous Media Contamination by Organic Compounds, 2. Numerical Simulation." Water Resour. Res. 21:19-26.
- Abriola, L. M. 1988. Multiphase Flow and Transport Models for Organic Chemicals: A Review and Assessment. EPRI EA-5976, Electric Power Research Institute, Palo Alto, California.
- Adam, K. M., and A. T. Corey. 1968. "Diffusion of Entrapped Gas from Porous Media." Hydrology Papers. Colorado State University, Fort Collins.
- Allen, M. B. 1985. "Numerical Modeling of Multiphase Flow in Porous Media." Adv. Water Resour. 8:162-187.
- Amersham Catalog. 1974/1975. Standardized Radioactive Solutions. Radiochemical Center, Amersham, England.
- Baehr, A., and M. Y. Corapcioglu. 1984. "A Predictive Model for Pollution from Gasoline in Soils and Groundwater." In Proceedings of the Petroleum Hydrocarbons and Organic Chemicals in Ground Water Conference, Houston, Texas, November 5-7.
- Bartell, F. E., and A. D. Wooley. 1933. "Solid-Liquid-Air Contact Angles and Their Dependence Upon the Surface Condition of the Solid." J. Amer. Chem. Soc. 55(3):3518-3527.
- Bartsch, H. J. 1968. Mathematische Formeln. VEB Fachbuchverlag, Leipzig.
- Bear, J. 1978. "Relations Between Microscopic and Macroscopic Descriptions in Porous Media." International Symposium on Fluid Mechanics and Scale Effects on Phenomena in Porous Media, Thessaloniki. International Association for Fluid Mechanics, Delft, Netherlands.
- Beilstein, F. K. 1929. Beilsteins Handbuch der Organischen Chemie. (Beilstein's Handbook of Organic Chemistry, Springer, Berlin.) Springer, Berlin.

- Bronstein, I. N., and K. A. Semendjajew. 1968. Taschenbuch der Mathematik. (Notebook for Mathematics.) Harri Deutsch, Zürich und Frankfurt/M.
- Bundesminister für Umwelt, Naturschutz, und Reaktorsicherheit (BUNR). 1986. Beurteilung and Behandlung von Mineralölschadensfällen im Hinblick auf den Grundwasserschutz, Teil 1: Die wissenschaftlichen Grundlagen zum Verständnis des Verhaltens von Mineralöl im Untergrund (Assessment and Treatment of Mineral Oil Spills for Groundwater Protection, Part 1: The Scientific Understanding of the Subsurface Behavior of Mineral Oil). LTWS No. 20, Herausgegeben vom Umweltbundesamt, Berlin.
- Cary, J. W., J. F. McBride, and C. S. Simmons. 1989. "Observations of Water and Oil Infiltration into Soil: Some Simulation Challenges." Water Resour. Res. 25:73-80.
- Childs, E. C. 1967. "Soil Moisture Theory." In Advances in Hydroscience, Vol. 4, pp. 73-117. Academic Press, New York.
- Collins, R. E. 1961. Flow of Fluids Through Porous Materials. Reinhold Publishing Corporation, New York.
- DISA. 1970. Wissenschaftliche Forschungsinstrumentierung. Herlev, Denmark.
- Dracos, Th. 1966. Physikalische Grundlagen und Modellversuche über das Verhalten und die Bewegung von nicht mischbaren Flüssigkeiten in homogenen Boden. (Physical Principles and experiments on the behavior and movement of immiscible fluids in homogeneous soils). VAW-72, Versuchsanstalt für Wasserbau, Zürich.
- Eckberg, D. K., and D. K. Sunada. 1984. "Nonsteady Three-Phase Immiscible Fluid Distribution in Porous Media." Water Resour. Res. 20:1891-1897.
- Eichler, E. 1879. "Beiträge zur Kenntnis der Octyl-derivate." Berichte der Deutschen Chemischen Gesellschaft, Band XIIb, pp. 1879-1880. (Contribution to the knowledge of Ochyl derivatives. Report of the German Chemical Society, Volume XIIb, p. 1879-1880.)
- Faust, C. R. 1985. "Transport of Immiscible Fluids within and below the Unsaturated Zone - A Numerical Model." Water Resour. Res. 21:587-596.
- Faust, C. R., and J. O. Rumbaugh. 1986. SWANFLOW: Simultaneous Water, Air, and Nonaqueous Phase Flow. Prepared by GeoTrans, Inc., Herndon, Virginia, for the U.S. Environmental Protection Agency, Washington D.C.
- Faust, C. R., J. H. Guswa, and J. W. Mercer. 1989. "Simulation of Three-Dimensional Flow of Immiscible Fluids within and below the Unsaturated Zone." Water Resour. Res. 25:2449-2464.
- Gilman, H., and R. E. Brown. 1930. "The Preparation of Mercury Dialkyls from Organomagnesium Halides." J. Am. Chem. Soc. 52:3314-3316.

Glocker R., and E. Macherauch. 1965. Roentgen- und Kernphysik. Georg Thieme Verlag, Stuttgart, 2. Aufl.

Grodstein, G. W. 1957. X-Ray Attenuation Coefficients from 10 keV to 100 MeV. National Bureau of Standards Circular 583, U.S. Government Printing Office, Washington, D.C.

Heath, R. L. 1964. Scintillation Spectrometry. Gamma-Ray Spectrum Catalog. 2nd Ed. IDO-16880, Phillips Petroleum Co., Atomic Energy Division, Idaho Falls, Idaho.

Heinhold, J., and K. W. Gaede. 1964. Ingenieur-Statistik. R. Oldenburg.

Hofacker, K. 1962. Baustatik II. ETH-Vorlesung, Zürich.

Høst-Madsen, J. 1988. "Laboratory Study of Three-Phase Flow in Porous Media Using Dual Gamma Attenuation Technique." In Proceedings of the Nordic Hydrological Conference, Rovaniemi, Finland. Preprints 2:240-262.

Kaluarachchi, J. J., and J. C. Parker. 1989. "An Efficient Finite Element Method for Modeling Multiphase Immiscible Flow Through Soils." Water Resour. Res. 23:43-54.

Kuppusamy, T., J. Sheng, J. C. Parker, and R. J. Lenhard. 1987. "Finite Element Analysis of Multiphase Immiscible Flow Through Soils." Water Resour. Res. 23:625-631.

Lenhard, R. J., J. H. Dane, J. C. Parker, and J. J. Kaluarachchi. 1988. "Measurement and Simulation of One-Dimensional Transient Three-Phase Flow for Monotonic Liquid Drainage." Water Resour. Res. 24:853-863.

Lippock, W. 1966. Modellversuch über das Verhalten von Heizöl EL im Porösen Medium. Deutsch Gewässerkundliche Mitteilunge, Heft 5. (Model experiments on the behavior of fuel oil EL in a porous medium. German Hydrological Reports, No. 5.)

Manegold, E. 1955, 1960. Kapillarsysteme, Bd. I. II; Strassenbau, Chemie und Technik Verlagsgesellschaft m. b. H., Heidelberg.

Marmier, P. 1960. Kernphysik I, Vorlesung. Verein der Mathematiker und Physiker an der ETH-Zürich. (Nuclear Physics I, Lecture: Mathematics and Physics Section at the ETH-Zurich.) Swiss Federal Institute of Technology, Zurich.

Marvel, C. S., and H. O. Calvery. 1923. "The Preparation of Dialkyl Mercury Compounds from the Grignard Reagent. II. The Relative Stability of the Carbon-Mercury Linkage in Dialkyl Mercury Compounds." J. Am. Chem. Soc. 45:820-821.

- McCaffery, F. G., and N. Mungan. 1970. "Contact Angle and Interfacial Tension Studies of Some Hydrocarbon-Water-Solid-Systems." J. Can. Petrol. Technol. 9(3):185-196.
- McKee, C. R., and A. C. Bumb. 1988. "A Three-Dimensional Analytical Model to Aid in Selecting Monitoring Locations in the Vadose Zone." Ground Water Monitor. Rev. 8(2):124-136.
- Mull, R. 1969. Modellmassige Beschreibung der Ausbreitung von Mineraloelprodukten im Boden. (Model-like description of the propagation of mineral oil products in soil)s. Mitteilungen aus dem Institut für Wasserwirtschaft und Landwirtschaftlichen Wasserbau der Tech Hochschule, Hannover, Heft 15.
- Muskat, M. 1934. "Two Fluid Systems in Porous Media. The Encroachment of Water Into an Oil Sand." Physics 5:250-264.
- Nuklidkarte. 1963. Bundesministerium für wissenschaftliche Forschung. (Federal Ministry for Scientific Research.) Bad Godesberg, BRD.
- Osborne, M., and J. Sykes. 1986. "Numerical Modeling of Immiscible Organics Transport at the Hyde Park Landfill." Water Resour. Res. 22:25-33.
- Parker, J. C., R. J. Lenhard, and T. Kuppusamy. 1987. "A Parametric Model for Constitutive Properties Governing Multiphase Flow in Porous Media." Water Resour. Res. 23:618-624.
- Radiochemical Manual. 1966. Radiochemical Center, Amersham, England.
- Rakow, A. 1962. Tabelle zur Identifizierung unbekannter Gammaspectren; Karl Thiemig KG, München. (Table for the identification of unknown gamma spectra. Karl Thiemig KG, Munich.)
- Richards, L. A. 1931. "Capillary Conduction of Liquids Through Porous Mediums." Physics 1:318-333.
- Scheidegger, A. E. 1960. The Physics of Flow Through Porous Media, Revised Ed. University of Toronto Press, Toronto.
- Schiegg, H. O. 1975. Probleme und Möglichkeiten der Simulation der Verunreinigung eines mit Wasser und Luft erfüllten, porösen Mediums durch eine nicht mischbare Flüssigkeit. Réunion internationale AIRH/SIA sur les nappes souterraines, Rapperswil. (Problems and possibilities on the simulation of non-miscible fluid contamination of a porous medium filled with water and air. International Meeting of AIRH/SIA on Aquifers, Rapperswil.)
- Schiegg, H. O. 1977a. Methode zur Abschätzung der Ausbreitung von Erdölderivaten im mit Wasser und Luft Erfüllten Boden. (Methods of estimating the propagation of petroleum derivatives in soils filled with water and air.) VAW-22, Versuchsanstalt für Wasserbau, Zurich.

Schiegg, H. O. 1977b. Modellvorstellung und Konzepte zur Abschätzung von Verunreinigungen von Grundwasser-trägern durch Erdölderivate; "Wasser, Energie, Luft" 10.

Schiegg, H. O. 1979. Verdrängungs-Simulation Dreier Nicht Mischbarer Fluide in Poröser Matrix. (Simulation of Three-Immiscible Fluid Displacement in Porous Media.) VAW-40, Versuchsanstalt für Wasserbau, Hydrologie, und Glaziologie: Eidgenössischen Technischen Hochschule (ETH), Zürich.

Schiegg, H. O. 1980. Grundlagen, Aufbau und Resultate von Laborexperimenten zur Erforschung von Oelenausbreitungen in Grundwasserträgern. (Fundamentals, Setups and Results of Laboratory Experiments on Oil Propagation in Aquifers.) VAW-43, Versuchsanstalt für Wasserbau, Hydrologie und Glaziologie: Eidgenössischen Technischen Hochschule (ETH), Zürich.

Schiegg, H. O. 1984. "Considerations on Water, Oil, and Air in Porous Media." Water Sci. Technol. 14:467-476.

Schiegg, H. O. 1985. Ausbreitung von Mineralöl im Boden; Vergleich von Theorie und Praxis. (Subsurface Propagation of Hydrocarbons; Comparison between Theory and Practical Experience.) DGMK-Project 373, Deutsche Gesellschaft für Mineralölwissenschaft und Kohlechemie E.V., Hamburg.

Schiegg, H. O. 1988. "The 'Transition Potential' Defining the Moving Boundaries in Multiphase Porous Media Flow." Adv. Water Resour. 11:144-149.

Schiegg, H. O., and J. F. McBride. 1987. "Laboratory Setup to Study Two-Dimensional Multiphase Flow in Porous Media." In Proceedings of the Petroleum Hydrocarbons and Organic Chemicals in Ground Water Conference, pp. 371-385. Houston, Texas.

Schiegg, H. O., and F. Schwille. 1989. "Hydrocarbons in Porous Media." In Transport Processes in Porous Media. NATO Advanced Study Institute. In press.

Schwille, F. 1971a. "Die Migration von Mineralöl in Porösen Medien, Dargestellt Anhand von Modellversuchen." Gwf-Wasser/Abwasser 112:307-311.

Schwille, F. 1971b. "Die Migration von Mineralöl in Porösen Medien, Dargestellt Anhand von Modellversuchen, Teil 2." Gwf-Wasser/Abwasser 112:331-339.

Schwille, F. 1971c. "Die Migration von Mineralöl in Porösen Medien, Dargestellt Anhand von Modellversuchen, Teil 3." Gwf-Wasser/Abwasser 112:465-472.

SSVO. 1976. Strahlenschutzverordnung vom 30. Juni 1976, Bundeskanzlei, EDMZ, Bern.

Stablein, G. 1966. Dosis- und Dosisleistungsmessung (q-Strahlung); 5. Kurs über Strahlenschutz, Kernforschungszentrum Karlsruhe.

Streile, G. P., and C. S. Simmons. 1986. Subsurface Flow and Transport of Organic Chemical: An Assessment of Current Modeling Capability and Priority Directions for Future Research (1987-1995). PNL-6043, Pacific Northwest Laboratory, Richland, Washington.

Strominger, D., J. M. Hollander, and G. T. Seaborg. 1958. "Table of Isotopes." Rev. Modern Phys. 30:585-904.

Swiss Atomic Handbook. 1963. Atomenergie und Strahlenschutz in der Schweiz. Schweiz. Vereinigung für Atomenergie, Bern. (Atomic energy and radiation protection in Switzerland. Swiss Union for Atomic Energy, Bern.)

Truesdell, C., and R. A. Toupin. 1960. "The Classical Field Theories." In Hanbuch der Physik, Vol. III/I, pp. 226-793. Springer Verlag, Berlin.

van Dam, J. 1967. Die Ausbreitung von Mineraloel in Grund- Wasserführenden Schichten; Deutsche Gewasserkundliche Mitteilungen, Heft 1.

Versluys, J. 1931. "Can Absence of Edge-Water Encroachment in Certain Oil Fields be Ascribed to Capillarity?" Bull. Am. Assoc. Petrol. Geol. 15(2):189-200.

von Engelhardt, W. 1960. Der Porenraum der Sediments. Springer Verlag, Berlin.

Wolf, K. L. 1957. Physik und Chemie der Grenzflächen. Springer Verlag, Berlin.

Wyckoff, R. D., and H. G. Botset. 1936. "The Flow of Gas-Liquid Mixtures Through Unconsolidated Sands." Physics 7:325-345.

Zilliox, L., and P. Muntzer. 1976. Mécanismes de la pollution des eaux souterraines et aménagement de l'environnement. (Determination quantitative d'une source de pollution des eaux souterraines par des produits pétroliers); XIV^{es} Journées de l'Hydraulique - Question IV, Rap. 7A, Paris. (Mechanisms of ground-water pollution and management of the environment: Quantitative determination of a source of ground-water pollution by petroleum products: XIV Journées de l'hydraulique-Question IV, Dept. 7a, Paris.)

10.2 BIBLIOGRAPHY

The following additional references were cited in Schiegg (1979, 1980). They are included here as a bibliography.

Adam, N. K., and R. S. Morrell. 1934. "The 'Bloom' of Varnish Films." J. Soc. Chem. Ind. 53:255-262.

Andreas, J. M., E. A. Hauser, and W. B. Tucker. 1938. "Boundary Tension by Pendant Drops." J. Phys. Chem. 42:1001.

Bartz, J., and W. Kass. 1972. Heizoelversickerungsversuche in der Oberrheinebene. Geolog. Landesamt Baden-Württemberg, Heft 7. (Fuel oil experiments in the Uper Rhine Plain. Geolog. Landesamt BadenWurttemberg, No. 7.)

Bear, J. 1972. Dynamics of Fluids in Porous Media. American Elsevier, New York.

Botset, H. G. 1940. "Flow of Gas-Liquid Mixtures Through Consolidated Sand." Trans. AIME 136:91-103.

Buckingham, E. 1907. Studies in the Movement of Soil Moisture. U.S. Department of Agriculture Bureau of Soils Bulletin 38, Washington, D.C.

Buckley, S. E., and M. C. Leverett. 1942. "Mechanism of Fluid Displacement in Sands." Trans. AIME 146:107-116.

Handbook of Chemistry and Physics. 1961. Chemical Rubber Publishing Co., 44 Ed., Cleveland, Ohio.

Childs, E. C. 1969. An Introduction to the Physical Basis of Soil Water Phenomena. J. Wiley, New York.

Childs, E. C., and N. Collis-George. 1950. "The Permeability of Porous Materials." Proc. Roy. Soc. A201:392-405.

Collatz, L. 1955. Numerische Behandlung von Differential-Gleichungen. (Numerical Treatment of Differential Equation.) Springer, Berlin.

Darcy, H. 1856. Les Fontaines Publiques de la Ville de Dijon. (The Public Fountains of the City of Dijon.) Dalmont, Paris.

Dracos, Th. 1966. Physikalische Grundlagen und Modellversuche über das Verhalten und die Bewegung von Nicht Mischbaren Flüssigkeiten in Homogenen Böden. (Physical principles and model experiments on the behavior and movement of non-miscible fluids in homogenous soils. VAW-Mitteilung Nr. 72, Zurich.

Dracos, Th. 1976. Pollution des Nappes par les Hydrocarbures. Société Hydrotechnique de France, XIV^{es} Journées de L'Hydraulique, Paris. (Pollution of aquifers by hydrocarbons. Societe hydrotechnique de France, XIV Journees de l'hydraulique, Paris.)

Eagleson, P. S. 1970. Dynamic Hydrology. McGraw-Hill, New York.

Flügge, S. 1958. Handbuch der Physik, Band XXXIV, Korpuskeln und Strahlung in Materie II. (Handbook of Physics, Vol. XXXIV, Particles and radiation in matter II.) Springer, Berlin.

Gaudin, A., A. F. Witt, and T. G. Decker. 1963. "Contact Angle Hysteresis - Principles and Application of Measurement Methods." Trans. AIME 226:107.

- Gilman, H., and R. E. Brown. 1929. "Improvements in the Method for the Preparation of Mercury Dialkyls from Organomagnesium Halides." J. Am. Chem. Soc. 51:928-929.
- Hart, J. A., K. R. Lawther, and E. Szomanski. 1966. "Fluid Flow in Packed Beds." In Proceedings on the Second Australasian Conference on Hydraulics and Fluid Mechanics, University of Auckland, Auckland, New Zealand.
- Hubbert, M. K. 1940. "The Theory of Ground Water Motion." J. Geol. 48(8)pt.1.
- Lamb, H. 1932. Hydrodynamics. 6th Ed. Dover, New York.
- Leverett, M. C. 1939. "Flow of Oil-Water Mixtures Through Unconsolidated Sands." Trans. AIME 132:149-169.
- Leverett, M. C., and W. B. Lewis. 1940. "Steady Flow of Gas-Oil-Water Mixtures Through Unconsolidated Sands." Trans. AIME 142:107-115.
- Leverett, M. C. 1941. "Capillary Behaviour in Porous Solids." Trans. AIME 142:152-168.
- Lucassen-Reynders, E. H. 1963. "Contact Angles and Adsorption on Solids." J. Phys. Chem. 67:969.
- McCaffery, F. C., and N. Mungan. 1970. "Contact Angle and Interfacial Tension Studies of Some Hydrocarbon-Water-Solid-Systems." J. Can. Petr. Tech. 9(3):185-196.
- Milgram, J. H., and R. G. Bradley. 1971. "The Determination of the Interfacial Tension Between Two Liquids." J. Fluid Mech. 50:469-480.
- Mull, R. 1969. Modellmässige Beschreibung der Ausbreitung von Mineraloelprodukten im Boden. Mitt. aus dem Inst. f. Wasserwirtschaft und landwirtschaftlichen Wasserbau, Techn. Univ. Hannover, Heft 15. (Model-like description of the propagation of mineral oil products in the soil. Report from the Inst. for Hydroeconomic and Agricultural Hydraulics, Techn. Univ. Hannover, No. 15).
- Muskat, M., and M. W. Meres. 1936. "The Flow in Heterogeneous Fluids Through Porous Media." Physics 7:346-363.
- Muskat, M., R. D. Wykoff, H. G. Botset, and M. W. Meres. 1937. "Flow of Gas-Liquid Mixtures Through Sands." Trans. AIME 123:69-96.
- Muskat, M. 1946. The Flow of Homogeneous Fluids Through Porous Media. Edwards, Ann Arbor, Michigan.
- Muskat, M. 1949. Physical Principles of Oil Production. McGraw-Hill, New York.

O'Brien, W. J., R. G. Craig, and F. A. Peyton. 1968. "Capillary Penetration Between Dissimilar Solids." J. Coll. Interface Sci. 26:500-508.

Philip, J. R. 1969. "Theory of Infiltration." In Advances in Hydroscience, Vol. 5, pp. 216-296. Academic Press, New York.

Schiegg, H. O., and Th. Dracos. 1971. "Migration of Oil in Unconfined Aquifers." IUTAM/IUGG-Symposium: Flow of Multiphase Fluids in Porous Media. Calgary, Alberta, Canada.

Schwille, F. 1969. Resp. Arbeitskreis 'Lasser und Mineraloel; Beurteilung und Behandlung von Mineraloelunfällen auf dem Lande im Hinblick auf den Gewässerschutz; Bundesministerium für Gesundheitswesen, Bad Godesberg.

Schwille, F. 1974. Die Grundwasserverunreinigung durch Mineraloelprodukte - ein hydrologisches Problem. Symposium "La pollution des eaux souterraines," Commission interministerielle de la politique scientifique, Services du premier ministre, Rue de la science 8, Bruxelles. (Ground-water contamination by mineral oil products - a hydrologic problem. Symposium "The pollution of ground water" Inter-Ministerial Commission of Scientific Politics, Services of the First Minister, 8 rue de la Science, Brussels.)

Shuttleworth, R., and G. L. J. Bailey. 1948. "Spreading of a Liquid Over a Rough Solid." Trans. Discuss. Faraday Soc. 15(3):16-22.

Stallmann, R. W. 1967. "Flow in the Zone of Aeration." In Advances in Hydroscience, Vol. 4, pp. 151-195. Academic Press, New York.

Stauffer, C. E. 1965. "The Measurement of Surface Tension by the Pendant Drop Technique." J. Phys. Chem. 69:1933.

Stauffer, F. 1977. Einfluss der kapillaren Zone auf instationäre Drainagevorgänge. (Influence of the capillary zone on unstable drainage processes.) IHR-ETH-Zürich.

Tietjens, O. G. 1957. Fundamentals of Hydro- and Hydro Aeromechanics. Dover, New York.

Topp, G. C., A. Klute, and D. B. Peters. 1967. "Comparison of Water Content-Pressure Head Data Obtained by Equilibrium, Steady-State and Unsteady-State Methods." Soil Sci. Soc. Amer. Proc. 31:312-314.

van Duin, R. H. A. 1955. "Tillage in Relation to Rainfall Intensity and Infiltration Capacity of Soils." Neth. J. Agric. Sci. 3:3.

Vollmer, E. 1967. Encyclopaedia of Hydraulics, Soil and Foundation Engineering. Elsevier, New York.

Weisflog, D. 1966. Mikroskopische Untersuchungen über das Verhalten von Wasser und Mineralöl im porösen Medium. Deutsche Gewässerkundliche Mitteilungen, Heft 5. (Microscopic investigations on the behavior of water and mineral oil in a porous medium.) German Hydrological Reports, No. 5.

White, J. R. 1949. "A Preferentially Oil Soluble Carrier for Radiocobalt-60." Journal Chem. Phys. 17:1000.

Whitmore, F. C. 1921. C-Quecksilberverbindungen. 1. Verbindungen, die vom Typus R•HgH ableitbar sind. A. Derivate der Kohlenwasserstoffe. Beilsteins Handbuch der Organischen Chemie, erstes Ergänzungswerk. (C-Mercury compounds. 1. Compounds which are derivable from types R HgH. A. Derivates of hydrocarbons. Beilstein's Handbook of Organic Chemistry, First Supplement, 1929.) Springer, Berlin.

Yih Chia-Sun. 1969. Fluid Mechanics. McGraw-Hill, New York

Young, T. 1805. "Essay on the Cohesion of Fluids." Phil. Trans. R. Soc. London 95:65-87.

APPENDIX A

EXPLANATION OF SYMBOLS AND INDICES

APPENDIX A

EXPLANATION OF SYMBOLS AND INDICES

The following is an abridged listing of the symbols and indices appearing in this report. The appendix is divided into four sections: 1) upper-case symbols, 2) lower-case symbols, 3) greek symbols, and 4) general indices. The section listing lower-case symbols begins on page A.7, the section listing greek symbols begins on page A.9, and the section listing general indices begins on page A.11. The page number indicates when the symbol is first used and/or defined in this report.

Upper Case Symbols

		<u>Page</u>
A	Activity in Curies	6.81
A	Atomic weight	5.6
A	Cross-sectional flow area	4.40
A	Support load	5.23
A'	Fictitious support load	5.26
AA	Number of atoms per molecule	6.19
A_K	Nuclear disintegrations per second	6.81
A_{emit}	Activity emitted by source accounted for self absorption	6.85
A_{tot}	Total activity	6.85
A^*	Weight-specific activity produced by neutron irradiation	6.39
A_{max}^*	Weight-specific theoretical maximum activity	6.29
$A_{\text{(Tm-170)}}^*$	Required weight-specific theoretical activity of the Tm-170 source	6.82
AC	Capillary rise curve	2.9

		<u>Page</u>
ACSB	Capillary rise curve	8.5
ACOL	Capillary rise curve for oil and air	2.11
ACWL	Capillary rise curve between water and air	2.11
ACWO	Capillary rise curve between water and oil	2.11
ACOLIM	ACSB for oil-air imbibition	8.56
ACWLDR	ACSB for water-air drainage	8.56
ACWLIM	ACSB for water-air imbibition	8.56
ACWODR	ACSB for water-oil drainage	8.56
B	Inside cross-sectional width of flume	6.57
B	Support load	5.22
B	Thickness or width of porous medium in the irradiation direction	3.4
B'	Fictitious support load	5.26
ΔB	Tolerated deviation in flume cross-sectional width	3.11
C _i	Curie	5.6
C _s	Cesium	5.2
D	Determinant	6.9
D	Inside diameter of calibration vessel	6.58
D _d	Coefficient of molecular diffusion	2.5
D _{ij}	Coefficient of mechanical dispersion	2.5
DR	Drainage	2.2
E	Location of point source	8.20
E	Modulus of elasticity	4.17
E _I	First radiation source (specific monochromatic energy)	6.65
E _{II}	Second radiation source (specific monochromatic energy)	6.64

		<u>Page</u>
$E_{1,2}$	Reference planes one and two	6.57
E_i	Expected value of i^{th} variable	6.53
F_K	Collimator cross-sectional area factor	6.32
G_i	Area-specific weight of i^{th} component	6.18
G_T	Area-specific total weight of compound	6.18
$G_{\text{Cs-Absc!}}$	Weight of cesium source lead shield	5.9
$G_{\text{Tm-Absch}}$	Weight of thulium source lead shield	5.7
ΔH_c	Hysteresis	8.41
H_E	Nonwetting fluid bubbling pressure head of porous probe	4.8
HC	Capillary pressure head curve	2.10
HCSB	Capillary pressure head curve	8.5
HCWL	Capillary pressure head curve for water and air	7.1
HCOL	Capillary pressure head curve for oil and air	7.1
HCWO	Capillary pressure head curve for water and oil	7.1
HCWLIM	HC for water-air imbibition	8.4
HCWLDR	HC for water-air drainage	8.2
I	Current intensity	6.42
I	Moment of inertia	5.22
IM	Imbibition	2.2
J	Attenuated (exiting) radiation intensity or impulse count rate	5.3
J_K	Constant entering impulse count rate	6.53
J_L	Impulse count rate measured through empty calibration vessel	6.59
J_N	Null impulse count rate	6.7

		<u>Page</u>
J_0	Initial (entering) impulse count rate (before passing through attenuating material)	5.3
J_T	Dry impulse count rate (null impulse count rate through oven-dried sand filling)	6.8
J_V	Volume-specific impulse count rate produced from a radioactive tracer in the porous medium	6.11
J_p	Internally produced impulse count rate from a radioactive tracer in the porous medium	6.11
J_{grEl}	Impulse count rate per gram of radioactive element	6.35
J_{grJ}	Impulse count rate per gram of isotope (compound)	6.35
$J_{gr}^{prodgef}$	Weight-specific impulse count rate capable of being being produced by an isotope	6.35
$J_{grEl}^{prodgef}$	Required weight-specific impulse count rate	6.35
J_{prod}	$J_{prod_{tot}}$ reduced by geometric attenuation within the isotope mass	6.30
$J_{prod_{max}}$	Weight-specific theoretical maximum producible activity	6.29
$J_{prod_{tot}}$	Infinitesimal volume-specific maximum impulse count of a given energy theoretically producible from a pure radioisotope per unit time	6.29
J_{prod}^{vol}	Volume-specific produced impulse count rate	6.31
$J_{prodgef}^{vol}$	Required volume-specific impulse count rate	6.35
K	Intrinsic permeability	2.6
K	Lump term in divisor	6.47
L	Air, from the German "luft"	2.3
L	Conductance	4.6
L	Length of beam serving as cart rails	5.22
L	Liter (also ℓ)	7.43
L	Loschmidt's number	6.29

		<u>Page</u>
M	Bending moment	5.24
M	Molecular weight	6.19
M'	Bending moment under virtual load condition (i.e., fictitious moment)	5.24
M_i	Partial area moment	5.26
M_0	Minimum thickness of lens of oil in residual state in vicinity of horizontal propagation surface	8.20
M_{red}	M_0 reduced to lens having uniform pendular residual oil saturation	8.56
N	Lump term in divisor	6.48
P_{Cs}	Total weight of Cesium source-detector cart	5.22
P_{Tm}	Total weight of thulium source-detector cart	5.22
OLDR	Fully-developed drainage oil-air capillary rise curve	7.1
OLIM	Fully-developed imbibition oil-air capillary rise curve	7.1
Q	Flow rate	4.6
Q	Infiltration rate	8.14
Q	Transverse load	5.28
R	Effective capillary radius of porous medium	8.2
R	Roentgen, unit of radiation dosage	5.2
R	Radius of pressure transducer diaphragm	4.17
R	Resultant (i.e., load on middle of beam)	5.23
R_{max}	Maximum horizontal radius of oil plume during vertical migration phase	8.21 8.34
RBW	Relative biological activity	5.3
RS	Residual saturation	2.1
RSL	Residual air saturation	2.2
RSO	Residual oil saturation	7.40

		<u>Page</u>
RSW	Residual water saturation	2.2
RRSL	Representative residual air saturation	8.4
RRSW	Representative residual water saturation	8.4
S	Saturation in percentage of pore volume	2.6
S_i	Center of gravity	5.27
SAI	Representative petroleum derivative composed of Super-Ad-It in organic solvent diluted in an extra-light petroleum fraction	3.8
SP	Intersection point above which a water-air capillary rise curve exists and below which water-oil and oil-air capillary rise curves exists at equilibrium with free-fluid levels.	2.9
ΔS	Unoccupied funicular saturation range	8.29
T	Day, from the German "tag"	3.18
T	Half-life of radionuclide	6.29
T	Response time of pressure gage system	4.39
ΔT	Temperature change	4.37
T_m	Thulium	5.2
U_o	Size of representative elementary volume	2.5
V	Volume	4.30
ΔV	Volume displacement	4.18
V_D	Specific diffusion volume through tubing wall	4.29
V_J	Isotope volume	6.32
V_M	Specific volume change caused by deflection of pressure transducer diaphragm	4.41
V_P	Specific volume change in flexible Vibon tubing caused by pressure change	4.33
V_T	Specific volume change in flexible Vibon tubing caused by temperature change	4.37

		<u>Page</u>
V_{tot}	Total exchange volume in pressure gage system	4.37
W	Water	2.3
WLDR	Fully-developed drainage water-air capillary rise curve	7.1
WLIM	Fully-developed imbibition water-air capillary rise curve	7.1
(WO $_$)	Undeveloped water-oil capillary rise curve	7.56
WODR	Fully-developed drainage water-oil capillary rise curve	7.1
WOIM	Fully-developed imbibition water-oil capillary rise curve	7.1
W-L level	Water-air level, i.e., water table height or elevation	
X	Distance between cesium cart and support B	5.22
Y_J	Thickness of isotope	6.32
$Y_{(99.9\%)}$	Thickness of isotope yielding 99.9% of maximum impulse count rate	6.32
Z	Atomic number	5.6
Z	Lump term in numerator	6.48

Lower Case Symbols

a	Distance between the center of each cart	5.22
a	Maximum deflection of pressure transducer diaphragm	4.16
a	Net subsidence of meniscus in capillary	4.28
a_c	Capillary rise	2.10
a_c^-	Representative capillary rise in a porous medium	8.20
a_o	Distance between center of cart and support	5.22
b	Pre-stress position	4.16
c	Concentration of solute	2.5
c	Constant variable	2.7

		<u>Page</u>
c	Velocity of light	6.3
c_0	Distance between wheels on cart	5.22
d	Pressure transducer diaphragm thickness	4.16
e	Distance between infiltration source and horizontal propagation surface	8.34
eV	Electron volt	6.3
g	Gravitational constant	2.10
g_i	Weight of i^{th} component element	6.18
gr	Abbreviation for grams in German text, also g	6.29
h	Planck's constant	6.3
Δh	Pressure head difference	4.6
Δh	Change in water table elevation	8.13
h_c	Capillary pressure head = piezometric height	2.10
Δh_c	Capillary pressure head reduction	7.1
h_M	Head of flattest meniscus	8.18
h_S	Free-fluid level (i.e., interface) between two fluids in large diameter tube	2.11
Δh_S	Change in free-fluid level	8.41
k^r	Relative permeability	2.6
l	Liter	8.14
l	Tube length	4.29
l	Bonding length	4.10
m_p	Tolerable pressure gage error	4.44
m_i	Standard error of i^{th} variable	6.46
m_e	Resting mass of electron	6.17
n	Porosity, effective porosity	2.6

		<u>Page</u>
n	Number of events	6.50
p	Probability of positive action	6.51
Δp	Pressure difference across diaphragm	4.17
p_H	Pressure in rigid steel tube	4.39
p_0	Atmospheric pressure	4.19
p_S	Pressure in flexible Vibon tubing	4.39
p_c	Capillary pressure	2.10
p_i	Pore fluid pressure to be determined	4.38
q_α	Macroscopic flux of fluid phase α	2.5
q	Probability of negative action	6.51
r	Distance from center of diaphragm	4.17
rad	100 erg/g	5.3
rem	Rad-equivalent in man	5.9
t	Time variable	2.5
t	Time of exposure to radiation	6.39
t_A	Time at which oil front reaches horizontal propagation surface	8.20
t_U	Time at which oil source is shut off	8.20
Δt_{\min}	Minimum measuring time of pressure gage system	4.44
tg	Tangent function	6.97
x	Displacement of oil drop in capillary	4.33
x	Thickness of the irradiated material (i.e., irradiation width or path length)	5.3
x	Moving variable	5.22
x_K	Collimator width	6.32
Δx_i	Distance between load points on beam	5.27

		<u>Page</u>
$\Delta X S_i$	Distance between load point and center of gravity	5.27
$Y S_i$	Moment resulting from virtual load condition	5.27
Z_K	Collimator height	6.32
 <u>Greek Symbols</u>		
α	Fluid phase	2.5
β	Dispersed phase	2.5
δ	Deflection	5.22
$\Delta \delta$	Change in deflection	5.22
ϵ	Quantum energy	6.3
ϵ_i	Element i^{th}	6.19
η	Efficiency in producing gamma-radiation within deceleration spectrum of x-ray tube	6.42
θ	Volumetric moisture content	6.1
θ_α	Volumetric fraction of fluid α in representative elementary volume	2.5
κ	Attenuation caused by pair-production	6.15
κ_M	Proportionality constant between M_{red} and $a_{\text{C}}^- \frac{L}{W}$	8.56
λ	Wavelength	6.3
λ	Proportionality constant between pressure change and oil drop displacement	4.33
λ	Reciprocal of response time of pressure gage system	4.40
μ	Dynamic viscosity	2.6
μ	Attenuation coefficient	6.15
μ	Poisson number	4.17
(μ/ρ)	Mass attenuation coefficient	5.3
ν	Frequency	6.3

		<u>Page</u>
ρ	Density	2.5
σ	Capture cross-section of the irradiated element	6.39
σ	Attenuation caused by Compton scattering	6.15
σ_A	Attenuation caused by production of Compton electron	6.15
σ_J	Standard deviation of exiting impulse count rate	6.51
σ_{J_0}	Standard deviation of entering impulse count rate	6.51
σ_R	Attenuation caused by Rayleigh scattering	6.15
σ_S	Attenuation caused by Compton scattering (inelastic collision)	6.15
σ_{SA}	Attenuation caused by self-absorption	6.31
σ_g	Geometric attenuation between source and detector	6.30
σ_g	Geometric attenuation within mass of isotope	6.30
σ_m	Attenuation caused by material between source and detector	6.33
σ^*	Attenuation coefficient for scattering	6.15
$\sigma _A^T$	Geometric attenuation between anode and target	6.42
$\sigma _T^D$	Geometric attenuation between target and detector	6.42
τ	Attenuation caused by photoabsorption	6.15
Φ	Neutron flux	6.39
Φ	Total fluid potential	2.6
Φ^r	Relative oil potential, also Φ_r	7.5 8.7
Φ^{rtM}	Relative transition oil potential	8.51
ϕ	Mean grain diameter	3.4
ϕ	Outside diameter	5.8
ϕ_K	Diameter of capillary	4.29

		<u>Page</u>
Ω	Scaling factor between capillary rise curves of different fluid combinations in a porous medium	7.3
$\Omega _0^L$	Scaling factor between oil-air capillary rise curve and virgin water-air capillary rise curve	7.3
<u>Indices</u>		
Cs	Cesium	5.16
DR	Drainage	8.2
El	Element	6.35
Eu	Europium	6.77
G	Compound	6.18
I	First radiation source (specific monochromatic energy)	6.9
II	Second radiation source (specific monochromatic energy)	6.9
J	Isotope	6.31
J	Impulse count rate	6.53
KWB	Carbon-water-lead compound	6.69
L	Air, from the German "luft"	2.7
M	Meniscus	8.18
O	Oil, petroleum derivative	2.7
RRSL	Representative residual air saturation	8.2
S	Sand	6.4
S	Level	2.11
SAI	Representative petroleum derivative composed of Super-Ad-It in organic solvent diluted in an extra-light petroleum fraction	6.103
Tm	Thulium	5.16
W	Water	2.7

		<u>Page</u>
b	Wetting fluid	2.10
befl	Contaminated	7.1
g	Glass	6.4
ins	Insular	2.1
jfrl	Virgin, uncontaminated	7.1
max	Maximum	2.1
nb	Nonwetting fluid	2.10
pend	Pendular	2.1
x	coordinate on longitudinal axis	2.7
y	coordinate on horizontal axis	2.7
z	coordinate on vertical axis	2.7

APPENDIX B

THE HALLUX PHENOMENON AND ITS EXPLANATION

INTERNATIONAL IAHR SYMPOSIUM ON SCALE EFFECTS IN POROUS MEDIA
Thessaloniki, Greece, Aug.29 - Sept.1, 1978

THE HALLUX PHENOMENON AND ITS EXPLANATION

HANS OLIVIER SCHIEGG

Laboratory of Hydraulics, Hydrology and Glaciology
annexed to the Federal Institute of Technology
Zürich - Switzerland

SYNOPSIS

In the experiment it is shown, that during a change from drainage to imbibition a zone is formed between the funicular and insular region, in which even the insular region is vastly replenished by the wetting fluid. This effect is called hallux phenomenon. The hallux phenomenon is physically explained. Therefore, microscopic view is necessary. Therefrom results, that the averaged, double thickness of the hallux gives a size for the statistical pore diameter in the flow direction within the widest pore threads.

RESUME

Dans l'expérience il est montré que lors du change du drainage à l'imbibition, entre le domaine funiculaire et le domaine insulaire, se forme une zone dans laquelle même le domaine insulaire est rempli pour la plus grande partie par le fluide mouillant. Cette apparition est désignée comme le phénomène du hallux. Le phénomène du hallux est physiquement expliqué. Ceci implique une observation microscopique. Il en résulte que la double épaisseur moyenne du hallux représente une grandeur pour le diamètre statistique des pores dans la direction du courant à l'intérieur des veines les plus larges.

INTRODUCTION

For the hallux phenomenon several conditions must be satisfied. This might be the reason why it has not been mentioned yet in the literature. Nevertheless, the hallux phenomenon can be of practical interest. For example, a hallux will continue to subsist at level fluctuations, the double amplitudes of which are smaller than the level distance of the transition to the insular region at drainage, see Fig. 2b. Furthermore, the measurement of the medium, double hallux thickness can be used as a method to determine the statistical pore diameter in the flow direction within the widest pore threads. Finally, there is some interest in the hallux phenomenon in connection with displacements of three, non-mixing fluids, due to the fact that the hallux is formed at the place of the lowest potential of the fluid with the medium density, i.e. in the region of its propagation surface, Schiegg (1977).

EXPERIMENT

The aim of the experiment is to provide information about the hallux formation, as observed in the laboratory, while the saturation distribution normal to the level, $a_c(S_b)$ develops after a reversal of the moving direction of the level from drainage to imbibition.

The function $a_c = a_c(S_b)$ is called capillary rise head curve, ACSB respectively. S_b means the saturation of the wetting fluid. a_c is the capillary rise head, i.e. the distance of the occurrence of the saturation S_b from the level. With a wetting angle hysteresis or a variable size of the cross sections of the pore threads an ACSB is subject to a hysteresis. Thus, following a reversal of the moving direction of the level, an ACSB must change from one extreme form to the other. This happens continuously and as long as the level has not moved from its reversal point for more than the maximum thickness of the hysteresis region of the ACSB.

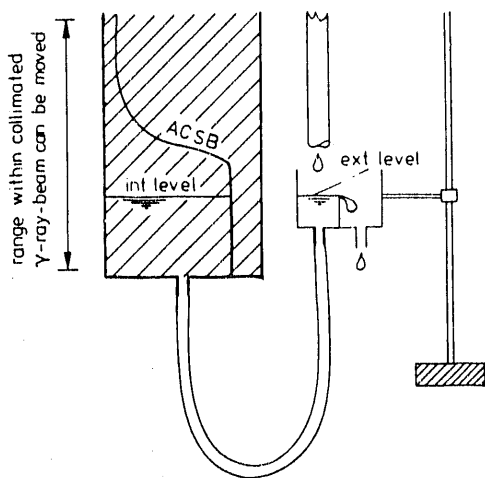


Fig.1 Experimental device

Fig.1 is a schematic drawing of the experimental device to observe the development of an ACSB during its change from one to the other extreme form.

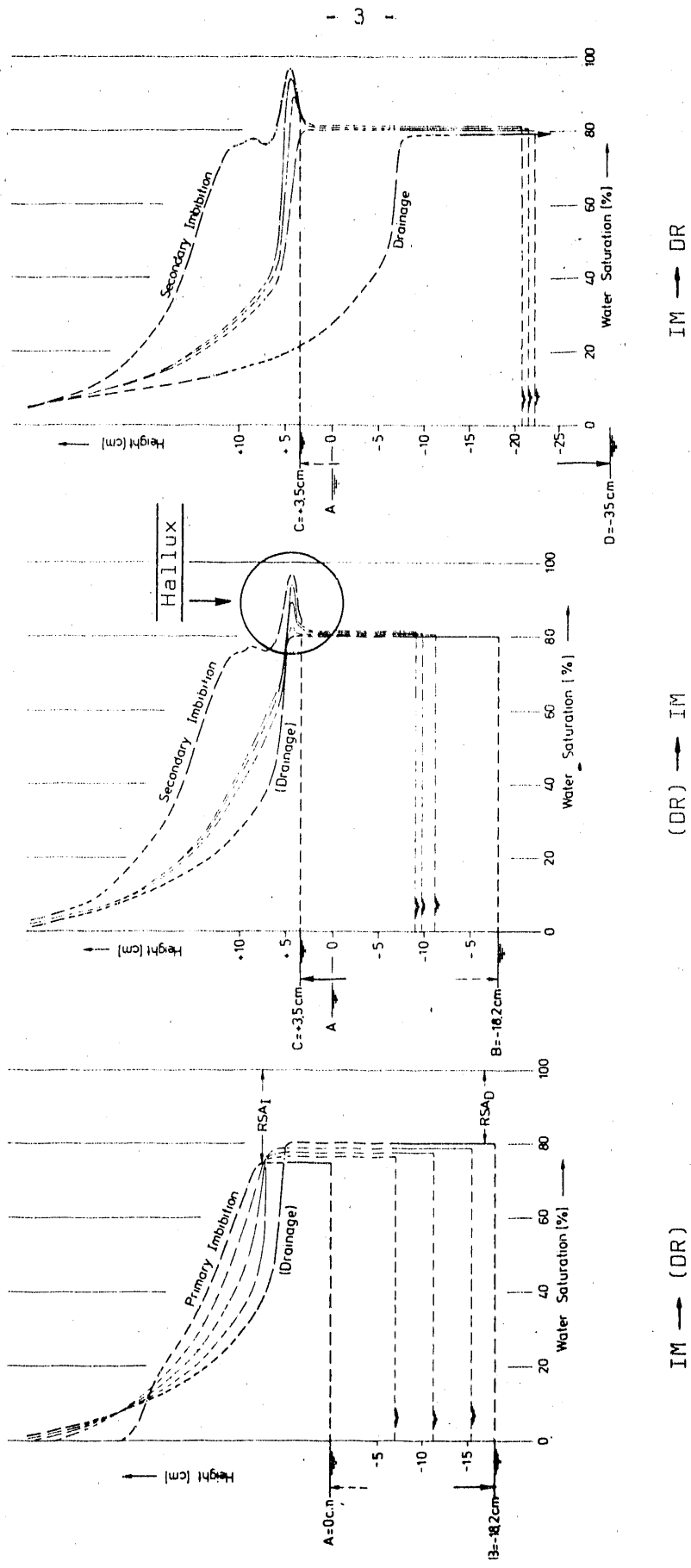


Fig. 2. Results

The porous matrix was a homogeneous and isotropic, unconsolidated fill of dry quartz sand. The grain size distribution curve was steep, i.e. between .1 and .6 mm. The medium grain size was .3 mm and the porosity .43. The hydraulic permeability amounted to $1.9 \cdot 10^{-2}$ cm/sec. Water was the wetting and heavier fluid. Air represented the non-wetting and lighter fluid. The measurement of saturation over the height was carried out by absorption of γ -rays. The isotope was Cs-137. The cross section of the collimated beam amounted to 5x20 millimeters. A saturation measurement was done each centimeter in the height. The internal level was adjusted by the external level in a movable reservoir. The measured ACSB were formed by removing the external level for 7 millimeters at one pull and then leaving it constant. At the following day the distribution of saturation was measured. Then the external level was removed for 7 millimeters again.

Fig.2 shows some of the measured ACSB during changes from imbibition to drainage and vice versa. Primary imbibition means imbibition into dry sand. The symbol DR between paranthesis means, that the drainage curve in question has not yet reached its final shape. The figures 2 show the well known dependency of a residual saturation on history, which can be explained at microscopic view, see Schiegg (1978). The residual saturation of air for imbibition, RS_{AI} , is smaller than that one for drainage, RS_{Aq} .

From fig.2a it can be seen, that during a change from imbibition to drainage no hallux is formed. In contrast, a hallux develops during a change from drainage to imbibition, which is shown in fig.2b. According to fig.2c the hallux disappears when the level is lowered more than it was for the (DR)-curve in fig.2a.

EXPLANATION OF THE HALLUX PHENOMENON

An ACSB implies macroscopic view. At macroscopic view a reduction of residual saturation of air can only be explained by diffusion or by floating. Yet, it is not possible to explain the special form of a hallux by these mechanisms. Thus, the concept of a macroscopic continuum, which usually is required by the application of Darcy's law, must be dropped and must be replaced by a microscopic view. Microscopic view means a resolution below the size of a pore diameter, of a meniscus respectively. Parameters, which shall describe the average conditions within a porous matrix of unknown microscopic geometry, for instance the Radius \bar{R} of a pore or a meniscus etc., must have the meaning of a statistical expectation.

The micro-macro-transition is normally done by the definition of the statical ACSB in dependence on the microscopic notion of \bar{R} , which means the statistical meniscus, pore radius respectively, according to eq. (3). It states the function $S_b = S_b(h_c)$. S_b is the macroscopic notion of the saturation of the wetting fluid. The capillary pressure head, h_c , can be written according to Laplace's equation of capillarity as

$$h_c = \gamma \left(\frac{1}{R_I} + \frac{1}{R_{II}} \right) / (\Delta \rho g) \quad (1)$$

γ is the interfacial tension. R_I and R_{II} are the radii of main curvature. $\Delta \rho$ is the density difference, g the acceleration of gravity. In case of spherical menisci the relation $R_I = R_{II} = \bar{R} \cos \alpha$ holds. α is the wetting angle. Hence the pore radius \bar{R} can be written in function of the appertaining capillary pressure head, $h_c \bar{R}$, as

$$\bar{R} = (2\gamma \cos \alpha) / (h_c \bar{R} \Delta \rho g) \quad (2)$$

The integral

$$S_b = 1 - \int_{\bar{R} = (2\gamma \cos \alpha) / (h_c \bar{R} \Delta \rho g)}^{\bar{R}_{\max}} f(\bar{R}) d\bar{R} \quad (3)$$

states, that for a capillary pressure head $h_c \bar{R}$ all pores, pore threads respectively, the decisive radius of which is larger than \bar{R} , are still filled with the non-wetting fluid, compare Scheidegger (1960,55). Not that eq.(3) implies the possibility of an analytical determination of the statical ACSB; this, because the volume radius function, $f(\bar{R})$, as the statical ACSB, i.e. $S_b = S_b(h_c)$, with unknown, microscopic geometry of the pores can be determined only experimentally. But eq.(3) shows, what the decisive parameters are and how they enter into the calculation. The function $S_b(h_c)$, $S_b(\bar{R})$ respectively, is limited by the regions of residual saturation.

The hallux phenomenon occurs in the transition zone to insular saturation. Hence, there is for its explanation some interest in the development of the function of saturation, eq.(3), in the region of the upper limit of the integral and thus in the region of the flattest menisci, i.e. of the menisci with a maximum, statistical radius \bar{R}_{\max} .

A movement of the menisci can on the average only be simultaneous with the movement of the level. But in reality the movement is jumpwise, i.e. it is composed of single jumps, provided the cross section of the pore thread is of variable size, as it can be seen in the experiment even with the naked eye. The size of a jump is given by the distance of the next

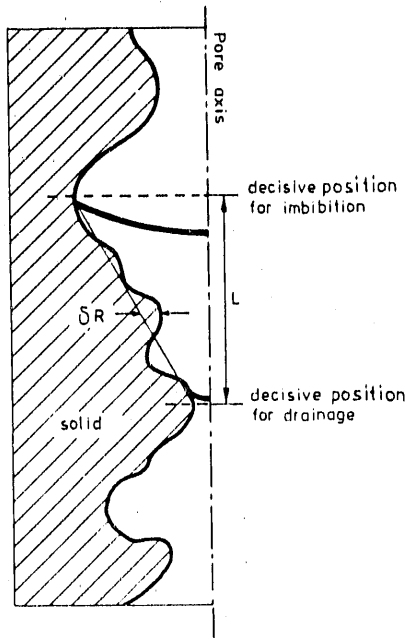


Fig.3 Decisive positions

Decisive position of equal type and is thus on the average equal to $2L$, see Fig.3. At imbibition the decisive positions are determined by the wide passages, at drainage by the narrow ones. In a homogeneous, porous matrix the decisive positions repeat statistically. L is the statistical distance between the wide and the narrow passages of a pore thread and thus equal to one half of the statistical pore diameter in the flow direction. A jump from one decisive position to the next one happens still then, when the level has moved for $2L$ since the last jump. The jumpwise movement of a meniscus consists of various subjumps, depending on the variance of the radius of the pore thread, δR .

The jumpwise movement of the flattest menisci explains the formation of insular saturation; this, because the displaced fluid is not able to escape at certain conditions, which differ depending on the history of the displacement. The sum of these entrapped residues of the displaced fluid are on the average about constant. At macroscopic view they form the insular saturation.

As long as the flattest menisci move on the average simultaneously with the level, the insular saturation is formed in any case, because of the jumpwise motion. The non-wetting fluid can not be displaced anymore. Under these circumstances a practically complete replenishment of the pore space by the displacing fluid and hence the formation of a hallux is not possible. According to the experiment the formation of a hallux stipulates a change of the moving direction of the level. This implies a change from drainage to imbibition or from imbibition to drainage. Until the level has not moved from its reversal point for more than the hysteresis of a meniscus, such a change means, that the meniscus alters from one to the other extreme form while it moves for one half of the pore diameter only. This happens very slowly compared with the posterior, macroscopic changes, because of the microscopic change in position, which is in contrast to the following, jumpwise movement continuous.

Fig.4 is a schematic drawing of the microscopic picture of the transition zone to insular saturation. It shows the distribution of the air on principle. The menisci are those with the maximum radius, they are the flattest menisci. Fig.4 can particularly be interpreted as the picture at the moment of a reversal of the moving direction of the level.

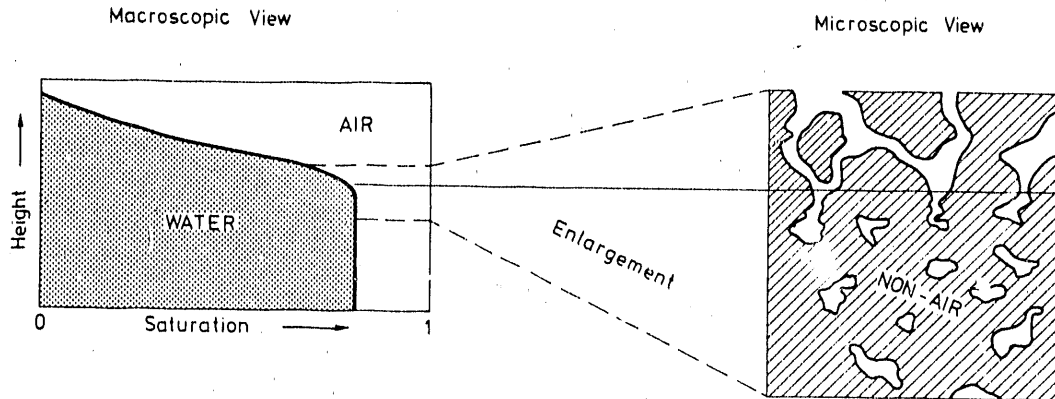


Fig.4 Microscopic view of the transition zone between funicular and insular saturation

After a change from imbibition to drainage the picture in fig.4 is on principle still valid, except that the free menisci change from the imbibition into the drainage form. They will retreat, where the pore space is narrow, and thus move within the same pore from the decisive position for imbibition to that one for drainage. Hence the free menisci will move on the average for the microscopic distance L , meanwhile the level must move for the macroscopic distance of the hysteresis range at the transition zone to insular saturation. Subsequently the picture of the air distribution in fig.4, changed in the way mentioned, will move within the porous matrix simultaneously with the level, whereas the single, free menisci will move jumpwisely.

In contrast to that a change from drainage to imbibition will alter the distribution of air in the picture of fig.4 fundamentally. The very slow and continuous change of the positions of the free menisci over only one half of a pore diameter and thus statistically over the distance L during their change from the drainage form into that one for imbibition causes, that the wetting fluid is enabled to escape practically completely. This means, that a layer is formed, the thickness of which is L and in which the insular saturation is practically zero. Hence, the pore space is practically completely filled up with the displacing, wetting fluid. Subsequently the free imbibition menisci move jumpwisely over distances with the statistical value of $2L$. Nevertheless they follow the level on the average simultaneously. Therefore an insular saturation must then again be formed necessarily. Hence, the formation as well as the special form of the hallux is explained.

CONCLUSIONS

- A hallux is a protrusion, an encroachment of the function between saturation and capillary pressure head into the range of insular saturation within the transition zone from the funicular to the insular region.
- The formation of a hallux is explainable at microscopic view only.
- The experimental experience, that a hallux can be formed during a change from drainage to imbibition only, can be explained.
- The hallux phenomenon is not a result of a displacement, but of the non-forming of insular saturation.
- The average thickness of a hallux is a measure for one half of the statistical pore diameter in the flow direction of the widest pore threads.
- The hallux phenomenon can be observed likewise in connection with displacements of three non-mixing fluids and that in a double way, Schiegg (1978).

REFERENCES

- Scheidegger, A.E. (1960); The physics of flow through porous media; 2nd ed., University of Toronto Press.
- Schiegg, H.O. (1977); Modellvorstellung und Konzepte zur Abschätzung von Verunreinigungen von Grundwasserträgern durch Erdölderivate; Wasser, Energie, Luft, 10:251-258.
- Schiegg, H.O. (1978); Verdrängungs-Simulation dreier, nicht mischbarer Fluide in poröser Matrix; Mitteilungen der Versuchsanstalt für Wasserbau, Hydrologie und Glaziologie, ETH-Zürich, be printed.

APPENDIX C

FIELD INFILTRATION AS A METHOD FOR THE DISPOSAL OF OIL-IN-WATER
EMULSIONS FROM THE RESTORATION OF OIL-POLLUTED AQUIFERS

Reprinted with permission from Water Research, Vol. 14, Copyright 1980, Pergamon Press plc

FIELD INFILTRATION AS A METHOD FOR THE DISPOSAL OF OIL-IN-WATER EMULSIONS FROM THE RESTORATION OF OIL-POLLUTED AQUIFERS

HANS-OLIVIER SCHIEGG*

Laboratory of Hydraulics, Hydrology and Glaciology at the Swiss Federal Institute of Technology,
ETH, CH-8092 Zurich, Switzerland

(Received August 1979)

Abstract--Oil may be crude oil or one of its derivatives. An oil accident involves the unintended infiltration of oil into the ground. If the propagation of the oil along the water table is stopped by pumping water, oil-in-water emulsions with low oil content may occur. Their disposal by infiltration in the proximity of the oil accident is called field infiltration.

The idea of field infiltration is based on the retention of oil by the soil as well as on the microbial degradation of oil. Advantages of field infiltration are its simplicity and its low cost as well as the minimum consumption of fresh water during pumping. Disadvantages are the unknown degree of microbial degradation and in some cases the uncertainty as to whether the Jamin effect, which governs retention, is operative at all, which can be proved by experiment only.

In the present paper hydromechanical fundamentals of field infiltration are examined and the maximum retention of oil by the Jamin effect is determined experimentally.

INTRODUCTION

If an oil accident happens above an aquifer which is used for the drinking-water supply and which is not protected by a relatively impermeable upper layer, it is most important to minimize the acute danger of pollution of the aquifer as well as to keep any pollution as slight as possible.

The first period of propagation of oil which infiltrates above the capillary fringe between water and air into a homogeneous and isotropic porous medium consists in a mainly vertical infiltration (Fig. 1). At the moment when the oil front reaches the propagation plane, the second period of propagation begins, during which the oil migrates along the propagation plane. The propagation plane is situated within the capillary fringe between water and air, parallel to the groundwater table and at a distance "a" from it. Schiegg (1977, p. 254). If the pressure of the oil is high enough, the oil penetrates transiently below the water-air table.

After a failure to hold up an oil front during the first period of propagation, a method often applied to prevent a further migration of the oil consists in pumping water in order to create a sink. Figure 2 shows the case of sinking a pump in the center of the oil infiltration area. With an inclined water table the vertical pump axis must be placed nearer to the momentary position F of the front in the flow direction when the pumping rate is lower. At the draw-down thus formed the oil is unable to propagate further and flows to point D, (Fig. 2).

* Present address: Electrowatt Engineering Services Ltd, CH-8022 Zurich, Switzerland.

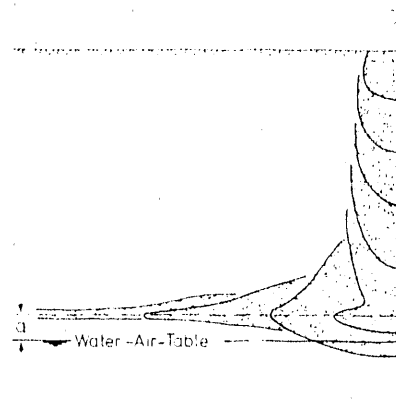


Fig. 1. Diagrammatic sketch of oil propagation Schiegg (1977, p. 252)

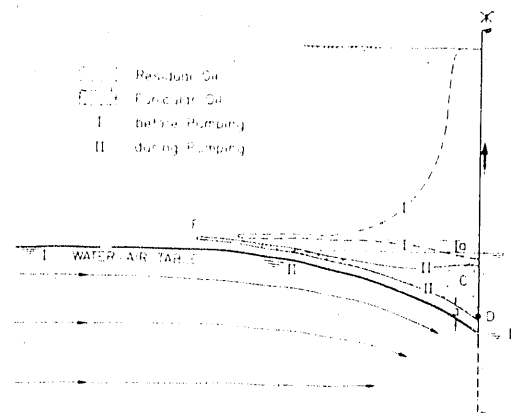


Fig. 2. Preparing a sink to stop oil propagation.

If we assume that the inlet to the water pump lies below point D, it is advisable, when a certain amount of oil has collected, not to pump water and oil with the same pump, but to raise the oil with a separate pump at point D. However, at least a small amount of oil will get into the water pump, whereby an emulsion of oil in water will be produced. Even if the oil content is small, it will in general be so high that the water should not be led into a river or lake in the untreated condition, as the following estimate shows. At a pumping rate of 10 l. s^{-1} and with an oil content of 5 ml l^{-1} , 130,000 l. of oil would be transported in the emulsion in a pumping time of 1 month.

The reduction of the oil content of such emulsions can be achieved by passing them through a filter or over an oil separator by gravity. If these installations are only improvised, as frequently happens, the separation of the oil will in most cases not be at all complete. For the disposal of such oil-in-water emulsions with low oil content the field infiltration method, as described in the following, is proposed.

DISPOSAL BY FIELD INFILTRATION

Disposal by field infiltration is based on the facts (i) that a soil has a certain capacity of retention for oil and (ii) that a substantial microbial degradation of the retained oil takes place in a relatively short time. This is the case with aerobic conditions (Zobell, 1973; Bringmann, 1969, 1972; Walker & Colwell, 1974; Kappeler, 1976; Bailey *et al.*, 1973), as long as no other nutrients, such as nitrates or phosphates are limiting factors.

Disposal by field infiltration consists in the infiltration of the pumped emulsion over the area B, see

Fig. 3. The size of the area B must be chosen in such a way, according to the retention capacity of the soil, that the total amount of infiltrated oil will be retained within the region A, defined by the area B and the height H. Pumping is necessary as long as a certain quantity of oil can be collected by it, i.e. until the oil in the region C in Fig. 3 has been reduced practically to residual saturation. After the interruption of pumping and hence of infiltration in area B, aerobic conditions, which are necessary for substantial microbial degradation, are restored within the region A. The centre Z of area B must be situated before the oil front F, but advisably not very far before it, so that the ground-water mound, caused by the recharging, becomes a barrier which makes for the prevention of further oil propagation and even pushes back the oil.

Compared with other methods, disposal by field infiltration has the advantage that, regardless of the duration of the drawdown, a minimum of fresh water is withdrawn from the aquifer to stop further propagation of the oil. This is because of the infiltration of the pumped emulsion and the equilibrium thereby reached between discharge and recharge.

The disadvantage of the pollution of the region A may not be so important for several reasons. On the one hand, for the precipitation water which infiltrates above the horizontal oil propagation, the probability of saturation with water-soluble oil derivatives is high anyway. On the other hand, an analogous pollution occurs if the groundwater level fluctuates, as it usually does. There is therefore in any case a possibility of long-time pollution by soluble organic compounds, as investigated by Dietz (1978), in the proximity of an oil

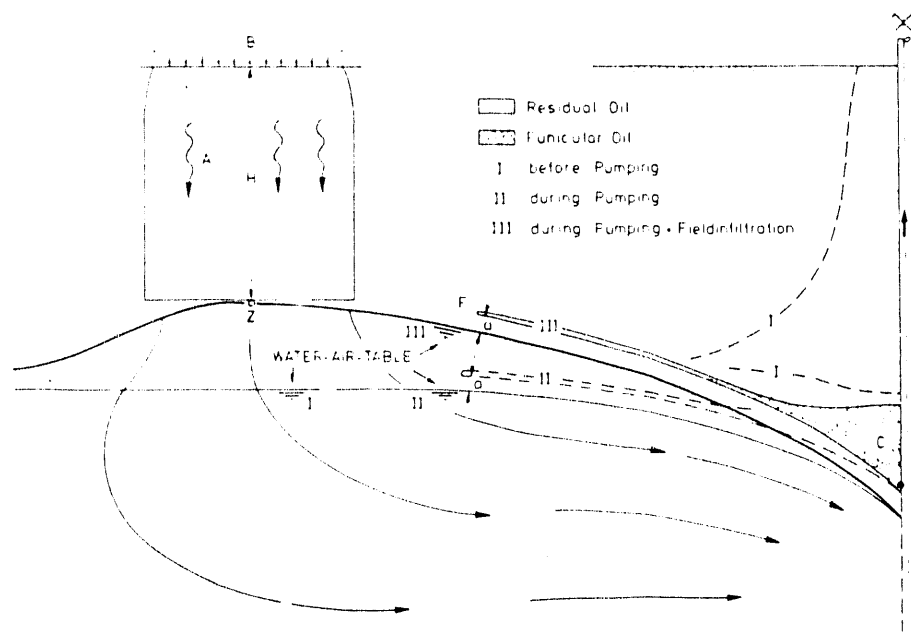


Fig. 3. Disposal by field infiltration.

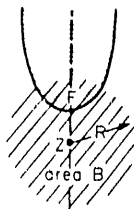


Fig. 4. Situation for inclined water-air table.

accident. Its slight increase by field infiltration should in general be negligibly small.

From an estimate of the necessary extension of a circular area B (Fig. 4) the radius for the example mentioned—with a volume V of 130 m^3 of oil in the $26,000 \text{ m}^3$ of emulsion, assuming a porosity n of 0.3, a retention capacity Ω of 5% of the pore volume and a distance H of 10 m between the groundwater table and the soil surface—works out at $R \approx 17 \text{ m}$, determined as the root of $V/\pi \cdot n \cdot \Omega \cdot H$.

For infiltration at a pumping rate Q of emulsion which is poured upon the soil surface over the point Z, the Darcy law holds in an extended form:

$$q = -k'_{(s)} \cdot k \cdot \nabla \Phi \quad (1)$$

where q is the vector of the specific flux of the emulsion, k' is the relative permeability, dependent on the saturation, k is the hydraulic permeability and $\nabla \Phi$ the gradient of the potential as a piezometric head. The minus sign indicates that the flow is in the opposite direction to increasing Φ . Because any flow is in the opposite direction to increasing Φ , q is per definitionem always a negative value; thus, the following $-q$ is positive. Assuming vertical infiltration due to gravity only, hence supposing a $\nabla \Phi$ equal to 1, then for a pumping rate Q of -10 l. s^{-1} —for the negative sign see Scheidegger, 1960, p. 70—over a circular area B with a radius R of at least 17 m, the following must hold for the permeability product $k' \cdot k$:

$$k'_{(s)} \cdot k \leq -(-q) = -\left(\frac{Q}{B}\right) = 10^{-3} \text{ cm s}^{-1}. \quad (2)$$

For a better permeability of the soil the emulsion for infiltration must be sprinkled over the area B with a radius R of 17 m. Otherwise the retention volume within the region A might be too small for the 130,000 l. of oil.

Disposal by field infiltration presupposes that the maximum retention capacity for oil due to the Jamin effect with gravity infiltration of an oil-in-water emulsion is of the magnitude of at least pendular saturation. Pendular saturation and Jamin effect are explained in the following theoretical exposition and experimental proof of these suppositions.

RETENTION CAPACITY AND RESIDUAL SATURATION

With displacements

Residual saturation consists in unconnected inclu-

sions of a displaced fluid. The formation of residual saturation is a consequence of the non-continuous, jump motion of the single menisci within a porous medium during a displacement, Schiegg (1979, p. 72). Residual saturation of the wetting fluid is called pendular saturation, that of the non-wetting fluid insular saturation. A funicular saturation is a non-residual saturation, Versluys (1931, p. 193).

For oil together with water and air in a porous matrix the residual saturation may be pendular as well as insular. With pendular saturation the oil occurs as the wetting fluid against the non-wetting air at the narrow places in the pore space. With insular saturation the oil remains as the non-wetting fluid against the wetting water at the widest places in the pore space, i.e. in the center of large pores. The different positions of the oil with pendular and insular saturation explain why the maximum pendular residual saturation of oil, $RSO_{pend,max}$, has not necessarily the same value as the maximum insular residual saturation of oil, $RSO_{ins,max}$. According to experimental results up to date, the following equation holds as a first approximation:

$$RSO_{ins,max} \approx 2 \cdot RSO_{pend,max} \quad (3)$$

where $RSO_{pend,max}$ can in general be taken as 3-6% of the pore volume depending on the type of soil.

With infiltration of an oil-in-water emulsion

The retention of oil from an infiltrated oil-in-water emulsion is based on an effect which was mentioned by Jamin (1860). The Jamin effect is—in a qualified sense, see Jamin (1860, p. 175), Versluys (1931, p. 197), Scheidegger (1960, p. 215)—the obstructing effect a non-wetting fluid may have. The effect of a plug occurs if the diameter of a narrow passage of a pore thread is smaller than the diameter of the part of the non-wetting fluid which floats in the percolating wetting fluid. The tendency of such a plug to grow results from its coalescence with the following dispersed droplets and bubbles respectively, of the non-wetting fluid. The maximum retention capacity, i.e. the maximum residual saturation of oil by retention, $RSO_{ret,max}$, is a function of the maximum height of a plug. This height depends on the specific properties of the media, such as density, interface tension and wetting angle. But it is also a function of the potential gradient in the transporting fluid and, last but not least, of the geometry of the pore space. This can be seen from the following equations for the determination of the maximum height of oil plugs.

MAXIMUM HEIGHT OF OIL PLUGS DUE TO THE JAMIN EFFECT

If the oil plug in Fig. 5 is to pass through the passage I, its radius of curvature, assuming the meniscus to be spherical, must be $\leq R_1$. The orientation of the menisci in Fig. 5 presupposes water as the wetting and oil as the non wetting fluid. Thus, the passing of

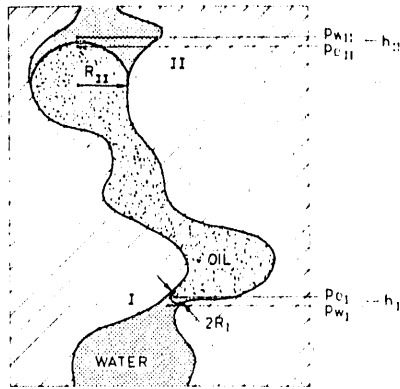


Fig. 5. Jamin effect.

the plug implies a higher pressure in the oil than in the water. The pressure difference is defined as

$$p_c \geq p_o - p_w \quad (4)$$

and is called capillary pressure. p_c , p_o is the pressure in the oil. p_w is the water pressure. The capillary pressure is defined, in dependence on the characteristic parameters of the media and the geometry of the pore space, with the aid of the Laplace equation of capillarity for place I as

$$p_{cI} = \gamma \cdot \cos \alpha \cdot \frac{2}{R_I} \quad (5)$$

where γ is the interface tension between water and oil and α represents the wetting angle of this liquid combination relative to the solid of the porous medium.

The capillary pressure at place I is determined in dependence on the unknown maximum height of an oil plug, $(h_{II} - h_I)_{\max}$, as

$$\begin{aligned} p_{cI} &= p_{oI} - p_{wI} \\ &= \{p_{wII} + p_{cII} + \rho_o \cdot g \cdot (h_{II} - h_I)_{\max}\} - p_{wI} \quad (6) \\ &= (p_{wII} - p_{wI}) + p_{cII} + \rho_o \cdot g \cdot (h_{II} - h_I)_{\max} \end{aligned}$$

The pressure difference in the water between places I and II is a function of $\nabla\phi_w$, of the potential gradient in the water. $\nabla\phi_w$ can be approached as the differential quotient of the piezometric heads in a macroscopic view as

$$\nabla\phi_w \approx \{(p_{wII} - p_{wI})/(\rho_w \cdot g) + (h_{II} - h_I)\} / (h_{II} - h_I) \quad (7)$$

The pressure-difference results explicitly as

$$(p_{wII} - p_{wI}) = (\nabla\phi_w - 1) \cdot \rho_w \cdot g \cdot (h_{II} - h_I) \quad (8)$$

Eliminating $(p_{wII} - p_{wI})$ in equation (6) with equation (8) and with p_{cII} analogous to equation (5), it follows that

$$\begin{aligned} p_{cI} &= (\nabla\phi_w - 1) \rho_w \cdot g \cdot (h_{II} - h_I) + \gamma \cdot \cos \alpha \cdot \frac{2}{R_{II}} \\ &\quad + \rho_o \cdot g \cdot (h_{II} - h_I)_{\max} \quad (9) \end{aligned}$$

By equalizing the terms on the right-hand side of

equations (5) and (9), it results for $(h_{II} - h_I) = (h_{II} - h_I)_{\max}$, which implies $R_I = R_{I\min}$, that

$$(h_{II} - h_I)_{\max} = 2 \cdot \gamma \cdot \cos \alpha \left(\frac{1}{R_{I\min}} - \frac{1}{R_{II}} \right) / \{g[\rho_o + \rho_w(\nabla\phi_w - 1)]\} \quad (10)$$

Vertical gravity flow is defined by a potential gradient equal to 1, hence by a constant pressure, see equation (8). With $\nabla\phi_w = 1$, equation (10) is reduced to

$$\begin{aligned} (h_{II} - h_I)_{\max} &= 2 \cdot \gamma \cdot \cos \alpha \left(\frac{1}{R_{I\min}} - \frac{1}{R_{II}} \right) / (\rho_o \cdot g) \quad (11) \end{aligned}$$

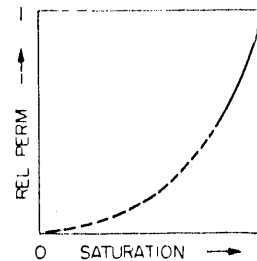
In general, R_{II} will be large compared with R_I . Thus, the height of a plug of oil which is necessary for it to pass at vertical gravity flow of the water can be written in a first approximation as

$$\left\{ \begin{array}{l} \nabla\phi = 1 \\ R_I \ll R_{II} \end{array} \right\} (h_{II} - h_I)_{\max} \approx 2 \cdot \gamma \cdot \cos \alpha / (R_{I\min} \cdot \rho_o \cdot g) \quad (12)$$

MOTION OF THE LIQUIDS

The retained oil changes the relative permeability for the emulsion. The form of the function $k'_{(S)}$ for an emulsion of which the dispersed part is a non-wetting one must in principle correspond to the function for a wetting fluid as measured by Wykoff & Botset (1936), shown in Fig. 6. The plausible argument for this statement is that insular parts must be situated similarly within the pores, independently of whether they are formed by a displacement or by retention due to the Jamin effect. The exact form of the $k'_{(S)}$ -curve for retention due to the Jamin effect can be determined by experiment only, see last comment before conclusions. The full curve in Fig. 6 shows the substantial reduction of the relative permeability by even small amounts of the non-wetting fluid, which is comprehensible in view of its plug effect.

If the dispersed fluid is to float with the emulsion within a porous medium and hence to move relative to the porous medium, the dimensions of the dispersed oil droplets must be smaller than the diameters

Fig. 6. $k' = k'_{(S)}$.

of the cross-sections of the pore threads. A fluid part which is blocked as a plug as a result of the Jamin effect cannot pass through the narrow passage unless the plug has reached its maximum height, determined with equation (11). The renewed motion of at least one part of such a blocked fluid before the plug has reached its maximum height is possible only if the growing plug comes into contact with another one and an outflow through another passage than the one momentarily obstructed is thereby made possible. Such contact means, in the macroscopic view, the beginning of the transition to funicular flow of the oil.

Oil particles which are small enough not to get blocked by the Jamin effect nor to coalesce with oil already retained pass through the matrix floating in the water. Nevertheless, such oil will be repumped and with great probability will be retained within the region A during its next infiltration cycle.

EXPERIMENTAL DETERMINATION OF:
 (I) THE MAXIMUM RETENTION CAPACITY
 OF OIL DUE TO THE JAMIN EFFECT,
 $RSO_{ret,max}$; (II) THE RELATIVE
 PERMEABILITY FOR $RSO_{ret,max}$

The experiment is meant to show the maximum oil retention capacity due to the Jamin effect of several soils upon the infiltration of oil-in-water emulsions with low oil content at gravity flow.

The grain-size distributions of the sands used are shown in Fig. 7. Obviously the Jamin effect is more likely to hold when the pore conjunctions are smaller and hence the grain-size-distribution is flatter. Thus relatively unfavourable conditions have been chosen for the experiments.

Unconsolidated, homogeneous and isotropic samples of the various sands were prepared, see Wygal (1963). As Fig. 8 shows, the axes of the cylindrical samples were positioned vertically. The upper front of the samples was charged with oil-in-water emulsions in such a way that $\nabla\phi = 1$ was maintained.

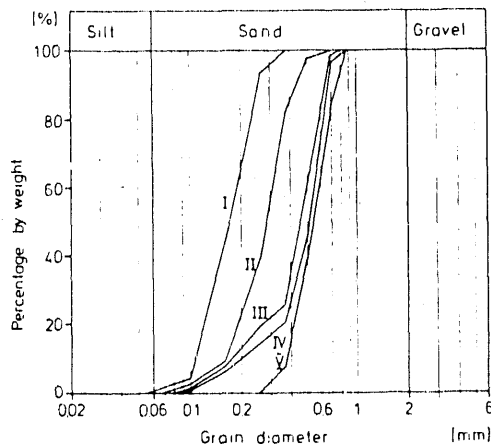


Fig. 7. Grain-size distributions for soils I—V.

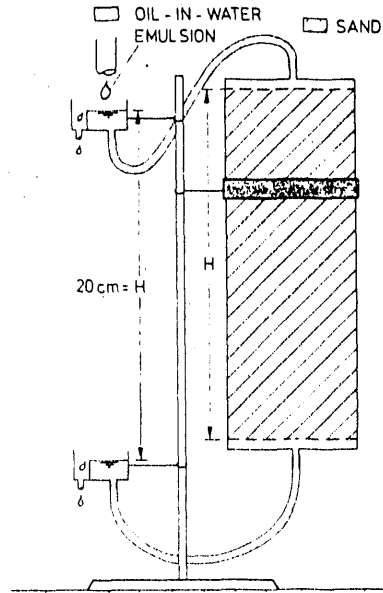


Fig. 8. Diagrammatic sketch of experiment.

The oil content of the infiltrating emulsion was kept constant during each experiment. It was chosen as 0.25, 0.50 or 1%.

For the determination of the maximum retention capacity the infiltration had to be maintained until the oil content of the outflow was equal to that of the inflow. Then, the relative permeability for the emulsion was measured. Finally the oil in the sample was washed out and its volume was determined.

Table I of the experimental results shows that the retention capacity for oil due to the Jamin effect in free infiltration of an oil-in-water emulsion is from 2 to 4 times as large as the maximum pendular saturation of 3-6%. Hence, the condition for field infiltration mentioned earlier, viz.

$$RSO_{ret,max} \geq RSO_{pend,max} \quad (13)$$

is fulfilled. But the 10-20% of oil saturation retained due to the Jamin effect during infiltration is reduced to pendular saturation during the drainage which follows the interruption of pumping, i.e. of the surface infiltration. Thus, the zone A and the extension B of surface infiltration must be determined for a given depth in dependence on the pendular saturation and not on the maximum retention capacity due to the Jamin effect.

For sand V the retention capacity was very weak. The oil passed through the sample nearly simultaneously with the water and the emulsion did not change. Practically no oil was retained, i.e. no Jamin effect was observed. Hence it must be inferred that the diameters of the narrow passages of the pore threads of the samples of sand V must have been larger than the diameters of the dispersed oil droplets.

No exact explanation can be given at the moment for the tendency of the maximum retention capacity

Table 1. Maximum oil retention capacity due to the Jamin effect at $\nabla\phi = 1$

Soil	Volumetric content of dispersed oil in infiltrated emulsion:			Max. oil retention capacity in % of the pore volume†			Relative permeability‡			
	0.25%	0.50%	1%	0.25%	0.50%	1%	0.25%	0.50%	1%	
I	50			(7)	(10)	(11)	§	(0.6)	(0.4)	(0.3)
II	42			10	17	21		0.7	0.4	0.3
III	36			13	15	20		0.5	0.3	0.2
IV	37			15	18	19		0.4	0.3	0.2
V	38						¶			

* With residual air before infiltration of emulsion.

† After deduction of the still movable, i.e. unblocked oil.

‡ At the end of the experiment

§ No steady flow was reached in the time allowed.

¶ Practically no retention of dispersed oil.

to increase with increasing content of dispersed oil in the infiltrated emulsion. But its existence is confirmed by the relative permeabilities at the end of the experiments. According to the results of Table 1, the drop of the relative permeability for the wetting fluid as a function of saturation is even steeper after the retention of the non-wetting fluid by the Jamin effect than after a displacement, as shown by Fig. 6.

CONCLUSIONS

The retention capacity for oil during infiltration of an oil-in-water emulsion at gravity flow can be valued as definitely greater than the pendular saturation, i.e. $RSO_{rel,max} > RSO_{pend,max}$. The drop of the relative permeability for the wetting fluid is even steeper after the retention of the non-wetting fluid by the Jamin effect than after a displacement.

Because $RSO_{rel,max} > RSO_{pend,max}$, field infiltration, as shown in Fig. 3, can be considered as one possible method of disposing of oil-in-water emulsions with low oil content such as may occur during the restoration of oil-polluted aquifers. This on the assumption that the Jamin effect is operative and that the microbial degradation is satisfyingly high.

REFERENCES

Bailey N. J. L., Jobson A. M. & Rogers M. A. (1973) Bacterial degradation of crude oil: comparison of field and experimental data. *Chem. Geol.* **11**, 203-221.

- Bringmann G. (1969) Quantitative Befunde an Kohlenwasserstoff-Oxydanten aus Mineralöl-infundierten Bodenproben. *Gesundheits-Ingenieur* **11**, 330-333.
- Bringmann G. (1972) Mikrobiologische Befunde an Sickerwasser- und Bodenproben petrochemisch infundierter Lysimeter. *Gesundheits-Ingenieur* **9**, 271-280.
- Dietz D. N. (1978) Large scale experiments on ground-water pollution by oil spills—interim results. *H₂O* **4**, 77-80.
- Jamin M. J. (1860) Mémoire sur l'équilibre et le mouvement des liquides dans les corps poreux. *C.r. hebd. Acad. séanc. Sci. Paris*.
- Kappeler T. (1976) Ueber den mikrobiellen Abbau der wasserlöslichen Heizöl EL-Fraktion im Grundwasser. *Diss. ETH* 5688.
- Scheidegger A. E. (1960) *The Physics of Flow through Porous Media* p. 313. Univ. of Toronto Press, London.
- Schiegg H. O. (1977) Modellvorstellung und Konzepte zur Abschätzung von Verunreinigungen von Grundwasserträgern durch Erdölderivate. *Wasser, Energie, Luft* **10**, 251-258.
- Schiegg H. O. (1979) Verdrängungs-Simulation dreier, nicht mischbarer Fluide in Poröser Matrix. *VAW-Mitteilung* No. 40.
- Versluys J. (1931) Edge-water Encroachment. *Bull. Am. Ass. Petrol. Geol.* **15**, 189-200.
- Walker J. D. & Colwell R. R. (1974) Microbial petroleum degradation: use of mixed hydrocarbon Substrates. *Appl. Microbiol.* **27**, 6, 1053-1060.
- Wygal R. J. (1963) Construction of models that simulate oil reservoirs. *J. Soc. Petrol. Engng.* Dec. 1963.
- Wykoff R. D. & Botset H. G. (1936) The flow of gas-liquid mixtures through unconsolidated sands. *Physics* **7**, 325-245.
- ZoBell C. E. (1973) Microbiol degradation of oil: present status, Problems and perspectives. *The Microbial Degradation of Oil Pollutants, Workshop Georgia State Univ., Atlanta*, Publ. No. LSU-SG-73-01.

APPENDIX D

EXPERIMENTAL CONTRIBUTION TO THE DYNAMIC CAPILLARY FRINGE

EXPERIMENTAL CONTRIBUTION TO THE DYNAMIC CAPILLARY FRINGE

by H.O. Schiegg
Laboratory of Hydraulics, Hydrology and Glaciology
annexed to the Federal Institute of Technology
Zürich - Switzerland

Synopsis

In solving displacement problems of two non mixing fluids there is a general interest in the functions firstly of the capillary pressure and the saturation, secondly of the saturation distribution, defining the capillary fringe, as well as specially in their dependence on the dynamics of a displacement, supposed that capillarity is considered. The laboratory experiment consisted in displacements of air by water at constant displacement velocities, induced by potential gradients ≤ 1 .

The results of the experiments show for the distribution of the saturation a clear dependence on the displacement dynamics. Yet, in the relation between capillary pressure and saturation no dependence on the displacement dynamics can be observed.

Résumé

Pour résoudre les problèmes de déplacement de deux fluides qui ne se mélangent pas, l'intérêt est porté sur les fonctions, premièrement de la pression capillaire et la saturation, deuxièmement de la distribution de la saturation, définissant la zone capillaire, tout comme particulièrement leur dépendance de la dynamique de déplacement, supposé que la capillarité soit considérée. Les essais de laboratoire ont consisté en déplacements de l'air par l'eau, par des vitesses constantes de déplacement causées par des gradients potentiels ≤ 1 .

Les résultats expérimentels montrent pour la distribution de la saturation une nette dépendance de la dynamique de déplacement. Contrairement, dans la relation entre la pression capillaire et la saturation, il ne peut pas être observé une dépendance de la dynamique de déplacement.

Theory

A table is defined as the locus, where the capillary pressure is zero. An interface separates two non mixing media. A medium can be a solid or a fluid, i.e. a liquid or a gas. The capillary pressure, p_c , is defined by the difference of the pressure in the non wetting fluid, p_{nb} , minus the pressure in the wetting fluid, p_b ,

$$p_c = p_{nb} - p_b \quad (1)$$

The wetting fluid is characterised by a contact angle smaller than $\pi/2$. The contact angle, α , is the angle between the tangent of the interface of the two fluids and the tangent of the interface between the solid and the fluid considered along the intersection line of the interfaces.

A pressure difference over an interface implies, that it must be curved. Therefore a capillary pressure can be defined in terms of the main curvatures, R_1 and R_2 , and the interface tension, δ , by the so-called Laplace equation of the theory of capillarity

$$p_c = \delta \left(\frac{1}{R_1} + \frac{1}{R_2} \right) \quad (2)$$

This equation represents the force equilibrium due to interface tension and capillary pressure. It stands for a differential equation, because R_1 and R_2 are dependent on the first and second order derivation of the interface function.

Under the assumption, that the interface is spherical and the curvature radius equal R_0 , we have $R_1 = R_2 = R_0$. A limited, spherical interface is a calotte, what is called spherical meniscus, in the following simply meniscus. Such a meniscus implies a limitation by a solid, of which the interfaces must be rotationally symmetric. The intersection line of the three interfaces - the interface between the two fluids and the two interfaces between the solid and each one of the two fluids - is a circle with radius R . In practice R is the effective radius of a capillare or a pore respectively. The curvature radius R_0 can be formulated in function of the capillare or pore radius and the contact angle as

$$R_0 = R / \cos \alpha \quad (3)$$

With this equation and $R_1 = R_2 = R_0$ Eq.(2) can be written for a spherical meniscus as

$$\{\text{spherical meniscus}\} \quad p_c = \delta \cdot \cos \alpha \cdot \frac{2}{R} \quad (4)$$

p_c has the dimension of a pressure.

The capillary pressure head, h_c , with the dimension of a length, is obtained by dividing the capillary pressure by $(\rho_b - \rho_{nb}) \cdot g$:

$$h_c = \frac{p_c}{(\rho_b - \rho_{nb}) \cdot g} \quad (5)$$

Both, the idea of the fictitious interface tension and the concept of a contact angle assume the change of a molecular view to a microscopic view. They can be explained by superpositions of the force fields of the molecules near the interface. The tendency of curving of an interface, i.e. of the development of a capillary pressure, which is based on interface tension and wettability, is called capillarity. Due to capillarity the wetting fluid is encroaching upon the region of the non wetting fluid on the other side of the table.

The distance of a meniscus from the table is called capillary rise head, a_c . The position of a meniscus is defined by the place, where the difference of the pressure in the non wetting fluid minus the pressure in the wetting fluid is equal to the capillary pressure, computed by Eq.(4). In static situations capillary rise head and capillary pressure head are equal.

In general flow problems through a porous medium can not be treated by using the Navier-Stokes equation at a microscopic view. Practically they are solvable only with the equation of Darcy, based on a macroscopic view.

Macroscopic view is tantamount to assuming a continuum. The transfer to a continuum is achieved by smearing out discontinuities, which are realizable only at a microscopic view.

In a porous medium an interface consists of the effective menisci and their connections. The effective menisci are the menisci with the greatest normal distance from the table, but still in contact with the table over the wetting fluid. The more various the pore sizes are, the more differentiated are capillary pressure head and capillary rise head of the effective menisci, the less monotonous is the topography of the interface at microscopic view.

The concept of the saturation assumes a continuum. It expresses that part of the pore volume, which is occupied by the considered fluid. The saturation results from a macroscopic view of the microscopic replenishment of the pore volume, which is given by position and form of the menisci within the single pores.

By plotting the relationship between the saturation of the wetting fluid and the distance of the place of its occurrence from the table, which equals the capillary rise head at macroscopic view, the capillary rise head curve is obtained, $a_c(S_b) \equiv ACSB$. The less monotonous the topography of an interface in a porous medium at microscopic view is, the more gradual is the capillary rise head curve. Representing instead of the capillary rise head the corresponding capillary pressure head in function of the saturation of the wetting fluid yields the capillary pressure head curve, $h_c(S_b) \equiv HCSB$. For static cases the ACSB and HCSB coincide, because then $a_c = h_c$.

Displacement signifies a moving interface. The displacement of a non wetting fluid by a wetting fluid is called imbibition.

Drainage means the displacement of a wetting fluid by a non wetting one. A displacement is induced by a potential gradient normal to the table. For a displacement the static pressure field in each of both fluids is changed by the pressure loss due to the interior friction. The smaller the permeability and the greater the viscosity and the velocity are, the bigger is the pressure loss.

The more the viscosities of the two non mixing fluids differ, the more different is the change of the two pressure fields due to interior friction, the nearer at the table is the locus, where the pressure difference is equal to a certain capillary pressure, and hence the smaller is the capillary rise head, and the lower is the capillary rise head curve. These considerations are valid for imbibition as well as for drainage. Yet, they assume that the wetting fluid is the more viscous one and that the afore mentioned capillary pressure with increasing displacement velocity does not increase more than the difference of the pressure fields of the two fluids.

For the discussion of a possible dependence of the capillary pressure on the displacement dynamics it ought to be remembered, that the capillary pressure is defined by the interface tension, γ , the contact angle, \mathcal{L} , and the capillary or pore radius, R , see Eq.(4). The interface tension can be assumed as independent on the displacement dynamics. Assuming a circular cylindrical capillare the radius R is constant and hence independent on the displacement dynamics. With regard to a possible dependance of the contact angle on the displacement dynamics it could be expected, that \mathcal{L} is for imbibition at most larger, for drainage -supposed \mathcal{L} is not equal zero as for total wettability- at most smaller than its static value. But equally possible is independence of \mathcal{L} on the displacement dynamics, at least for such relatively small displacement velocities as they are implied by Darcy's law.

In a pore space, which is composed of single pores and their connections, the pore radius along a way of a moving meniscus varies heavily, what causes a corresponding large variation of the capillary pressure. This explains the jumpwise motion of the single menisci from one effective position to the next one, a phenomenon easly realizable by eye in an experiment. For imbibition the effective positions are defined by the places of the largest pore diameters, but slightly shifted towards the table. For drainage the effective positions are given by the sites of the smallest pore diameters, but slightly shifted away from the table. The difference in capillary pressure, which is induced by the difference of the radii between the largest and the smallest passages in a pore space, causes the hysteresis of capillarity.

The variation of the pore radius along the way of a moving meniscus as well as the resulting jumpwise motion of the

menisci at microscopic view have no influence on the description of a displacement at macroscopic view, which is necessary for the applicability of Darcy's law. The explanation is firstly, that the variations of the time functions of the individual capillary pressures at microscopic view are not realizable by macroscopic measurements of the capillary pressure and secondly, that the medium fluctuation of the capillary rise head - which is equal to the distance between two effective positions and hence in the order of a medium pore diameter - is negligibly small compared with the capillary rise head. Thus an interface, which follows the table at microscopic view jumpwisely, can at macroscopic view be regarded as moving synchronically with the table. This is the picture of a displacement in a pore space with constant radius R . Due to these considerations the parameters of the interface tension, σ , and of the radius, R , in Eq(4) can at macroscopic view be assumed as independent on the displacement dynamics. Hence, a dependence of the capillary pressure head curve on the displacement dynamics implies dependence of the contact angle on the displacement dynamics.

The experiment should prove qualitatively the postulated dependence of the capillary rise head curve on the displacement dynamics and should referring to this give quantitative informations. Furthermore it should be shown by the experiment, how far the capillary pressure head curve and thus also the contact angle are depending on the displacement dynamics.

Because the viscosity of a gas is lower than that of a fluid by at least one order of magnitude, the expected dependence of the capillary rise head curve on the displacement dynamics must be particularly pronounced for a liquid gas displacement. As density and viscosity of a gas are very small - compared with density and viscosity of a liquid - for a gas static pressure change and pressure loss due to interior friction can be neglected in comparison to the corresponding pressure changes in the liquid. Therefore the pressure in the gas can be assumed to be practically constant for the static as well as for the dynamic situation. When the gas is atmospheric air its constant pressure is normally taken equal to zero. With $p_{nb} \approx 0$ the measured suction in the liquid corresponds in piezometric form and with a negativ sign according to Eq.(1) to the capillary pressure head, h_c , see Eq.(5).

Experiment

The experiment consisted in steady uniform displacements of air by water. Thereby the capillary pressure head and the saturation of the wetting water were measured. The pressure measurement was achieved by a pressure probe and a pressure transducer. The measurement of the saturation was based on the ab-

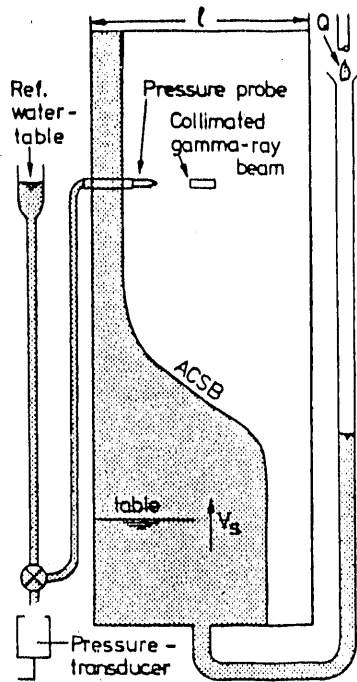


Fig.1 Experiment

sorption of a collimated gamma ray beam, Cs-137. The measurements of pressure and saturation were achieved continuously and simultaneously, as well as at the same place within the porous matrix. Porous matrix, pressure probe and gamma ray beam were constant in place. The horizontal water table moved upwards with a constant speed, whereby uniform imbibition was induced. The porous matrix was homogeneous and isotropic. It consisted of non consolidated, fine quartz sand. The uniform corn had a medium diameter of 0,3 mm. The porosity was 0,43. The hydraulic permeability was $2 \cdot 10^{-2}$ cm/sec.

The various, constant displacement hence table velocities, v_s , resulted from the various constant infiltration rates:

$$v_s = \frac{q}{n \cdot \Delta S} = \frac{Q}{l^2 \cdot n \cdot \Delta S} \quad (6)$$

q [cm/sec] is the specific discharge defined by the quotient of infiltration rate, Q [cm³/sec], and the cross section, l^2 [cm²]. n is the porosity and ΔS is the largest available part of the pore volume for funicular, i.e. non residual water. ΔS is defined by $[1 - (RSW + RSL)]$, wherein RSW and RSL mean the residual saturation of water and air. With the knowledge of v_s and because the table passes the measuring level at that moment, at which the measured pressure in the water is equal to the reference pressure, see Fig. 1, every momentary table position can be determined.

Knowing the time-dependent position of the table as well as the saturation of water in function of time the capillary rise head curve, ACSB, can be drawn. With the measurements of pressure and saturation in function of time the capillary pressure head curve, HCSB, is determined. The ACSB and HCSB for the various displacement velocities can be seen in Fig. 2.

For the generalisation of the displacement dynamics referable to the porous matrix the ACSB and HCSB are not shown in a parameter representation of the displacement or table velocity respectively, but of the potential gradient, $\nabla \phi^o$, in the water behind the backside of the front, i.e. for saturated flow. The potential gradient in the water in piezometric form, $\nabla \phi^o$, results from the law of Darcy as

$$\nabla \phi^o = \frac{q}{k} \quad (7)$$

k [cm/sec] is the hydraulic permeability for saturated flow.

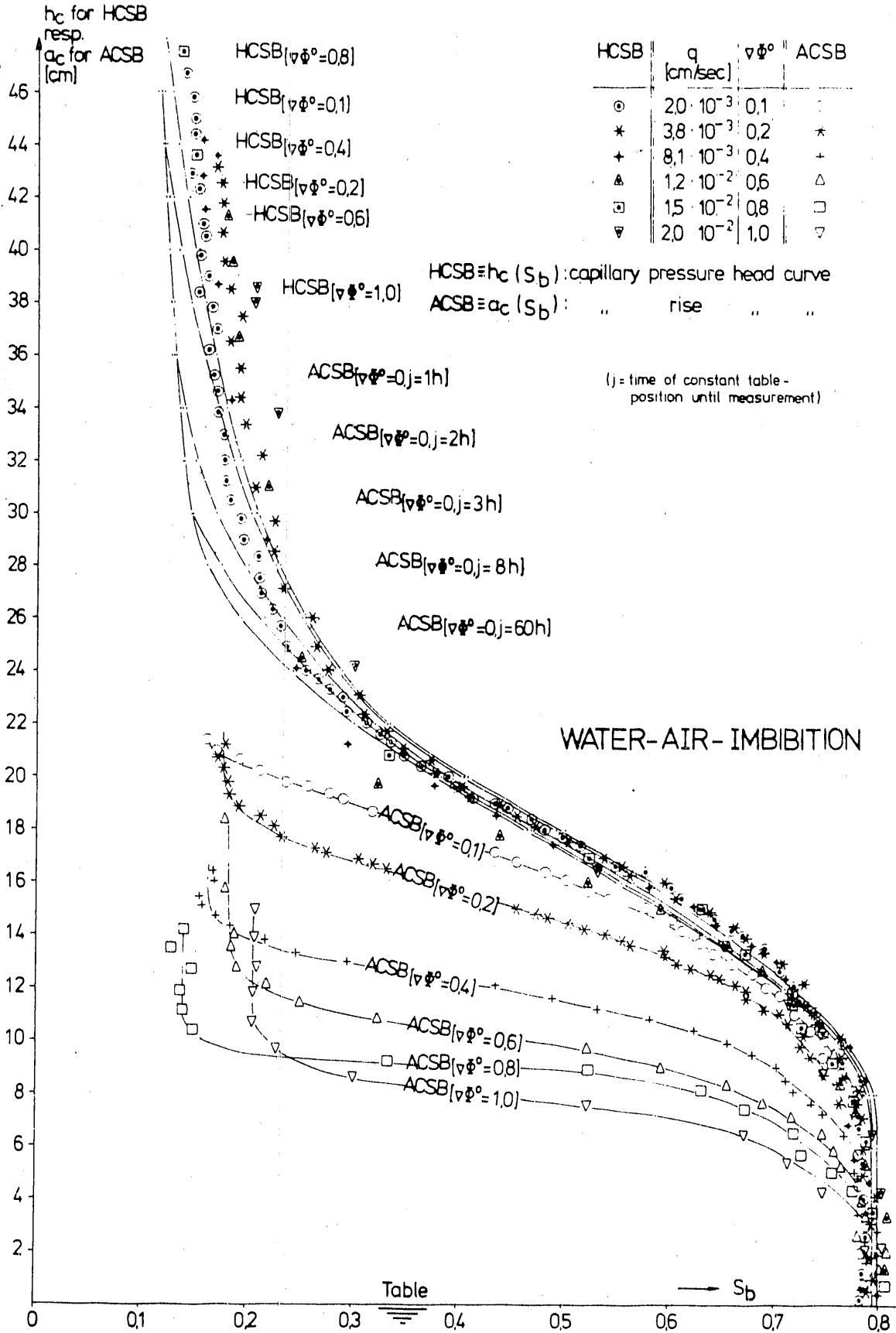


Fig.2 Results

C-9

Conclusions

Considering the experimental facts the following conclusions are valid for water air imbibition at gradients ≤ 1 . But a more general validity of the statements is probable.

The greater the potential gradient is, the flatter and lower is the capillary rise head curve, ACSB. At gradient 1 a reduction of the capillary rise head of more than half of its static value can be seen, and furthermore that the capillary rise head curve is flattened to a near parallel to the table.

The capillary pressure head curve, HCSB, is practically independent on the dynamics of a displacement and hence constant.

These experimental experiences lead to the following cognitions:

- Independence of the capillary pressure head curve on the displacement dynamics implies that the pressure condition along a moving boundary - which is assumed to be known for an arithmetic treatment of a displacement problem - is equal to the boundary condition for the static situation.
- The flatter the capillary rise head curve is, the better a displacement can be simulated by a piston like displacement.
- Simple infiltrations can be described analytically. To that it is necessary to suppose a piston like displacement and a constant medium capillary pressure head, which is usually determined by the static capillary pressure head curve. The near coincidence of the results of analytical simulations with the measurements from experiments, see Schiegg (1975), shows, that these assumptions represent the reality astonishingly well. The explanation for this statement is given by the both preceding cognitions.
- As mentioned, the constance of the capillary pressure head curve implies, that the contact angle is independent on the displacement dynamics.

Schiegg, H.O.; Liquid air displacements in a homogeneous, isotropic, unlimited, porous media; XVIth IAHR Congress, Sao Paulo, Vol. 3; 1975

APPENDIX E

LIQUID-AIR-DISPLACEMENTS IN A HOMOGENEOUS, ISOTROPIC,
UNLIMITED, POROUS MEDIA

INTERNATIONAL ASSOCIATION FOR HYDRAULIC
RESEARCH

LIQUID-AIR-DISPLACEMENTS IN A HOMOGENEOUS,
ISOTROPIC, UNLIMITED, POROUS MEDIA.

by H.O. Schiegg
Laboratory of Hydraulics, Hydrology and Glaciology
annexed to the Federal Institute of Technology
Zürich - Switzerland

Synopsis

It will be shown, that for the simulation of the transient front position of a liquid-air-displacement in a homogeneous, isotropic, unlimited, porous media in the field of gravity under consideration of capillarity and provided, that the liquid pressure at the source stays constant,

- in case of a plane-source, for the vertical, one-dimensional displacement, instead of the analytical solution, $T = \xi' - G(\xi'+1)$, just as well the function $T = \xi' - \alpha \eta \xi'$ can be taken,
- in case of a point-source, due to the experimentally proved, simultaneous constance of the infiltration rate, the displacement can be described by the known solution for one-fluid-flow, caused by a point-source in a parallel stream,
- and thus independent of the source geometry the advance of the front along the vertical can be described by the function $T = \xi' - \alpha \eta \xi'$.

Résumé

Il va être montré que pour la simulation de la position instationnaire d'un déplacement d'air par un liquide, dans un milieu poreux, homogène, isotropique et illimité, dans le champ de gravitation, sous considération de la capillarité et sous condition que la pression du liquide reste constante à la source,

- en cas d'une source en plan, pour un déplacement vertical, la fonction $T = \xi' - \alpha \eta \xi'$, peut tout aussi bien être admise à la place de la solution analytique, $T = \xi' - G(\xi'+1)$.
- en cas de source en un point, en raison de la constance simultanée du taux d'infiltration prouvée par expérience, le déplacement peut être décrit à l'aide de la solution connue pour l'écoulement à phase unique, causé par une infiltration d'une source en un point dans un écoulement parallèle,
- ainsi indépendamment de la géométrie de la source, l'avancement du front le long de la verticale peut être décrit par la fonction $T = \xi' - \alpha \eta \xi'$.

INTRODUCTION

In connection with the necessary precautions for prophylaxis and restoration of an aquifer pollution by environphobic liquids there is a great interest in the first period of an infiltration before the front reaches the depth, where the horizontal migration gets dominant. Referable to this first period, the main interest consists in the time dependent position of the front in the vertical direction below the source; furthermore wanted is sometimes the maximum horizontal extension for this period of mainly vertical migration.

THEORY

For a displacement of two nonmixing fluids an analytical solution is generally not possible; one of the reasons is the nonlinearity -caused by the dependence of the relative permeability, k_r , of the saturation, S , and thus finally of the potential, ϕ , - of the known, a displacement describing differential-equation-type, which in assumption, that the density, ρ , the viscosity, μ , the permeability, K , and the porosity, n , are constant, can be written as : $n \cdot \partial S / \partial t = K / \mu \cdot \sigma \cdot (k_r \cdot \rho \cdot g)$. For pistonlike displacement the relative permeability gets a constant and can thus be put before the nabla-operator, whereby the differential-equation gets linear; nevertheless displacements -excepted linear, cylindrical- or sphericsymmetrical spreadings- are not analytically solvable, because mostly just the time dependent position of the front, which is likewise a boundary, is searched, and therefore the place of the boundary condition along the front is transient and unknown, whereby the boundary condition is dependent of the searched potentials and thus becomes nonlinear. Accordingly solving a displacement problem requires a numerical treatment, generally a computer.

CONCEPTION FOR AN APPROXIMATE SOLUTION

For the organisation of the crew and the necessary equipment with the aim to minimise and restaure the infiltration and spreading out of an environphobe liquid, there is less interest in accuracy, than in a simple method to determine the time function of the front position, whenever possible at the place of the accident, and before the front has reached the ground water level. Approximated, but closed solutions for liquid-air-displacements in a porous media are from equal interest for soil-physicists, hydrologists, glaciologists etc..

For the one-fluid-flow caused by a plane-, line, or point-source in a parallel flow the time function of the front position along the axis of symmetry can be found by analytical integration. This fact in mind it is comprehensible to ask, as far these solutions could be taken to simulate the corresponding displacements, that means, how far and by which influences a displacement differs from a one-fluid-flow, even if such a comparison by no means results of analytical considerations, although it might be physically evident. These for a displacement specific influences are caused by the density- and viscosity-differences, as well as by capillarity.

Preliminary the influence of gravity shall be neglected, thus the influence of density difference is eliminated as well. For the case of additional negligence of the capillarity influence Miskat (1934) has given analytical solutions for the one- two- and three-dimensional, that means for the linear, cylindrical and spherical displacement with the quotient of the viscosities as a parameter. The graphic representations of his results show, that for a liquid-air-displacement in case of a line- or a point-source the influence of the viscosity-difference is practically negligible, because the curve for the one-fluid-flow, speci-

fied by the parameter l , and the displacement curve with the parameter equal to the quotient of the viscosities of the liquid and the air are very near to each other, whereupon for a line- and a point-source results a dominating influence of geometry. — For the one-dimensional displacement the influence of viscosity-difference can not be neglected, what can be seen by the fact, that at the beginning of a one-dimensional infiltration the pressure in the source and the infiltration rate not both can be simultaneously constant, as shown by many experiments of infiltration theory.

Consideration of capillarity means having regard to the generally gradual transition of saturation between two nonmixing fluids in a porous media, whereby the wetting fluid stands under the saturation dependent capillary pressure. Corresponding to the suction the front might be accelerated, on the other hand the gradual transition of saturation might lead to a reduced permeability, thus to a retardation. Experiments show, that not taking into consideration this gradual transition of saturation, -equivalent to the assumption of pistonlike displacement, as well as to the average consideration of the influence of the capillarity, involving the negligence of the resulting retardation influence, - is not at all an unrealistic supposition. Consideration of capillarity, specially of the suction at the front is physically and mathematically equivalent to the addition of the corresponding, positive, averaged capillary pressure to the liquid pressure in the source. In default of a dynamic capillary pressure curve generally this averaged capillary pressure will be taken corresponding to the static capillary pressure curve.

The hypothesis, that the consideration of the until now neglected influence of the gravitation, the density difference respectively, can be done by superposing a vertical parallel flow caused by gravity only -thus called gravitation flow, which is characterized by a potential gradient l - might seem to be rather arbitrary; a reason for doing so might be the consideration, that it should not be important for the spreading fluid, by which fluid it is surrounded, as long as the pressure distribution is the same, and that for the flow with a potential gradient l the pressure must be constant anywhere, as it is practically in the displaced air.

In assumption of the possibility of considering the differences between a liquid-air-displacement and an analogous one-fluid-flow, which are density- and viscosity-differences, as well as capillarity, in the described manner the relationships for a line- or a point-source-displacement in a homogeneous, isotopic, unlimited, porous media can be represented by the known functions of the corresponding one-fluid-flow, provided the pressure in the source is increased by the averaged capillary pressure. The experimental prove for the negligence of the influence of the viscosity difference, for the proposed simulation respectively, would be given by the fact, that the infiltration rate and the liquid pressure in the source are simultaneously constant. — Because of its geometrical simplicity the one-dimensional-flow of a plane-source in the field of gravity a displacement can be solved analytically, even if the viscosity difference can not be neglected; consideration of capillarity influence can as well be done by addition of the averaged capillary pressure. How realistic these assumptions are, must be shown by experiments.

EXPERIMENTS

In the following comparison of the experimental data of one-dimensional, as well as three-dimensional displacements with the solutions for the analogous one-fluid-flow " $g.O.F.[t-i]$ " means "geometrical place (Ort) of elementary fluid volumes, which have simultaneously left the source at the time i "; $g.O.F.[0]$ is identical

tical with the front; $g.O.F.[\infty]$ describes a g.O.F. within the final extension of the practical steady state of a displacement long time afterwards of its beginning, which for all parameters are practically constant; $g.O.F.[E]$ means a g.O.F. for any time i of the steady one-fluid-flow. -- The important parameters for the several experiments are given in the annexed table.

Plane-source; one-dimensional, vertical displacements in the gravity field.

The curves 2, 3 and 4 in Fig. 1 result of experiments in three-dimensional models; curve 5 shows the data from a tube experiment; the curves 6 and 7 represent the classical results of Bodman and Colman (1943).

A displacement implies a potential gradient, which is a function of gravitation, capillarity, as well as pressure. The time dependent position of the front of a one-dimensional, vertical displacement by gravity flow must be described by the linear function 1 with an inclination of \sqrt{t} , which is equally valid for any steady, one-dimensional one-fluid-flow. The curve 5 shows the front position in function of time received from a displacement experiment, which for solely the influence of gravity and of the over pressure in the source -equal to the pressure difference of the liquid at the point of the source with an without the source influence, briefly called as pressure in the source or source pressure- were important, what means, that the capillarity influence is negligible, the averaged capillarity potential, $\bar{\psi}$, is relatively small compared with the source pressure, $p_s/\rho g$ respectively. The curves 2, 3 and 4 resulted from experiments, which for the source pressure was taken to zero, and the displacements were caused only by gravity and capillarity. Curves 3 and 4 represent the transient position of the front, equivalent to the $g.O.F.[0]$; curve 4 for a front, which enters into a dry porous media, curve 3 for a front, which meets an already existent residual saturation of the liquid. Curve 2 shows the transient position of the $g.O.F.[one\ hour]$. Displacements influenced by gravity, as well as by capillarity and source pressure have not been carried out.

The usual, analytical solution for a one-dimensional, vertical liquid-air-displacement in the gravity field is given by function 8, $T = \xi' - G(\xi'+1)$, where- at T means the dimensionless time, ξ' the dimensionless distance of the front vertical downwards referred to the source. In consideration, that the front speed converges against the steady front speed for gravity flow and that the analytical solution for the transient front position along the symmetry axis in case of a point source is given by function 9, $T = \xi' - \operatorname{arctg} \xi'$, it might be asked, whether the asymptotic function 9 might not better describe the converging, one-dimensional, vertical liquid-air-displacement, than function 8 without an asymptote; an idea, which seems to be confirmed by the experiments. -- Curve 5 coincides practically with function 8 at the beginning of the displacement, but for a much bigger part it is vastly identical with function 9. The curves 3 and 4 are flatter than curve 5, which for a reason might be the fact, that until the capillary fringe has been completely build up, until the front has reached a distance two to three times the averaged capillary pressure height respectively, the averaged consideration of capillarity influence can not be correct, although the dynamic capillary pressure curves will be lower than the static one. The position of curve 2 is comprehensible, because a $g.O.F.[i]$ with increasing index i converges against curve 1.

Summarizing can be postulated, that function 9, $T = \xi' - \operatorname{arctg} \xi'$, represents rather well the time dependent front position of a one-dimensional, vertical liquid-air-displacement in the gravity field, except at the beginning, which for the differences between the more correct function 8 and function 9 are relatively small, and that a predicted, transient front position according to function 9 would be on the sure side in connection with the infiltration of an environphobe liquid.

Point-source; three dimensional displacement in the gravity field.

Sketch 2 for one-fluid-flow in Fig.2 shows rather good accordance of the experimental points, *, with the theoretical ones, o, given by the analytical solution, quite well fitting in of the experimental front lines, —, between those got by numerical integration, ****, respectively. The rather good fitting in of experimental data of a liquid-air-displacement in the gravity field between the results for one-fluid-flow, as well as the fact, that the source pressure and the infiltration rate during the whole experiment stood constant, shows, that the proposed simulation of a liquid-air-displacement, caused by a point source infiltration, as well as the involved assumptions seem to be reasonable. Poorest accordance between one-fluid-flow displacement exists at the stagnation point; this is comprehensible by the fact, that the pressure in the stagnation point for one-fluid-flow exceeds the pressure at this same place in case there is no source; but for a displacement the pressure in the stagnation point, that means at the highest point of the front, must be, as anywhere else along the front, equal to the pressure at this place without the source; therefore the distance between stagnation point and source, choosen equal to unity for one-fluid-flow, for a displacement must be greater than 1. Generally more important than the distance between source and stagnation point is the maximal horizontal spreading of the liquid; because there is a convergence to gravity flow in any case the maximum horizontal extension must be equal for one-fluid-flow, as well as for a displacement, a fact, which easily can be proved by consideration of the mass balance.

By comparing sketch 2 and 4 results, that the time dependent positions of a g.O.F. [∞] coincides with those of a g.O.F. [E]. Provided the already in the porous media existing liquid saturation, which the front meets, is less than the maximum residual saturation, of the liquid, ΔS will be larger, that means the front advances slower, than any g.O.F. with $i > 0$, because parts of the liquid coming out of the front first will fill up residual saturation; an effect, which can be seen by comparing sketch 3 with the other ones.

CONCLUSION

Considering that,

- for a one-fluid-flow by a point-source in a parallel flow the analytical solution for the time dependent position of a g.O.F. [E] along the symmetry axis is given by function 9, $T = \xi' - \alpha c / g \xi'$, and the transient front position in case of a point-source-liquid-air-displacement in the gravity field can be simulated by it, as well as
- the function 9, due to the summarizing remarks to the results for the one-dimensional displacements, also represents the time dependent front position in case of a plane source in the gravity field, and
- a line source represents geometrically an intermediate form between a plane- and a point-source,

the transient front position along the vertical can be described for any liquid-air-displacement in the gravity field, independent of the source geometry by function 9, $T = \xi' - \alpha c / g \xi'$.

REFERENCES

Muskat, M.; Two Fluid Systems in Porous Media. The Encroachment of Water into an Oil Sand; Physics, 5, 250 - 264; Sept. 1934.

Bodman, G.B. and E.A. Colman; Moisture and energy conditions during downward entry of water into soils; Soil Sci. Soc. Amer. Proc. 8, 116 - 122; 1943.

FIGURES AND TABLES

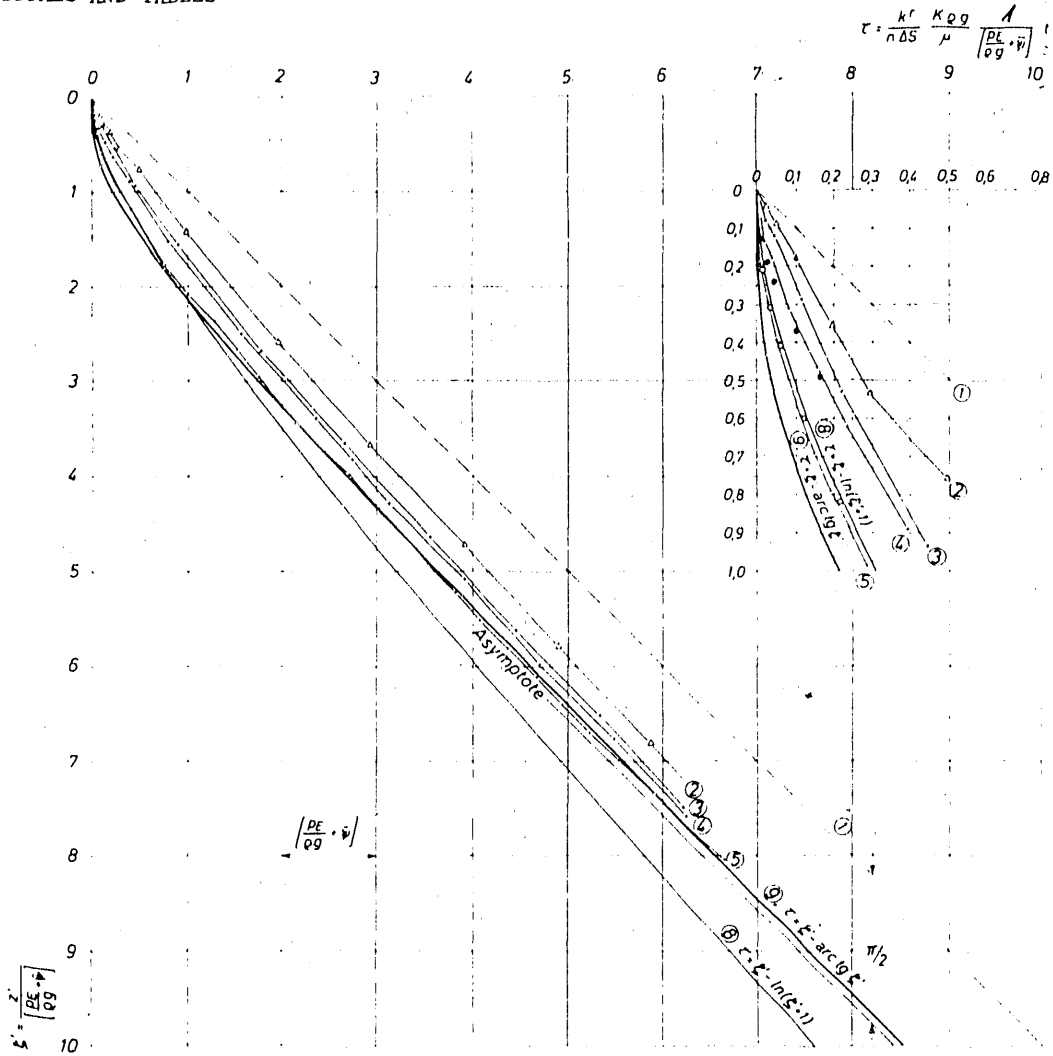


Fig.1 Plain-source; one-dimensional, vertical displacements in the gravity field.

	1	---	g.O.F. [E]; g.O.F. [0; $\nabla \phi = 1$] \equiv Front [Gr-fl.]; g.O.F. [∞]
threedim. models	2	- Δ -	g.O.F. [1 hour]
	3	-x-	Front \equiv g.O.F. [0; 0 cm \sim p _E / g.g « $\bar{\psi} \sim 33$ cm; SFO = RSF]
	4	-+-	" \equiv " [0; 0 " \sim " « $\bar{\psi} \sim 33$ "; " = 0]
Tube exp.	5	-o-	" \equiv " [0; 100 " = " » $\bar{\psi} \sim 1,5$ "; " = 0]
Bodman and Colman, 1943	6	••	" \equiv " [0; 0 " \sim " « $\bar{\psi} \sim 50$ "; " = 0]
	7	o o	" \equiv " [0; 0 " \sim " « $\bar{\psi} \sim 80$ "; " = 0]
analytical solutions	8	—	
	9	—	

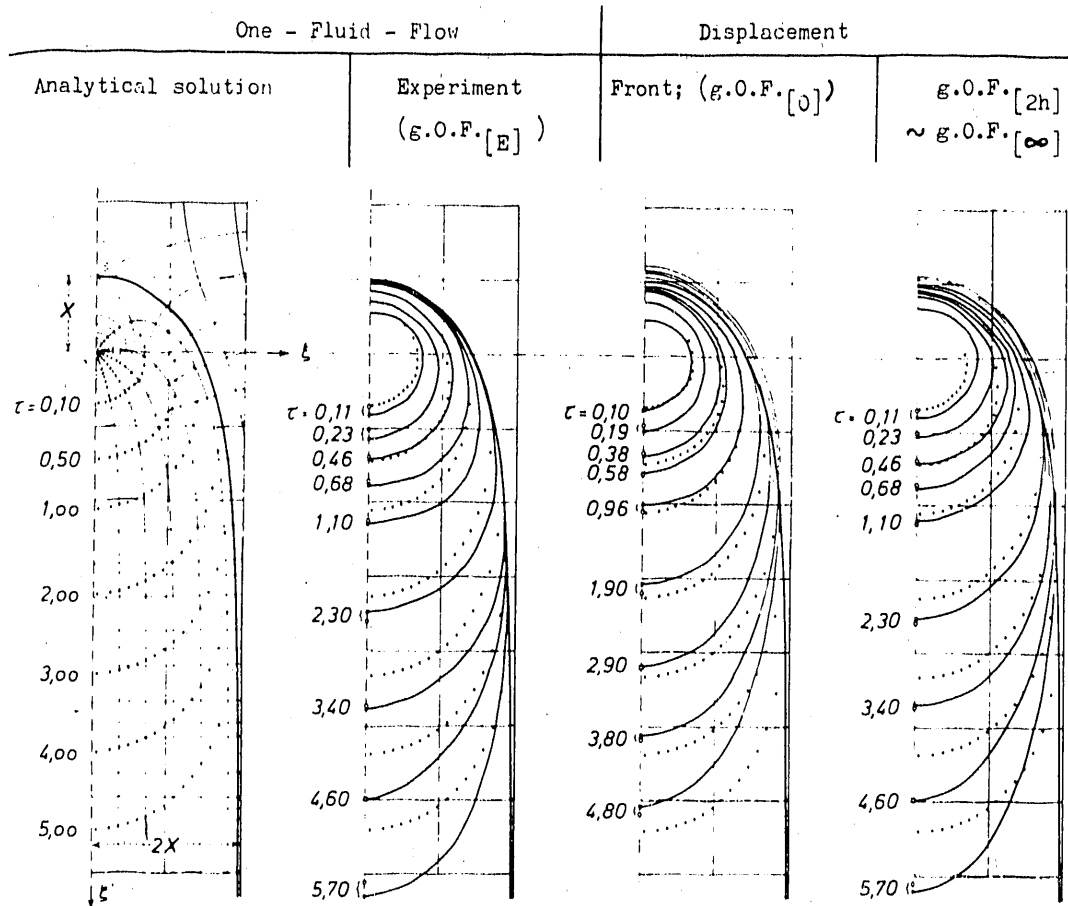


Fig. 2 Point source, three dimensional displacement in the gravity field.

$$\tau = \frac{k^r}{n \cdot \Delta S} \cdot \frac{K \cdot \varphi \cdot g}{\mu} \cdot \frac{1}{X} \cdot t \quad \text{O; o o o Theory} \quad \text{x; — Experiment}$$

$$\xi = \frac{x}{X}; \quad \xi' = \frac{z'}{X}; \quad X = \sqrt{\frac{Q \cdot \mu}{4\pi \cdot K \cdot \varphi \cdot g}} = \sqrt{\frac{r_E}{\varphi \cdot g} \cdot (P_E + P_{\bar{c}})}$$

(r_E = source radius)

Dimensionality	One - dimensional						Three-dimensional	
	Kind of sand	Quarzsand			Yolo loam			Quarzsand
		QI	QII	QIII	sandy	silt		
Number and signature of curve	1 ---	2 -Δ-	3 -X-	4 -+-	5 -o-	6 ●●	7 O O	Quarzsand QIII
Porosity, n,		←-0,62-→			0,32	0,415	0,42	0,465
Permeability, $k^k [1-RSL] \cdot \frac{K}{\mu} \cdot e.g., [cm/s]$		←-9,7 \cdot 10^{-3}-→			7,6 \cdot 10^{-3}	4 \cdot 10^{-7} \cdot g	7 \cdot 10^{-8} \cdot g	9,8 \cdot 10^{-3}
Averaged capillary potential, $\bar{\psi}, [cm]$	0	32	35	32	1,5	50	80	1,5
Residual saturation of liquid, RSF		←-0,25-→			0,05	0,29	0,18	0,15
Residual saturation of air, RS_A^l			0,15	0	0	0,03	0,04	0,05
Liquid saturation met by front, SFO		←-0-→			100			0
Pressure height in the source, $\frac{PE}{e.g.}, [cm]$	E 10,00	1h			-0			0
Time index of R.O.F. $[i]$, i,		←-0,60-→			0,95	0,68	0,78	0,80
AS								0,95
								E 0 2h-∞

TRANSLATION OF CAPTIONS IN SATURATION DIAGRAMS AND POTENTIAL
TIMELINE OF EXPERIMENTS 1-8, CHAPTER 9.0

The legend for the potential histograms and the saturation diagrams are provided in Section 9.4 of the report. The timeline on the left is for the profile underneath the oil application site, and the timeline on the right is for the profile 59 cm to the right of the oil application site. A translation is provided only as new terms are encountered in the timelines of Experiments 1-8.

EXPERIMENT 1

Vor Oeileingabe - Before oil application
Zeit - Time
Oeileingabe - Oil application
Rückseite - Back side

EXPERIMENT 2

EXPERIMENT 3

Wsp. Neigung 4 1/2% - Water table established with 4-1/2% slope

EXPERIMENT 4

EXPERIMENT 6

unregelmässig - Irregular

Absenkung des W-L-Sp im Eing.-Querschnitt um 1 1/2 cm infolge Neigung auf 1 1/2% (Δ W-Sp: links= 0 cm, rechts= -4 cm) - Water table lowered about 1-1/2 cm in the area of the right-hand measurement profile and a 1-1/2% slope established (Δ water table on the left side = 0 cm; on the right = -4 cm)

geneigter Wasserspiegel um 10 cm gehoben - Inclined water table raised about 10 cm

nach 20 Tagen Wasser-Luft-Spiegel horizontiert auf 13 cm unter Ausgangs-Wasser-Luft-Spiegel - After 20 days, water table made horizontal and lowered 13 cm below the original water table

horiz. Wasser-Luft-Spiegel auf 39 cm über Ausgangs-Wasser-Luft-Spiegel angehoben - Horizontal water table raised 39 cm above original water table.

TRANSLATION OF CAPTIONS IN SATURATION AND POTENTIAL TIMELINE OF
EXPERIMENTS 1-8, CHAPTER 9.0 (continued)

horiz. Wasser-Luft-Spiegel um 39 cm d.h. auf Höhe des Ausgang-Wasser-Luft-Spiegels abgesenkt - Horizontal water table at 39 cm lowered to the elevation of the original water table

EXPERIMENT 8

Beginn 1.0elingabe - Begin first oil application

Wasserspiegel um 12 cm abgesenkt - Water table lowered 12 cm

Wasserspiegel um 38 cm heraufgesetzt - Water table raised 38 cm

Neigung des W'Sp. auf 4.5% - Water table slope = 4.5%

Absenken des geneigten W'Sp um 38 cm - Inclined water table lowered 38 cm

Horizontierung des W'Sp. auf Basis - Water table made horizontal at datum

W'Sp. unterhalb Rinne abgesenkt, dann 30' beregnet - Water table lowered below flume, then 30-min sprinkling of water

nach Absenkung - After lowering

nach Beregnungsbeginn - After start of water sprinkling

anschliessend 11 Tage Drainage - After 11 days of drainage

Beregnung während 9h, Absaugen während 9 1/2h - Sprinkling of water during 9 h, equilibration during 9-1/2 h

ganze Rinne mit Vakuumpumpe drainiert (wegen Endeffekt) - Entire flume drained by using a vacuum pump (because of end effect)

Modell von unten langsam mit Wasser gefüllt - Flume was slowly filled with water

Modell drainiert, W'Sp. horizontal auf 12 cm (=Ausg. W'Sp.) - Flume drained, horizontal water table established at 12 cm (= original water table elevation)

Wassersp. auf 4 1/2% geneigt. Drehpunkt in Eingabevertikalen - Water table inclined 4-1/2%. Center of rotation at vertical application site

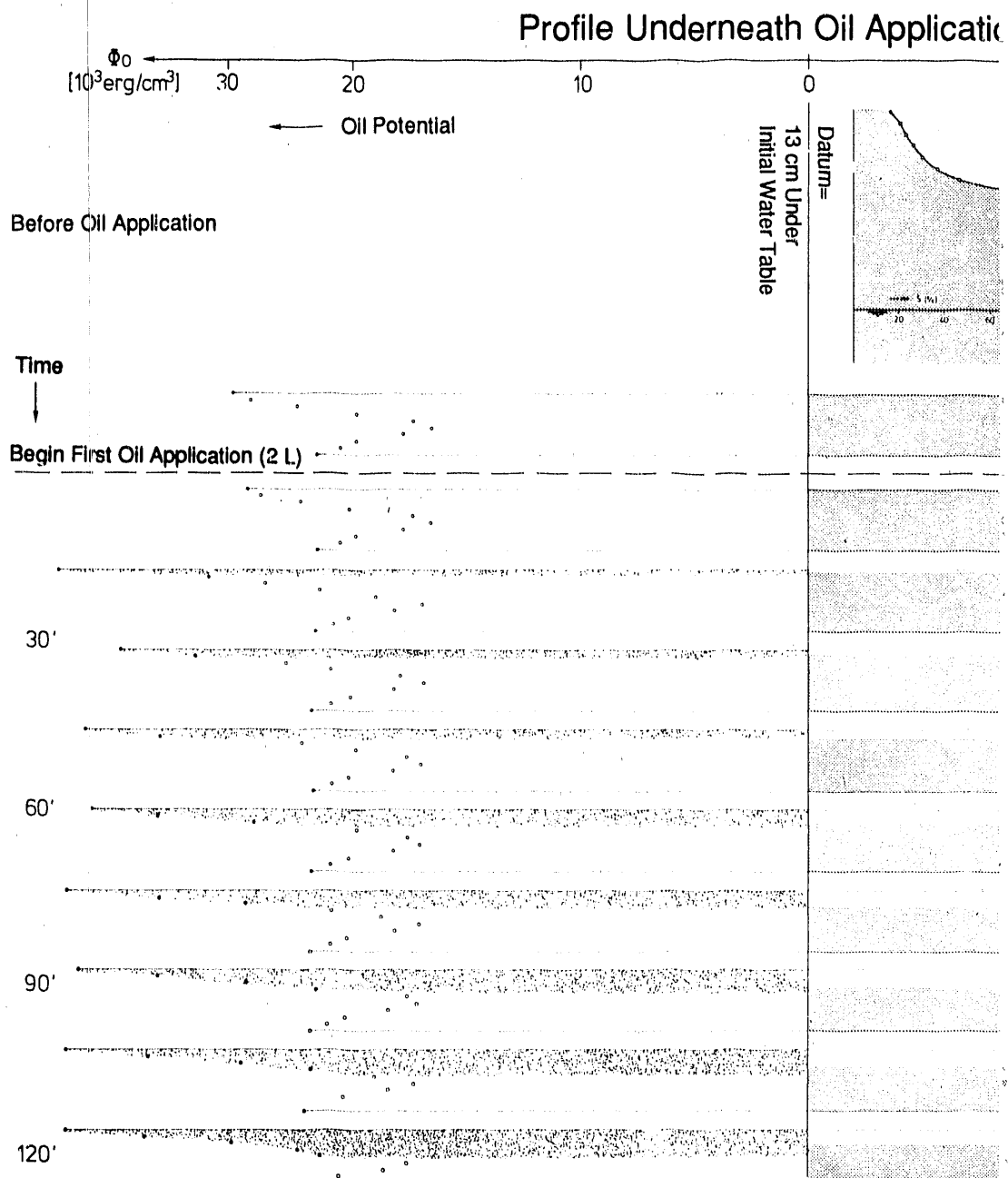
Mit Vakuumpumpe drainiert, dann IM (links 50 cm, rechts 0 cm über Basis) - Drained by using vacuum pump, then imbibed (left = 50 cm, right = 0 cm above datum)

TRANSLATION OF CAPTIONS IN SATURATION AND POTENTIAL TIMELINE OF
EXPERIMENTS 1-8, CHAPTER 9.0 (continued)

Mit Vakuumpumpe drainiert, Modell langsam gefüllt, horiz. W'Sp. auf 12 cm=
Ausg. W'Sp. - Drained by using vacuum pump, flume slowly filled with water,
horizontal water table established at 12 cm = original water table elevation

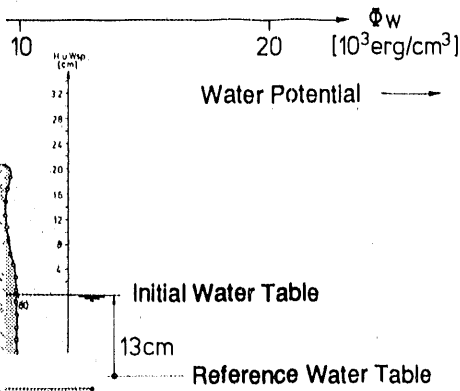
9

TABLE α . Potential and Saturation Measurements



Results During Experiment A

Site



Initial Water Table
(Compare to Photographs)

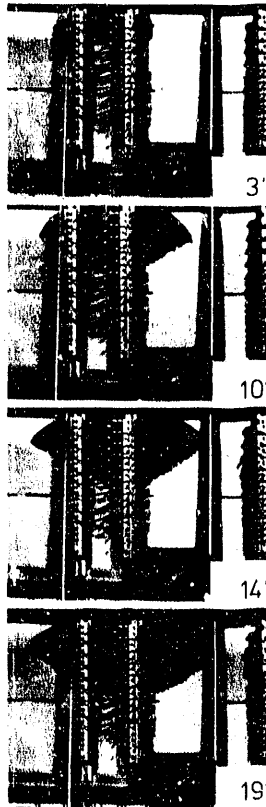
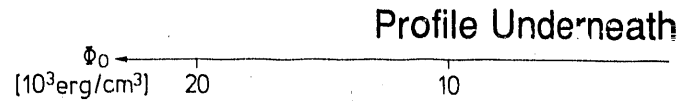


TABLE B. Potential an



Before Oil Application

Time

Begin Oil Application (4 L)

3'

10'

14'

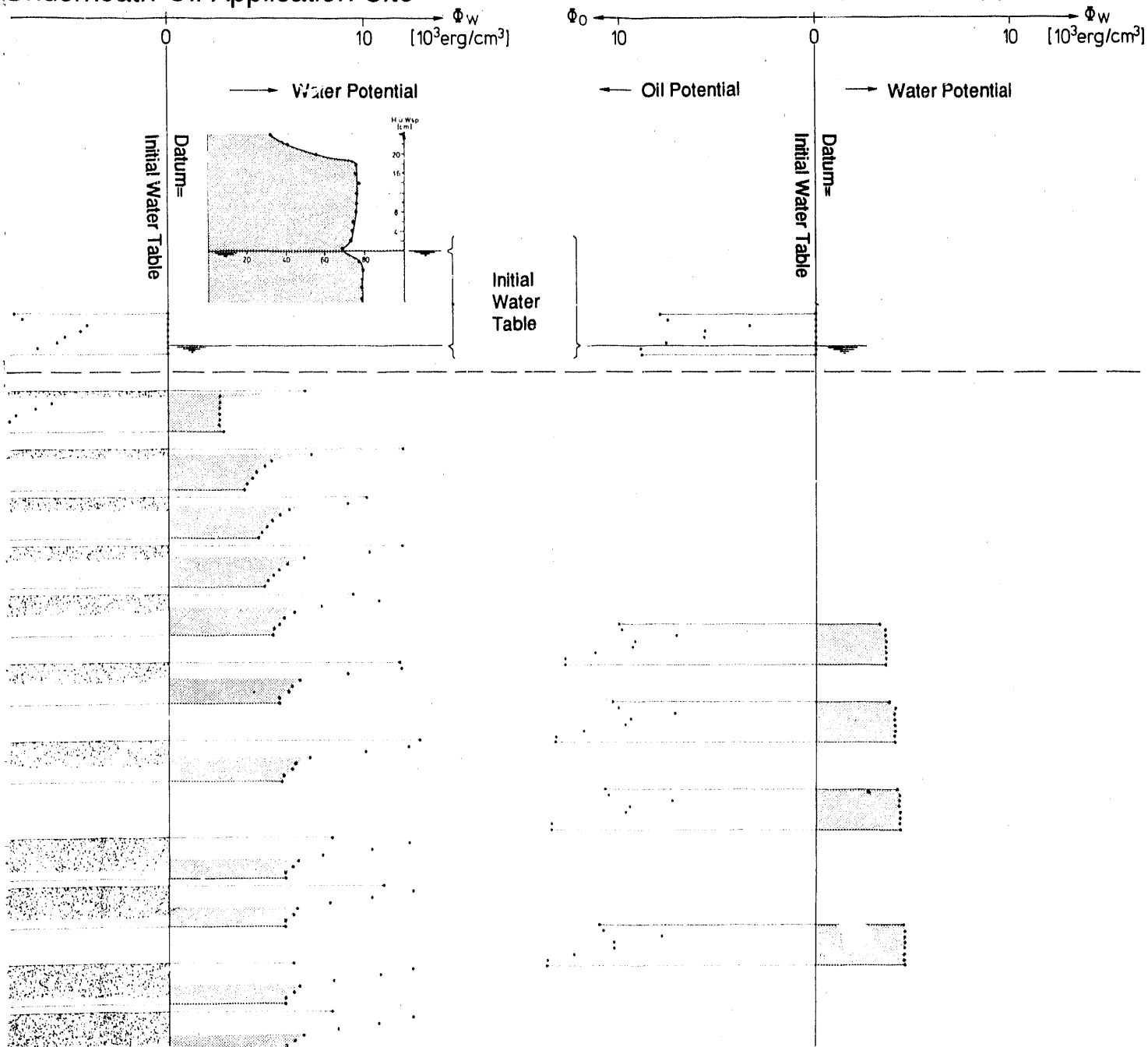
19'

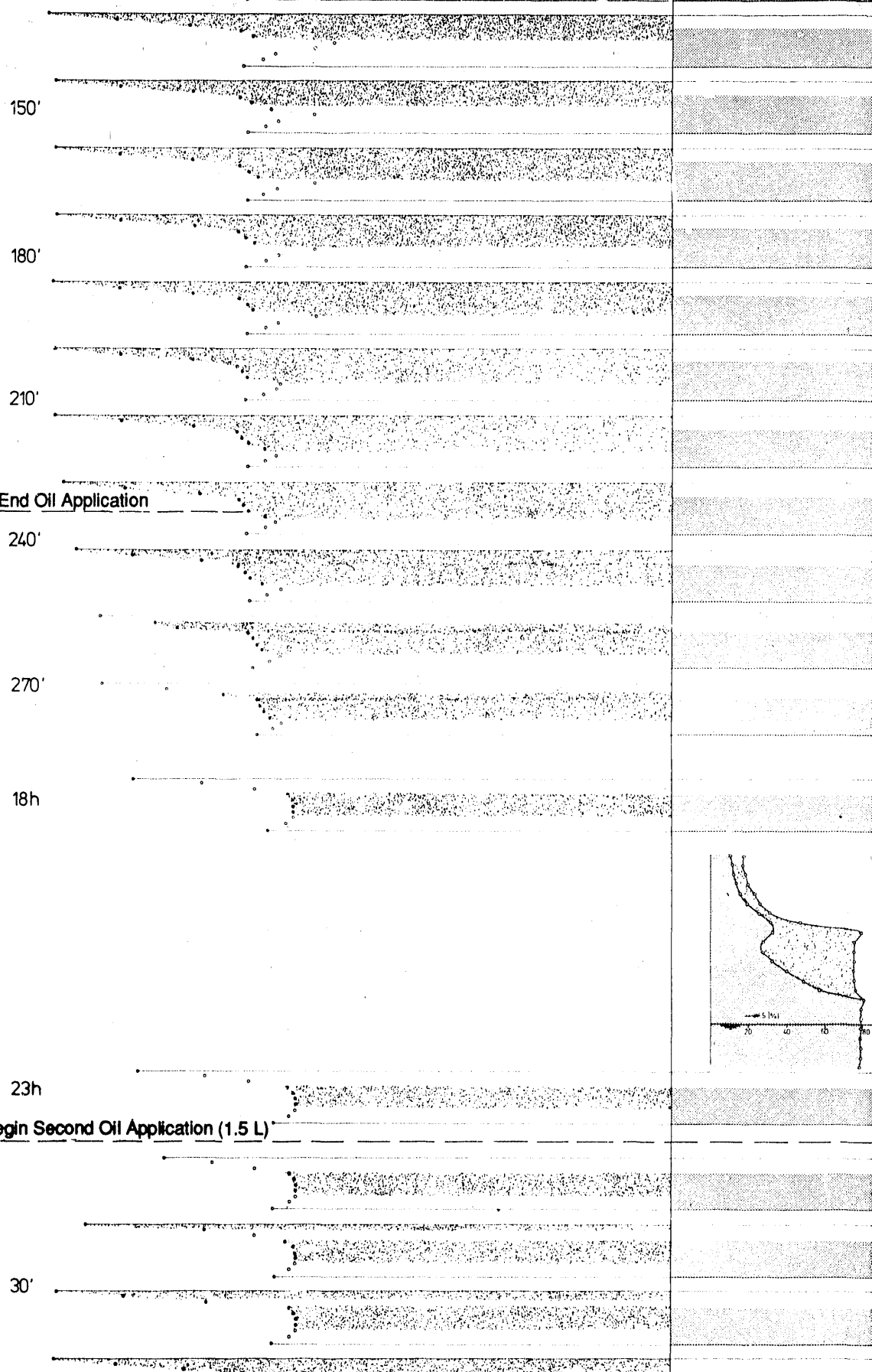
End Oil Application

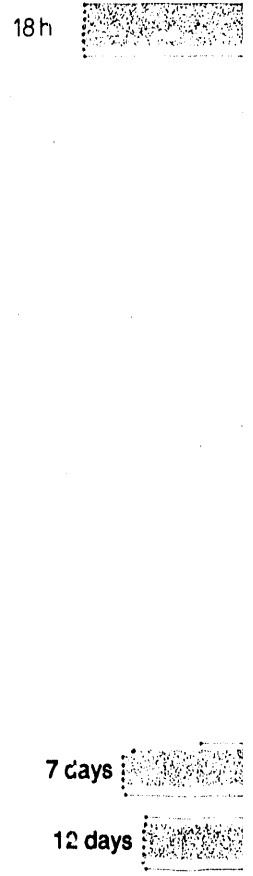
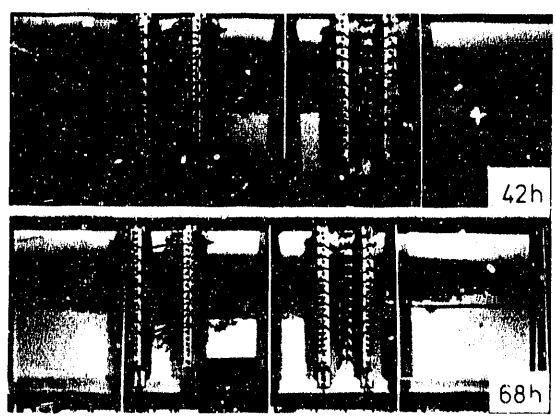
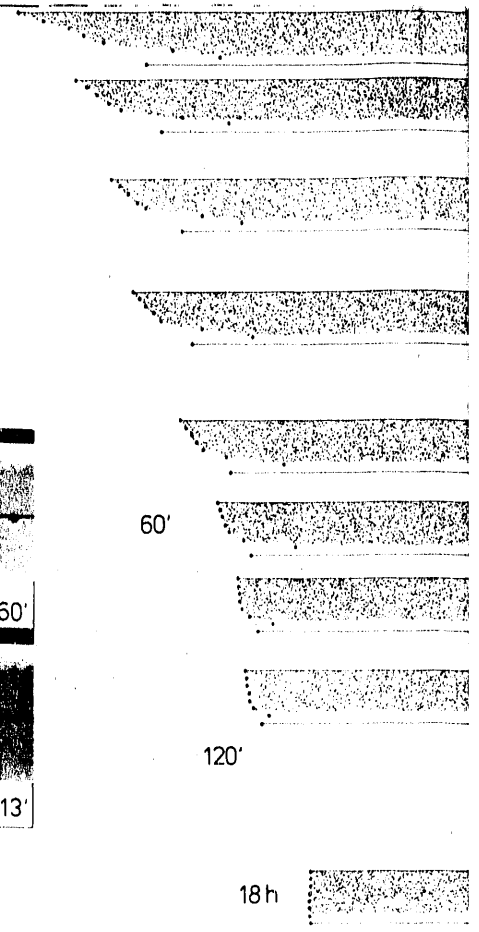
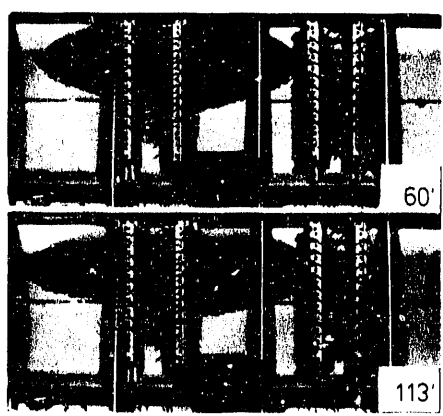
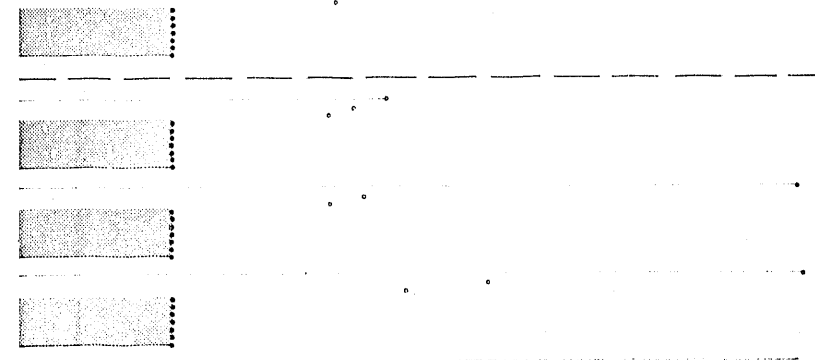
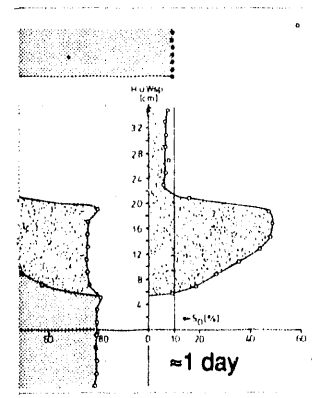
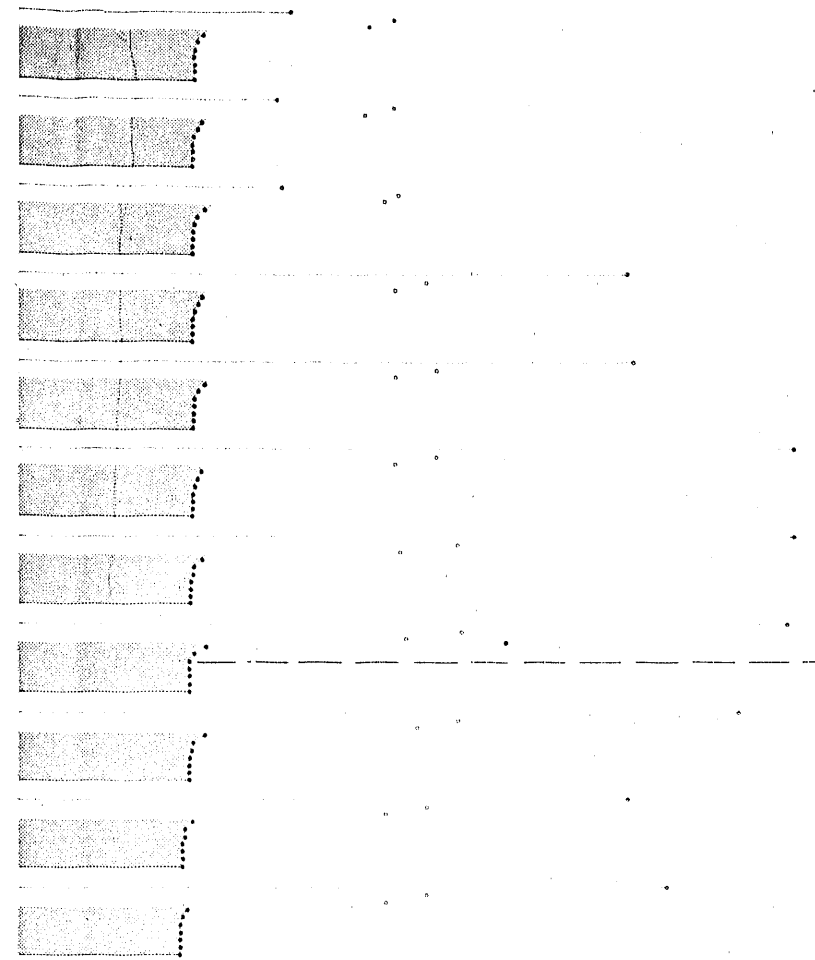
Potential and Saturation Measurements During Experiment B

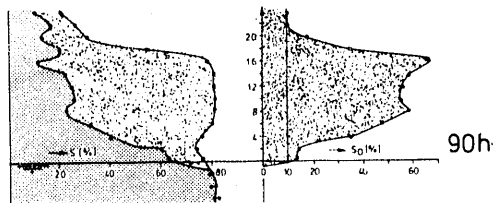
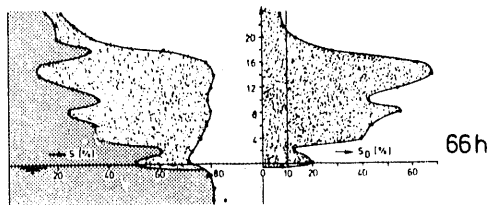
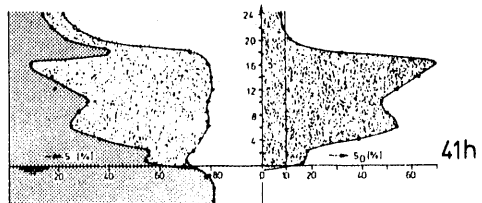
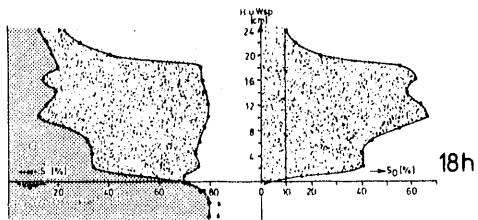
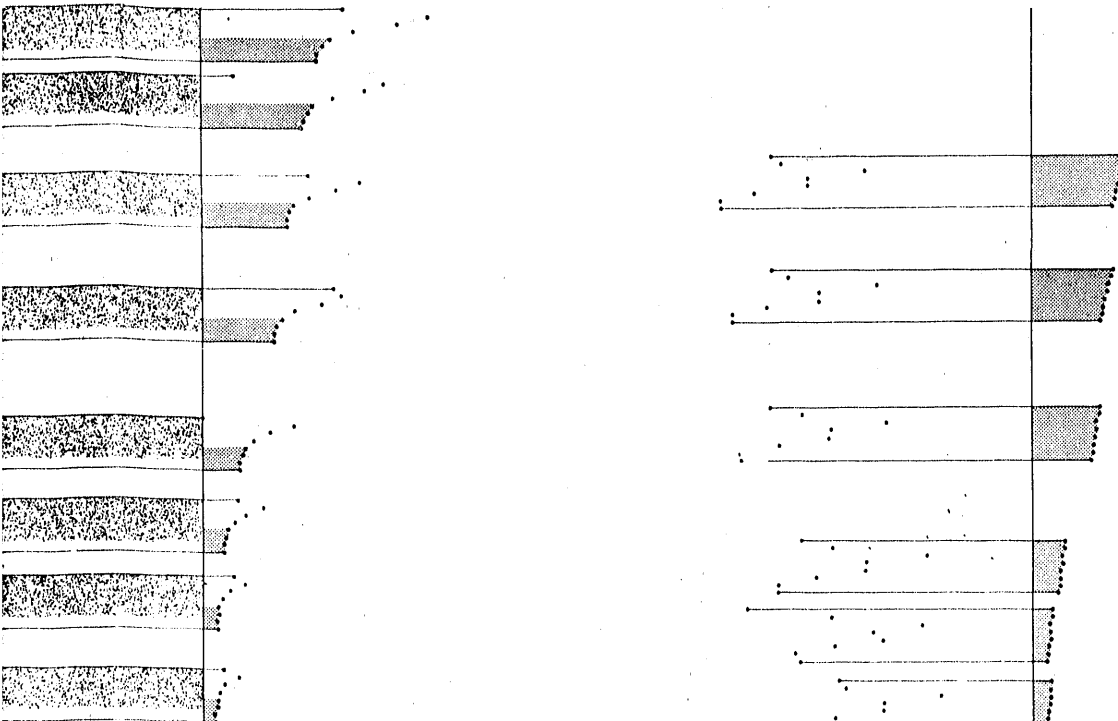
Underneath Oil Application Site

Profile 62 cm to the Right of Oil Application Site



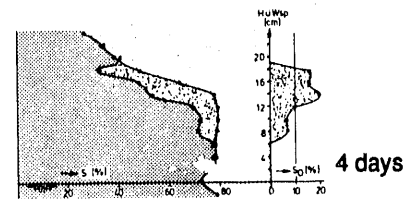
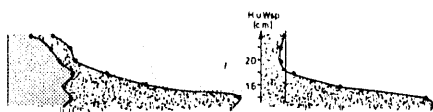






1 days

2 days



60'

90'

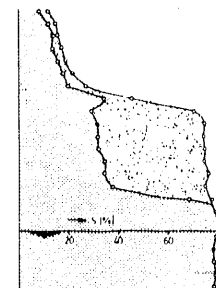
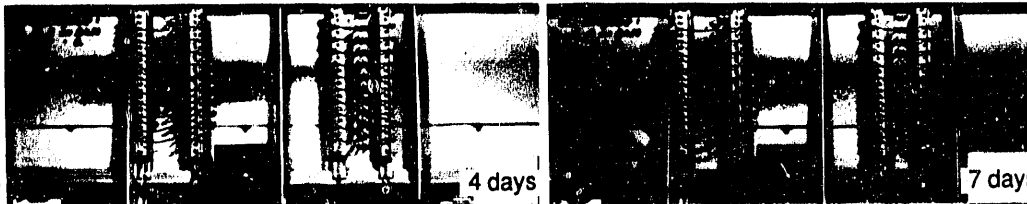
End Oil Application

2h

3h

4h

68h



6 days 143h

Begin Third Oil Application (1 L)

5'

13'

21'

29'

45'

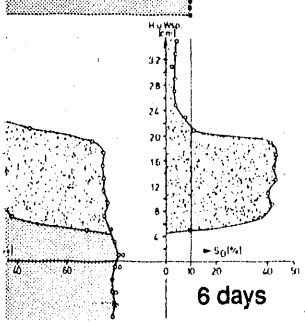
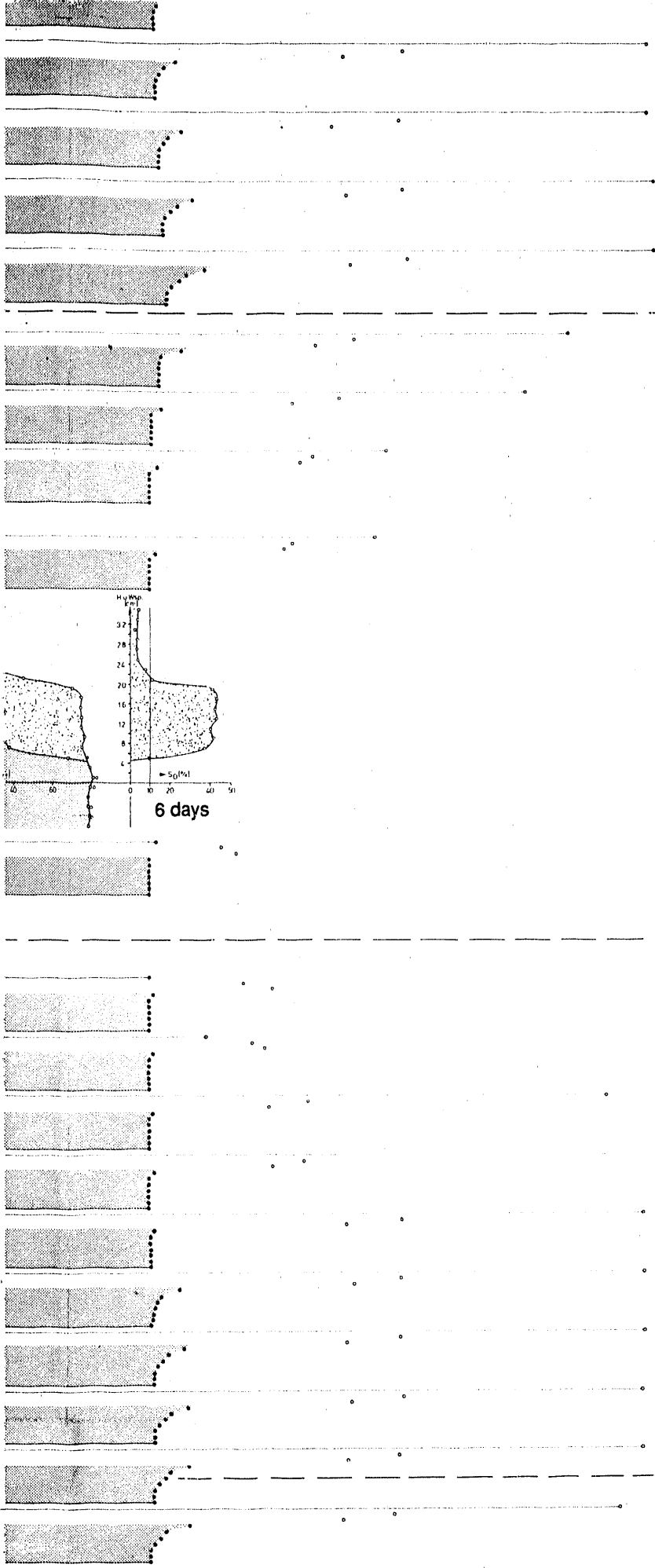
61'

77'

93'

109'
End Oil Application

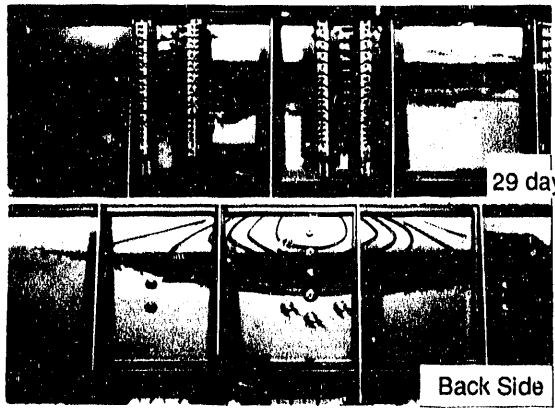
125'



6 days

18 days

24 days



29 days

Back Side

31 days

35 days

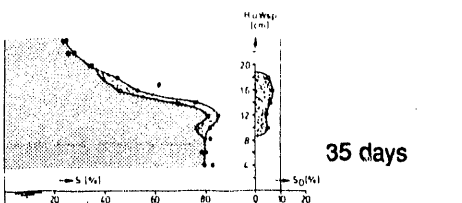
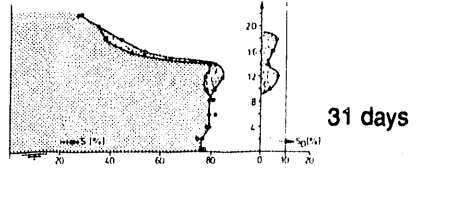
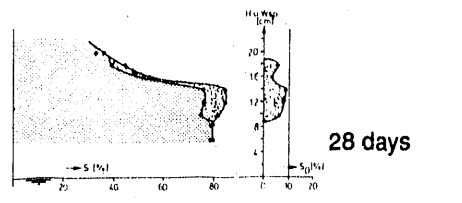
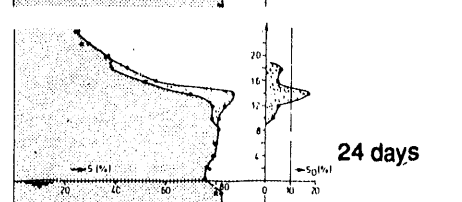
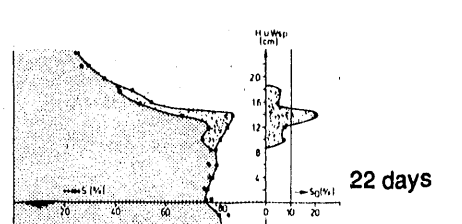
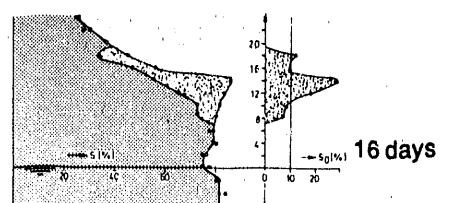
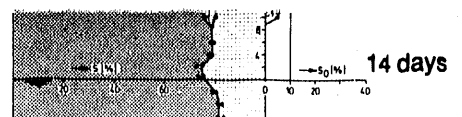
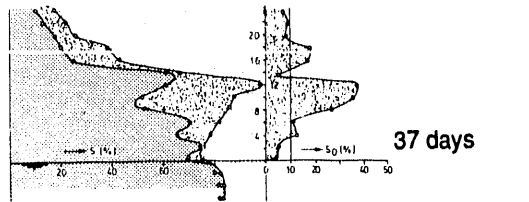
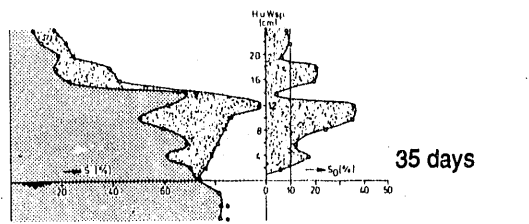
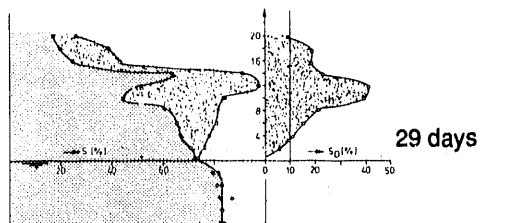
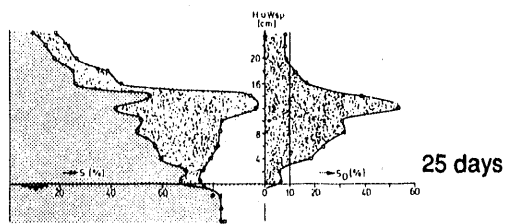
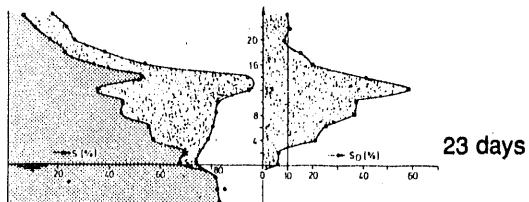
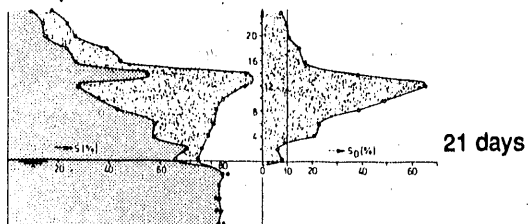
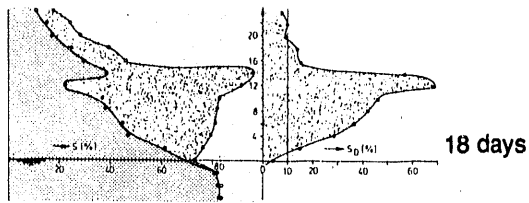
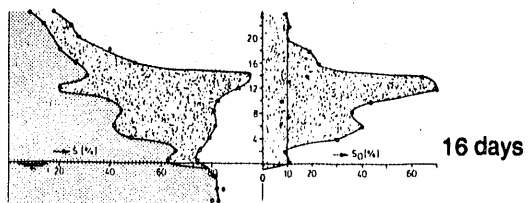
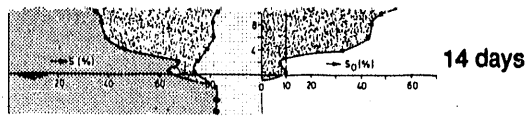


Table α (cont.)

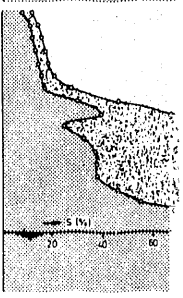
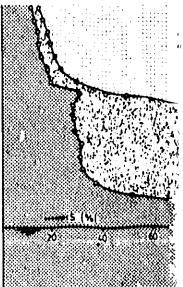
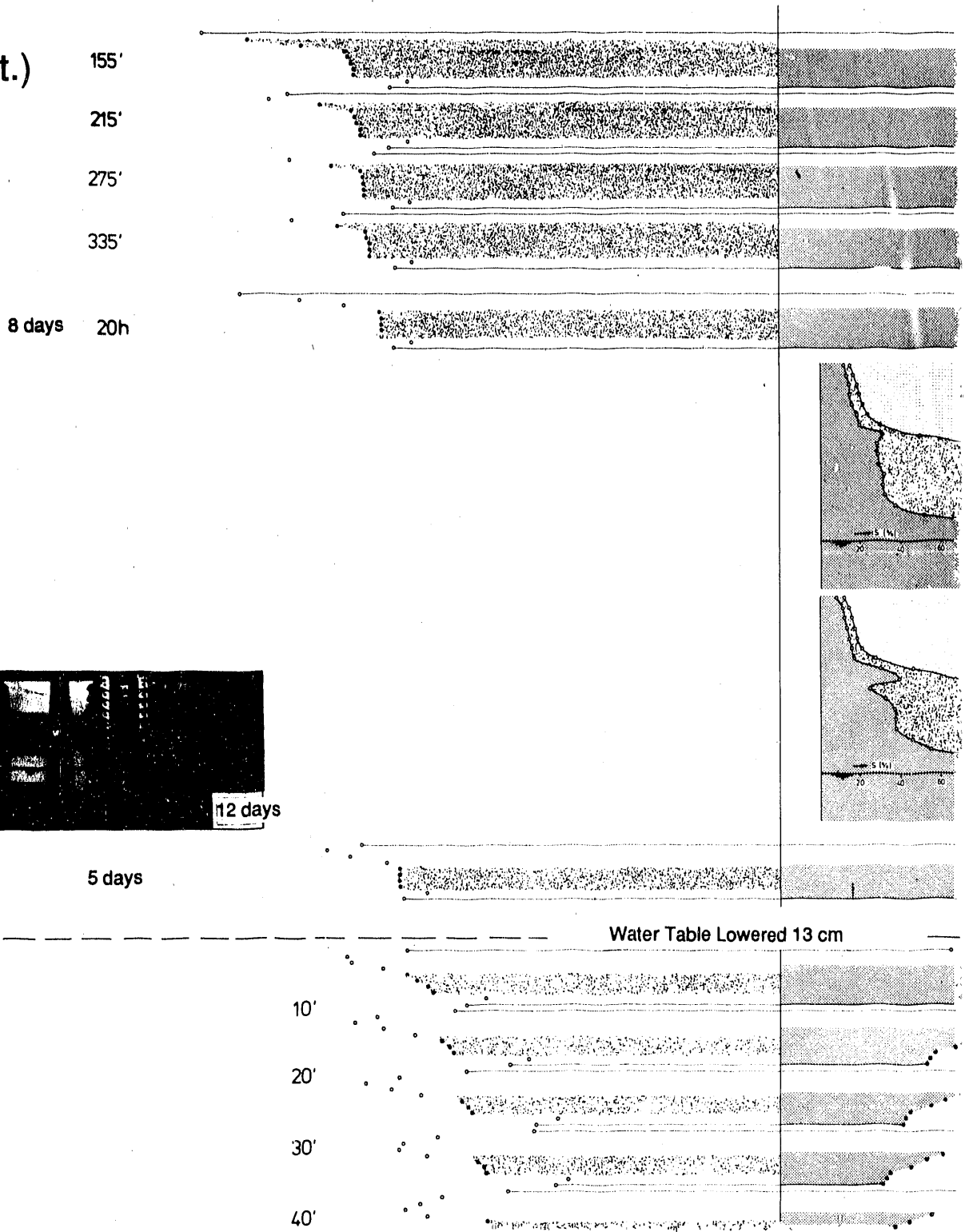
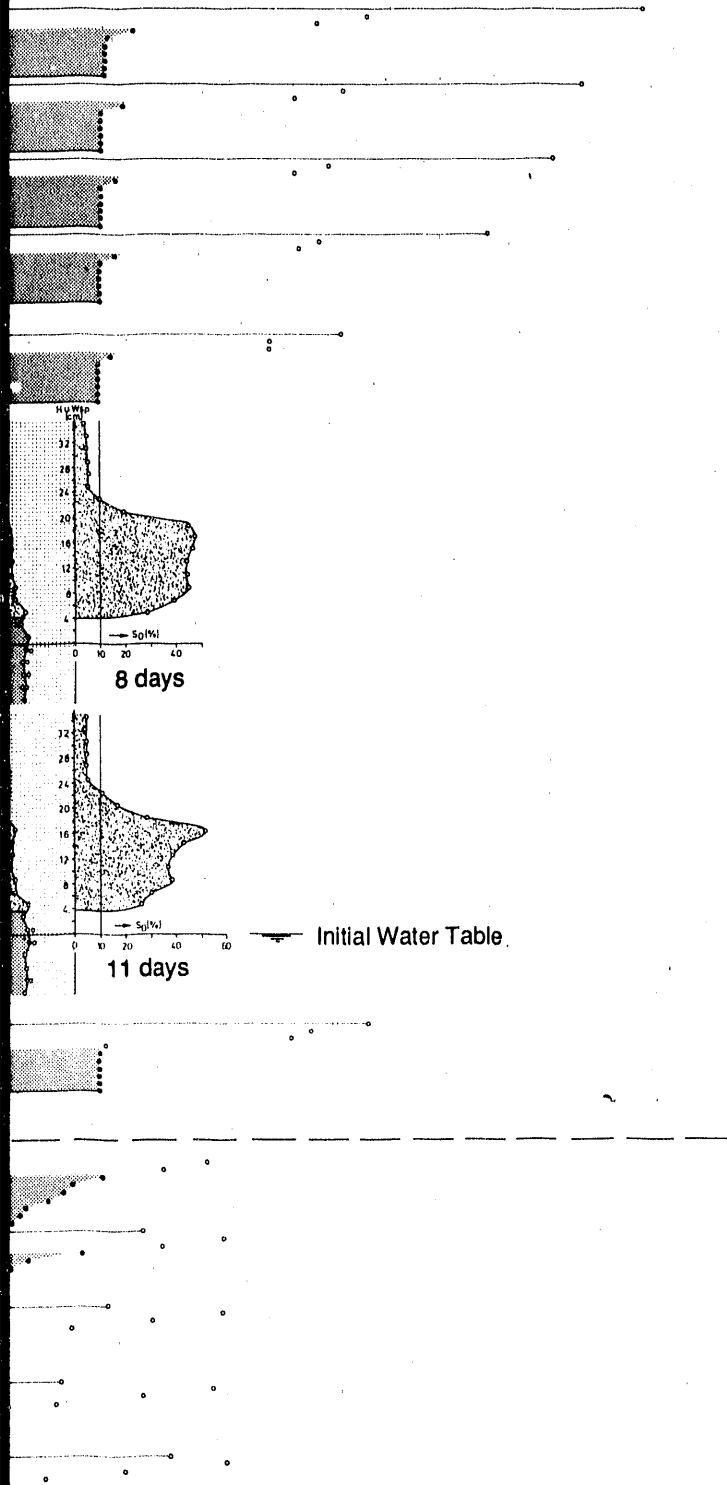
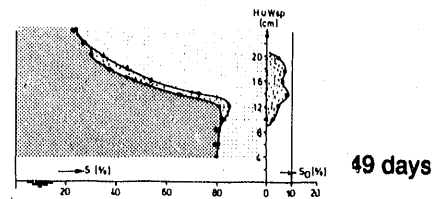
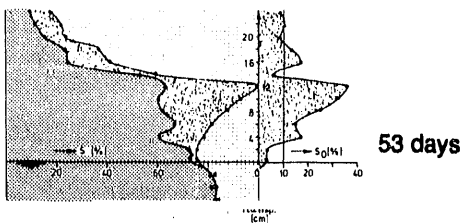
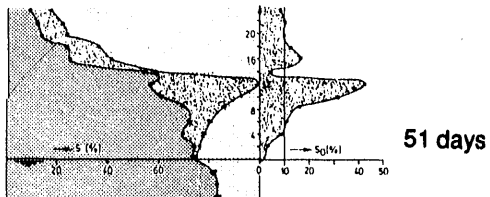
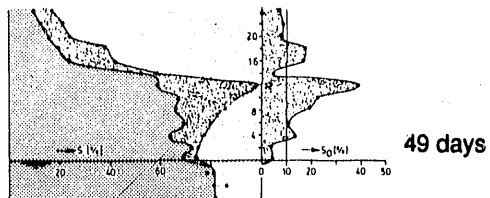
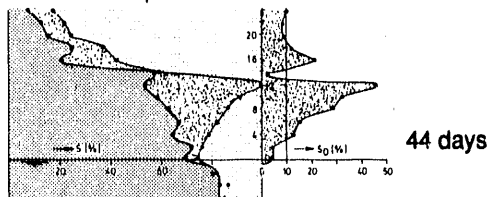
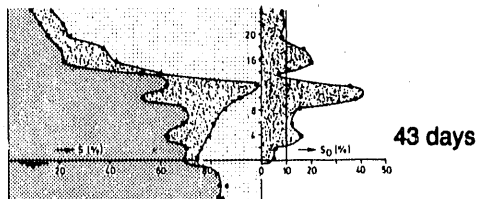
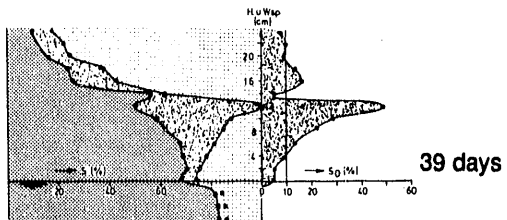
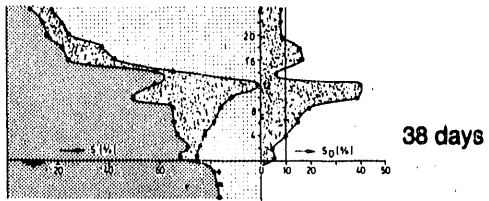


Table β (cont.)

39 days



53 days



50'

60'

70'

80'

90'

100'

110'

120'

150'

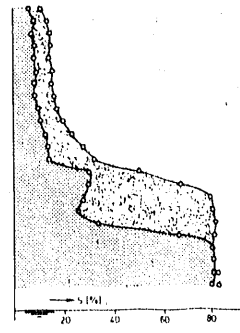
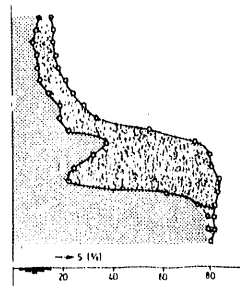
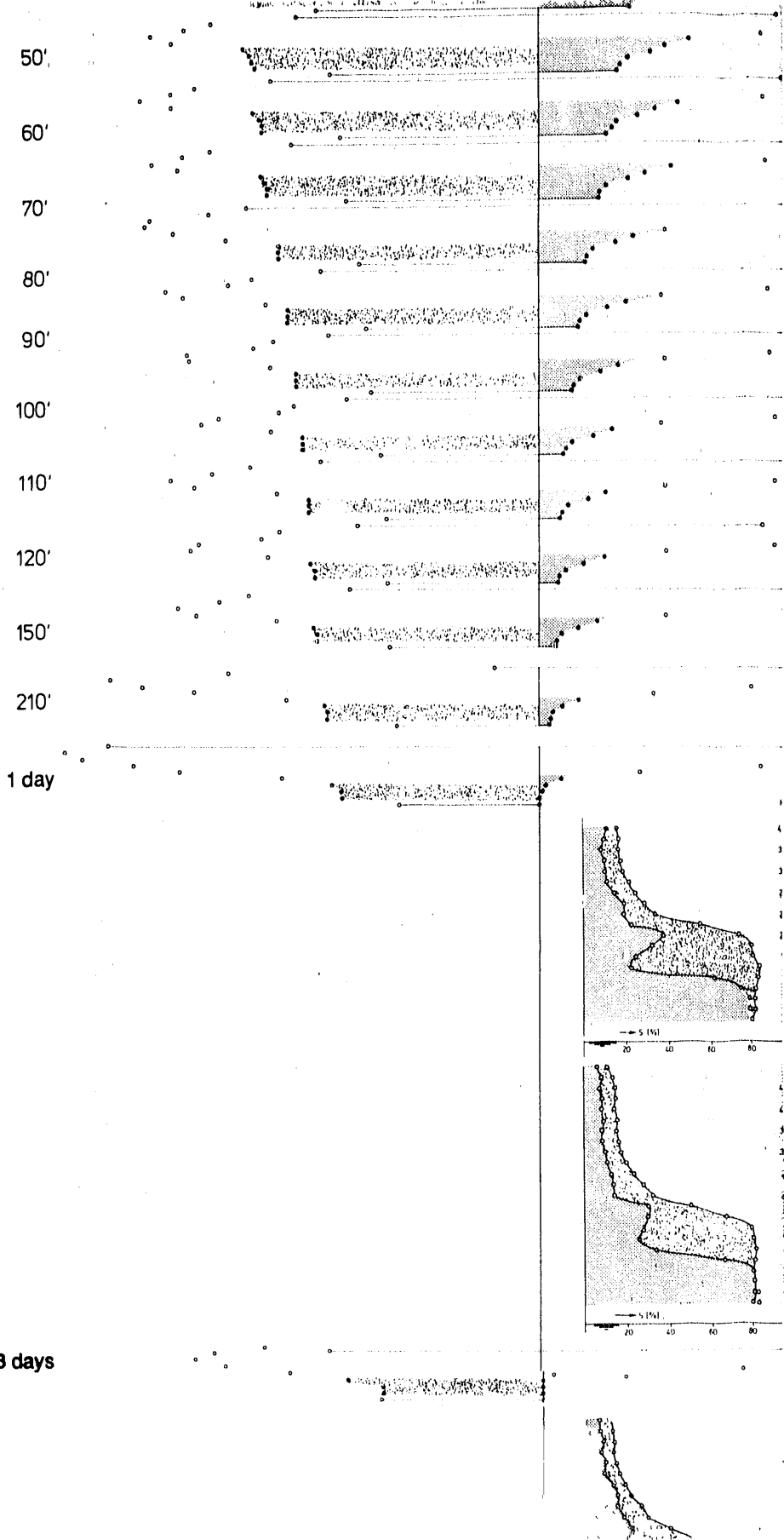
210'

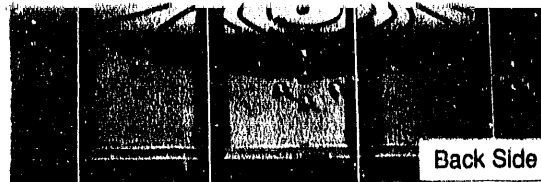
1 day

13 days

8 days

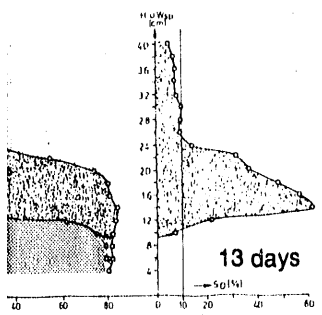
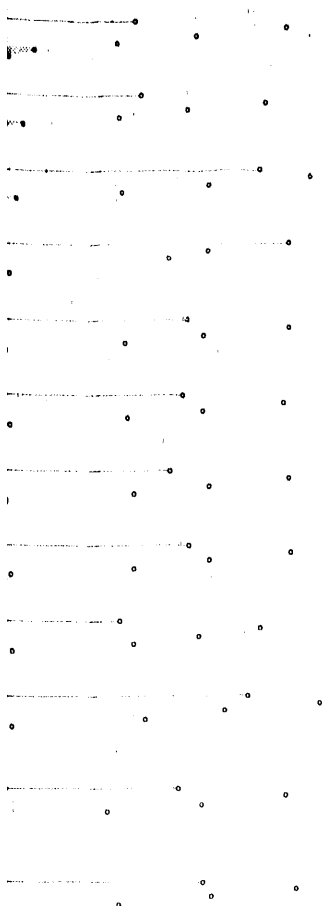
20 days



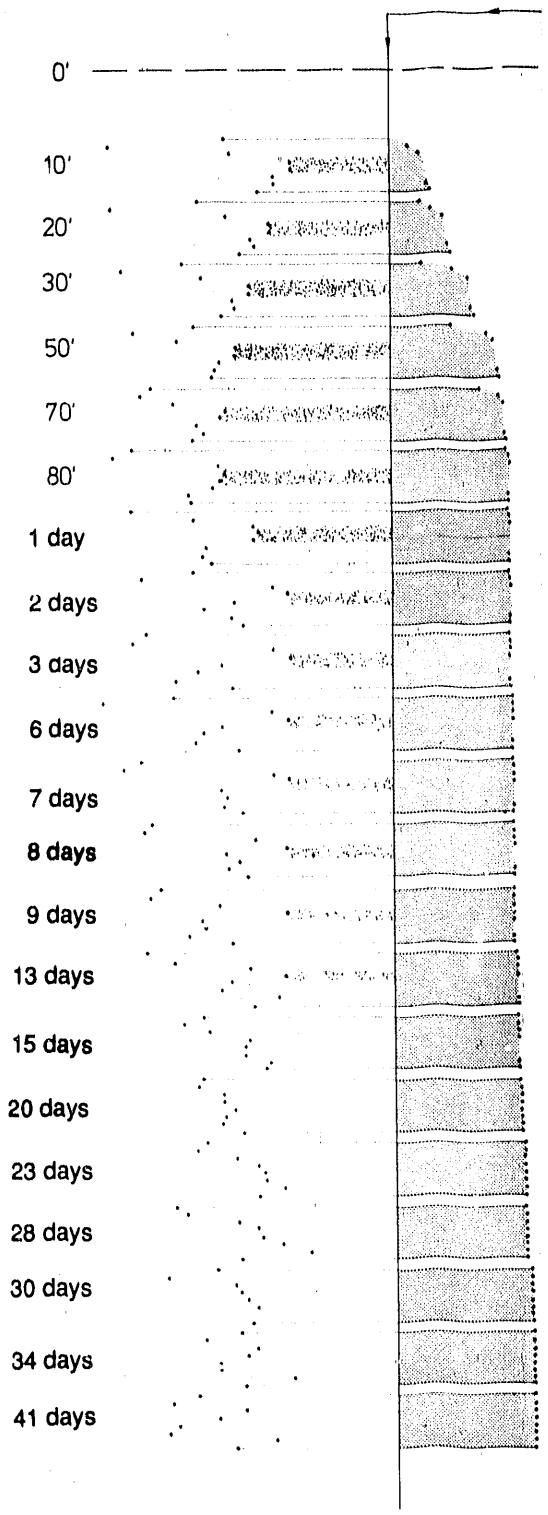
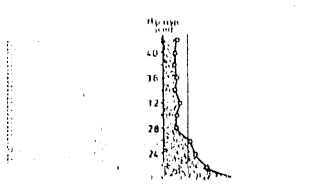
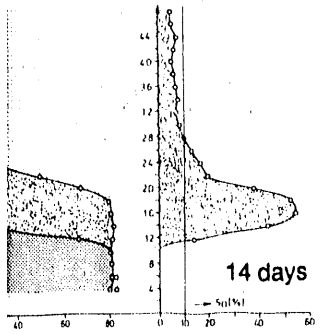


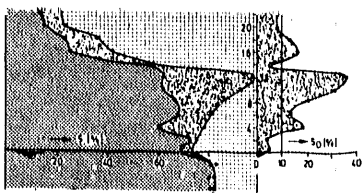
57 days

MSR

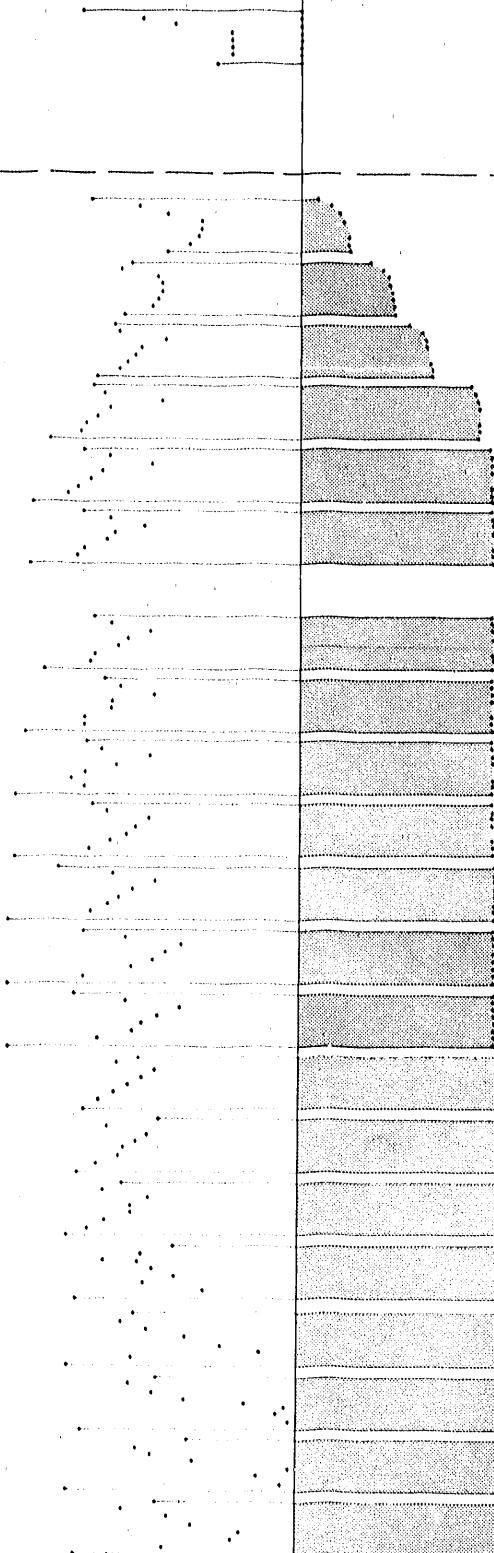
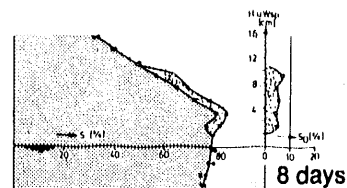
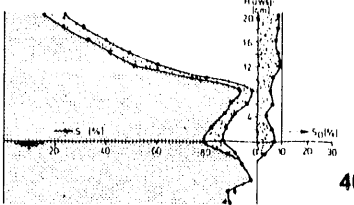
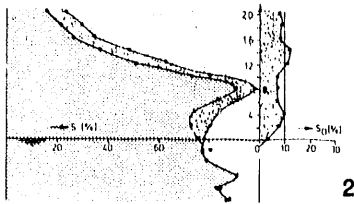
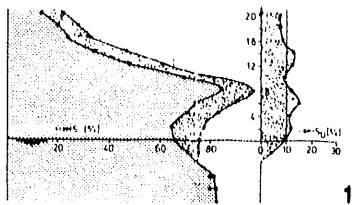
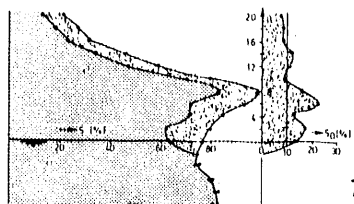
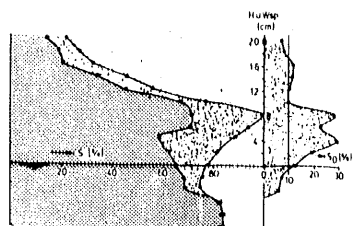


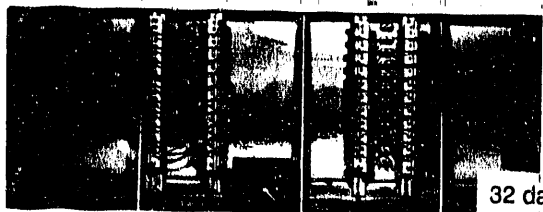
On the Basis of Lowered Water Table Level





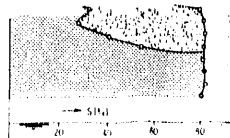
Begin Adjusting Slope of Water Table at ~4%





22 days

32 days



34 days

Water Table Raised 35 cm

20'

50'

80'

110'

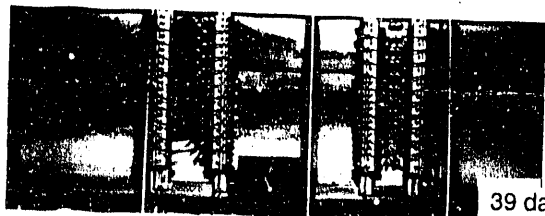
140'

290'

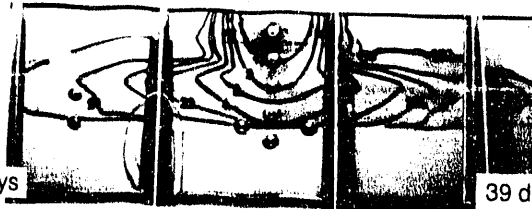
22 1/2 h

2 days

5 days

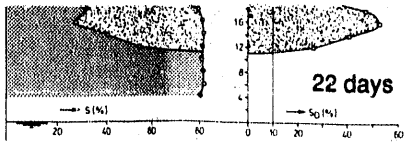


39 days



39 days

Back Side



35 cm

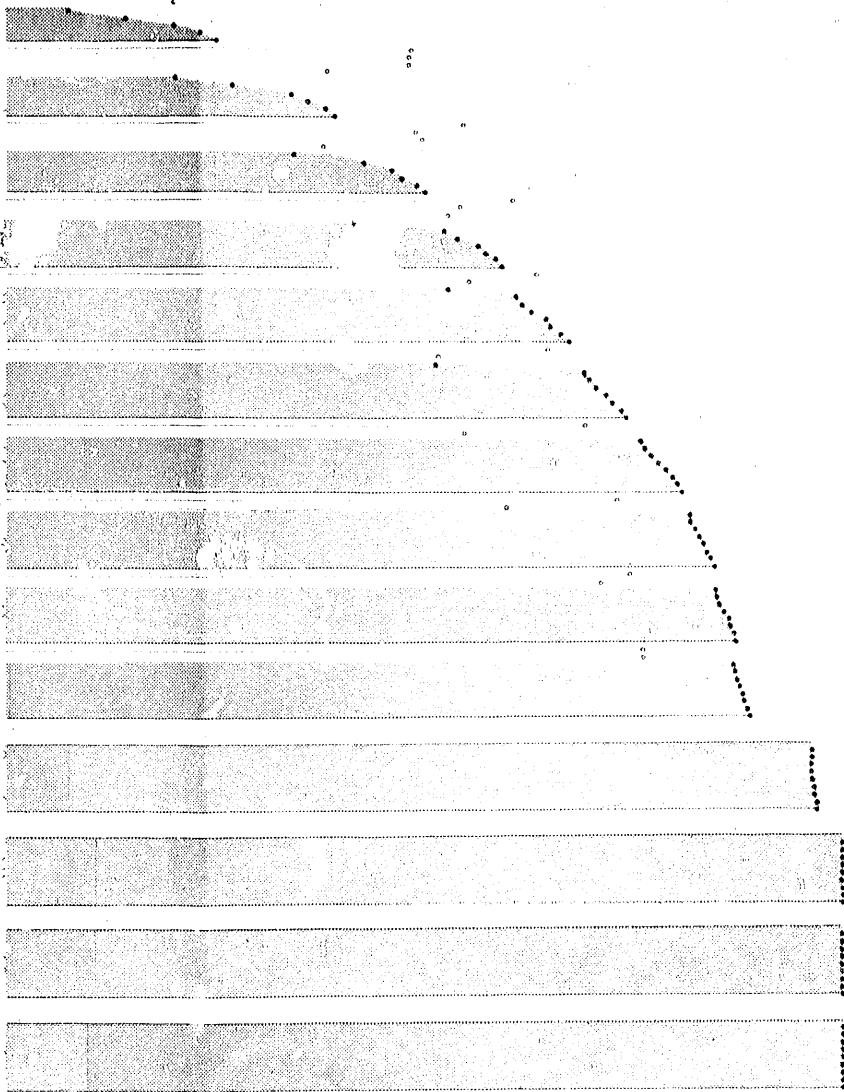


TABLE 8 Potential and Satur

Horizontal Distance from the
Oil Application Profile, cm

109,0

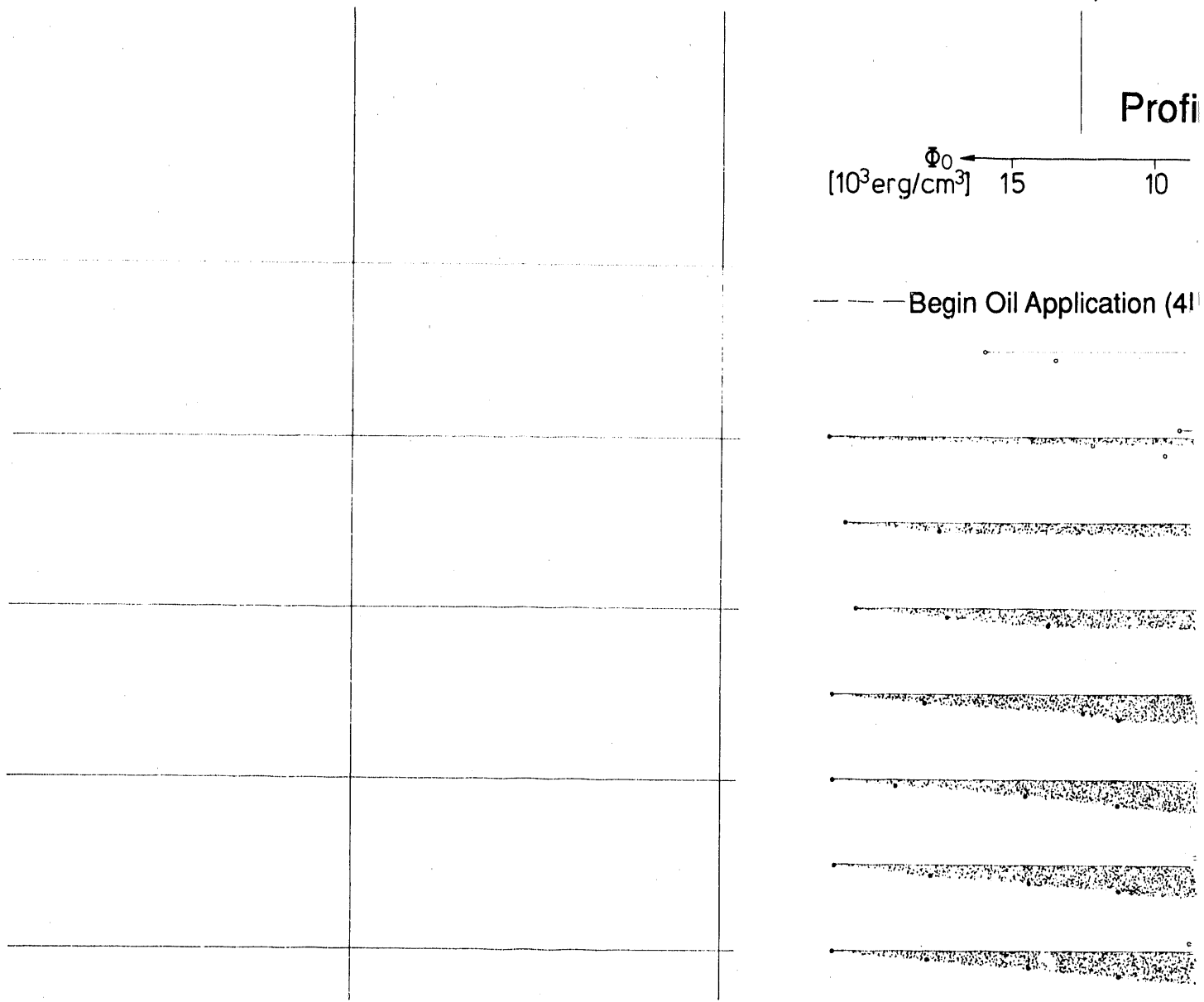
101,5

96,5

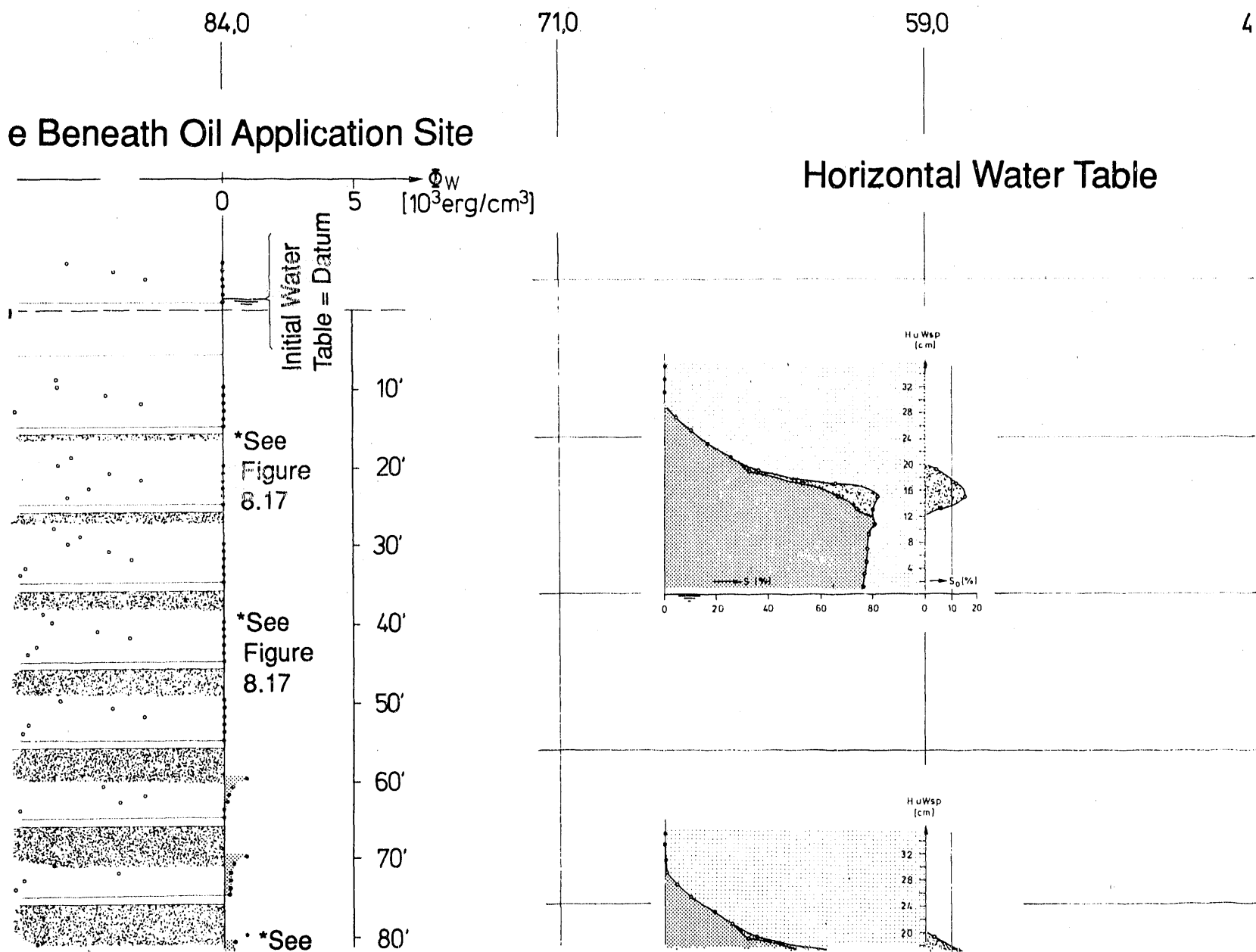
Profi

Φ_0
[10^3erg/cm^3] 15 10

— — — Begin Oil Application (41



Position Measurements During Experiment D

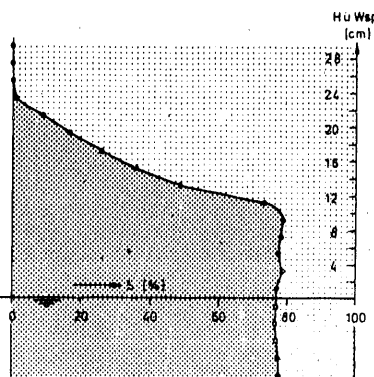


40,0

20,0

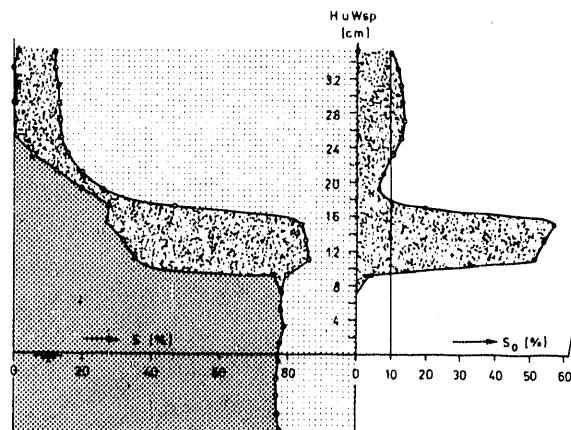
0

Initial Water
Table = Datum



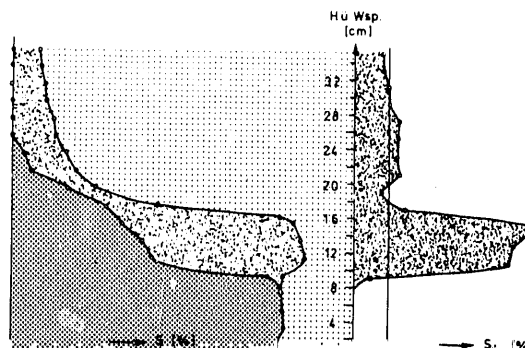
Time

Days
0



1

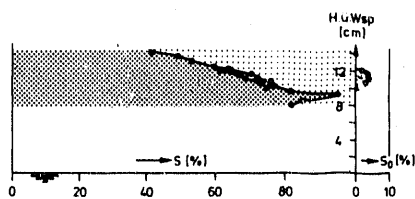
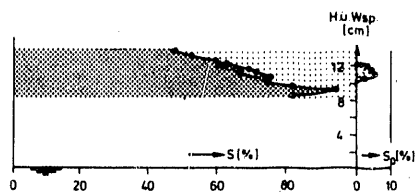
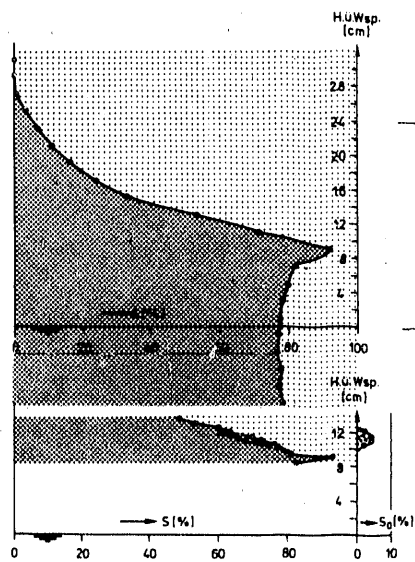
2

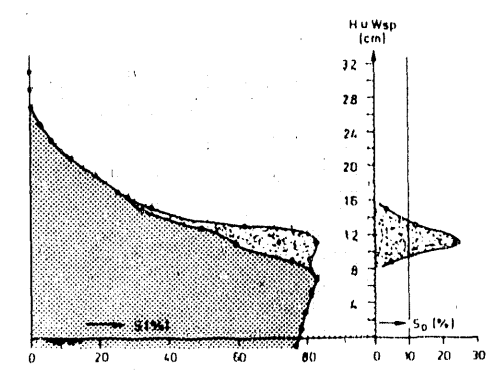
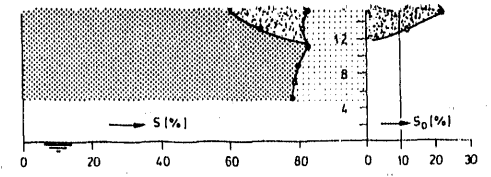
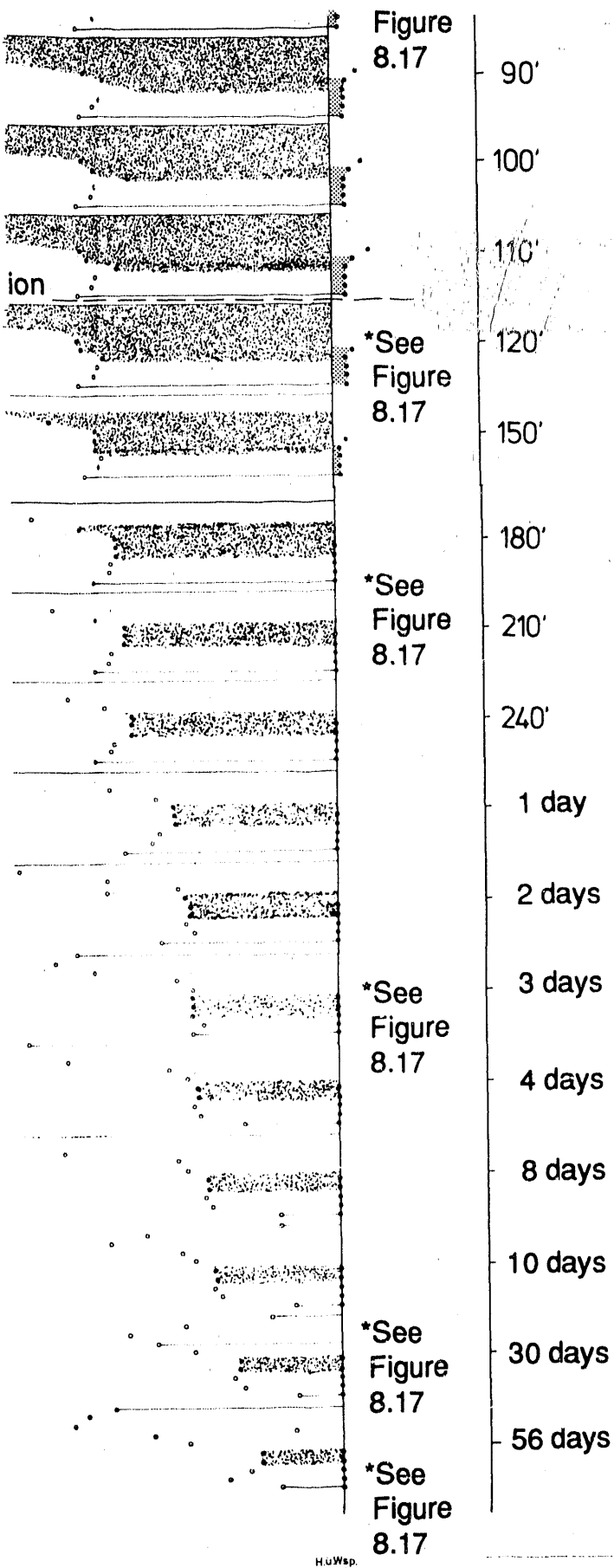


3

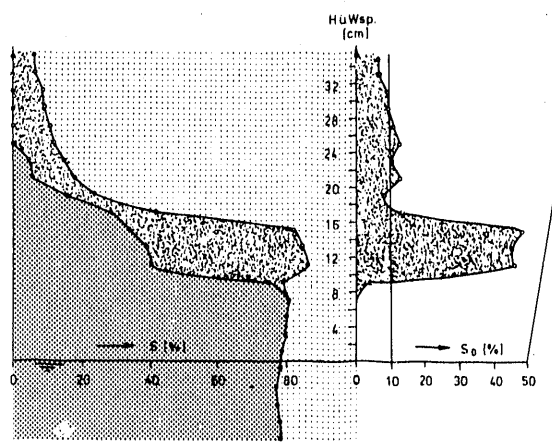
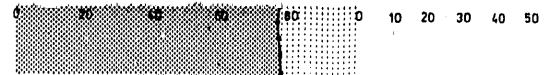
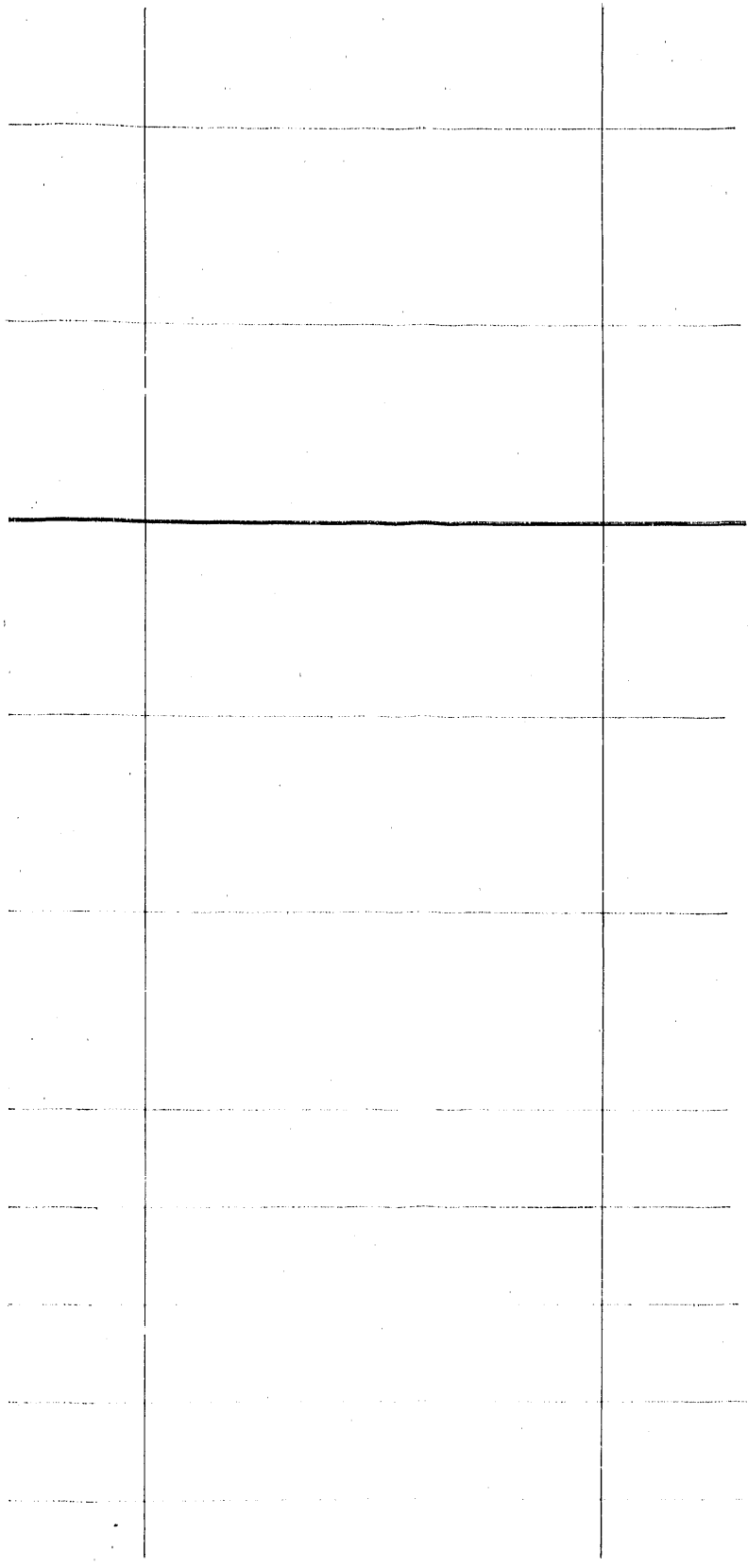
4

End Oil Application

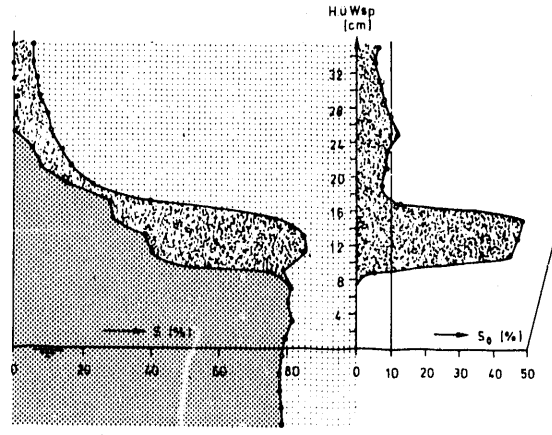




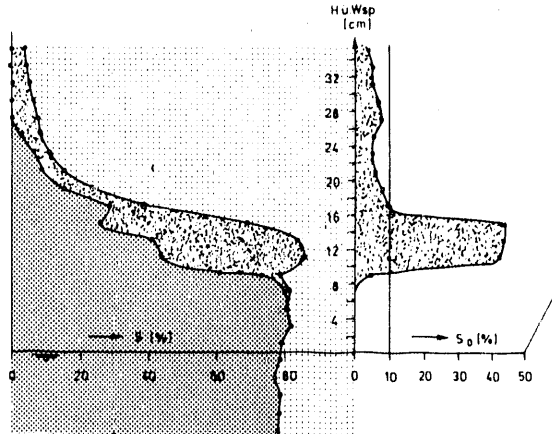
H u Wsp.



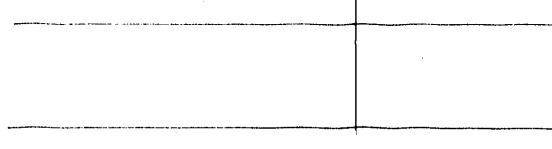
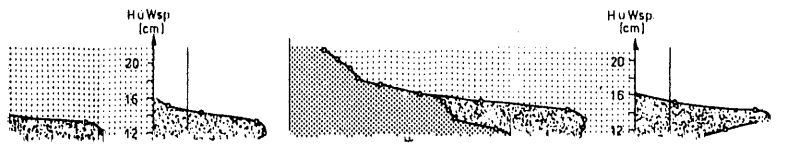
5



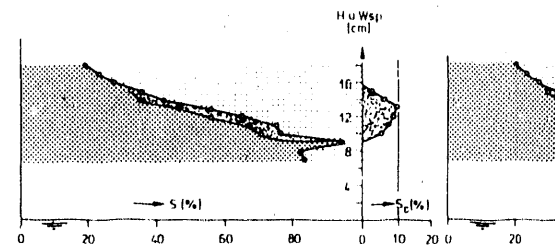
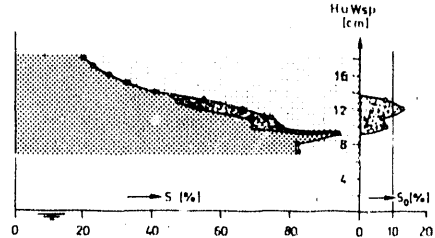
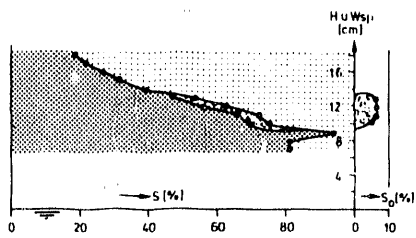
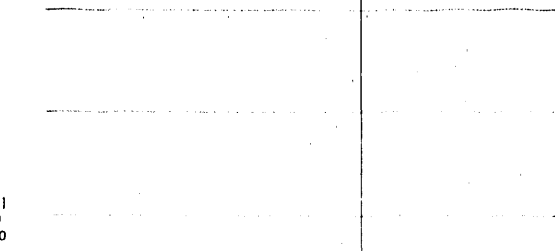
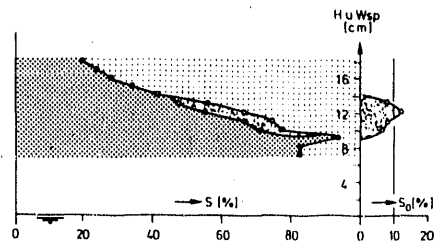
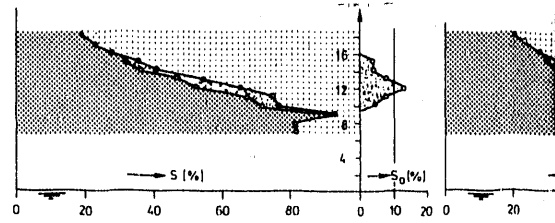
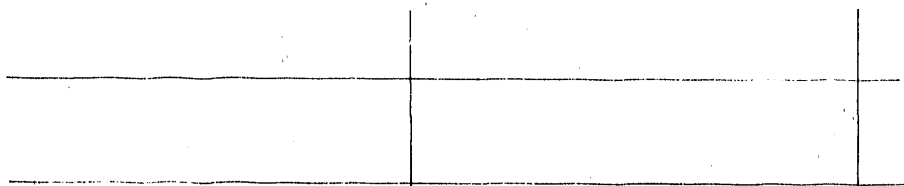
7

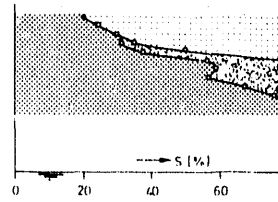
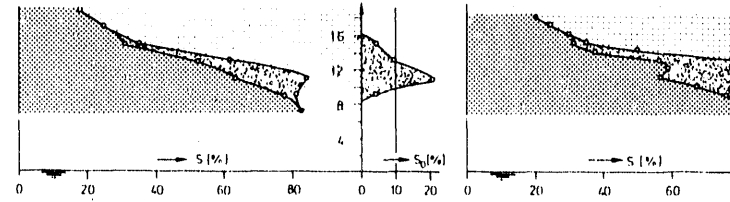
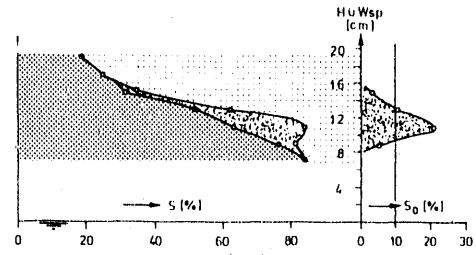
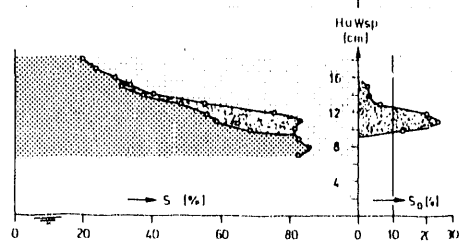
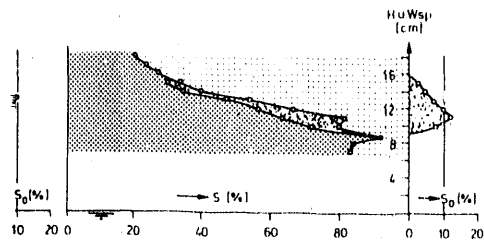
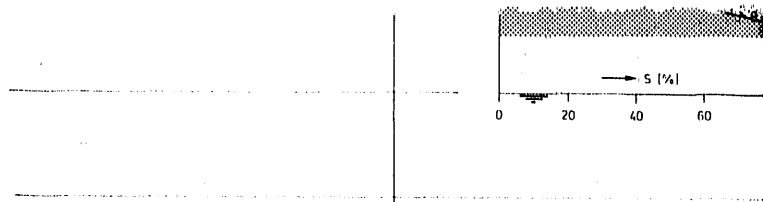
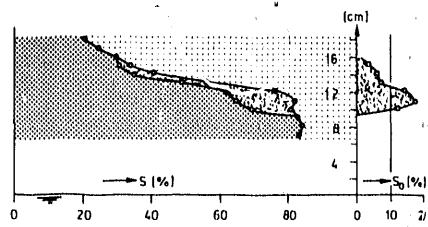
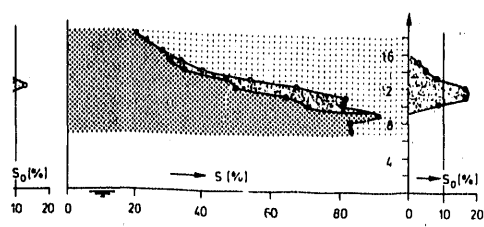


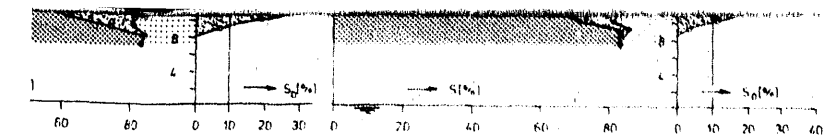
10



16



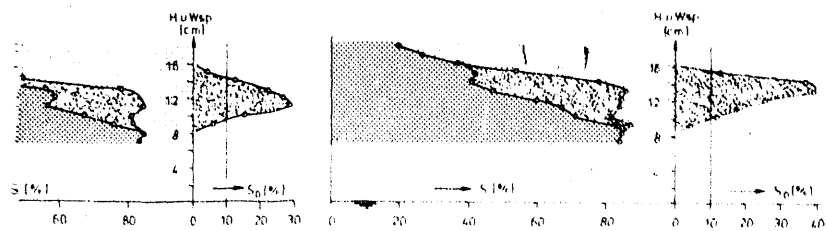




17

18

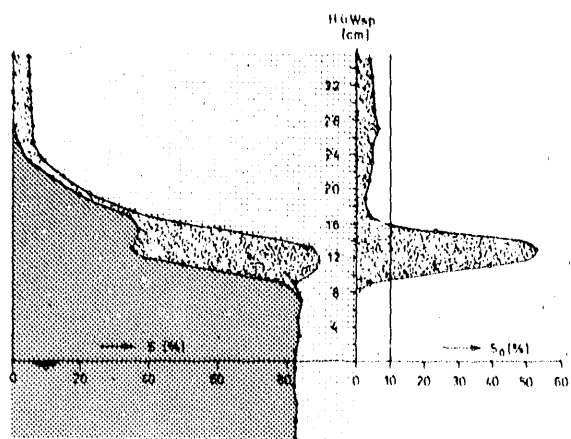
19



20

21

22



23

24

25

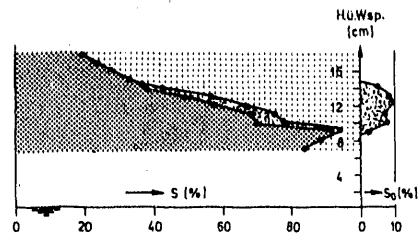
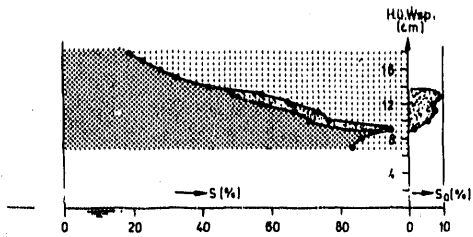
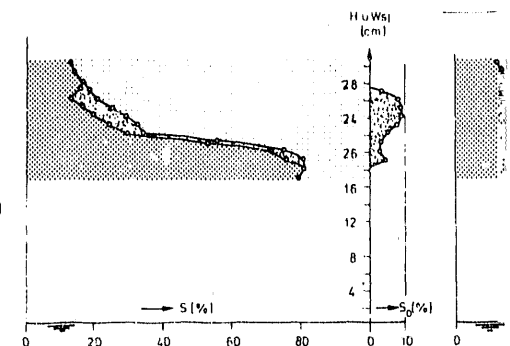
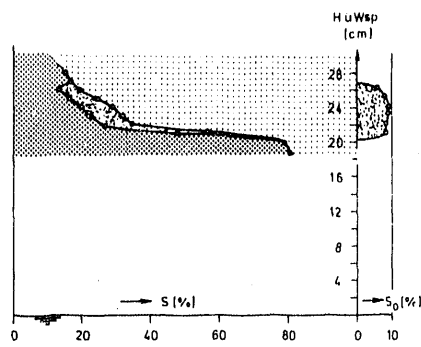
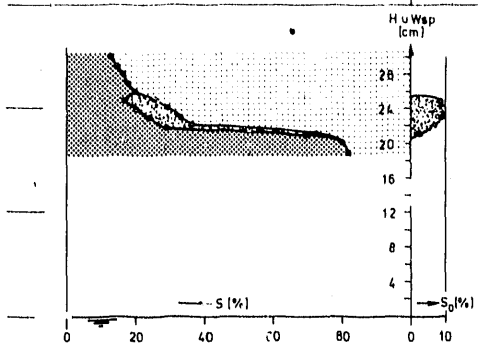
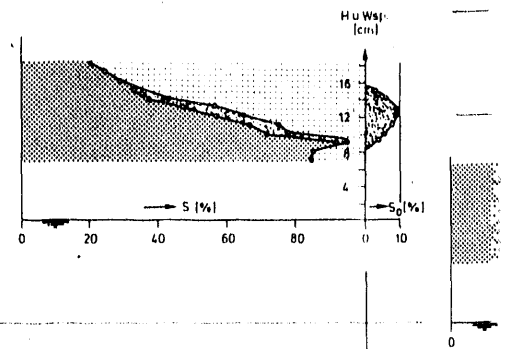
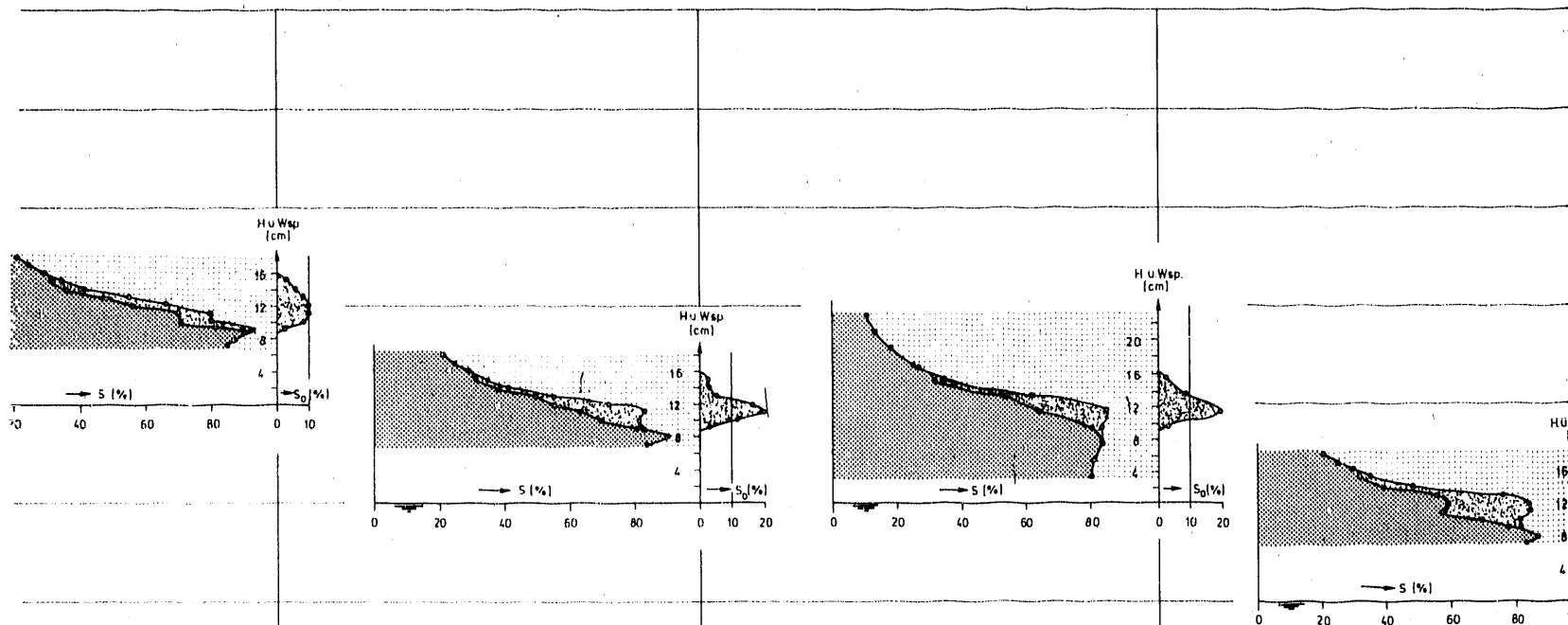


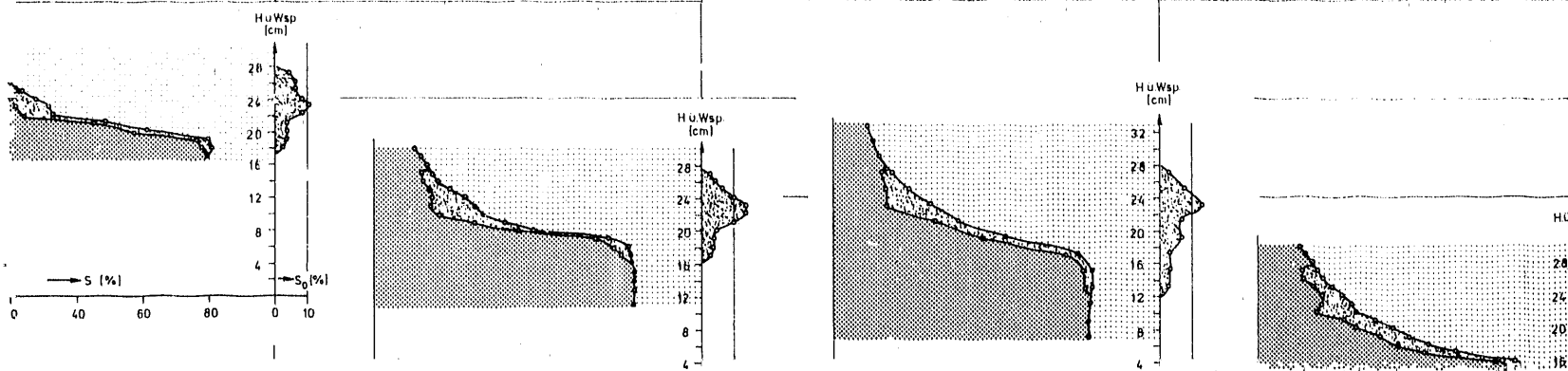
Table δ



(Cont.)



Water Table Lowered 12 cm



46

47

48

49

50

51

52

53

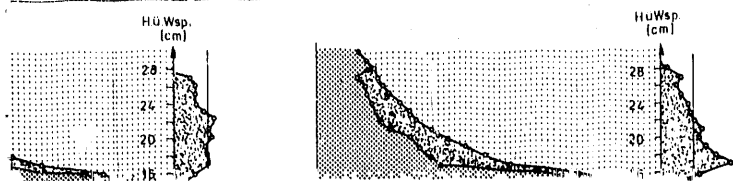
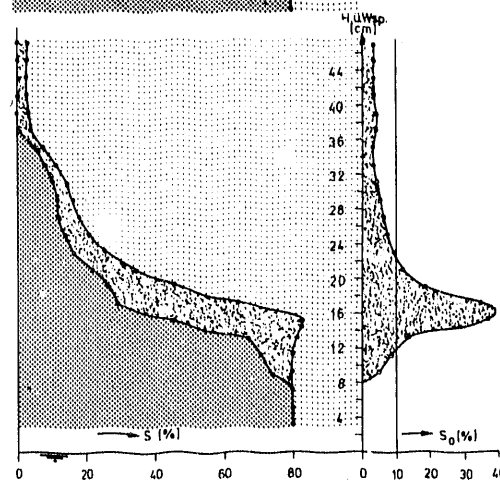
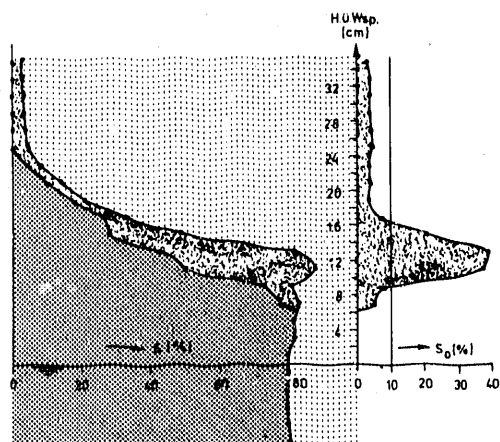
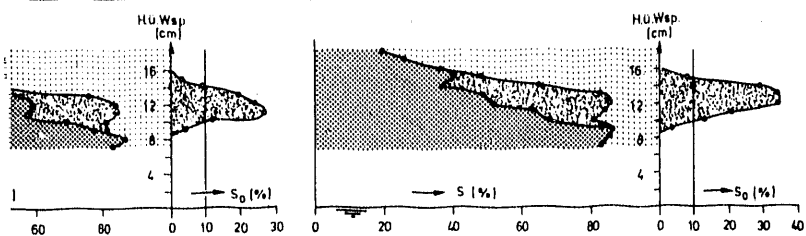
54

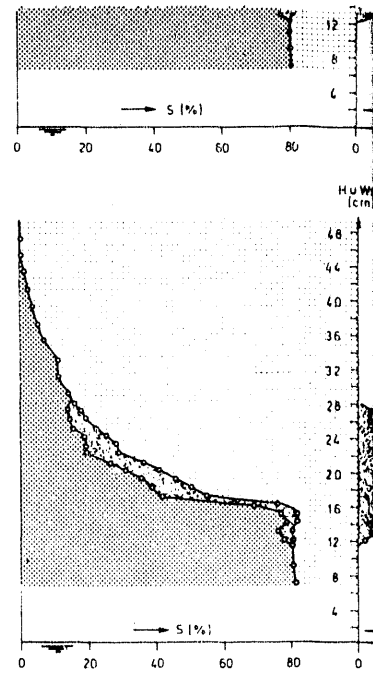
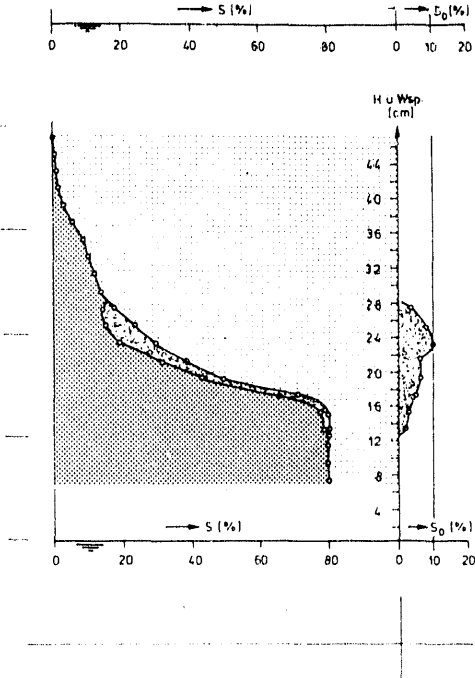
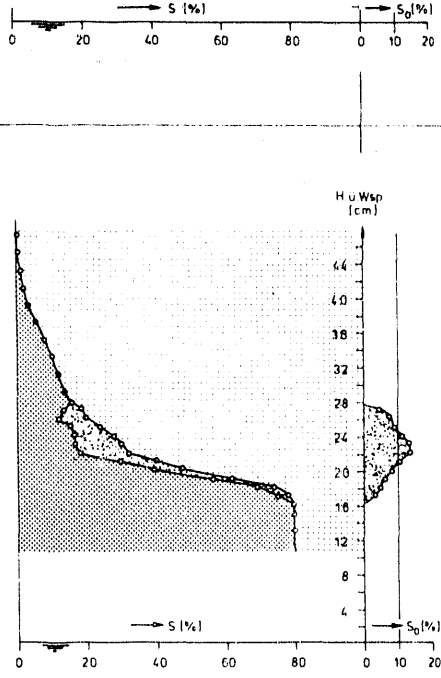
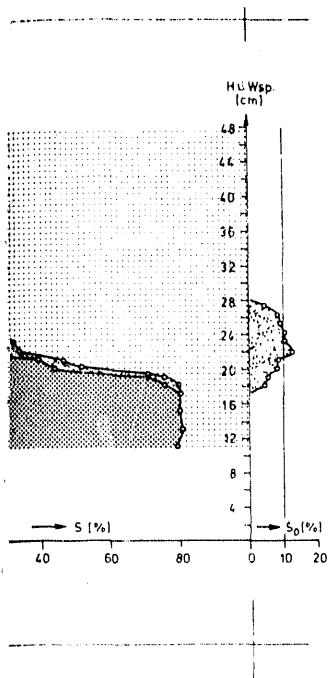
55

56

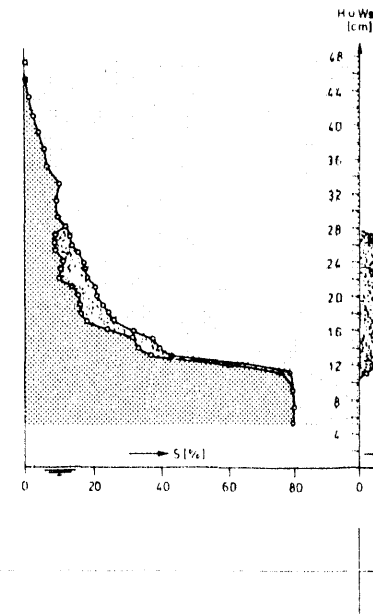
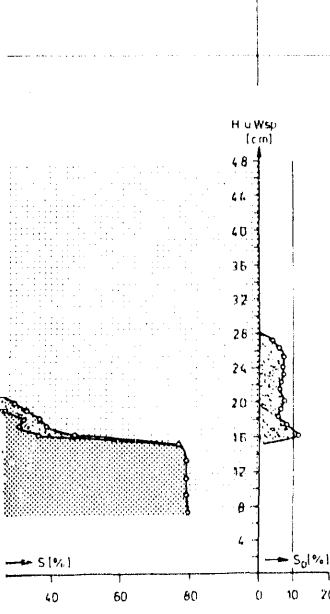
57

58





Slope of Water Table is 4%



59

60

61

62

63

64

65

66

67

68

69

70

71

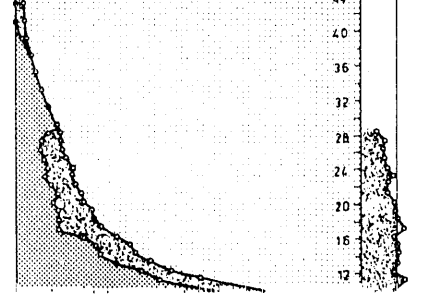
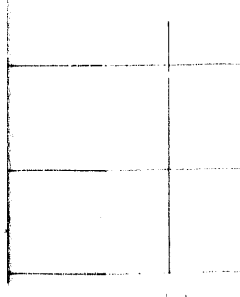
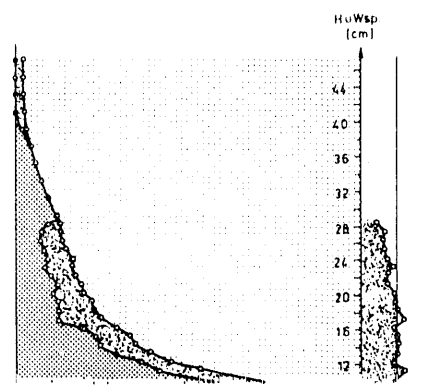
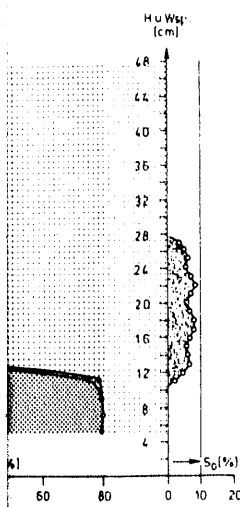
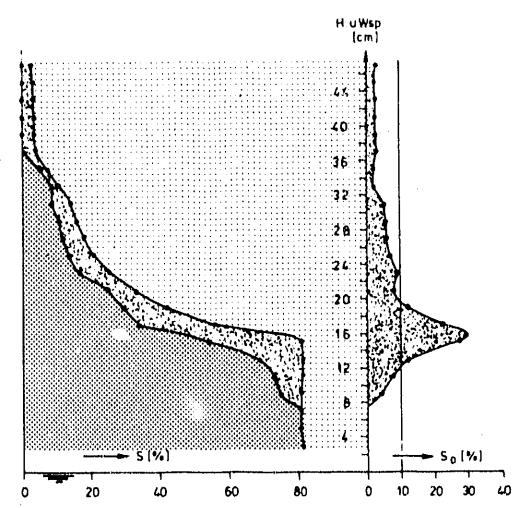
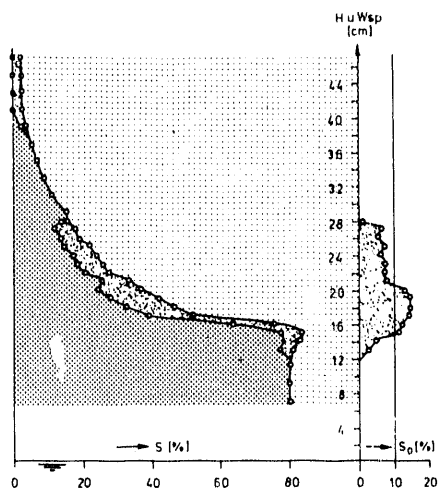
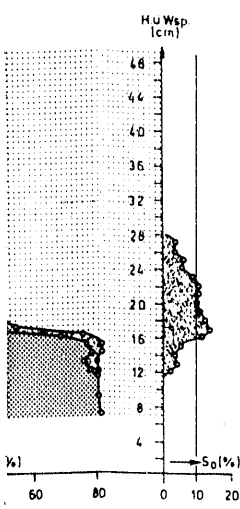
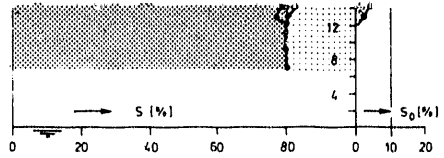
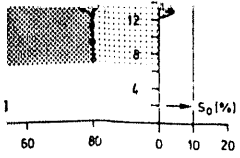
72

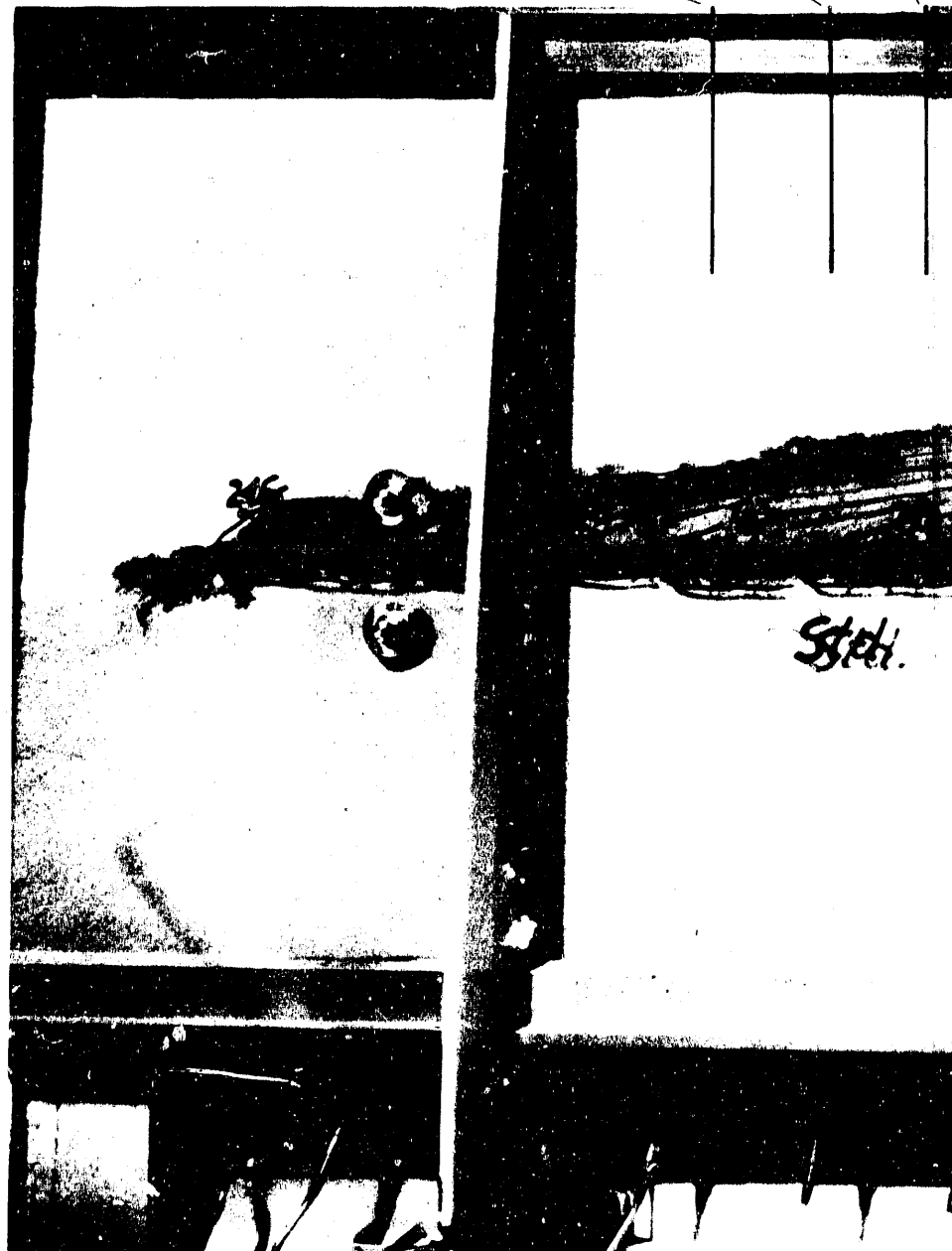
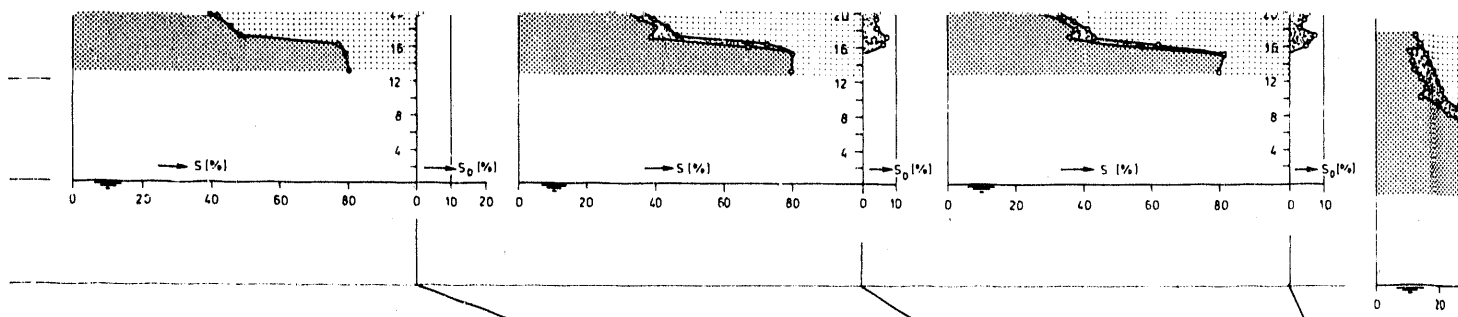
73

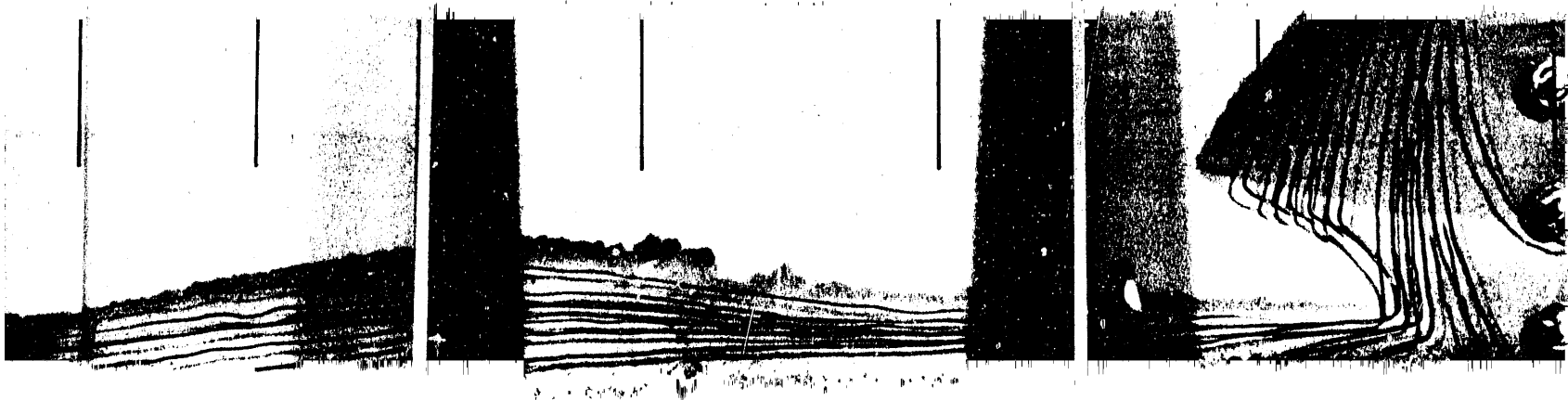
74

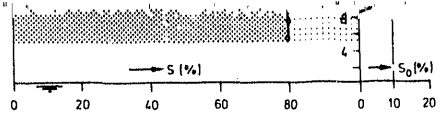
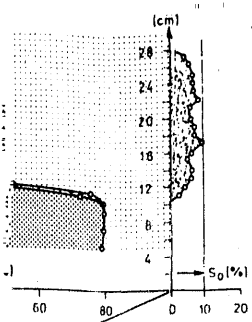
75

76





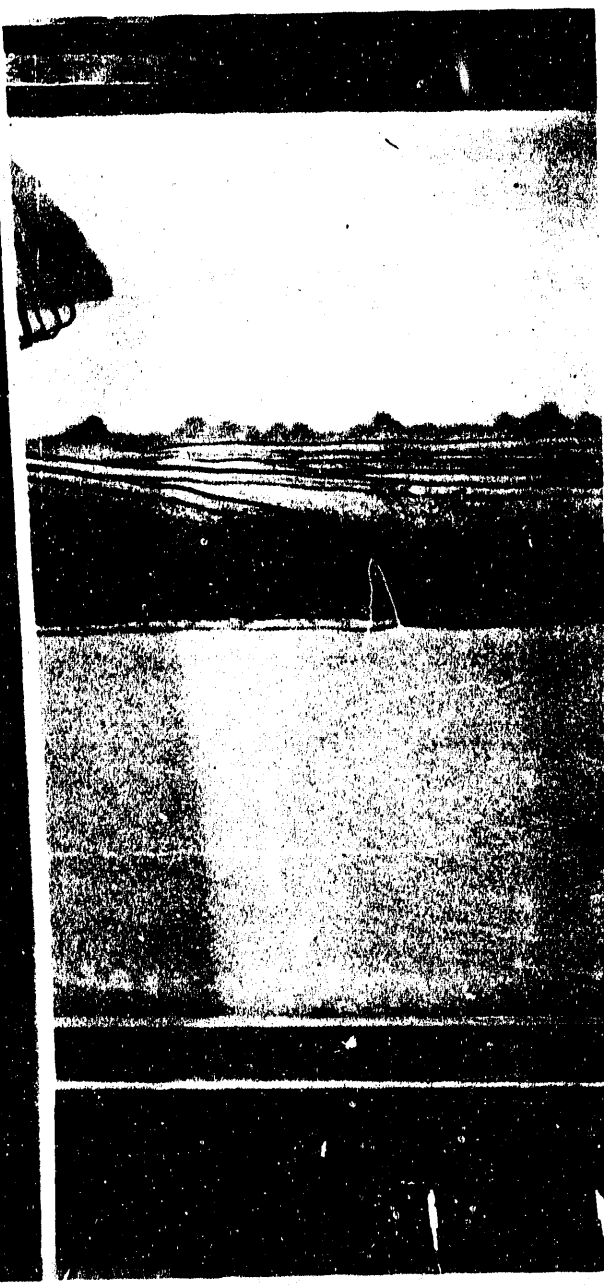




77

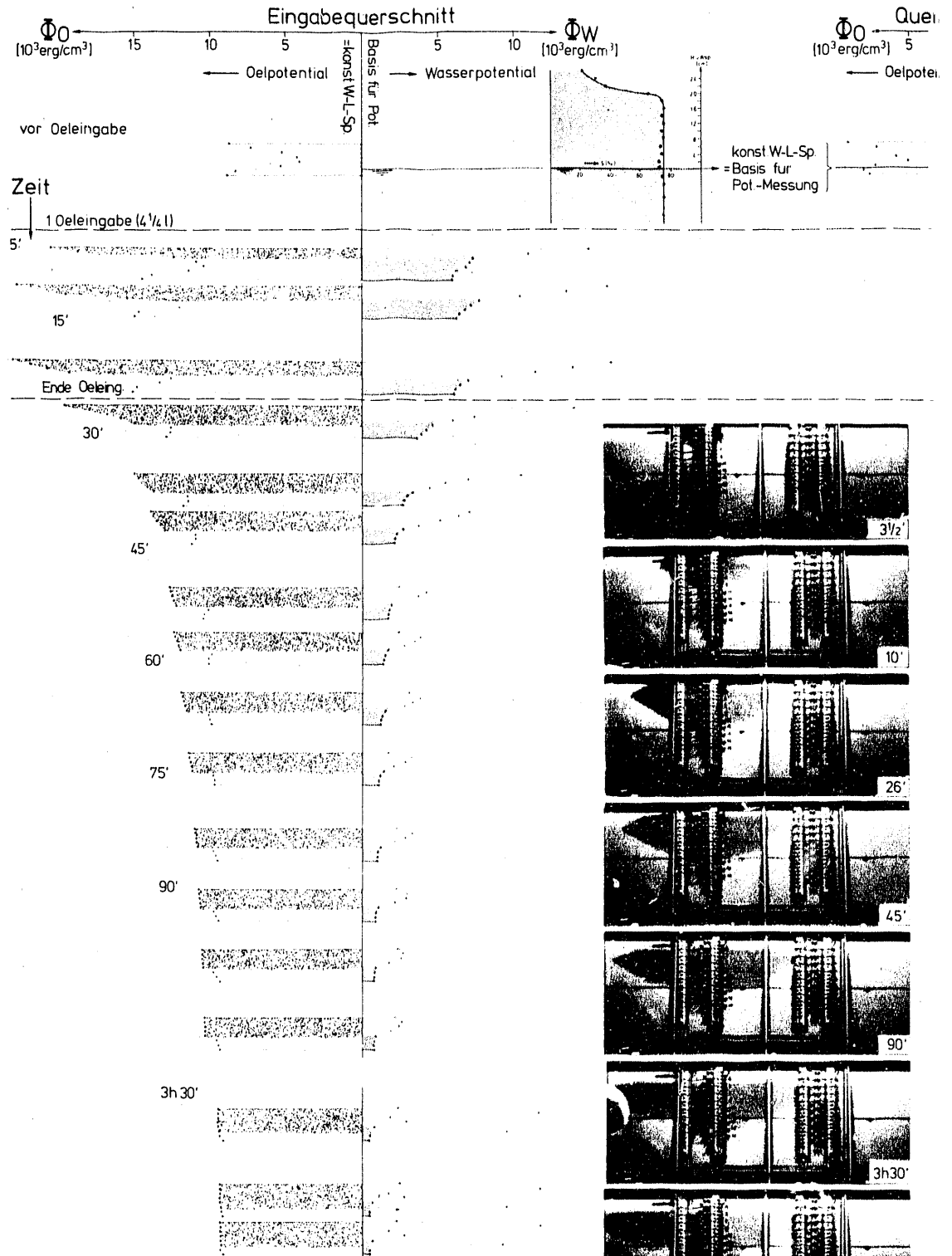
78

79



POTENTIAL-UND SAETTIGUNGSMESSUNGEN WAEHREND

(Versuchscharakteristika sowie Legende siehe VI.2 bis



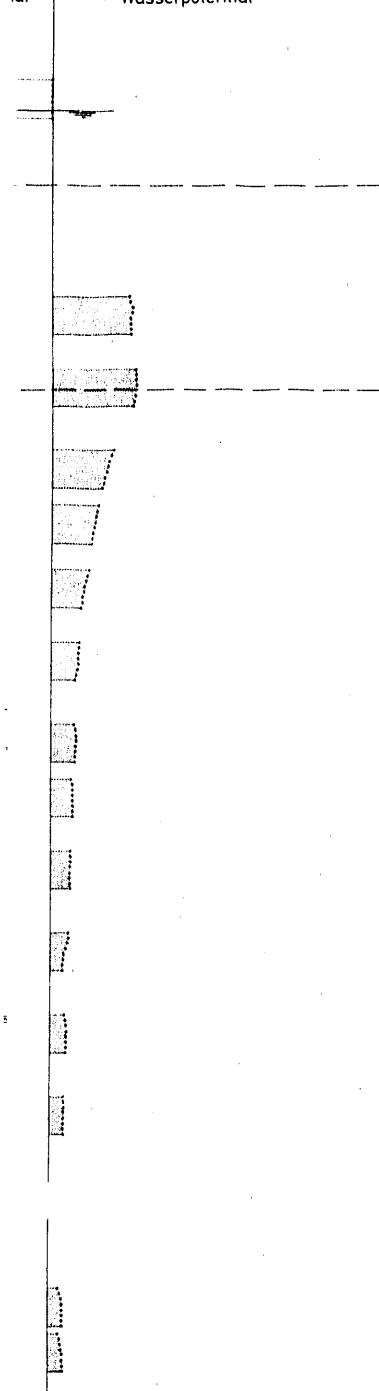
ERSUCH 1

I.4)

chnitt rechts

Wasserpotential Φ_W [10³erg/cm³]

ial



POTENTIAL-UND S

(Versuchschare

Eingabequerschn

Oelpotential Φ_O [10³erg/cm³]

Basiss für Pot

vor Oeileingabe

Zeit

Oeileingabe (4l)

3 1/2'

7 1/2'

Ende Oeileingabe

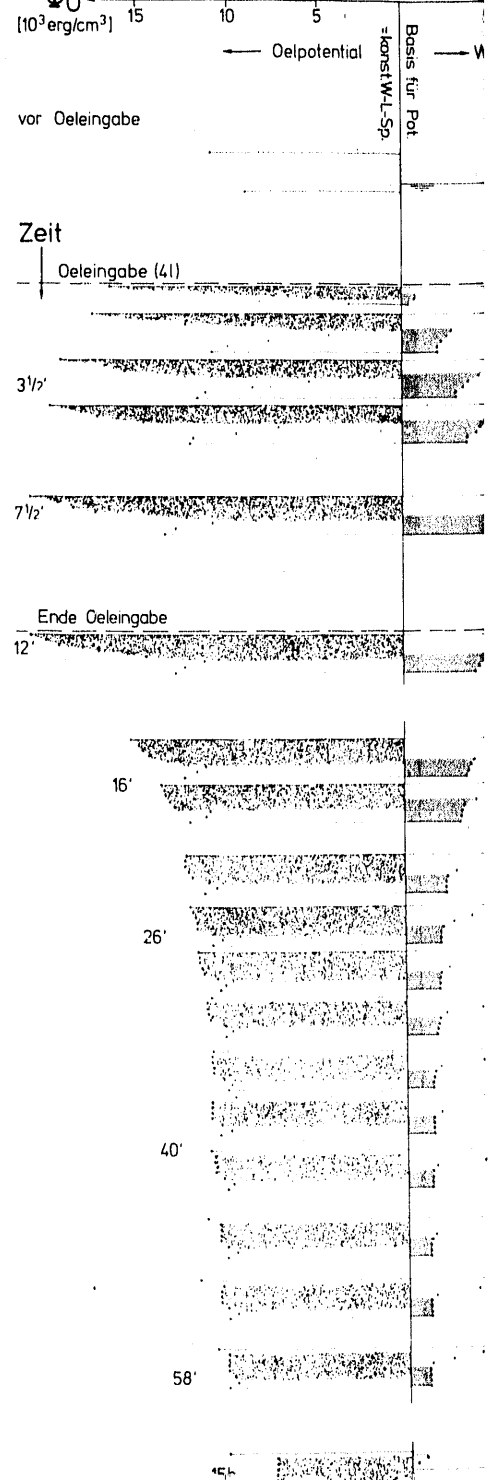
12'

16'

26'

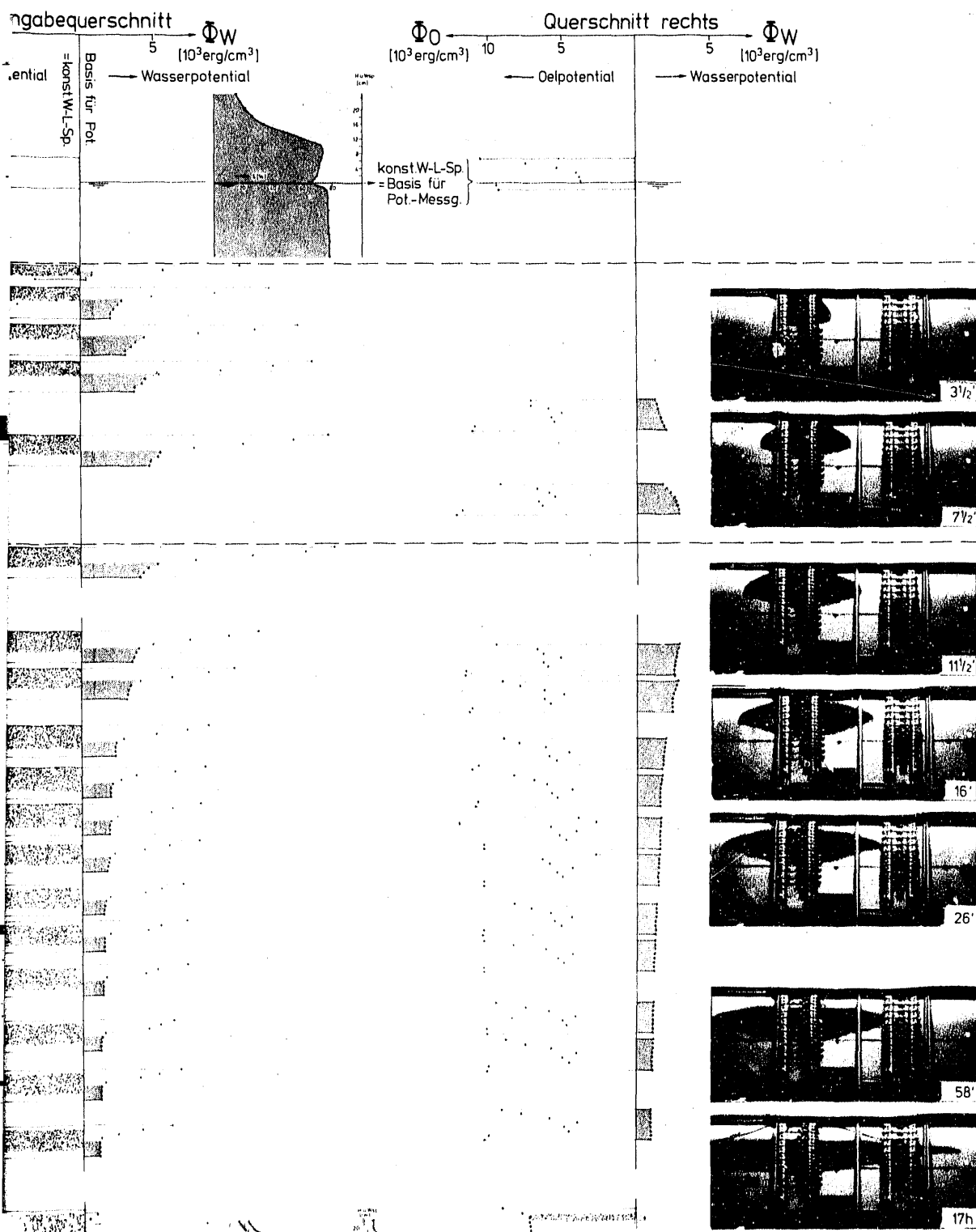
40'

58'

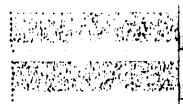


IAL- UND SAETTIGUNGSMESSUNGEN WAEHREND VERSUCH 2

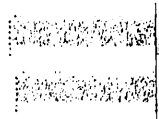
versuchscharakteristika sowie Legende siehe VI.2 bis VI.4)



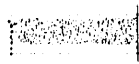
5h



31h

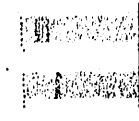


4T

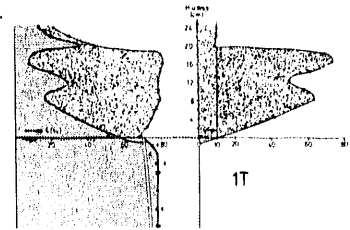


6T

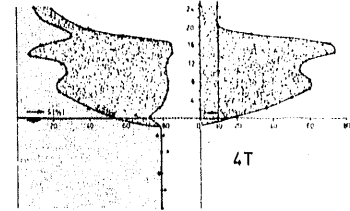
6T



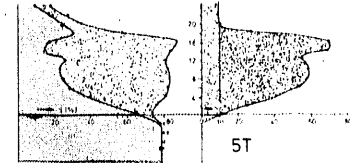
5h



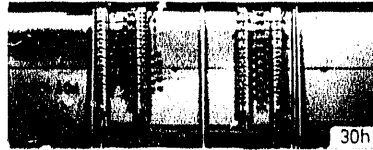
1T



4T



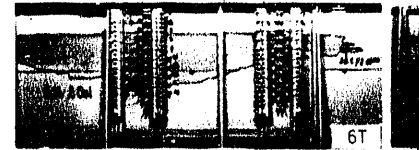
5T



30h



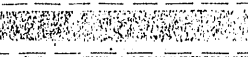
Rückseite



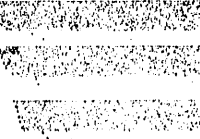
6T

2. Oeleingabe (1 1/2 l)

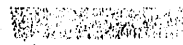
Ende Oeleingabe



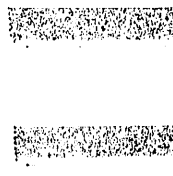
15'



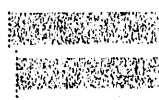
30'



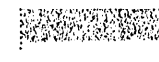
45'



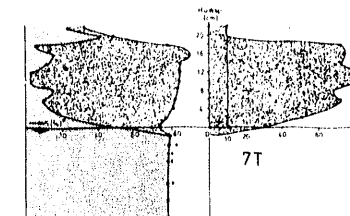
2h



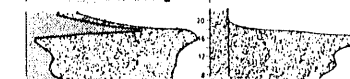
8h



1T



7T



4T



5

7T

10T

13T

16T

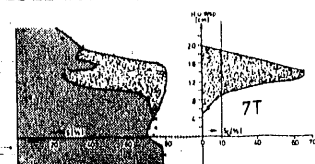
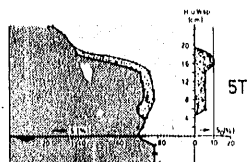
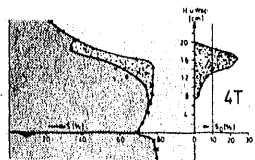
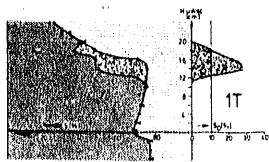
19T

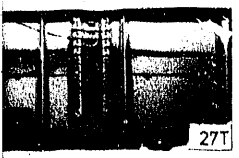
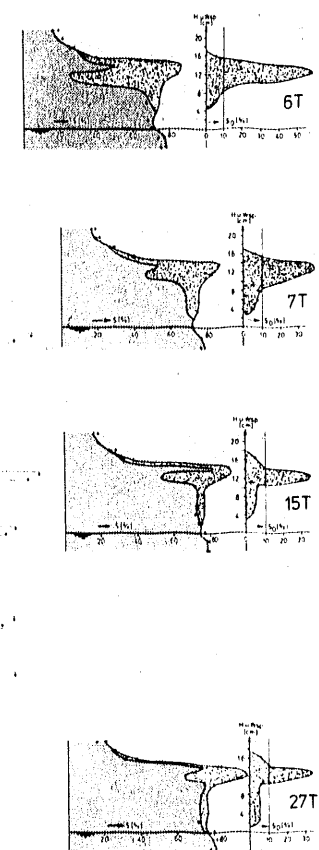
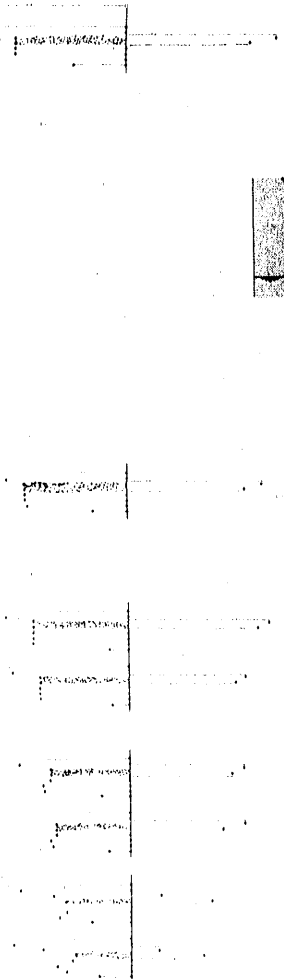
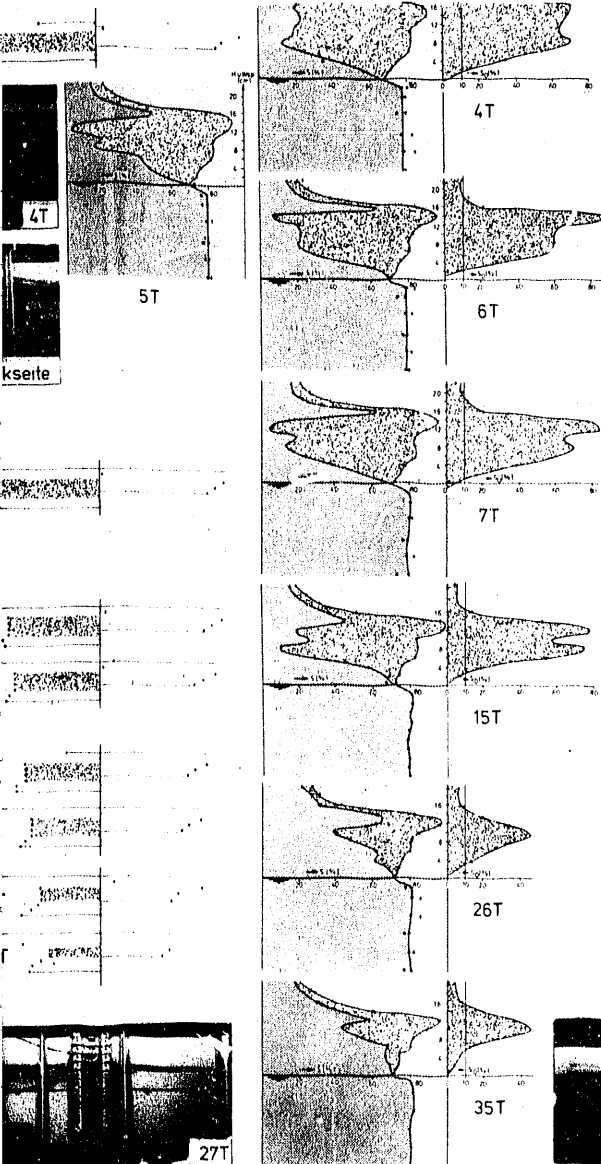
25T

34T



5h

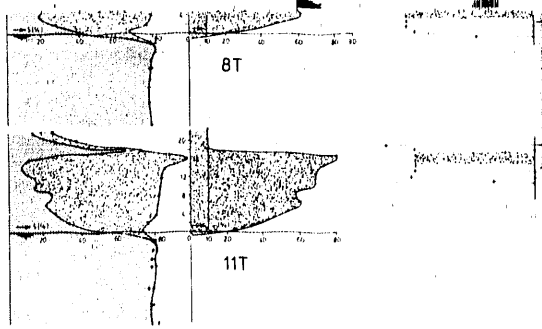




kserte

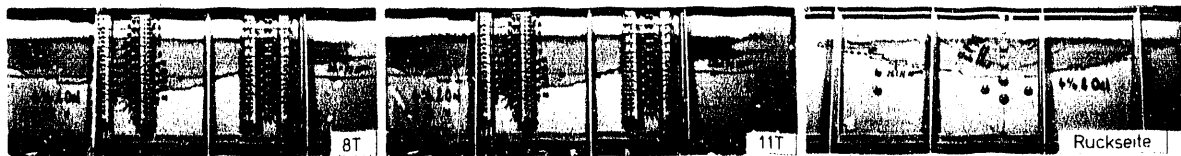
8T

21



11T

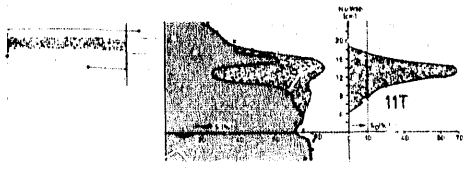
5T



8T

11T

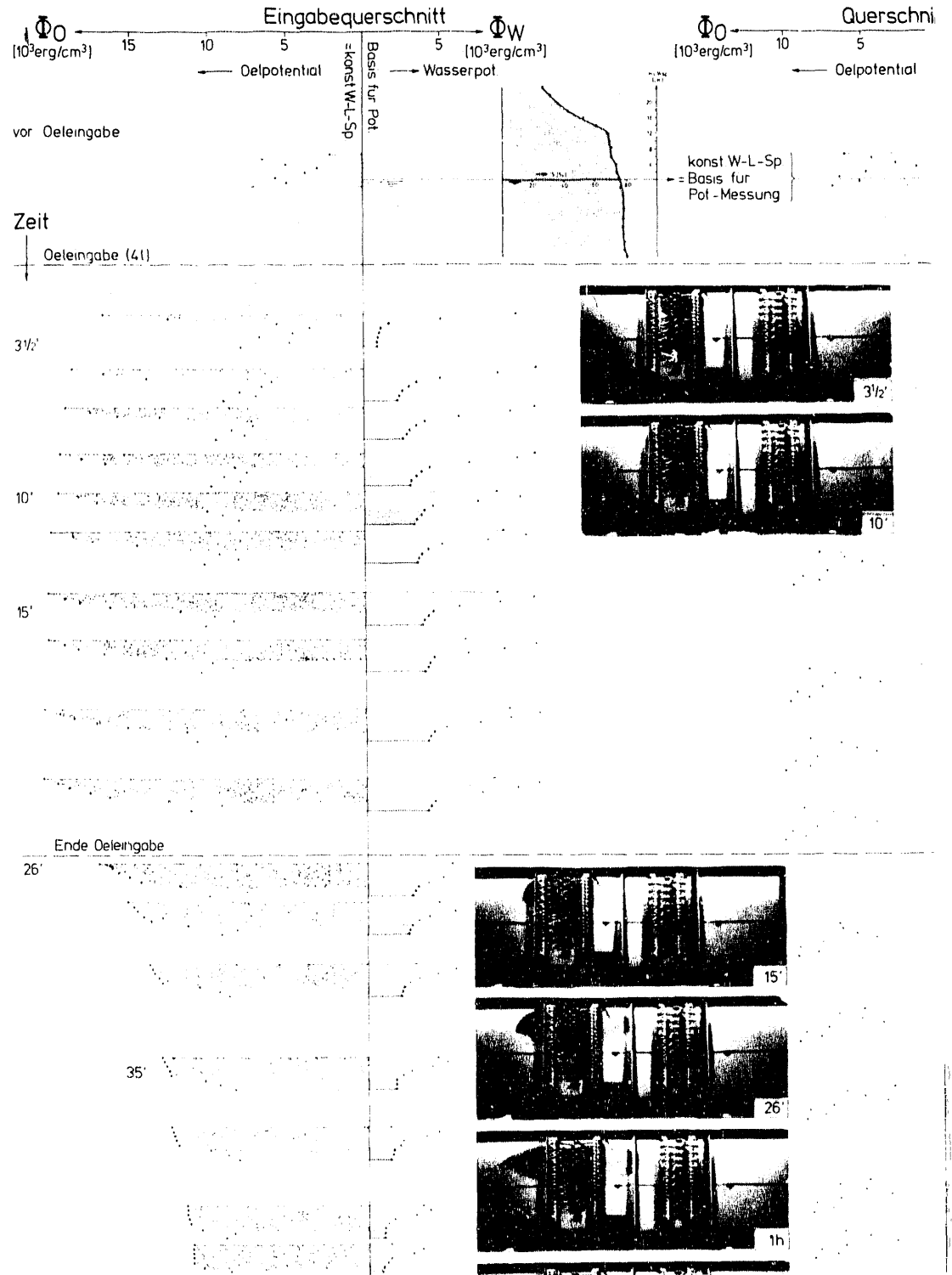
Ruckseite



Rückseite

POTENTIAL-UND SÄTTIGUNGSMESSUNGEN WAHREND

(Versuchscharakteristika sowie Legende siehe VI.2 bis VI.4)



VERSUCH 3

VI.4)

i rechts
5 10 Φ_W
(10^3erg/cm^3)
→ Wasserpotential

POTENTIAL-UN

(Versuchs

Φ_0 → 25
(10^3erg/cm^3)

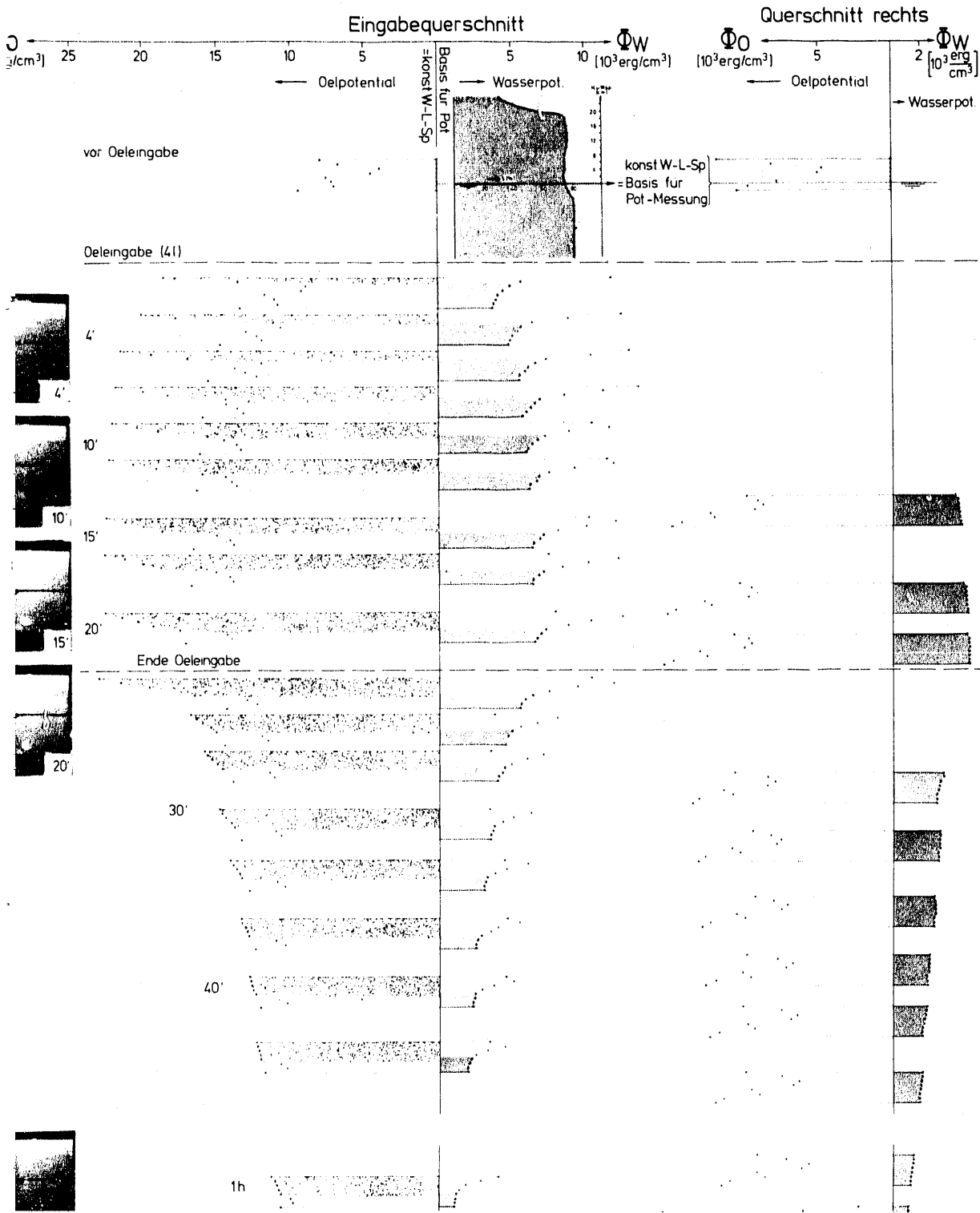
vor Oel

Oeleing

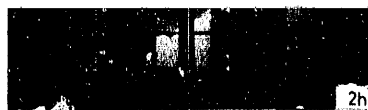


PHOTONEN-UND SÄTTIGUNGSMESSUNGEN WAHREND VERSUCH 4

(Versuchscharakteristika sowie Legende siehe VI.2 bis VI.4)



1h



2h



17h

2h



2T

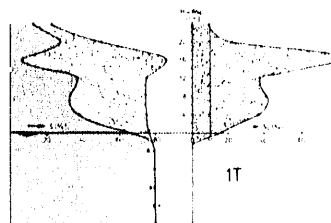
17h

2T

5T

8T

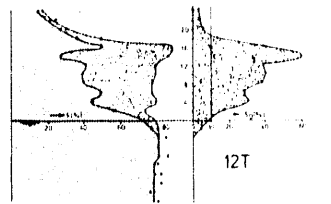
11T



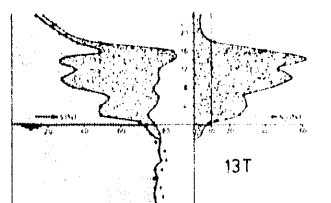
1T



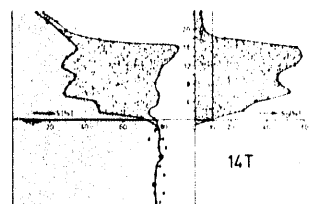
6T



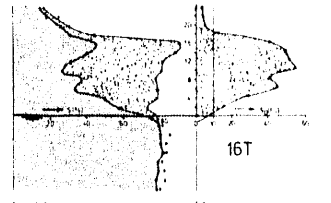
12T



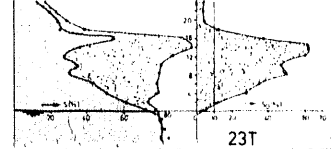
13T



14T



16T



23T



36T



Rückseite

14T

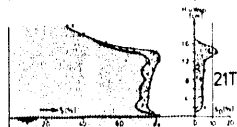
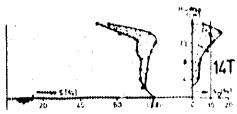
16T

21T

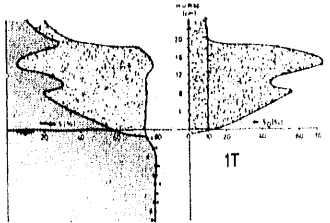
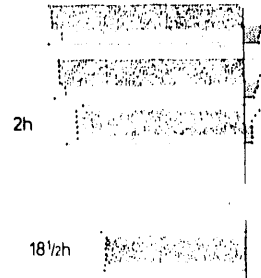
23T

26T

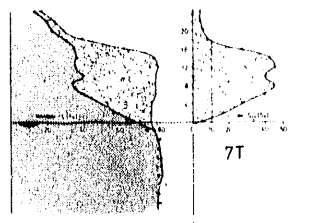
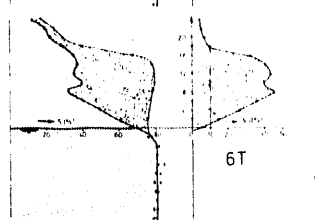
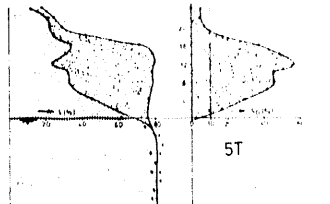
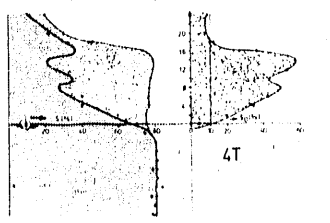




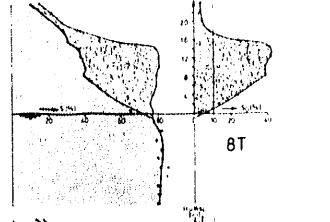
m
2h
18h



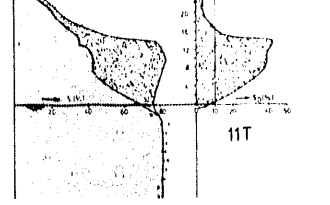
4T



8T



11T

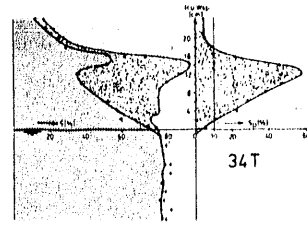


36T

33T

36T

Wsp. Neigung 4 1/2%



34T

15'

30'

45'

2h 35'

5h 45'

20h

30h

41T

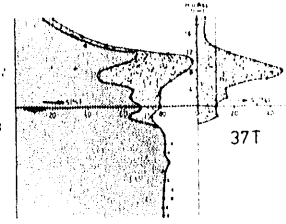
5T

6T

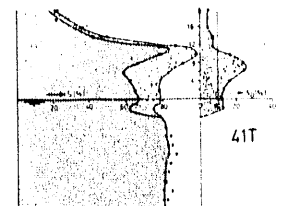
15T

61T

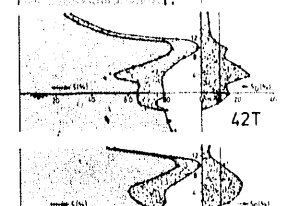
25T



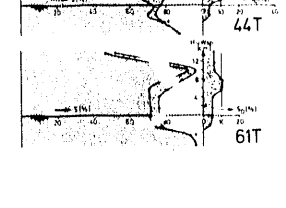
37T



41T



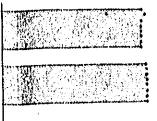
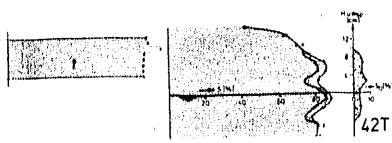
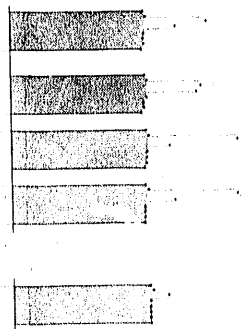
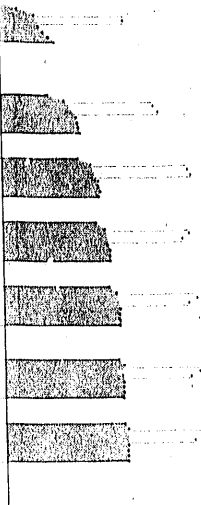
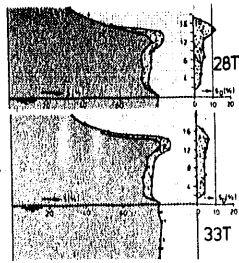
42T



44T

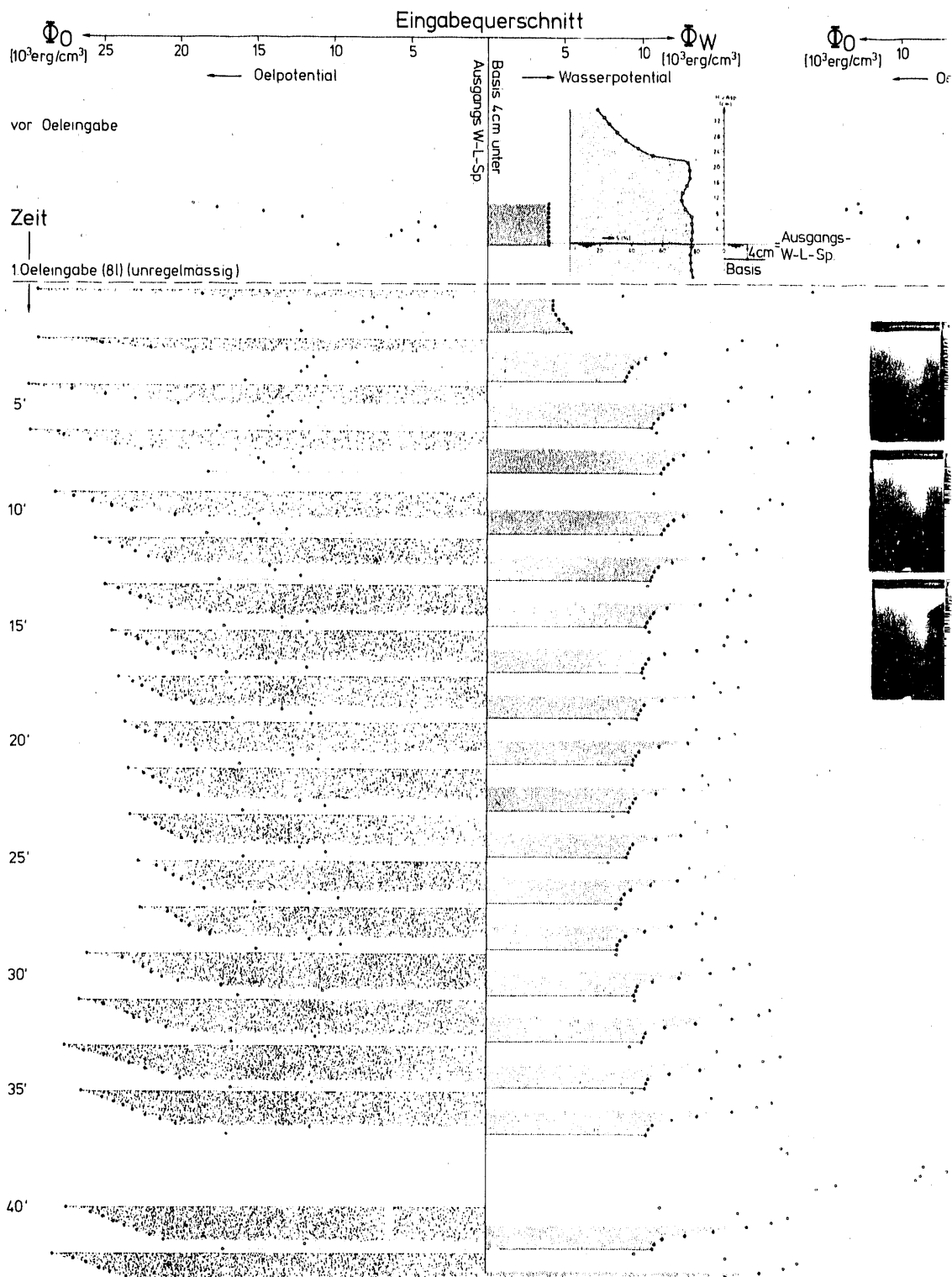


61T



POTENTIAL-UND SAETTIGUNGSMESSUNGEN WAEHREND

(Versuchscharakteristika sowie Legende siehe VI.2 bi

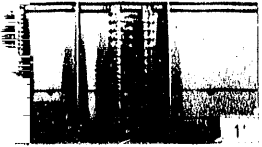
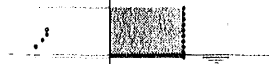


VERSUCH 6

VI.4)

Querschnitt rechts

potential Φ_W [10³erg/cm²]
→ Wasserpotential



6T



7T

8'

24'

40'

56'

72'

88'

3h

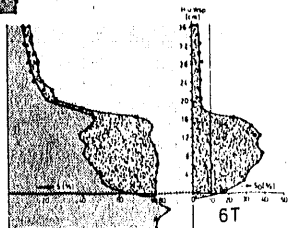
4h

18h



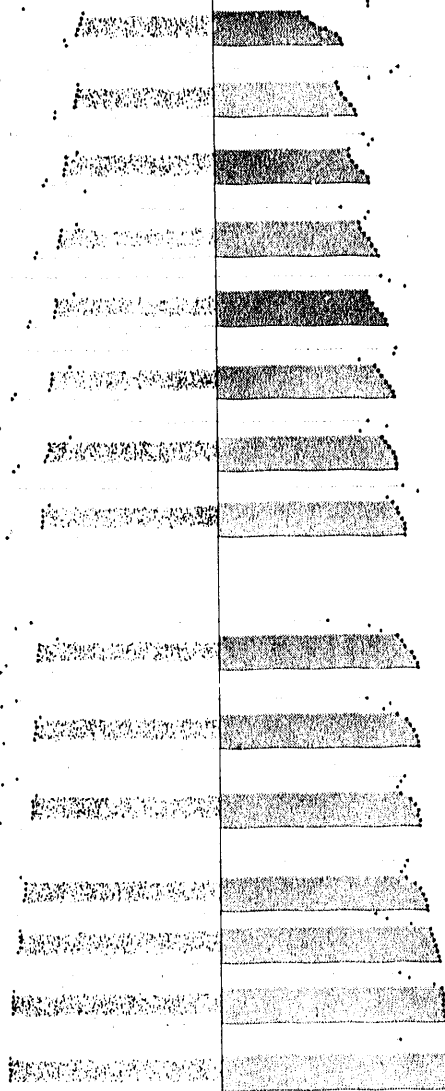
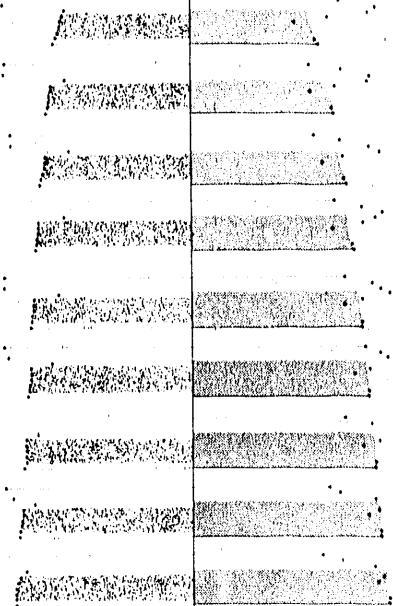


7T



6T

geneigter Wasserspiegel um 10 cm gehoben



7T

45'

Ende Oeleingabe

50'

55'

60'

68'

84'

100'

120'

240'

255'

260'

266'

272'

330'

390'

Absenkung des W-L-Sp. im Eing-Qerschnitt um 1 1/2 cm
infolge Neigung auf 1 1/2% (ΔW -Sp links = 0 cm, rechts = -4 cm)



19T

12T



20T

nach 20 Tagen Was



22T

horiz. Wasser-Luft



, rechts = -4cm)



27T

horiz. Wasser-Lu

29T

2. Oeileingabe 2l

2'

Ende Oeileingabe

4'

6'

8'

8T

17T

19T

21T

gen Wasser-Luft-Spiegel horizontalert auf 13cm unter Ausgangs-Wasser-Luft-Spiegel



22T

ser-Luft-Spiegel auf 39cm über Ausgangs-Wasser-Luft-Spiegel angehoben

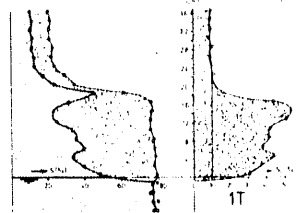
26T

27T

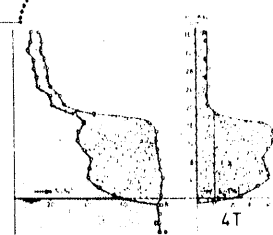
Wasser-Luft-Spiegel um 39cm dh auf Höhe des Ausgangs-Wasser-Luft-Spiegels abgesenkt

28T

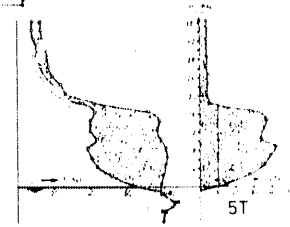
1T

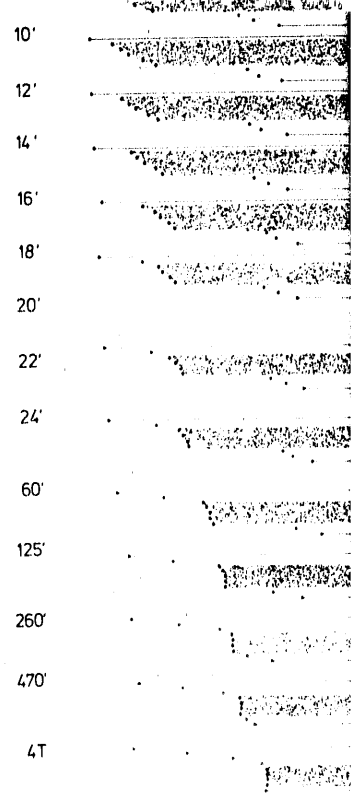
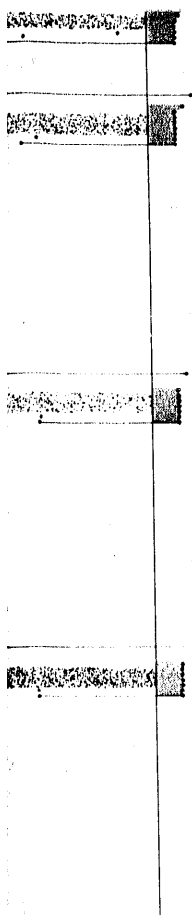


4T



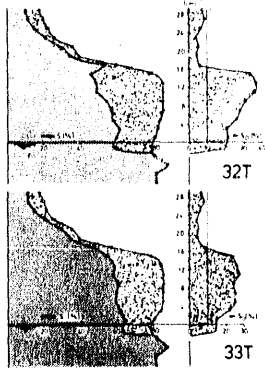
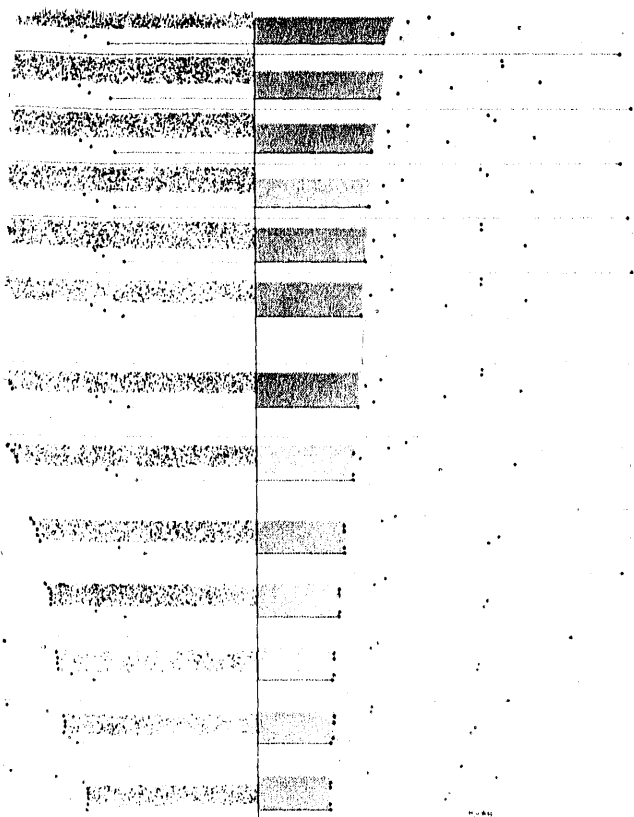
5T





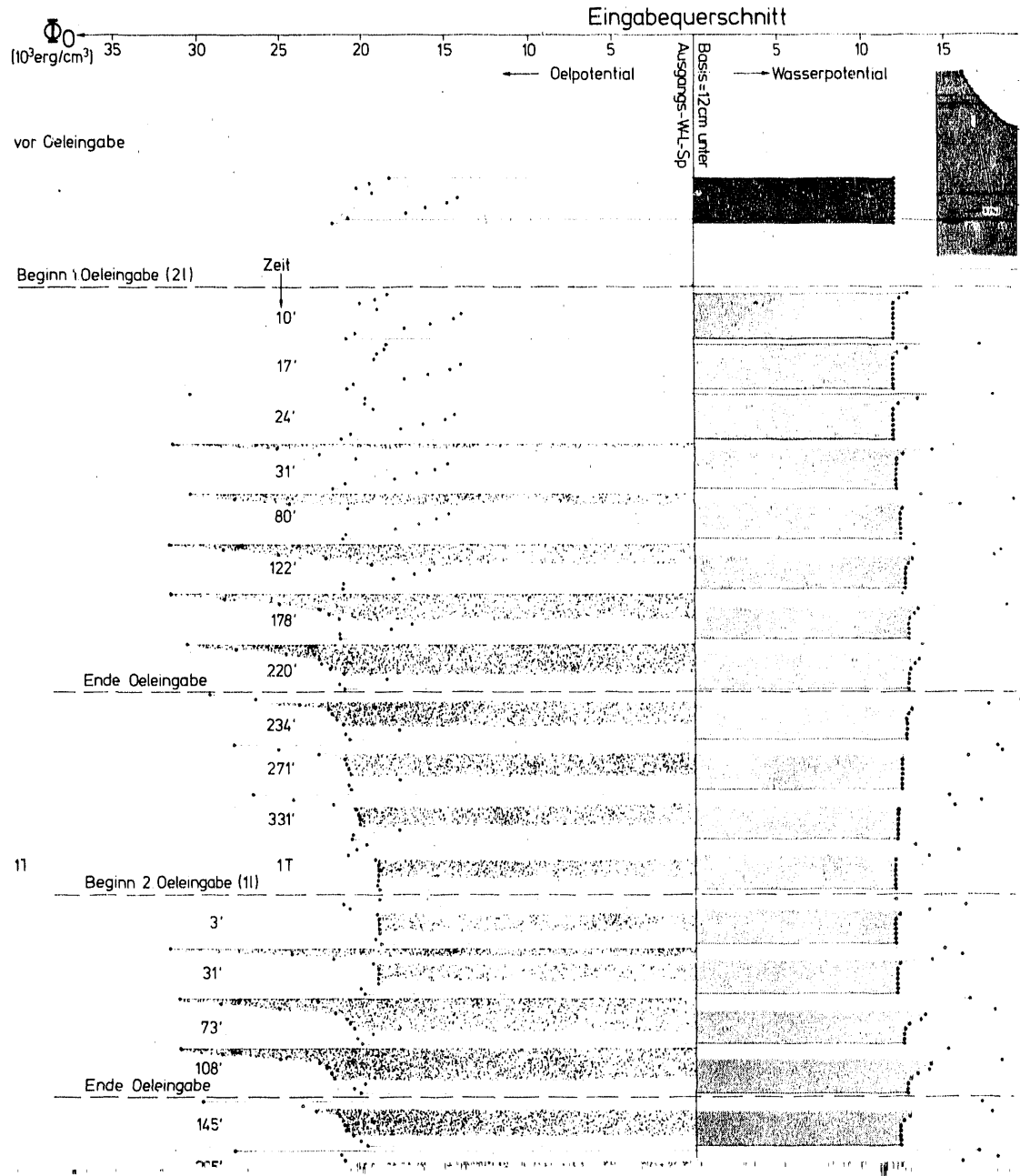
33T

4T



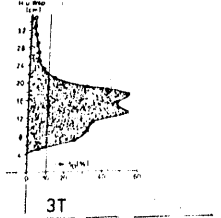
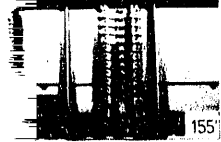
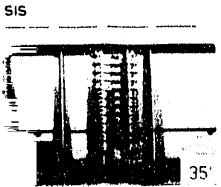
POTENTIAL-UND SAETTIGUNGSMESSUNGEN WAEHREND

(Versuchscharakteristika sowie Legende siehe VI.2 b)



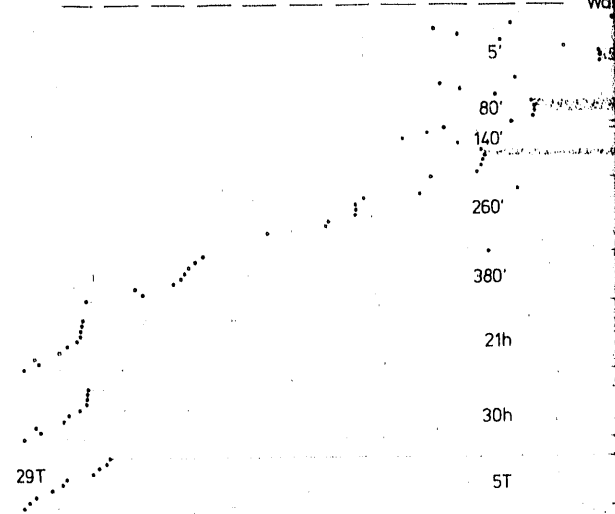
Φ_W
3L 35 [10³erg/cm²]

Ausgangs-W-L-Sp.



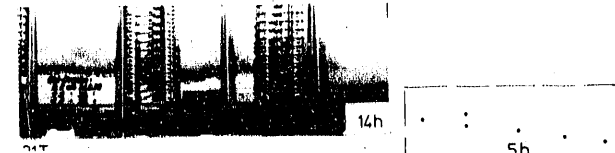
24T

7T



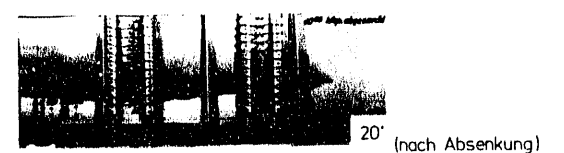
29T

30T



31T

32T



43T



44T

46T

49T

Beginn 40eleingabe (31)

10'

17'

24'

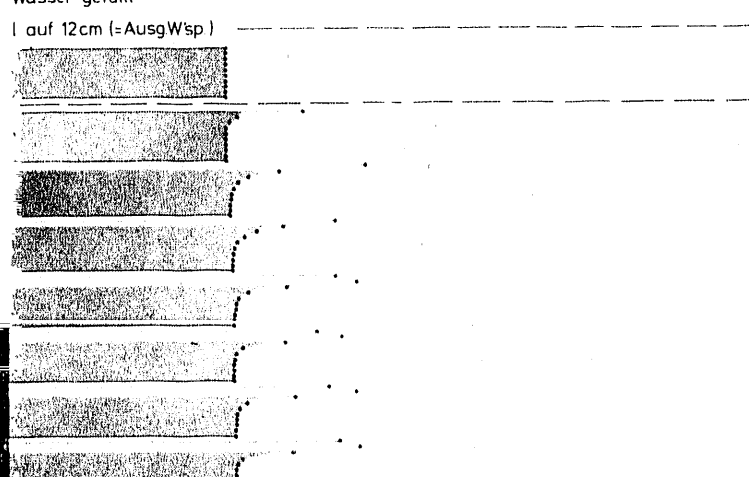
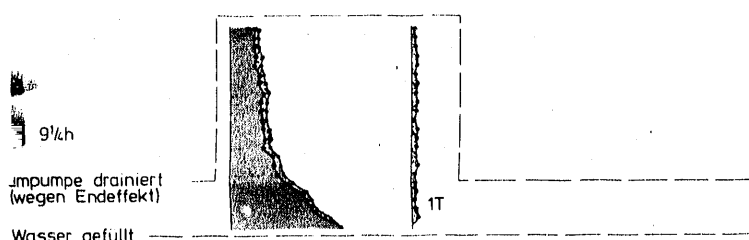
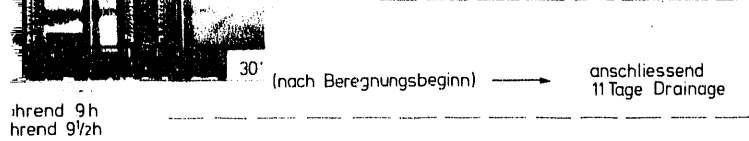
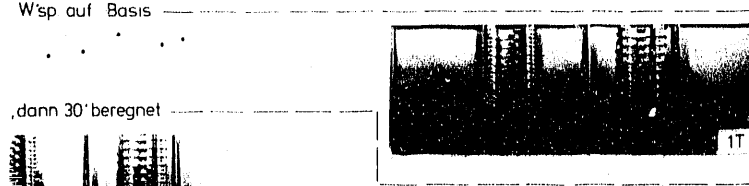
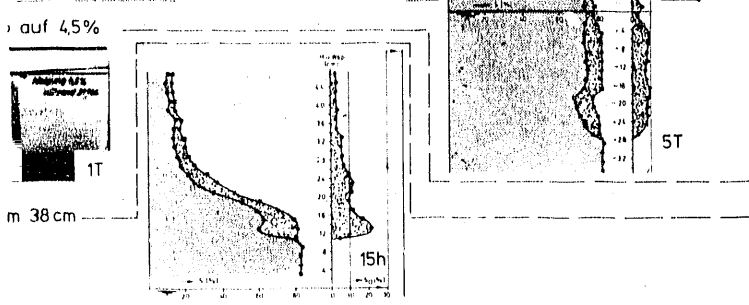
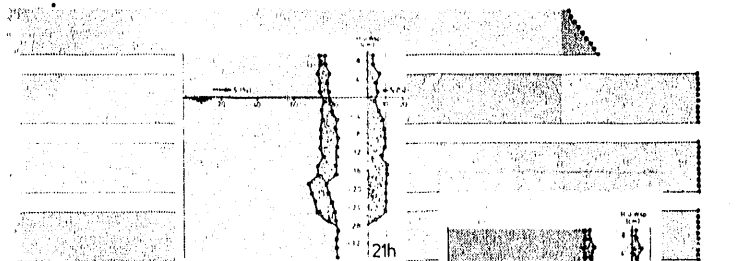
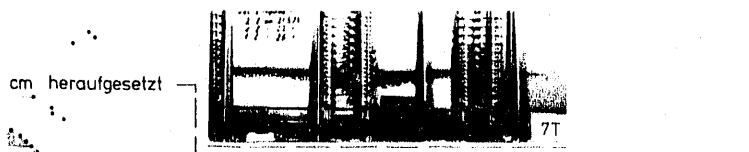
59'

93'

128'

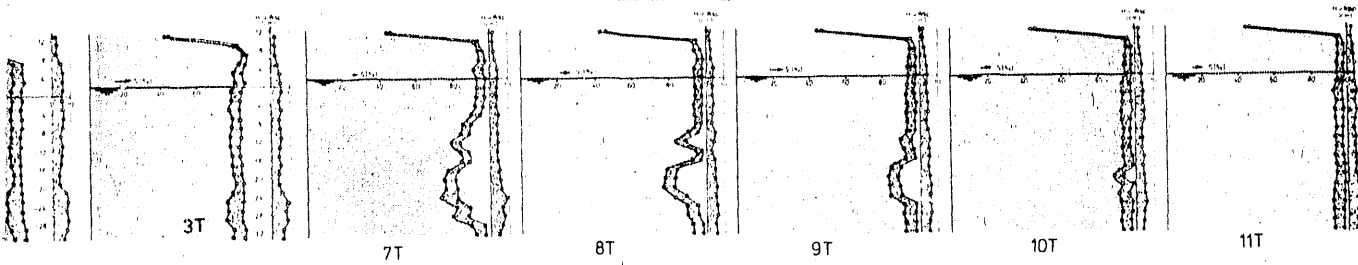
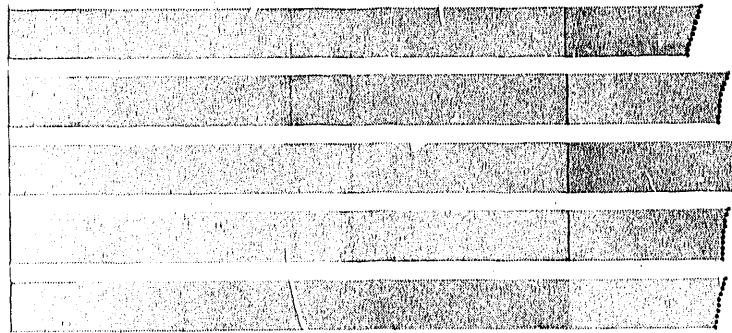
163'

233'



Mit Vakuumpumpe drainiert, dann IM (links 50cm, rechts 0cm über Basis)

1T
3T
8T
10T
11T

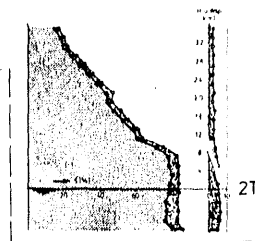
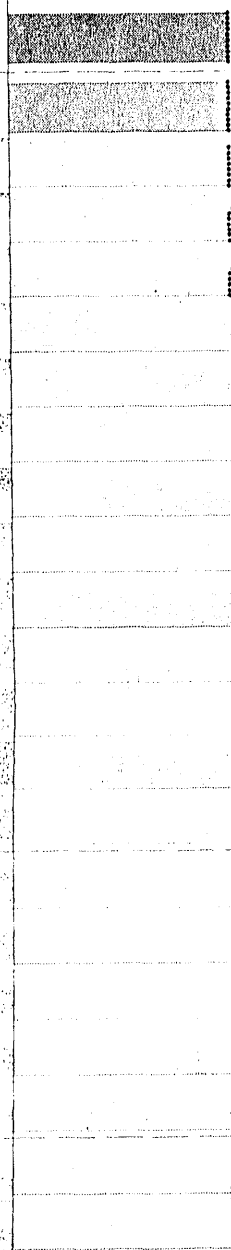


mit Vakuumpumpe drainiert, Modell langsam gefüllt, horiz. W'sp auf 12cm = Ausg. W'sp

3T

n 5 Oeileingabe (21)

10'
17'
24'
31'
38'
52'
66'
80'
94'
108'
136'
164'



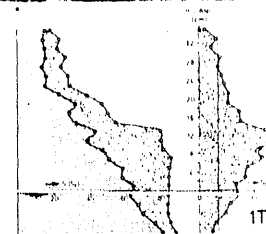
de Oeileingabe

227'
241'
301'
361'



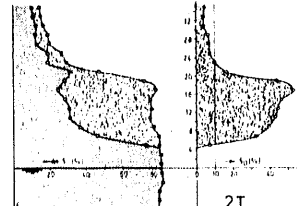
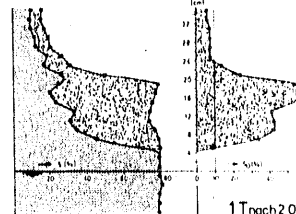
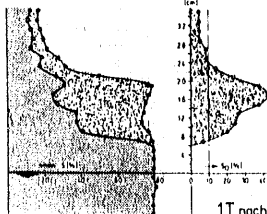
ginn 6 Oeileingabe 11

1T
3'
24'



4T

3T



1T nach 10eileing

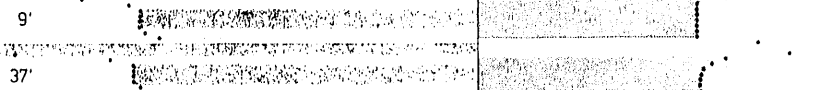
1T nach 20eileing

2T

4T

Beginn 3. Oeileingabe (1l)

9'



37'

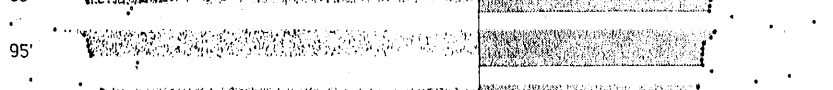


Ende Oeileingabe

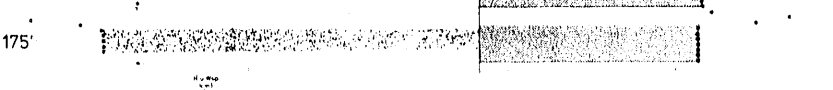
58'



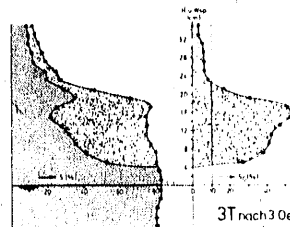
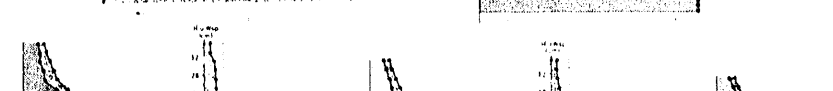
65'



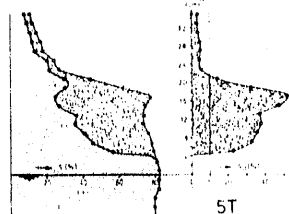
95'



175'



3T nach 3 Oeileing

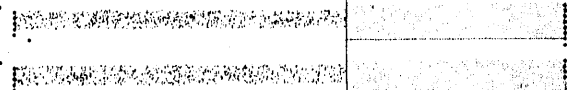


5T



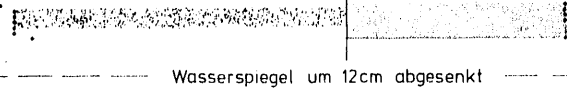
15T

11T



17T

13T



17T

Wasserspiegel um 12cm abgesenkt

2'

34'

66'

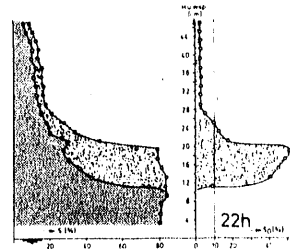
106'

210'

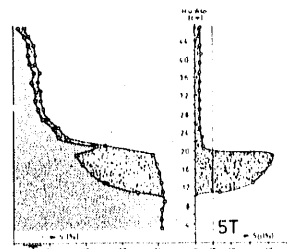
390'

22h

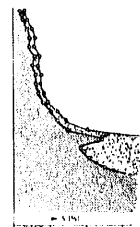
5T

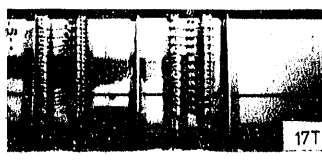
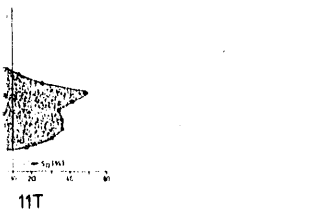
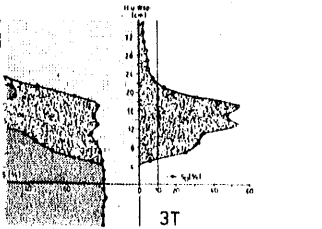


22h



5T





43T -----

44T ----- Mod

46T ----- Mod

49T Beginn 4.Oeleingabe (3l)

10'

17'

24'

59'

93'

128'

163'

233'

303'

Ende Oeleingabe 338'

345'

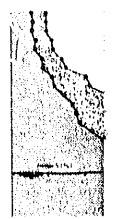
359'

373'

387'

416'

50T 20h



53T ----- 4T ----- Wasser

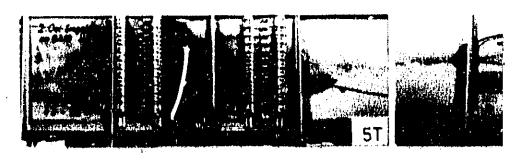
3T

4T

5T

59T ----- Mit Vakuumpumpe

4T

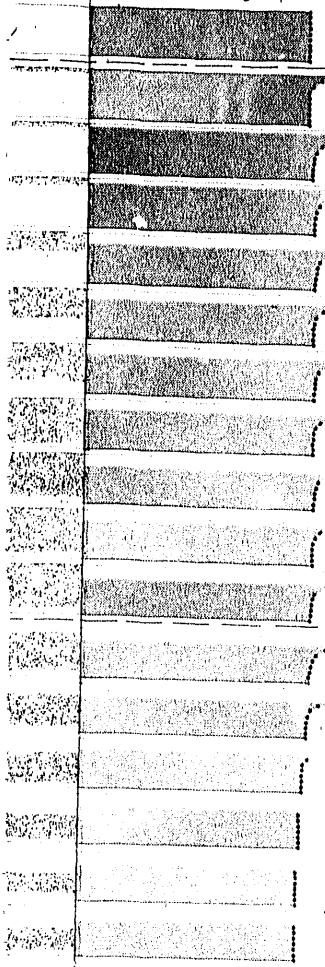


15T

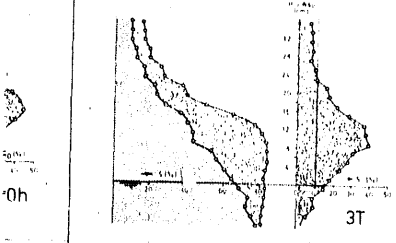
...e mit Vakuumpumpe drainiert
(wegen Endeffekt)

...ngsam mit Wasser gefüllt

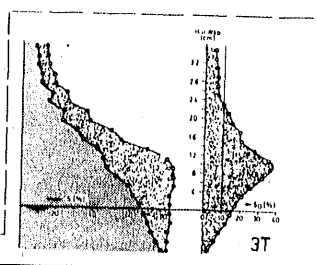
...horizontal auf 12cm (=AuszgWsp.)



341



3T



3T

...neigt, Drehpunkt in Eingabevertikalen

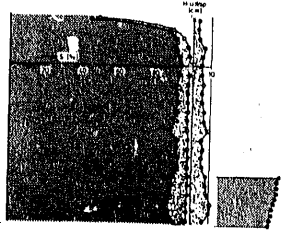


3T

...hks 50cm, rechts 0cm über Basis)



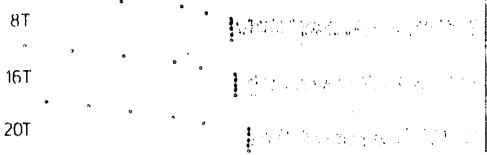
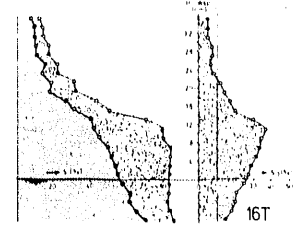
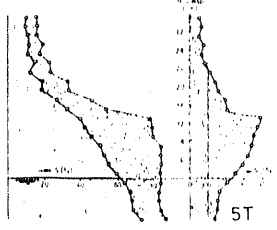
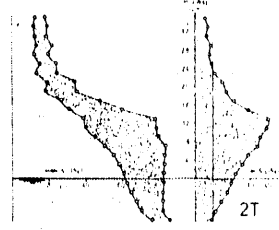
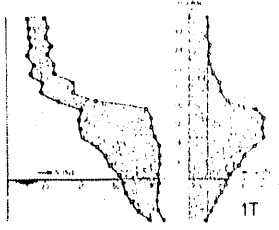
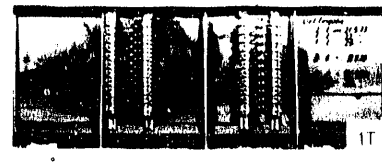
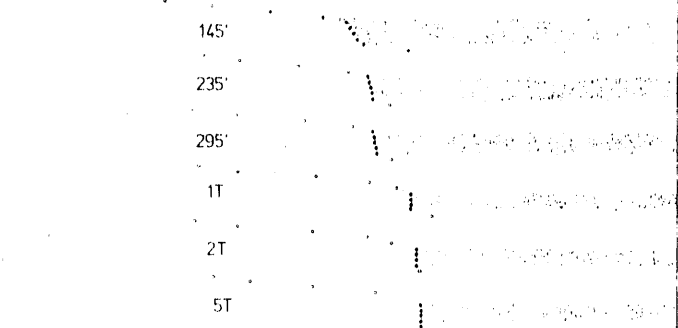
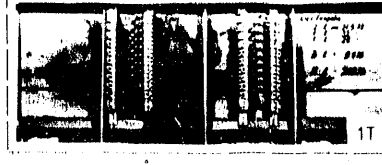
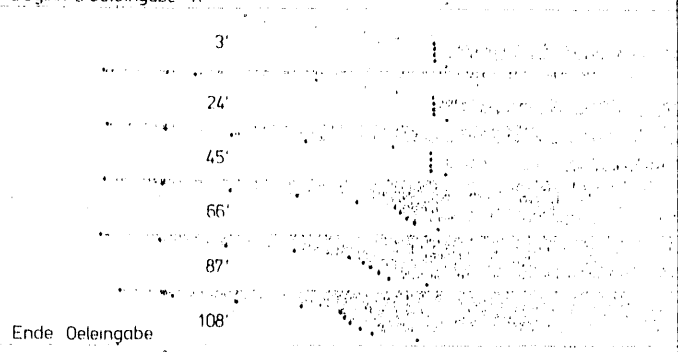
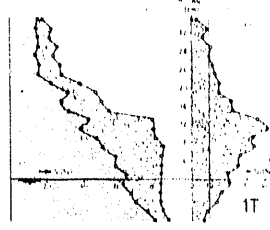
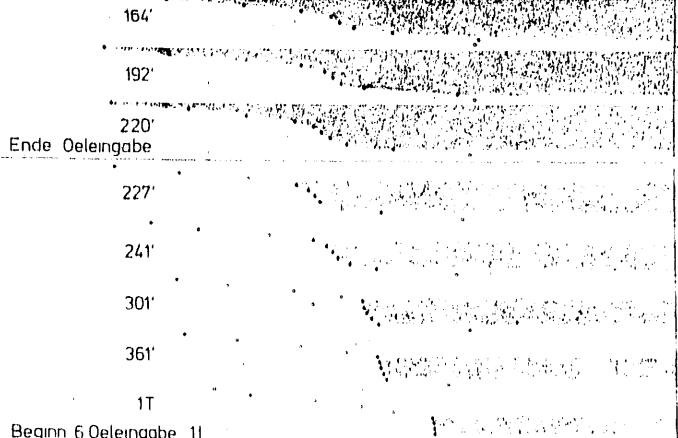
Rückseite

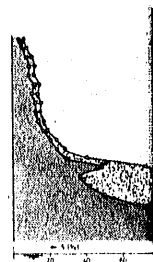
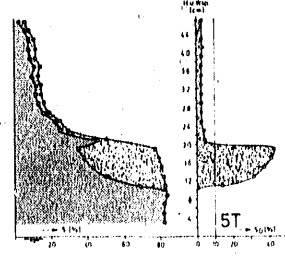
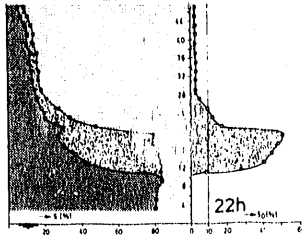


93T

98T

113T





4T



15T

- END -

DATE FILMED

02 / 20 / 91

